The Circulation of the Southern Ocean and the adjacent ocean basins determined by inverse methods

by

Bernadette M. Sloyan, BSc, Grad. Dip. ASOS (Hons)

Submitted in fulfilment of the requirements
for the degree of
Doctor of Philosophy

Institute of Antarctic and Southern Ocean Studies
University of Tasmania
October, 1997

For James, my Father and in
memory of my Mother

Declaration

This thesis contains no material which has been accepted for a degree or diploma by the University or any of other institution, except by way of background information and duly acknowledged in the Thesis. To the best of my knowledge and belief no material previously published or written by another person, except where due acknowledgement is made in the text of the Thesis.

Bernadette M. Sloyan

Authority of Access

This thesis may be made available for loan and limited copying in accordance with the *Copyright Act 1968.*

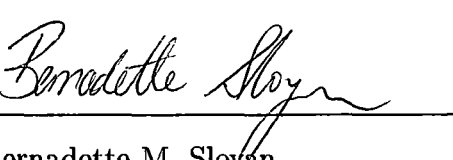

Bernadette M. Sloyan

Abstract

Inverse methods which conserve mass, heat and salt are applied to high resolution hydrographic data in the Southern Ocean and adjacent ocean basins. Dianeutral fluxes are incorporated into the inverse model by including a separate dianeutral flux unknown for each property. Further model development includes the addition of air-sea forcing (wind stress, air-sea heat flux and freshwater flux). The inverse model is then used to test different circulation hypotheses, including the estimated size of the heat loss over the Weddell Sea and the strength of the Malvinas Current.

The accuracy of inverse methods are tested using the Fine Resolution Antarctic Model. This shows that the lateral and dianeutral fluxes are well determined by inverse methods and that the "true" effective diffusion across neutral surfaces in the inverse model can be much larger, and in some cases of opposite sign, to the explicit diffusion in the numerical model when layers outcrop or undercrop. The latter results has implications for how diffusivity estimates obtained from inverse models should be interpreted.

In the initial inverse model the Antarctic Circumpolar Current transport varies from $133\pm2\times10^6 m^3 s^{-1}$ at Drake Passage to 148 ± 4.5 south of Australia. There is a $-15\pm8\times10^6 m^3 s^{-1}$ southward transport through the Indian Ocean and a similar sized northward transport into the Pacific Ocean at 32°S. The addition of air-sea fluxes results in a $5\times10^6 m^3 s^{-1}$ decrease in the southward, eastward and northward transport in the Indian ocean, south of Australia and across 32°S in the Pacific. The imposition of a large northward Malvinas Current ($60\times10^6 m^3 s^{-1}$), adjacent to the South American coast maintains a similar eastward transport at Drake Passage, south of Africa and south of Australia. The southward and northward transport through the Indian Ocean and across 32°S in the Pacific is decreased further to $-8.3\pm5.1\times10^6 m^3 s^{-1}$ and $8.8\pm14.2\times10^6 m^3 s^{-1}$, respectively.

By including air-sea forcing and interior dianeutral fluxes, the water mass production and modification that occurs in the regions defined by the hydrographic sections, can be quantified. In the Indian Ocean sector, the

Agulhas Current transports warm Indonesian throughflow thermocline water into the Southern Ocean. The thermocline water ($10\times10^6 m^3 s^{-1}$) is transferred to SAMW by air-sea (cooling and evaporation) processes and interior dianeutral fluxes. As the SAMW moves eastward with the ACC, Antarctic surfaces water ($16\times10^6 m^3 s^{-1}$) is converted to SAMW across the Polar Front Zone resulting in progressive cooling and freshening of SAMW. $10\times10^6 m^3 s^{-1}$ of the locally produced SAMW in the Southern Ocean Indian exits the region northward across 32°S ventilating the subtropical gyre, while the remaining $15\times10^6 m^3 s^{-1}$ moves eastward with the ACC into the Southern Ocean Pacific sector. In the Southern Ocean Pacific sector $11\times10^6 m^3 s^{-1}$ of SAMW is transferred into thermocline water by air-sea fluxes and exported northward in the Pacific Ocean across 32°S. This circulation path of thermocline water between the Indian and Pacific Oceans describes the Indonesian throughflow as a circum-Australia feature.

North Atlantic Deep Water ($20\times10^6 m^3 s^{-1}$) moves southward across 15°S in the Atlantic and is the major source of Lower Circumpolar Deep Water. Lower Circumpolar Deep Water salinity and oxygen maxima are eroded during the eastward progression of the Antarctic Circumpolar Current. Strong deep overturning circulation are found in the Indian ($26\times10^6 m^3 s^{-1}$) and Pacific ($30\times10^6 m^3 s^{-1}$) Oceans. The northward transport of Antarctic Bottom Water and Circumpolar Deep Water into the Indian and Pacific Oceans is essentially balanced by the return of slightly less dense, low oxygen Indian and Pacific Deep water. The southward inflow of Indian and Pacific deep water to the Southern Ocean results in the formation of Upper Circumpolar Deep Water.

The eastward flow of Antarctic Bottom Water, by the Antarctic Circumpolar Current, into the Southern Ocean Pacific sector is not sufficient to balance the northward export of Antarctic Bottom Water into the Pacific Ocean across 32°S. This implies there are sources of Antarctic Bottom Water within the Southern Ocean Pacific sector.

The circulation results in a meridional heat flux at 30°S of -0.51 PW. The southward heat flux is dominated by a large southward heat flux in the Indian Ocean (-0.94±0.18 PW), a northward heat flux in the Atlantic (0.34±0.13 PW) and a small northward heat flux in the Pacific (0.09±0.26 PW).

Acknowledgements

I am indebted to my thesis supervisor, Dr. Steve Rintoul. His knowledge and direction steered me through the learning process. I acknowledge his enthusiasm, continual encouragement and patience. Dr. Nathan Bindoff filled another supervisory role, dealing with the university and Antarctic CRC on my behalf and more importantly provided critical comments on the content and structure of the thesis.

I thank the staff of CSIRO Marine Division for their openness and friendliness. Many people at CSIRO Marine aided my scientific development particularly, Drs. Peter McIntosh, Trevor McDougall, Susan Wijffels and Stuart Godfrey. I acknowledge the work of Dr. Phil Morgan who wrote much of the inverse model software and Dr. David Jackett who wrote the neutral surface labelling software. I also thank Drs. John Church and Gary Meyers for their interest in and support of this research.

My family have provided moral support without which I would not have embarked on or completed this degree. Finally to James Anderson, your love, support and calm reassured me and gave me confidence in my own ability. You, Bridget and Fiona make my life so enjoyable.

This research was supported by an Australian Postgraduate Award (APA) and an Antarctic CRC "top-up" scholarship.

Contents

List of Figures

List of Tables

Chapter 1

Circulation and water masses of the Southern Ocean and adjacent ocean basins

1.1 Introduction

The Southern Ocean is an area of intense scientific interest due to its unique features and the influence is has on the global climate. The Southern Ocean occupies 20% of the worlds ocean area. It provides a conduit through which water masses from the Atlantic, Indian and Pacific Oceans can exchange properties. This connection plays an important role in the redistribution of heat, salt, freshwater and other properties throughout the worlds oceans. It is also a region of active water mass formation and conversion. Water masses are generally formed at the ocean surface and their properties are due to the interaction of the ocean with the overlying atmosphere, while water mass conversion are essentially an interior mixing process that results in modification of particular water masses.

The water mass formation processes result in modifications to the global climate by the sequestering of carbon and other greenhouse gases, heat, salt and freshwater from the atmosphere and upper ocean into the deep ocean reservoir. The importance of the bottom water on the global climate is due to its long time-scale overturning circulation (1000's of year) and its penetration into all the world oceans. Water mass conversions also act to redistribute greenhouse gases, heat, salt, freshwater and other nutrients vertically and meridionally

within the oceans.

Although the ocean circulation, water mass formation and conversion process have important impacts on the global climate these processes are still largely unknown. This study is undertaken to provided an improved picture of the Southern Ocean and the adjacent oceans basins circulation, inter-ocean mixing, intra-ocean water mass formation and conversion processes within a dynamically consistent inverse model.

A brief review of our current understanding of Southern Ocean and the adjacent ocean basins circulation is given below.

1.2 Oceanic Fronts

Ocean fronts are one of the most obvious ocean features. Fronts are regions on the surface or at depth where either vertical or horizontal gradients in temperature, salinity, density and concentrations of dissolved gases and nutrients are observed. These changes in water properties over a comparably short distance can lead to observable changes in sea colour and surface wave height (Muench 1990).

1.2.1 Antarctic Polar Front

The existence of the Antarctic Polar Front (APF) was recognised by Meinardus in 1923. The *Discovery* cruises between 1932 and 1933 enabled Deacon to describe the circumpolar extent of the APF (Deacon 1937; Whitworth 1980). Many criteria have been proposed to define the position of the APF. The commonly accepted method describes the APF as a subsurface feature located at the northern extremity of the 2°C minimum contour (Taylor et al. 1978)

The latitude of the APF varies dramatically in each region of the Southern Ocean: approximately 50°S in the South Atlantic Ocean; 52°S in the Indian Ocean and; 62°in the Pacific Ocean (Deacon 1982) (Figure 1.1). This movement can be summarised as a general southward trend of the APF from the Atlantic basin eastward to Drake Passage, where the Antarctic Polar Front reaches its maximum southward extent. Major southward trends of the APF have been linked to bottom topography (Kort 1966).

This classical description of the APF conveniently ignores the complexities of the front. The position of the APF also varies on seasonal and inter-seasonal time scales. The APF has shown seasonal movements of 1°to 2°of latitude, and long-term variations of 4°latitude (Gordon 1971). Frontal movement may be due to the existence of eddies an meanders within the polar front zone (Ikeda et al. 1989; Edwards and Emery 1982).

1.2.2 Subantarctic Front

The existence of a separate frontal system north of Antarctic Polar Front has been suggested since Böhnecke(1936) found a sea surface temperature gradient halfway across the Subantarctic region (Deacon 1982). Emery (1977), using expendable bathythermography (XBT) data from 100°E through the Pacific basin to 60°W, established a northern and southern frontal boundary which separated Antarctic waters from Subantarctic waters. The region between the northern and southern fronts was called the Polar Front Zone. The southern front corresponds to the APF, while the northern boundary corresponds to the Australasian Subantarctic Front, due to the circumpolar nature of the front the preferred name is the Subantarctic Front (SAF) (Figure 1.1).

The SAF is identified by a subsurface temperature gradient centred around the most vertically orientated isotherms (Sievers and Emery 1978). It reaches it's northernmost position in the Atlantic basin and then shifts southward to the east, reaching its most southern position through Drake Passage. The strength (temperature gradient) of the SAF varies dramatically throughout the Southern Ocean (Hofmann and Whitworth 1985). The temperature gradient is strongest from 100°W to 60°W and 140°E to 170°E where the SAF is a narrow feature. The narrowness of the front is the result of bottom topography. Between these two regions the SAF temperature gradient weakens and broadens (Emery 1977). The SAF temperature gradient also strengthens and appears to be displaced northwards when eddies or meanders are within the Polar Frontal Zone (Sievers and Emery 1978; Ikeda et al. 1989).

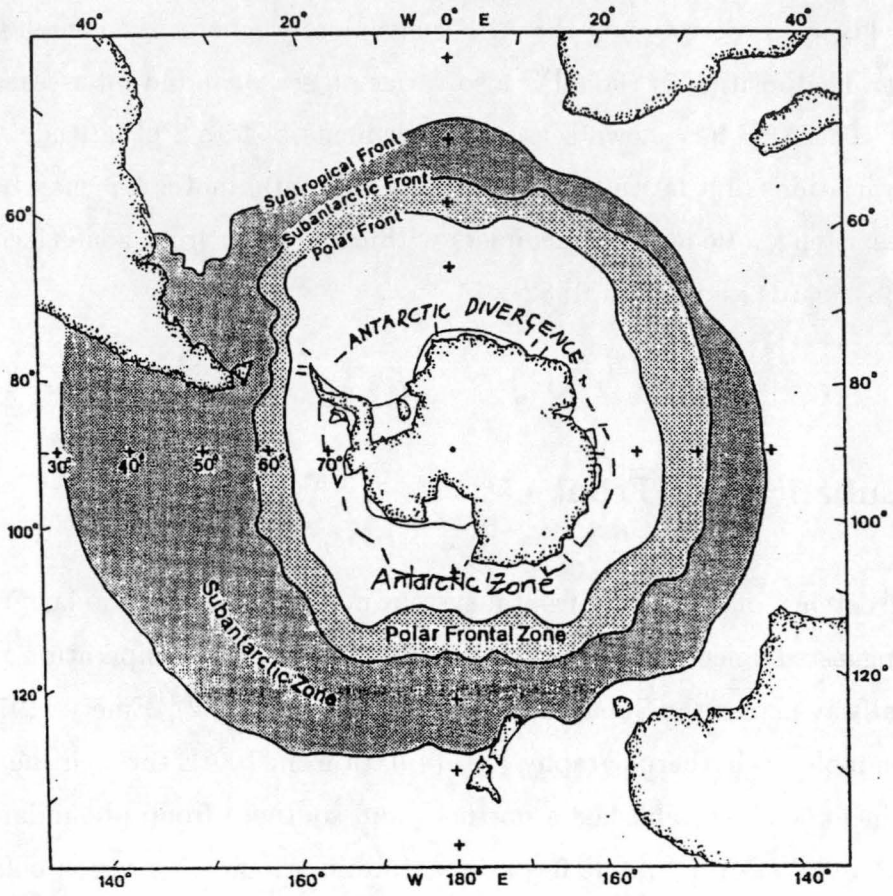

Figure 1.1: Surface regimes of the Southern Ocean (after Nowlin and Klinck, 1986)

1.2.3 Subtropical Front

The Subtropical Front (STF) is the boundary between the warm, saline Subtropical water and the colder, less saline water of the Subantarctic. The STF is generally recognised by a subsurface salinity maximum (Wyrtki 1962b). The STF represents the northern boundary of the Southern Ocean and has a mean position of 40°S, except in the eastern Pacific Ocean where the STF runs northwards to 25°S parallel to the South American coast (Sverdrup et al. 1946).

In summer the surface temperature across the STF, from south to north, is 14°C to 18°C and winter between 10°C to 14°C (Tchernia 1980; Deacon 1982). The STF is essentially a circumpolar feature, but not as well defined as the SAF or APF (Figure 1.1).

1.3 Water Masses

1.3.1 Antarctic Bottom Water

Antarctic bottom water formation appears to be concentrated on the continental margin, where mixing between deep water and shelf water occurs (Jacobs 1986). Early investigations into Antarctic Bottom Water (AABW) highlighted the Weddell Sea as the location for AABW formation (Sverdrup et al. 1946). Later studies identified AABW formation also occurring off the Adelie coast (ALBW) and in the Ross Sea (RSBW) (Gordon 1972; Gordon and Tchernia 1972; Jacobs et al. 1985; Rintoul 1997).

Weddell Sea Bottom Water (WSBW) (< -0.7 °C) forms near 30°W and to the west along the Antarctic Peninsula shelf edge (Gill 1973). Weddell Sea Deep Water (WSDW) (-0.7°C to 0.0°C and salinity 34.64) results from mixing between WSBW and CDW (Orsi et al. 1993), which moves northward into the deep basins of the Southern Ocean and adjoining ocean basins. Two varieties of Ross Sea Bottom Water (RSBW) have been identified a high salinity type (> 0.5°C and salinity of 34.70) and a low salinity type (-0.16°C and salinity of 34.65) (Jacobs et al. 1985; Carmack 1990). AABW formed off the Adelie coast has similar properties to the WSBW (Gordon and Tchernia 1972).

1.3.2 Antarctic Surface Water

Antarctic Surface Water (AASW) is found between the Antarctic Polar Front (APF) and the Antarctic continent (Figure 1.2). It is a relatively cold (-1.9°C - 2°C), low salinity water mass (34.0 - 34.5) which varies in depth from about 50 m near the continent to between 150 - 250 m at the APF (Sverdrup et al. 1946; Sievers and Nowlin 1988; Carmack 1990).

Two regimes influence the character of AASW, a winter and summer regime. In summer the upper water column warms, and a seasonal thermocline develops in the upper 50 m. The surface temperature and salinity may not be as constant in spring and autumn, mainly due to the presence of sea-ice and the distance from the continent. In winter the layer is homogeneous with depth. Surface heat loss from the ocean to the atmosphere and sea-ice production, resulting in cooling and a salinity increase, enhance the convective mixing of the

water mass to a depth of 150 m to 250 m (Carmack 1990).

1.3.3 Circumpolar Deep Water

Circumpolar Deep Water (CDW) forms the largest body of water, by volume, in the Southern Ocean. CDW has an average depth of 1500 to 2000 m in the mid-latitudes. It begins to shoal near the Subantarctic Front and reaches a minimum depth at or south of the Antarctic Divergence (Figure 1.2).

CDW is the result of mixing between several deep water masses that enter the Southern Ocean from the South Atlantic, South Pacific and Indian Oceans and AABW within the ACC. The continual movement of water in the ACC promotes mixing resulting in a relatively homogeneous water mass. However, due to the different northern sources slightly different water properties result allowing for the identification of two types of CDW: Upper Circumpolar Deep Water (UCDW) and; Lower Circumpolar Deep Water (LCDW).

UCDW is identified by a dissolved oxygen minimum and a nutrient maximum, placing its source in the Pacific and Indian Oceans (Patterson and Whitworth 1990). North Atlantic Deep Water (NADW) flows into the Southern Ocean in the Atlantic sector to form LCDW. LCDW is identified by a salinity and relative oxygen maximum.

1.3.4 Antarctic Intermediate Water

Antarctic Intermediate Water (AAIW) is identified by a salinity minimum at a depth of 1000 m north of the Subantarctic Front. It has a temperature range of between 3°C and 7°C and also has a relatively high oxygen concentration (Sverdrup et al. 1946; Georgi 1979).

Significant property changes occur in AAIW across the different ocean basins (Figure 1.3). The differences in the salinity values of AAIW between the different ocean basins are mainly due to the different properties of Subantarctic waters within the basins (Carmack 1990). Apart from the salinity changes between the ocean basins the potential temperature of AAIW generally increases to the east of the Pacific Ocean.

Many theories on the formation of AAIW have been proposed. Early

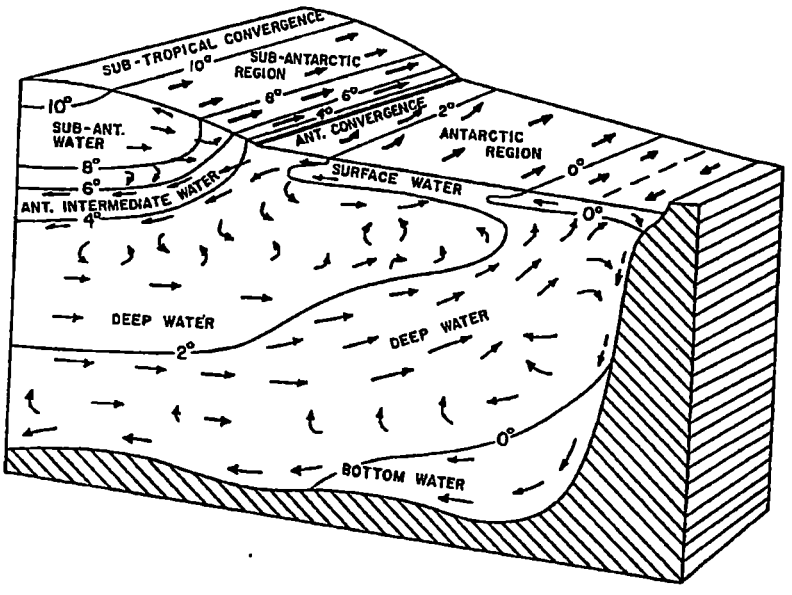

Figure 1.2: Water Masses of the Southern Ocean, from Sverdrup et al (1942)

investigations proposed that AAIW formation was circumpolar near the APF due to wind convergence (Piola and Georgi 1982). Another suggested mechanism states that AAIW is formed by mixing of AASW and Subantarctic surface water. This would require an isopycnal, cross-frontal mixing process between the Antarctic region and the Subantarctic region (Georgi 1979; Molinelli 1981; Piola and Georgi 1982). McCartney (1977) has suggested that AAIW is formed in Subantarctic waters from the cooling of Subantarctic Mode Water in the southeast Pacific which passes through Drake Passage. It then turns north into the South Atlantic to form the low salinity mode AAIW. Georgi (1979) found that this process of SAMW cooling could form the low salinity variety of AAIW, found within the South Atlantic, but did not account for the high salinity AAIW variety also found in the region. There appears to be two explanations for the high salinity AAIW found in the region. Firstly, old recirculated AAIW, or secondly, there may be two different formation mechanisms producing AAIW. Gordon (1975) suggested that water of AAIW characteristics could be formed from the mixing of warmer, high salinity Subantarctic surface water and colder, low salinity transition water found in the PFZ.

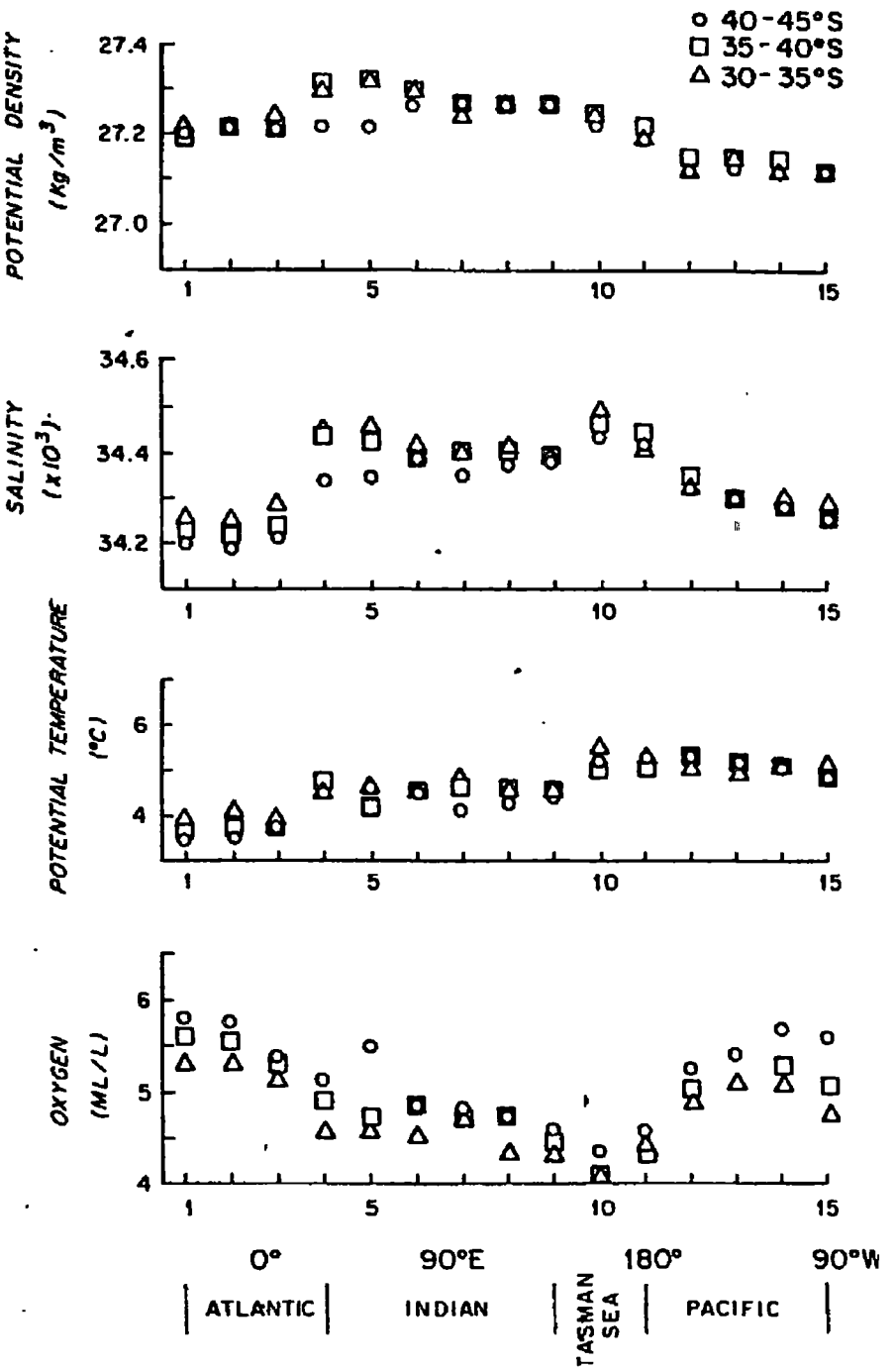

Figure 1.3: Mean potential density (upper panel), salinity (second panel), potential temperature (third panel), and dissolved oxygen (lower panel) in AAIW for three latitude zones between 30°S and 45°S (from Piola and Georgi, 1982)

1.3.5 Subantarctic Mode Water

Subantarctic Mode Water (SAMW) is defined by a thick thermostad (constant temperature) above the AAIW salinity minimum north of the SAF (Figure 1.2). SAMW is formed in late winter by convective overturning which results from surface water cooling in autumn and winter (McCartney 1977). The thermostad is then capped in spring by the development of a seasonal thermocline.

SAMW temperature and salinity, although constant at a given longitude, varies considerably zonally in the Southern Ocean. The zonal difference in temperature and salinity is mainly due to the different properties of Subantarctic water in each of the ocean basins. SAMW is characterised by water of approximately 14°C between 40°W and 20°E. There is then a general cooling of the thermostad to the east. At 65°E the temperature is 12.7°C. From 120°E and 160°E the thermostad is approximately constant between 8°C to 9°C. At 130°W the thermostad reaches its minimum temperature of 5.5°C to 4°C (McCartney 1977).

SAMW is generally found to a depth of 800 m in the Subantarctic region, reaching its maximum depth in the southeast Indian ocean. The depth of the thermostad may indicate the severity (coldness) of the winter, while annual changes in the depth of the thermostad indicate the variability of winter cooling from year to year (Carmack 1990).

McCartney (1977) suggested that the cold, low salinity variety of SAMW found in southeast Pacific may form AAIW in the South Atlantic ocean. This form of SAMW has a temperature of 4°C to 5.5°C and a salinity of 34.2 psu, which corresponds to the temperature and salinity characteristics of AAIW within the South Atlantic ocean.

1.3.6 North Atlantic Deep Water

North Atlantic Deep Water (NADW) originates from dense Norwegian Sea water that flows over three sills between Greenland and northern Scotland (Warren 1981b). These waters mix together and also entrain resident North Atlantic water to form NADW (Warren 1981a; Dickson and Brown 1994). It is

generally thought that between $13\times10^6 m^3 s^{-1}$ to $17\times10^6 m^3 s^{-1}$ of NADW enters the South Atlantic, although the contribution of each of the original sources in this flux has not yet been determined (Rintoul 1991; Dickson and Brown 1994).

NADW enters the South Atlantic in the southward western boundary current below the Brazil Current. It turns east with the Malvinas-Brazil Confluence, with a portion returning to the South Atlantic in the subtropical gyre, while the remainder joins the ACC mixing with LCDW and is distributed by the Southern Ocean into the Indian and Pacific oceans.

1.3.7 North Indian Deep Water

As Antarctic Bottom and Deep water moves northwards in the Indian Ocean it is altered by mixing with overlying deep water which results in slightly less dense deep water. The input of organic material from the Indus and Ganges rivers result in increased nutrient concentrations (Mantyla and Reid 1995). A southward moving high silica, low oxygen water mass is the result of this modification - known as North Indian Deep Water (NIDW) (Wyrtki 1971). The southward transport of high silica NIDW results in siliceous sediments in the eastern Indian Ocean between 5°S and 15°S (DeMaster 1981).

1.3.8 Pacific Deep Water

Pacific Deep Water (PDW) is identified by an oxygen minimum and silica maximum that flows southward, slightly removed from the western boundary, at depth of 2000 to 3000 m (Warren 1981a). Although Banks et al. (1995) see a high silica PDW between 2500 to 3500 m adjacent and east of the Tonga-Kermadec ridge at 17.5°S.

1.4 Circulation

1.4.1 Antarctic Circumpolar Current

The Southern Ocean contains the world's largest current, the Antarctic Circumpolar Current (ACC) (Figure 1.4). The ACC is described as having two current cores separated by a transition zone (Nowlin and Klinck 1986). The two currents are the Subantarctic Front and Antarctic Polar Front , while the

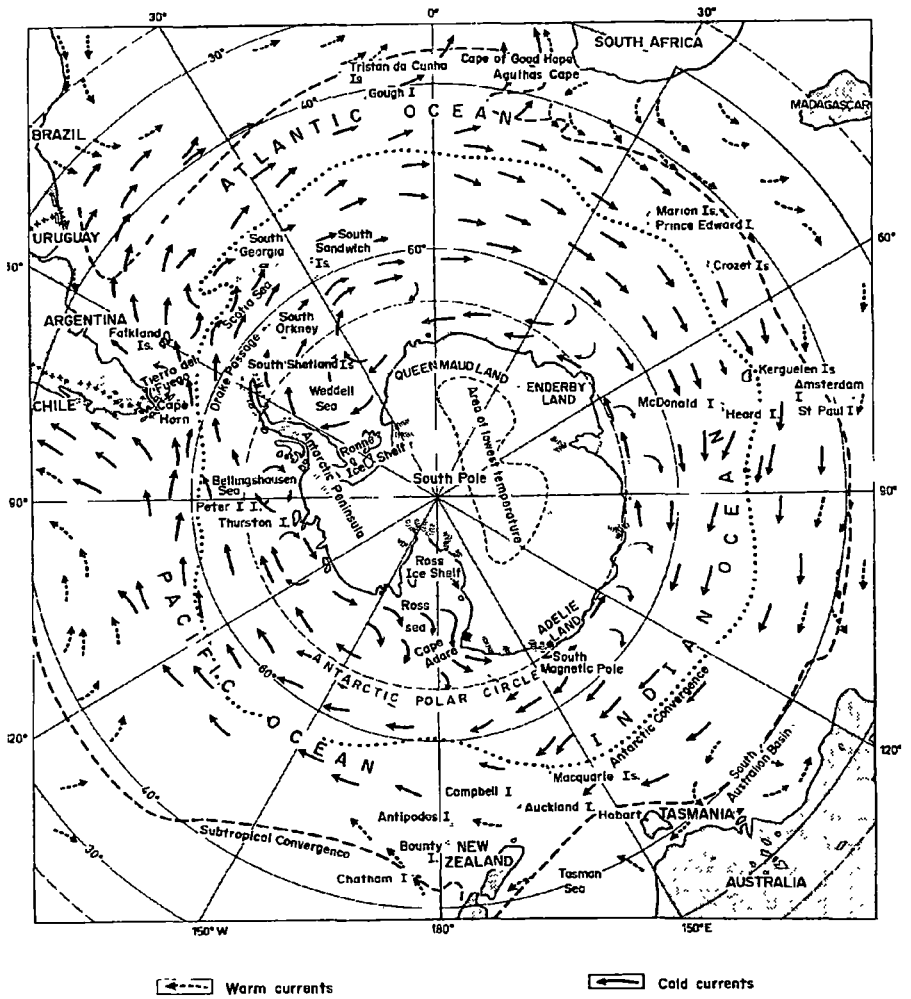

Figure 1.4: Regime of surface currents of the Southern Ocean. Warm currents (dotted arrows) and cold currents (solid arrows) (from Tchernia, 1980)

transition zone is the Polar Front Zone (Figure 1.1). The ACC simply defined is a continuous region of net eastward water transport.

Estimates of surface velocity associated with the SAF include $26cms^{-1}$ at the Greenwich meridian, relative to the bottom, and $> 20cms^{-1}$ at Drake Passage, relative to 2500 dbars. and $40cms^{-1}$ south of Australia, relative to the bottom (Nowlin and Klinck 1986; Whitworth and Nowlin 1987). Velocity estimates associated with the APF at Drake Passage and south of Australia are greater than $30cms^{-1}$ and $20cms^{-1}$ respectively (Savchenko et al. 1978; Nowlin and Klinck 1986). Movements in the position of the fronts affect the calculated velocity and strength of the ACC.

The fronts that occur within the ACC have been estimated to account for 75 % of the baroclinic transport (Nowlin and Clifford 1982). Estimates of the ACC transport are 125 $\pm$ 10$\times 10^6 m^3 s^{-1}$ at Drake Passage (relative to 2500 dbars), 162 $\times 10^6 m^3 s^{-1}$ at Greenwich meridian (relative to the bottom), and 156 $\times 10^6 m^3 s^{-1}$ south of Australia (relative to the bottom) (Nowlin and Klinck 1986; Whitworth and Nowlin 1987).

1.4.2 Weddell Gyre

The Weddell Sea is one of the major regions of Antarctic bottom water formation in the Southern Ocean. Within the Weddell Sea a cyclonic gyre extends from the Antarctic Peninsula ($\approx$ 60°W) to between 30°E and 20°E and from the Antarctic coast to between 60°S and 55°S (Orsi et al. 1993; Gordon et al. 1981).

Major water masses within the Weddell gyre are Antarctic Surface Water, Circumpolar Deep Water (CDW), Weddell Sea Bottom Water (WSBW) and Weddell Sea Deep Water (WSDW). CDW is the only water mass that is advected southwards into the Weddell Sea region (Orsi et al. 1993).

The mixing of CDW water with shelf waters in the southwestern part of the gyre forms the most extreme form of WSBW (Foster and Middelton 1980). WSBW circulates around the cyclonic gyre mixing with CDW to form WSDW (Orsi et al. 1993). WSDW flows northward out of the Weddell Sea into the Scotia and Georgia Basins, ultimately entering the deep ocean basin of the Atlantic Ocean.

1.4.3 Subtropical Gyre

In all three adjacent oceans the mid-latitudes are dominated by an anti-cyclonic surface circulation which is linked to the surface wind pattern (Figure 1.5). The South Atlantic, Indian and Pacific subtropical gyres are similar in general respects, having two zonal segments and two meridional segments (Tchernia 1980). These are most pronounced in the South Atlantic and the Pacific basins. The Indian Ocean northern circulation is complicated by the marked seasonal variability in the wind field and the eastern boundary by a

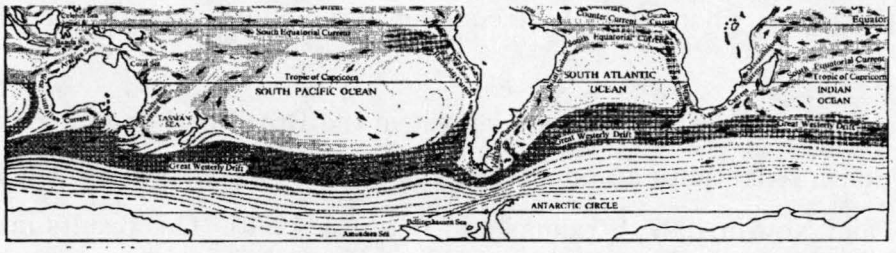

Figure 1.5: Subtropical gyre circulation (from Tchernia(1980)

narrow southward coastal boundary current.

The specific currents which dominate the subtropical gyre in each basin is discussed below.

South Atlantic

The northern boundary of the South Atlantic subtropical gyre is the westward South Equatorial Current (SEC). The current is the result of the consistent south-east trade winds that dominate between the equator and 30°S. These result in a broad westward SEC between 20°S and 2°-3°N. The current deepens from 100m near the African coast to 200m off the South American coast and has a mean transport of $23\times10^6 m^3 s^{-1}$ (Tchernia 1980).

On reaching the South American coast the SEC bifurcates. The southern branch forms the western boundary of the Subtropical gyre, the Brazil Current (BAC). The BAC is a weak, shallow current, with a transport of less than $11\times10^6 m^3 s^{-1}$ between 19°and 25°S, relative to 1400 to 1500 m (Gordon and Greengrove 1986; Garzoli and Garraffo 1989; Gordon 1989). The current intensifies and deepens south of 24°S, and the transport increases to $70\times10^6 m^3 s^{-1}$ - $76\times10^6 m^3 s^{-1}$ (relative to 3000m) at 37°S (Peterson and Stramma 1991).

Between 33°S and 38°S the Brazil Current meets the northward Malvinas current, resulting in the Brazil-Malvinas Confluence zone. The juxtaposition of subantarctic water against subtropical waters enhances mixing. The Brazil Current appears to form semi-permanent meanders directly off-shore which are thought to enhance the air-sea heat fluxes (Gordon 1981a). The movement of the Brazil Current eastwards between 33°S and 38°S forms the southern limb of

the subtropical gyre, where east of the confluence the South Atlantic Current (SAC) is evident.

Surface velocities of the SAC are largest in the Brazil basin and decrease across the South Atlantic to a minimum in the eastern Cape basin (Roden 1986; Whitworth and Nowlin 1987; Stramma and Peterson 1990). This results in a transport variation across the South Atlantic of $37\times10^6 m^3 s^{-1}$ to $30\times10^6 m^3 s^{-1}$ in the top 1000m, relative to 3000 m in the Brazil basin, to $15\times10^6 m^3 s^{-1}$ in the Cape basin (Stramma and Peterson 1990). Approaching southern Africa a portion of the SAC turns north while the remainder continues with the ACC south of Africa. The northern portion of the SAC feeds the Benguela current, which forms the closing eastern boundary of the subtropical gyre (Stramma and Peterson 1990).

The Benguela Current spreads from a width of 270 km in the south to between 550 and 650 km in the north. The prevailing winds deflect the current to the left (off-shore), resulting in upwelling along the African coast. Transport estimates of the Benguela Current range from 16 to $21\times10^6 m^3 s^{-1}$ (relative to 1000m) (Peterson and Stramma 1991). The current leaves the coast at 30°S and flows northwest across the South Atlantic with estimates of $18\times10^6 m^3 s^{-1}$ crossing 28°S (Peterson and Stramma 1991).

Indian Ocean

The South Equatorial Current (SEC) of the Indian Ocean forms the northern boundary of the subtropical gyre. It has a major seasonal transport variation of $14\times10^6 m^3 s^{-1}$ (minimum in austral summer of $40\times10^6 m^3 s^{-1}$ and maximum in winter of $54\times10^6 m^3 s^{-1}$) (Tchernia 1980).

Madagascar forms an island barrier to the SEC between 12°S and 25°S. This results in the bifurcation of the SEC. The southern branch forms the East Madagascar Current (EMC) which has an estimated transport of $41\times10^6 m^3 s^{-1}$ at 23°S (Lutjeharms et al. 1981). South of Madagascar the EMC forms numerous eddies. It is suggested that these eddies are the mechanism by which heat and mass is transferred from the EMC to the Agulhas Current (Gründlingh et al. 1991). It is now thought that the Mozambique current has little influence on the Agulhas current to the south (Sætre and da Silva 1984;

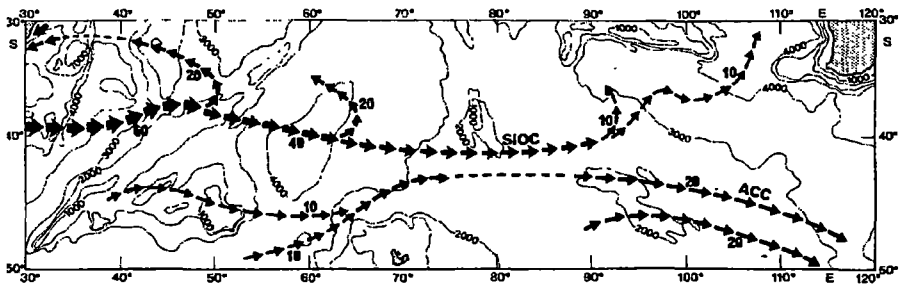

Figure 1.6: Schematic illustration of the flow field in the south Indian Ocean. The transport ($\times 10^6 m^3 s^{-1}$) of the South Indian Ocean Current (SIOC) and of the northern part of the Antarctic Circumpolar Current (ACC) are shown. (from Stramma, 1992)

Gründlingh et al. 1991).

The Agulhas Current has its origins at 28°S adjacent to the African coast. Similar to the EMC, the Agulhas Current is a southward, western boundary current. Transport has been estimated at $62 \times 10^6 m^3 s^{-1}$ at 31°S and increasing downstream at a rate of $6 \times 10^6 m^3 s^{-1}$ per 100 km (Gründlingh 1980). The Agulhas follows the African coast southwards and veers southwest off the south coast to approximately 19°E. At this point it retroflects and flows eastward at 40°S, north of the STF. The Agulhas Return Current (ARC) has an estimated transport of $84 \times 10^6 m^3 s^{-1}$ to $103 \times 10^6 m^3 s^{-1}$ (Read and Pollard 1993). Not all Indian Ocean water returns with the Agulhas retroflection with eddy shedding on the western extension into the South Atlantic Ocean (Gordon 1986; Fine et al. 1988; Peterson and Stramma 1991; Gordon et al. 1992).

East of the ARC, Stramma (1992) found a strong eastward current band, north of the STF along 40°S within the Indian Ocean. He called this current the South Indian Ocean Current (SIOC). Near the African coast the SIOC has a transport of $60 \times 10^6 m^3 s^{-1}$ in the upper 1000 m (relative to 3000m) which decreases as it moves across the Indian Ocean to $10 \times 10^6 m^3 s^{-1}$ near Australia as it turns northeast into the Indian Ocean (Figure 1.6).

The northeast movement of the SIOC near the Australian coast marks the weak northward closing arm of the subtropical gyre. This eastern boundary of the Indian Ocean is unique. The northward subtropical flow is not support by the upwelling of water off the coast of Australia. There is actually a southward

current directly off-shore, the Leeuwin Current. The Leeuwin Current is a warm, relatively fresh current that opposes the wind stress in the region, which would support an equatorward flow. It is observed as a broad, shallow current in low latitudes that tapers to a deep narrow current off the coast of southwest Australia (Church et al. 1989; Smith et al. 1991). The current is strongest in autumn and winter. The origin of the flow is uncertain but high meridional steric heights gradients exist on the eastern boundary which are comparable to those that exist along the western ocean boundaries. It is thought that this drives the southward flow (Godfrey and Ridgway 1985; Church et al. 1989; Smith et al. 1991). This gradient is thought to be setup by the warm inflow of Pacific waters into the Indian Ocean via the Indonesian Through-flow.

Pacific Ocean

The northern current of the South Pacific subtropical gyre is the South Equatorial Current (SEC) between 20°S and 5°N. This current results from the persistent southeast trade winds. The current is well defined from South America to 180°W, with an estimated transport of $50\times10^6 m^3 s^{-1}$ (Tchernia 1980). The SEC has a branch the turns south at 180°W, while the remainder continues west to the Australia coast. At the Australian continent the remaining SEC forms the southward East Australia Current (EAC).

The EAC is a warm shallow current that flows along the coast of Australia, with transport estimates of between $15\times10^6 m^3 s^{-1}$ to $45\times10^6 m^3 s^{-1}$ (Wyrtki 1962a; Hamon 1965; Andrews et al. 1980; Ridgway and Godfrey 1994). The EAC is much weaker and more variable than other western boundary currents. Between 34°S and 36°S it separates from the coast and meanders eastward across the Tasman Sea towards New Zealand with the Tasman Front (Bennett 1983; Stramma et al. 1995). The current eventually turns southward along the east coast of New Zealand. The SPC forms the southern limb subtropical gyre. The SPC maintains a weak transport of $5\times10^6 m^3 s^{-1}$ from New Zealand across the South Pacific and gradually moves north. Between 115°W and 85°W its separates into two weak currents, which develop a more pronounced northward component east of 83°W (Stramma et al. 1995). This northward movement forms the closing northward meridional boundary of the subtropical gyre, the

off-shore Chile-Peru Current and the coastal Peru or Humbolt Current.

1.4.4 Deep Circulation

The deep circulation in each ocean basin is restricted and directed by topographic barriers. Deep water enters each ocean in deep western boundary currents adjacent to major topographic features.

South Atlantic

Antarctic Bottom Water and Circumpolar Deep Water enter the Brazil Basin in the deep western boundary current adjacent to South America. It moves into the Argentine basin via deep troughs in the Rio Grande Rise, namely the Vema and Hunter channels, while CDW passes over the Lower Santos Plateau (Speer and Zenk 1993). Hogg et al. (1982), using current moorings estimate the transport of AABW through the Vema channel at $4\times10^6 m^3 s^{-1}$. Speer and Zenk (1993) estimate $2\times10^6 m^3 s^{-1}$ across the Lower Santos Plateau, $3.9\times10^6 m^3 s^{-1}$ in the Vema channel and $0.7\times10^6 m^3 s^{-1}$ in the Hunter channel.

There is also a western boundary current along the mid-Atlantic ridge that allows bottom water to flow into the Cape basin in the eastern South Atlantic . The northward flow of this water below 4000 m is restricted by the Walvis Ridge. The water below 4000 m north of the Walvis Ridge in the Angola basin enters from the north over the Guinea Rise via the Argentine basin (Warren and Speer 1991).

Indian

Bottom and deep water enters the Indian Ocean via a series of deep western boundary currents adjacent to major north-south orientated topographic feature. In the Madagascar Basin, which connects to the northern Mascarene Basin, the coldest form of bottom water is found (Warren 1981a). This water originates in the Weddell-Enderby Basin were water properties are mainly derived from the Weddell Sea (Mantyla and Reid 1995).

In the eastern Indian Ocean bottom water enters the West Australian Basin as a deep western boundary current adjacent to the Ninetyeast Ridge. The water that enters this basin has a higher salinity than that found in the

Madagascar Basin placing its source in the Ross Sea and a small portion originating off the Adelie coast (Gordon and Tchernia 1972; Mantyla and Reid 1995). Rintoul (1997) suggests that Adelie bottom water is the major contributor to AABW within the eastern Indian and Pacific basins.

The most extreme deep water in the Central Indian Basin is found in the eastern portion of the basin adjacent the Ninetyeast ridge. This deep water results from flow across the Ninetyeast ridge through deep fracture zones (Warren 1982). A deep western boundary current is observed in the Central Indian Basin between 2000 and 3500 m. This carries CDW from the Antarctic Circumpolar Current into the Central Indian basin and connected northern basins (Warren 1981a).

Pacific

Bottom and deep water enters the Pacific in the deep western boundary current adjacent to New Zealand and the Tonga-Kermadec Ridge and in the interior of the Southeast Pacific Basin (Warren 1981b; Banks et al. 1995). The Lord Howe Rise in the Tasman Sea and the Chile Rise restrict the passage of the deep water in the far west and east Pacific basin, respectively. Northward deep transports of $20\times10^6 m^3 s^{-1}$ have been estimated at both 43°S and 28°S (Warren 1981b). Whitworth et al. (1996), from two-year current mooring data, estimate a northward transport (between 2000m to the bottom) of $13.6 \pm 12.6\times10^6 m^3 s^{-1}$ adjacent the Tonga-Kermadec ridge This deep western boundary current is the primary source of deep water for the entire Pacific Basin.

1.4.5 Heat Fluxes

The northward heat flux within the South Atlantic has been estimated by various methods between $0.25PW$ and $0.68PW$ ($1PW = 10^{15}W$) (Bennett 1978; Hastenrath 1982; Hsiung 1985; Fu 1981; Rintoul 1991; Macdonald and Wunsch 1996; Boddem and Schlitzer 1995; Saunders and King 1995). The northward heat flux is counter-intuitive to the expected heat distribution and results because the southward export of cold NADW is balanced by the northward flux of warmer intermediate and thermocline water. The sign of the heat flux in the Atlantic is well determined but the magnitude of the northward heat flux is not.

The estimated Indian Ocean heat flux varies greatly, some of which is explained by different techniques and assumptions used in the individual calculations. Toole and Raymer (1985) estimate a heat flux of $-0.6PW$, but this is calculated assuming no net mass flux associated with the Indonesian throughflow. Other estimates vary from $-0.49PW$ to $-1.4PW$ (Hastenrath 1982; Georgi and Toole 1982; Hsiung 1985; Toole and Warren 1993; Macdonald 1993; Macdonald and Wunsch 1996). These estimates are made from a combination of techniques including hydrographic, direct and bulk methods. Although the size of the heat flux estimates varies considerable the sign of the heat flux is consistently southward, apart from an early estimate by Bennett (1978) who estimates a northward heat flux of between $0.46PW$ to $1.76PW$.

In the Pacific Ocean the heat flux varies considerably in size and direction from small equatorward or poleward to large poleward heat fluxes. Hsiung (1985) estimates a southward heat flux of $-0.2PW$ at 30°S and northward heat flux of $0.09PW$ at 40°S. Georgi and Toole (1982) estimate a northward heat flux of $0.04PW$ at 40°S, while Wunsch et al. (1983) estimated a southward heat flux of $-0.03PW$ at 43°S. Other estimates include a large southward heat flux at 30°S of between $-1.16PW$ and $-1.92PW$, and at 43°S a northward heat flux of $0.42PW$ (Bennett 1978; Hastenrath 1982). Recent inverse studies by Macdonald (1993) and Macdonald and Wunsch (1996) estimate a northward heat flux at 30°S of $0.3PW$.

These studies show that the magnitude of the heat flux in each ocean basin is not well determined. The direction of the heat flux in the Atlantic Ocean is consistent in all studies but in the Indian and Pacific Oceans there is still uncertainty in both the direction and size of the heat flux.

1.4.6 Salt Fluxes

In the Atlantic, Bennett (1978) estimates a salt flux of $-3.4 \times 10^6 kgs^{-1}$ to $2.2 \times 10^6 kgs^{-1}$ at 24°S and $-7.0 \times 10^6 kgs^{-1}$ to $0.6 \times 10^6 kgs^{-1}$ at 43°S. Recently, Wijffels et al. (1992) estimate a southward salt flux of $-26.7 \times 10^6 kgs^{-1}$ within the Atlantic Ocean. This estimate is based on the inflow of Pacific water into the Atlantic, via the Bering Strait, of $0.8 \times 10^6 m^3 s^{-1}$ with an average salinity 32.5 psu.

In the Indian Ocean Toole and Warren (1993) estimate a southward heat flux of $-236.8 \times 10^6 kgs^{-1}$, which results from the input of Pacific water into the Indian Ocean via the Indonesian throughflow. In the Pacific (Wunsch et al. 1983) ran a series of inverse models, using different constraints, which results in a salt flux range of between $-0.59 \times 10^6 kgs^{-1}$ to $294 \times 10^6 kgs^{-1}$ at 43°S and $-0.49 \times 10^6 kgs^{-1}$ to $-3.8 \times 10^6 kgs^{-1}$ at 28°S.

Estimates of meridional salt fluxes are not widely provided in the literature. Of the studies that investigate the meridional salt flux there is little consensus on either the size or the direction of the salt flux within any of the ocean basins.

1.5 Thesis Structure

This study provides a description of the Southern Ocean and the adjacent ocean basins circulation, inter-ocean mixing, intra-ocean water mass formation and conversion processes within a dynamically consistent inverse model. Chapter 2 gives a brief review of inverse methods and also addresses the accuracy of circulations determined by inverse methods. Chapter 3 gives a basic hydrographic description of the sections used in the study and outlines the initial inverse model. Chapter 4 provides a detailed description of the inverse solution, highlighting the circulation and the water mass formations and conversions that occur within the Southern Ocean on a region by region basis. In Chapter 5 the dianeutral fluxes are separated into sea-surface fluxes resulting from air-sea interactions and interior mixing processes. This model describe the mixing and conversion process that results in the water mass characteristics in the Southern Ocean and adjacent ocean basins. Chapter 6 investigates alternative circulation hypotheses and a brief summary of the study in given Chapter 7.

Chapter 2

Inverse Theory

Inverse methods are widely used to determine ocean basin circulation (Rintoul 1991; Wijffels 1993; Macdonald 1995; Harris 1996). The use of inverse methods to describe oceanic circulation was initiated by Wunsch (1978). Prior to this the inverse method had been used in geophysical studies (Parker 1977).

In this chapter a brief review of the principles underlying inverse methods is given. Following this, the accuracy of the inverse method to determine the reference velocity and dianeutral property fluxes is determined using "quasi-hydrographic" data from the Fine Resolution Antarctic Model (FRAM, Group 1991). This study follows the criteria develop by McIntosh and Rintoul (1997). I then extend the study of McIntosh and Rintoul (1997) examining the ability of the inverse method to explicitly solve dianeutral mean property advection and effective property diffusion. Finally I discuss the most appropriate form of the conservation equations when using non-synoptic hydrographic data.

2.1 Inverse Models: an Overview

This section is a brief overview of the principles and approaches used to define inverse methods. For a more thorough treatment of the principles and development of inverse theory the reader is directed to Wunsch (1978), Parker (1977) and Roemmich (1980). For more details on the mathematical approach used to solve the underdetermined problem the reader is directed to Lanczos (1961), Lawson and Hanson (1974), Menke (1984) and Tarantola (1987).

Inverse models use two oceanographic techniques to define the general

circulation: simple dynamics and water mass analysis. When defining the system of simultaneous equations these two principles are heavily relied upon.

Simple dynamic constraints are applied to the ocean region defined by the hydrographic sections and land boundaries. The ocean is assumed to be in hydrostatic and geostrophic balance:

$$\frac{\partial p}{\partial z} = -g\rho \tag{2.1}$$

$$fv = \frac{1}{\rho}\frac{\partial p}{\partial x} \tag{2.2}$$

Equation 2.1 and Equation 2.2 can be combined to give an expression for the vertical velocity shear between two adjacent stations along a hydrographic section.

$$f\frac{\partial v}{\partial z} = \frac{-g}{\rho_o}\frac{\partial \rho}{\partial x} \tag{2.3}$$

Equation 2.3 defines the velocity shear at all depths. Integrating Equation 2.3 from z_0 gives

$$v(x,z) = \frac{-g}{\rho_o f}\int_{z_0}^{z}\frac{\partial \rho}{\partial x}dz + v(x,z_0) = v_r + b \tag{2.4}$$

The first term of Equation 2.4 depends on the density gradient and is called the relative velocity (v_r). The second term is the integration constant, and as is known as the reference velocity (b). The relative velocity (v_r) is determined from the hydrographic data but some assumption about the unknown reference velocity is required to determine the absolute velocity.

In order to solve for **b** Wunsch (1978) defined an oceanic region bounded by hydrographic sections. Within the region he assumed that mass was conserved in discrete horizontal layers enabling a set of conservation equations to be written. The conservation equation did not allow mass to be transfered from one layer to the next. Further development and improved ocean physics have been incorporated by subsequent inverse studies (Wunsch et al. 1983; Fu 1986; Rintoul and Wunsch 1990; Macdonald 1991; Rintoul 1991; Wijffels 1993; McIntosh and Rintoul 1997). These studies have lead to the inclusion of heat, salt and nutrients within the suite of conserved properties and an improvement

in the physical representativeness of these models by the addition of diapycnal fluxes. Diapycnal fluxes enables mixing to occur between different layers. The form of the conservations equations is then

$$\sum_{j=1}^{N} \Delta x_j \int_{h_m}^{h_{m+1}} (\rho C_j (v_r + b)_j) + E_j C_j + (w_c AC)_m - (w_c AC)_{m+1} \approx 0 \tag{2.5}$$

C_j property value/unit mass at pair j

$h_{m,m+1}$ depth of surfaces bounding layer m

v_r relative velocity

b reference velocity

$E_j C_j$ Ekman property flux at station pair j

$(w_c AC)_{m,m+1}$ property dianeutral flux. A is the interface area of density surfaces $m, m+1$. C is the mean interface property and, w_c is the unknown interfacial property "velocity"

The resulting system of conservation equations can be written in matrix form as

$$\mathbf{Ab} = -\mathbf{d} \tag{2.6}$$

where

A matrix element product of area × C at each station pair in each layer

b vector of unknowns including reference velocities (b_j) and diapycnal "velocities" ($(w_c)_{m,m+1}$)

d property divergence in each layer due to relative ($\Delta x_j \times C_j v_r$) and Ekman ($E_j C_j$) fluxes

The linear system described by Equation 2.5 and written in matrix form in Equation 2.6 generally has more unknowns than equations. In this case it is an underdetermined problem and will have an infinite numbers of solutions. A least squares technique is used to find a unique solution.

An appropriate solution of Equation 2.6 is found by defining the inverse $\mathbf{A}^+$ to the matrix $\mathbf{A}$ by

$$\mathbf{A}^+ = \mathbf{A}^\mathbf{T}(\mathbf{A}\mathbf{A}^\mathbf{T})^{-1} \tag{2.7}$$

This is know as the Moore-Penrose inverse (Wunsch 1978). From this one obtains one possible specific solution

$$\mathbf{b} = \mathbf{A}^\mathbf{T}(\mathbf{A}\mathbf{A}^\mathbf{T})^{-1}(-\mathbf{d}) \tag{2.8}$$

The specific $\mathbf{b}$ chosen by the Moore-Penrose inverse is the solution such that $\|\mathbf{b}^t\mathbf{b}\|$ is as small as possible, the minimum norm (L^2 norm). The Moore-Penrose inverse is used when the data that describe the model parameters ($\mathbf{b}$) are exact and completely independent, a well-conditioned problem (Menke 1984). The oceanographic data that forms the conservation equations contain instrument and non-synoptic errors and the equations may not be completely independent. These errors result in an ill-conditioned problem. The non-independency of the equation formed from hydrographic data may result in $\mathbf{A}\mathbf{A}^\mathbf{T}$ being singular. In such a system the Moore-Penrose solution cannot compute the inverse ($\mathbf{A}^+$) (Wunsch 1978). To solve such a system of equations the singular value decomposition (SVD) is used (Lanczos 1961). The SVD decomposes $\mathbf{A}$ into a coupled eigenvector-eigenvalue problem. This allows $\mathbf{A}$ to be defined as a product of three matrices.

$$\mathbf{A} = \mathbf{U}\Lambda\mathbf{V}^\mathbf{T} \tag{2.9}$$

where

$\mathbf{A}$ is an $m \times n$ matrix (m = number of equations, n = number of unknowns)

$\mathbf{U}$ matrix that spans the row (m) space of $\mathbf{A}$ eigenvectors

$\mathbf{V}^\mathbf{T}$ transpose of matrix $\mathbf{V}$ that spans the column (n) space of $\mathbf{A}$ eigenvectors

$\mathbf{\Lambda}$ diagonal matrix of eigenvalues λ (strictly finite and positive)

Using the SVD, Equation 2.6 can be written

$$\mathbf{U\Lambda V^T b} = -\mathbf{d} \tag{2.10}$$

and solved for $\mathbf{b}$

$$\mathbf{b} = \sum_{i=1}^{k} \frac{U_i \cdot (-d)}{\lambda_i} V_i \tag{2.11}$$

where k is the number of non-zeros eigenvalues retained in the solution.

The SVD allows us to truncate $\mathbf{A}$ removing the small eigenvalues which should be zero, but because the equations contain errors are actually small finite values. The retention of small eigenvalues in Equation 2.11 causes the solution ($\mathbf{b}$) to differ markedly from the original choice, as the solution is inversely proportional to the eigenvalue. The number of non-zeros eigenvalues retained in the solution is known as the rank (k). The solution of $\mathbf{b}$ excludes the null-space of $\mathbf{A}$. The exclusion of the null-space vectors makes this solution the minimum norm solution of Equation 2.6. The unique solution is the one where the deviation from the original choice of $\mathbf{b}$ is small (solution norm $||\mathbf{b^t b}||$) given the misfit of each equation (residual norm $||\mathbf{Ab} + \mathbf{d}||$) is reduced to a reasonable value.

Before solving the system of equations, weights are applied to the elements of $\mathbf{A}$ (Wunsch 1978). The rows of $\mathbf{A}$ are made non-dimensional by normalising with respect to layer property means. The solution elements b_i are proportional to corresponding elements of $\mathbf{A}$ (Rintoul 1988). This results in large velocities a deep, wide stations pairs. To remove the bias resulting from unequal station pair areas the columns of $\mathbf{A}$ are normalised with respect to station pair area. Inverse methods that solve for both the reference velocity and dianeutral flux unknowns also include a column scaling that effectively partitions the unknowns (reference velocity versus dianeutral fluxes) in importance within the conservation equations. The most appropriate column scaling factor is one which minimises the condition number (ratio of largest to smallest eigenvalues) (McIntosh and Rintoul 1997).

As stated at the beginning, the inverse method uses two oceanographic tools. I have discussed the dynamical assumptions and methods used to solve the conservation system of equations. The second tool used is water mass analysis. This analysis is important in defining the initial choice of reference level and reference velocity. The reference level is generally assumed to be a boundary between two water masses that flow in opposing directions i.e. the boundary between North Atlantic Deep Water and Antarctic Bottom Water. At this level the reference velocity is generally assumed to be zero. The solution, **b**, is solved by adding the simplest possible structure. Therefore, the most accurate initial choice of **b** should be used. The importance of this initial choice cannot be over emphasised. The accuracy of the solution depends on the appropriate choice of and confidence in the initial choice.

A powerful aspect of the inverse method is the ability to add *a priori* information into the system. The addition of *a priori* information enables aspect of the circulations thought to be known to be used in determining the reference velocities. It also enables the testing of circulation theories by determining if a circulation consistent with the hydrographic data can be found.

2.2 Validation of Inverse Methods

The skill of inverse methods to determine the reference velocity or dianeutral property flux has not been extensively studied. Neither has the form the conservations equations may take to make them more consistent with the ocean dynamics they are attempting to describe. Killworth and Bigg (1988) studied the reliability of solutions obtained using inverse models. This study has been extended by McIntosh and Rintoul (1997). McIntosh and Rintoul (1997) investigated the ability of the inverse to reproduce numerical model results and suggest criteria that may be used in finding the optimum inverse solution.

In this study I investigate the philosophy behind inverse methods by assessing the accuracy of the inverse solution against the known solution provided by the Fine Resolution Antarctic Model (FRAM) (FRAM, Group 1991). The study uses the criteria developed by McIntosh and Rintoul (1997) and considers whether these are appropriate for this ocean region. I then

investigate the ability of inverse methods to explicitly diagnose the dianeutral mean property advective flux and diffusive flux.

2.2.1 Numerical Model Data and Inverse Region

FRAM is a Bryan-Cox model that encompasses the Southern Ocean south of 24°S. During its first 6 years FRAM was restored, at the surface and in the vertical, to Levitus (1982) climatology. The FRAM numerical model captures the banded nature of the Antarctic Circumpolar Current (ACC) and the eddy and meandering nature of the frontal features within the ACC. South of Australia the FRAM model shows the southeastward movement of the ACC. This shift of the ACC is thought to be due to the interaction of the current with the complex bottom topography within the region.

I use model output from a snap-shot at the end of the final year 6 model simulation within the region south of Australia (117°E to 147°E). This region is subdivided into four smaller boxes which define the water zones found within this region (Figure 2.1). The domain of these boxes and the water zones they enclosed are:

1. The Subtropical zone from the Australian continent to 42°S.

2. The Subantarctic zone defined between 42°S and 46°S.

3. The Polar Frontal zone which included the Subantarctic and Antarctic Polar Fronts defined between 46°S and 58°S

4. The Antarctic zone which encompasses the region south of 58°S to the Antarctic Continent.

At each of the sections the FRAM model provides the "hydrographic data" used to assemble the conservation equations (mass, heat and salt). The velocity is taken directly from the FRAM numerical model. This velocity field is the absolute velocity field (sum of the reference, relative and Ekman velocities) from which the velocity at our chosen reference level is removed. The deepest common depth is chosen as the reference level for all sections. The salinity conservation equation are written using the salinity anomaly value (S - 35).

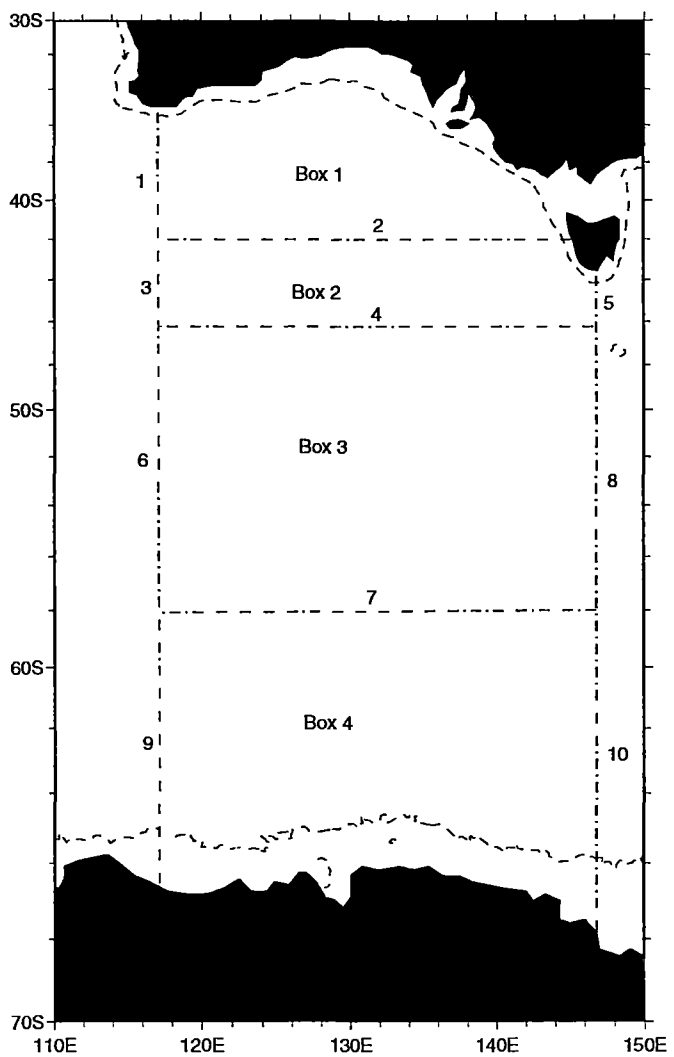

Figure 2.1: Inverse Model Box Regions South of Australia. Boxes are numbered 1-4, and sections are numbered 1-10. The ocean region between the Australian mainland and Tasmania (Bass Strait) is closed FRAM.

Using the anomaly value reduces the error in the salt conservation equations and increases the independency of these equations from the mass conservation equations (McDougall 1991). The inverse model has 21 layers. The layers are defined by neutral surfaces (McDougall 1987a) and computed as described by Jackett and McDougall (1997).

The relaxation of FRAM to the Levitus climatology results in source and sink terms of heat and salt which are known and included in the right-hand side of Equation 2.6 (McIntosh and Rintoul 1997). The tracer time-dependent (storage) terms are diagnosed and the Ekman flux across each section is also known and included in the right-hand side of Equation 2.6. Figure 2.2 show the relative mass transports across each section from FRAM, while Figure 2.3 shows the total mass transport across each section within FRAM.

The reference transport at sections 1, 2, and 7 are larger and of opposite sign to the relative transports at these sections, resulting in a total westward mass flux at section 1 and northward mass transports at sections 2 and 7 (Figure 2.3). At the remaining section the reference transport increases (sections 5, 8, 9 and 10) or decreases (sections 3, 4 and 6) the relative transport resulting in a larger or smaller total mass flux, respectively.

2.2.2 Accuracy of Inverse Solution

Traditionally, dianeutral (interfacial) unknowns are incorporated into an inverse problem by the addition of one dianeutral flux per layer. The interfacial variable w^* represented all types of transport including vertical advection, diffusion, cabelling and other eddy process (Wunsch 1984). This allowed layer mass to be balanced by vertical and lateral advection. McDougall (1987b) questions any conclusions about vertical velocities from these inverse models, stating that it is inconsistent to included diapycnal advection of properties without including diapycnal diffusion fluxes.

Advection and diffusion have been incorporated into a least squares problem by Hogg (1987). This inverse is based upon the β-spiral technique using Levitus data in a region of the North Atlantic surrounding the Mediterranean salt tongue. Hogg (1987) shows that the residual of the least squares problem decreases with the inclusion of vertical advection and diffusion.

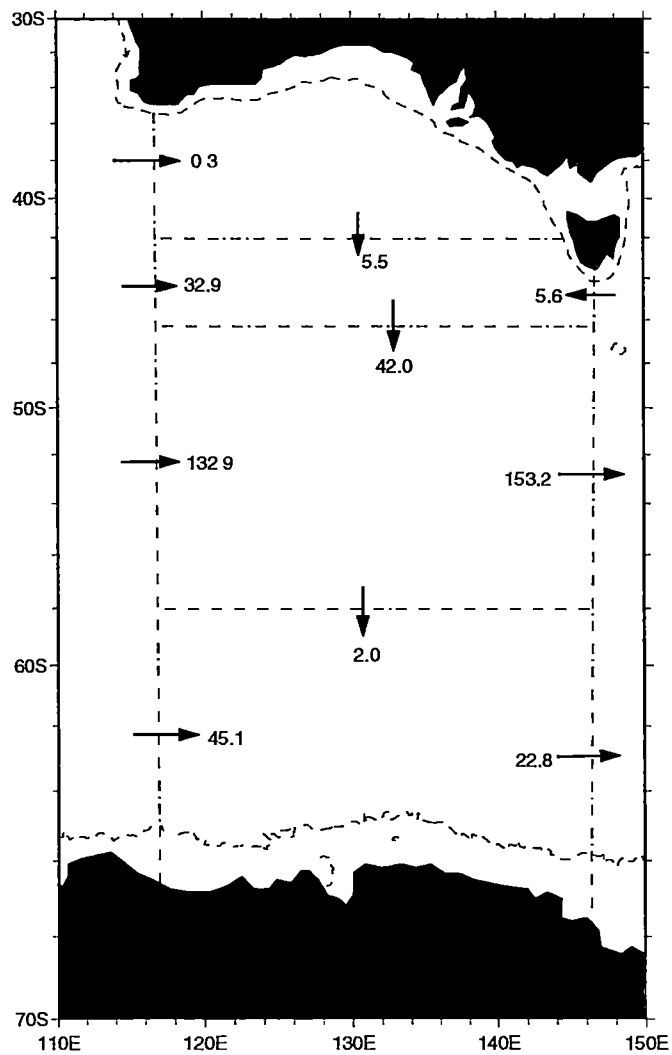

Figure 2.2: Relative and Ekman mass transport ($\times 10^6 m^3 s^{-1}$) (and other miscellaneous terms in FRAM that are treated as known) within FRAM.

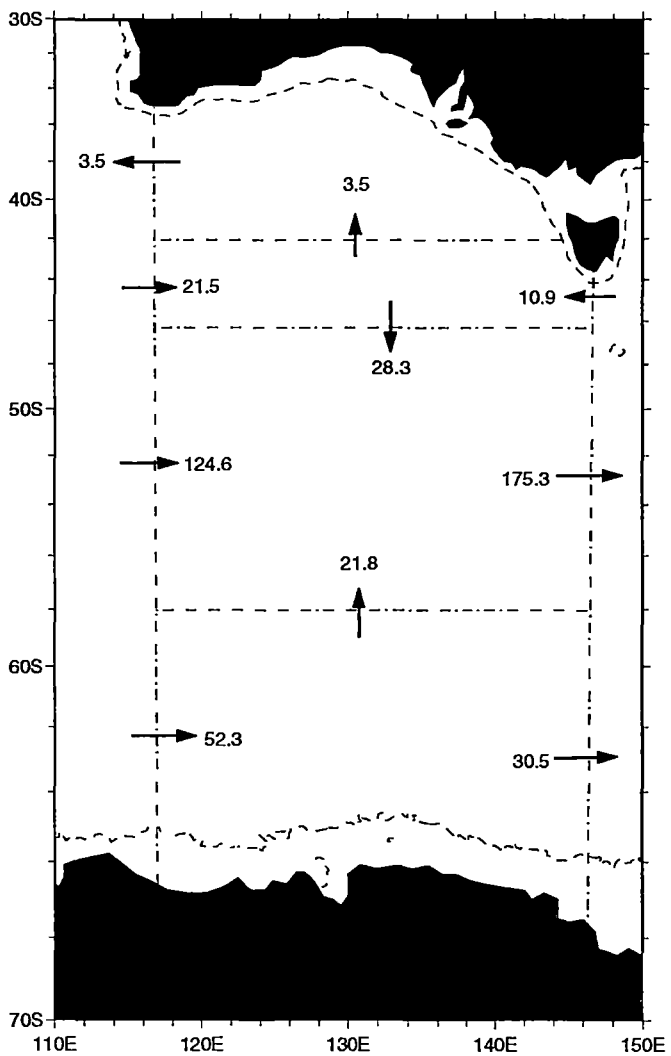

Figure 2.3: Total mass transport ($\times 10^6 m^3 s^{-1}$) of FRAM at each section defined in Figure 2.1. This is the "true" solution, inverse total transports will be compared to these section transports

McIntosh and Rintoul (1997) find that an inverse model which ignores diapycnal property fluxes is sensitive to error due to its large condition number and results in a nearly worthless inversion. Following McIntosh and Rintoul (1997) an independent dianeutral flux for each layer of each conserved property is incorporated into the inverse model (Equation 2.5). The dianeutral fluxes are written as the horizontal surface area and surface-averaged property times dianeutral property "velocity" (ACw_m, ACw_h, ACw_s m-mass, h-heat and s-salt). The dianeutral heat and salt fluxes include the advective and diffusive fluxes, while the dianeutral mass flux is purely an advective flux (McIntosh and Rintoul 1997).

McIntosh and Rintoul (1997) suggest that minimising the condition number (the ratio of largest eigenvector to smallest eigenvector) is an appropriate way to choose the rank of the system. Minimising the condition number is achieved by choosing the scaling factor between the reference velocity unknowns and the dianeutral flux unknowns. The scaling factor trades off the size of reference level velocities and diapycnal fluxes in the overall solution vector **b**.

In the four box region south of Australia there are 210 equation and 641 unknowns (401 reference velocity and 240 dianeutral flux unknowns). Choosing the weights as described above results in a condition number of ≈ 269 using all eigenvalues (k) in Equation 2.11. Layer residuals for each box (Figure 2.4) are small with mass residuals less than $0.5\times10^6 m^3 s^{-1}$, heat residuals less than 4×10^6 °C $m^3 s^{-1}$ and salt less than 6×10^{-4} (s-35) $m^3 s^{-1}$.

The inverse reference velocities are a heavily smoothed representation of the FRAM field with the overall trend resolved (Figure 2.5). The reference velocities at 117 °E and 147 °E of this model are similar to those of McIntosh and Rintoul's (1997) Southern Ocean box (their Figure 8). Although the reference velocities are smooth compared to the FRAM reference velocities, the mass, heat and salt transports in each layer agree well with the FRAM model (Figure 2.6). (For comparison purposes FRAM fluxes are resolved into the neutral surface coordinate system.) The amount of structure added to the initial reference velocities is appropriate and enables the inverse solution to reproduce the "true" transport.

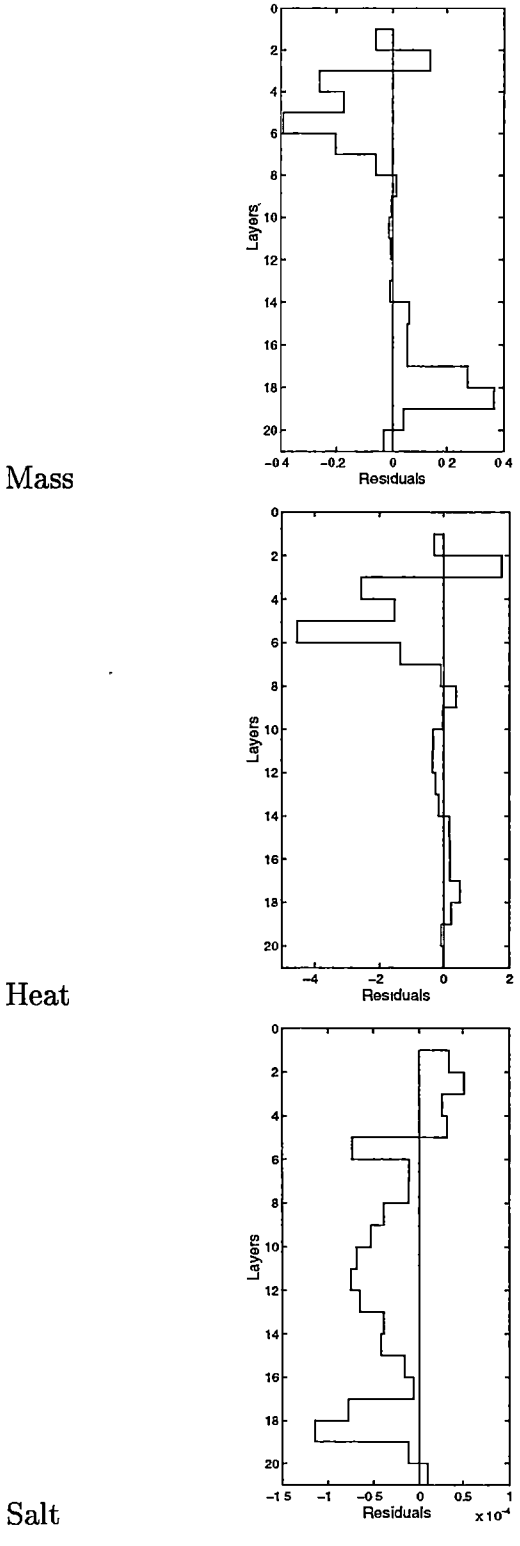

Figure 2.4: Inverse model (mod_fram) Mass, Heat and Salt Residuals in each layer for Box 2. Units: mass ($\times 10^6 m^3 s^{-1}$), heat ($\times 10^6$ °C $m^3 s^{-1}$) and salt ((psu-35)$m^3 s^{-1}$)

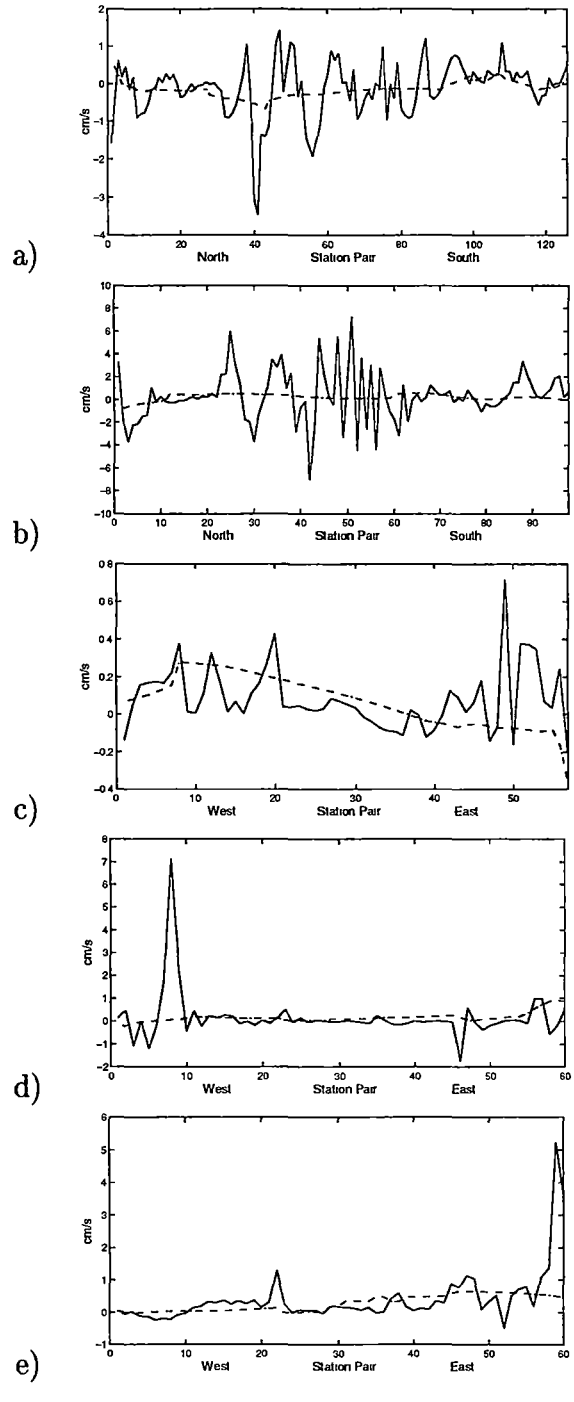

Figure 2.5: Comparison of reference velocities (cms^{-1}) from FRAM (continuous line) and inverse solution (mod_fram, dashed line) at a) 117°E b) 147°E c) 42°S d) 46°S e) 58°S

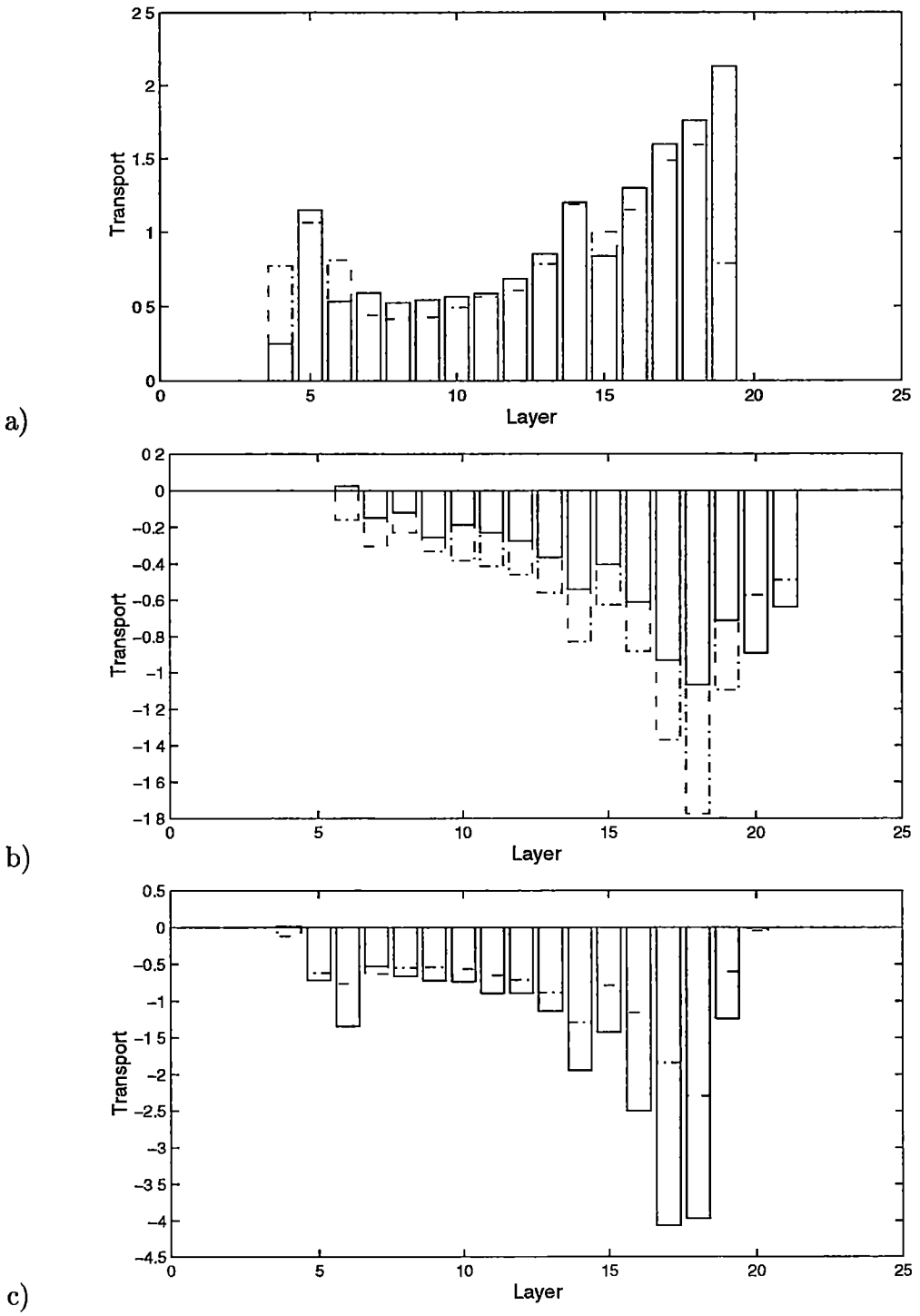

Figure 2.6: Comparison of mass fluxes in each layer ($\times 10^6 m^3 s^{-1}$) from FRAM (continuous line) and inverse solution (mod_fram, dash line) at a) Section 4 b) Section 6 c) Section 8

Figure 2.7 shows the comparison of FRAM and the inverse solution dianeutral mass, heat and salt fluxes for box 3. In FRAM the horizontal and vertical mixing components are diagnosed across each neutral surface. These terms are added to give the total dianeutral FRAM property flux. This shows that the total dianeutral property flux is well reproduced for mass, heat and salt. A similar reproduction is achieved for box 1, box 2 and box 4.

Figure 2.8 shows the total mass transport from the inverse model. A comparisons of Figure 2.8 with the "true" FRAM total transport (Figure 2.3) highlights that some total sections transports are well reproduced (to within $3\times10^6 m^3 s^{-1}$) by the inverse model (sections 1, 2, 3, 4, 5, 6 and 10). The largest difference between the "true" FRAM mass transport and the inverse model solution occurs at section 8 where the difference is $8\times10^6 m^3 s^{-1}$ and smaller differences occur at sections 7 and 9 ($\approx 5\times10^6 m^3 s^{-1}$). A comparison of the inverse solution total heat and salt flux with the "true" FRAM heat and salt fluxes is given in Table C.1.

In this inverse model (model_fram) the dianeutral advective and diffusive heat and salt terms are combined within ACw_h and ACw_s terms respectively. These represent:

$$ACw_c = A\left(\overline{ec} + \overline{e'c'} + \kappa\frac{dc}{dz}\right) \tag{2.12}$$

where

$\overline{ec}$ mean dianeutral property advection

$\frac{dC}{dz}$ dianeutral property gradient

κ diffusivity

$\overline{e'c'}$ dianeutral property advection perturbations from the mean ($\overline{ec}$)

It is desirable to separate the advective and diffusive fluxes. This would enable us to determine the magnitude of dianeutral advective velocities and dianeutral heat and salt diffusivities within ocean regions. These could then be be compared to similar parameters in numerical models enabling assessment of

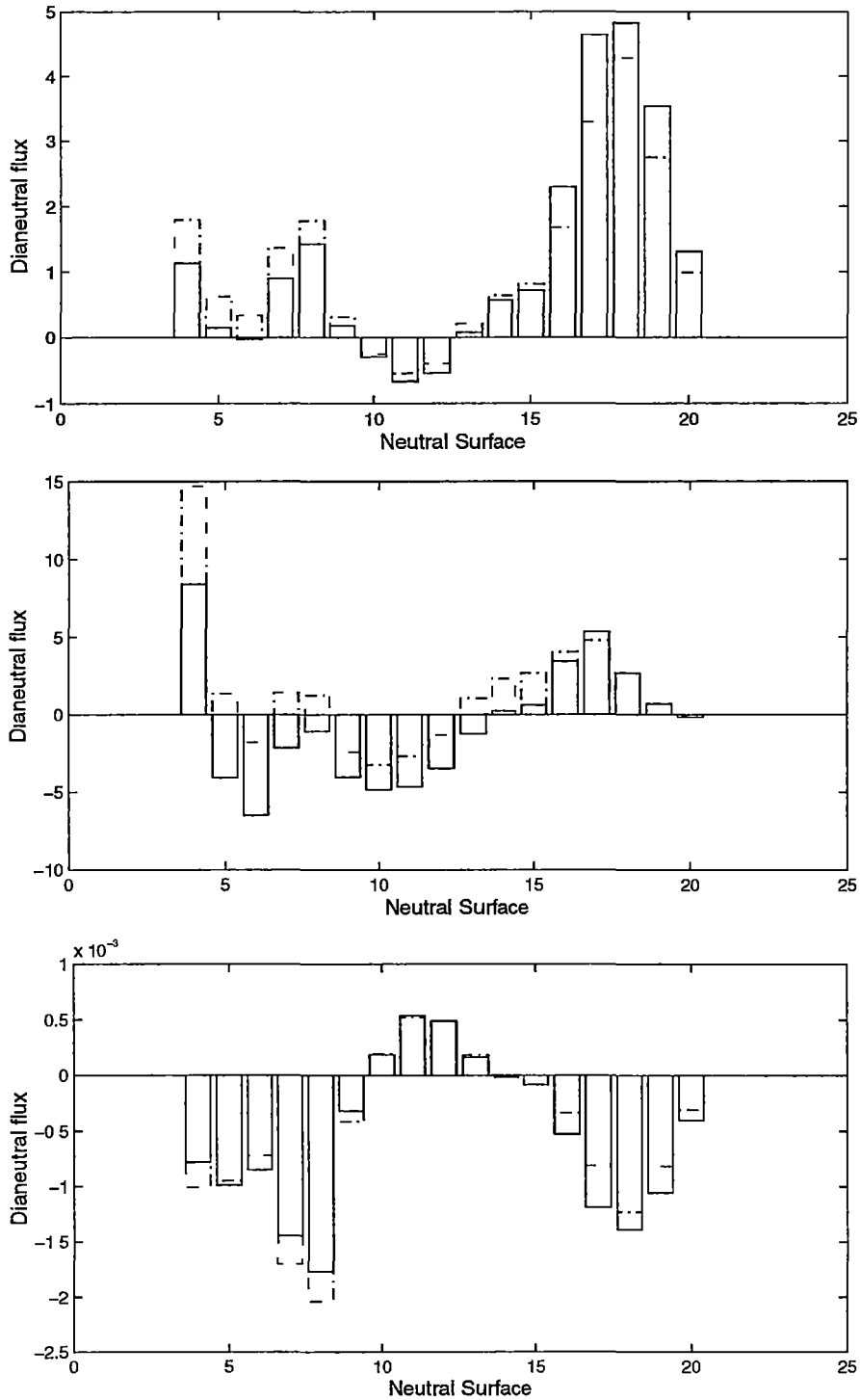

Figure 2.7: Comparison of total dianeutral fluxes within box 3 from FRAM (continuous line) and inverse solution (mod_fram, dash line) a) Mass ($\times 10^6 m^3 s^{-1}$) b) Heat ($\times 10^6$ °C $m^3 s^{-1}$) c) Salt ($\times 10^6$ (psu-35) $m^3 s^{-1}$)

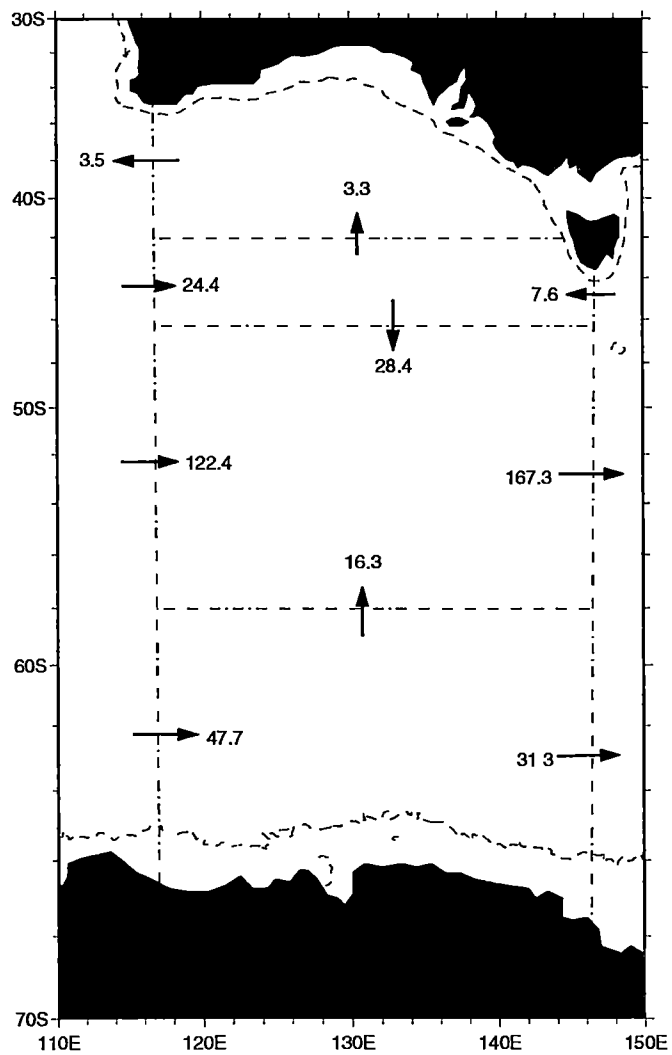

Figure 2.8: Total mass transport ($\times 10^6 m^3 s^{-1}$) from inverse solution at each section defined in Figure 2.1

.

their appropriateness (or lack of) in these models. This may lead to an improvement in the parameterisation of mixing processes in numerical model.

The mass dianeutral "velocity" (w_m) represents the mean dianeutral velocity. Using (w_m) we can find the mean dianeutral heat and salt advective flux. Removing the mean dianeutral advective component from the total dianeutral flux (ACw_c) leaves the effective dianeutral diffusive flux. The term effective dianeutral diffusive flux is used because this term includes not only the dianeutral diffusive flux but also the correlation of grid point variation in layer properties and dianeutral advective velocity ($\overline{e'c'}$) and other eddy processes.

The mean dianeutral advective heat and salt flux is shown in Figure 2.9 (negative transport represents downwelling while positive values indicate upwelling). Figure 2.9 shows that deriving the mean dianeutral property advective flux from the mass flux accurately reproduces the sign of the dianeutral heat and salt mean advective flux, apart from box 4 dianeutral heat advection. n some boxes the magnitude of the dianeutral property advective flux is also well reproduced, while for other boxes (particularly box 3 and 4) the inverse fluxes are 25% to 5o% less than the "true" Fram fluxes.

Figure 2.10 shows a comparison of inverse model effective dianeutral heat and salt diffusion flux with FRAM. A striking feature of Figure 2.10 is that in all boxes and for each property, there are a few layers in which the effective dianeutral diffusion is large. Figure 2.11 shows the size of $\overline{e'c'}$ on particular layers within box 3. Layers 7 and 8 have large $\overline{e'c'}$ on their outcropping edges, while on layer 17, which doesn't outcrop the $\overline{e'c'}$ flux very small. Figure 2.10 shows that the layers in which the $\overline{e'c'}$ dominates the effective dianeutral property diffusion are those which outcrop within the box.

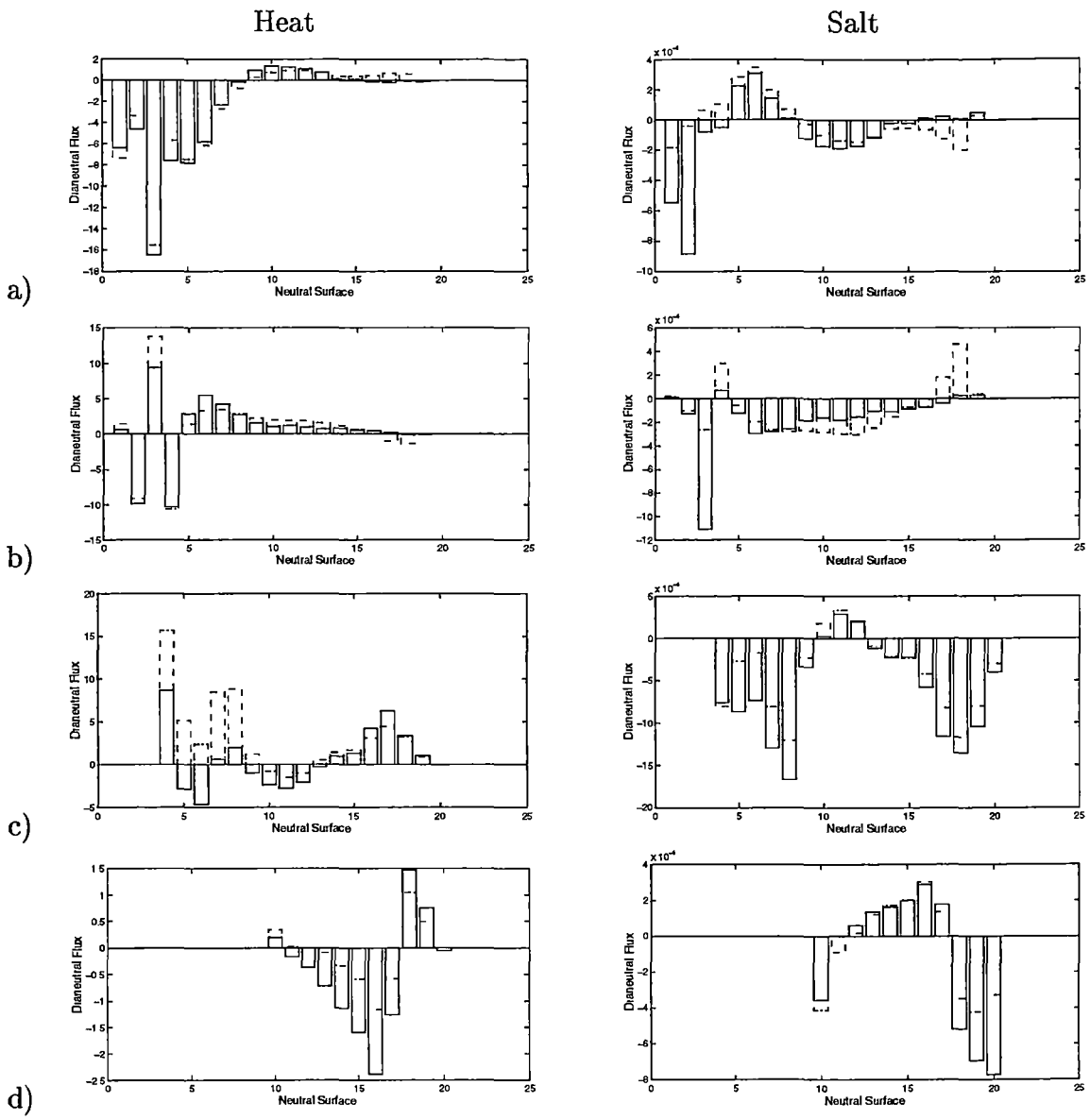

Figure 2.9: Comparison of Layer Mean Dianeutral Heat and Salt Advection between FRAM (continuous line) and inverse solution (dashed line) for a) Box 1 b) Box 2 c) box 3 d) Box 4 Heat ($\times 10^6$ °C $m^3 s^{-1}$) and Salt ($\times 10^6$ (psu-35) $m^3 s^{-1}$)

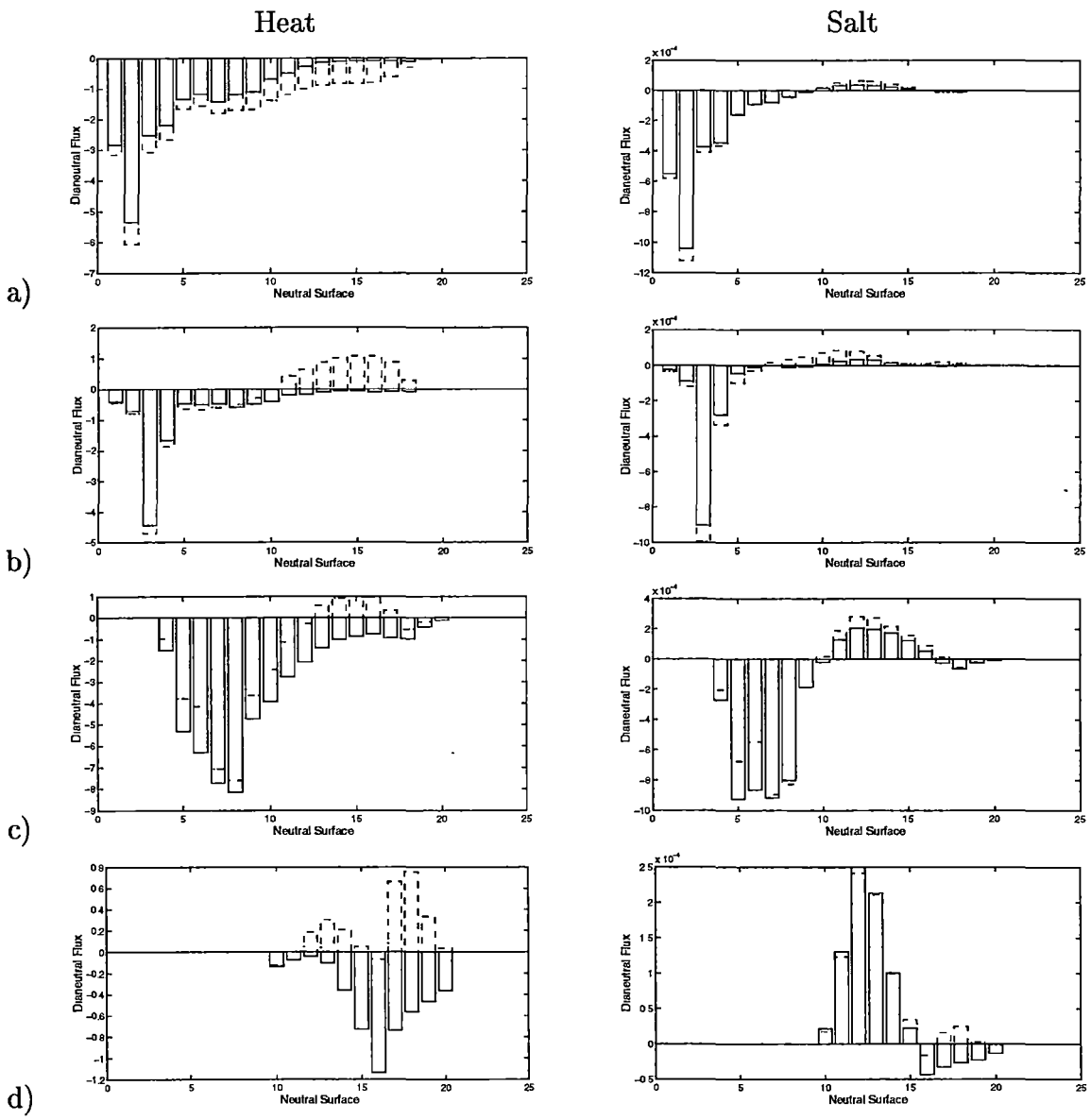

Figure 2.10: Comparison of Layer Dianeutral Effective Heat and Salt Diffusive flux between FRAM (continuous line) and inverse solution (dashed line) a) Box 1 b) Box 2 c) Box 3 d) Box 4 Heat ($\times 10^6$ °C $m^3 s^{-1}$) and Salt ($\times 10^6$ (psu-35) $m^3 s^{-1}$)

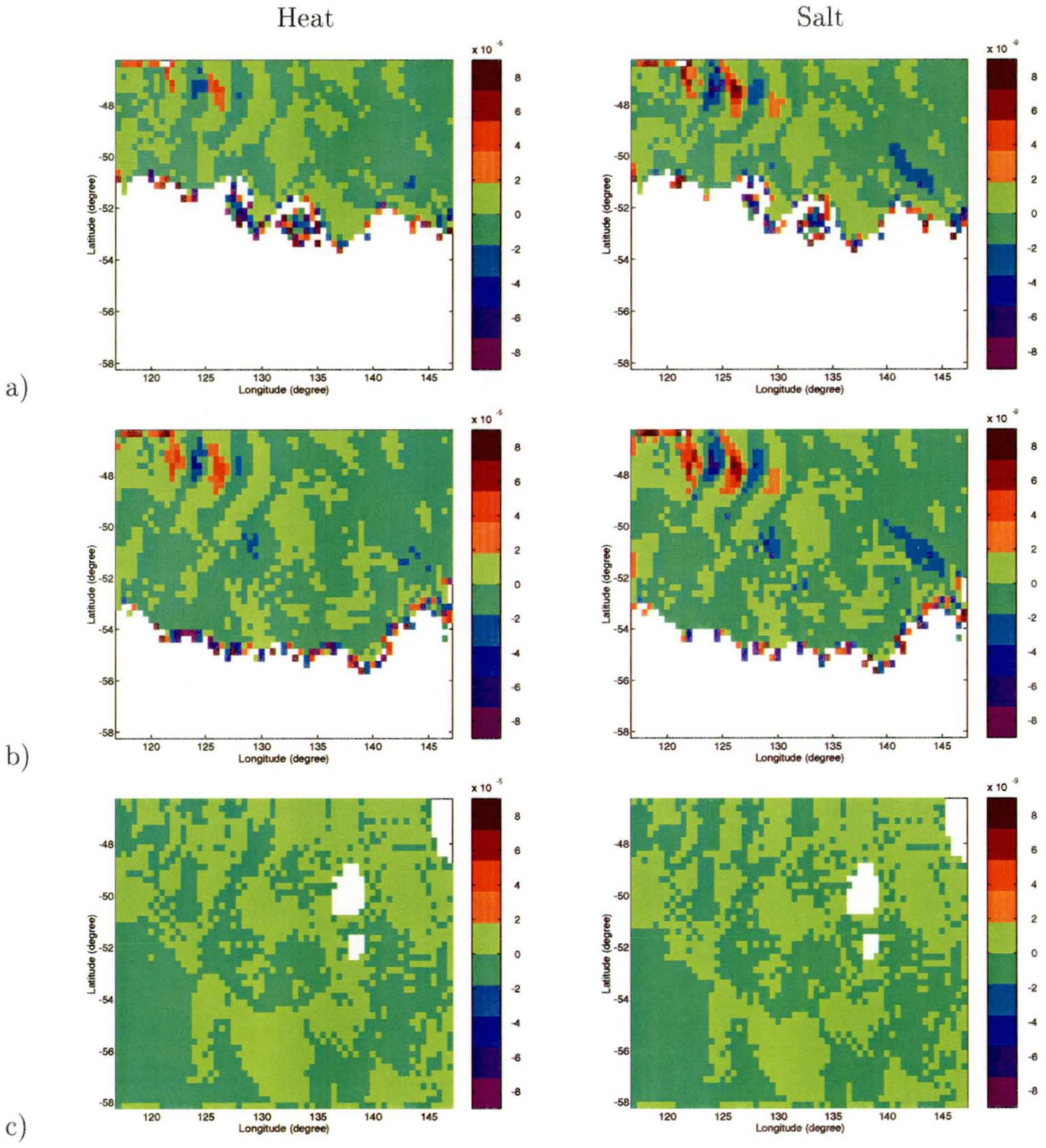

Figure 2.11: Evaluation of $\overline{e'c'}$ in Box 3 for heat and salt on Neutral Surface Layers a) Layer 7 b) Layer 8 c) Layer 17 Heat ($\times 10^6$ °C $m^3 s^{-1}$) and Salt ($\times 10^6$ (psu-35) $m^3 s^{-1}$)

This shows that it is possible to break-down the total dianeutral heat and salt flux their mean dianeutral advection and effective dianeutral diffusion components, although there are some boxes where the fluxes are not reproduced as well as others. Another way of determining the dianeutral property advection and effective diffusion, which may reproduce well all dianeutral advective and effective diffusion fluxes is to include these terms explicitly within the conservation equation. The inverse method then determines the dianeutral advective velocity, effective dianeutral property diffusivity, along with the reference velocity.

Explicit Advection and Effective Diffusion

The conservation equation of the previous inverse model are rewritten to include the dianeutral advection and effective dianeutral property diffusion fluxes, explicitly. Including the dianeutral advective and effective diffusive flux modifies the conservation equation in the following way:

$$\sum_{j=1}^{N} \delta_j \Delta x_j \int_{h_m}^{h_{m+1}} (\rho C_j (v_r + b)_j) + E_j C_j \\ (eAC)_m - (eAC)_{m+1} + \\ (\beta_c A \frac{dC}{dz})_m - (\beta_c A \frac{dC}{dz})_{m+1} \approx 0 \qquad (2.13)$$

In Equation 2.13 variables are as defined in Equation 2.5 apart from $(eAC)_{m,m+1}$, which is the dianeutral advective property flux and $(\beta_c A \frac{dC}{dz})_{m,m+1}$ which represents the effective dianeutral property diffusion. The unknowns solved by this inverse method (mod_expl) are: b, station pair reference velocity; e, the mean dianeutral advective velocity for each neutral density surface and all properties and; β_c, the effective diffusion for each neutral density surface and each property. The matrix system defined still has 210 equations and 641 unknowns. The property gradients $\frac{dC}{dz}$ are diagnosed directly from FRAM.

In this model (mod_expl) there are large off-diagonal terms in matrix **A** associated with the dianeutral terms in the conservation equations. These off-diagonal terms results in a large condition numbers, when the appropriate weights are are applied to the matrix system. (Slight changes to the criteria

used to define the column weights did not improve the condition number.) Although the condition number is large the full rank solution still produces an accurate solution (shown below).

The residuals of this model (mod_expl) are shown in Figure 2.12. The residual are small for each property in each box. Comparing the residuals of this model with the previous model (mod_fram, Figure 2.4) highlights the similarities in the magnitude and sign of the residuals between these models.

The reference velocities (Figure 2.13) are a smoothed representation of the FRAM velocities. A comparison with the previous model reference velocities (Figure 2.5) highlights the similarity between these two models. Although the inverse reference velocities are smooth they still contain enough information to reproduce the associated mass, heat and salt fluxes (Figure 2.14).

This model solves the dianeutral advection and effective diffusion explicitly. A comparison of the mean dianeutral heat and salt flux of this model and FRAM is shown in Figure 2.15. The inverse model provides an accurate description of the mean dianeutral property flux. The model is able to diagnose the vertical structure and magnitude of this flux for all boxes, apart from the surface layers of the advective heat flux in box 3. The comparison of Figure 2.15 with a similar figure for the previous model (Figure 2.9) highlights the similarity of the dianeutral advective flux for these models.

Figure 2.16 show the comparison of the effective dianeutral diffusion between this model (mod_expl) and FRAM. As shown previously the large effective diffusion at certain neutral surfaces result from large $\overline{e'c'}$ terms exist in layers that outcrop within the box region. A comparison of the dianeutral effective property diffusion flux with the previous model (Figure 2.10) shows the similarities between the two inverse models.

The total section transport are shown in Figure 2.17. A comparison of section transport from this model and the "true" FRAM transport (Figure 2.3) shows that the total section transport are well reproduced for sections 1, 2, 4, 9 and 10, to within $3\times10^6 m^3 s^{-1}$. The eastern and western boundaries of box 2 (sections 3 and 5) have a transport error of about $5.5\times10^6 m^3 s^{-1}$. These transport errors compensate each other resulting in good transport estimates at the bounding northern and southern section of box 2 (sections 2 and 4). The

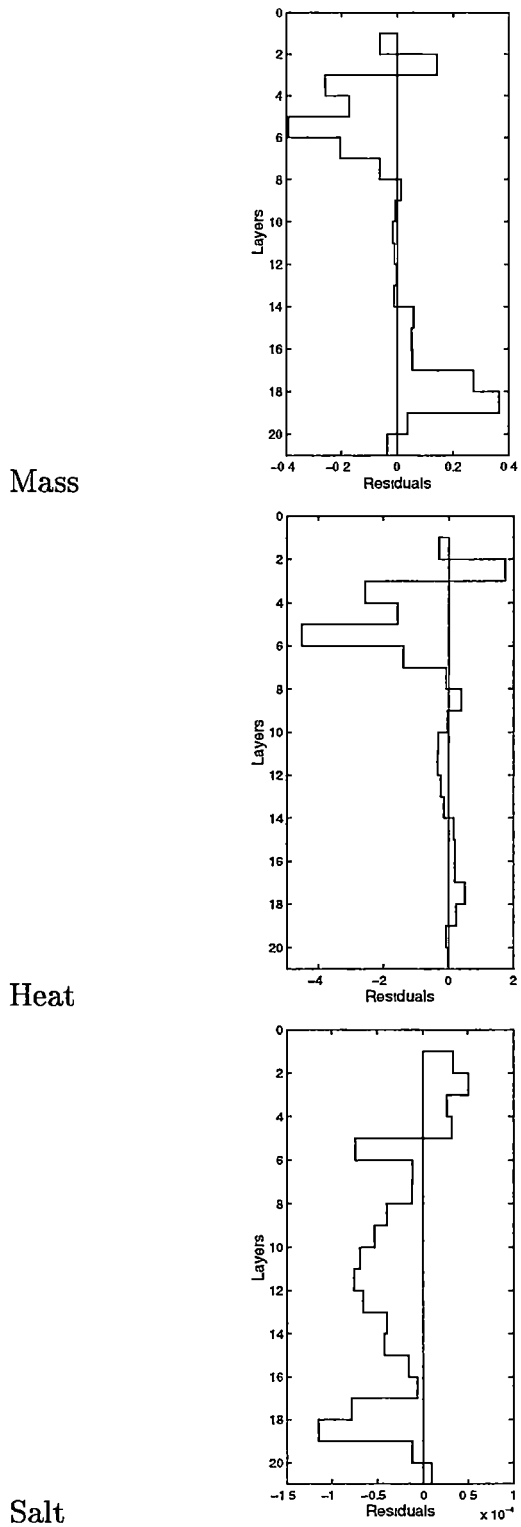

Figure 2.12: Mass, Heat and Salt Residuals in each layer for inverse model that explicitly solves the dianeutral advection and effective diffusion(mod_expl) a) Box 1 b) Box 2 Units: mass ($\times 10^6 m^3 s^{-1}$), heat ($\times 10^6$ °C $m^3 s^{-1}$) and salt ($\times 10^6$ (psu-35) $m^3 s^{-1}$)

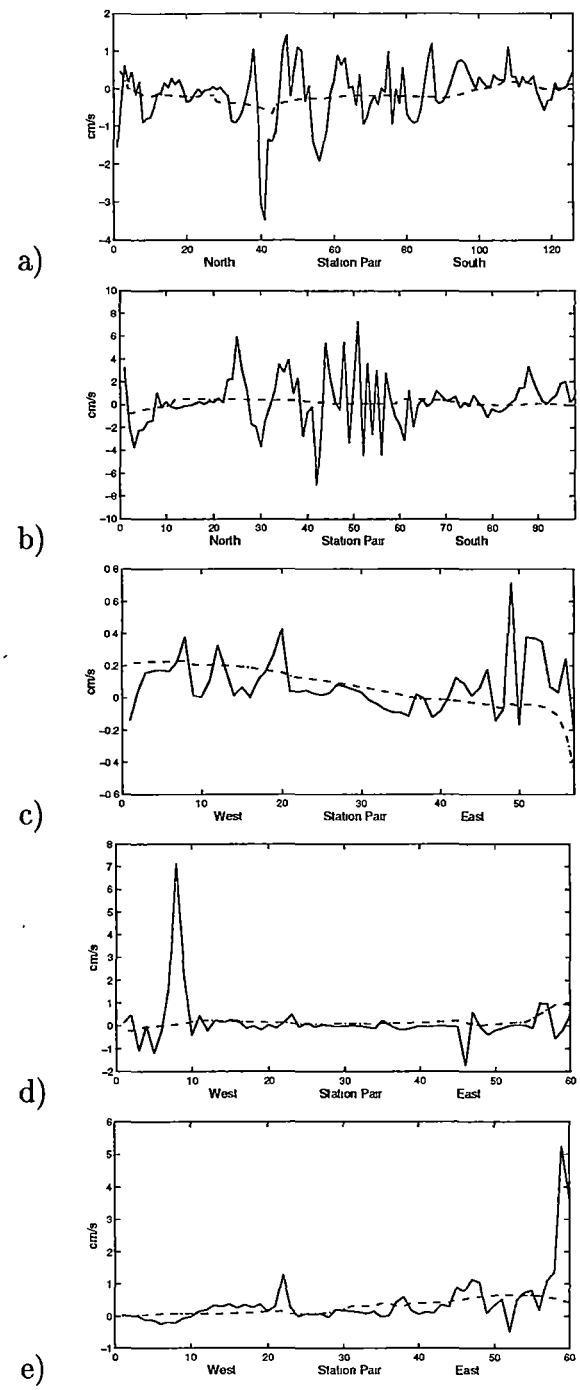

Figure 2.13: Comparison of reference velocities (cms^{-1}) from FRAM (continuous line) and inverse solution with explicit dianeutral mixing (dashed line) at a) 117°E b) 147°E c) 42°S d) 46°S e) 58°S

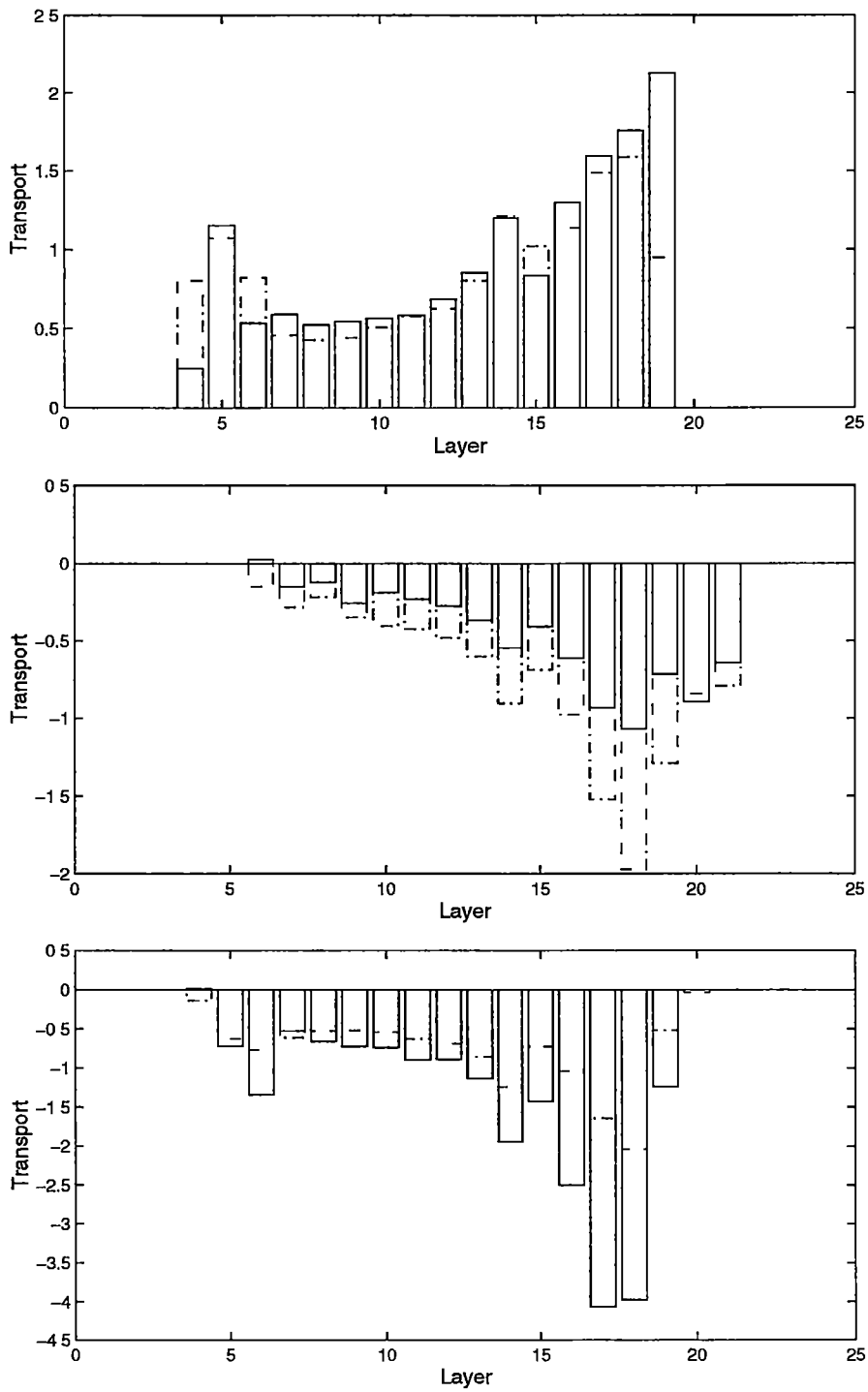

Figure 2.14: Comparison mass reference layer fluxes ($\times 10^6 m^3 s^{-1}$) from FRAM (continuous line) and inverse solution with explicit dianeutral mixing (dash line) at a) Section 4 b) Section 6 c) Section 8

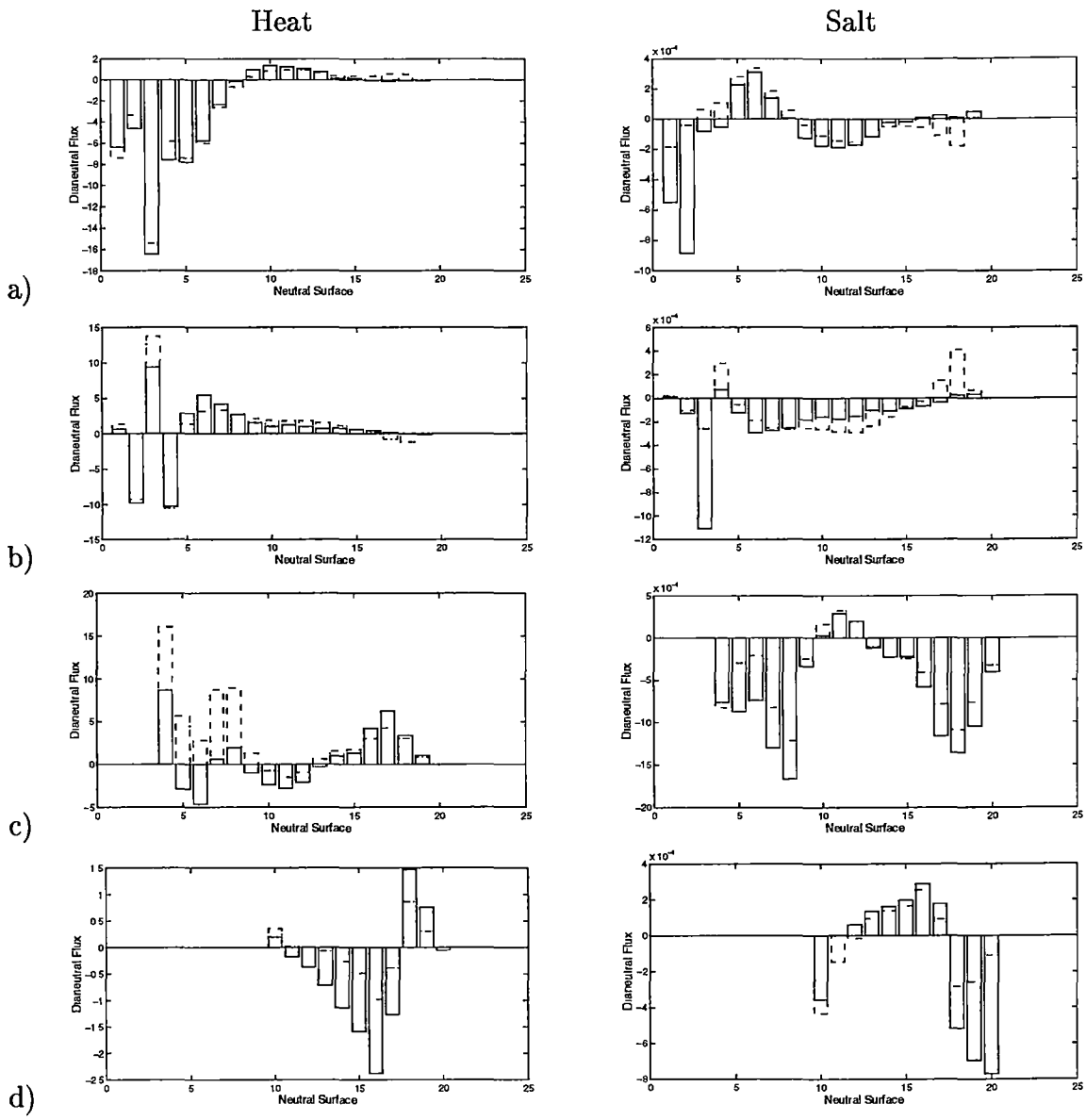

Figure 2.15: Comparison of Layer Mean Dianeutral Heat and Salt Advection between FRAM (continuous line) and inverse solution with explicit dianeutral flux (dashed line) for a) Box 1 b) Box 2 c) box 3 d) Box 4 Heat ($\times 10^6$ °C $m^3 s^{-1}$) and Salt ($\times 10^6$ (psu-35) $m^3 s^{-1}$)

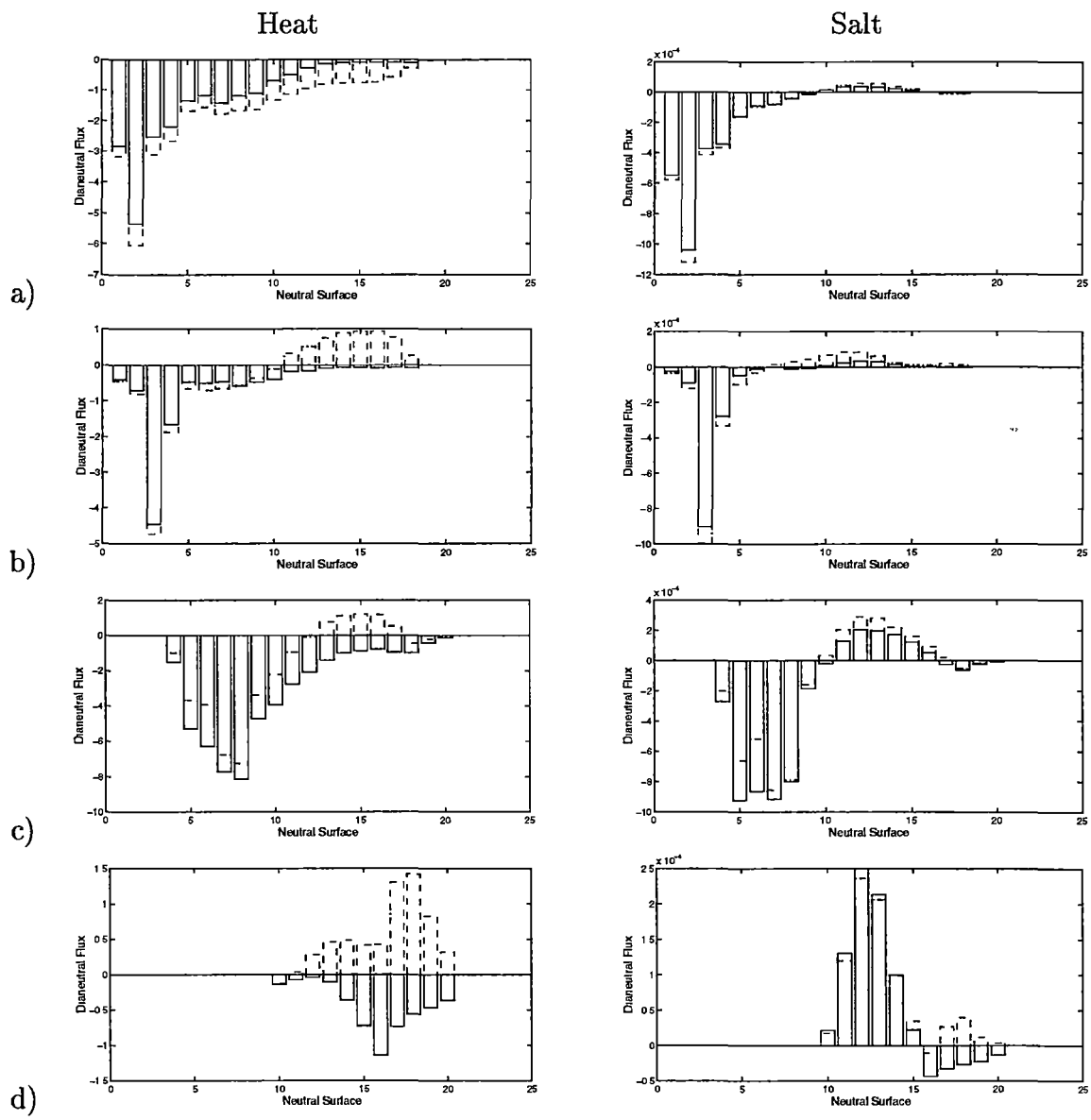

Figure 2.16: Comparison of Layer Dianeutral Effective Heat and Salt Diffusive flux between FRAM (continuous line) and inverse solution with explicit dianeutral flux (dashed line) for a) Box 1 b) Box 2 c) Box 3 d) Box 4 Heat ($\times 10^6$ °C $m^3 s^{-1}$) and Salt ($\times 10^6$ (psu-35) $m^3 s^{-1}$)

largest transport errors of $11\times10^6 m^3 s^{-1}$, $5\times10^6 m^3 s^{-1}$ and $16\times10^6 m^3 s^{-1}$ occur in box 3 across the eastern, southern and western sections (6,7, and 8), respectively. The magnitude of the transport error at section 6 and 8 is two times larger than the transport error in the previous model (Figure 2.8). The transport error at section 7 is similar in both inverse models (mod_fram and mod_expl).

Solving the dianeutral flux explicitly into the advection and effective property diffusion provides an estimate of the mean dianeutral velocity and heat and salt diffusivity across each neutral surface within the box region. Figure 2.18 shows the comparison of between the FRAM and the inverse model dianeutral velocity. The inverse model derived dianeutral velocities agree with the FRAM velocities across most neutral surfaces although there is a divergence in the agreement of the velocities across the deepest neutral surfaces. The velocities across the deepest neutral surfaces in box 1 are an order of magnitude smaller than the remaining boxes, but are of the same order as previous estimates of deep vertical velocities in the Atlantic and Indian Oceans (Warren and Speer 1991; Speer and Zenk 1993; Robbins and Toole 1997). In the remaining three boxes the dianeutral velocities are $O(10^{-4} cms^{-1})$, which are an order of magnitude larger than previous estimates of the vertical velocity south of the Polar Front Zone (Metzl et al. 1990).

Figure 2.19 and Figure 2.20 shows the comparison between the heat and salt inverse and "true" FRAM diffusivities (calculated from both the horizontal and vertical dianeutral fluxes), also plotted is the "actual" FRAM heat and salt diffusivity (dotted $5 \times 10^{-5} m^2 s^{-1}$). The heat and salt dianeutral inverse and "true" FRAM diffusivities are approximately an order of magnitude larger than previous estimates (Olbers 1991). These figures show that: the "true" dianeutral FRAM heat and salt diffusivities are different from the prescribed actual diffusivity in FRAM particularly across outcropping or undercropping layers; the "true" FRAM and inverse dianeutral diffusivities are not always positive; the heat and salt "true" FRAM and inverse dianeutral diffusivities are different and; inverse dianeutral diffusivities are largest across outcropping and undercropping neutral surfaces. The salt (and across some neutral surfaces for heat) diffusivity across completely internal neutral surfaces in boxes 1 and 2 are

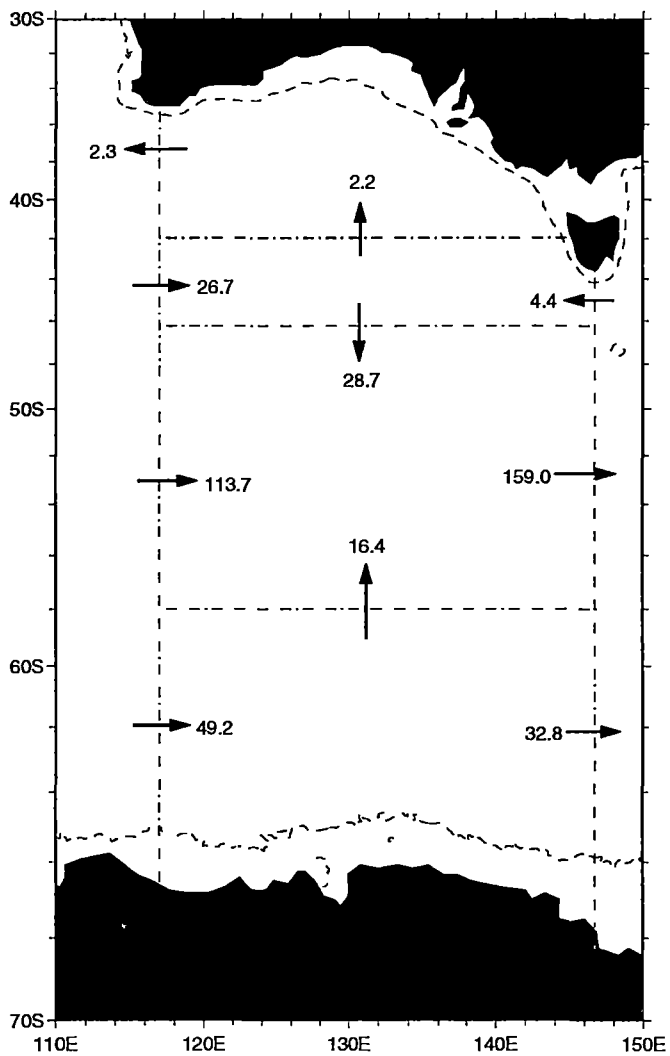

Figure 2.17: Total mass transport ($\times 10^6 m^3 s^{-1}$) from inverse solution with explicit dianeutral flux at each section defined in Figure 2.1

.

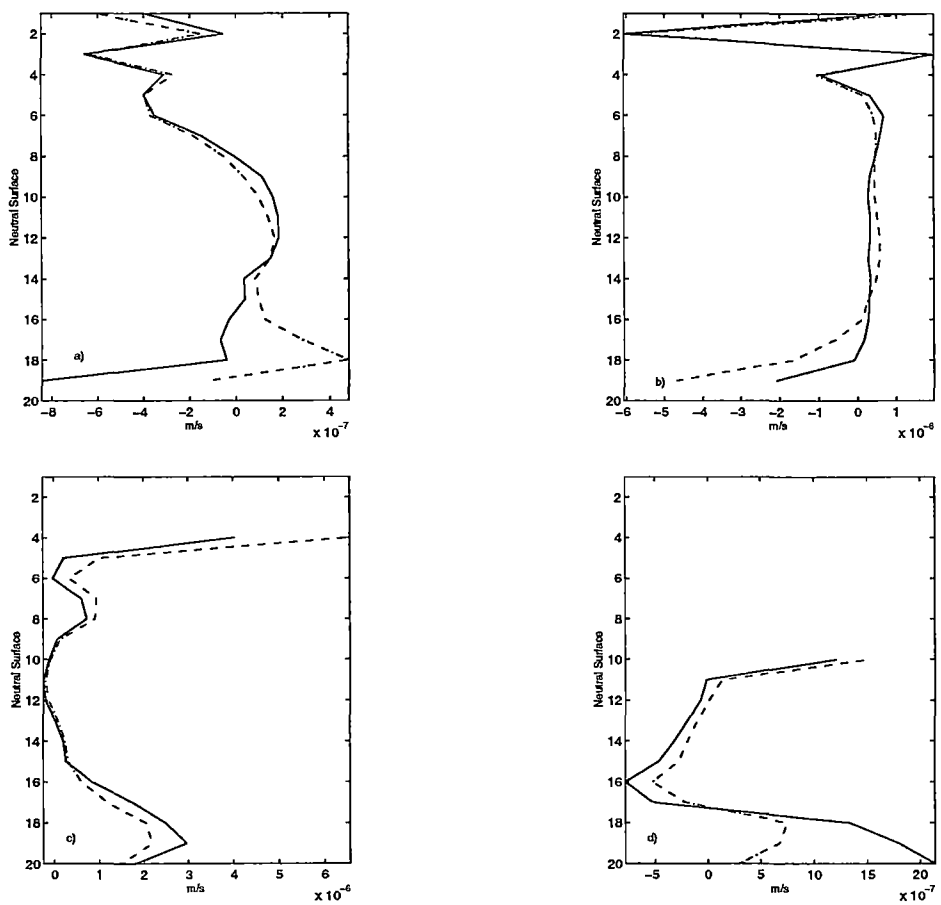

Figure 2.18: Comparison of dianeutral velocity between FRAM (continuous line) and inverse model (dot-dashed line) with explicit dianeutral advection and effective diffusion. a) Box 1 b) Box 2 c) Box 3 d) Box 4

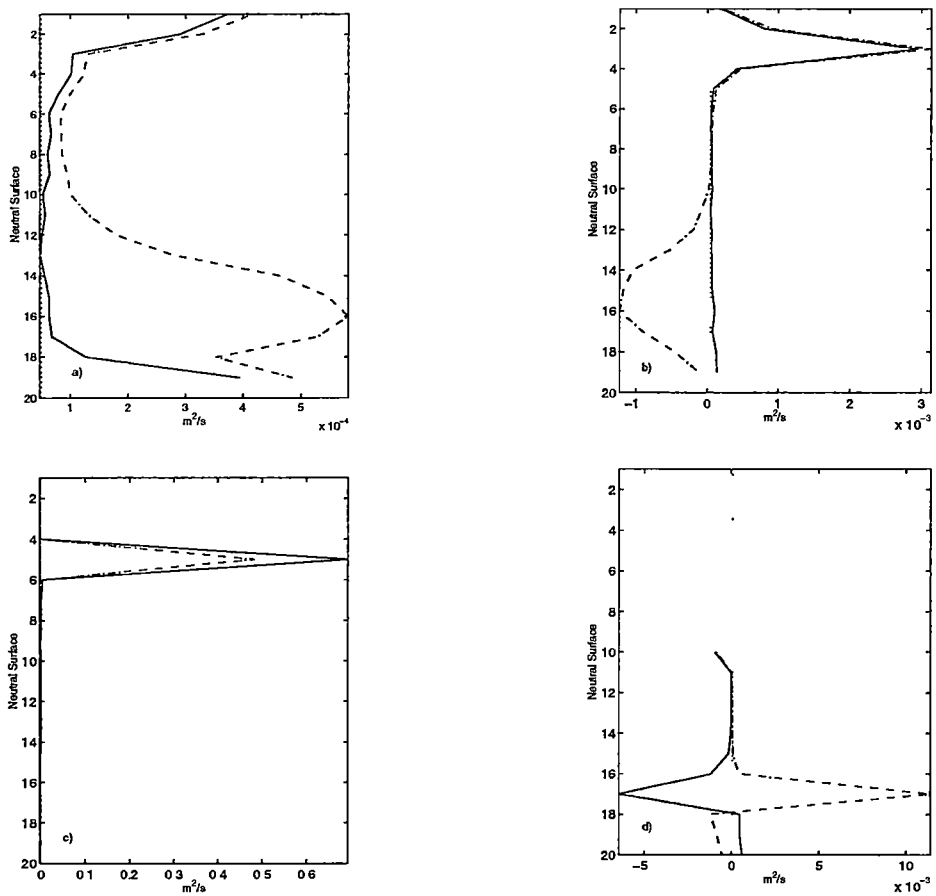

Figure 2.19: Comparison of Dianeutral Effective Heat diffusivity between "true" FRAM (continuous line), and inverse solution with explicit dianeutral velocity and heat diffusivity (dot-dashed line) for a) Box 1 b) Box 2 c) Box 3 d) Box 4. The actual FRAM heat and salt diffusivity of $5 \times 10^{-5} m^2 s^{-1}$ is shown as dotted line

small, and agree with the actual FRAM diffusivity. This suggests that for inverse models that have defined boxes in low latitudes, where only the upper and lower layer outcrop or undercrop parameterising the diffusivity as Fickian diffusion (where the diffusion flux is given as a positive diffusivity multiplied by a vertical gradient and neutral surfaces area) is appropriate. For regions (such as the Southern Ocean box 3 and 4) where numerous layers outcrop or undercrop the Fickian parameterisation of diffusion may not be appropriate because of the size and dominance of other eddy processes such as $\overline{e'c'}$

The above discussion shows that both inverse models, model_fram for which the advection and effective property diffusion fluxes are found implicitly

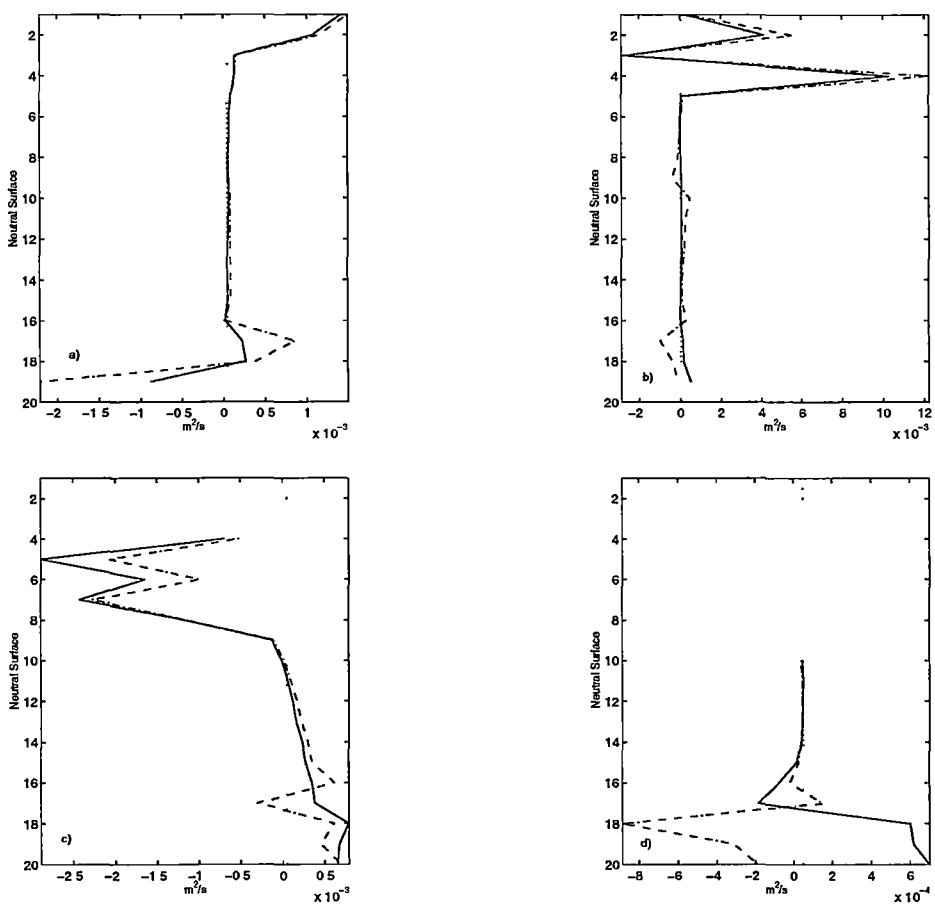

Figure 2.20: Comparison of Dianeutral Effective Salt Diffusivity between FRAM (continuous line) and inverse solution with explicit dianeutral velocity and salt diffusivity (dot-dashed line) for a) Box 1 b) Box 2 c) Box 3 d) Box 4
. The actual FRAM heat and salt diffusivity of $5 \times 10^{-5} m^2 s^{-1}$ is shown as dotted line

from the total dianeutral property fluxes and model_expl which solves explicitly the advection and effective property diffusion fluxes, reproduce well the "true" FRAM lateral and dianeutral property fluxes. In the "FRAM" inversion the errors such as storage terms, and source/sink terms are treated as known within Equation 2.5 and Equation 2.13. Resulting in the conservation equation that contain no errors. Inverse methods applied to actual hydrographic data contain errors including non-synoptic and instrument errors, adding random error to the FRAM "data" will recreate the inherent error contained in actual hydrographic data used in inverse models.

Random error (10%) is added to the FRAM "data" and the inverse models using the two forms of the conservation equations (Equation 2.5 and Equation 2.13) are re-calculated. The addition of the 10% random error to the FRAM "data" results in small changes to the total section transport using both the implicit and explicit dianeutral advective and effective diffusive forms of the conservation equations (Table C.3 and Table C.4, respectively).

2.2.3 Dianeutral Fluxes - Implicit or Explicitly Resolved

Mod_fram and mod_expl include dianeutral property fluxes for each conserved property. Mod_fram has a dianeutral statement for each property on each layer. The dianeutral mass flux represents the mean dianeutral advection flux. This allows the heat and salt dianeutral flux to be separated into their mean advective and effective diffusive flux. Mod_expl solves the dianeutral property advective flux and effective dianeutral property diffusive flux explicitly.

The solutions obtained from mod_fram and mod_expl are similar. The reference velocities are smoothed representations of the FRAM field (Figure 2.5 and Figure 2.13). Although the inverse reference velocities contain minimal structure the inverse reference layer fluxes reproduced well the "true" FRAM reference layer fluxes (Figure 2.6 and Figure 2.14). The dianeutral advective and effective diffusivity fluxes resolved by both models are similar and agree well with the FRAM dianeutral advective and effective property diffusion flux. A comparison of the total section flux between each inverse model and FRAM (Table C.1 and Table C.2) shows that although the inverse reference velocities are similar (overall) the small differences between mod_fram and mod_expl

result in mod_fram agreeing closer to the "true" FRAM flux.

In the inverse models using FRAM "data" I have investigated the form the conservation equation may take to improve the accuracy of the inversion. Mod_fram solves the total dianeutral flux for each property. The total dianeutral property flux is then separated into the mean dianeutral advection and dianeutral effective diffusive components. In model_expl the dianeutral property advective and effective property diffusive fluxes are included explicitly and provide estimates of the dianeutral velocity and effective heat and salt diffusivity. The property gradients used in mod_expl are determined directly from FRAM. Both forms of the conservation equations reproduce well the "true" FRAM solution, but which is more appropriate when using actual hydrographic data in inverse methods?

Mod_fram provides a better representation of the total transport across the bounding "hydrographic" sections. Mod_expl requires knowledge of the property gradients across or surrounding the neutral surfaces in the regions encompassed by the hydrographic sections. There are a number of difficulties associated with estimating the property gradients when using actual hydrographic data. The gradients could be derived as a composite from the bounding hydrographic sections, but the non-synoptic nature of the hydrographic sections could bias these gradients, particularly in the thermocline. The gradients could be determined from climatological data. The question then arises as to what is the appropriate integral range, surrounding the neutral surface, to compute the property gradients. The hydrographic data allows the gradients to be calculated over a small interval while the climatological data could have to be interpolated into a finer vertical resolution or the gradients would be calculated over a layer depth interval. The calculation of the gradients will introduce more errors to the conservation equations, which may be significant.

In the FRAM study the dianeutral effective property diffusion fluxes are shown to not only contain the property diffusion but also other eddy processes. Figure 2.11 shows the large dianeutral effective property diffusion flux is associated with the dianeutral flux of $\overline{e'c'}$ at the outcropping regions of the neutral surfaces. The effect of the other eddy processes contained in the dianeutral effective property diffusion flux make interpretation of the "effective

diffusivity" solved by the inverse solution difficult particularly in regions where numerous upper and deep neutral surfaces outcrop or undercrop, respectively.

There appears to be no gain, in solution accuracy, in determining the dianeutral property advection and effective diffusion fluxes explicitly in inverse models. The uncertainty in determining the property gradients, when actual hydrographic data is used in inverse methods and the interpretation of the inverse derived "effective diffusivity" in regions of the ocean where numerous layer outcrop or undercrop (such as the Southern Ocean) suggest that it is more practical to use conservation equations that have separate dianeutral flux for each property as given in Equation 2.5 and used in mod_fram.

Chapter 3

Model Description

In the previous section I investigated the most appropriate form of the conservation equations in inverse methods. In this section I will give a brief description of hydrographic sections used in this study of the Southern Ocean and adjacent ocean basins circulation, and give specific details about the design of the inverse model.

3.1 Description Hydrographic Data

The position of the hydrographic sections and the regions they define are shown in Figure 3.1. Table 3.1 gives the year and season of the hydrographic sections. The sections in this study are recent high quality hydrographic sections, apart from the Ind18 section. The Pac32 section (World Ocean Circulation Experiment (WOCE) P6) was made available by John Toole and John Church. Other WOCE sections include the S. Aust (SR3_1994) and the Drake P. (S1) sections.

A brief description of the hydrographic data in this study is given. Some sections have been described previously, in other studies. The reader is referred to these where appropriate.

3.1.1 Atlantic 17°S (SAVE 2)

At the SAVE 2 section (South Atlantic Ventilation Experiment) the thermocline deepen from the east to the west (Figure 3.2). At 1000 dbars the salinity minimum associated with AAIW is evident (Figure 3.3). The salinity

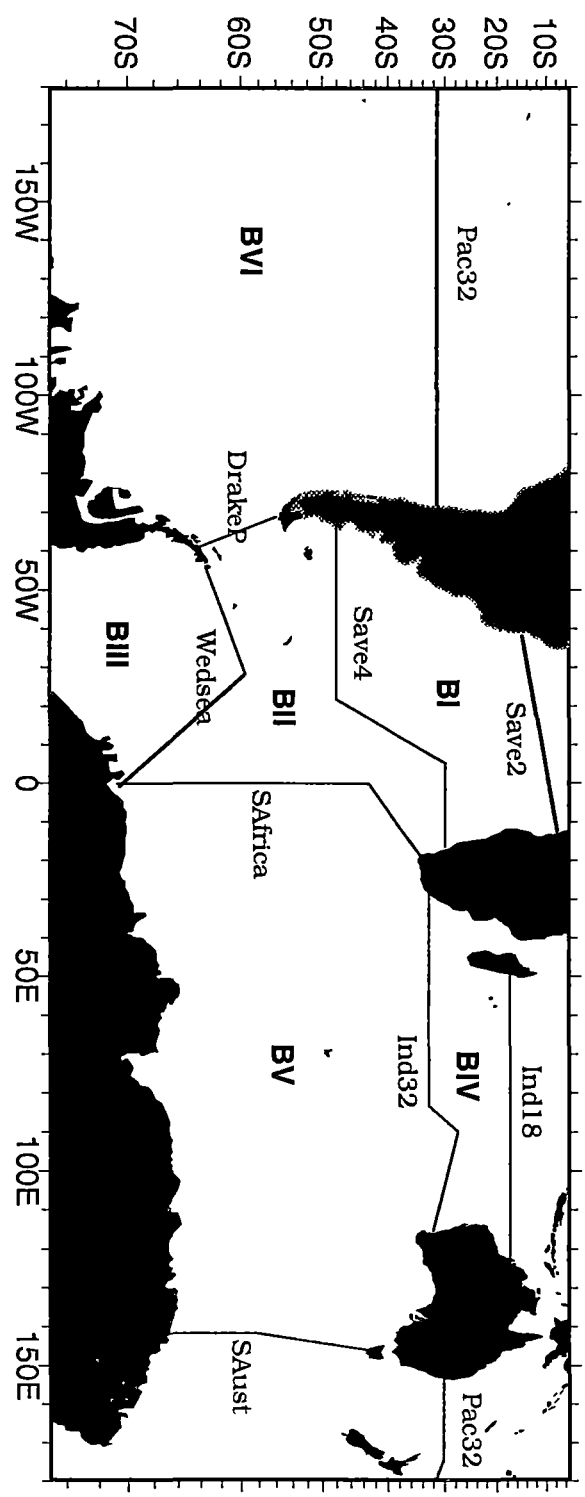

Figure 3.1: Position of Hydrographic sections and box regions used in the inverse model

Section	Year	Season
SAVE 2	1988	Summer
SAVE 4	1989	Summer
Drake P	1990	Summer
S. Africa	1984	Summer
Weddell Sea	1984	Summer
Ind18	1976	Winter
Ind32	1987	Summer
S. Aust (SR3)	1994	Summer
Pac32	1992	Winter

Table 3.1: The hydrographic section (month and year) used in this study.

minimum is strongest in the Brazil basin and weakens to the east. In the eastern boundary an oxygen minima is evident at 500 dbars (Figure 3.4). These low oxygen concentration result from fallout and regeneration of biogenic material within the euphotic zone (Reid 1989).

The salinity maxima (> 34.9) of NADW is present below the AAIW salinity minima. NADW has a temperature of between 3°C to 2 °C. The NADW salinity maxima is seen across the section in both the Brazil and Angola basins, although it thins slightly from west to east (Figure 3.3). The oxygen maxima associated with NADW is strongest in the Argentine basin with values > 250 μmol.kg^{-1} (Figure 3.4).

Below 4000 dbars there are major difference in the property profiles between the Brazil and Angola basins. Within the Brazil basin a temperature minimum of < 0.2°C is seen on the western slope, with associated oxygen maximum and salinity minimum (Figure 3.2, Figure 3.4 and Figure 3.3). The temperature, salinity and oxygen sections are more uniform in the Angola basin. The difference in property characteristics between the Brazil and Angola basins highlights how the bottom circulation is guided by topography. AABW flows directly into the Brazil basin via a deep western boundary current. In the Angola basin water below 4000 dbars enters from the north over the Guinea Rise (Warren and Speer 1991).

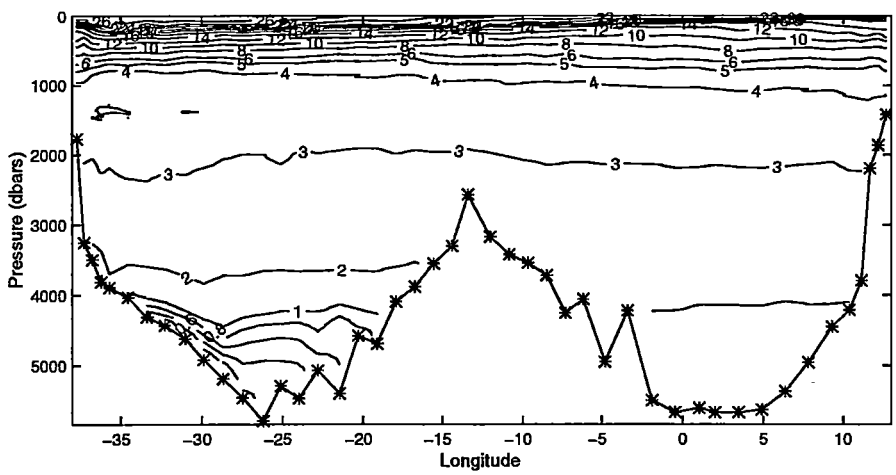

Figure 3.2: Potential Temperature (°C) at SAVE 2

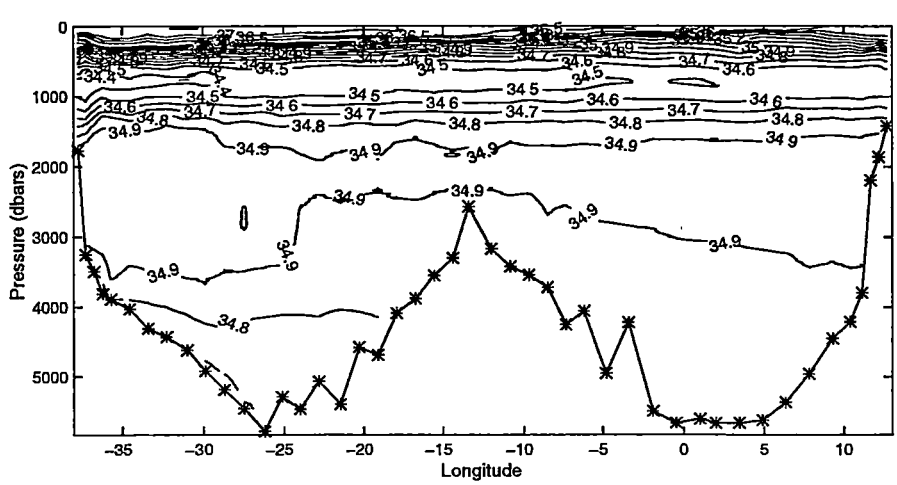

Figure 3.3: Salinity (psu) at SAVE 2

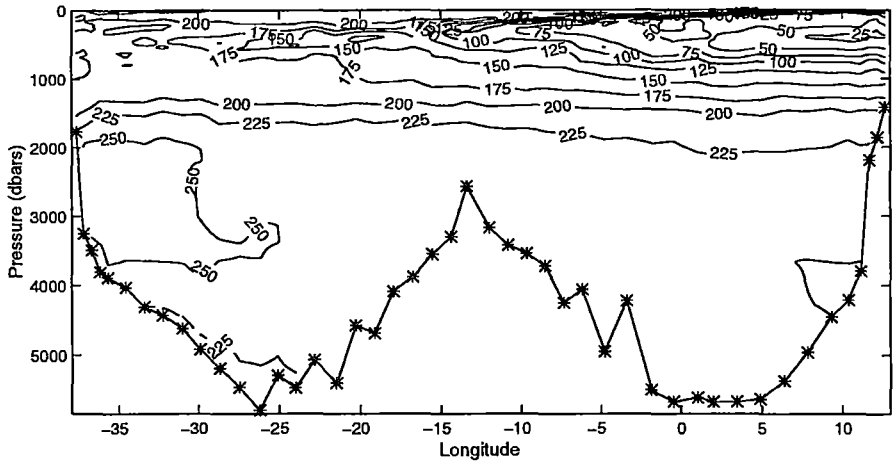

Figure 3.4: Oxygen (μmol.kg^{-1}) at SAVE 2

3.1.2 Atlantic 30°S-40°S (SAVE 4)

The SAVE 4 section is at 30°S from the African coast to the Mid-Atlantic ridge, runs parallel to the ridge between 30°S and 47°S and is completed along 47°S to the South American coast. These three portions sample water masses of varying origins and shows the interaction between Antarctic and subtropical waters.

Eastern Basin 30°S

The surface water is warm, salty and depleted in oxygen (Figure 3.5, Figure 3.6 and Figure 3.7). Centred at 800 dbars is the salinity minimum (< 34.4) which marks AAIW (Figure 3.6). The AAIW salinity minimum is strongest near the western boundary (Figure 3.6). Associated with the salinity minimum is an oxygen maximum of > 200 μmol.kg^{-1} (Figure 3.7).

The oxygen minima between 1000 - 2000 dbars highlights UCDW (Figure 3.7). The salinity maxima (> 34.8) shows the core of NADW, and is associated with a nitrate minimum < 25 μmol.kg^{-1} and oxygen maximum > 225 μmol.kg^{-1} (Figure 3.8 and Figure 3.7). In the Cape basin, below 4000 dbars, temperatures < 1 °C and oxygen maximum (> 225 μmol.kg^{-1}) identify AABW (Figure 3.5 and Figure 3.7).

Mid-Atlantic Ridge

Over the mid-Atlantic ridge strong vertical and horizontal gradients in temperature and salinity identify numerous fronts. The temperature and salinity gradients at 15°W identify the SAF (Figure 3.5 and Figure 3.6). At the SAF, the AAIW salinity minimum deepens to 800 dbars and the surface temperature increases from 8°C to 12°C (Figure 3.5 and Figure 3.6). This front marks the boundary between PFZ and SAZ. Slightly further east is the STF (10 ° W). At this front the temperature increases from 13°C to 16°C and the salinity increases 35.2 to 35.5 (Figure 3.5 and Figure 3.6). The STF forms the southern boundary of the subtropical gyre. Its associated current is the South Atlantic Current (SAC) (Stramma and Peterson 1990). Surface waters north of the STF are warm and salty and the salinity minimum of AAIW is at 1000 dbars (Figure 3.6).

Western Basin 47°S

This portion of SAVE 4 samples the Argentine Basin. The SAF, after passing through Drake Passage forms a northward western boundary current, the Malvinas Current, adjacent the South American coast (Peterson 1992). A salinity minimum is found at or near the surface, apart from where warm, salty meanders or eddies are found (Figure 3.6). The warm, salty meanders or eddies result from meanders in the Brazil-Malvinas Confluence. A thermostad (5°C to 3°C) is present in the upper 500 m which characterises Subantarctic Mode Water (SAMW) in this region.

An oxygen minimum layer at 1200 dbars highlights the presence of UCDW (Figure 3.7). The salinity maxima (> 34.9), nitrate minima (< 28 μmol.kg^{-1}) and relative high oxygen at 2500 dbars identifies NADW (Figure 3.6, Figure 3.7 and Figure 3.8).

AABW is seen below 3000 dbars (temperature < 1 °C). The temperature minimum of < -0.2 °C and oxygen maximum of > 225 μmol.kg^{-1} identifies WSDW within the Argentine basin (Figure 3.5,Figure 3.6 and Figure 3.7).

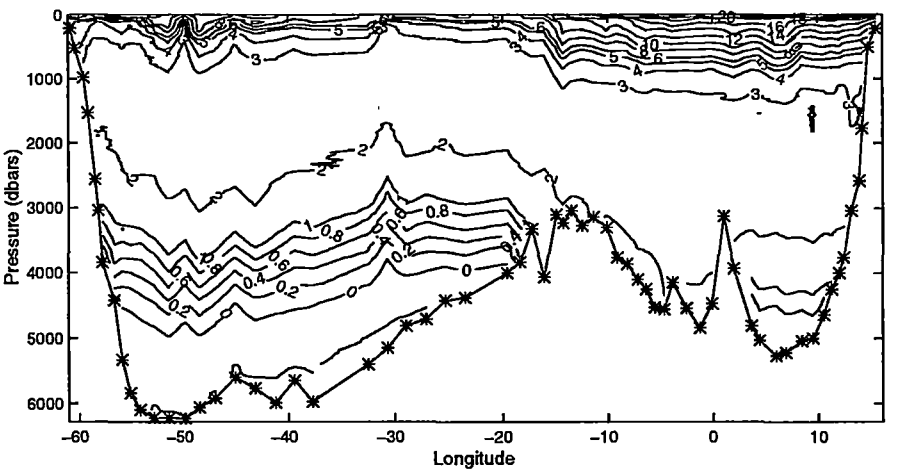

Figure 3.5: Potential Temperature (°C) at SAVE 4

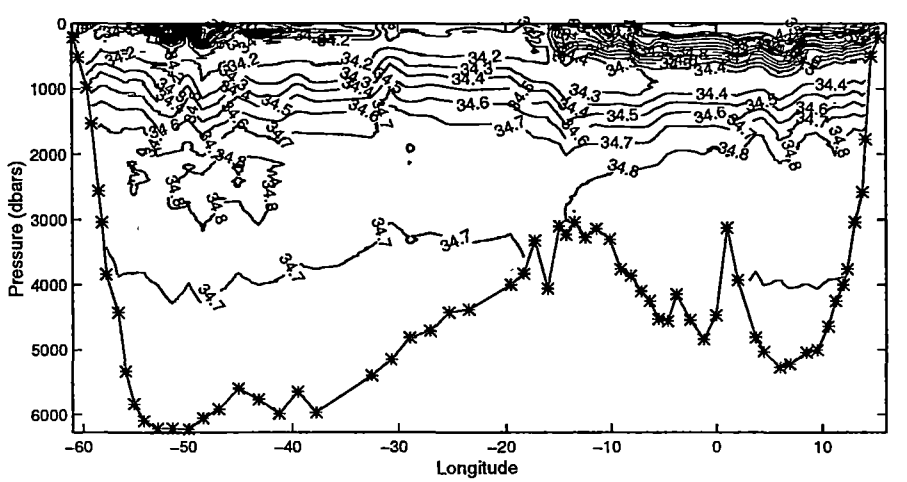

Figure 3.6: Salinity (psu) at SAVE 4

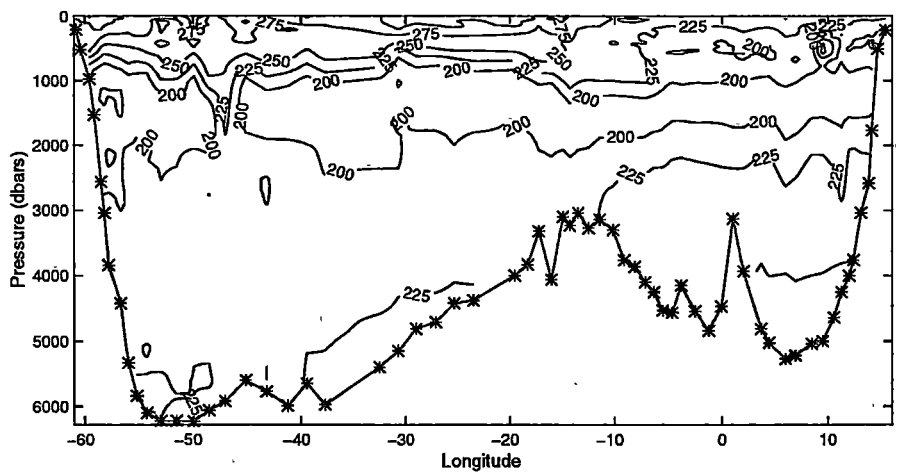

Figure 3.7: Oxygen (μmol.kg^{-1}) at SAVE 4

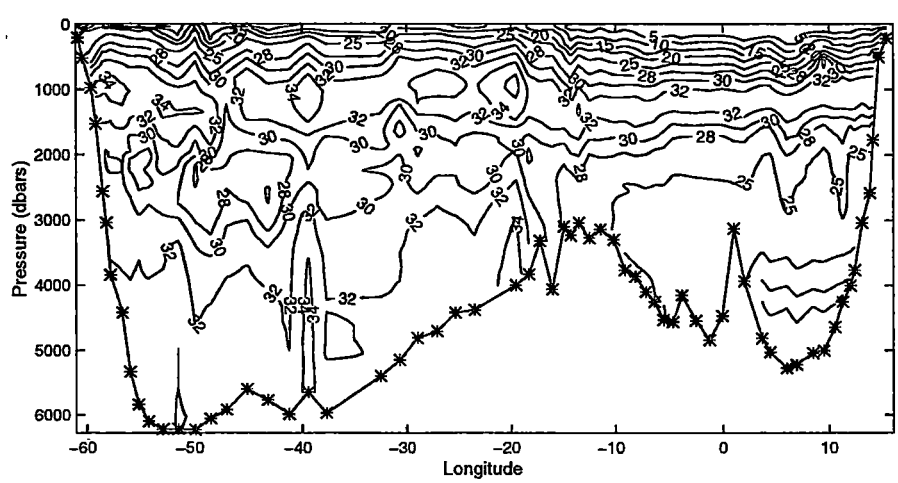

Figure 3.8: Nitrate (μmol.kg^{-1}) at SAVE 4

3.1.3 Drake Passage (DrakeP)

A detailed description of the Drake Passage properties is given by Roether et al. (1993).

Frontal positions identified by Roether et al. (1993) include the APF at 61°S and the SAF at 58 °S. These features have associated sharp vertical and horizontal gradients in temperature and salinity (Figure 3.9 and Figure 3.10). A secondary Polar Front was identified at 60 °S. This feature is similar to a secondary front identified by (Sievers and Nowlin 1984).

Within the temperature and salinity profiles CDW (temperature between 3°C and 1°C and oxygen < 200 μmol.kg^{-1}) can be identified (Figure 3.9 and Figure 3.11). An oxygen minimum (< 175 μmol.kg^{-1}) associated with UCDW dominates the CDW, particularly north of 58.5°S (Figure 3.11). The southward shoaling of CDW is highlighted by the 34.7 salinity contour.

South of the APF the surface waters are cold and fresh. A shallow seasonal thermocline caps the subsurface temperature minimum (< -0.2 °C) of Antarctic Surface Water (Figure 3.9).

Inflow of bottom water from the Pacific, adjacent to the Antarctic continental slope, results in high oxygen and silica concentrations (Figure 3.11 and Figure 3.12). Roether et al. (1993) note that the APF is identified further south than previous studies, therefore restricting the influence of Pacific bottom water within Drake Passage.

3.1.4 South of Africa 0°S (SAfrica)

The properties and structure of the section south of Africa (AJAX 2) are described in detail by Whitworth and Nowlin (1987). The section used in this studies differs to that used by Whitworth and Nowlin (1987) by the addition of stations from AJAX 1 to fill gaps from the African coast to the beginning of AJAX 2. The two AJAX sections are separated by two months.

A weak Subtropical Front (STF) is located between 40°S and 45°S. Strong vertical and horizontal gradients in temperature and salinity identify the Subantarctic Front (SAF) at 48°S and the Polar Front (APF) at 52°S (Figure 3.13 and Figure 3.14).

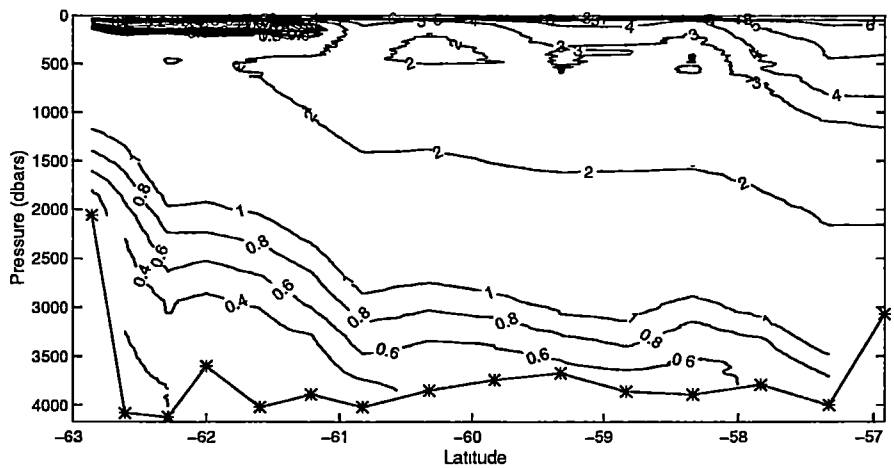

Figure 3.9: Potential Temperature (°C) at Drake Passage

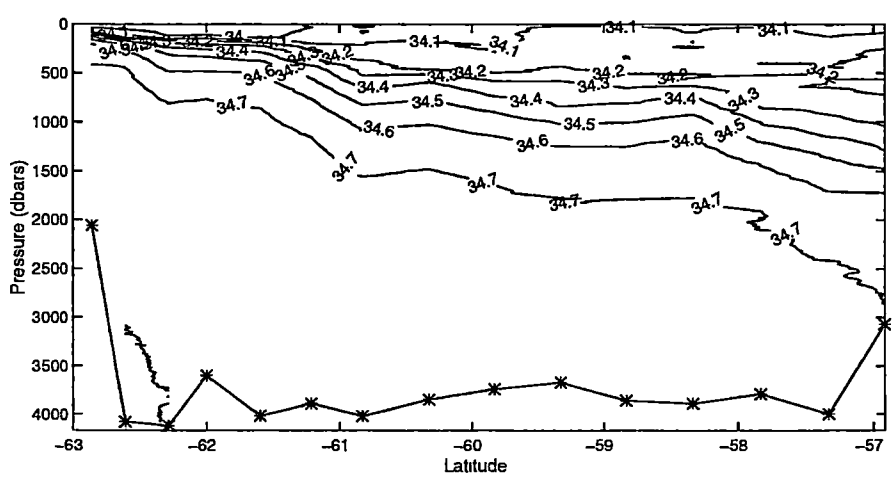

Figure 3.10: Salinity (psu) at Drake Passage

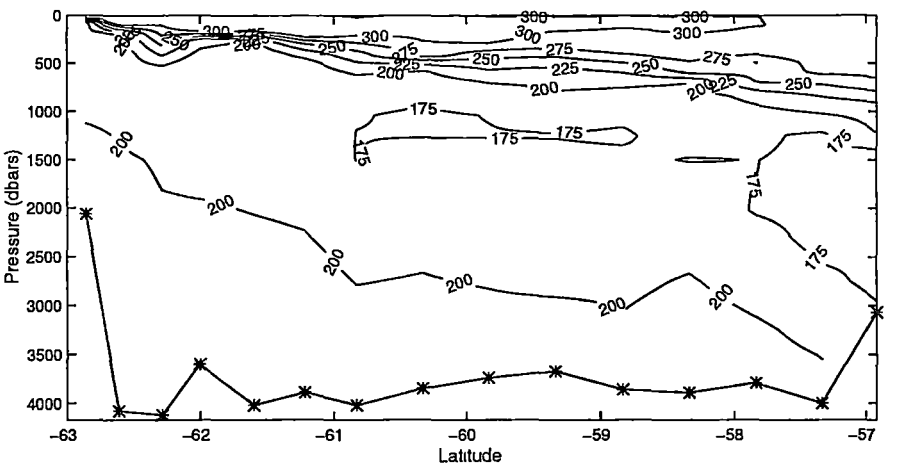

Figure 3.11: Oxygen (μmol.kg^{-1}) at Drake Passage

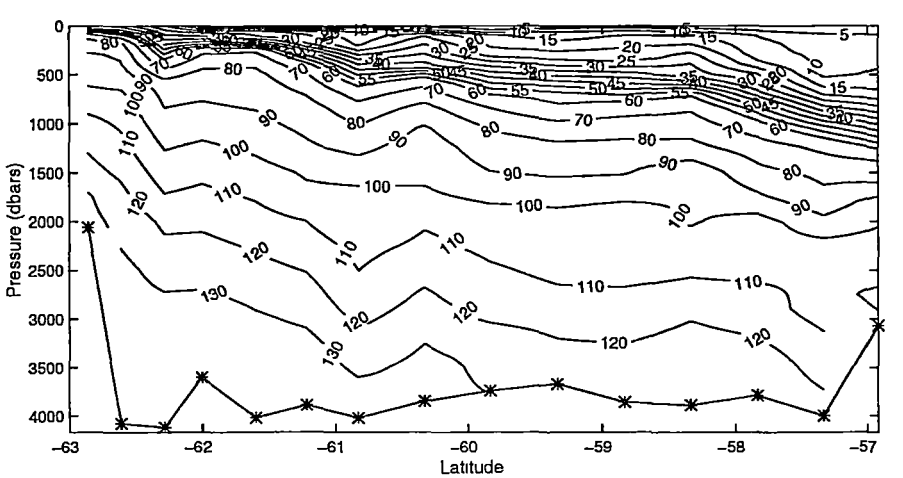

Figure 3.12: Silicate (μmol.kg^{-1}) at Drake Passage

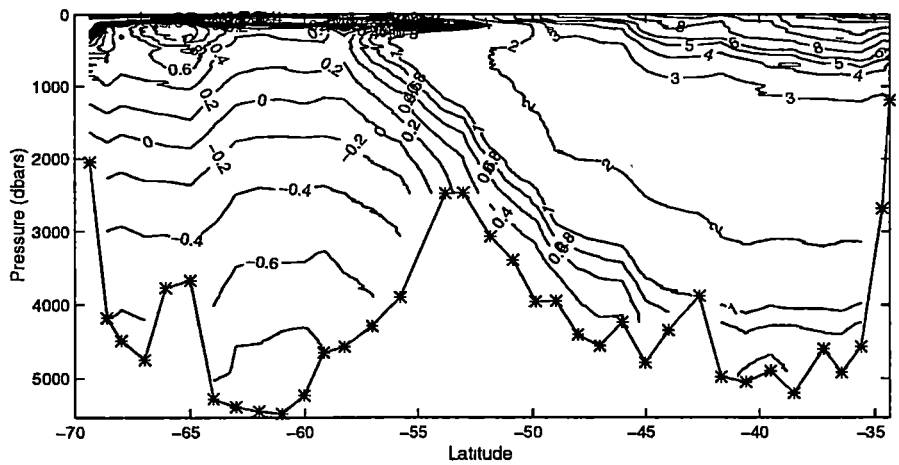

Figure 3.13: Potential Temperature (°C) at South Africa

Parallel to the South African coast to 37°S warm, salty subtropical water is identified above 200 dbars. North of the SAF, centred at 600 dbars, a thermostad of 8 °C to 10°C identifies SAMW (Figure 3.13). Lying below SAMW is the salinity minimum and high oxygen concentrations (1000 dbars) of AAIW (Figure 3.14 and Figure 3.15).

The oxygen minimum at 1500 dbars identifies UCDW, while the salinity maximum (> 34.7) at 2000 dbars identifies LCDW (Figure 3.14 and Figure 3.15). The distinct salinity maximum of NADW (> 34.8) north of 45°S bifurcate CDW. The presence NADW, adjacent the south Africa indicates NADW entering the Southern Ocean directly from the South Atlantic. South of the Subantarctic Front CDW begins to shoal reaching 500 dbars at 53°S (Figure 3.13 and Figure 3.14).

The Weddell Sea gyre is seen south of the Indian-Atlantic ridge (55°S). WSDW (temperature between 0 °C and −0.7 °C) and WSBW (< −0.7 °C) are evident below 1500 dbars (Figure 3.13). Within the Weddell gyre, CDW is identified by the presence of warm and salty intrusions (Figure 3.13 and Figure 3.14).

3.1.5 Weddell Sea (Wedsea)

The western portion of AJAX 2 (west of 8 °W) forms a section across the Weddell Sea. The section moves north across the Weddell Abyssal Plain to the

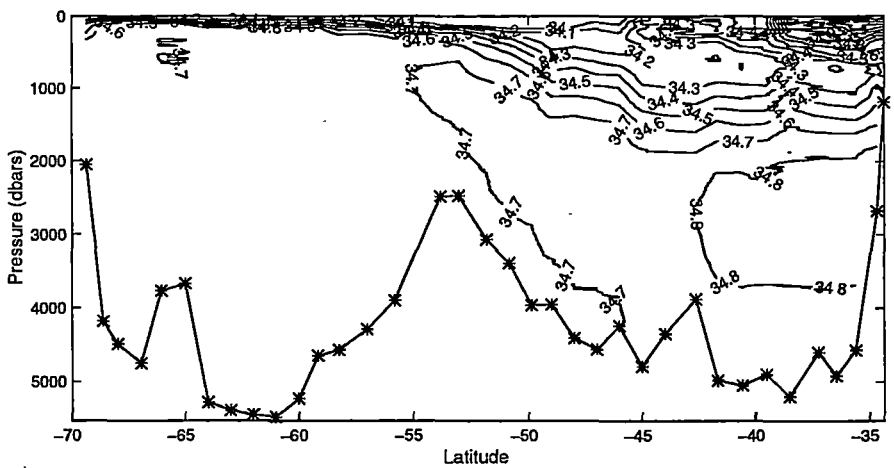

Figure 3.14: Salinity (psu) at South Africa

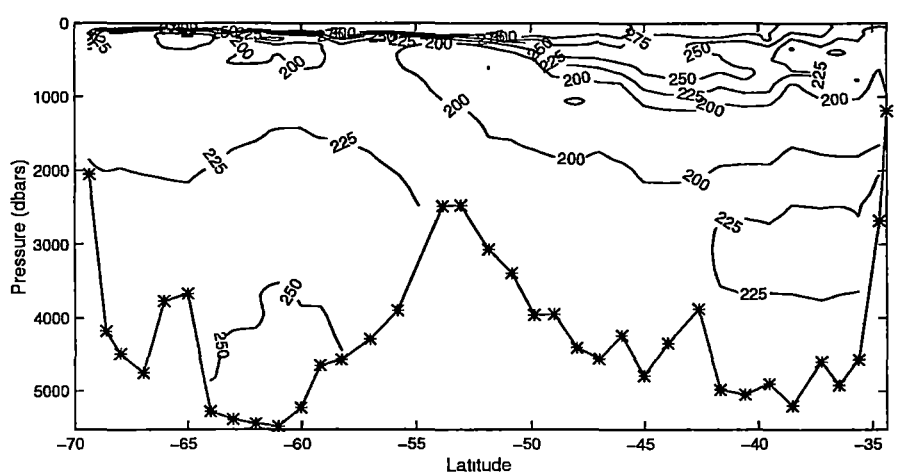

Figure 3.15: Oxygen (μmol.kg^{-1}) at South Africa

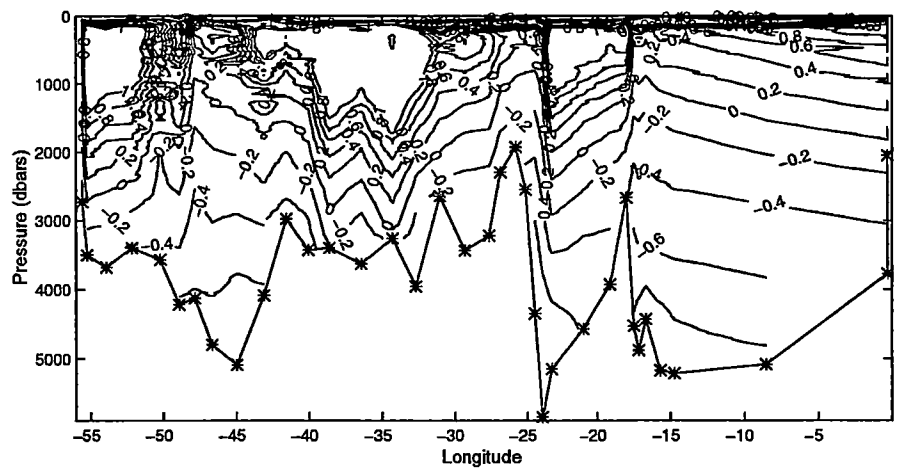

Figure 3.16: Potential Temperature (°C) at Weddell Sea

American-Antarctic ridge. On reaching the ridge the section turns west and runs parallel to the Scotia Ridge to 42°W, where it turns southwest, crossing the Scotia ridge and ending on the northern edge of the Antarctic Peninsula.

The path of the section explains the large discontinuities in temperature along the section (Figure 3.16). In the eastern and western ends of the section WSDW (temperature between 0.0°C and < -0.7 °C) and WSBW (< 0.7 °) are present below 1500 dbars. These water masses have salinity values < 34.6 (Figure 3.17). WSBW is also defined by an oxygen maximum (> 250 μmol.kg^{-1}) in the Weddell Abyssal Plain (Figure 3.18).

CDW is identified by temperatures > 0 °C and salinity > 34.7. These features are most striking near the American-Antarctic and Scotia ridges between 20°W and 40°W and adjacent the Antarctic Peninsula (Figure 3.16 and Figure 3.17).

3.1.6 Indian Ocean 18°S (Ind18)

A detailed description of water properties is given by Warren (1981a). There is a salinity maximum (< 35.5) at 300 dbars and an associated oxygen minimum < 150 μmol.kg^{-1} (Figure 3.20 and Figure 3.21). This near surface salinity maximum is derived from the south between 25°S and 35°S and is thought to be due to excess evaporation over this region (Wyrtki 1971; Baumgartner and Reichel 1975; Warren 1981a; Toole and Warren 1993).

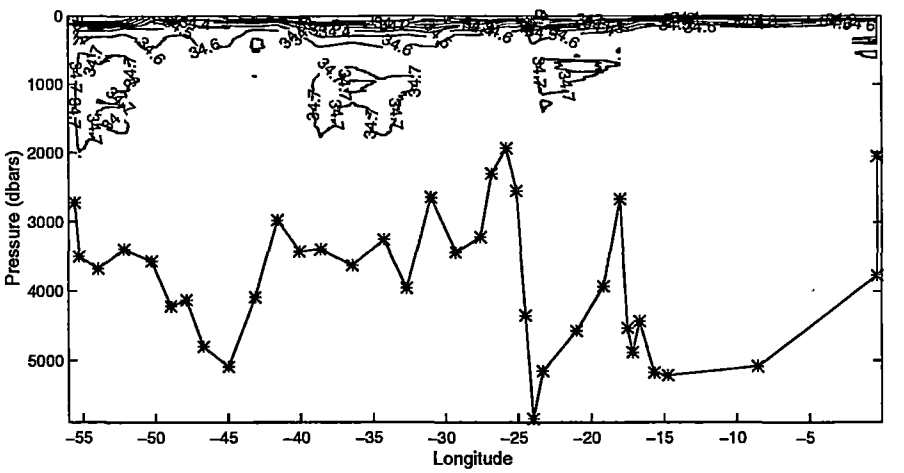

Figure 3.17: Salinity (psu) at Weddell Sea

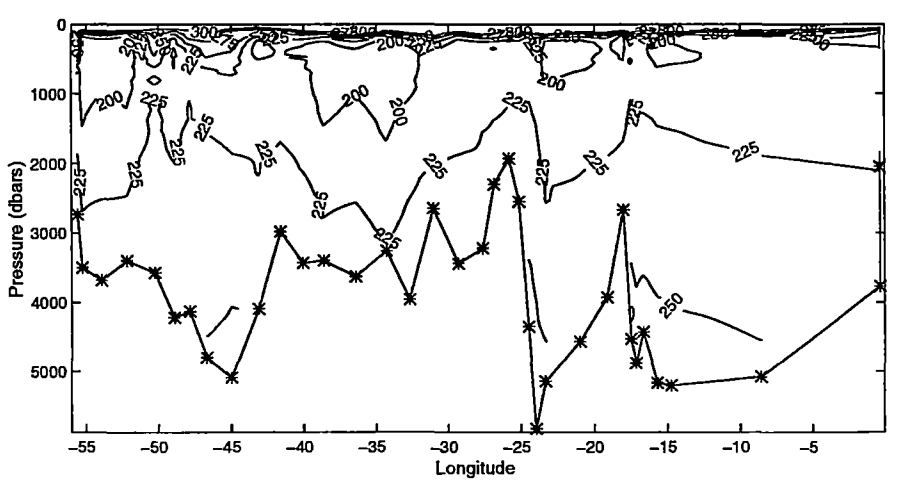

Figure 3.18: Oxygen (μmol.kg^{-1}) at Weddell Sea

Warren (1981a) suggest the oxygen minimum layer is due to *in situ* consumption of oxygen as the water moves northwards.

A thermostad (14°C to 8°C) and associated oxygen maximum (> 225 $\mu mol.kg^{-1}$), between 500 and 700 dbars, identify SAMW (Figure 3.19 and Figure 3.21). Below the oxygen maxima lies a salinity minimum (< 34.6) which marks AAIW. The depth of AAIW decreases slightly from east to west, with a mean depth of 1000 dbars (Figure 3.20). The decreased oxygen concentration from SAMW to AAIW suggest a slower northward passage of AAIW (Warren 1981a).

Immediately below the salinity minimum is an oxygen minimum (< 125 $\mu mol.kg^{-1}$) which identifies Indian Deep Water (IDW) (Figure 3.21). The low oxygen concentration is due to *in situ* oxygen consumption and indicates that the water is older than those lying above and below this layer (Warren 1981a).

The coldest water, found adjacent to Madagascar, has a potential temperature of < 0.6°C and an associated oxygen maximum identifies AABW (Figure 3.19 and Figure 3.21). This AABW enters the basin via the deep western boundary currents of the Madagascar and Mascarene basins.

The most extreme AABW in the Central Indian basin is found at 5000 dbars adjacent the Ninety-East Ridge (Figure 3.19). This water enters the Central Indian basin from the Perth basin via deep passages in the Ninetyeast ridge. Circumpolar Deep Water, identified by with temperature < 2 °C and high oxygen concentrations, enters the Central Indian basin directly from the south (Figure 3.19 and Figure 3.21).

Within the West Australian basin, below 5000 dbars, an oxygen maximum (> 200 $\mu mol.kg^{-1}$) adjacent to the Ninety-East ridge identifies more AABW (Figure 3.21). Between 3000 and 4000 dbars, silica maxima (> 130 $\mu mol.kg^{-1}$) and a relative oxygen minimum (between 175-200 $\mu mol.kg^{-1}$) identifies North Indian Ocean Water (NIDW) (Figure 3.22 and Figure 3.21).

3.1.7 Indian Ocean 32°S (Ind32)

The southern Indian Ocean section has a mean latitude of 32°S, but the latitude varies from 29°S in the Central Indian basin to 34°S in the Crozet and Perth basins. The reader is referred to Toole and Warren (1993) for a detailed

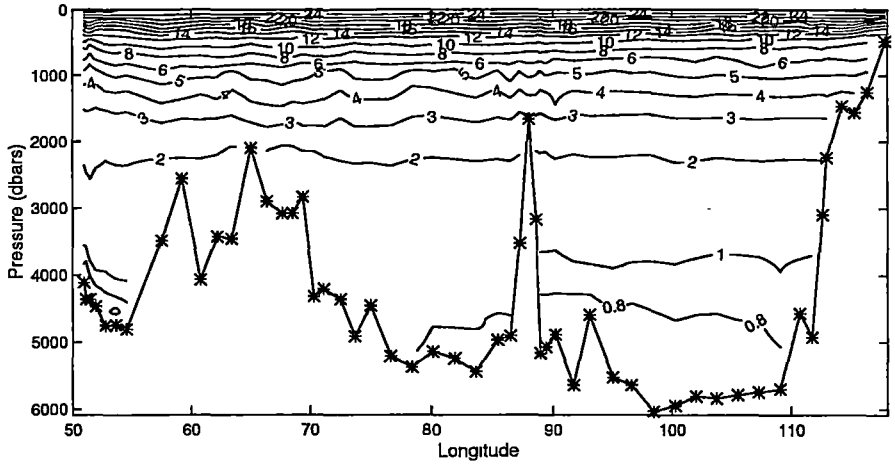

Figure 3.19: Potential Temperature (°C) at Indian 18°S

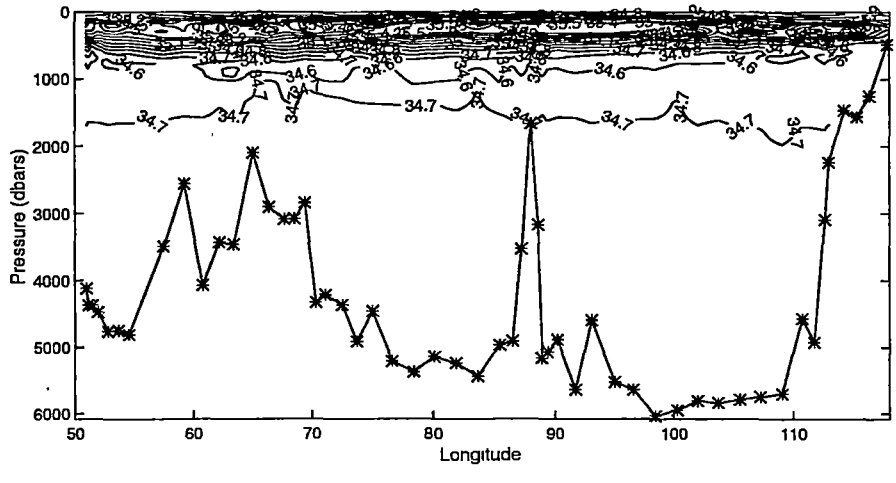

Figure 3.20: Salinity (psu) at Indian 18°S

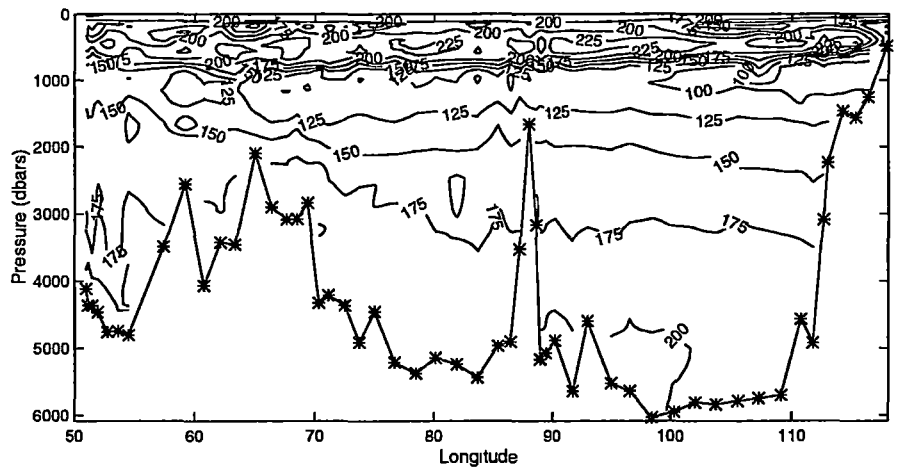

Figure 3.21: Oxygen (μmol.kg^{-1}) at Indian 18°S

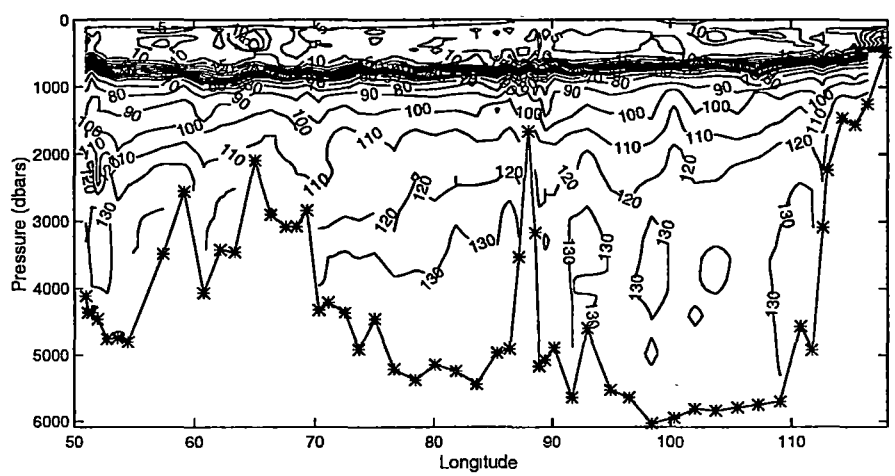

Figure 3.22: Silicate (μmol.kg^{-1}) at Indian 18°S

property description.

The temperature profile generally slopes upwards, after reaching its deepest depth off-shore of Africa (Figure 3.23). The highest surface salinity is east of 70°E, reflecting the excess evaporation against precipitation in the subtropics (Figure 3.24) (Toole and Warren 1993).

The SAMW thermostad (600 dbars) decreases from 14°C to 10°C east of 60°E to 12°C to 8°C in the Perth basin (105°E) (Figure 3.23). The AAIW salinity minimum layer (< 34.4) is seen at 1200 dbars in the Crozet basin and rises to 1000 dbars over Broken ridge and in the Perth basin (Figure 3.24). The salinity minimum is strongest in the Crozet and Perth basins.

At 1500 dbars, below the AAIW salinity minimum, is an oxygen minimum layer and a high silicate (Figure 3.26 and Figure 3.25) which identifies the southward moving IDW. The oxygen minimum layer is strongest in the Natal basin, the Central Indian basin and east of the Ninety-east ridge.

The northward flow of CDW and AABW across 32°S is guided by complex bottom topography into numerous individual ocean basins: the Natal; Mozambique; Madagascar; Crozet and; Perth basins. In the Natal and Mozambique basins, at 3000 dbars, the salinity maximum (> 34.8) identifies NADW which enters the Indian Ocean via the Agulhas basin south of Africa (Figure 3.24). AABW is identified in the Mozambique, Madagascar, Crozet and Perth basins, below 4000 dbars, by temperatures < 1 °C and oxygen > 200 $\mu mol.kg^{-1}$ (Figure 3.23 and Figure 3.24). The coldest temperatures are seen within the Mozambique and Crozet basin (< 0.2 °C) (Figure 3.23).

3.1.8 South of Australia 140°E (SAust)

This section is one of the repeat transects within the World Ocean Circulation Experiment (WOCE) and was occupied in summer 1994.

At 46°S there is a rapid decrease in salinity from 35.0 to 34.7 indicating the STF. Further south between 51°S and 52°S a sharp decrease in temperature and salinity is associated with the SAF. At 54°S a subsurface temperature minimum identifies the APF. These fronts from the boundaries between the Subtropical, Polar Front and Antarctic zones.

North of the STF warm, salty subtropical water dominate the upper 300

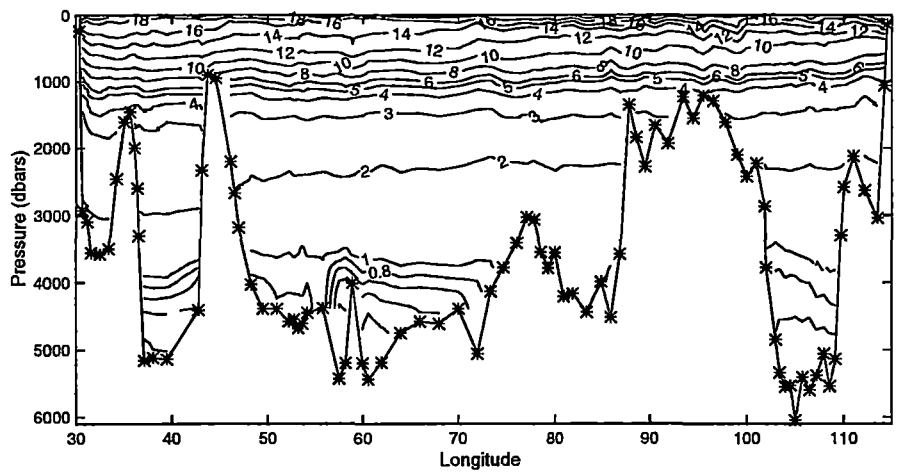

Figure 3.23: Potential Temperature (°C) at Indian 32°S

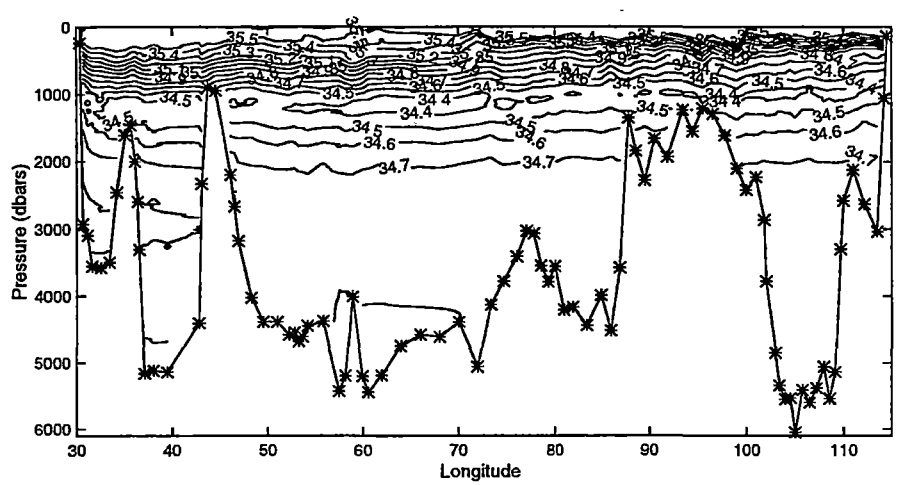

Figure 3.24: Salinity (psu) at Indian 32°S

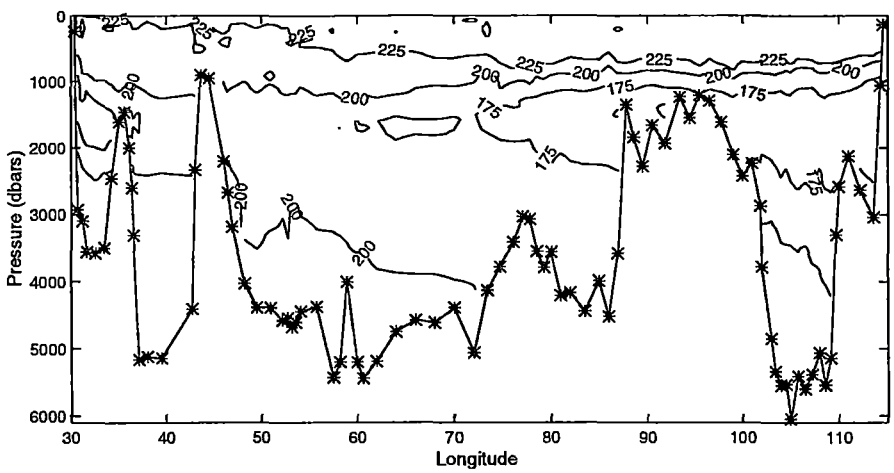

Figure 3.25: Oxygen (μmol.kg^{-1}) at Indian 32°S

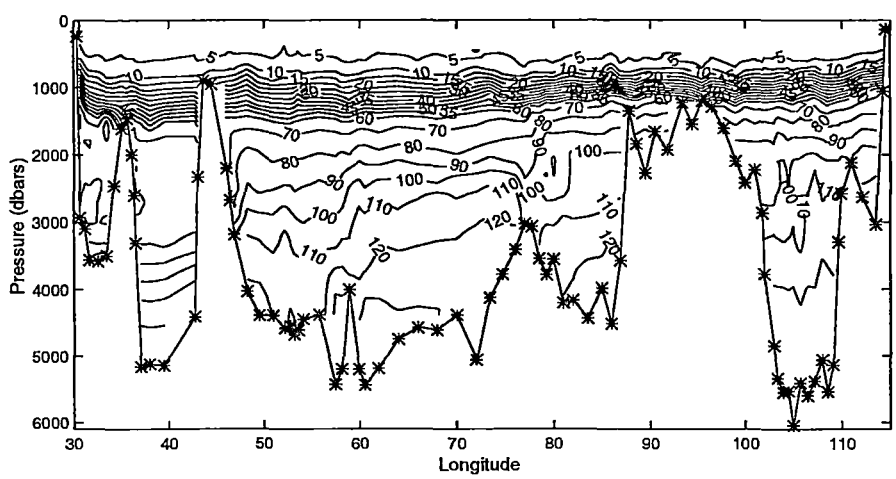

Figure 3.26: Silica (μmol.kg^{-1}) at Indian 32°S

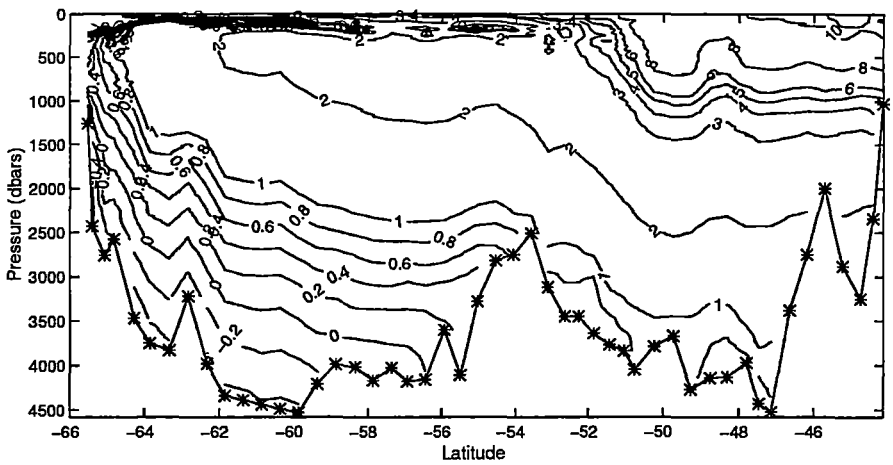

Figure 3.27: Potential Temperature (°C) south of Australia at 140°E

dbars (Figure 3.27 and Figure 3.28). A thermostad of 10°C to 8 °C at 800 dbars and associated high oxygen values identify SAMW (Figure 3.27 and Figure 3.29). Below SAMW at, 1000 dbars, is the salinity minimum associated with AAIW (Figure 3.28).

An oxygen minimum layer ($< 200\ \mu mol.kg^{-1}$), at 1500 dbars identifies UCDW (Figure 3.29), while at 2000 dbars the salinity maximum layer (> 34.7) highlights LCDW (Figure 3.28). Both of these water masses shoal south of Antarctic Polar Front reaching a depth interval of 500 to 1500 dbars south of 57°S.

Cold, low salinity surface water south of the Antarctic Polar Front identifies Antarctic Surface Water (Figure 3.27 and Figure 3.28). The coldest temperature (< -0.5°C) is found on the continental slope and within the Australian-Antarctic basin (< 0.0°C). These cold temperatures and maximum oxygen concentrations ($> 225\ \mu mol.kg^{-1}$) are representative of locally produced AABW (Rintoul 1997).

3.1.9 Pacific 32°S (Pac32)

The temperature section shows the characteristic subtropical gyre with an upward slope of isotherms from west to east (Figure 3.30). In the Tasman Sea warm, salty water dominates the upper 500 dbars (Figure 3.30 and Figure 3.31). The salinity and oxygen profiles between 200 and 1000 dbars, adjacent the Chile

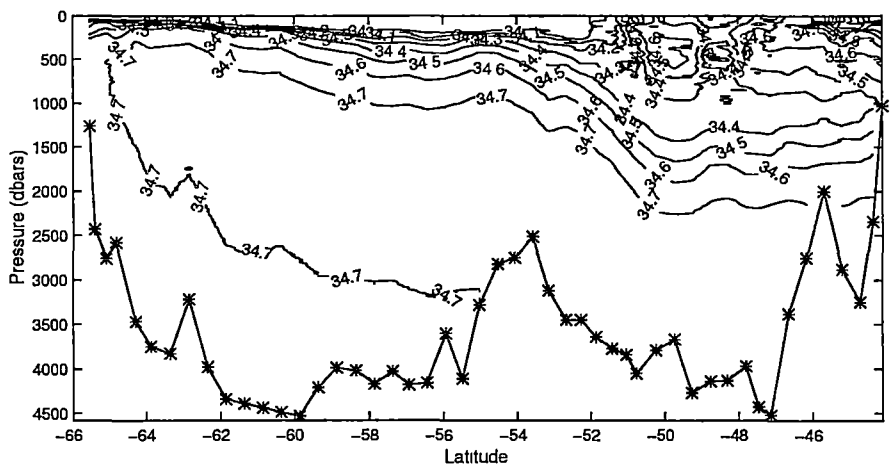

Figure 3.28: Salinity (psu) south of Australia at 140°E

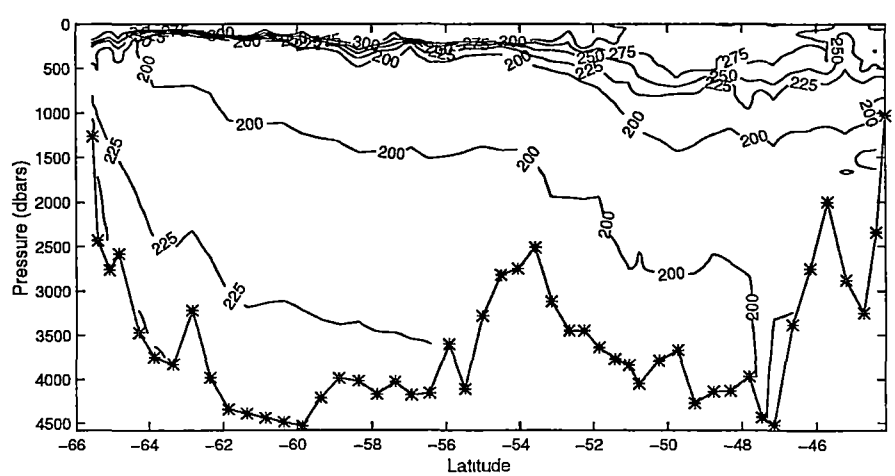

Figure 3.29: Oxygen (μmol.kg^{-1}) south of Australia at 140°E

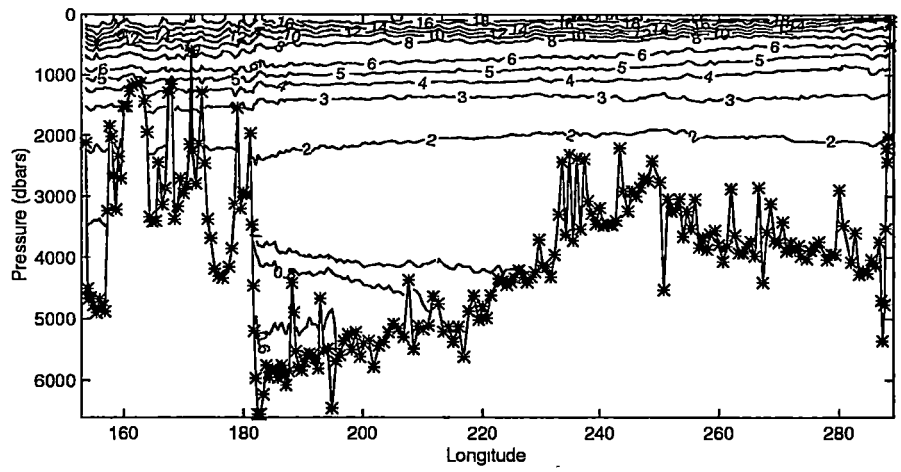

Figure 3.30: Potential Temperature (°C) Pacific Ocean 32°S

coast, show local maxima and minima, respectively (Figure 3.31 and Figure 3.32). These features represent the southward subsurface counter-current (Wooster 1961).

A thermostad between 10°C to 6°C identifies SAMW (Figure 3.30). The thermostad is deepest in the Tasman Sea (800 dbars) and shallowest in the eastern basin. At 1000 dbars the AAIW salinity minimum layer is found (Figure 3.31). The AAIW salinity minimum is strongest east of the East Pacific Rise (230°E) and only a weak reflection is seen west of the Kermadac ridge (180°E). The associated oxygen maximum is found only in the central and eastern basins (Figure 3.32).

The oxygen minimum (< 125 μmol.kg^{-1}), at 1200 dbars, in the Chile basin and over the Broken Ridge identifies North Pacific Deep Water (NPDW) (Figure 3.32). The oxygen minimum at 2200 dbars in the Southwest Pacific basin identifies UCDW, below 2200 dbars the oxygen and salinity increases identifying LCDW (Figure 3.31 and Figure 3.32).

Within the Southwest Pacific basin the coldest temperatures (< 0.6 °C) and oxygen maximum (> 200 μmol.kg^{-1}) identify AABW (Figure 3.32 and Figure 3.30).

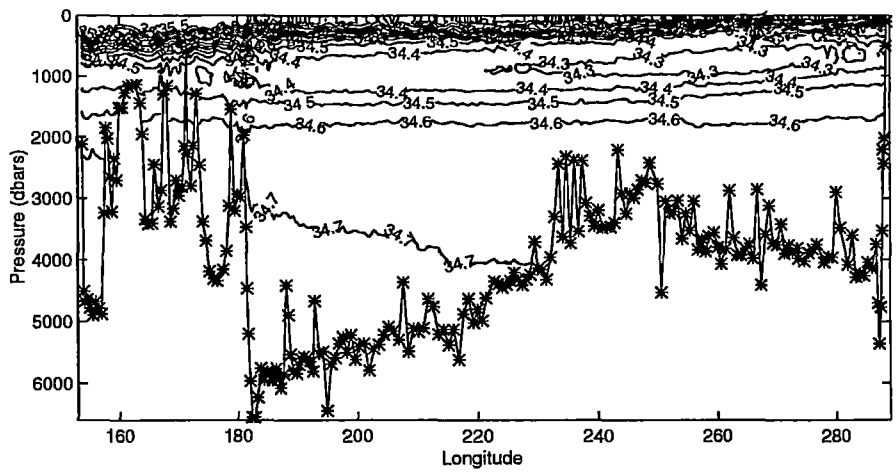

Figure 3.31: Salinity (psu) Pacific Ocean 32°E

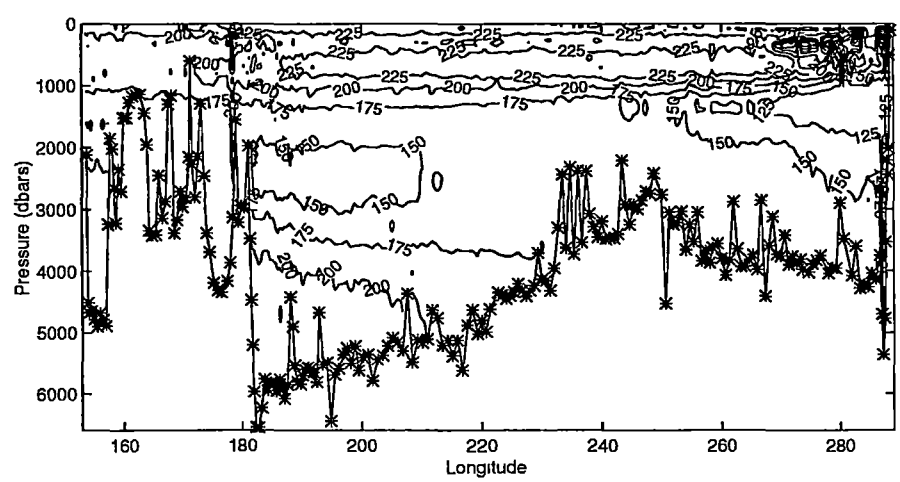

Figure 3.32: Oxygen (μmol.kg^{-1}) Pacific Ocean 32°E

3.2 Inverse Model Design

The study of inverse methods using the FRAM numerical model (Section 2.2) showed that the appropriate structure is added to the reference level velocities such that total transports were well reproduced. This study highlights that the appropriate form of the conservation is Equation 2.5 (reproduced below), when actual hydrographic data is used:

$$\sum_{j=1}^{N} \delta_j \Delta x_j \int_{h_m}^{h_{m+1}} (\rho C_j (v_r + b)_j) + E_j C_j + (w_c AC)_m - (w_c AC)_{m+1} \approx 0$$

δ_j unit normal

Δx_j stations spacing at pair j

C_j property value/unit mass at pair j

$h_{m,m+1}$ depth of surfaces bounding layer m

v_r relative velocity

b reference velocity

$E_j C_j$ Ekman property flux at station pair j

$(w_c AC)_{m,m+1}$ property dianeutral flux

This section provides the reader with particular information about the inverse model design for the Southern Ocean and adjacent ocean basins.

3.2.1 Ekman Fluxes

The Ekman fluxes are calculated normal to the station pairs along the hydrographic section. The depth of the Ekman layer is assumed to be 60 dbars for all sections. The property Ekman fluxes are calculated as a weighted mean property flux from the sea surface to 60 dbars assuming an exponential decay of the Ekman velocity. The Ekman property fluxes, are then added to the top layer of the inverse model.

3.2.2 Wind Data

The Ekman transport, normal to the hydrographic sections is calculated using the Hellerman and Rosenstein (1983) annual mean wind stress data. The Hellerman and Rosenstein (1983) wind stress data set was compiled from observation covering the world ocean (1870-1976). The Southern Ocean generally has < 50 observations per $2°\times 2°$box (Hellerman and Rosenstein 1983). This data set was chosen over the Trenberth et al. (1990) wind stress, which is based on seven years (1980-1986) of twice daily 1000 hectopascal wind analyses from the European Centre for Medium Range Weather Forecasts (ECMWF), due to the presence of data over the high latitudes of the Southern Ocean.

The quality of both the Hellerman and Rosenstein (1983) and Trenberth et al. (1990) wind stress data sets has been questioned by Chelton et al. (1990) and Mestas-Nuñez et al. (1994), respectively. Their studies are based on two months of Seasat-A satellite scatterometer near surface wind data. Some of the differences may be due to the short period for which the wind field was observed during the two months of operation by Seasat. The quality of the data may be questionable but the choice is dictated by the coverage of the data over the Southern Ocean and as a consequence I use the Hellerman and Rosenstein (1983) wind stress data set.

3.2.3 Neutral Surfaces and the layers defined

As in the FRAM study (Section 2.2) layers are bounded by neutral surfaces. Neutral surfaces in this study are calculated from the Jackett and McDougall (1997) *gamma_n* and *neutral_surfaces* algorithms. The algorithms allow labelling of sections and climatological data, in the interior of the boxes, onto neutral surfaces (*gamma_n*). The Levitus and Boyer (1994) climatological data are used to define the neutral surfaces and mean property values on these neutral surfaces within the boxes defined by the hydrographic sections. The chosen neutral surfaces subdivide the sections (Figure 3.33 to Figure 3.35) and the interior of the boxes into particular water mass. The layers defined by these neutral surfaces and the mean layer properties and the water masses defined at

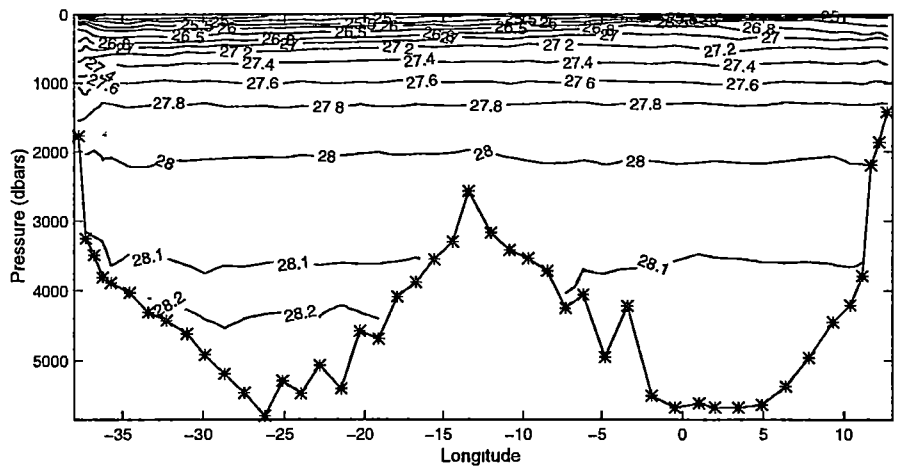

Figure 3.33: Neutral Surfaces (γ_n) at SAVE 2

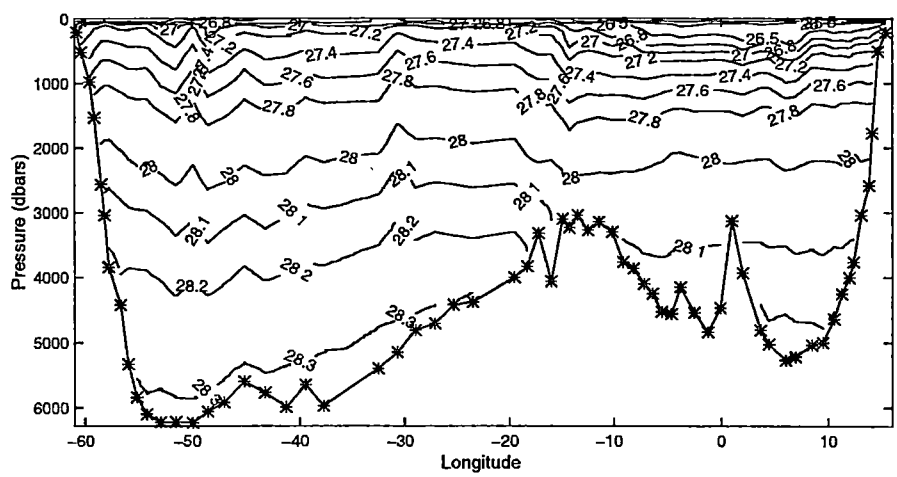

Figure 3.34: Neutral Surfaces (γ_n) at SAVE 4

the hydrographic section are shown in Table 3.2.

Table 3.2 defines the 23 layers, bounded by neutral surfaces (22), used in the Southern Ocean inverse and the mean property temperature and salinity of these layers at the hydrographic sections. It is noted that the north-south sections have layers in which cold, fresh Antarctic surface water bias the layer mean property values.

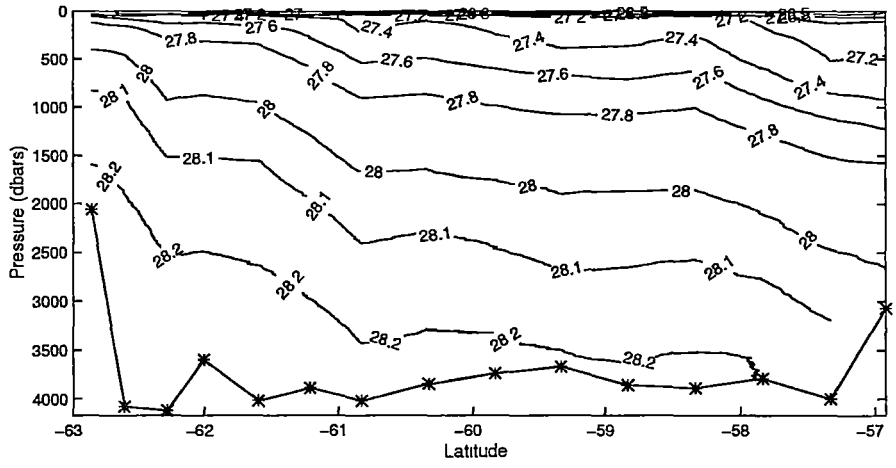

Figure 3.35: Neutral Surfaces (γ_n) at Drake Passage

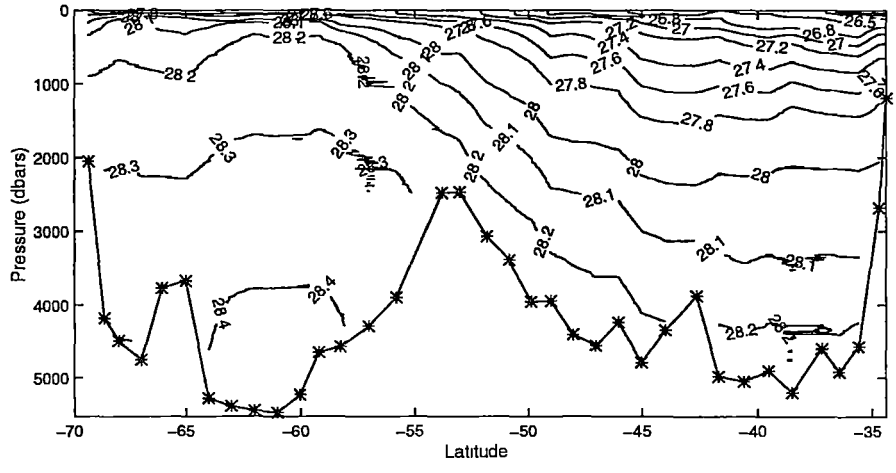

Figure 3.36: Neutral Surfaces (γ_n) at South Africa

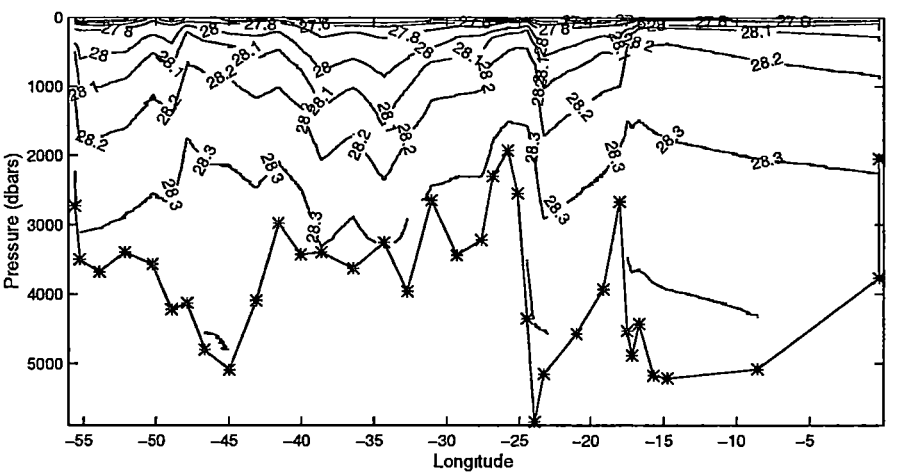

Figure 3.37: Neutral Surfaces (γ_n) at Weddell Sea

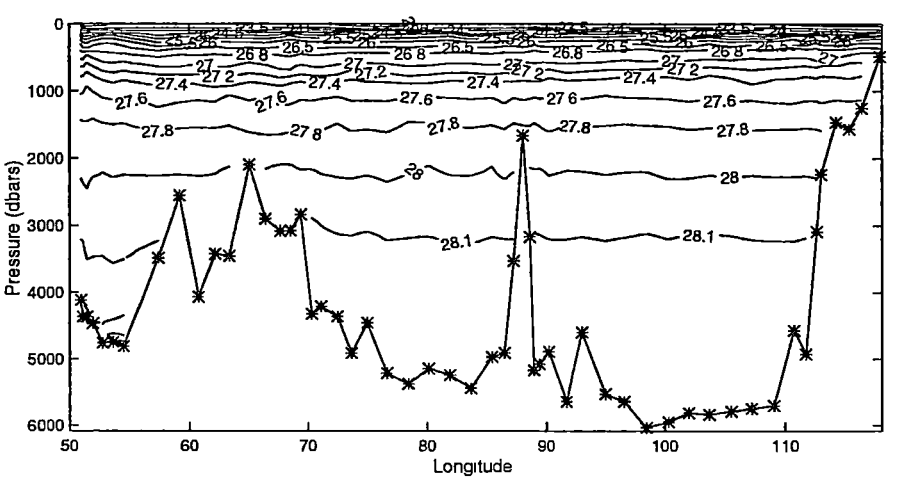

Figure 3.38: Neutral Surfaces (γ_n) at Indian 18°S

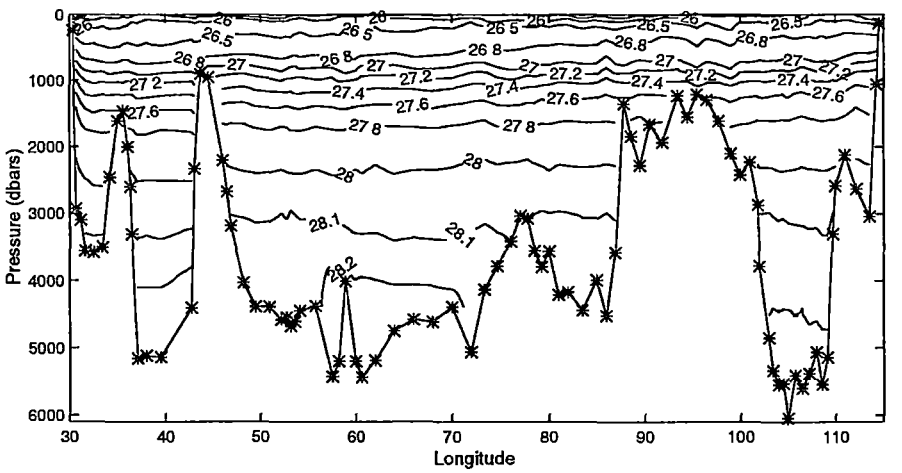

Figure 3.39: Neutral Surfaces (γ_n) at Indian 32°S

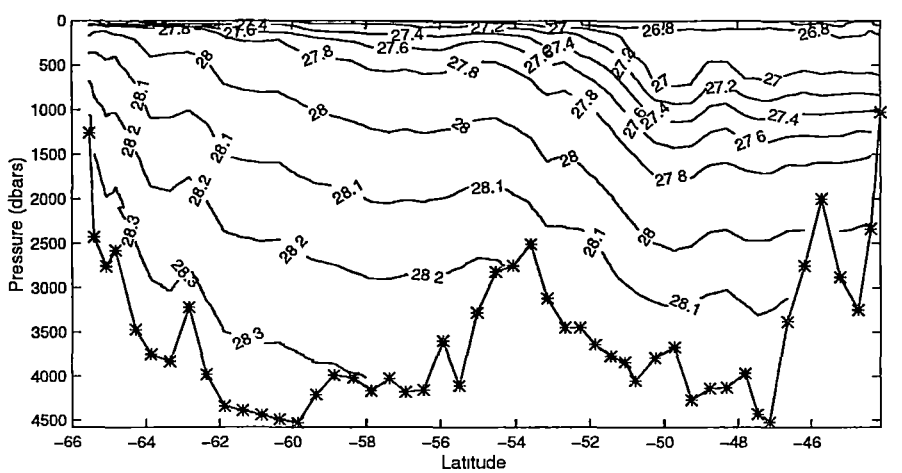

Figure 3.40: Neutral Surfaces (γ_n) south of Australia at 140°E

Layer	Surf.	Sections									water mass
		SV 2	SV 4	DrakeP	SAfrica	Wedsea	Ind18	Ind32	SAust	Pac32	
1	top	*	*	*	*	*	*	*	*	*	
	22.0	*	*	*	*	*	*	*	*	*	
2	22.0	*	*	*	*	*	*	*	*	*	
	22.5	*	*	*	*	*	*	*	*	*	
3	22.5	*	*	*	*	*	26.10	*	*	*	
	23.0	*	*	*	*	*	34.858	*	*	*	
4	23.0	*	*	*	*	*	25.01	*	*	*	surface
	23.5	*	*	*	*	*	34.844	*	*	*	
5	23.5	26.59	*	*	*	*	23.65	*	*	*	thermo-
	24.0	36.307	*	*	*	*	34.984	*	*	*	
6	24.0	26.53	*	*	*	*	22.15	22.49	*	*	cline
	24.5	36.872	*	*	*	*	35.110	35.294	*	*	
7	24.5	24.52	20.68	*	20.89	*	20.73	20.95	*	19.25	water
	25.0	36.766	35.449	*	35.522	*	35.220	35.441	*	34.906	
8	25.0	22.77	20.12	*	19.37	*	19.26	19.72	*	18.13	
	25.5	36.603	35.659	*	35.418	*	35.375	35.645	*	35.016	
9	25.5	19.86	17.528	*	17.27	*	17.61	18.13	*	16.26	
	26.0	36.217	35.489	*	35.337	*	35.457	35.696	*	35.054	
10	26.0	15.93	13.64	8.72	12.77	*	15.34	15.61	12.28	13.82	
	26.5	36.626	35.009	34.055	34.859	*	35.432	35.554	34.880	34.978	
11	26.5	12.75	10.42	7.77	9.56	*	12.81	12.65	9.97	10.99	interm-
	26.8	35.195	34.661	34.062	34.479	*	35.215	35.170	34.544	34.753	ediate
12	26.8	10.54	8.54	5.94	7.86	*	10.30	9.90	7.01	8.70	water
	27.0	34.944	34.532	34.052	34.404	*	35.892	34.777	34.273	34.549	
13	27.0	8.40	6.50	4.44	6.00	1.399	8.12	7.71	5.06	6.79	
	27.2	34.724	34.382	34.048	34.293	33.725	34.644	34.567	34.155	34.406	
14	27.2	6.00	4.39	2.86	3.37	1.33	6.33	5.61	2.88	5.22	(SAMW
	27.4	34.519	34.254	34.059	34.140	33.872	34.574	34.432	34.075	34.346	AAIW)
15	27.4	4.31	3.18	1.55	1.81	0.48	5.15	4.05	1.79	4.01	
	27.6	34.472	34.302	34.146	34.154	34.030	34.631	34.437	34.174	34.408	
16	27.6	3.87	2.78	1.86	1.08	0.07	3.98	3.20	1.80	3.07	Deep
	27.8	34.652	34.485	34.387	34.335	34.220	34.679	34.550	34.390	34.521	water
17	27.8	3.57	2.67	2.06	0.95	0.27	2.66	2.53	1.91	2.16	(NIDW
	28.0	34.895	34.727	34.639	34.560	34.490	34.720	34.691	34.634	34.638	NPWD
18	28.0	2.73	2.23	1.66	1.30	0.60	1.82	1.93	1.64	1.71	NADW
	28.1	34.906	34.809	34.721	34.709	34.628	34.732	34.747	34.729	34.688	CDW)
19	28.1	2.09	1.52	1.12	0.98	0.55	1.32	1.31	1.08	1.23	
	28.2	34.857	34.766	34.720	34.718	34.675	34.721	34.727	34.720	34.712	
20	28.2	0.95	0.60	0.69	0.50	0.12	1.02	0.82	0.38	1.06	Bottom
	28.3	34.739	34.692	34.708	34.693	34.670	34.714	34.701	34.691	34.708	water
21	28.3	*	0.26	*	-0.27	-0.20	*	*	-0.03	*	(AABW
	28.4	*	34.66	*	34.658	34.658	*	*	34.676	*	WSDW
22	28.4	*	*	*	-0.44	-0.45	*	*	*	*	WSBW
	28.5	*	*	*	34.652	34.647	*	*	*	*	RSBW
23	28.5	*	*	*	*	*	*	*	*	*	ALBW)
	bottom	*	*	*	*	*	*	*	*	*	

Table 3.2: The 22 neutral surfaces which bound the 23 layers and the water masses they define at the hydrographic sections. Also shown are the layer average potential temperature (upper °C) and salinity (lower, psu) at each station. * indicates layer not present in section

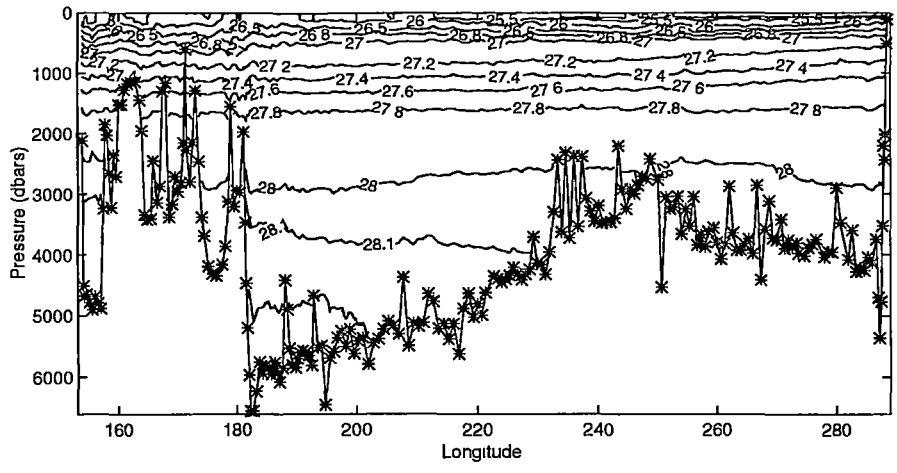

Figure 3.41: Neutral Surfaces (γ_n) Pacific Ocean 32°S

3.2.4 Reference levels

Across the meridional sections (SAVE 2, SAVE 4, Ind18, Ind23 and Pac32) the reference level is the boundary between the northward flowing AABW and southward NADW, IDW and PDW, neutral surface 18 (28.1), although at SAVE 4 in the western Argentine basin a deepest common reference level is chosen. At the three Southern Ocean choke point sections (DrakeP, SAfrica and SAust) a deepest common reference level is chosen, reflecting the dominance of the Antarctic Circumpolar Current at these sections.

3.2.5 Constraints - *A priori* Information

Four initial constraints where placed on the particular hydrographic section used in the study, based on *a priori* information. These constraints are added to the inverse problem as additional equations.

Long term current mooring data in the Bering Strait gives a mean flow of Pacific water into the Atlantic of $0.8\times10^6 m^3 s^{-1}$ (Coachman and Aagaard 1988). Hogg et al. (1982) estimated northward flow of AABW into the Argentine basin, via the Vema channel at $4\times10^6 m^3 s^{-1}$. This study was based on current moorings and hydrographic data. Speer and Zenk (1993) estimated the northward transport of AABW between the Argentine and Brazil basins at $6\times10^6 m^3 s^{-1}$, this includes transport in the Vema and Hunter channels and flow

over the Lower Santos Plateau. Based on these estimates, the total and bottom transport at SAVE 2 was constrained at:

- Total transport of -0.8×$10^6 m^3 s^{-1}$ across SAVE 2 (southwards).
- Bottom water transport in the Argentine basin below neutral surface 19 (CDW and AABW) of 4.5×$10^6 m^3 s^{-1}$ (northwards).

Gordon (1981b) estimated oceanic heat loss of $31 W m^{-2}$ between 60°S and 70°S. Applying this to the Weddell Sea, defined in this study, implies a southward heat flux of 0.1 PW (1 PW = 10^{15} W). Constraining the heat flux also implies that there is zero net mass flux across the Weddell Sea section. Based on these estimates the AJAX Weddell Sea section has the following constraints:

- 0.1 PW southward heat flux
- 0×$10^6 m^3 s^{-1}$ total mass flux

3.2.6 Weights

The importance of appropriate column and row weighting was discussed previously (Section 2.1) and by McIntosh and Rintoul (1997). The rows are weighted by the property norm and the columns are weighted by the area norm. A scaling factor is also applied to the reference velocity and the dianeutral property flux unknowns such that the condition number is minimised.

3.2.7 Choosing the Rank

As discussed in Chapter 2 the use of actual hydrographic sections introduces errors into the system. In this model those errors result in choosing a rank where the data residual norms are of O(1 to 2×$10^6 m^3 s^{-1}$).

Table 3.3 provides a quick reference table of the inverse models in this study and the ×$10^6 m^3 s^{-1}$ a priori constraints applied (in addition to conserving mass heat and salt).

Constraint	Model_int	Model_surf	Model_wsh	Model_malv
-0.8×$10^6 m^3 s^{-1}$ net southward transport at SAVE2	√	√	√	√
4×$10^6 m^3 s^{-1}$ northward bottom transport in Brazil basin	√	√	√	√
0×$10^6 m^3 s^{-1}$ net tranport across Wedsea	√	√	√	√
31Wm^{-2} heat loss over Weddell Sea	√	√		
air-sea fluxes		√	√	√
16Wm^{-2} heat loss over Weddell Sea			√	√
60×$10^6 m^3 s^{-1}$ northward Malvinas Current				√
6×$10^6 m^3 s^{-1}$ northward transport AABW across Argentine basin				√
11×$10^6 m^3 s^{-1}$ northward transport across WOCE PCM9 (Pac32)				√

Table 3.3: All inverse models used in this study and the different *a priori* constraints applied. All models conserve mass, heat and salt.

Chapter 4

Circulation of the Southern Ocean - the initial model

The initial mass imbalances for each layer bounded by hydrographic sections are shown in Figure 4.1 (+ve is a convergence in the layer, -ve represents a divergence). Within the subtropical Atlantic region (BI) there is a divergence from intermediate water (layer 11 to 15) and a convergence into bottom water (layers 19 and 20) (Figure 4.1 a). The Southern Ocean Atlantic sector (BII) has a convergence into lower intermediate (layers 14 and 15), deep layers (16 to 18) and bottom water (layers 21 and 22) but divergence from upper intermediate water (layers 12 and 13) and lower deep water (layers 19 and 20) (Figure 4.1 b). In the subtropical Indian region (BIV) there is a convergence into upper thermocline water (layers 3 and 4). There is a smaller convergence into upper intermediate water (layers 11 and 12) and divergence from lower thermocline water (layers 7 to 10) and lower intermediate water (layers 13 to 15) and upper deep water (layers 16 and 17) (Figure 4.1 c). In the Southern Ocean Indian sector (BV) there is a divergence from upper intermediate water (layers 11 to 13), lower deep (layers 18 and 19) and bottom (layers 20 to 21) waters, while there is convergence into upper thermocline (layers 6 to 10), lower intermediate (layers 14 and 15) and upper deep (layers 16 and 17) waters (Figure 4.1 d). The Pacific region (BVI) shows a divergence from thermocline (layers 9 and 10) and intermediate (layers 11, 13 to 15) water, and a convergence into upper deep (layers 16 to 18), and bottom (layers 20 and 21) water (Figure 4.1 e). Similar layer imbalances exist for heat and salt within each region. Figure 4.1 layer imbalances are large, showing that the relative and

Ekman transport alone do not conserve mass within layers, even when a reasonable reference level is chosen. The inverse method solves the unknown reference velocities and dianeutral property fluxes such that property conservation, in each region, is achieved.

This chapter discusses the resultant circulation of the Southern Ocean and adjacent ocean basins derived from inverse methods.

4.1 Reference Velocities

Figure 4.2 through to Figure 4.10 show the absolute velocity profile for each section, with the reference velocity given in the upper plot. The reference velocities, although different for each section, are smooth and generally less than $\pm 1 cms^{-1}$, apart from stations pairs over steeply sloping topography on the boundaries and over mid-ocean ridges of the hydrographic sections. These higher reference velocities result from the way in which the inverse model reduces layer imbalances: placing large velocities over steeply sloping topography. The propensity of the inverse method to place large reference (barotropic) velocities over sloping topography is explained by Stommel and Veronis (1981). The inverse method takes advantage of the structure of the layers to balance the conservation equations, where large reference velocities over narrow region where the layer thickness differs are effective in achieving conservation while minimising $||\mathbf{b}^t\mathbf{b}||$.

On the western boundary of SAVE 2 the absolute velocities are southward, associated with the Brazil Current (Figure 4.2). The absolute velocity structure at SAVE 4 in the Argentine basin (60°W to 40°W) highlights the complicated north/south structure associated with the Brazil-Malvinas Confluence (Figure 4.3). Over the mid-Atlantic ridge the stronger southward current indicate the position of the Polar Front, Subantarctic Front and Subtropical Front, while in the eastern, Cape basin the northward current identifies the Benguela Current. The Drake Passage (Figure 4.4) and the section south of Africa (Figure 4.5) show to the banded eastward current structure synonymous with the ACC, although adjacent the south African coast (35°S) a shallow westward flow is seen. The velocity structure at the Weddell Sea section has

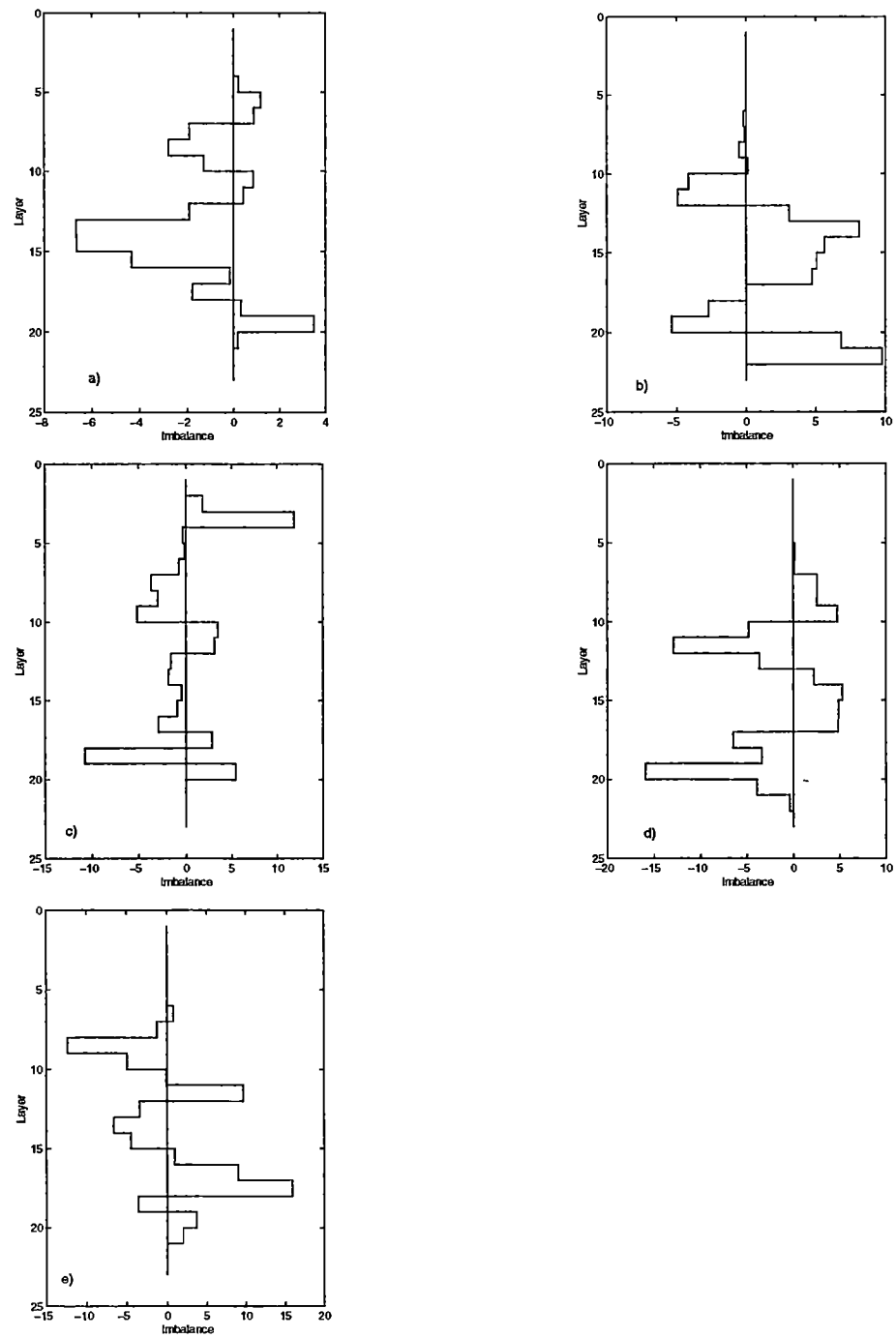

Figure 4.1: Initial layer imbalance for each region shown in Figure 3.1 a) BI b) BII c) BIV d) BV , and e) BVI ($\times 10^6 m^3 s^{-1}$)

alternating southward and northward flow (Figure 4.6). The velocities are small across the Ind18 section, apart from a large southward current adjacent Madagascar (50°E) associated with the East Madagascar Current and stronger northward and southward current both east and west of the Ninetyeast Ridge (88°E) (Figure 4.7). The largest southward velocities at the Ind32 section are in Natal basin associated with the Agulhas Current (Figure 4.8). South of Australia the banded current structure of the ACC is evident between 48°S and 58°S, also shown are counter-currents at 47°S and 49°S (Figure 4.9). The absolute velocity at 32°S in the Pacific highlights the small alternating northward and southward currents of the subtropical gyres (Figure 4.10). The largest velocities are adjacent to Australia and the Tonga-Kermadac Ridge.

4.2 Dianeutral Property Flux

In Chapter 2 I outlined how the dianeutral flux unknowns are incorporated into the conservation equations. The accuracy of decomposing the property dianeutral flux into its advective and effective diffusive components is discussed in Section 2.2.2. The reader is reminded that the dianeutral property advection is the layer property mean × dianeutral mass flux, and the dianeutral effective property diffusion is the remainder of the total dianeutral property flux once the advective component is removed. The dianeutral effective diffusion incorporates not only the actual diffusion but also other eddy processes.

In the subtropical Atlantic region (BI) (Figure 3.1) the dianeutral advective flux is downwards across upper thermocline (6 to 8) neutral surfaces and upwards across lower thermocline (9 to 11) neutral surfaces (Figure 4.11). There is an upward dianeutral advective flux across lower intermediate (14 and 15) and deep (16) neutral surfaces, and a downward flux across lower deep (17 and 18) neutral surfaces. The dianeutral advective fluxes result in the redistribution of upper thermocline (6 and 7) layers into lower thermocline (8 to 10) layers and deep (17 and 18) layers into overlying intermediate (14 and 15) layers and underlying lower deep (19) layers (Figure 4.11).

The dianeutral effective heat diffusion is downwards across the thermocline (4 to 8) neutral surfaces, and upward across intermediate (11 to 15)

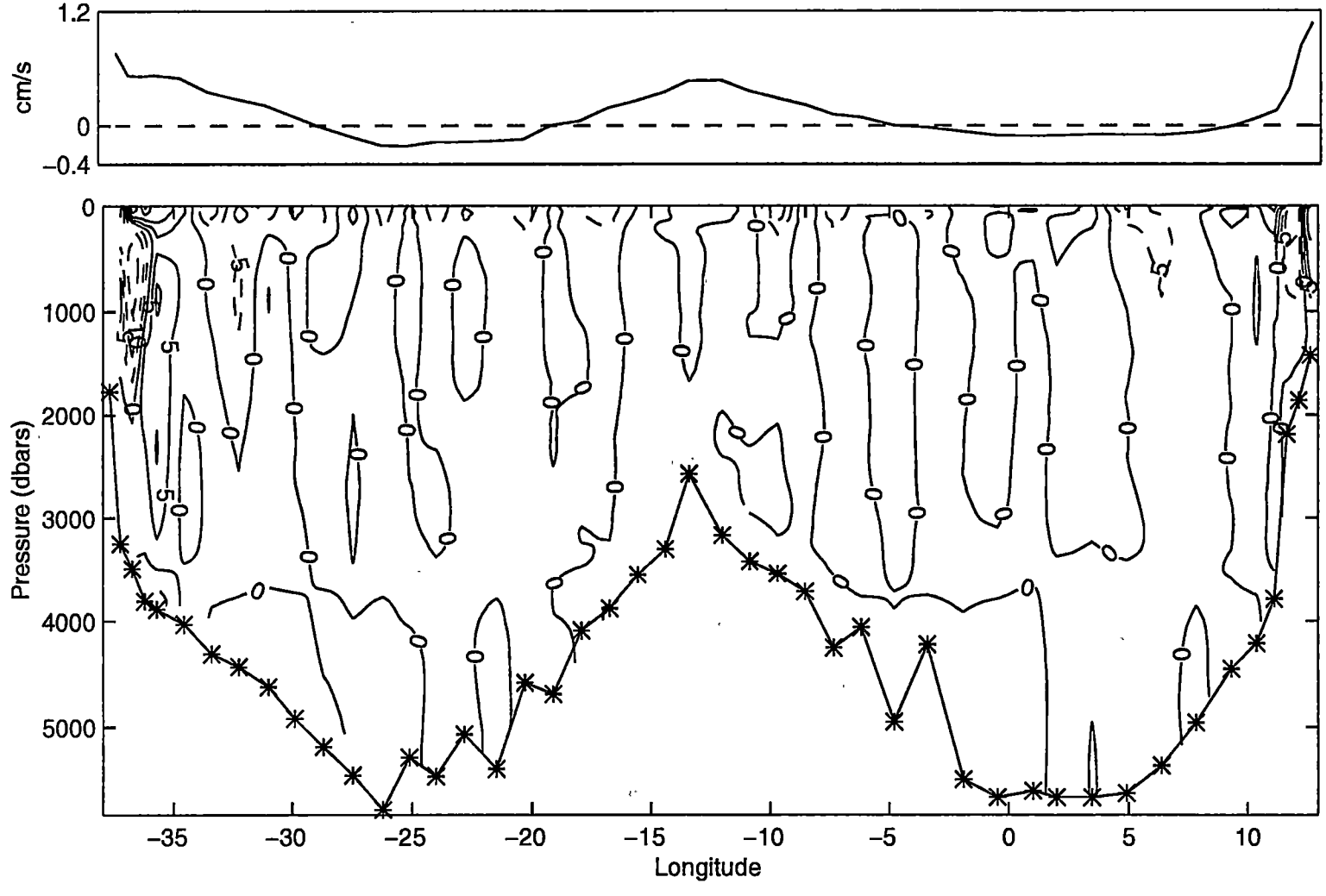

Figure 4.2: Absolute velocity at the SAVE 2 section. Solid and dashed contours refer to north and south velocities, respectively. Upper plot is reference level velocity.

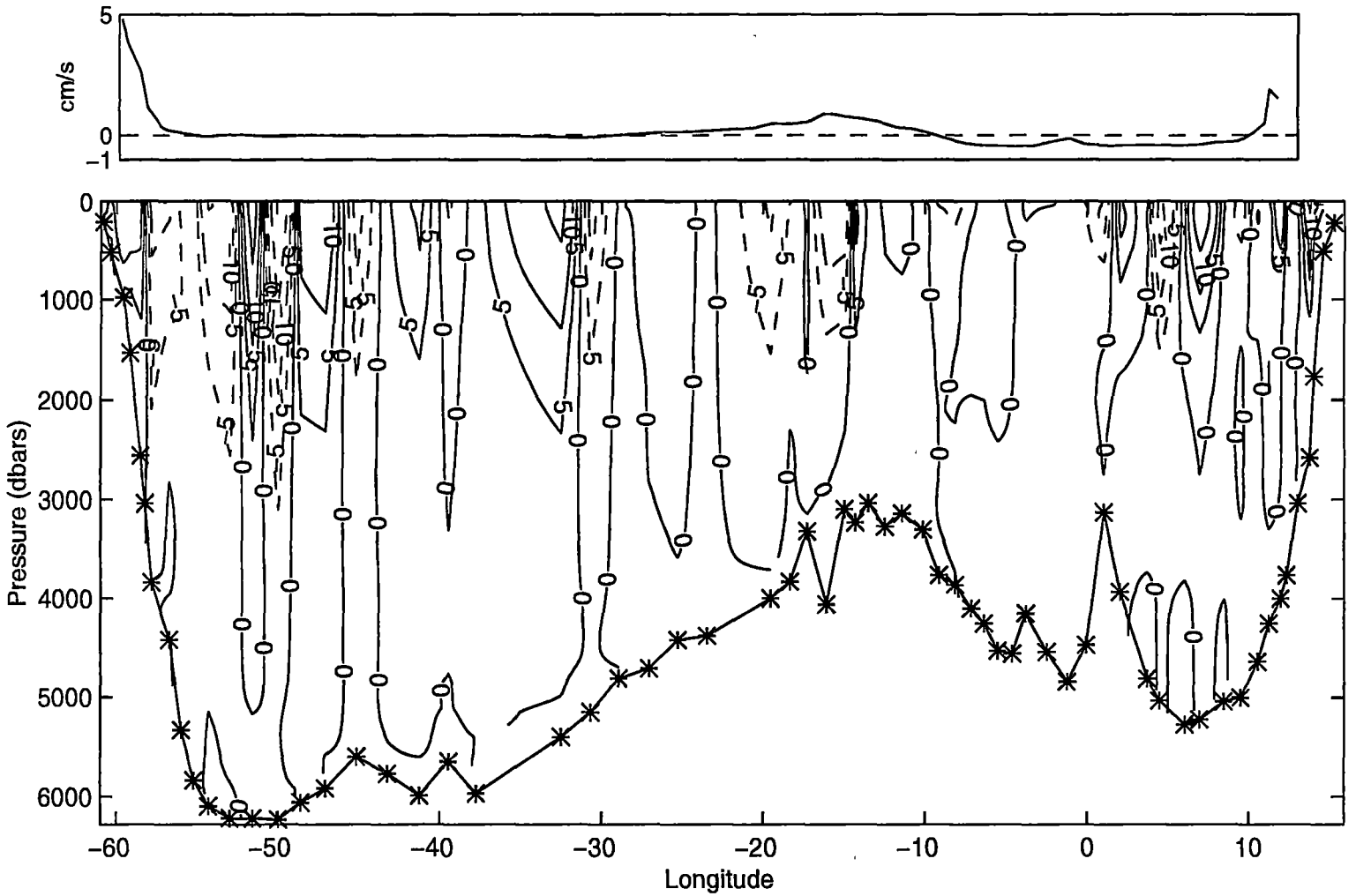

Figure 4.3: Absolute velocity at the SAVE 4 section. Solid and dashed contours refer to north and south velocities, respectively. Upper plot is reference level velocity.

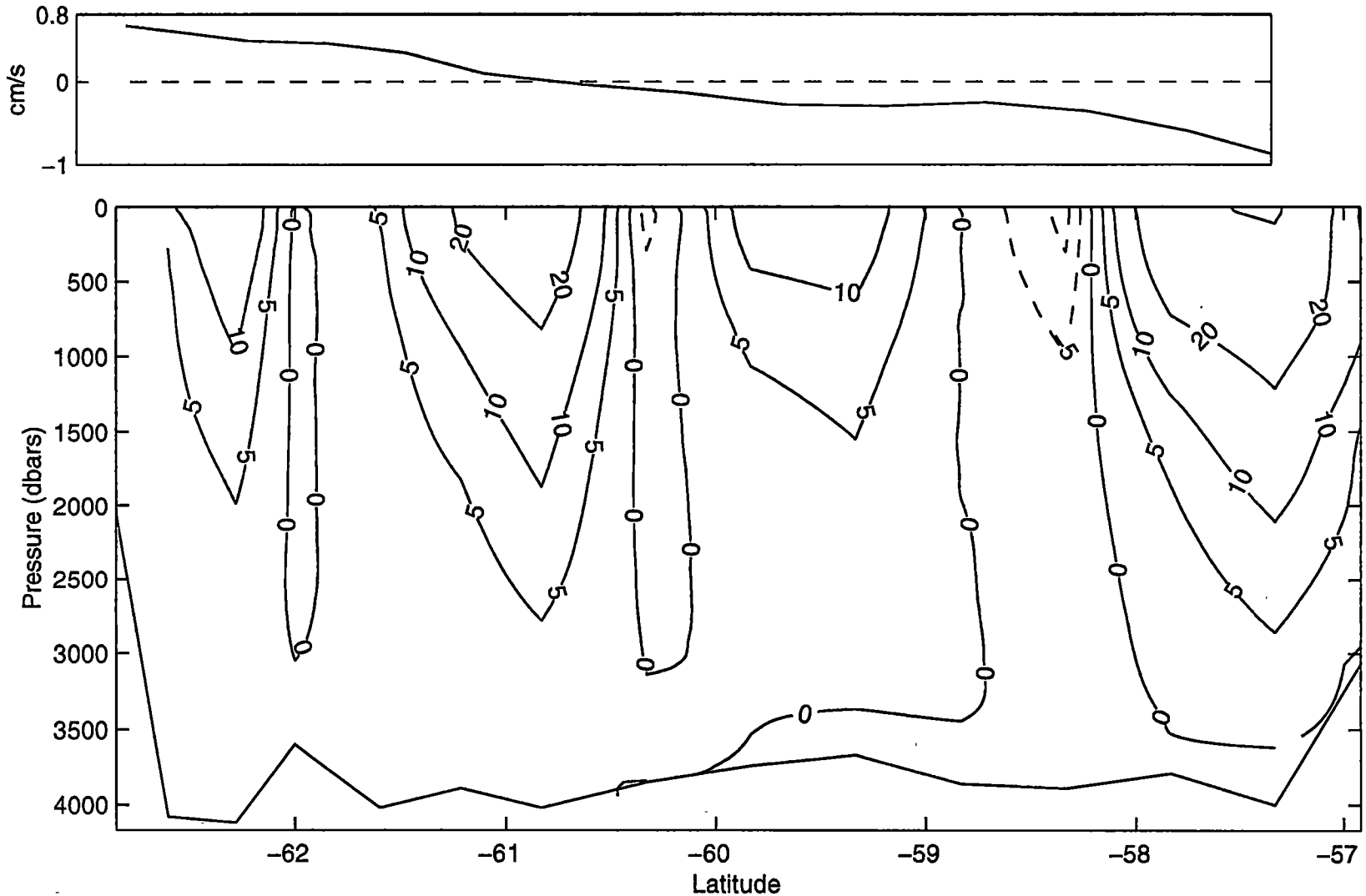

Figure 4.4: Absolute velocity at the Drake Passage section. Solid and dashed contours refer to east and west velocities, respectively. Upper plot is reference level velocity.

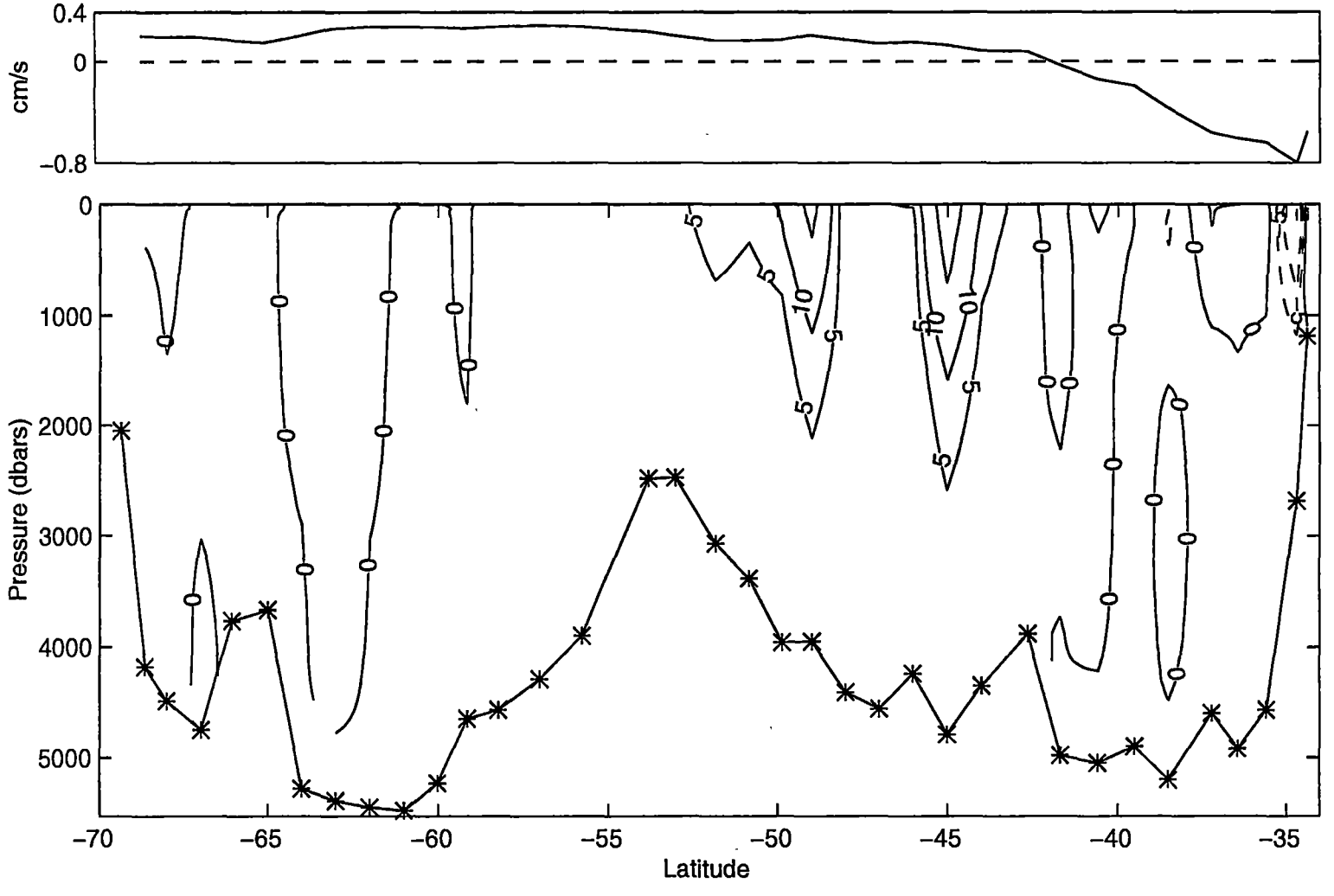

Figure 4.5: Absolute velocity at the section south of Africa. Solid and dashed contours refer to east and west velocities, respectively. Upper plot is reference level velocity.

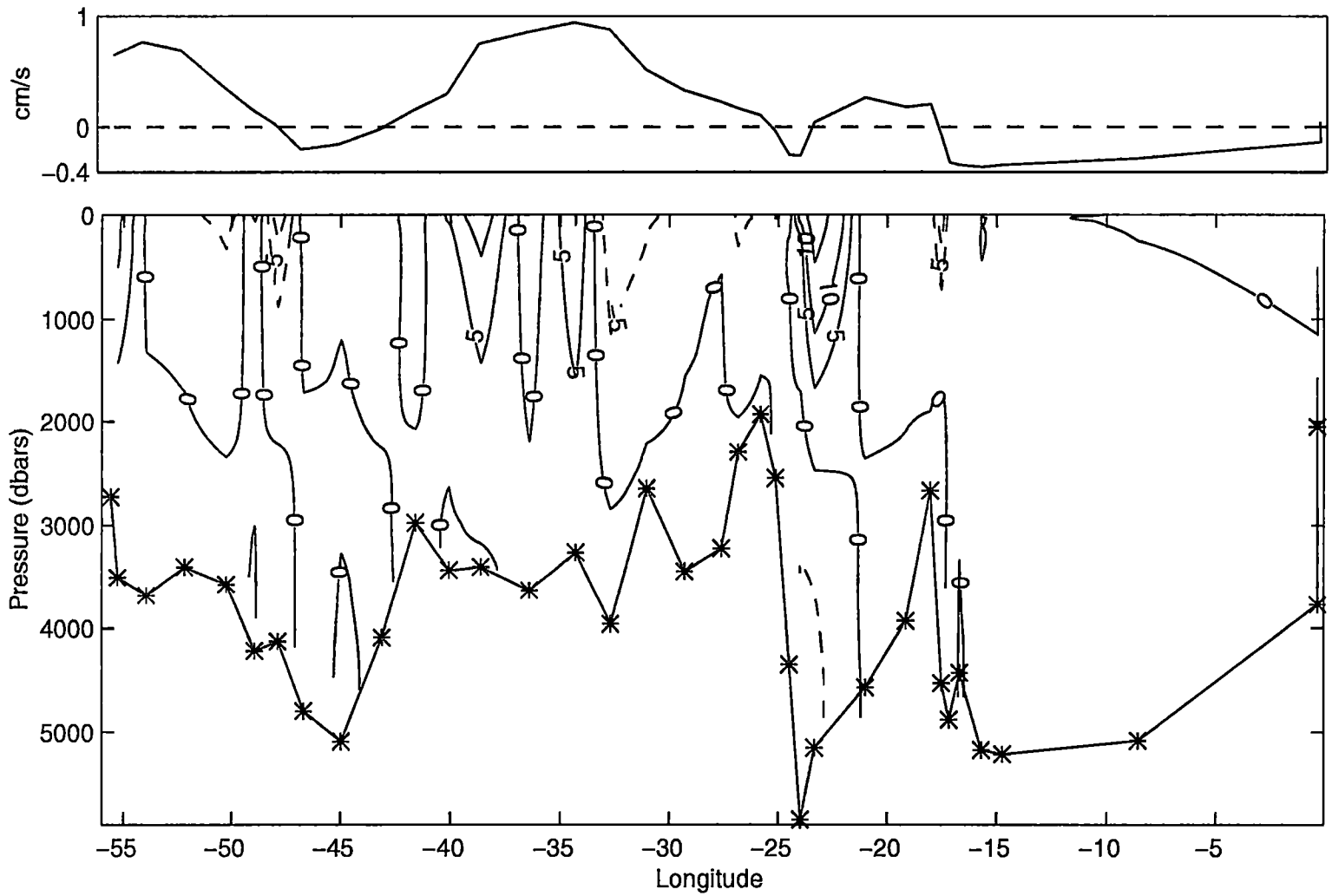

Figure 4.6: Absolute velocity at the Weddell Sea section. Solid and dashed contours refer to north and south velocities, respectively. Upper plot is reference level velocity.

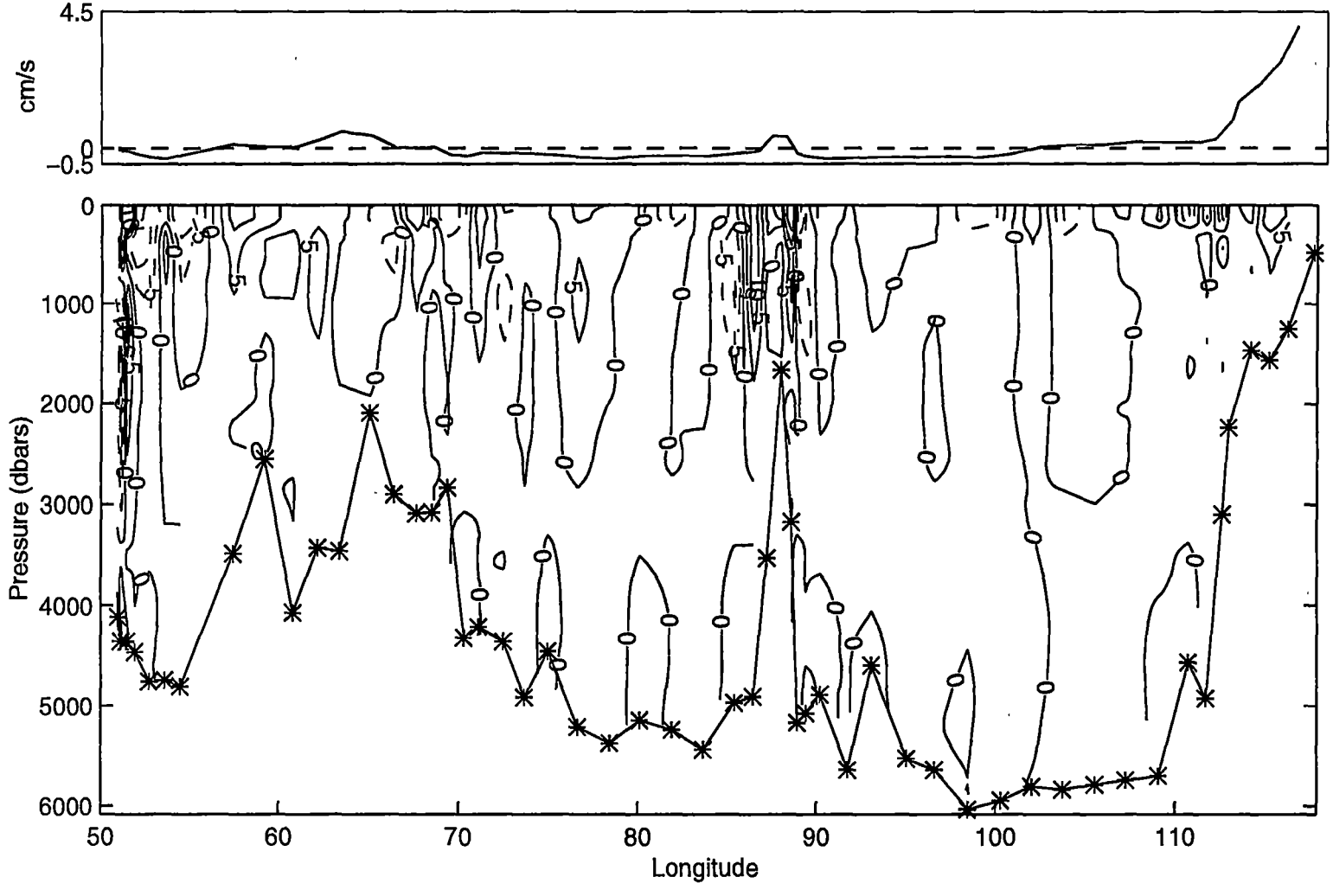

Figure 4.7: Absolute velocity at the Indian 18°S section. Solid and dashed contours refer to north and south velocities, respectively. Upper plot is reference level velocity.

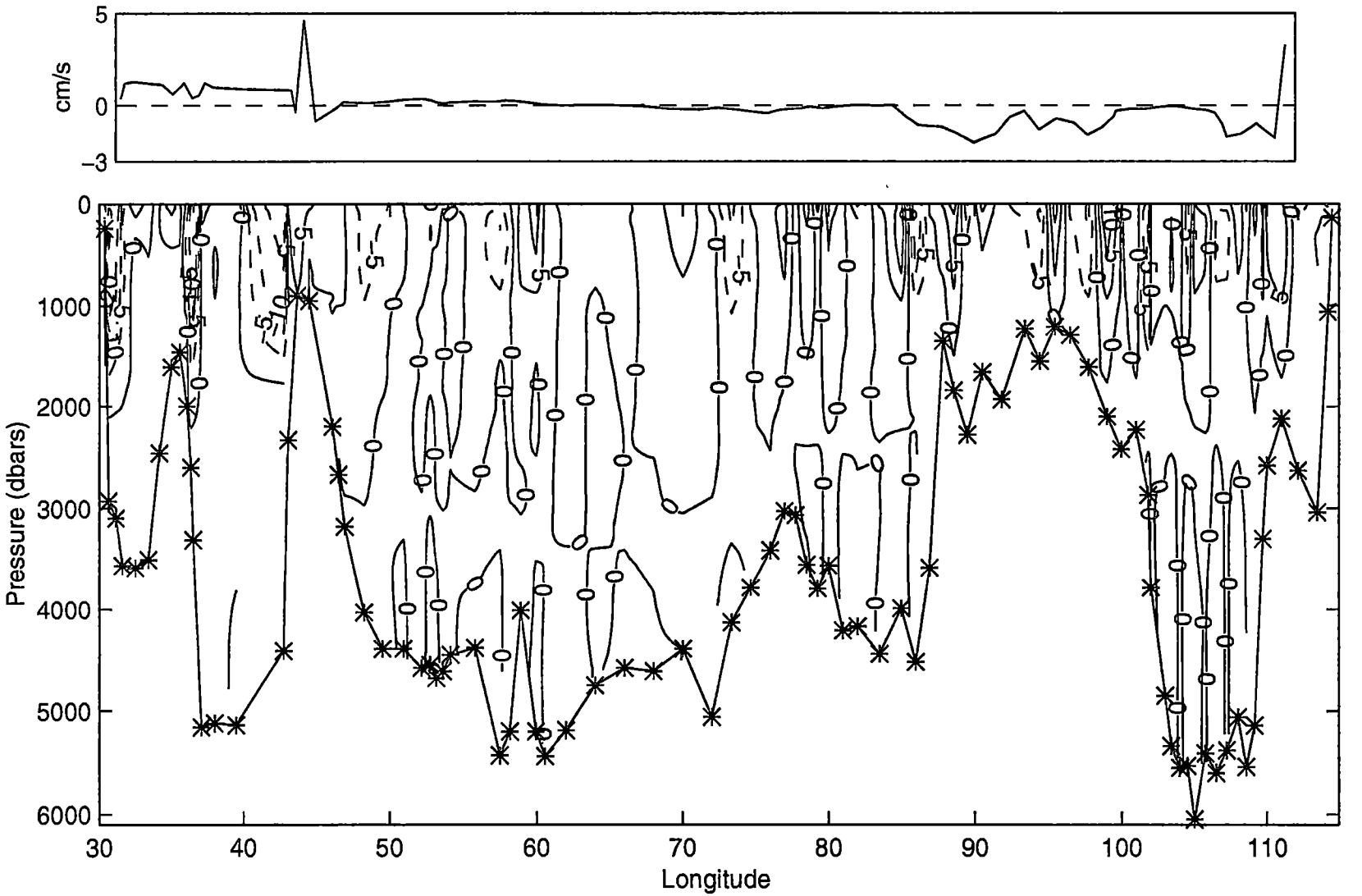

Figure 4.8: Absolute velocity at the Indian 32°S section. Solid and dashed contours refer to north and south velocities, respectively. Upper plot is reference level velocity.

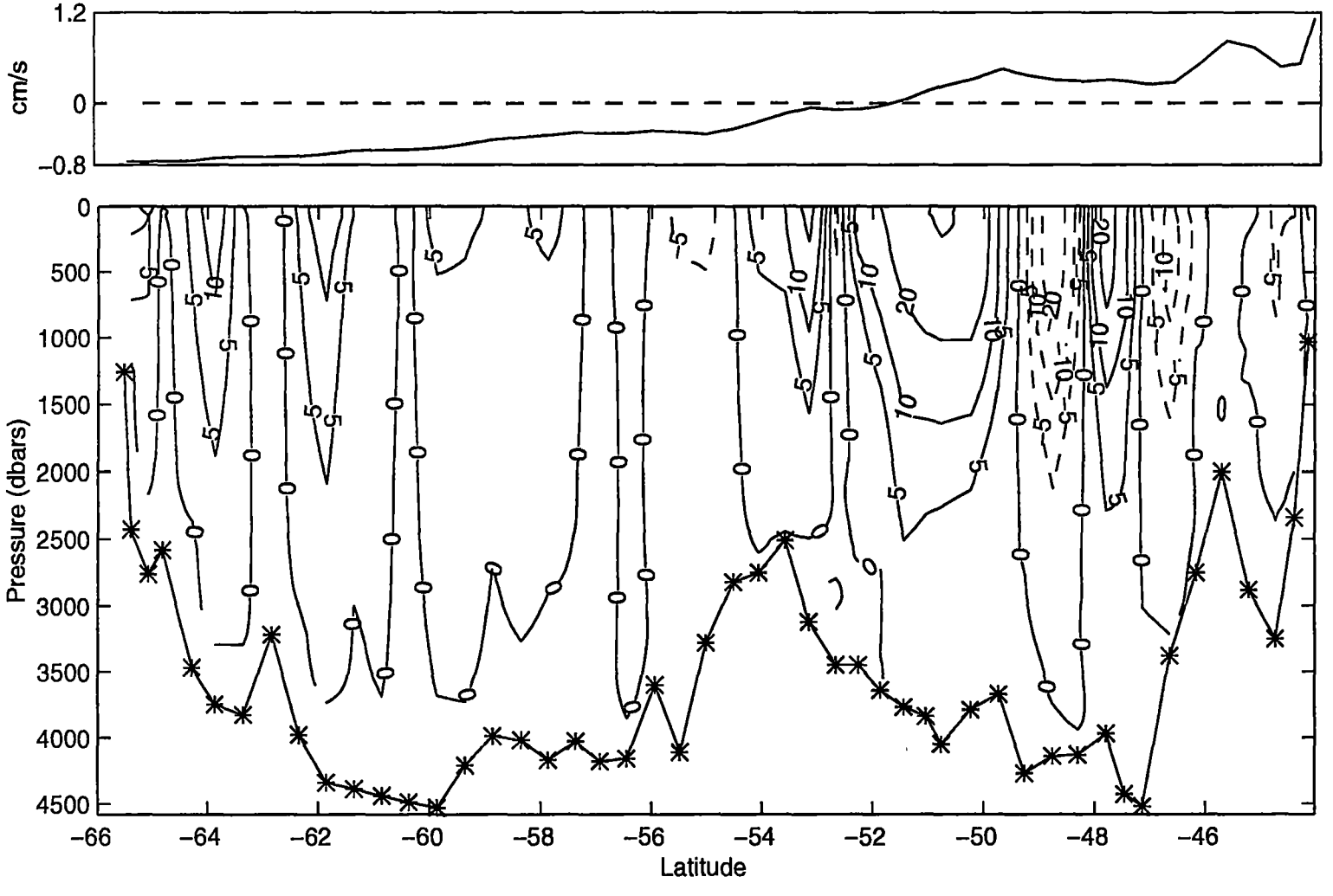

Figure 4.9: Absolute velocity at the section south of Australia. Solid and dashed contours refer to east and west velocities, respectively. Upper plot is reference level velocity.

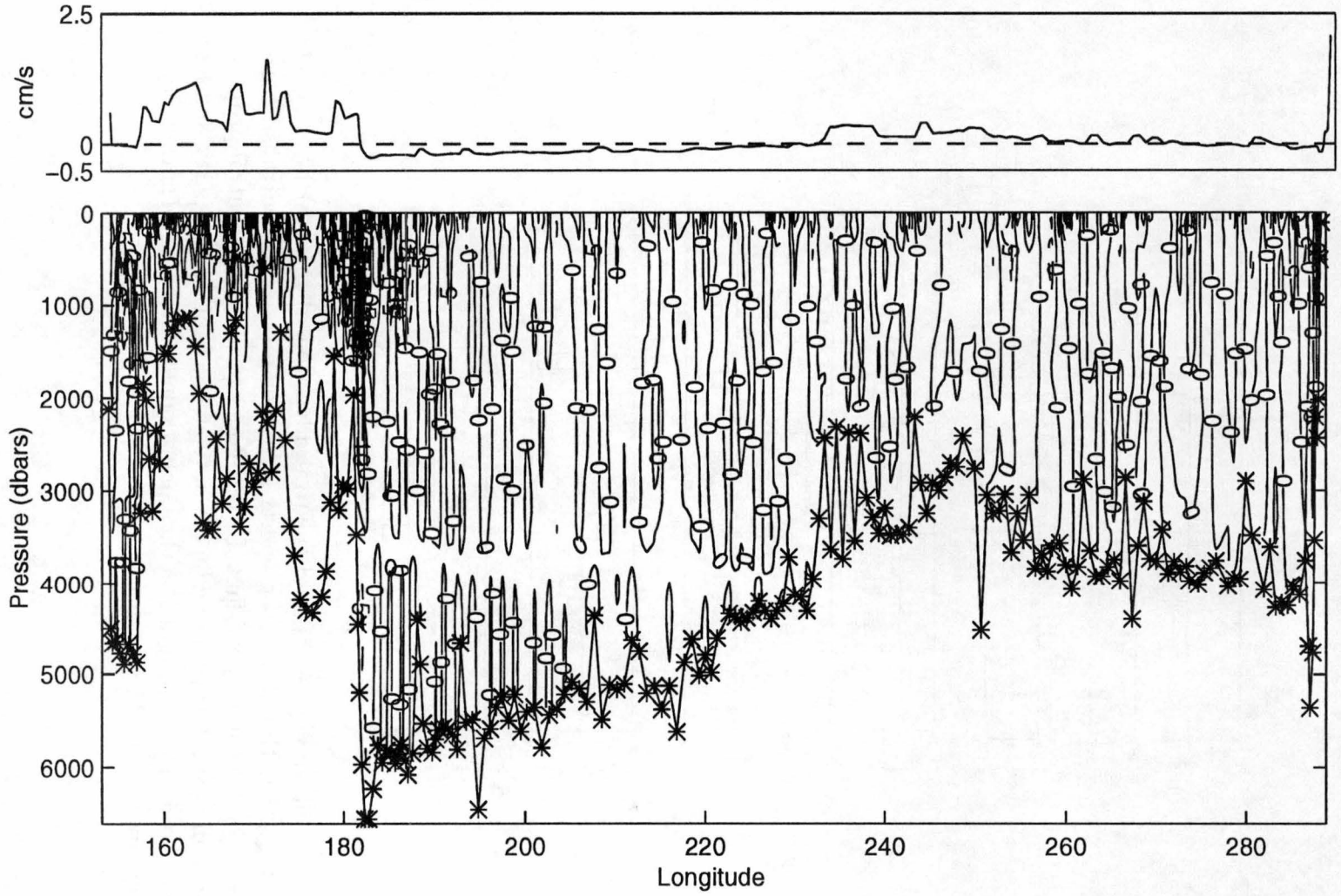

Figure 4.10: Absolute velocity at the Pacific 32°S section. Solid and dashed contours refer to north and south velocities, respectively. Upper plot is reference level velocity.

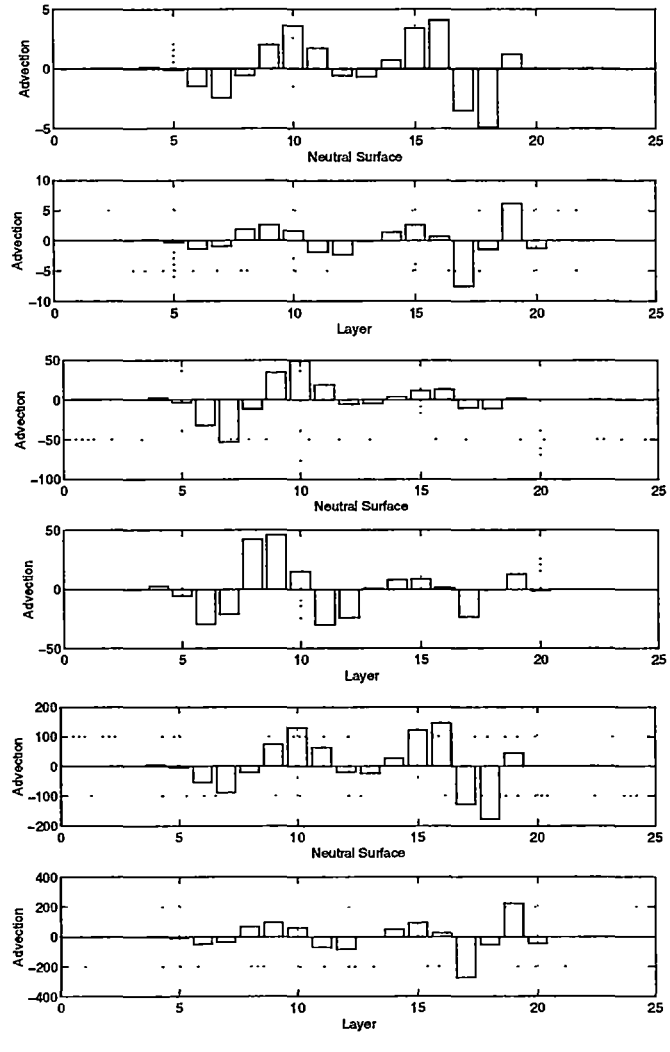

a)

b)

c)

Figure 4.11: Subtropical Atlantic dianeutral advection a) mass b) heat c) salt (prop$\times 10^6 m^3 s^{-1}$). Upper plots - property advection flux across neutral surfaces, +ve upward flux, -ve downward flux. Lower plots - resultant dianeutral property convergence in layer, +ve property flux gain (convergence), -ve property flux loss (divergence). Layer m is bounded on the upper boundary by neutral surface $m-1$ and on the upper boundary by neutral surface m

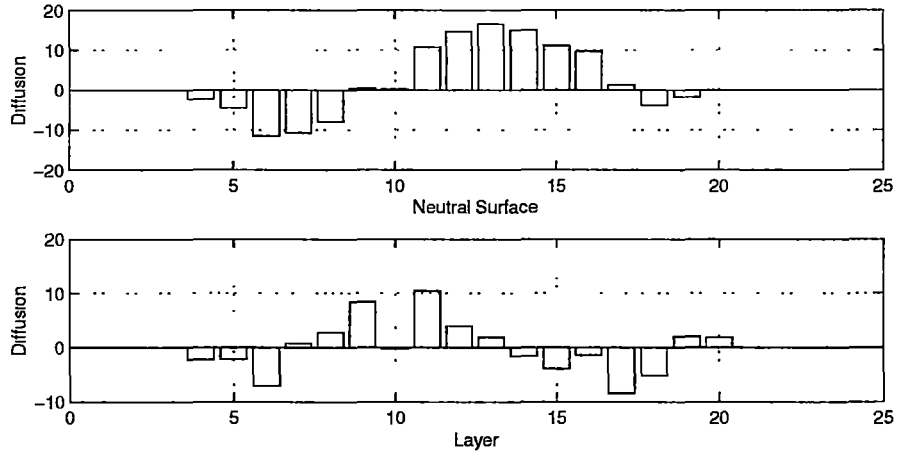

Figure 4.12: Subtropical Atlantic dianeutral effective heat diffusion ($\times 10^6$ °C $m^3 s^{-1}$). Upper plot - effective heat diffusion flux across neutral surface, +ve upward flux, -ve downward flux. Lower plot - resultant dianeutral effective heat convergence within layers, +ve heat flux gain (convergence), -ve heat flux loss (divergence)

and upper deep (16 and 17) neutral surfaces (Figure 4.12). This results in a redistribution of heat from the upper thermocline (4 to 6) into the lower thermocline (7 to 9), and a redistribution of lower intermediate layers (14 and 15) and upper deep layers (16 and 17) into upper intermediate water (11 to 13). There is also a conversion of heat from the lower deep layers (18) into bottom layers (19 and 20), respectively.

The effective salt diffusion is upwards across upper thermocline (4 and 5) neutral surfaces and downwards across underlying thermocline layer (6) (Figure 4.13). There is a smaller upward salt flux across deep (17 to 19) neutral surfaces (Figure 4.13). The salt diffusion redistributes salt from the upper thermocline layers (6) into underlying thermocline (7 to 9) and intermediate (12 to 15) layers.

The dianeutral "velocity", for each property is largest in the the upper thermocline layers (3 to 6) (Figure 4.14). These layers outcrop at the sea-surface and are substantially modified by sea-surface heat and freshwater fluxes that result in advection into lighter and denser water layers. Below the surface outcropping layers the dianeutral velocities are small ($O(10^{-7} ms^{-1})$ for all properties. The deep (18) and bottom (19 and 20) dianeutral mass velocity

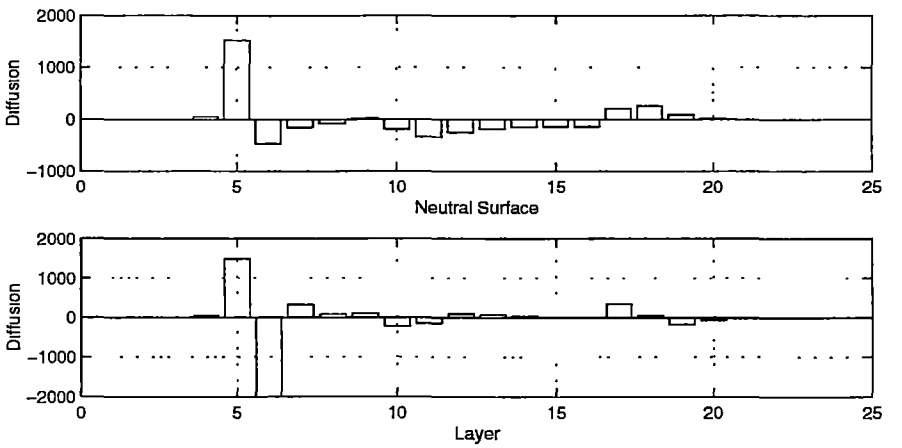

Figure 4.13: Subtropical Atlantic dianeutral effective salt diffusion ($\times 10^6$ psu $m^3 s^{-1}$). Upper plot - effective salt diffusion flux across neutral surface, +ve upward flux, -ve downward flux. Lower plot - resultant dianeutral effective salt convergence within layers, +ve salt flux gain (convergence), -ve salt heat flux loss (divergence)

is similar to previous estimates (Warren and Speer 1991; McCartney 1993; Speer and Zenk 1993).

In the Atlantic sector of the Southern Ocean (BII) (Figure 3.1) the advection flux is upwards across intermediate (11 to 14) and bottom (20 and 21) neutral surfaces and downward flux across deep (16 to 19) neutral surfaces (Figure 4.15). This results in a redistribution of lower intermediate layers (13 to 15), which identify AAIW, into upper intermediate layers (11 to 12, SAMW). The advection across bottom layer (21 and 22, WSDW and WSBW) and deep (16 to 18, NADW and CDW) layers results in a redistribution of NADW, from above, and WSDW and WSBW, from below, into CDW (layer 19) and generic AABW (layer 20). (The density on the classical Southern Ocean water masses (e.g. SAMW, AAIW) varies somewhat from basin to basin. In order to make the discussion easier to follow, I have used the water mass names to refer to particular density layers rather than using layer numbers only. The reader interested in the properties of a particular layer at a particular section is referred to Table 3.2).

The dianeutral effective heat diffusion is upwards across thermocline (8 to 10), intermediate (11 to 15) and deep (16 to 18) neutral surfaces and downward

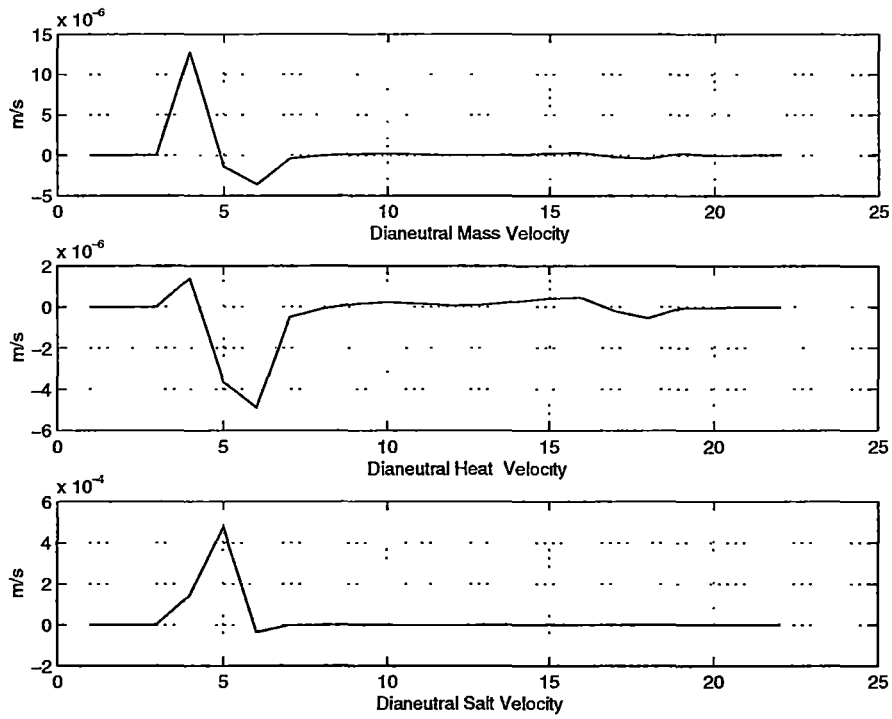

Figure 4.14: Subtropical Atlantic Mass, Heat and Salt Dianeutral "velocity" (ms^{-1}). +ve -upwards, -ve -downwards

across lower deep (19) and bottom (20) neutral surfaces (Figure 4.16). The dianeutral effective heat diffusion results in a redistribution of heat from deep layers (16 to 18) and lower intermediate layers (14 and 15) into upper intermediate (12 and 13) and thermocline layers (8 to 10). There is also a redistribution of heat from lower deep (19) and bottom (20) layers into extreme bottom water (layers 21 and 22, WSDW and WSBW respectively)

The dianeutral effective salt diffusion is downwards across all surfaces, with local maxima across the thermocline (10) and deep (17 and 18) neutral surfaces (Figure 4.17). This results in a salt loss from lower thermocline (9 and 10) layers into the intermediate (11 and 14, SAMW/AAIW) layers and a further redistribution of salt from upper deep (16 and 17, NADW) into lower deep (18 and 19, CDW) and bottom (20, AABW) layers.

The property "velocity" profiles are largest across the bottom layers (Figure 4.18). These large "velocities" result from the modification of Weddell Sea Deep and Bottom water (layers 21 and 22) into slightly less dense Antarctic

a)

b)

c)

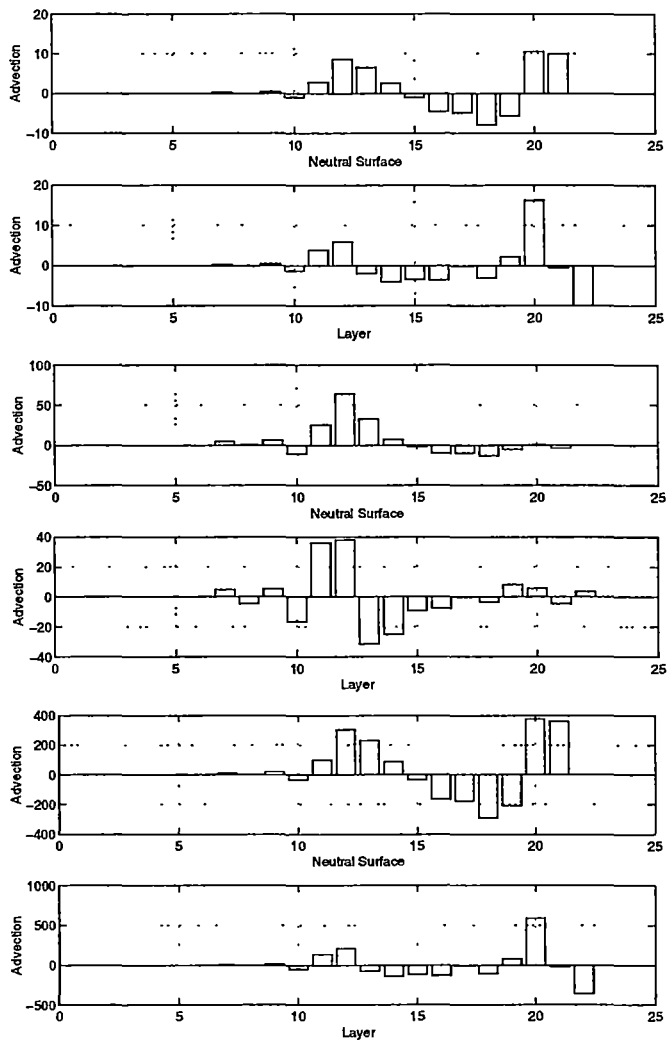

Figure 4.15: Southern Ocean Atlantic dianeutral advection a) mass b) heat c) salt (prop$\times 10^6 m^3 s^{-1}$). Upper plots - property advection flux across neutral surfaces, +ve upward flux, -ve downward flux. Lower plots - resultant dianeutral property convergence in layer, +ve property flux gain (convergence), -ve property flux loss (divergence). Layer m is bounded on the upper boundary by neutral surface $m-1$ and on the upper boundary by neutral surface m

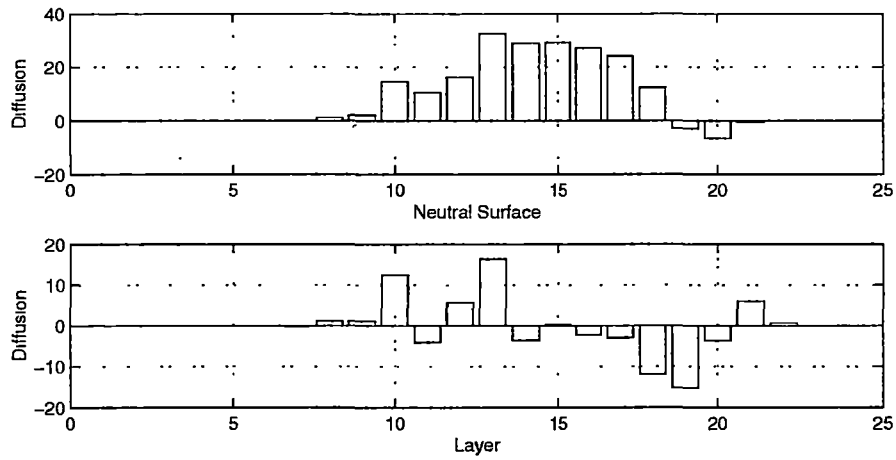

Figure 4.16: Southern Ocean Atlantic dianeutral effective heat diffusion ($\times 10^6$ °C $m^3 s^{-1}$). Upper plot - effective heat diffusion flux across neutral surface, +ve upward flux, -ve downward flux. Lower plot - resultant dianeutral effective heat convergence within layers, +ve heat flux gain (convergence), -ve heat flux loss (divergence)

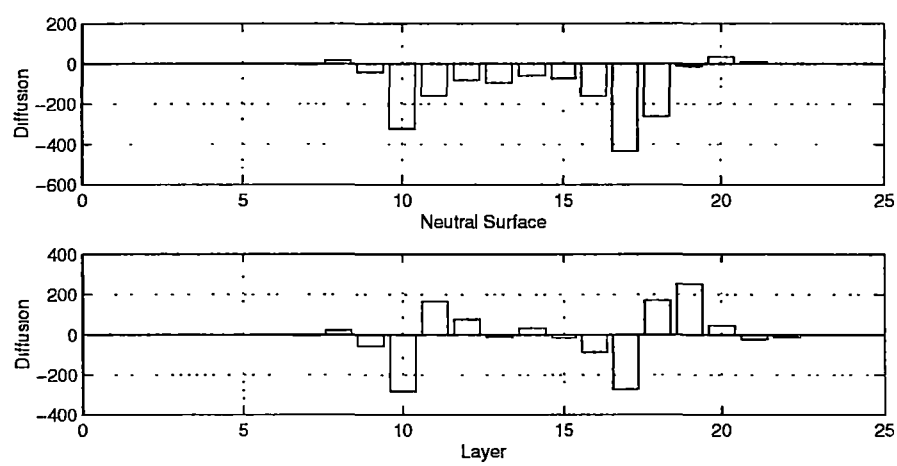

Figure 4.17: Southern Ocean Atlantic dianeutral effective salt diffusion ($\times 10^6$ psu $m^3 s^{-1}$). Upper plot - effective salt diffusion flux across neutral surface, +ve upward flux, -ve downward flux. Lower plot - resultant dianeutral effective salt convergence within layers, +ve salt flux gain (convergence), -ve salt heat flux loss (divergence)

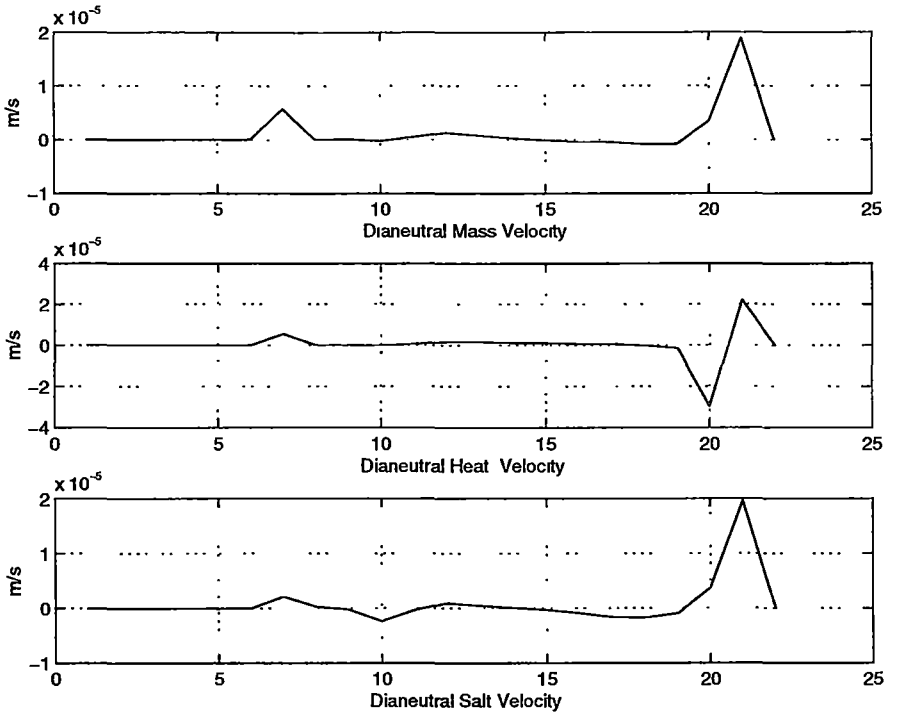

Figure 4.18: Southern Ocean Atlantic Mass, Heat and Salt Dianeutral "velocity" (ms^{-1}). +ve -upwards, -ve -downwards

Bottom Water (layers 20) and Lower Circumpolar Deep Water (layers 19).

The property advection in the subtropical Indian region (BIV) (Figure 3.1) shows two distinct modes: downward advection across thermocline (3 to 10) neutral surface and upward advection across lower intermediate (13 to 15), deep (16 to 18) and bottom (19) neutral surfaces (Figure 4.19). This results in a convergence of the upper thermocline layers (3 and 4) into the remaining thermocline layers (5 to 10) and upper intermediate layers (11 and 12), while lower deep (18 and 19, CDW) and bottom water (20, AABW) are converted into upper deep (16 and 17, UCDW/IDW) and lower intermediate (13 and 15) layers.

The dianeutral effective heat diffusion is upward across thermocline (3 and 10) neutral surfaces and downwards across lower intermediate (13 to 15), deep (16 to 18) and bottom (19 and 20) neutral surfaces (Figure 4.20). This results is a redistribution of heat from the lower thermocline layers (5 to 10) into upper thermocline layers (3 and 4), and a smaller conversion of lower intermediate (13

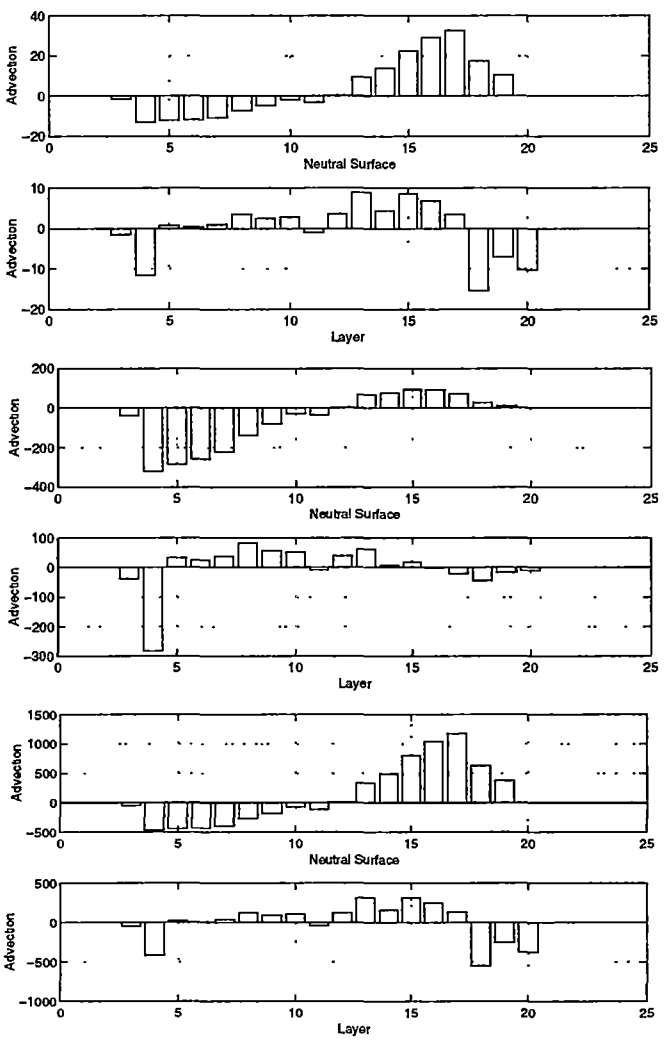

Figure 4.19: Subtropical Indian Ocean dianeutral advection a) mass b) heat c) salt (prop$\times 10^6 m^3 s^{-1}$). Upper plots - property advection flux across neutral surfaces, +ve upward flux, -ve downward flux. Lower plots - resultant dianeutral property convergence in layer, +ve property flux gain (convergence), -ve property flux loss (divergence). Layer m is bounded on the upper boundary by neutral surface $m-1$ and on the upper boundary by neutral surface m

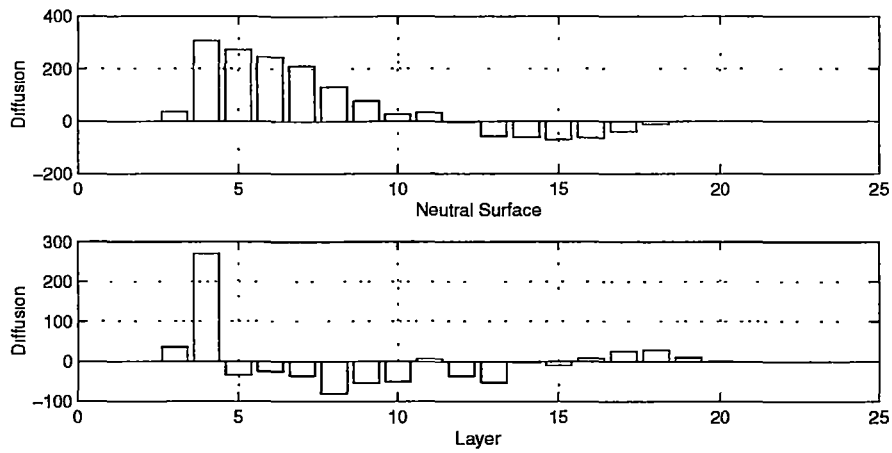

Figure 4.20: Subtropical Indian Ocean dianeutral effective heat diffusion ($\times 10^6$ °C $m^3 s^{-1}$). Upper plot - effective heat diffusion flux across neutral surface, +ve upward flux, -ve downward flux. Lower plot - resultant dianeutral effective heat convergence within layers, +ve heat flux gain (convergence), -ve heat flux loss (divergence)

to 15) into deep (16 to 18) and bottom (19 and 20) layers.

The salt effective diffusion is dominated by an upward flux across thermocline (10 to 4) and upper intermediate (11) neutral surfaces and a downward flux across lower intermediate (12 to 15) and deep (16 to 18) neutral surfaces (Figure 4.21). This results in a redistribution of salt from the intermediate layer (12) into the upper thermocline layers (4 to 10).

The largest dianeutral property "velocities" are present across deep (16 to 18) and bottom (19) neutral surfaces indicating that these layers undergo major modification within this region (Figure 4.22). The salt dianeutral "velocity" is also large across the upper thermocline and upper intermediate layers. This results in the redistribution of salt within the thermocline and upper intermediate layers.

The Southern Ocean Indian sector advection flux is downwards across the thermocline (6 to 10) and upper deep (16 to 17) neutral surfaces, while there is an upward flux across intermediate (12 to 14), lower deep (18 and 19) and bottom (20 and 21) neutral surfaces (Figure 4.23). This results in a convergence from thermocline layers (7 to 10) into upper intermediate layers (11 to 13, SAMW), and a convergence from upper deep layers (16 and 17, UCDW/IDW)

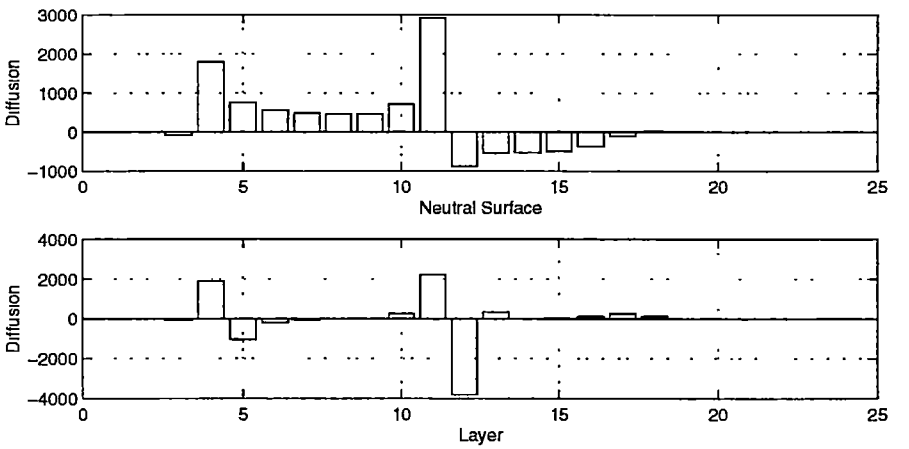

Figure 4.21: Subtropical Indian Ocean dianeutral effective salt diffusion ($\times 10^6$ psu $m^3 s^{-1}$). Upper plot - effective salt diffusion flux across neutral surface, +ve upward flux, -ve downward flux. Lower plot - resultant dianeutral effective salt convergence within layers, +ve salt flux gain (convergence), -ve salt heat flux loss (divergence)

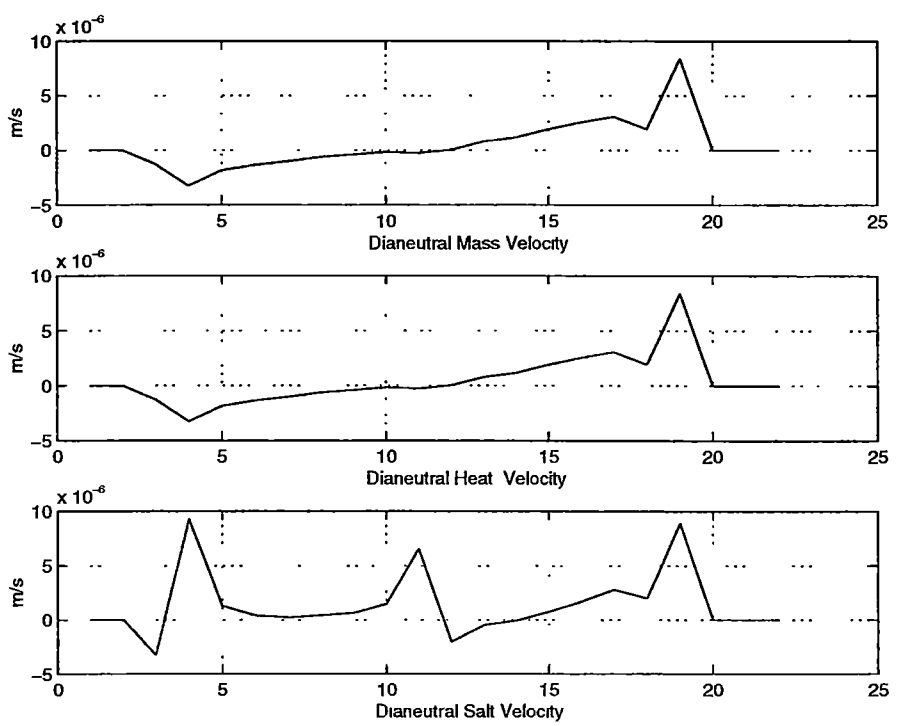

Figure 4.22: Subtropical Indian Ocean Mass, Heat and Salt Dianeutral "velocity" (ms^{-1}). +ve -upwards, -ve -downwards

into lower deep (17, CDW), and a conversion of extreme bottom water (21 and 22, WSDW, WSBW, RSBW, ALBW) into lower deep layers (18 and 19, CDW).

The dianeutral effective heat diffusion flux is downwards across all surfaces, although there are two maxima: at the lower thermocline (10) and upper intermediate (11 and 12) neutral surfaces; and across deep (16 to 18) neutral surfaces (Figure 4.24). This results in a net convergence of heat from the thermocline layers (7 to 10) and upper intermediate layers (11 and 12) into lower intermediate layers (13 and 14). The net convergence into lower deep (18 to 19) and bottom layers (20 to 21) results from a redistribution of heat from the lower intermediate layers (15) and upper deep layers (16). Salt diffusion is downward across the thermocline (8 and 9) neutral surfaces, and upwards across all other surfaces (Figure 4.25). The results in a redistribution of salt in the thermocline layers (8 to 10).

The dianeutral "velocities" are largest across the thermocline neutral surfaces reflecting the conversion of thermocline layers into upper intermediate layers (Figure 4.26). The large salt "velocities" across thermocline neutral surfaces result from the redistribution of salt within thermocline layers.

The advective flux in the Pacific is upward across lower thermocline (9 and 10) and upper intermediate (11) neutral surfaces and downwards across the deep (16 to 19) neutral surfaces, with smaller downwards fluxes across intermediate (12 to 15) neutral surfaces (Figure 4.27). This results in a convergence of upper intermediate layers (11 and 12, SAMW) into lower thermocline layers (9 and 10). There is also a significant convergence of upper deep layers (16 to 18, UCDW/LCDW) into lower deep layers (19 LCDW, AABW) and bottom layers (20 and 21, RSBW ALBW).

The dianeutral effective heat diffusion is downward across the upper thermocline (7 and 8) neutral surfaces and upwards across the lower thermocline (9 and 10), intermediate (11 to 15) and deep (16 to 19) neutral surfaces (Figure 4.28). This results in a convergence into lower thermocline layers (9 and 10) from the intermediate layers (12 and 15). There also a convergence of the heat into the bottom layers (20) from lower deep layers (19).

The dianeutral effective salt diffusion is upward across upper thermocline (7 and 8) and deep (16 to 19) neutral surfaces, while there is a downward flux

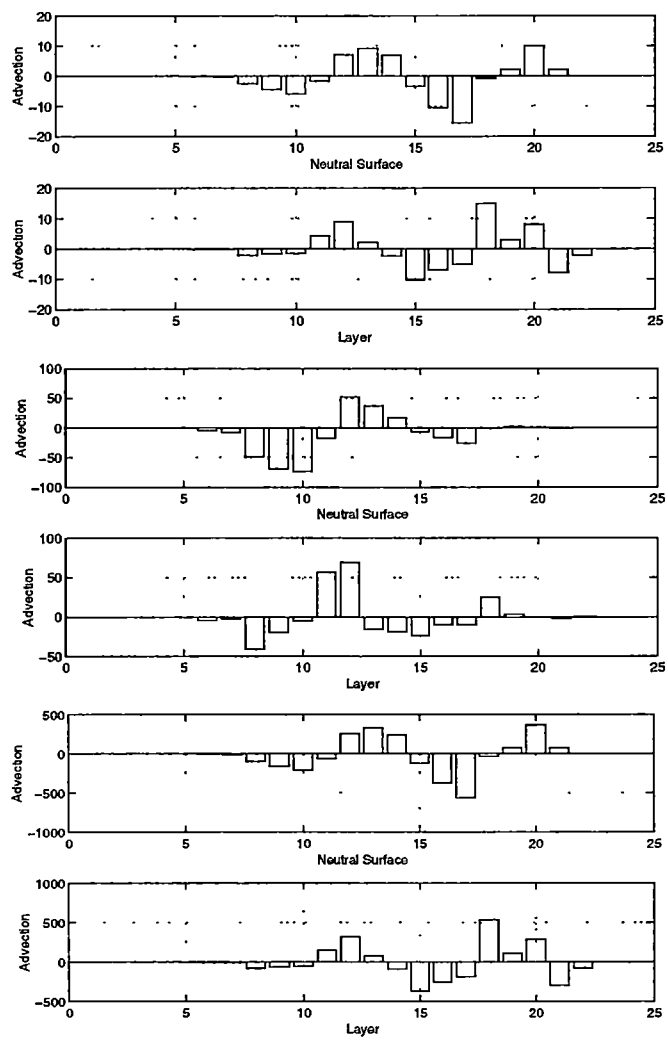

Figure 4.23: Southern Ocean Indian dianeutral advection a) mass b) heat c) salt (prop$\times 10^6 m^3 s^{-1}$). Upper plots - property advection flux across neutral surfaces, +ve upward flux, -ve downward flux. Lower plots - resultant dianeutral property convergence in layer, +ve property flux gain (convergence), -ve property flux loss (divergence). Layer m is bounded on the upper boundary by neutral surface $m-1$ and on the upper boundary by neutral surface m

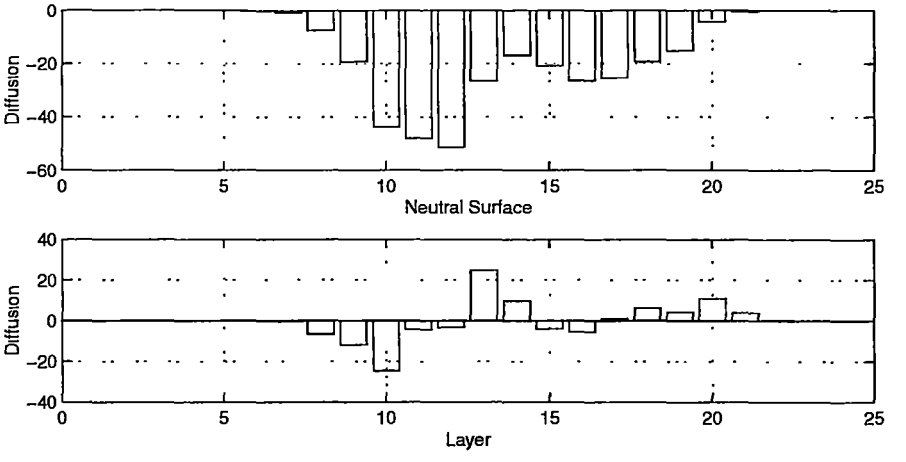

Figure 4.24: Southern Ocean Indian sector dianeutral effective heat diffusion ($\times 10^6$ °C $m^3 s^{-1}$). Upper plot - effective heat diffusion flux across neutral surface, +ve upward flux, -ve downward flux. Lower plot - resultant dianeutral effective heat convergence within layers, +ve heat flux gain (convergence), -ve heat flux loss (divergence)

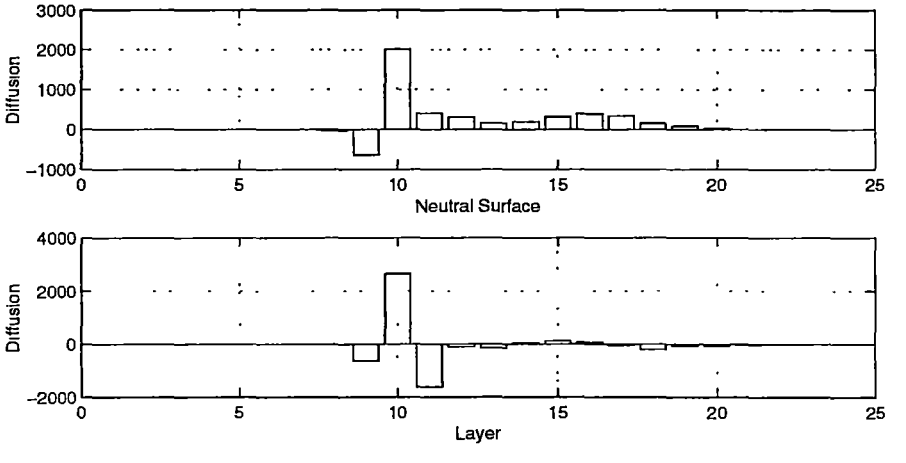

Figure 4.25: Southern Ocean Indian sector dianeutral effective salt diffusion ($\times 10^6$ psu $m^3 s^{-1}$). Upper plot - effective salt diffusion flux across neutral surface, +ve upward flux, -ve downward flux. Lower plot - resultant dianeutral effective salt convergence within layers, +ve salt flux gain (convergence), -ve salt heat flux loss (divergence)

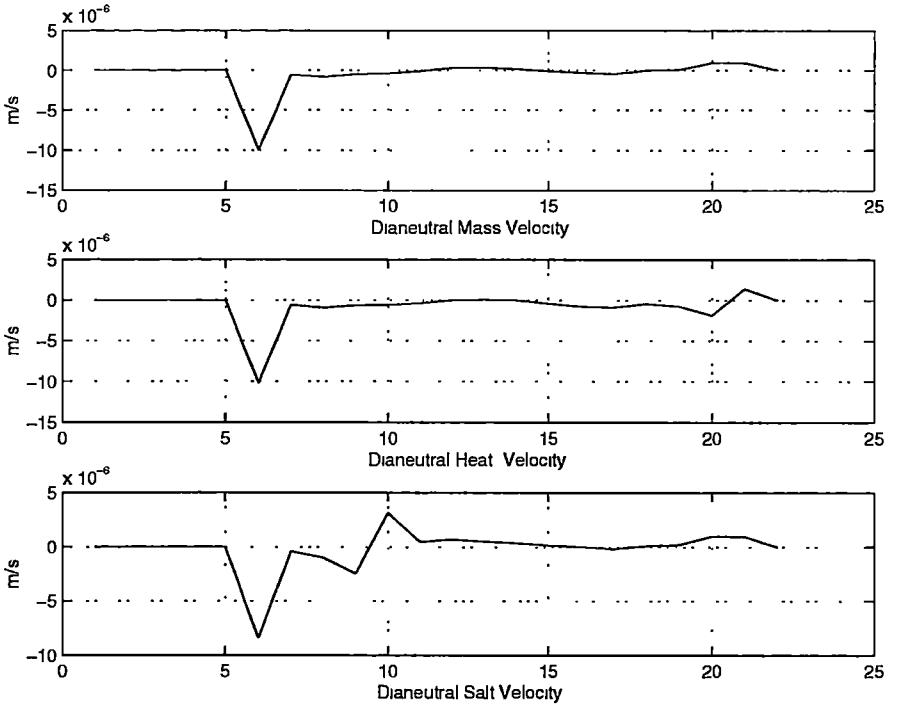

Figure 4.26: Southern Ocean Indian Mass, Heat and Salt Dianeutral "velocity" (ms^{-1}). +ve -upwards, -ve -downwards

across lower thermocline (9 and 10) and intermediate (11 to 15) neutral surfaces (Figure 4.29). This results in a net convergence of salt into upper thermocline layers (7 and 8) and upper intermediate layers (12 and 13) from lower thermocline layers (9) and a smaller convergence of salt from deep layers (17 to 19) into lower intermediate layers (15).

The dianeutral "velocity" of the Pacific sector are small compared to the other regions. The property "velocities" have a similar size across all neutral surfaces (Figure 4.30). The maintenance of similar sized property "velocities" across all neutral surfaces shows that thermocline, intermediate, deep and bottom water modification is occurring in the region.

As shown in Chapter 2 in principle it is possible to calculate diffusivities by dividing the effective property diffusion by the neutral surface area and the property gradient (which is poorly known). The diffusivity calculated in this way "parameterises" a wide range of process including deviations from the mean advective flux, air-sea interactions and other eddy processes which act on spatial scales of a few kilometres to basins-scale (or box scale). The implied

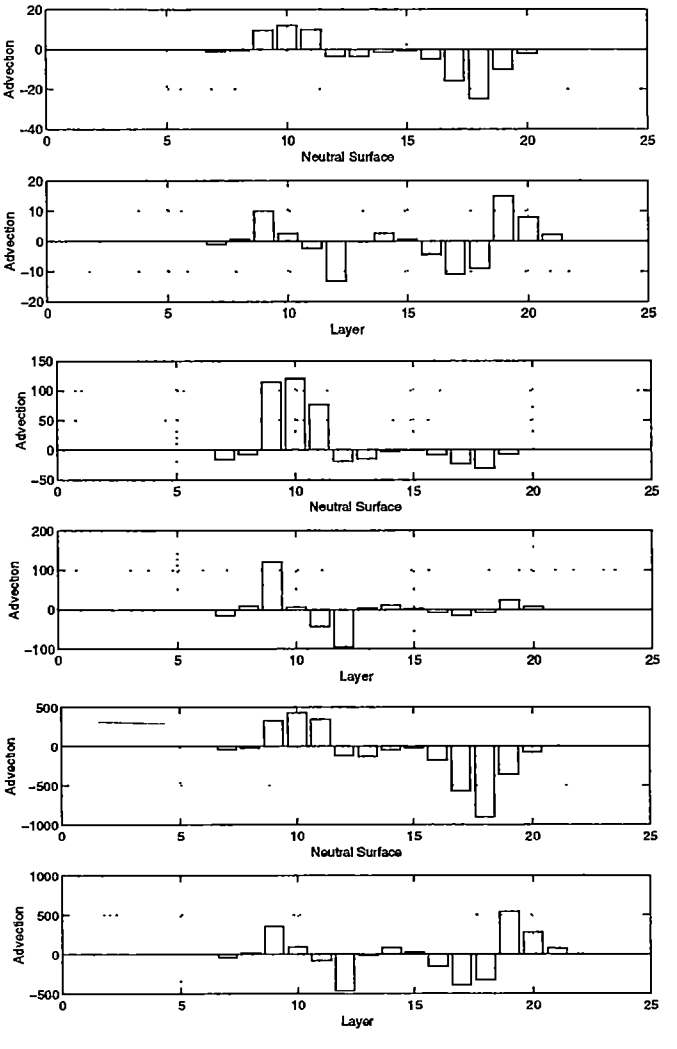

a)

b)

c)

Figure 4.27: Southern Ocean Pacific sector dianeutral advection a) mass b) heat c) salt (prop$\times 10^6 m^3 s^{-1}$). Upper plots - property advection flux across neutral surfaces, +ve upward flux, -ve downward flux. Lower plots - resultant dianeutral property convergence in layer, +ve property flux gain (convergence), -ve property flux loss (divergence). Layer m is bounded on the upper boundary by neutral surface $m-1$ and on the upper boundary by neutral surface m

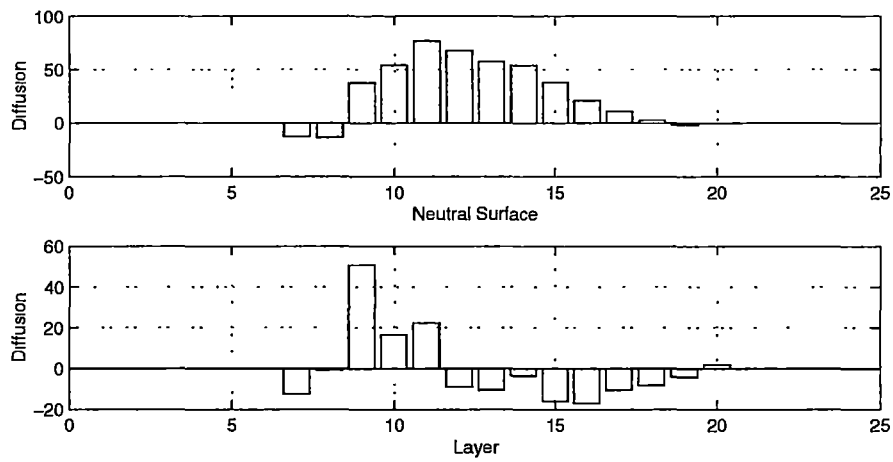

Figure 4.28: Southern Ocean Pacific sector dianeutral effective heat diffusion ($\times 10^6$ °C $m^3 s^{-1}$). Upper plot - effective heat diffusion flux across neutral surface, +ve upward flux, -ve downward flux. Lower plot - resultant dianeutral effective heat convergence within layers, +ve heat flux gain (convergence), -ve heat flux loss (divergence)

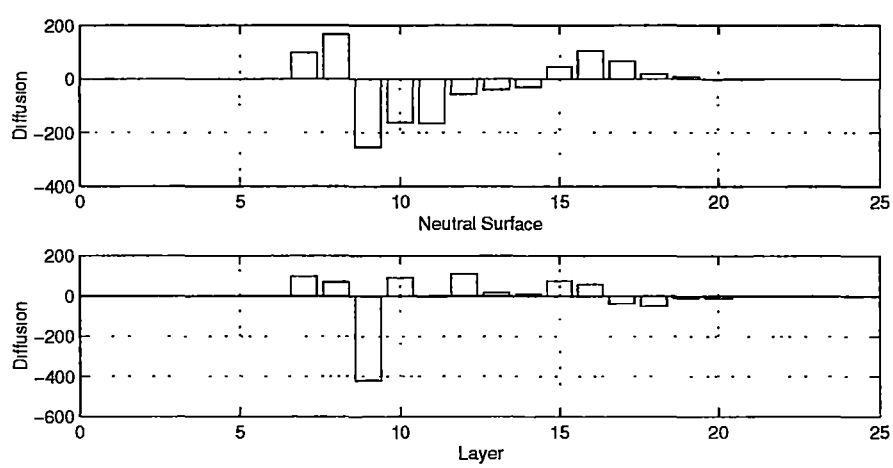

Figure 4.29: Southern Ocean Pacific sector dianeutral effective salt diffusion ($\times 10^6$ psu $m^3 s^{-1}$). Upper plot - effective salt diffusion flux across neutral surface, +ve upward flux, -ve downward flux. Lower plot - resultant dianeutral effective salt convergence within layers, +ve salt flux gain (convergence), -ve salt heat flux loss (divergence)

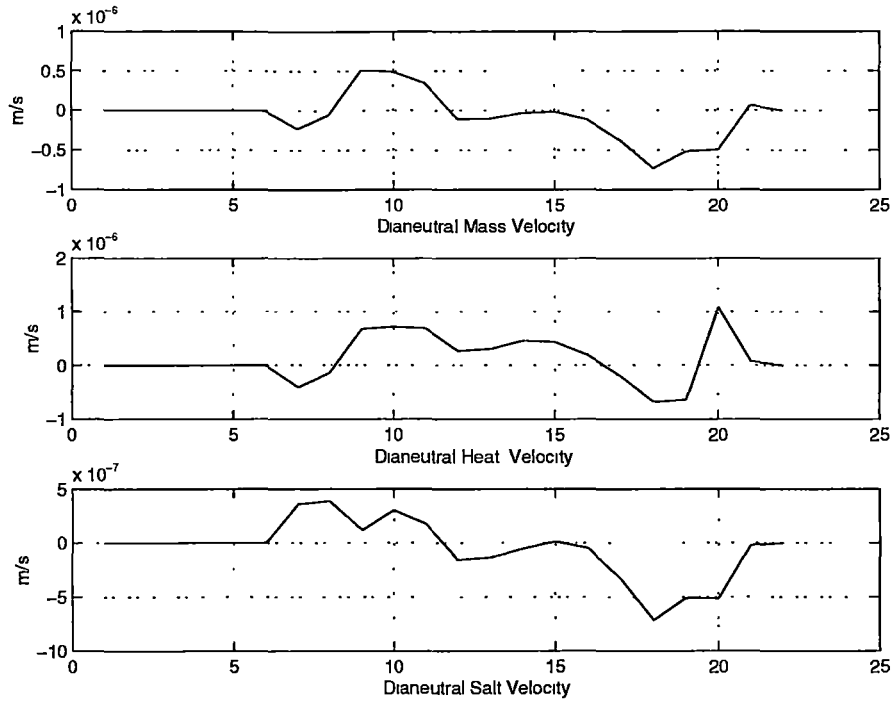

Figure 4.30: Southern Ocean Pacific Mass, Heat and Salt Dianeutral "velocity" (ms^{-1}). +ve -upwards, -ve -downwards

diffusivities (not shown here) are not strictly positive and result in diffusive fluxes that oppose the property gradient (ie. some fluxes are up-gradient) The interpretation of the diffusivities and comparison with other studies is unclear (e.g. see the comparison between calculated effective diffusivities and the explicit diffusivity in the FRAM experiments in Chapter 2, Figure 2.19 and Figure 2.20). For this reason a detailed study of the diffusivities is not given. The focus in the following sections is on the net dianeutral flux, which is what is important in terms of overall box budgets.

4.3 Mass, Heat and Salt Fluxes

The mass, heat and salt fluxes of the initial model are discussed in detail, and the discussion of subsequent model focus on the difference from this initial model. In this model (model_int) some aspects of the circulation (e.g. large Indonesian throughflow) are inconsistent with previous studies, prompting the development of the further models in Chapter 5 and Chapter 6. The best

estimate of the mass, heat and salt fluxes are discussed in Chapter 7.

The total property flux across each section is given in Table 4.1. The errors given in Table 4.1 are the "formal" errors from the inverse method, namely the noise and null space error. By minimising the condition number, small eigenvalues are avoided which minimise the errors due to the noise (see Appendix B). By weighting the problem to ensure it is well-conditioned, the rank is increased which reduces the null space error. The method of calculating of these errors is given in Appendix B. The errors do not contain an estimate of the ocean variability or the error associated with the non-synoptic sections and therefore probably underestimate the real uncertainty of the variability of section property fluxes.

The Atlantic Ocean has a small southward mass and salt flux, and a northward heat flux which are all comparable to previous estimates (Rintoul 1988; Coachman and Aagaard 1988; Wijffels et al. 1992; Macdonald and Wunsch 1996). The southward (-15$\pm$7$\times10^6 m^3 s^{-1}$) net transport in the Indian Ocean results in a large southward heat, salt and freshwater flux. The mass, heat and salt fluxes, from the Indian Ocean, carried into the Southern Ocean are balanced by an increased eastward flux of all properties south of Australia. The circulation pattern resolved by the inverse method is discussed in detail in the following sections.

4.3.1 Atlantic Region

The Atlantic region includes the subtropical (BI) and Southern Ocean sector (BII) (Figure 3.1). The subtropical Atlantic Ocean is divided into a western and eastern regime by the mid-Atlantic ridge (Figure 4.31). There is a further division of the western basin into the Brazil and Argentine basins by the Rio Grande rise, while the eastern basin is divided into the Angola and Cape basins by the Walvis ridge. The Weddell gyre is found south of the America-Antarctic ridge, with deep passages in this and the Scotia ridge allowing AABW northward passage into the Atlantic Ocean.

section	Mass($\times 10^6 m^3 s^{-1}$)	Heat($\times 10^6$ °C $m^3 s^{-1}$)	Salt($\times 10^6 kg s^{-1}$)	Freshwater($\times 10^9 kg s^{-1}$)	Silica ($kmol s^{-1}$)
SAVE2	-0.71±8.8	108.94±38.9	-24.93±32.9	-0.79±0.9	8.7±354.7
SAVE4	-0.58±5.1	109.21±16.8	-19.13±64.5	-0.63±5.1	-311.9±317.6
Drake P	133.11±2	339.86±3.8	4720.1±30.3	132.34±2.1	8911.7±191.1
S. Africa	133.64±6.8	206.22±14.2	4735.7±83.4	132.89±6.9	9972.1±586.1
Weddell Sea	0.01±2.9	-24.40±0.9	0.68±37.7	0.05±2.9	193.7±358.1
Ind18	-14.73±6.4	-256.48±31.66	-524.31±57.0	-14.62±6.6	-758.0±623.8
Ind32	-14.73±7.4	-256.57±36.1	-524.72±65.0	-14.52±7.6	213.6±490.1
S. Aust	148.37±4.1	462.60±10.1	5262.30±56.1	147.48±4.1	8085.5±314.3
Pac32	15.28±8.5	122.70±37.5	543.96±117.8	15.18±8.7	755.2±678.6

Table 4.1: Total property flux for all sections. +ve - northwards or eastward flux, -ve - southward or westward flux. Units: mass $\times 10^6 m^3 s^{-1}$ and heat $\times 10^6$ °C $m^3 s^{-1}$ relative to 0°C, salt $\times 10^6 kg s^{-1}$, freshwater $\times 10^9 kg s^{-1}$ and silica $kmol s^{-1}$

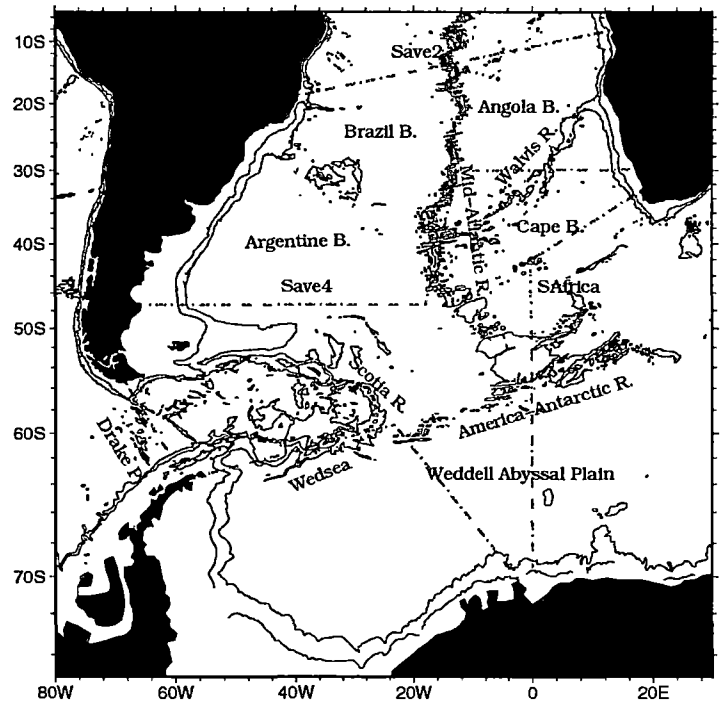

Figure 4.31: Topographic features of the Atlantic Ocean with position of hydrographic section (dot-dash). Contours 1000, 3000 metres

Mass Flux

The small southward total mass flux across SAVE2 and SAVE4 results as the Atlantic Ocean north of 18°S is not a closed basin. There is a small inflow of fresh, cold Pacific water into the Atlantic via the Bering Strait of $0.8\times10^6 m^3 s^{-1}$ (Coachman and Aagaard 1988). The overall section flux is achieved by a northward transport of thermocline layers (5 to 10), intermediate layers (11 to 15) and bottom layers (19 and 20) and an opposing southward transport deep layers (16 to 18) which characterise NADW. The NADW mass transport across SAVE2 is $20\times10^6 m^3 s^{-1}$, of which $14\times10^6 m^3 s^{-1}$ enters in the Brazil basin and $6\times10^6 m^3 s^{-1}$ flows southward in the Angola basin (Figure 4.32). McCartney (1993) estimates a net flow $20.4\times10^6 m^3 s^{-1}$ of NADW into the South Atlantic. He highlights that this transport is achieved within recirculating gyres of similar magnitude, with the deep boundary current transporting twice the amount of NADW into the northern Brazil basin. Further estimates of NADW southward transport into the South Atlantic vary between $13.3\times10^6 m^3 s^{-1}$ to $17\times10^6 m^3 s^{-1}$ (Rintoul 1991; Dickson and Brown 1994; Schmitz 1995).

There is a weak, shallow western boundary current at SAVE2 of $3\times10^6 m^3 s^{-1}$ (relative to 1500 dbars) which identifies the beginnings of the Brazil Current. Much of the Atlantic South Equatorial Current (SEC) is lost to the northern hemisphere which results in a weak northern Brazil Current (Peterson and Stramma 1991). There is no evidence of strengthening of the Brazil Current between 10°S and 20°S, with an average transport of $4\times10^6 m^3 s^{-1}$ in the region (Stramma et al. 1990). The Brazil Current intensifies and deepens further to the south.

Figure 4.32 shows the layer fluxes in the Brazil basin and the Angola basin. In the Angola basin southward transport dominates the intermediate layers (11 to 15, SAMW/AAIW) and deep layers (16 to 18). The bottom layer (19, AABW) has a small northward transport (not shown) (Appendix D, Table D.1). The flow pattern of Reid (1989) also has a southward transport of intermediate layers within the Angola basin, fed by an implied eastward flow (dashed lines) of intermediate water south of the equator (Figure 4.33). The eastward flow of AAIW south of the equator is highlighted by a low salinity,

high oxygen tongue extending eastwards from the western boundary (Suga and Talley 1995). The salinity maximum (> 34.9) of deep layers in the Angola basin indicate that some NADW enters the South Atlantic in the eastern basin (Figure 3.3). The small northward transport of AABW in the Angola basin is not consistent with topographic barriers and previous studies. The Angola basin is closed, at its southern end, by the Walvis ridge below 4000 dbars, thus restricting direct input of AABW. McCartney and Curry (1993) find an unquantified amount of AABW moving eastward through the Romanche Fracture Zone, while Warren and Speer (1991) identify southward transport of AABW ($1.2\times10^{6}m^{3}s^{-1}$) in the Angola basin which enters to the north over the Guinea Rise. AAIW and AABW moves northward in the Brazil basin providing the main route for these waters to penetrate into the North Atlantic.

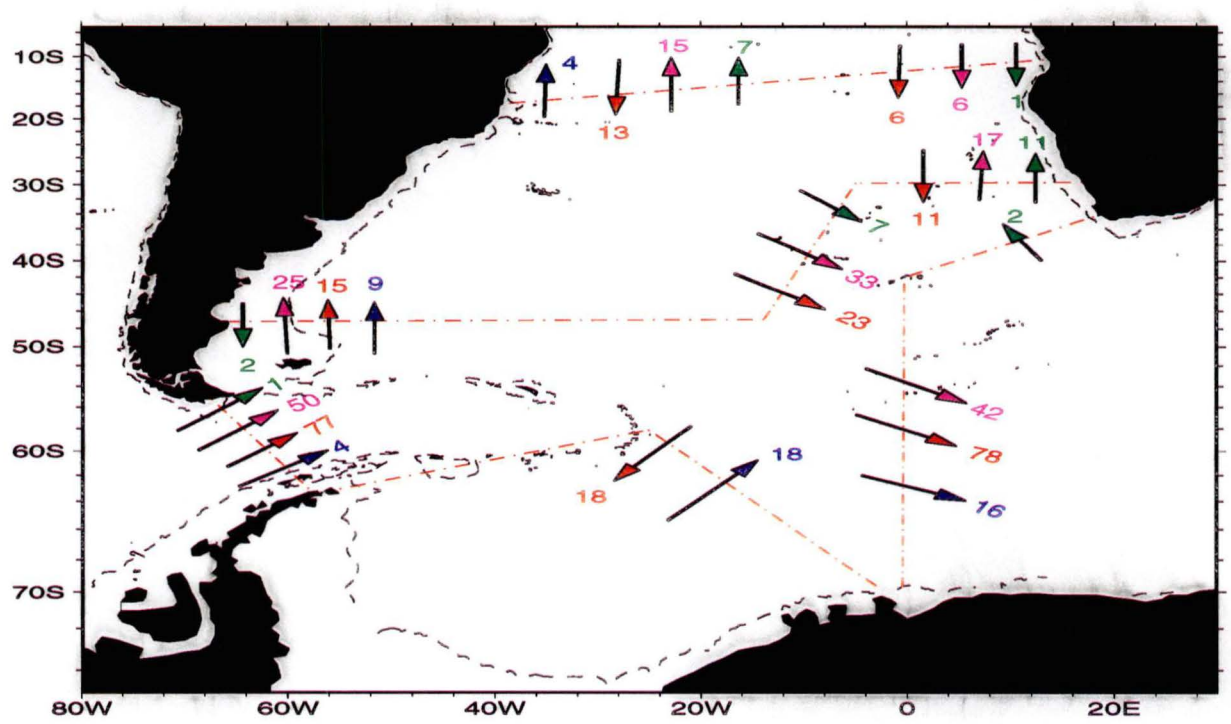

Figure 4.32: Transport ($\times 10^6 m^3 s^{-1}$) of particular layers in the Atlantic Region. Thermocline layers 5 to 10 (green), Intermediate layers 11 to 15 (magenta), Deep layers 16 to 18 across SAVE2, SAVE4 and 16 to 19 across Drake Passage, south Africa and Weddell Sea (red) and Bottom layers 20 to 22 (dark blue). Dashed line 1000 dbar contour

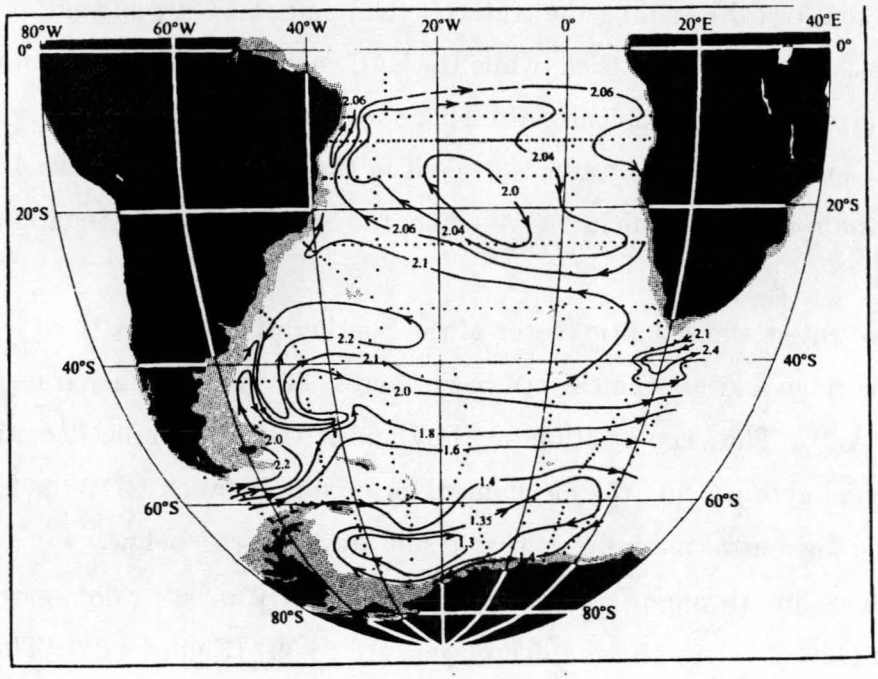

Figure 4.33: Adjusted steric height ϕ_A at 800 dbar ($10m^2s^{-2} or 10Jkg{-}1$). Depths less than 1000 m are shaded (after Reid 1989).

In the Argentine basin (47°S) the Malvinas (Falkland) Current has a transport of $19\times10^6m^3s^{-1}$, which is in agreement with previous estimates (Gordon and Greengrove 1986; Piola and Bianchi 1990). Recently, Peterson and Stramma (1991) have identified that the Subantarctic Front (SAF) turns northwards east of Drake Passage essentially becoming the Malvinas Current. Peterson (1992) suggests that the actual strength of the Malvinas Current could be $60\times10^6m^3s^{-1}$ to $70\times10^6m^3s^{-1}$, which represents the mass transport through Drake Passage north of the SAF. The effect, on the circulation, of imposing a large Malvinas Current will be discussed in a later chapter (Chapter 6).

There is northward transport in all water classes (Figure 4.32) in the Argentine basin. The northward flow continues along the coast to between 38°S and 33°S where it meets the southward Brazil Current forming the Brazil-Malvinas Confluence which moves eastward across the South Atlantic forming the South Atlantic Current (SAC). AABW continues northwards along the coast as a deep western boundary current. The eastward SAC and SAF are evident over the mid-Atlantic ridge and in the Angola basin (Figure 4.32). The

SAF moves southward rejoining the Antarctic Circumpolar Current and continues eastward south of Africa, while the SAC moves northwards forming the closing arm of the subtropical gyre. This northward transport of intermediate and thermocline water is evident in the Cape basin (Figure 4.32). This is the main route by which AAIW enters the South Atlantic (Suga and Talley 1995).

NADW enters the Atlantic sector of the Southern Ocean over the mid-Atlantic ridge and via the eastern basins across 30 °S with a net transport of $12\times10^6 m^3 s^{-1}$. The juxtaposition of CDW and NADW of similar densities in the subtropical gyre provide the mechanism for mixing between CDW and NADW. The dianeutral mass fluxes that result are discussed below.

The mass flux through Drake Passage is $133\pm2\times10^6 m^3 s^{-1}$, dominated by intermediate layers (11 to 15) and deep layers (16 to 19) (Figure 4.32). This mass flux through Drake Passage is consistent with previous estimates which range between $117\times10^6 m^3 s^{-1}$ to $137\times10^6 m^3 s^{-1}$ (Nowlin and Klinck 1986). Rintoul (1991) also found that intermediate ($83\times10^6 m^3 s^{-1}$) and deep ($43\times10^6 m^3 s^{-1}$) layers were the dominant water classes through Drake Passage. The ACC leaves the Atlantic sector south of Africa, with a transport of $133.6\pm2\times10^6 m^3 s^{-1}$. The slight increase in the size of the ACC through the region is due to the small mass input from the South Atlantic. South of Africa the dominant layer transport again occurs in the intermediate and deep layers, although there is an increase in the eastward transport of bottom layers (20 to 22) (Figure 4.32).

Contained in the Atlantic sector of the Southern Ocean is the Weddell Sea region (BIII). This has a zero mass constraint across its bounding section (wedsea). This constraint is achieved by inflow of deep, warm salty water ($17\times10^6 m^3 s^{-1}$, layers 16 to 19) and the outflow of extreme AABW ($18\times10^6 m^3 s^{-1}$, layers 20 to 22), comprised of Weddell Sea Deep and Bottom water. The southward advection of deep water and the northward advection of Weddell Sea bottom water is consistent with other studies that find warm deep water is the only northern source water advected into the Weddell Sea (Orsi et al. 1993). The input of this Weddell Sea Deep and Bottom water into the Southern Ocean renews AABW in the Circumpolar Current. The strength of

the overturning cell is larger than previous estimates of $6\times10^6 m^3 s^{-1}$ to $9\times10^6 m^3 s^{-1}$ (Rintoul 1991; Fahrbach et al. 1994). Chapter 6 investigated the sensitivity of the northward transport of Weddell Deep and Bottom water to the estimated heat loss over the region.

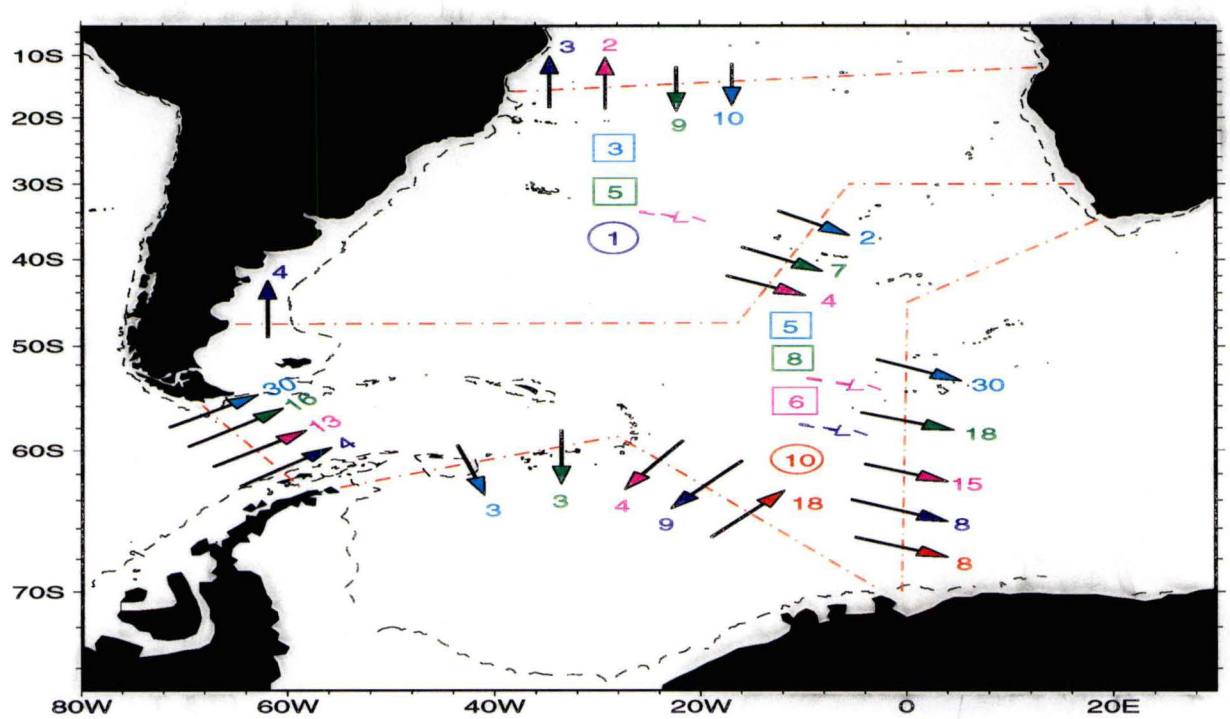

Figure 4.34: Mass transport and dianeutral flux ($\times 10^6 m^3 s^{-1}$) within Deep and Bottom water in the Atlantic Region (BI,BII). Upward Dianeutral flux- circle, Downward Dianeutral Flux - square, dashed arrow represent net production within layers due to dianeutral flux. UCDW/NADW (layer 17, light blue), UCDW/NADW/LCDW (layer 18, green), LCDW/AABW (layer 19, magenta), AABW (layer 20, dark blue), and extreme AABW (layer 21 and 22, red). Dashed line 1000 dbar contour

The mass transport shown in Figure 4.32 results from lateral and dianeutral fluxes across neutral surfaces. The dianeutral flux results in the transfer of mass and other properties between layers. In the Atlantic region the largest dianeutral fluxes occurs across deep and bottom layers. These dianeutral fluxes convert NADW (layers 17 and 18) into CDW (layers 18 and 19), the resulting changes in CDW characteristics highlight these mixing process. To examine the dianeutral advection occurring it is appropriate to examine the deep and bottom water layers in finer detail by considering individual layers.

In the subtropical Atlantic southward moving NADW (layers 17 and 18) mixes with both overlying intermediate layers (layer 15, not shown) and underlying CDW (layer 19) and AABW (layer 20) (Figure 4.34). NADW characteristics are dispersed into both denser and lighter surrounding layers by dianeutral heat and salt fluxes. The dianeutral heat and salt fluxes drive the mass advection across both upper and lower bounding surface of NADW. AABW/CDW (layers 19 to 20) enters the subtropical Atlantic in the Argentine basin. Some of the CDW/AABW continues along the western boundary, being modified as it move northward by overlying NADW resulting in the warmer and saltier CDW/AABW which moves north across SAVE 2. Th remaining AABW/CDW moves eastward with the Falkland-Malvinas Confluence where the dianeutral heat and salt flux, from NADW and CDW modify AABW resulting in the dianeutral advection of AABW into less dense AABW and CDW (Figure 4.34).

The input of NADW into the Southern Ocean Atlantic sector from the north and Weddell Sea Deep and Bottom water from the south produces changes in the characteristics of CDW. The input of these water masses result in ventilation of CDW and the classical salinity and oxygen distinction between UCDW and LCDW. These changes show the differences in the properties of CDW entering through Drake Passage and those leaving south of Africa which are more influenced by NADW and WSDW (Figure 4.35 and Figure 4.36).

The Weddell Sea bottom water is produced by the cooling of imported CDW in the Weddell Sea region (BIII). The loss of CDW to the Weddell Sea, and its subsequent return as much colder and denser Weddell Sea Deep and Bottom water, is replenished by the input of warm, salty oxygen rich NADW

across SAVE4. The addition of this salty water results in a dianeutral salt flux from NADW (layers 17 and 18) into denser CDW and the further erosion of the strong salinity maximum associated with NADW. Figure 4.35 and Figure 4.36 highlight the changes in CDW between Drake Passage and south of Africa which result from the input of NADW into these water layer. At Drake Passage there is no salinity maximum associated with LCDW, with UCDW oxygen minimum dominating CDW. When CDW leaves the Atlantic sector south of Africa the salinity and oxygen maxima associated with LCDW has been re-established.

The extreme properties of AABW (Weddell Sea Deep and Bottom Water, layer 21 and 22) are eroded by the downward dianeutral heat flux from CDW (layer 18 and 19) and NADW (layers 17 and 18). This results in a major change in the dominance of extreme Weddell Sea Bottom Water (layer 22) at the Weddell Sea to generic AABW and Weddell Sea Deep Water south of Africa (layer 20 and 21, respectively) (Figure 4.34).

The effects of dianeutral heat and salt fluxes results in the mass advection of extreme AABW (mainly WSBW and WSDW) into slightly less dense AABW and the mass advection of NADW into LCDW and AABW (Figure 4.34). These mixing processes act to diffuse the NADW temperature and salinity signatures, which is evident by the distinction between UCDW and LCDW south of Africa and the dilution of the salinity maximum of NADW between SAVE4 and south of Africa, although there is still a distinct maximum adjacent to the Africa coast.

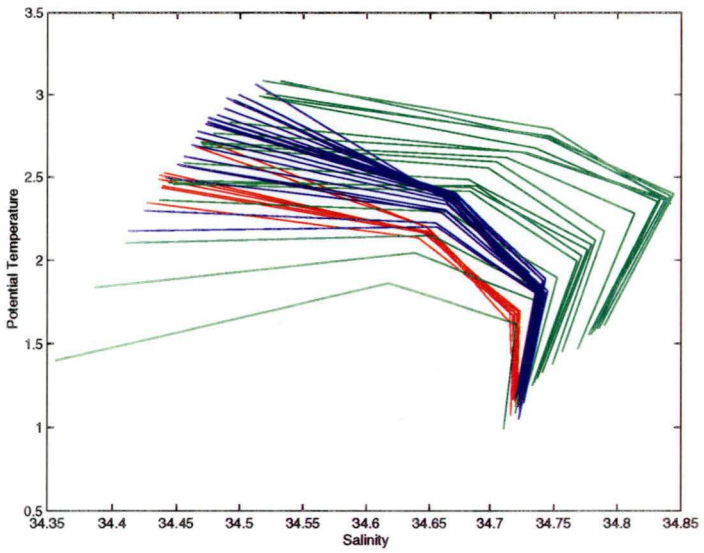

Figure 4.35: Circumpolar Deep Water (layers 16-19) Temperature (°C) - Salinity (psu) diagram. DrakeP (red), SAfrica (green) and SAust (dark blue)

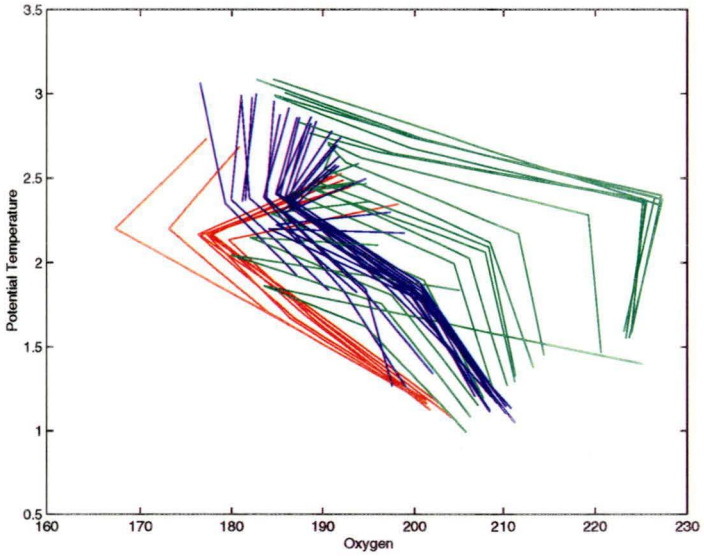

Figure 4.36: Circumpolar Deep Water (layers 16-19) Temperature (°C) - Oxygen(μmol.kg^{-1}) diagram. DrakeP (red), SAfrica (green) and SAust (dark blue)

The circulation pattern for the South Atlantic subtropical gyre derived, in this study, is similar to previous studies (Reid 1989; Stramma and Peterson 1990). This consists of a subtropical gyre between 10 °S and 30 °S. The Brazil-Malvinas Confluence forms the southern limb of the gyre which moves eastward across the Atlantic. The returning northward limb, on the eastern boundary, is the main route by which SAMW and AAIW (layers 11 to 15) enter the Atlantic Ocean. NADW penetrates southward adjacent the South American coast at 19 °S with underlying northward AABW flowing northwards along the western boundary from 47 °S. NADW moves eastward across the Mid-Atlantic ridge and southward in the Cape basin providing the route by which this water mass enters the Southern Ocean and renews CDW. The ACC in the Southern Ocean Atlantic sector is dominated eastward intermediate (layers 11 to 15) and deep (layers 16 to 19) transport. The circulation derived from this model agrees with previous studies, highlighting that the model has correctly captured the main features. The most important aspect of the circulation is that it is achieved within a 3-D mass conserving model. The model quantifies the vertical exchanges occurring between NADW, CDW, AABW, WSDW and WSBW. This mixing regime between these water masses quantifies the hypothesised mixing scheme proposed by Schmitz (1995) and Schmitz (1996a).

Heat Flux

The estimated heat flux across Save2 and Save4 is 0.46±0.07PW (1 PW = 10^{15}W) northwards. (The heat flux quoted are calculated relative to 0°C). This results from warmer thermocline (5 to 10) and intermediate (11 to 15) layers being the main layers that balance the colder southward NADW inflow into the Southern Ocean (Figure 4.37). At Save4 the intermediate heat transport is the largest component, while at Save2 the thermocline layers dominate the heat transport. The heat flux associated with the ACC through Drake Passage and south of Africa, of 1.10 PW and 0.88 PW respectively, is similar to that found by Macdonald and Wunsch (1996).

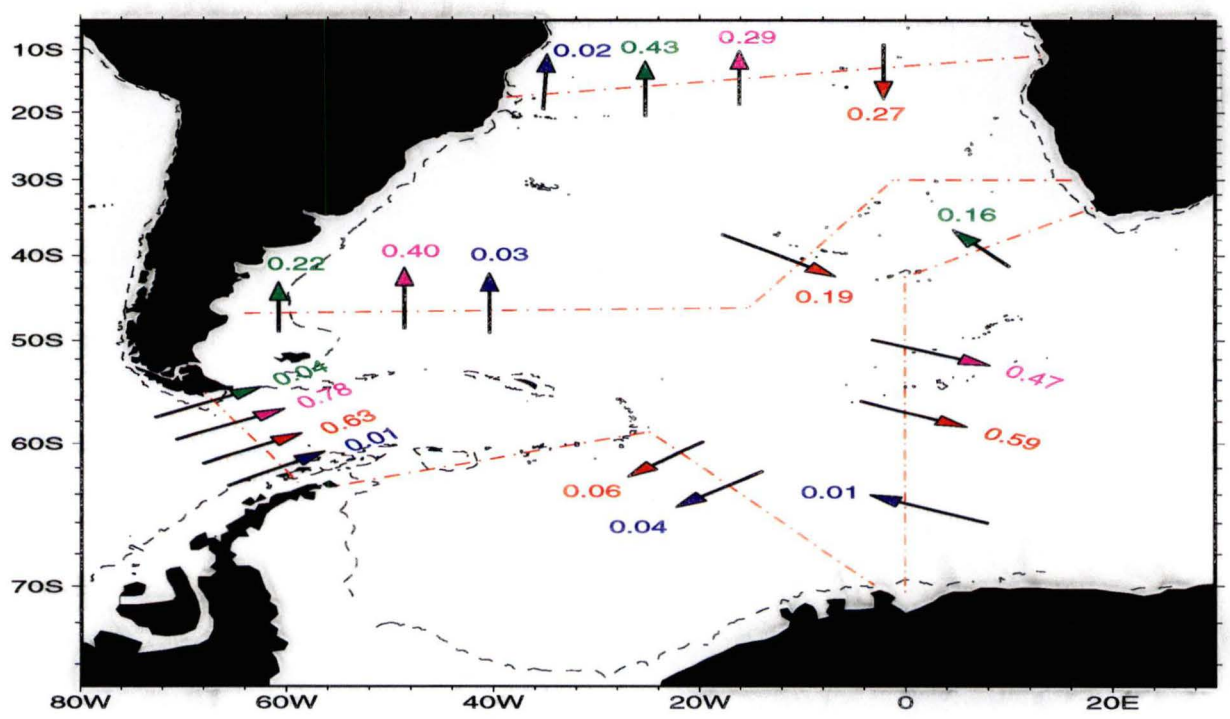

Figure 4.37: Heat flux (PW) of particular layers in the Atlantic Region. Thermocline layers 5 to 10 (green), Intermediate layers 11 to 15 (magenta), Deep layers 16 to 18 across SAVE2, SAVE4 and 16 to 19 across Drake Passage, south Africa and Weddell Sea (red) and Bottom layers 20 to 22 (dark blue). Dashed line 1000 dbars contour.

Study	Heat (PW)	Comments
Rintoul (1991)	0.25 ± 0.12	i
Fu (1981)	0.8	i
Saunders and King (1995)	0.5 ± 0.1	i
Macdonald and Wunsch (1996)	0.5 ± 0.3	i
Macdonald (1993)	0.3	i
Boddem and Schlitzer (1995)	0.35	i
Hsiung (1985)	0.38	b
Hastenrath (1982)	0.69	d
Bennett (1978)	0.16-0.68	d
This study	0.46±0.07	i

Table 4.2: Comparison of Heat flux (PW)estimates for the Atlantic Ocean at ≈ 30°S (in PW). i- inverse methods, b- bulk formula and d- direct

A comparison of the heat flux of this study with previous estimates is shown in Table 4.2 . Table 4.2 shows that recent estimates, using inverse techniques, give similar estimates of the heat flux at 30°S.

The Weddell Sea region (BIII) has an initial southward heat flux constraint of -0.1 PW, based on a heat loss between 60°S and 70°S of $31 Wm^{-2}$ (Gordon et al. 1981). Other estimates of the heat loss over the Weddell Sea vary from $16 Wm^{-2}$ to $41 Wm^{-2}$ which for the Weddell Sea region results in a heat flux of 0.05 PW to 0.13 PW (Gordon and Huber 1990; Fahrbach et al. 1994) The effect of imposing different southward heat fluxes across the Wedsea section is discussed later (Chapter 6).

Salt Flux

The salt flux across the SAVE2 and SAVE4 section is $24.93 \pm 32.9 \times 10^6 kgs^{-1}$ and $19.13 \pm 64.5 \times 10^6 kgs^{-1}$, respectively. Previous

estimates of the salt flux in the Atlantic, based on an input of $0.8 \times 10^6 m^3 s^{-1}$ through Bering Strait from the Pacific Ocean, are 26.7 kgs^{-1} (Wijffels et al. 1992). This salt flux is achieved against an overall northward salt flux in thermocline, intermediate and bottom water classes and a southward salt flux within deep water (Figure 4.38).

The salt flux in the Atlantic sector of the Southern Ocean (BII) is dominated by the Antarctic Circumpolar Current (ACC) (Figure 4.38). The salt flux through Drake Passage is $4.720 \pm 30.3 \times 10^9 kgs^{-1}$. This is the value of S_A in Wijffels et al. (1992) (her figure, figure 2b). The salt flux south of Africa is larger than that entering through Drake Passage by the addition of salt from the Atlantic across SAVE4.

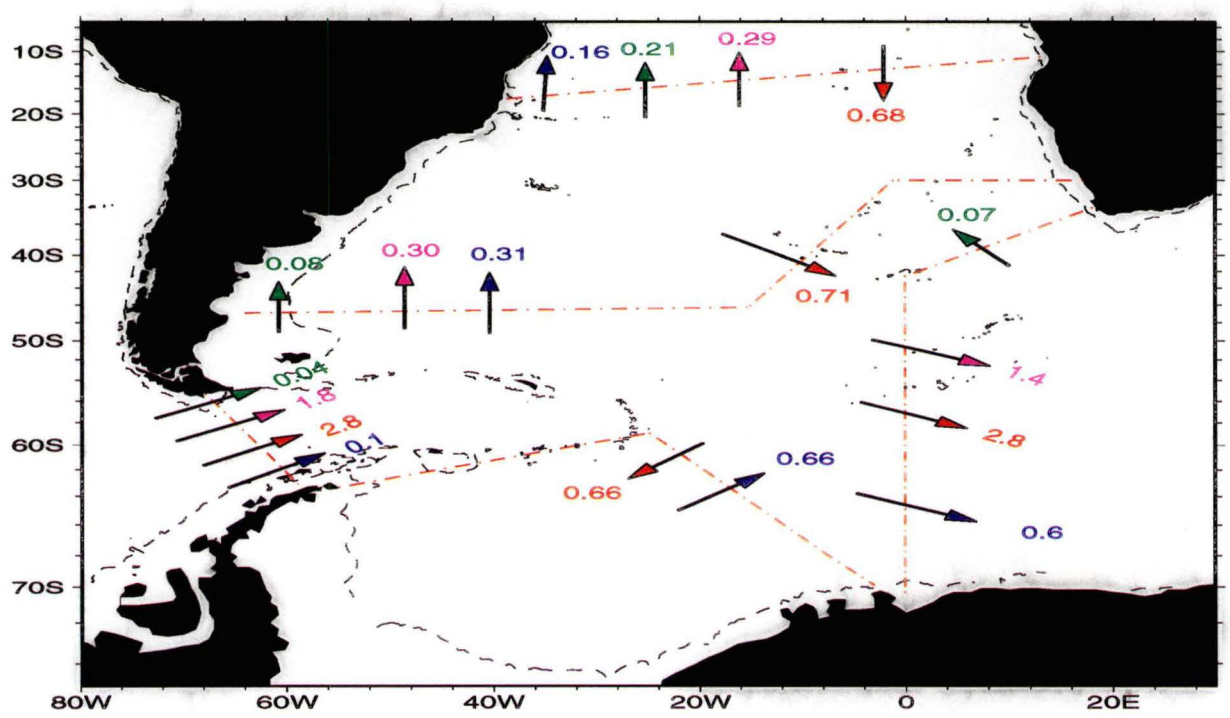

Figure 4.38: Salt flux ($\times 10^9 kgs^{-1}$) of particular layers in the Atlantic Region. Thermocline layers 5 to 10 (green), Intermediate layers 11 to 15 (magenta), Deep layers 16 to 18 across SAVE2, SAVE4 and 16 to 19 across Drake Passage, south Africa and Weddell Sea (red) and Bottom layers 20 to 22 (dark blue). Dashed line 1000 dbar contour.

Freshwater Flux

The freshwater flux across SAVE2 is $0.79 \pm 0.9 \times 10^9 kgs^{-1}$ and $0.63 \pm 5.1 \times 10^9 kgs^{-1}$ across SAVE4. This implies a small evaporative loss of freshwater ($0.16 \times 10^9 kgs^{-1}$) from the subtropical Atlantic region. Previous studies estimate the freshwater flux of $0.69 \times 10^9 kgs^{-1}$ at the equator, $0.6 \times 10^9 kgs^{-1}$ at 15°S and from $0.13 \times 10^9 kgs^{-1}$ to $0.3 \times 10^9 kgs^{-1}$ at 30°S (Wijffels et al. 1992; Macdonald 1995). The implied net evaporation, over the subtropical Atlantic, from these studies varies between $0.3 \times 10^9 kgs^{-1}$ and $0.56 \times 10^9 kgs^{-1}$, respectively. From this study the subtropical Atlantic is a net evaporative basin which agrees with Baumgartner and Reichel (1975), although the magnitude of the evaporative loss is smaller (as summed by Wijffels et al. (1992) and Macdonald (1995)). The freshwater flux presented by Wijffels et al. (1992) is only tentative. They suggest that small bias errors in the air-sea freshwater flux over a vast ocean can lead to large errors in the total freshwater transport.

Saunders and King (1995) use a zero net mass constraint, across a section with similar latitude variation as SAVE4, based on Wijffels et al. (1992) near cancelation of freshwater flux at 30°S. (This implies freshwater input from the Bering Strait is nearly equal to loss the freshwater loss by evaporation over the entire Atlantic.) They conclude that with a zero net mass flux a salt flux of $26.7 \times 10^6 kgs^{-1}$ is not consistent, suggesting that current estimates of the air-sea freshwater flux have large errors. The air-sea freshwater fluxes may have errors but a southward salt flux in the Atlantic may be achieved with zero mass flux if NADW is balanced by northward flow of less saline water.

Circulation impacts of Dianeutral Heat and Salt Fluxes

Before discussing the effects of the heat and salt dianeutral fluxes on the circulation the reader is reminded that the dianeutral fluxes are an expression for the mean basin dianeutral flux. With this model, only the net dianeutral fluxes acting over the area of each box can be determined, and not the magnitude of individual processes which contribute to this flux. In this section I sketch a plausible but not unique interpretation of these fluxes.

In the subtropical Atlantic Ocean region (BI) the upper thermocline (layer 5 to 8) dianeutral heat flux is downwards into denser layers. This downward dianeutral heat flux is the combination of the air-sea heat flux into the ocean on the outcropping layers and subsequent diffusion of this sea-surface heat gain into denser thermocline layers. Across the lower thermocline and intermediate dianeutral surfaces the heat flux is directed upwards. This upward heat flux could be the result of heat loss from these surfaces in their far southern outcropping areas. The dianeutral salt flux is upwards into the lightest thermocline layers (4 and 5). Below these layers the dianeutral salt flux is directed towards denser layers. The dianeutral salt flux transfers salt from the thermocline salinity maximum (layers 6 to 10) into the salinity minimum AAIW (layer 13 to 15). The dianeutral heat and salt fluxes are nearly in balance across the thermocline layers resulting in only minimal mass advection.

Major changes result from the input of warm, salty NADW (layers 17 and 18) into the subtropical Atlantic region (BI). The dianeutral heat flux transfers heat from NADW (layers 17 and 18) into underlying LCDW/AABW (layer 19) and AABW (layer 20) resulting in the advection of mass from AABW into LCDW. This downward heat flux accounts for the net warming of CDW/AABW between SAVE4 and SAVE2. The other major effect of NADW is the upward and downward dianeutral salt flux from these layer. The upward dianeutral salt flux into over-lying LCDW (layer 16) and AAIW (layers 13 to 15) results in the salinity increase of these layers within the subtropical Atlantic, while the downward dianeutral salt flux into LCDW increases the salinity of this water mass. The distribution of NADW heat and salt into surrounding denser and lighter water layers results in the erosion of the salinity maximum from > 34.9 at SAVE 2 (Figure 3.3) into a broad salinity maximum of > 34.7 at SAVE4 and only a core NADW salinity maximum > 34.8 in the eastern basin (Figure 3.6).

In the Southern Ocean Atlantic sector the dianeutral heat flux is upward across all thermocline layers (8 to 10) and intermediate layers (11 to 15). This upwards heat flux results from the heat loss of the ocean to the atmosphere where the neutral surface outcrops and the upward dianeutral heat flux from underlying warm NADW and CDW (layer 16 to 18) into the colder overly Antarctic surface waters in the southern region. The dianeutral salt flux is

downward through all layers, resulting in a salt flux from higher salinity thermocline water to less saline intermediate waters below. The downward dianeutral salt flux and upward dianeutral heat flux results in upward mass advection of intermediate water into lower thermocline layers.

Within the Southern Ocean Atlantic sector (BII) the dianeutral heat flux is upwards across all layers above AABW. Within this area deep layers outcrop in the southern region, exposing them to sea-surface heat loss. The heat loss from deep layers (16 to 19) is a combination of both the interior heat flux from the warm circumpolar deep water (layer 16 to 19) into colder surface waters and also the heat loss to the atmosphere from the outcropping areas of these layers.

The dianeutral heat and salt flux results in the mass advection of extreme AABW (layers 21 and 22 WSBW and WSDW) into slightly less dense AABW (layer 20) and downward mass advection of NADW into LCDW (layers 18 and 19) and AABW. These mixing process act to diffuse the NADW temperature and salinity signatures and results in the contrasting characteristics between UCDW (lower salinity and oxygen) and LCDW (maximum salinity and high oxygen) south of Africa and the erosion of the salinity maximum of NADW between SAVE4 and south of Africa. Although there is still a distinct maximum adjacent to southern Africa.

4.3.2 Indian Region

The Indian Ocean is divided into numerous basins by bottom topography (Figure 4.39). The topography forms barriers and guides bottom and deep circulation paths resulting in a complex northward circulation pattern of Antarctic origin water into the subtropical Indian Ocean.

Mass Flux

The Ind18 section forms the northern boundary of the subtropical Indian region (BIV) and has an overall southward mass flux of $14.7 \pm 6.4 \times 10^6 m^3 s^{-1}$. This transport represents the size of the Indian-Pacific mass exchange, known as in Indonesian through-flow. The East Madagascar Current (EMC) forms a western boundary current adjacent to Madagascar, with a southwards transport of $31.8 \times 10^6 m^3 s^{-1}$. Previous estimates vary from $41 \times 10^6 m^3 s^{-1}$ to

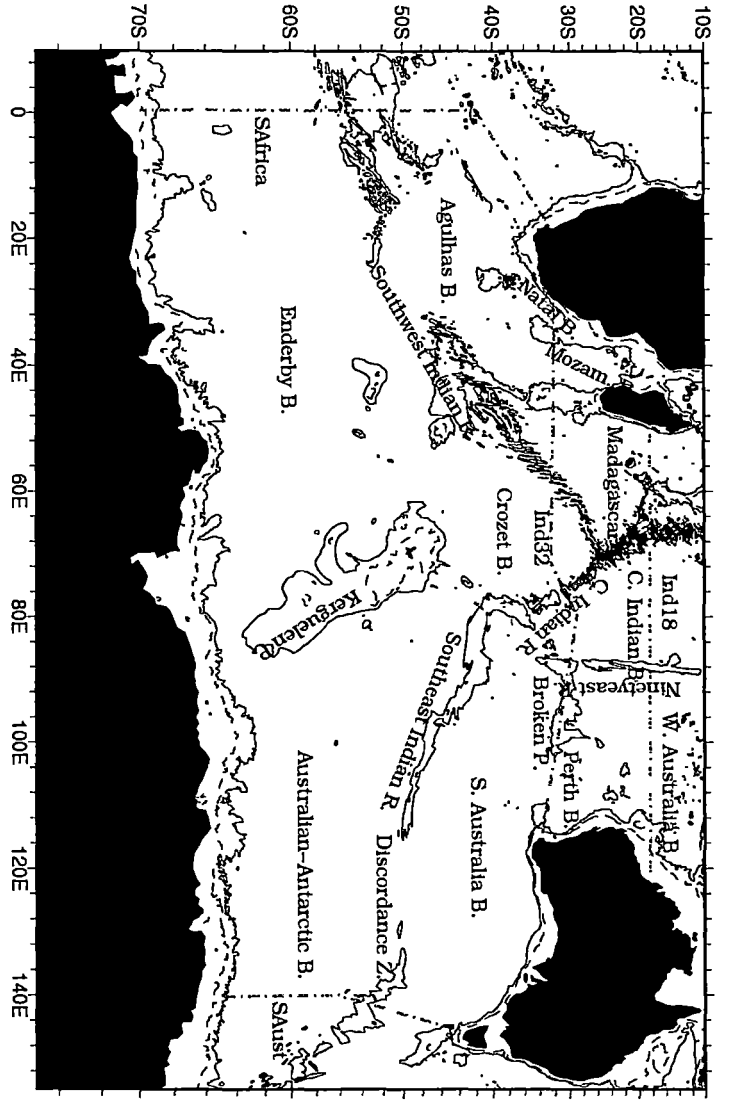

Figure 4.39: Topographic features of the Indian Ocean with position of hydrographic section (dot-dash). Contours 1000, 3000 metres

$20.6\times10^6 m^3 s^{-1}$ at 23°S (Lutjeharms et al. 1981; Swallow et al. 1988; Schott et al. 1988)

The net southward transport is mostly contained in the top two thermocline layer (3 and 4). These surface layers transport $14\times10^6 m^3 s^{-1}$ of warm, fresh water southward, which is evenly distributed across the section (Figure 4.40). The remaining thermocline (5 to 10), intermediate (11 to 15), deep (16 to 18) and bottom (19 to 20) layer transports are essentially in balance resulting in a small southward transport of $1.8\times10^6 m^3 s^{-1}$. The southward transport is concentrated in the EMC ($27\times10^6 m^3 s^{-1}$ below layer 4). The basin interior thermocline (5 to 10) and intermediate (11 to 15) layers transport $33\times10^6 m^3 s^{-1}$ northwards (Figure 4.40). The northward thermocline and (some) intermediate water balance the southward EMC. The remaining intermediate water, along with AABW (layers 19 to 20, $4\times10^6 m^3 s^{-1}$) and CDW (layers 16 to 18, $7\times10^6 m^3 s^{-1}$) (Figure 4.40), are modified in the northern Indian Ocean. The modified intermediate, deep and bottom water returns to the Subtropical Indian Ocean as low oxygen, high silica NIDW (layers 16 and 17) (Figure 4.40), in the Mascarene, Central Indian and West Australia basins. Figure 4.41 sketches the implied overturning circulation north of 18 °S in the northern Indian Ocean.

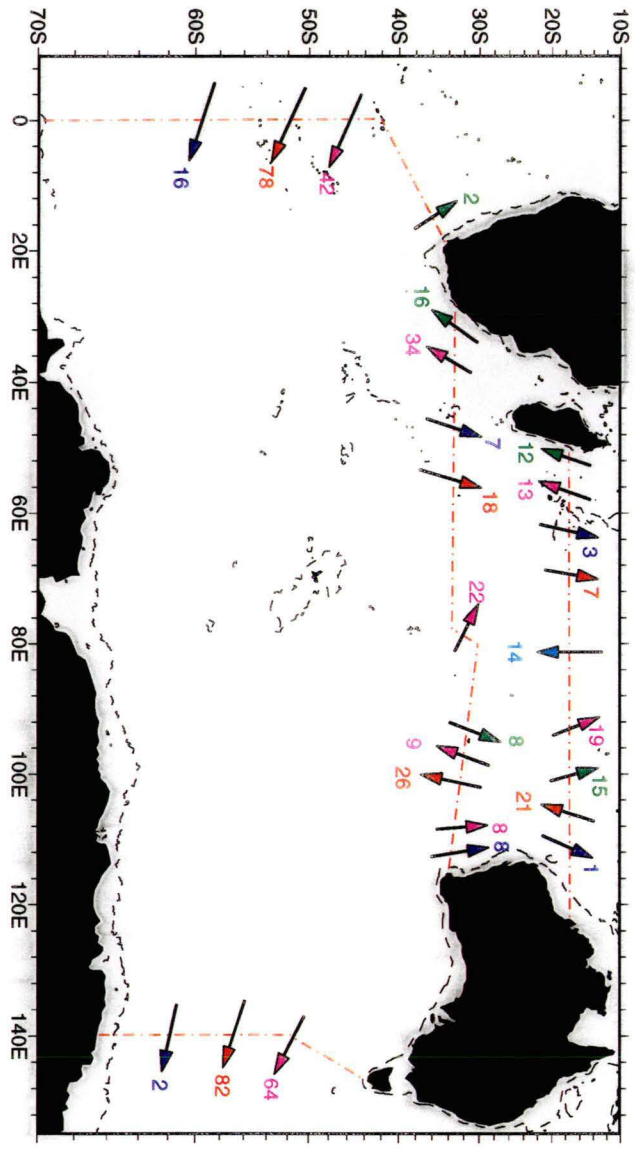

Figure 4.40: Transport ($\times 10^6 m^3 s^{-1}$)of particular layers in the Indian Region. Surface layers 3 and 4 (light blue), Thermocline layers 5 to 10 (green), Intermediate layers 11 to 15 (magenta), Deep layers 16 to 18 across Ind18, Ind32 and 16 to 19 south of Africa and Australia (red) and Bottom layers 20 to 22 (dark blue). Dashed line 1000 dbar contour.

Across 32°S in the Indian Ocean there is a net southward transport of -15±7.4×$10^6 m^3 s^{-1}$. This is achieved in a series of north/south transports within individual basins. The western boundary is dominated by the southward Agulhas Current of 47.3×$10^6 m^3 s^{-1}$. Previous estimates of the strength of the Agulhas Current vary from 21.4×$10^6 m^3 s^{-1}$ to 62×$10^6 m^3 s^{-1}$ at 31°S and 80×$10^6 m^3 s^{-1}$ using geostrophic and direct methods, respectively (Gründlingh 1980; Toole and Raymer 1985; Gründlingh et al. 1991). In recent years there has been some debate pertaining to the origins of the Agulhas Current, particularly the importance of the Mozambique channel and EMC on the Agulhas. Harris et al. (1978) using satellite images highlighted that surface water originating from the EMC turned westward and finally curved southwest (after northwest movement towards the Mozambique Channel) into the Agulhas Current. They also found water originating from the Mozambique Channel moving south adjacent to the south African coast into the Agulhas Current. The influence of the Mozambique Current on the Agulhas Current has been estimated at 6×$10^6 m^3 s^{-1}$ Fu (1986). A study of hydrographic data (between 1977 to 1980) off the Mozambique Coast and historical data in the Mozambique Channel indicates that the Mozambique Current is, if at all, only a minor tributary of the Agulhas Current (Sætre and da Silva 1984). Sætre and da Silva (1984) even question the concept of a continuous Mozambique Current. Gründlingh et al. (1991) studied eddies in the Mozambique Channel, between June 1978 and February 1988. No eddies were seen entering or leaving the Mozambique Channel over this period. Anticyclonic eddies found southeast of Madagascar were derived from the EMC. Eddies from the EMC represent the mechanism by which mass and heat are transfered to the Agulhas Current. Downstream strengthening of the Agulhas Current results from the local recirculation in the southwest subtropical Indian Ocean (Gordon et al. 1992).

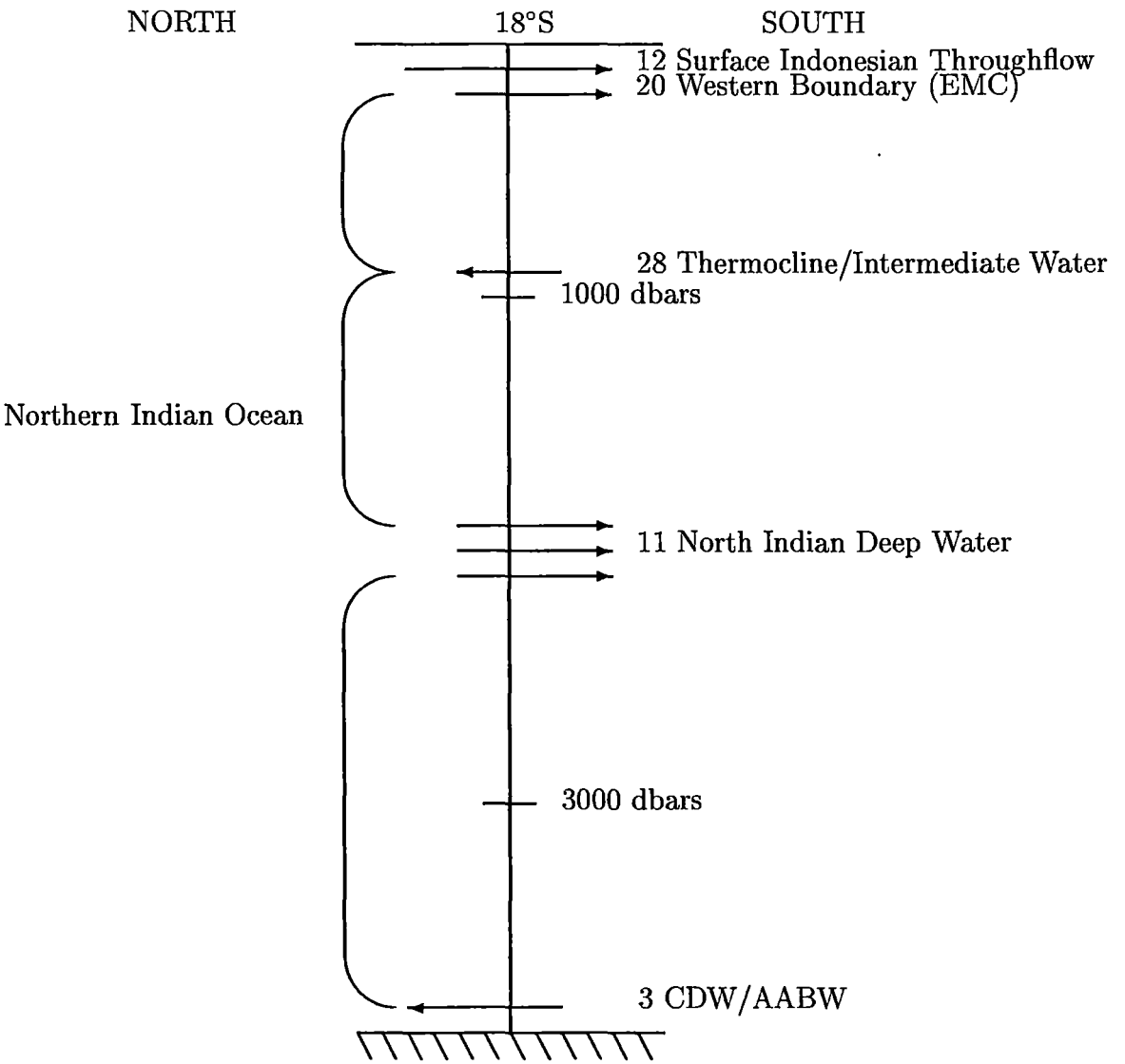

Figure 4.41: Schematic of overturning cell north ($\times 10^6 m^3 s^{-1}$) of 18°S in the Northern Indian Ocean. Southern origin Intermediate water important source of EMC and with AABW source of North Indian Deep Water after mixing and conversion in the northern Indian Ocean

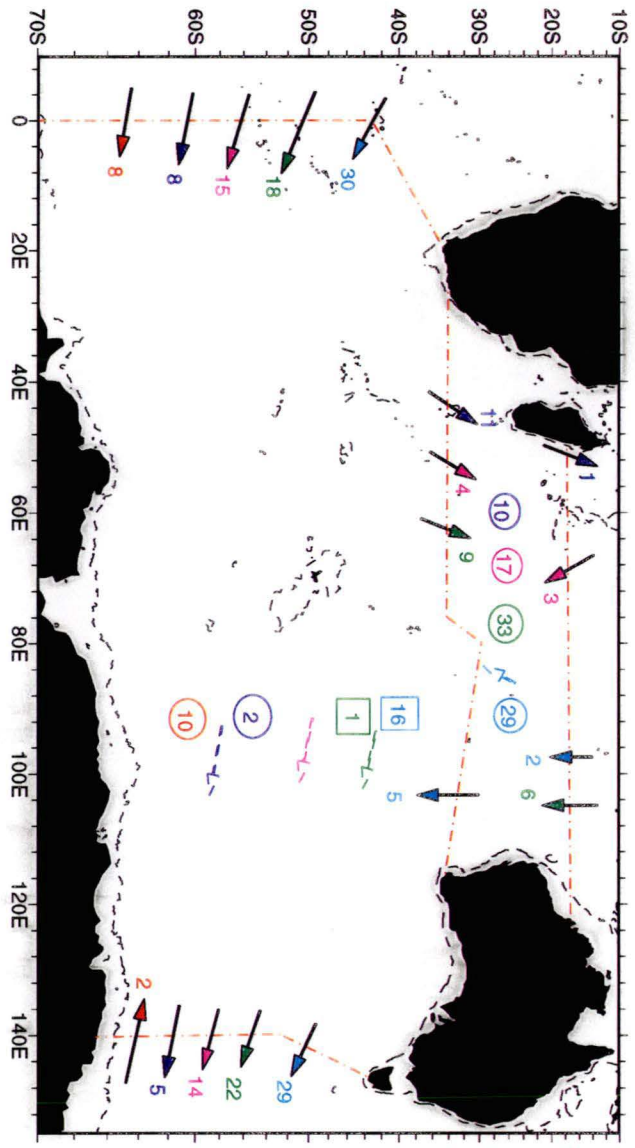

Figure 4.42: Mass transport and dianeutral flux ($\times 10^6 m^3 s^{-1}$) within Deep and Bottom water in the Indian Region (BIV, BV). Upward Dianeutral flux- circle, Downward Dianeutral Flux - square, dashed arrow represent net production within layers due to dianeutral flux. UCDW/NADW/NIDW (layer 17, light blue), UCDW/NADW/LCDW (layer 18, green), LCDW/AABW (layer 19, magenta), AABW (layer 20, dark blue), and extreme AABW (layer 21 and 22, red). Dashed line 1000 dbars

Across 32°S there is a total southward transport of intermediate (11 to 15) layers of $13\times10^6 m^3 s^{-1}$. This transport is achieved by southward transport in the Natal and Madagascar basins and over the Broken Plateau and opposing northward flow in the Crozet (60°to 70°E) and Central Indian (85°E) basins (for simplicity these are combined within Figure 4.40, individual transport are $15\times10^6 m^3 s^{-1}$ and $7\times10^6 m^3 s^{-1}$) and in the Perth basin (100°to 110°E) (Figure 4.40). The intermediate transport structure is similar to that suggested by Stramma (1992) for the upper 1000 m (Figure 1.6). He found that intermediate water moves northward, into the Indian Ocean, in the Madagascar ($20\times10^6 m^3 s^{-1}$), Crozet ($20\times10^6 m^3 s^{-1}$), Central Indian ($10\times10^6 m^3 s^{-1}$) and Perth ($10\times10^6 m^3 s^{-1}$) basins. Fine (1993) using chlorofluorocarbon (CFC) and oxygen analysis of the Ind32 section showed that the intermediate water entering the Indian Ocean via the Crozet and Central Indian Ocean is the most recently ventilated, with the F11/F12 indicating an age of 9 years. The F11/F12 age of the intermediate water entering in the Perth basin is 30 years. The difference in intermediate water age between these basins suggest very different circulation paths. The Crozet and Central Indian basins have the more direct connection to the source region of intermediate water. The intermediate water entering the Indian Ocean via the Crozet and Central Indian Oceans is the main source of AAIW, which ventilates the Indian Ocean. The age of the intermediate water in the Perth basin suggests a circulation pathway in which intermediate water first flows around the Pacific subtropical gyre and then flow westward south of Tasmania into the southeast Indian Ocean.

Topography plays a major role in directing the deep (16 to 18) and bottom (19 to 20) layer transports across Ind32. Deep (16 to 18) water moves northward in the western Natal, Mozambique, Madagascar and Crozet basins (Figure 4.40). The eastern basins, at similar depth are dominated by southward flow of low oxygen North Indian Deep waters (layers 16 and 17). Bottom (layers 19 and 20) water enters the Indian Ocean in a series of deep boundary currents, in the Mozambique, Madagascar, Crozet and Perth basins (Figure 4.40).

The deep (layer 18) northward flow in the Natal and Mozambique basins has a salinity of > 34.8 indicating NADW is transported into the southwest Indian Ocean via the Agulhas basin south of Africa (Figure 3.24). The deep (17

to 18) and bottom (19 to 20) layers that enter via the Mozambique, Madagascar and Crozet basins move northwards into the Indian Ocean through a series of deep passages in the Southwest Indian Ridge or upwell into overlying deep (16 and 17) and lower intermediate (15 to 13) layers. The other source of bottom water (layers 19 and 20) enters in the Perth basin. There are topographic barriers to the west that restrict the densest AABW, from the Weddell Sea, reaching the southeast Indian Ocean, namely the Kerguelen Plateau and the Southeast Indian Ridge, while there are passages south of Australia that enable AABW of Adelie Land and Ross Sea origin to penetrate into the southeast Indian Ocean and the Pacific Ocean. The potential temperature-salinity and potential temperature-oxygen diagrams (Figure 4.43 and Figure 4.44) show differences in the bottom layer properties between the Crozet and Perth basins. The coldest and freshest bottom layers are found in the Crozet basin. The persistence of the extreme bottom water characteristics highlight that bottom water in the Crozet basin is recently produced AABW from the Weddell Sea. Bottom water in the Perth basin is warm and has a relatively high salinity. The bottom water of the Perth basin are sourced from the Australia-Antarctic basin, adjacent to the Antarctic continent, through the South Australian basin (Mantyla and Reid 1995). The high salinity values of bottom water in the Australia-Antarctic basin is suggested to be the result of mixing between Weddell Sea and Ross Sea Bottom water (Carmack 1977). But Rintoul (1997), using recent data, finds that the bottom water in the Australia-Antarctic basin is principally derived from AABW formation along the Adelie coast. The bottom water entering the Perth basin is a very modified version of the AABW of the Australia-Antarctic basin, as highlighted by its relatively high temperature and salinity. The high temperature and salinity of bottom water in the Perth basin results from the mixing of bottom water with overlying warm, saline CDW as the bottom water moves northward from the Australia-Antarctic basin and not necessary an indication of a saline source of bottom water from the Ross Sea. The Perth basin bottom water has a higher oxygen concentration than the Crozet basin water at the same temperature again highlighting the eastern and western sources of the bottom water, respectively.

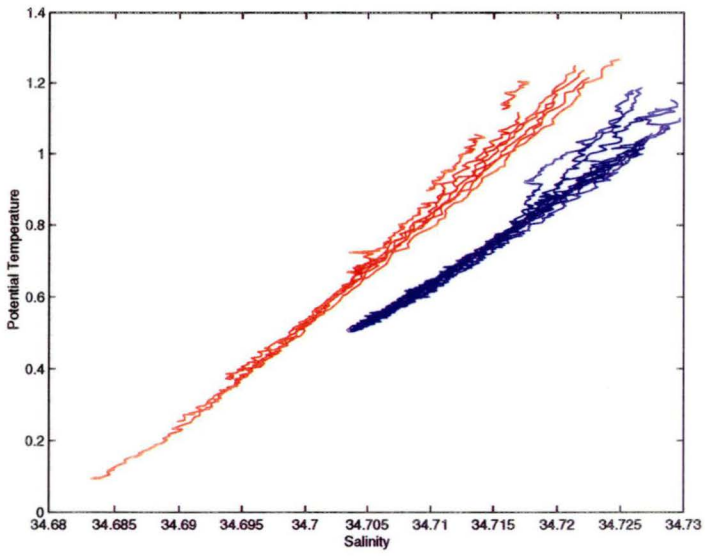

Figure 4.43: Indian 32°S Bottom Water Potential Temperature (°C) - Salinity (psu) diagram for the Crozet basin (red) and Perth basin (dark blue)

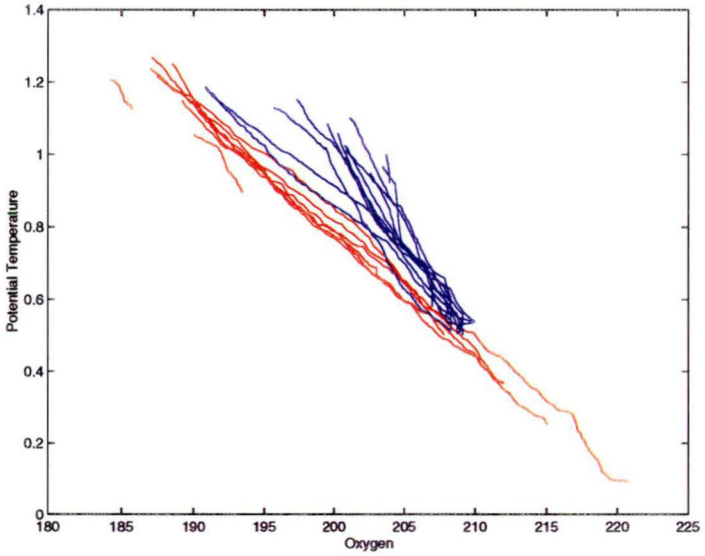

Figure 4.44: Indian 32°S Bottom Water Potential Temperature (°C) - Oxygen (μmol.kg^{-1}) diagram for the Crozet basin (red) and Perth basin (dark blue)

Within the subtropical Indian region (BIV) most of the AABW (layers 19 and 20) and LCDW (layer 17 and 18) ($25\times10^6 m^3 s^{-1}$) that enters from the south across Ind32 is modified into upper deep (17 and 16) and lower intermediate (13 to 15) layers and only a small portion moves northwards into the northern Indian Ocean. The subtropical Indian Ocean is a major region of water modification with mixing occurring between Southern Ocean (intermediate, CDW and AABW) and subtropical/tropical (thermocline, NIDW) water masses.

The most important mechanism for water mass conversion of LCDW and AABW, in subtropical Indian Ocean, is the downward dianeutral heat flux (through all surfaces). This results in the conversion of Southern Ocean AABW and LCDW to upper deep layers (16 and 17, IDW) and lower intermediate layers (13 to 15), which leave the exit the southward across 32°S (Figure 4.42). This overturning, in the subtropical Indian Ocean, is supported by previous studies (Toole and Warren 1993; Robbins and Toole 1997). There are some difference in the vertical extent of the overturning cell between this study and the studies of Toole and Warren (1993) (hereafter T&W) and Robbins and Toole (1997) (hereafter R&T) which are emphasised by the silica flux across the Ind32 section. These differences are discussed below.

Toole and Warren (1993) suggest that the strong overturning could be the result from boundary mixing process. The Indian Ocean is divided into numerous smaller basins and the complex topography may provide the mechanism required to enhance the downward dianeutral heat flux and subsequent strong overturning present in the deep subtropical Indian Ocean.

In the Southern Ocean Indian sector (BV) large changes occur in the volume flux of bottom layers (20 to 22) and deep layers (17 to 19) between the south African and south Australian sections. Extreme AABW (layers 21 and 22), from the Weddell Sea and Adelie/Ross Sea are modified by downward dianeutral heat flux. This downward heat flux results in the upward advection of mass from these extreme density layers into slightly less dense AABW (layer 20) and CDW (layer 19) (Figure 4.42).

The dianeutral heat flux has a major influence on the mixing processes in the Indian region. The downward advective mass flux results in the dispersal of

the surface warm, fresh thermocline layer into lower thermocline layers in the subtropical Indian Ocean. The mass advection into lower intermediate and upper deep layers is driven by the strong overturning of LCDW and AABW. It has been suggested that the strong overturning is the result of enhanced mixing induced by the complex bottom topography of the Indian Ocean, while the downward dianeutral heat flux maintains the deep temperature gradient.

Heat Flux

The Indian Ocean exports heat southwards. The heat flux is a combination of the heat associated with the Indonesian through-flow and *in situ* heat gain, from the atmosphere, in the Indian Ocean north of 32°S. The heat flux across Ind18 and Ind32 is 1.10±0.15 PW.

The southward heat flux at Ind18 is contained, mainly in the top thermocline layers (3 and 4) across the entire basin. Below these layers, the northward basin interior thermocline (5 to 10) and intermediate (11 to 15) layers heat flux dominates over the southward heat flux associated with the EMC resulting in an overall northward heat flux in these water classes (Figure 4.45). The deep layers (16 to 18) have a southward heat flux which results from a balance between the northward flow of cool CDW (layers 17 and 18) and the southward flow of relatively warm NIDW (layer 16 and 17).

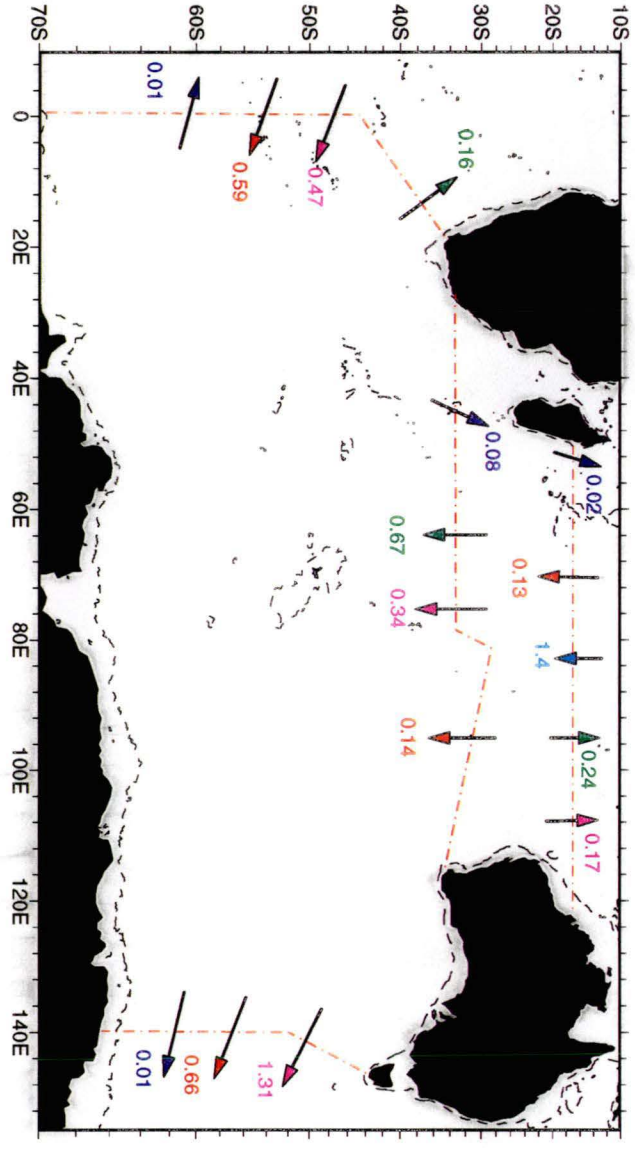

Figure 4.45: Heat flux (PW) of particular layers in the Indian region. Surfaces layers 3 and 4 (light blue), Thermocline layers 5 to 10 (green), Intermediate layers 11 to 15 (magenta), Deep layers 16 to 18 across Ind18, Ind32 and 16 to 19 south of Africa and Australia (red) and Bottom layers 20 to 22 (dark blue). Dashed layers 1000 dbar contour.

Study	Total Heat (PW)	Indo.	Heat Conv.	Comments
Toole and Warren (1993)	-1.67	6.7	-0.98	h
Macdonald and Wunsch (1996)	-1.3 ± 0.3	8.7	-0.4	i
Macdonald (1993)	-1.3	10.0	-0.27	i
This study	-1.10±0.15	15.0	0.45	i

Table 4.3: Comparison of Heat flux (PW) estimates for the Indian Ocean at $\approx$ 30 °S (in PW). Also shown given is the estimated size of the Indonesian Throughflow for each study. Heat flux associated with Indonesian Throughflow is calculated assuming a throughflow water temperature of 24°C (Toole and Warren, 1993). h- hydrographic data and i- inverse methods

At Ind32, the large southward heat flux, associated with the top thermocline layers (3 and 4) at Ind18, is redistributed into lower thermocline layers (5 to 10) and intermediate layers (11 to 15). The heat flux is transported southwards in the western basins (Natal, Madagascar) and over the Broken Plateau. This results in a total basin southward heat flux in thermocline and intermediate water classes (Figure 4.45). There is also a southward heat flux within deep layers (16 to 18). The only northward heat flux into the Indian Ocean is associated with bottom layers (19 and 20).

The redistribution of heat in the Indian subtropical gyre results in the warming of particular layers, which are returned to the Southern Ocean Indian sector in the Agulhas Current (thermocline and intermediate layers). Similarly, the downward dianeutral heat flux from intermediate (11 to 15) and upper deep (16 and 17) layers into CDW (17 to 19) and AABW (10 to 22) enhance modification and conversion of these waters into less dense upper deep and intermediate layers.

The ACC heat flux south of Australia (1.99±0.04PW) is larger than that entering south of Africa (0.88±0.06 PW). This reflects the cyclic nature of the Indian-Pacific mass transport where the Indonesian through-flow is balanced south of Australia.

Table 4.3 provides a comparison of the heat flux across 30°S between this

study and previous estimates. The total heat fluxes include the heat flux associated with the Indonesian throughflow. When accounting for the heat flux associated with the Indonesian throughflow the net convergence of heat into the Indian Ocean north of 30°S is southward in the previous studies and northward in this study. Macdonald (1993) when constraining the Indonesian through flow to $20\times10^6 m^3 s^{-1}$ obtain a total southward heat flux of -1.4 PW, when removing the heat contribution of the Indonesain throughflow a net northward heat convergence (0.66 PW) is obtained.

Salt Flux

At 18°S in the subtropical Indian Ocean (BIV) the EMC transports salt southwards, this is balanced by northward salt fluxes in the interior thermocline (5 to 10) and intermediate (11 to 15) layers. There is also a northward salt flux in the bottom layers (19 to 20). The southward salt flux, at 18°S, is achieved principally in the top two thermocline layer and in the deep layers (16 to 18) resulting in total salt flux of $524 \pm 57 \times 10^6 kgs^{-1}$ (Figure 4.46). At 32°S the salt flux in southward ($523 \pm 65 \times 10^6 kgs^{-1}$). The southward salt flux at Ind32 is contained mainly in the thermocline (6 to 10), intermediate (11 to 15) and upper deep (16 to 17) layers (Figure 4.46). Toole and Warren (1993) estimate a salt flux across 32°S, in the Indian Ocean, of 236.8 $\times 10^6 kgs^{-1}$.

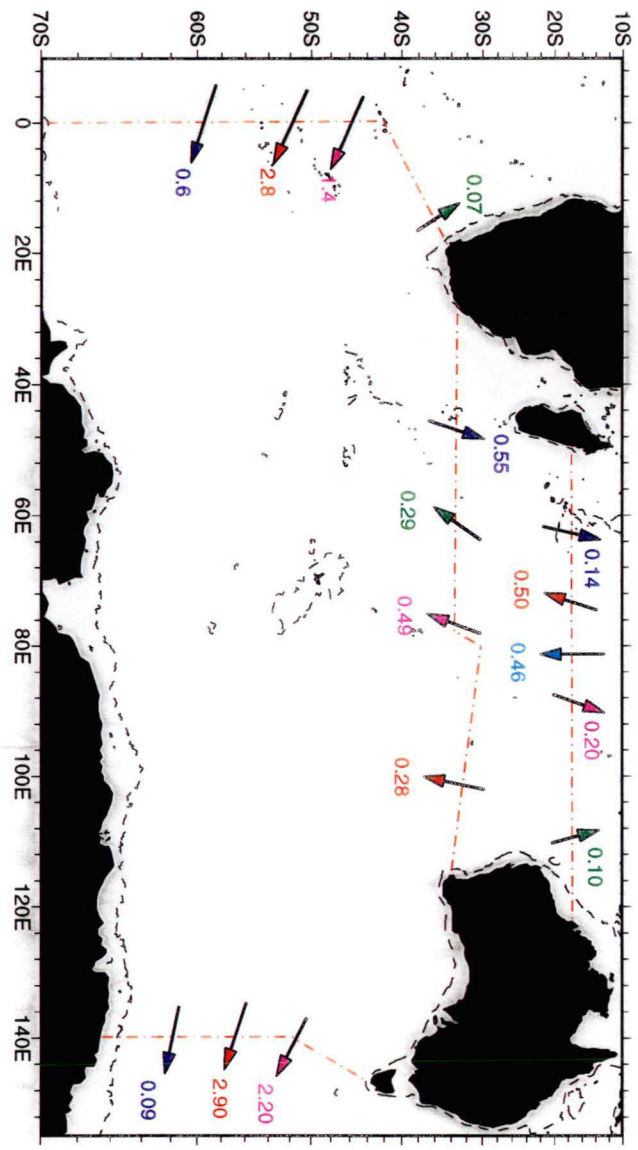

Figure 4.46: Salt flux ($\times 10^9 kgs^{-1}$) of particular layers in the Indian Region. Surface layers 3 and 4 (light blue), Thermocline layers 5 to 10 (green), Intermediate layers 11 to 15 (magenta), Deep layers 16 to 18 across Ind18, Ind32 and 16 to 19 south of Africa and Australia (red) and Bottom layers 20 to 22 (dark blue). Dashed line 1000 dbar contour.

The Indian Ocean is closed north of 32°S, except for the export of Pacific water into the Indian Ocean via the Indonesian through-flow. This flow results in a salt flux into the Indian Ocean. The salt flux out of the Indian represents the S_P in Wijffels et al. (1992), figure 2b. Toole and Warren (1993) assuming salt conservation, estimate the size of the Indonesian through-flow, based on mean temperature of 24°C and salinity of 34.5, to be $6.7\times10^6 m^3 s^{-1}$. Defining the through-flow in term of salt transport in the Indian Ocean I estimate a through-flow of $15.03\times10^6 m^3 s^{-1}$. This shows that the differences in salt flux between this study and Toole and Warren (1993) results from different estimates of the size of the Indonesian through-flow.

Freshwater Flux

The Indian freshwater flux of $14.6 \pm 7 \times 10^9 kgs^{-1}$, is dominated by the southward flux of the Indonesian through-flow. This freshwater flux is considerably larger than previous estimates (Toole and Raymer 1985; Macdonald 1995). Both of these studies do not include the freshwater flux associated with the Indonesian through-flow thus accounting for the large difference between these studies and the flux estimated here.

We have estimated the the Indonesian through-flow at $15\times10^6 m^3 s^{-1}$; assuming the through-flow has a mean temperature of 24°C, salinity of 34.5 and density of 1023 kgm^{-3} the estimated freshwater flux associated with the through-flow is $14.6 \pm 7.6 \times 10^9 kgs^{-1}$. The freshwater flux of the Indian, with Indonesian through-flow removed, is $-0.32 \times 10^9 kgs^{-1}$. Wijffels et al. (1992) estimate a freshwater flux of $-0.51 \times 10^9 kgs^{-1}$. There is agreement in the sign of the freshwater flux (Indian Ocean north of 32°S is a net evaporative basin) but the magnitudes differs.

Deep overturning circulation - The Silica Flux

Toole and Warren (1993) (T&W)emphasised a deep overturning cell in the subtropical Indian Ocean of $26\times10^6 m^3 s^{-1}$ which converts northward flowing AABW and CDW into lighter southward flowing thermocline and intermediate water. Robbins and Toole (1997) (R&T) show that the overturning scheme of Toole and Warren (1993) results in a large northward silica flux ($1532 kmols^{-1}$),

which is unrealistic given the current estimates of the global silica budget (DeMaster 1981; Nelson et al. 1995). Robbins and Toole (1997) revise the overturning cell in the Indian Ocean to $13\times10^6 m^3 s^{-1}$, such that the silica flux across 32°S is approximately zero. The Indian overturning cell ($25\times10^6 m^3 s^{-1}$) in this study is comparable to the Toole and Warren (1993) study, but the northward silica flux is much smaller ($214 \pm 490.1 kmols^{-1}$). (Note that no silica constraint was imposed on the solution. The silica flux is diagnosed from the absolute velocity field and is used as a test of the inverse solution.)

Table 4.4 compares the layer transports and silica fluxes of this study with the studies of T&W and R&T. The layers used in this study are grouped so they agree with the previous studies. There is a northward flow of deep and bottom water as deep western boundary currents into the Indian Ocean across 32°S. The most significant difference of this study with previous studies is the increased southward transports in layers 4 and 5 (in this study layers 14 and 15 and, 16 and 17, respectively). The vertical overturning cell in this study is contained below 1000 dbars while for the T&W and R&T studies it extend throughout the entire water column. Layers 4 and 5 contain silica values that vary from between 60 to 100 $kmols^{-1}$ while the thermocline layers are nearly depleted in silica (Figure 3.26). The larger southward transport in layers 4 and 5 and the higher silica concentration of these layers nearly balance the northward silica flux within deep (18 and 19) and bottom layer (20) resulting in a small northward silica flux. The southward silica fluxes in the lower intermediate layers (14 and 15) and the upper deep layers (16 and 17) occur in the Central and Perth basin and over the Ninetyeast ridge and are associated with the southward transport of low oxygen IDW (Appendix D,Table D.12).

The circulation derived from this study supports a large deep overturning cell as proposed by Toole and Warren (1993), but contains it below 1000 dbars. The confinement of the overturning cell to below 1000 dbars has a significant effect on the silica flux across 32°S, resulting in a small northward flux. The smaller northward silica is more consistent with the global silica balance.

Layers		Mass ($\times 10^6 m^3 s^{-1}$)			Silica ($kmols^{-1}$)		
T&W,R&T	int	T&W	R&T	int	T&W	R&T	int
1	1-10	-21	-16	-8	-97	-31	-83
2	11-12	-0.7	4	-1	-85	-64	-68
3	13	-8	-4	-5	-305	-226	-147
4	14-15	-5	-3	-14	-316	-208	-806
5	16-17	-0.5	-4	-12	-73	-417	-1155
6	18	11	2	10	731	-216	627
7	19	14	10	4	1509	1110	330
8	20	1	1	11	169	170	1463
Total		-10	-10	-15	1532	21	213±490

Table 4.4: A comparison of the layer silica flux ($kmols^{-1}$) and the mass transport ($\times 10^6 m^3 s^{-1}$) between Toole and Warren (1993) (T&W), Robbins and Toole (1997) (R&T) and this study. +ve northward flux, -ve southward flux

Circulation impacts of Dianeutral Heat and Salt Fluxes

In the subtropical Indian Ocean (BIV) the Indonesian through-flow dominates the thermocline layers. There is an upward dianeutral heat flux within this region across all thermocline layers (3 to 10). This represents the redistribution of heat gained from the atmosphere across the air-sea interface. The dianeutral salt flux is upward across thermocline layers (3 to 10). This is consistent with a salt flux from the salinity maximum thermocline layers (5 to 10) into the salinity minimum Indonesian through-flow layers (3 and 4). The salinity maximum layer is found at the surface in the southern half of the region but at 18°S is a subsurface features.

The downward dianeutral heat flux, in the subtropical Indian Ocean, into IDW and CDW (17 to 18) and AABW (layers 19 and 20) may be induced by the complex bottom topography that divides the Indian Ocean into numerous individual basins. Toole and Warren (1993) suggests that the maintenance of the vertical temperature gradient in the face of strong upwelling must result from downward diffusion of heat. The vertical temperature profiles between the Atlantic, SAVE2 and SAVE4 (Figure 3.2 and Figure 3.5), and the Indian Ocean (Figure 3.19 and Figure 3.23) highlight the differences in the structure and depth of particular isotherms and the strength of the vertical temperature gradient associated with the thermocline. In the Atlantic Ocean at SAVE4, the

input of AABW and LCDW is identified by the strong vertical gradient below 3000 dbars (Figure 3.5). An identifiable temperature gradient, between AABW and NADW is still evident at SAVE2 (Figure 3.2). At a similar depth, a temperature gradient is seen in the Indian Ocean at 32°S (Figure 3.23), but at 18°S (Figure 3.19) this is eroded and the deep temperature is much more uniform than at a similar latitude in the Atlantic Ocean. It is interesting also, to note, that the temperature gradient is slightly stronger in the West Australian basin, perhaps indicating that the mechanism for downward heat diffusion is not as strong in the eastern Indian Ocean. AABW moving northward in the eastern Indian Ocean encounters reduced topographic restrictions than that moving northwards in the western basins (Figure 4.39). The strength of the overturning cell could result from the combined effects of upwelling induced by topography and the enhanced vertical diffusion of heat, due to the ability of the Indian Ocean to effectively transfer surface heat to water below the thermocline.

In the Southern Ocean Indian sector the dianeutral heat flux is downwards across all layers. This results in a redistribution of heat from the thermocline layers (8 to 10) associated with the southward Agulhas current into intermediate layers. This heat flux results in the mass conversion of thermocline layers (8 to 10) into intermediate layers (12 to 15, SAMW/AAIW). The dianeutral salt flux redistributes the salt in the thermocline. There is a net conversion of heat into CDW (layer 18 to 19) and AABW (layer 20 to 22). This heat flux into these layers results in the warming of the LCDW and provides a mechanism by which extreme RSBW and ALBW (layers 21 and 20), in the Australian-Antarctic basin, is warmed resulting in the warmer and saltier AABW (layer 19 and 20) in the Perth basin. The dianeutral salt diffusion is upward across the salinity maximum CDW (layer 18 and 19). This results in a conversion of salt into the salinity minimum AAIW (layer 13 and 15). The erosion of the salinity maximum, which identifies LCDW, highlights the changing dominance of LCDW and UCDW in the composition of CDW within this region. The difference in composition of CDW is shown by changes in the potential temperature-salinity and potential temperature-oxygen diagrams between SAfrica and SAust sections (Figure 4.35 and Figure 4.36).

4.3.3 Pacific Region

The Pacific Ocean is bounded by Australia and New Zealand in the west and South America in the east. The Pacific Ocean is divided by the Pacific - Antarctic ridge and the East Pacific Rise, forming the Southwest Pacific basin and the Southeast Pacific basin (Figure 4.47). The deep western boundary current is not adjacent to the Australian coast but is displaced further east and found adjacent to the Campbell Plateau and the Kermadec-Tonga ridge. The Pacific Ocean western boundary current, the East Australian Current, leaves the coast at $\approx$ 30 °S and meanders eastwards across the Tasman Sea eventually reforming east of New Zealand.

Mass Flux

The Pacific Ocean sector of the Southern Ocean (BVI) is dominated by the eastward flow of the ACC. South of Australia the ACC attains its maximum strength of $148 \pm 4.1 \times 10^6 m^3 s^{-1}$ and decreases to $133 \pm 2 \times 10^6 m^3 s^{-1}$ at Drake Passage; the decrease in the ACC transport is compensated by a northward transport, into the subtropical Pacific Ocean, across Pac32 of $15 \pm 8.5 \times 10^6 m^3 s^{-1}$. The northward transport across Pac32 is dominated by thermocline waters (Figure 4.48). The northward transport of thermocline waters across Pac32 nearly balances the input of Pacific water to the Indian Ocean (the Indonesian Through-flow).

Intermediate layers (11 to 15) are transported northward in the eastern Pacific ocean, east of 168 °W, as part of the subtropical wind-driven gyre. Most of this water returns in the western Pacific Ocean, via the Tasman Sea, over the Kermadec-Tonga Ridge and in the western portion of the South-West Pacific basin, resulting in only a small southward transport of $1.7 \times 10^6 m^3 s^{-1}$ (Figure 4.48).

Southern Ocean deep (16 to 18) and bottom (19 to 20) layers enters the Pacific ocean in the South-West Pacific basin in a deep western boundary current adjacent to the Kermadec-Tonga Ridge. Stations occupied adjacent the ridge to 168 °W coincide with the WOCE mooring array PCM9. The integrated transport from the ridge to 168 °W below 2000 dbars (layer 17) is $13 \times 10^6 m^3 s^{-1}$

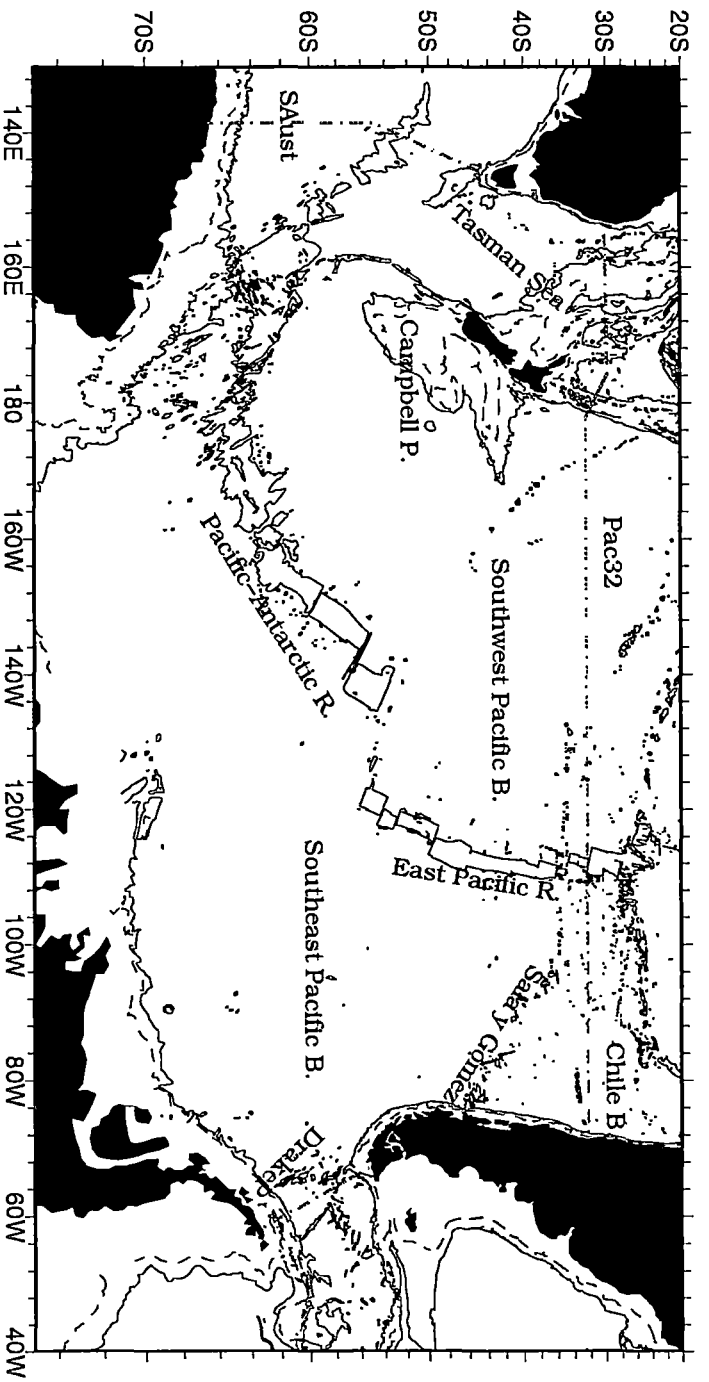

Figure 4.47: Topographic features of the South Pacific Ocean with position of hydrographic section (dot-dash). Contours 1000, 3000 metres

. This is in good agreement with the long term northward transport from the PCM9 mooring array of $11\times10^6 m^3 s^{-1}$ (Whitworth et al. 1996). At 17.5 °S Banks et al. (1995) estimate a northward transport of water colder than 1.2°C at $13.6\times10^6 m^3 s^{-1}$, while Johnson and Toole (1993) estimate a net transport of $9.6\times10^6 m^3 s^{-1}$ moving north across 10 °N. This is comprised of $14.3\times10^6 m^3 s^{-1}$ moving northwards in the east Mariana basin and the Central Pacific basin and a southward transport of $4.7\times10^6 m^3 s^{-1}$ in the Northeast Pacific basin.

Within the Chile basin, the Tasman Sea and over the Kermadec-Tonga Ridge, there is a southward flow of upper deep water (layer 16 and 17), which is associated with an oxygen minimum (Figure 4.48). The southward flow is Pacific Deep Water which results from modification of AABW and CDW and mixing with overlying intermediate water in the Pacific Ocean north of 32 °S.

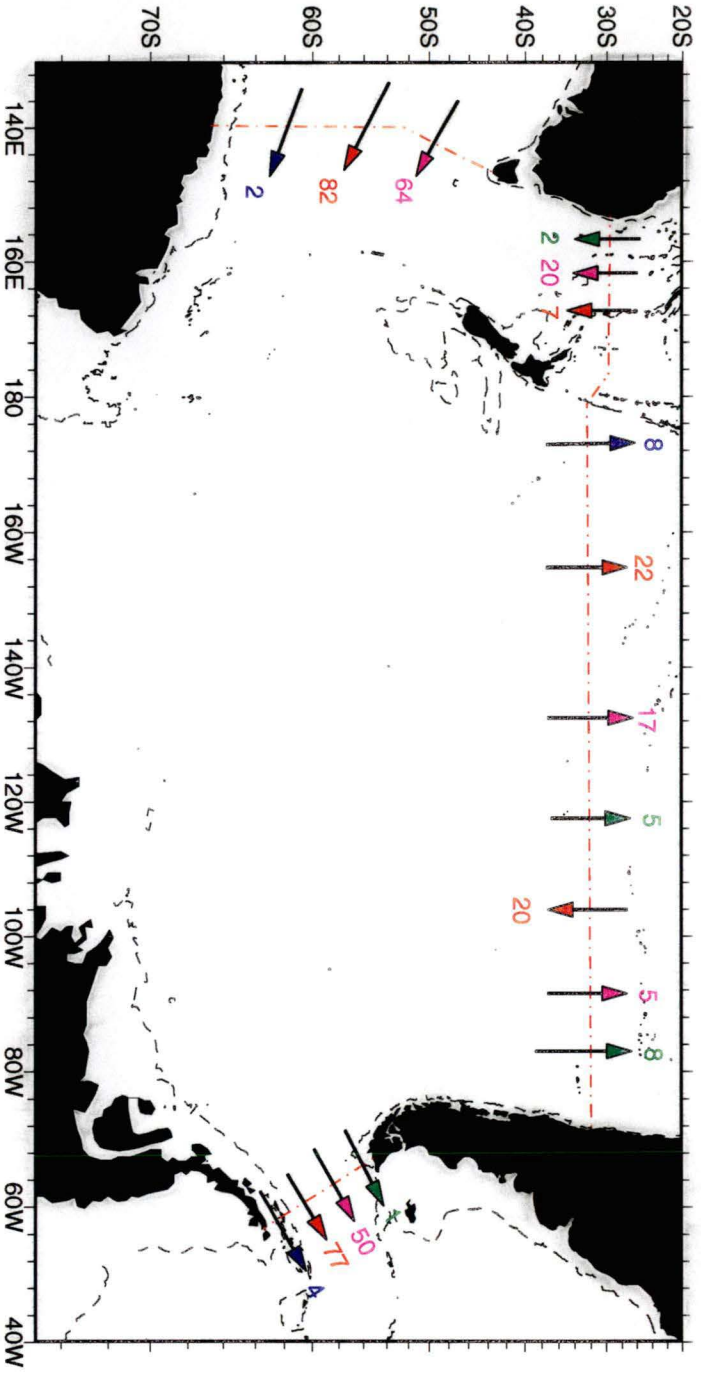

Figure 4.48: Transport ($\times 10^6 m^3 s^{-1}$) of particular layers in the Pacific Region. Thermocline layers 5 to 10 (green), Intermediate layers 11 to 15 (magenta), Deep layers 16 to 19 (red) and Bottom layers 20 to 22 (dark blue). Dashed line 1000 dbar contour.

In the Southern Ocean Pacific sector the densest water is found in the northwest Ross Sea and adjacent to the Adelie Coast. (θ -0.5°C, 34.65 and O_2 249.83 μmol.kg^{-1}). The salinity and temperature of this extreme bottom water identifies it as Adelie bottom water which Rintoul (1997) concludes is a significant contributor, second in volume to the Weddell Sea Bottom water, to global abyssal water colder than 0°C. This water is not found in either of the bounding sections at Drake Passage or south of Australia. Therefore the production of this extreme bottom water occurs in the Southern Ocean Pacific sector.

The extreme bottom water (layers 21 and 22) produced in the northwest Ross Sea and adjacent to the Adelie Coast mixes with overlying warmer CDW (layers 18 to 19) as it moves northward away from its source region (Figure 4.49). This mixing results in the modification of the extreme properties of Ross Sea and Adelie bottom water into the generic AABW (layer 20) which move northward as a deep western boundary current in the Southwest Pacific basin and fills the deep basins of the entire Pacific Ocean. As we lack a section adjacent to the Adelie coast and across the Ross Sea we are unable to determine the amount of extreme bottom water produced by cooling of CDW in the region.

The CDW is modified, producing denser water, by two mechanism: cooling adjacent to the Antarctic coast producing an unknown volume of extreme AABW and by direct mixing with extreme AABW as it moves northward away from the Antarctic continental shelf. Both of these processes result in the downward advection of CDW toward denser layers, which account for the large dianeutral mass advection ($25\times10^6 m^3 s^{-1}$) across the CDW layers (Figure 4.49).

The downward mass advection across UCDW (layers 16 and 17) replaces LCDW (layer 18 and 19) advected into AABW (layers 20 and 21). The mixing of lower salinity and oxygen minimum UCDW into LCDW in the Pacific Ocean results in the dilution of the salinity maximum and decreases the oxygen concentration of the LCDW in the Pacific region. The changes to LCDW properties in the Southern Ocean Pacific sector is shown when comparing potential temperature-salinity and potential temperature-oxygen diagrams south of Australia and at Drake Passage (Figure 4.35 and Figure 4.36). At Drake Passage the salinity maximum has decreased, reaching the minimum

value for all Southern Ocean choke-point sections. Even more dramatic is the decrease in oxygen concentration between the SAust and Drake Passage sections. The oxygen minimum results from the southward export of NPDW, which is a significant contributor to UCDW. At Drake Passage CDW is dominated by low oxygen UCDW which is composed of Indian Deep Water and Pacific Deep Water.

Upper intermediate layers (11 and 12, SAMW) are transfered into thermocline layers (9 and 10). This results from the upward dianeutral heat flux from SAMW into the thermocline which more than compensates the salt flux into the thermocline from underlying intermediate layers. The dianeutral heat flux from SAMW to thermocline layers may represent the sea-surface heat gain that occurs at the outcropping areas, which result in a buoyancy transport into the lighter thermocline layers. The lower thermocline layer moves northward across 32°S in the Pacific and compensates the Pacific thermocline water lost to the Indian Ocean through the Indonesian through-flow. There is also smaller downward advection from upper intermediate water (SAMW) into lower intermediate layers (AAIW) of $4\times10^{6}m^{3}s^{-1}$.

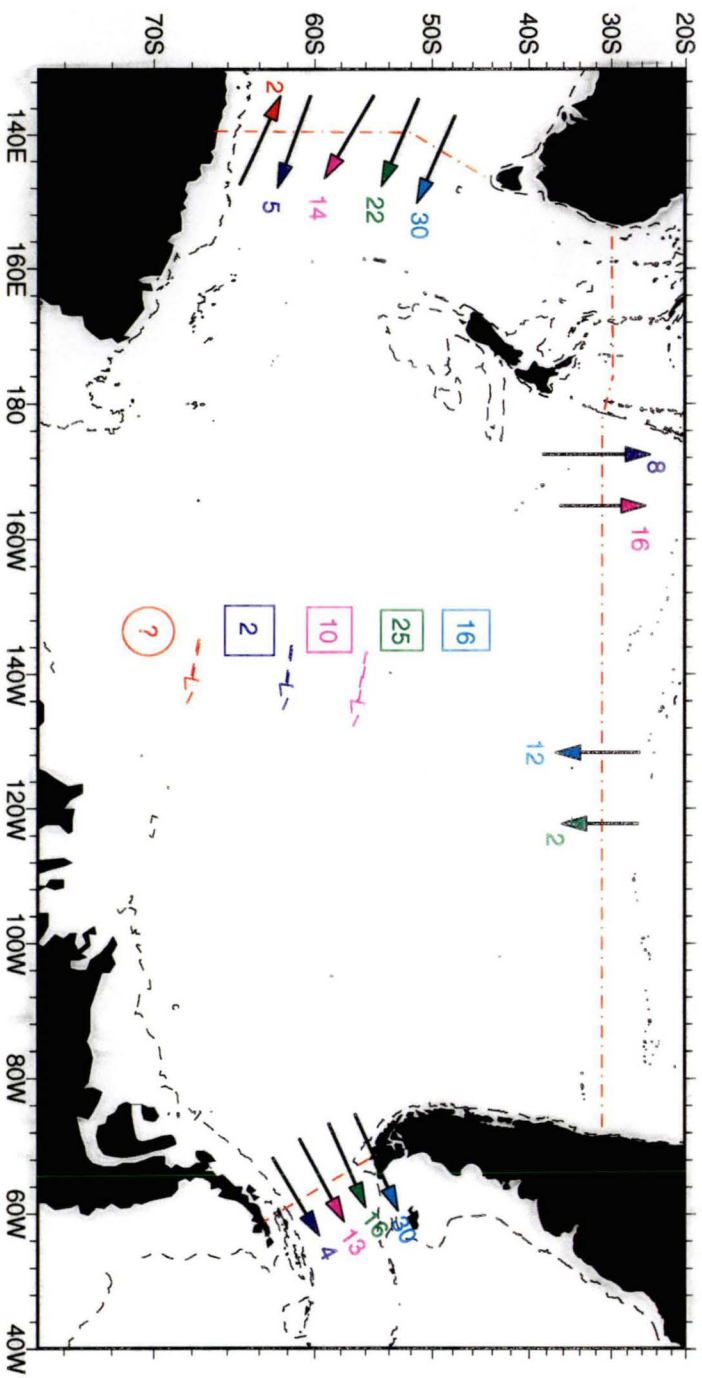

Figure 4.49: Mass transport and dianeutral flux ($\times 10^6 m^3 s^{-1}$) within Deep and Bottom water in the Pacific Region (BVI). Upward Dianeutral flux- circle, Downward Dianeutral Flux - square, dashed arrow represent net production within layers due to dianeutral flux. UCDW/NADW (layer 17, light blue), UCDW/NADW/LCDW (layer 18, green), LCDW/AABW (layer 19, magenta), AABW (layer 20, dark blue), and extreme AABW (layer 21 and 22, red). Dashed line 1000 dbar contour.

Study	Heat (PW)	Comments
Macdonald and Wunsch (1996)	0.3 ± 0.3	i
Macdonald (1993)	0.3	i
This study	0.53±0.16	i

Table 4.5: Comparison of Total Heat flux estimates (PW) for the Pacific Ocean at ≈ 30 °S. These estimates include a northward heat flux associated with the return flow of Indonesian Throughflow into the Pacific. i- inverse methods

Heat Flux

Across Pac32 there is a northward heat flux of 0.53±0.16 PW. The northward heat flux occurs in the thermocline layers (7 to 10), with only a small northward heat flux in bottom layers (19 and 20) (Figure 4.50). Southward heat flux occurs in intermediate (11 to 15) and deep (16 to 18) layers.

Table 4.5 gives a comparison of the Pacific heat flux estimated from this study with previous estimate. These studies include the heat flux associated with the return flow of the Indonesian Throughflow into the Pacific.

The Indian and Pacific Oceans are directly linked by the Indonesian through-flow and its return flow is principally south of Australia. This also means that the heat flux of these two oceans are entwined together. The estimated southward heat flux derived for the Indian-Pacific region at 30°S is -0.57 PW. Macdonald and Wunsch (1996) and Macdonald (1993) estimate an overall southward heat flux for the Indian-Pacific region of -1 PW. Toole and Warren (1993) estimate an Indian-Pacific southward heat flux of -0.98 PW.

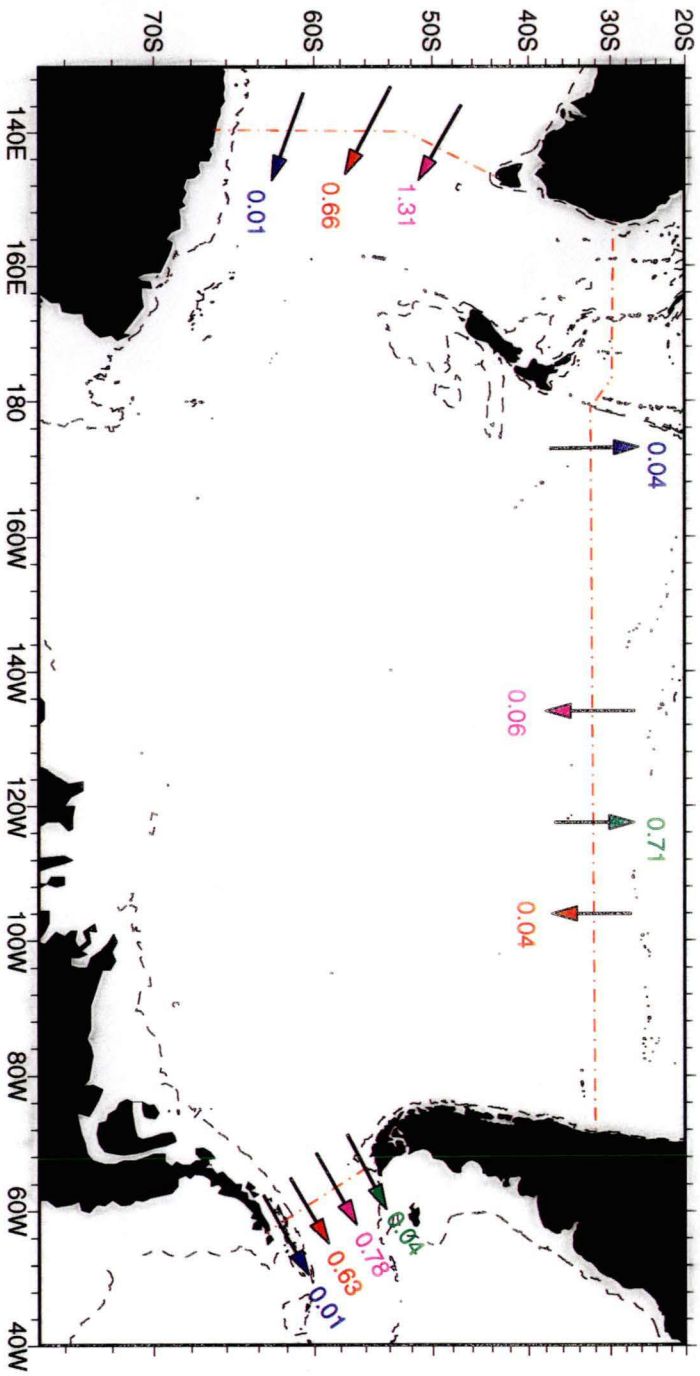

Figure 4.50: Heat flux (PW) of particular layers in the Pacific Region. Thermocline layers 5 to 10 (green), Intermediate layers 11 to 15 (magenta), Deep layers 16 to 18 across Pac32 and 16 to 19 across south of Australia and Drake Passage (red) and Bottom layers 20 to 22 (dark blue). Dashed line 1000 dbar contour.

Salt Flux

The northward salt flux across Pac32 again highlights the cyclic nature of the Indonesian through-flow around the Australian continent. The salt flux south of Australia, of $5262 \pm 56 \times 10^6 kgs^{-1}$, is greater than that entering the Southern Ocean Indian sector (BV), south of Africa or leaving the Southern Ocean Pacific sector through Drake Passage by the southward salt flux across 32°S in the Indian Ocean. The excess salt flux is contained in the lower thermocline layers (Figure 4.51).

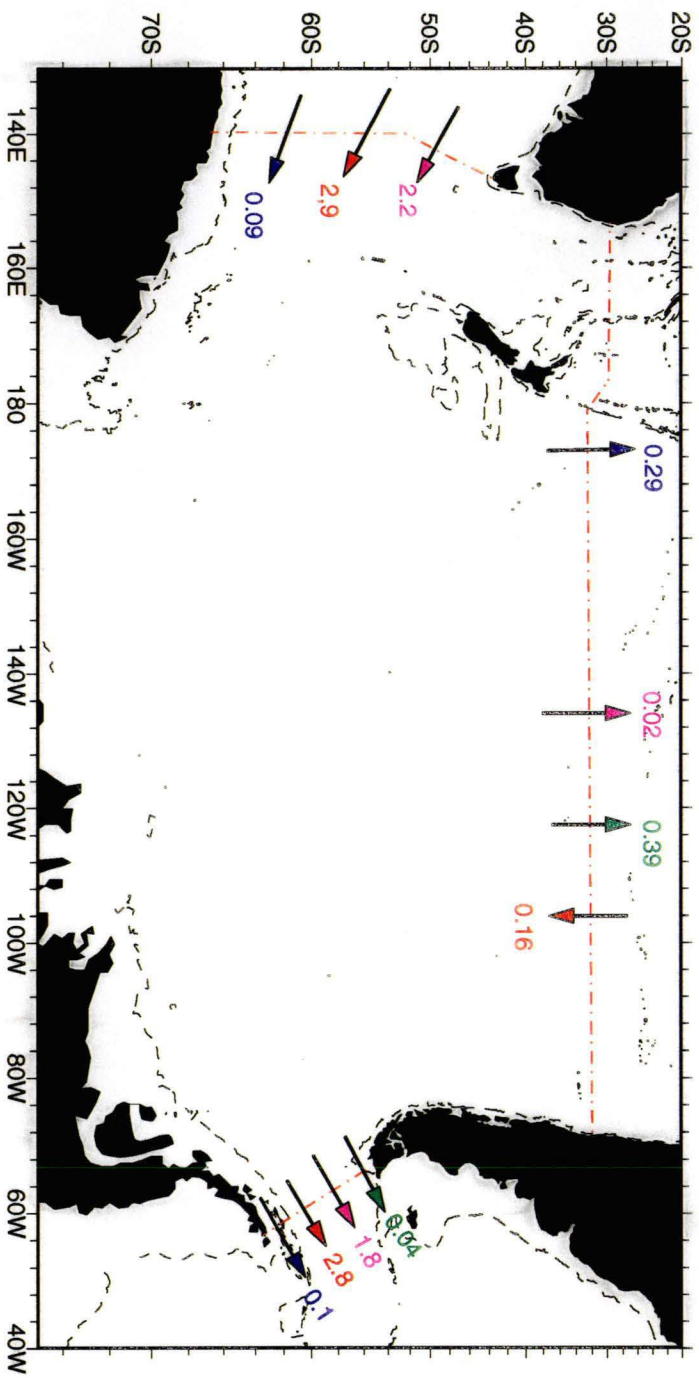

Figure 4.51: Salt flux ($\times 10^9 kgs^{-1}$) of particular layers in the Pacific Region. Thermocline layers 5 to 10 (green), Intermediate layers 11 to 15 (magenta), Deep layers 16 to 18 across Pac32 and 16 to 19 across south of Australia and Drake Passage (red) and Bottom layers 20 to 22 (dark blue). Dashed line 1000 dbar contour.

Across 32°S in the Pacific the northward salt flux occurs in the thermocline (7 to 10) and bottom (19 and 20) layers, while a smaller southward salt flux is seen in the deep layers (16 to 18) (Figure 4.51). This results in a total northward salt flux of $544 \pm 117.8 \times 10^6 kgs^{-1}$ into the Pacific Ocean, which accounts for the salt flux from the Pacific into the Indian ocean, via the Indonesian through flow, and into the Atlantic via the Bering Strait.

Freshwater Flux

The northward freshwater flux across 32°S in the Pacific ($15.2 \pm 8.7 \times 10^9 kgs^{-1}$), is dominated by the large cyclic transport, around Australia, between the Indian and Pacific Oceans. The combined Indian-Pacific freshwater flux results in a total northward flux of $0.7 \times 10^9 kgs^{-1}$. I have estimated the Indonesian through-flow at $15 \times 10^6 m^3 s^{-1}$; assuming the through-flow has a mean temperature of 24°C, salinity of 34.5 and density of $1023 kgm^{-3}$. The estimated freshwater flux associated with the Indonesian through-flow is $14.6 \pm 6.6 \times 10^9 kgs^{-1}$. The northward freshwater flux of the Pacific, with Indonesian through-flow removed, is $0.38 \times 10^9 kgs^{-1}$ which is in good agreement of the Pacific freshwater flux estimated by Wijffels et al. (1992).

Circulation impacts of Dianeutral Heat and Salt Fluxes

Within CDW (layers 17 to 19) there is an upward dianeutral heat flux into overlying lighter layers (13 to 14). These lighter layers outcrop in the far southern region, adjacent to the Antarctic coast where heat loss to the atmosphere results in cold sea-surface water. Therefore there is a heat flux into these cold surfaces water from underlying warm CDW. This upward heat flux and the upward dianeutral salt flux from the CDW into the cold sea-surface water (AASW) leads to a downward advection of mass into denser CDW and AABW layers resulting in the production of these denser water classes.

In the Southern Ocean Indian sector the dianeutral heat flux is downward across thermocline layers (6 to 10) while the dianeutral salt flux across these lower layers (10) is upwards into less dense layers. The effect of the dianeutral heat and salt fluxes across the thermocline layers results in the downward mass advection across thermocline layers into intermediate layers (11 to 15,

SAMW/AAIW). These layer flow eastward into the Pacific region (BVI) where they experience an upward dianeutral heat flux from intermediate (SAMW/AAIW) and deep (CDW) water, due principally to air-sea interaction. The salt diffusion in the Pacific region is generally downwards resulting in the redistribution of salt from the thermocline maximum into underlying salinity minimum intermediate water. Although the heat diffusion dominates, resulting in upward mass advection from SAMW into lower thermocline layers. The lower thermocline layer move northward across 32°S in the Pacific. The dianeutral mass, heat and salt fluxes describe the mechanism by which the Indonesian through-flow moving eastward south of Australia is returned northwards into the Pacific Ocean. This highlight the circum-Australia nature of the Indian-Pacific circulation.

4.4 Summary

The column and row weights of the present inverse model (model_int) and the scaling of the unknown reference level velocity and dianeutral flux unknowns minimised the condition number (ratio of largest to smallest eigenvalue) allowing the system to be solved to a high rank. The derived circulation is consistent with previous studies.

The total eastward transport of the ACC across the Southern Ocean choke point of $133\pm2\times10^6 m^3 s^{-1}$ at Drake Passage, $134\pm2\times10^6 m^3 s^{-1}$ south of Africa and $148\pm4\times10^6 m^3 s^{-1}$ south of Australia agree with recent estimates (Nowlin and Klinck 1986; Bindoff et al. 1997). The meridional transport across approximately 30°S are: Atlantic $-0.6 \pm 5\times10^6 m^3 s^{-1}$; Indian $-15 \pm 7\times10^6 m^3 s^{-1}$ and across the Pacific $15 \pm 9\times10^6 m^3 s^{-1}$.

The dianeutral fluxes provide a plausible explanation of how water masses exchange properties across bounding neutral surfaces. In the Southern Ocean Atlantic, Indian and Pacific sectors mixing between AABW, CDW, NADW, IDW and NPDW respectively results in changes to the characteristics of bottom and deep water masses within each region. NADW ($20\times10^6 m^3 s^{-1}$) enters the South Atlantic across SAVE2 (15°S). In the Subtropical Atlantic NADW mixes with overlying intermediate water ($4\times10^6 m^3 s^{-1}$) and underlying ($4\times10^6 m^3 s^{-1}$

) colder, fresher CDW. The downward dianeutral flux of NADW into AABW and CDW results in the temperature and salinity increase evident in these water masses as they move northward across 15°S into the North Atlantic. In the Southern Ocean Atlantic sector further downward dianeutral flux from NADW ($5\times10^6 m^3 s^{-1}$) results in the salinity maximum of LCDW. The input of NADW replaces CDW that moves southward into the Weddell Sea, which eventually returns the Southern Ocean Atlantic sector as cold, fresh WSDW and WSBW. WSDW and WSBW ($10\times10^6 m^3 s^{-1}$) is modified into less extreme AABW which moves northward into the adjacent subtropical oceans and eastward with the ACC.

The NADW influenced CDW (salinity maximum and high oxygen concentration) and cold fresh Weddell Sea influenced AABW moves eastward into the Southern Ocean Indian sector. Numerous deep western boundary currents direct $25\times10^6 m^3 s^{-1}$ of LCDW and AABW into the subtropical Indian Ocean, where it is modified into slightly less saline, oxygen poor water which returns to the Southern Ocean across 32°S as slightly less dense IDW. The slightly fresher, oxygen poor returning IDW mixes with underlying ($10\times10^6 m^3 s^{-1}$) LCDW resulting in the erosion of the salinity maximum and high oxygen concentration of LCDW and the definition of a deep oxygen minimum associated with UCDW.

In the Pacific Ocean a similar deep overturning cell is suggested with AABW and LCDW ($24\times10^6 m^3 s^{-1}$) moving northward across 32°S in the deep western boundary of the Southwest Pacific basin. The northward AABW and CDW are balance by southward flow across 32°S of as slightly less dense, less saline, oxygen poor NPDW. NPDW water mixes with underlying ($15\times10^6 m^3 s^{-1}$) CDW resulting in further erosion of the LCDW salinity maximum and oxygen concentration such that UCDW low oxygen dominates CDW as it move eastward through Drake Passage into the Atlantic. The northward and eastward transport of AABW across 32°S in the Pacific and Drake Passage is not balanced by the input of AABW south of Australia. This suggests that there is a local source of extreme AABW in the Southern Ocean Pacific sector. I am unable to determine the amount of locally produced extreme AABW as there is no hydrographic section parallel to the Antarctic coast. The northern and

eastern exit regions of AABW are far removed from suspected formation regions and by the time AABW reaches these point the extreme properties of newly formed AABW are modified by downward dianeutral flux of CDW (resulting in the generic AABW exiting the Pacific sector at 32°S and Drake Passage).

The combined meridional heat flux from the Atlantic, Indian and Pacific Ocean at approximately 30°S is -0.1 PW. This southward heat flux is considerably smaller than previous estimates which vary from $-0.9 \pm 0.3PW$ (Macdonald and Wunsch 1996), -1.62 PW (Hsiung 1985) and, -1.75 PW (Hastenrath 1982).

There are some aspects of the circulation of model_int that are not consistent with previous studies. Further development of the inverse model in this study would be the inclusion of the air-sea heat and freshwater divergences. Apart from adding a total heat and freshwater divergence, the explicit inclusion of air-sea heat, freshwater and Ekman flux at the outcropping neutral surfaces can also be included to determine the sea-surface dianeutral mass, heat and salt fluxes. The inclusion of sea-surface property dianeutral fluxes would allow distinction between sea-surface and interior dianeutral processes, enabling us to identify regions where air-sea fluxes and or interior dianeutral fluxes redistribute heat, salt and freshwater through-out the ocean. Explicitly dividing the dianeutral flux into air-sea and interior processes may remove some of the ambiguities in the interpretation of the dianeutral property fluxes in this model. Such a model is developed in the next chapter.

Chapter 5

Explicit Surface Buoyancy Forcing

The dianeutral terms of the previous model (model_int) represent all the physical processes that are involved in producing fluxes across neutral surfaces. These processes include advection, diffusion, eddy mixing processes and air-sea forcing upon outcropping layers by wind, heat and freshwater fluxes.

Recent studies have quantified the water mass conversion resulting from exchanges of heat and freshwater on outcropping layers (Tziperman 1986; Schmitt et al. 1989; Speer and Tziperman 1992). Following these studies, heat and freshwater fluxes and surface Ekman advection can be included explicitly in the inverse model as constraints on the mass, heat and salt equations. The explicit inclusion of air-sea forcing in the improves the physical representativeness of the inverse model.

This chapter briefly discusses the way in which sea-surface forcing terms act to change the sea-surface density and shows how these term are incorporated into the conservation equations. The resultant circulation is discussed, highlighting the interaction between interior and sea-surface dianeutral fluxes that result in the net convergence in outcropping layers.

5.1 Surface Buoyancy Fluxes

The interaction of the outcropping neutral surfaces with the overlying atmosphere can result in dianeutral mass, heat and salt fluxes. Previous inverse studies have overcome the problem of exchange between layers driven by air-sea

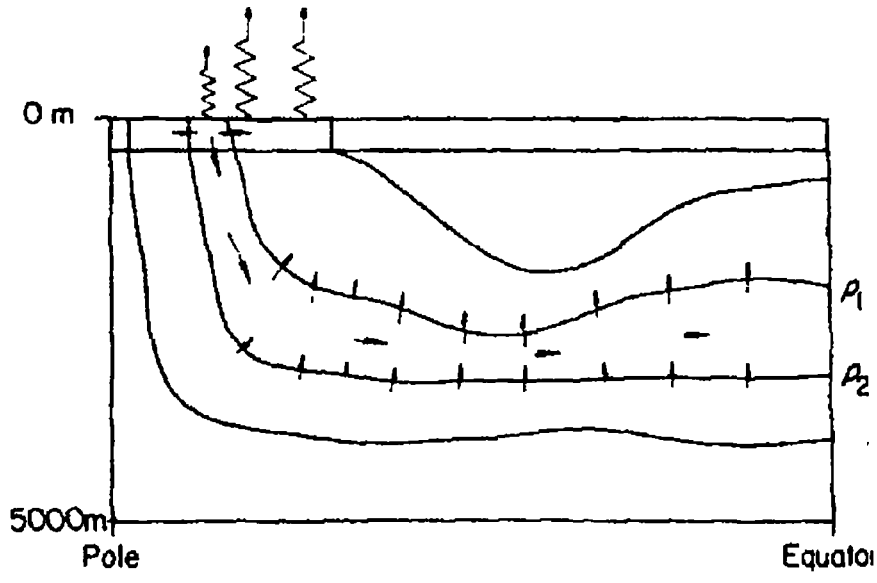

Figure 5.1: A schematic north-south vertical section showing the production of water of density between ρ_1 and ρ_2 by air-sea heat fluxes, and dissipation of this water type by interior mixing (from Tziperman, 1986)

fluxes by either down-weighting the conservation equations for the outcropping layers or ignoring the upper layers and applying the conservation constraint below the thermocline or mixed layer depth (Rintoul 1988; Metzl et al. 1990).

A schematic of the interactions between sea-surface production and interior dissipation is shown in Figure 5.1. Differences in the heat flux acting on the outcropped layers ($\rho < \rho_1$ and $\rho_1 < \rho < \rho_2$) results in production of water within layer $\rho_1 < \rho < \rho_2$. Interior mixing results in mass fluxes across ρ_1 and ρ_2 of which, in the case shown, more leaves across ρ_1 than enters across ρ_2. The loss of water in the layer by interior mixing balances input from the surface. The freshwater and Ekman fluxes have similar effects on the sea-surface water conversions and these are also balanced by interior mixing across density surfaces. In a steady state system, surface buoyancy fluxes must be balanced by interior dianeutral fluxes.

Following Tziperman (1986), Schmitt et al. (1989) and Speer and Tziperman (1992) the effect of surface forcing on mass, heat and salt dianeutral fluxes can be found. The mass flux (f_m) due to heat and freshwater flux and Ekman is:

$$f_m = \frac{-\alpha H}{C_p} + \rho\beta QS - \rho Q + \rho E \tag{5.1}$$

where

ρ sea surface density

α thermal expansion

β saline contraction

H heat flux

Q freshwater flux (Evaporation - Precipitation ms^{-1})

S sea surface salinity

E Ekman transport

C_p specific heat

All of these term are functions of time and position. The first two terms of Equation 5.1 represent the effect of heat and freshwater on density, while the last two terms are direct input/loss of freshwater and the horizontal Ekman mass advection across the density layer, respectively. The total mass flux, for one year, as a function of sea surface density is:

$$F_m(\rho) = \int_{year} dt \int\int_{area} dA\, f_m\, \delta(\rho - \rho') \tag{5.2}$$

where the δ function samples the density flux at surface ρ. Speer and Tziperman (1992) call this the transformation ($F_m(\rho)$), or the flux of water across density surface, ρ. The water that accumulates between ρ and $\rho + d\rho$ is:

$$C_m(\rho)\, d\rho = -\left[F_m(\rho + d\rho) - F_m(\rho)\right] \tag{5.3}$$

Equation 5.3 is known as the formation ($C_m(\rho)$) (Speer and Tziperman (1992) uses $M_m(\rho)$ as the symbol of formation).

Equation 5.2 and Equation 5.3 are expressions for the mass transformation and formation due to sea-surface forcing from heat and freshwater fluxes and wind stress. In a similar manner, the convergence of heat and salt in isopycnal

layers due to air-sea fluxes of heat, freshwater and momentum can be found. The heat flux (f_h) across outcropping density surfaces is:

$$f_h = \frac{-H}{C_p \rho} + \rho E \theta_{De} \tag{5.4}$$

and the total heat flux, as a function of sea surface density is:

$$F_h(\rho) = \int_{year} dt \int \int_{area} dA \, f_h \, \delta(\rho - \rho') \tag{5.5}$$

while the salt flux (f_s) is:

$$f_s = \rho E S_{De} \tag{5.6}$$

and the total salt flux, as a function of sea surface density is:

$$F_s(\rho) = \int_{year} dt \int \int_{area} dA \, f_s \, \delta(\rho - \rho') \tag{5.7}$$

where θ_{De} and S_{De} are the weighted mean temperature and salinity over the Ekman layer (De).

From expressions Equation 5.5 and Equation 5.7 the heat and salt convergence between ρ and $\rho + d\rho$ is

$$C_{prop}(\rho) = -dF_{prop}/d\rho \tag{5.8}$$

5.2 Inverse Model - Explicit Sea-Surface Forcing

In the inverse model, neutral density (γ_n) is used to define vertical layers, therefore property transformations are written in terms of γ_n. The property transformations across the area of each outcropping neutral surface are calculated from climatological data sets that are interpolated onto a 1°× 1°grid. As the data are discontinuous, the property transformations across outcropping neutral surfaces are summed over a discrete neutral density interval surrounding the outcropping neutral surface (Speer and Tziperman 1992). The delta function in now a boxcar (Π) of width $\Delta\gamma$.

$$F_m(\gamma) = \frac{1}{\Delta\gamma}\sum_{n=1}^{12}\Delta t\sum_{i,j}\Delta A_{i,j}\times \left[\frac{-\alpha H^n_{i,j}}{C_p}+\rho\beta Q^n_{i,j}S-Q^n_{i,j}+E^n_{i,j}\right]\Pi(\gamma-\gamma') \quad (5.9)$$

$$F_h(\gamma) = \sum_{n=1}^{12}\Delta t\sum_{i,j}\Delta A_{i,j}\times\left[\frac{H^n_{i,j}}{C_p\rho}+E^n_{i,j}\theta_{De_{i,j}}\right]\Pi(\gamma-\gamma') \quad (5.10)$$

$$F_s(\gamma) = \sum_{n=1}^{12}\Delta t\sum_{i,j}\Delta A_{i,j}\sum_{n=1}^{12}\left[E^n_{i,j}S_{De_{ij}}\right]\Pi(\gamma-\gamma') \quad (5.11)$$

The climatological data used to calculate the property transformations are:

Heat Flux (H) COADS by da Silva et al. (1994) (Figure 5.2);

Wind Stress (E) Hellerman and Rosenstein (1983) and;

Freshwater (Q) from GASP by Budd et al. (1995) (Figure 5.3)

The Levitus and Boyer (1994) oceanic climatology is used to find the sea-surface outcropping position of the neutral density surfaces for each month and the weighted mean Ekman depth temperature and salinity. Figure 5.4 shows the mean outcropping positions of neutral density surfaces.

The data sets used to calculate the sea-surface fluxes (or transformations) contain errors, including errors in the bulk formulae used to derive air-sea heat fluxes and a lack of observations, from oceanographic and meteorological data, at high latitudes and over subtropical regions away from commercial shipping routes (Speer and Tziperman 1992; Barnier et al. 1995). More errors are introduced from the averaging methods used to assemble the data sets (Speer and Tziperman 1992). Using the inverse technique we are able to find corrections to the climatological data sets that make these data sets consistent with the hydrographic data while still conserving mass, heat and salt in the model domain.

The total property fluxes calculated from the climatological data and an unknown sea-surface property flux correction term are added to the conservation equations. The form of the conservation equations is then:

$$\sum_{j=1}^{N} \delta_j \Delta x_j \int_{h_m}^{h_{m+1}} (\rho C_j (v_r + b)_j) + E_j C_j$$
$$+ (w_c AC)_m - (w_c AC)_{m+1}$$
$$+ (F_c + F_c^*)_m - (F_c + F_c^*)_{m+1} \approx 0 \tag{5.12}$$

where

F_c total property sea-surface flux across outcropping neutral surface m and m+1

F_c^* unknown correction to property sea-surfaces flux across outcropping neutral surface m and m+1

The first and second term of Equation 5.12 are present for all layers within the region, while the third term only exists for the neutral surfaces that outcrop with the region. The sea-surface transformation corrections are calculated for heat, freshwater and Ekman fluxes, from which the derived corrections can be added to the original air-sea heat flux, Ekman wind stress and freshwater flux.

5.3 Sea-Surface Forcing and Dianeutral Fluxes

In this section the inverse corrections to the air-sea heat, freshwater and Ekman fluxes and the interior dianeutral fluxes are discussed. The reference velocities for this model (model_surf) are shown in Figure 5.5 to Figure 5.13. These are similar to the reference velocity of the previous model (Figure 4.2 to Figure 4.10), apart from the reference velocity at SAVE4, Ind18 and Pac32. The reference velocity at SAVE4 is smaller, at Ind18 the velocity is smaller on the eastern boundary, while at PAC32 the velocity is larger when compared to the previous model (model_int).

5.3.1 Sea-Surface Forcing

As outlined in Section 5.2 heat, freshwater and wind stress climatologies are included as the initial guess in the inverse model with unknown correction terms determined by the inverse model. The correction terms allow these

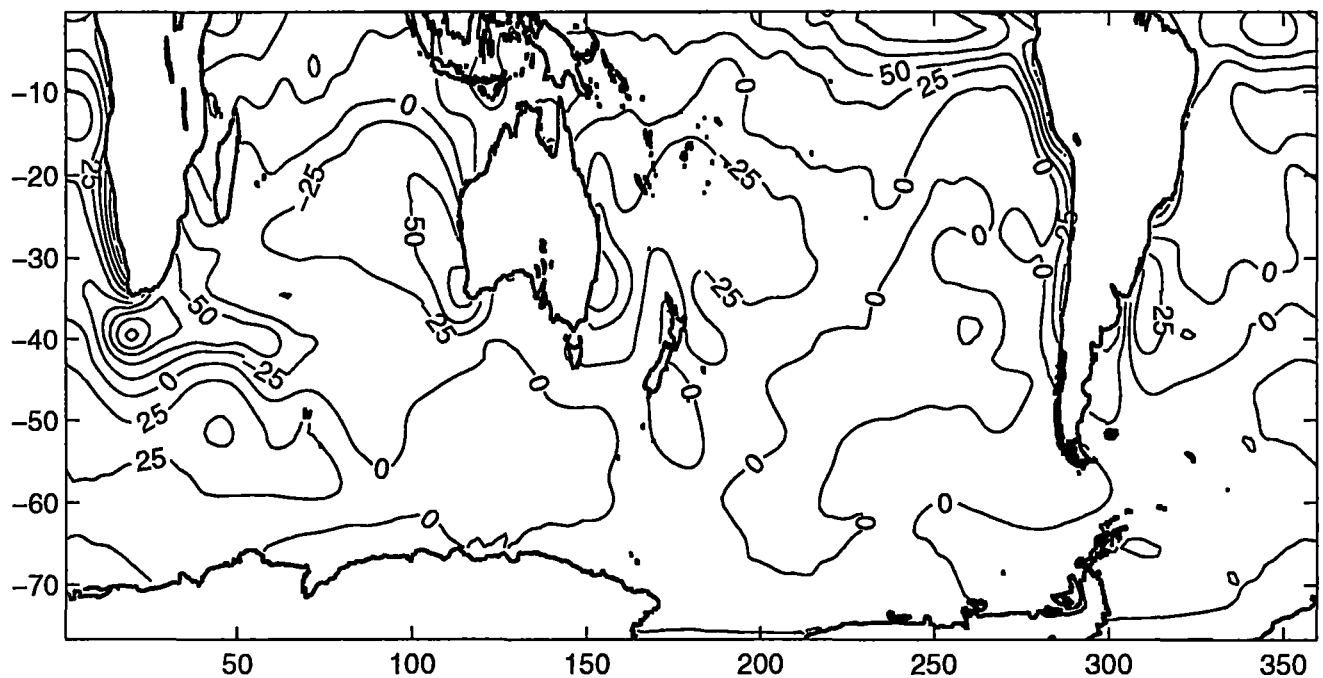

Figure 5.2: The COADS Annual Mean Heat Flux (Wm^{-2})

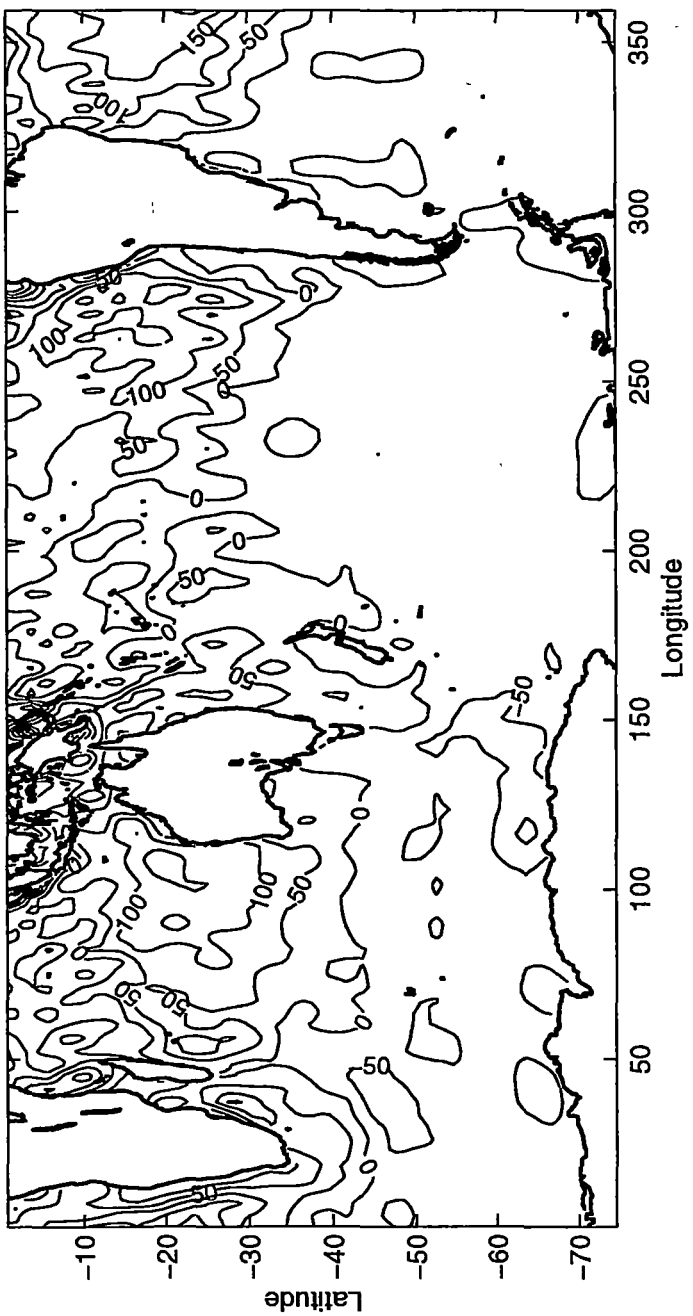

Figure 5.3: The GASP Freshwater Flux (E-P cm/year)

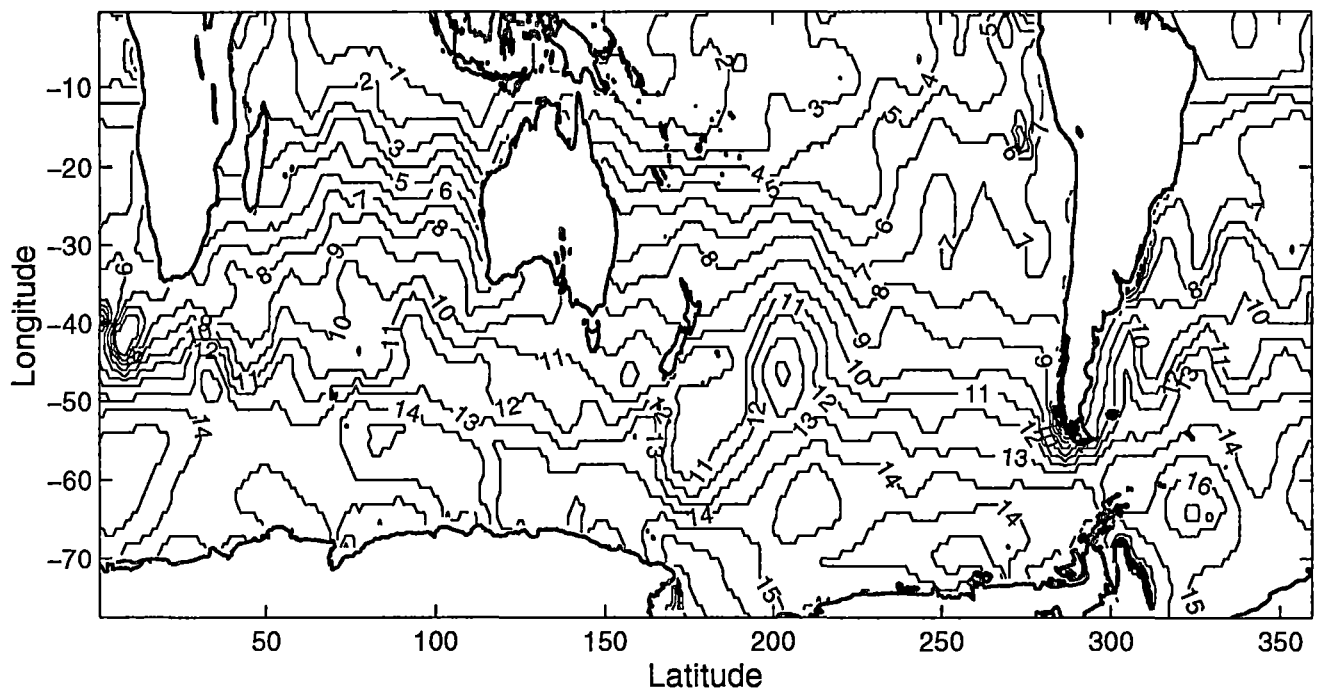

Figure 5.4: June outcropping position of neutral density surfaces, contours are labelled with neutral surface numbers. Unrealistic features, particularly in the Southern Ocean could be due interpolation errors resulting from the sparce data available in the Southern Ocean during winter

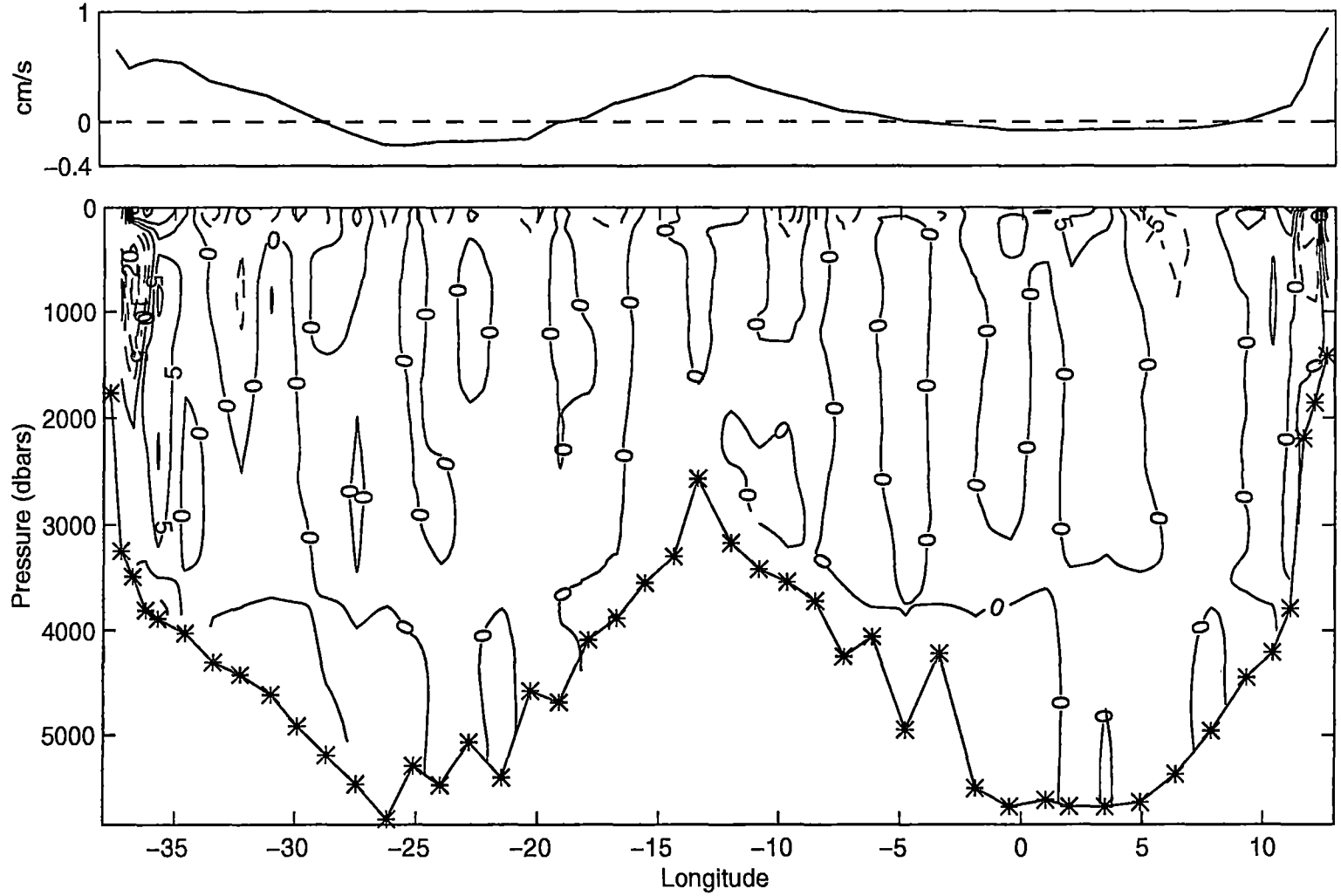

Figure 5.5: Absolute velocity at the SAVE 2 section. Solid and dashed contours refer to north and south velocities, respectively. Upper plot is reference level velocity.

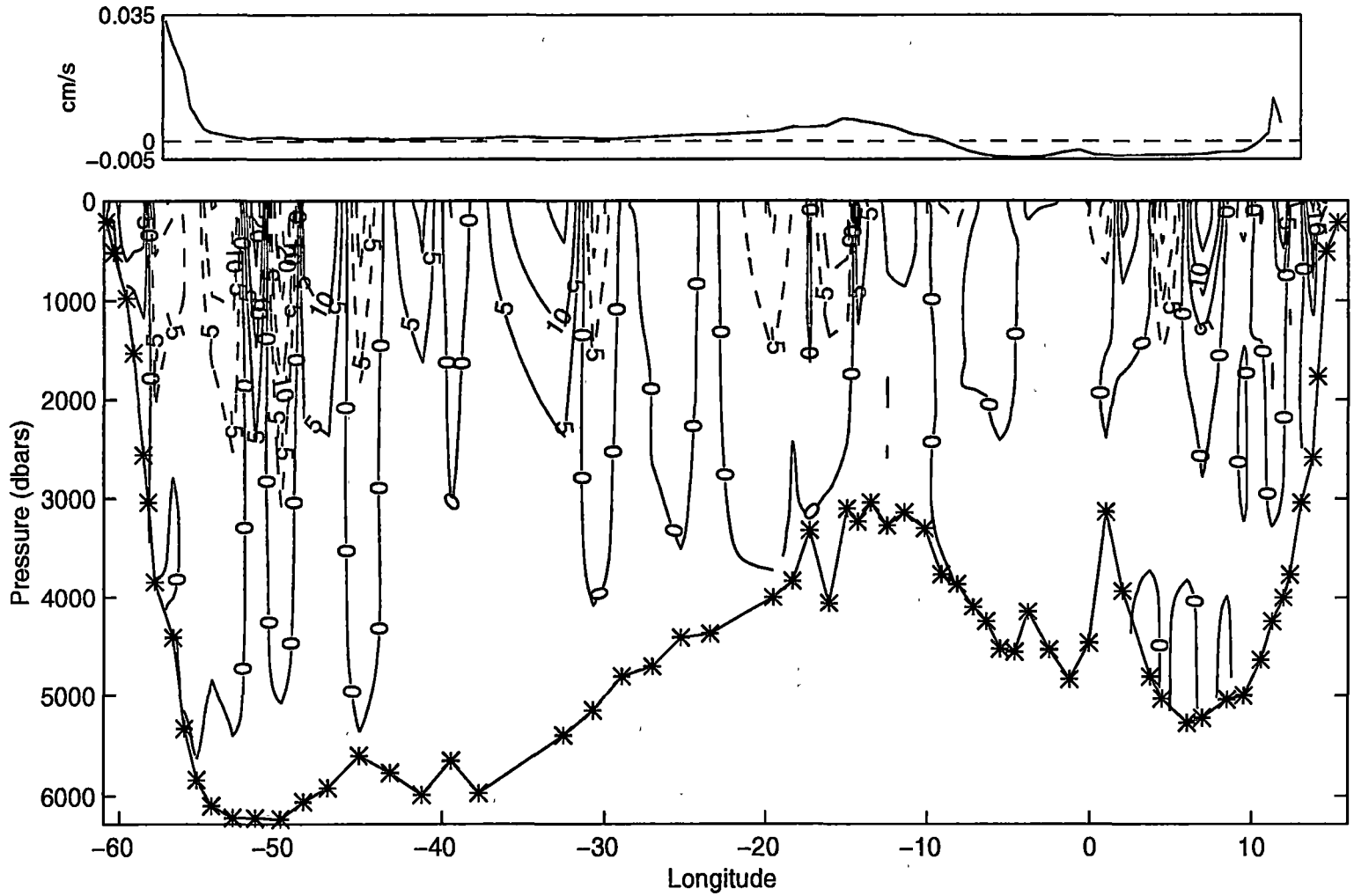

Figure 5.6: Absolute velocity at the SAVE 4 section. Solid and dashed contours refer to north and south velocities, respectively. Upper plot is reference level velocity.

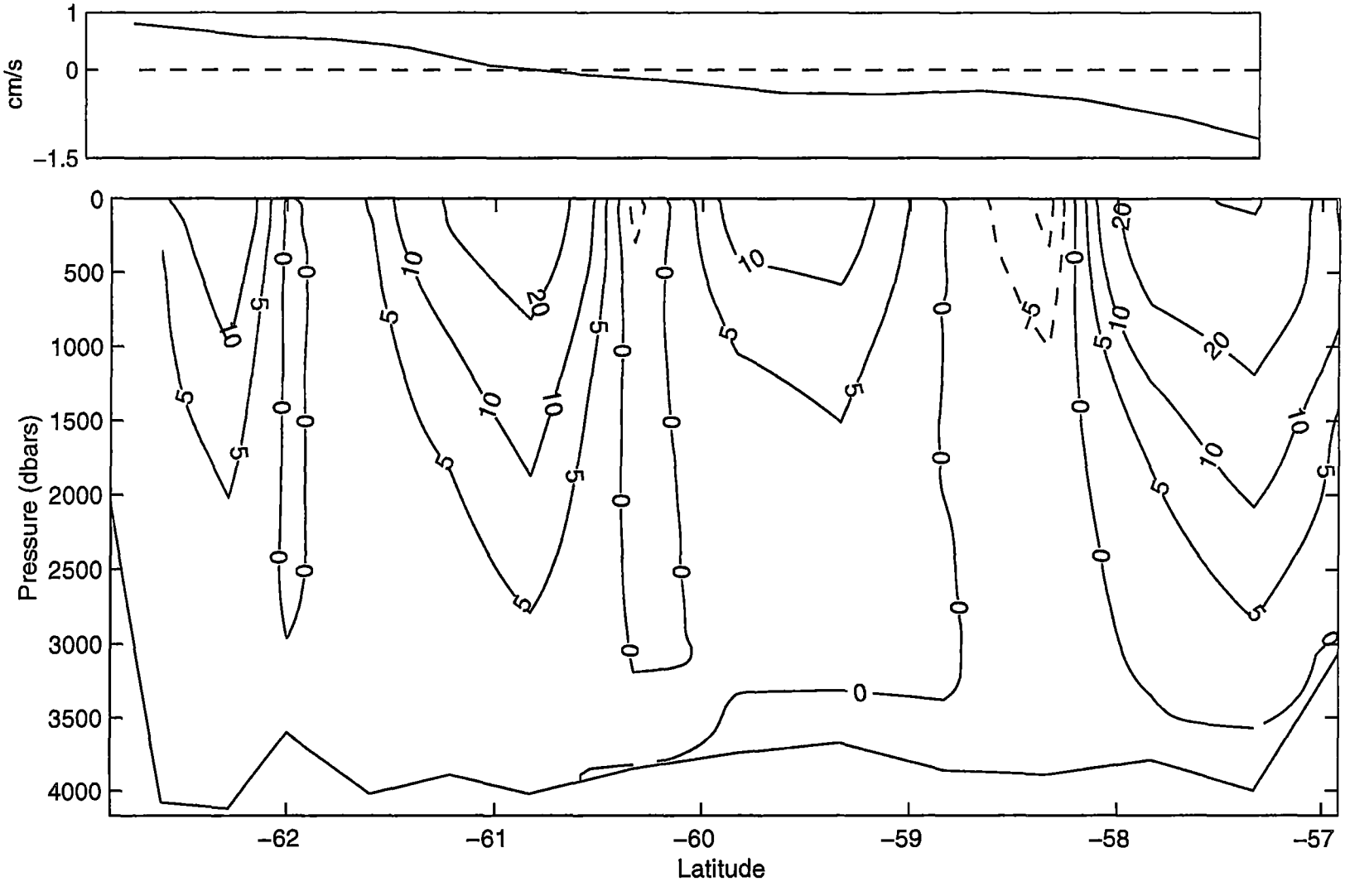

Figure 5.7: Absolute velocity at the Drake Passage section. Solid and dashed contours refer to east and west velocities, respectively. Upper plot is reference level velocity.

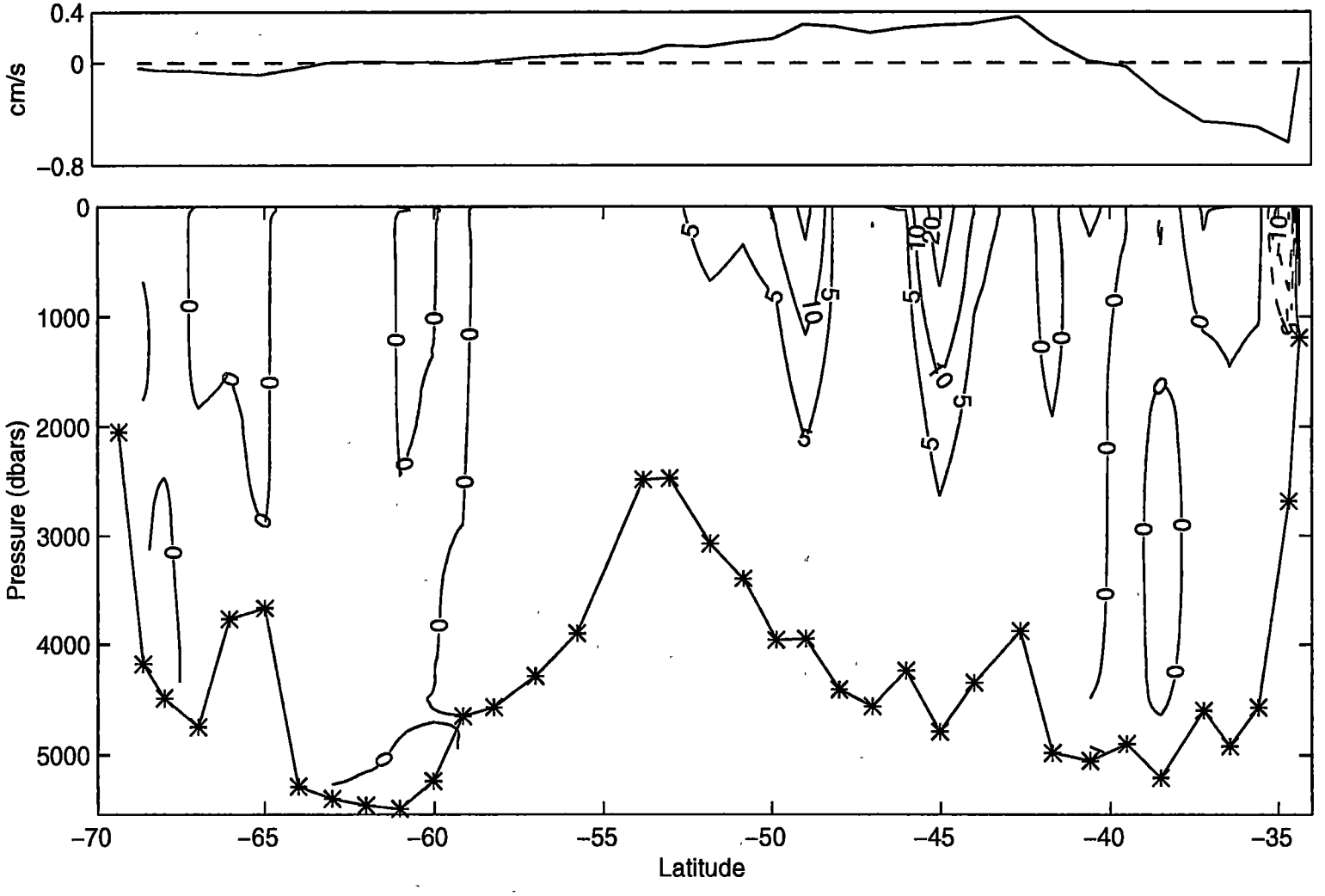

Figure 5.8: Absolute velocity at the section south of Africa. Solid and dashed contours refer to east and west velocities, respectively. Upper plot is reference level velocity.

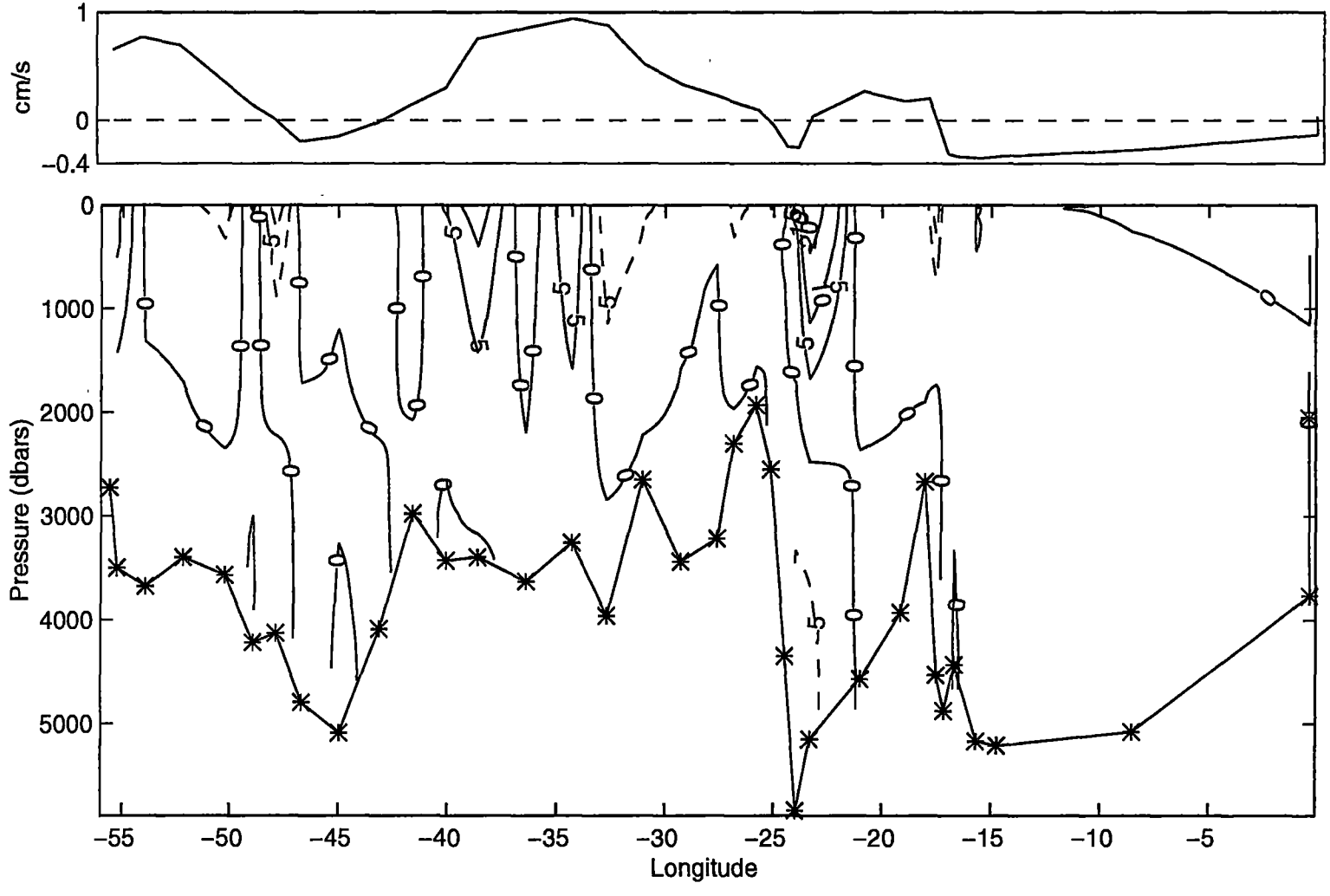

Figure 5.9: Absolute velocity at the Weddell Sea section. Solid and dashed contours refer to north and south velocities, respectively. Upper plot is reference level velocity.

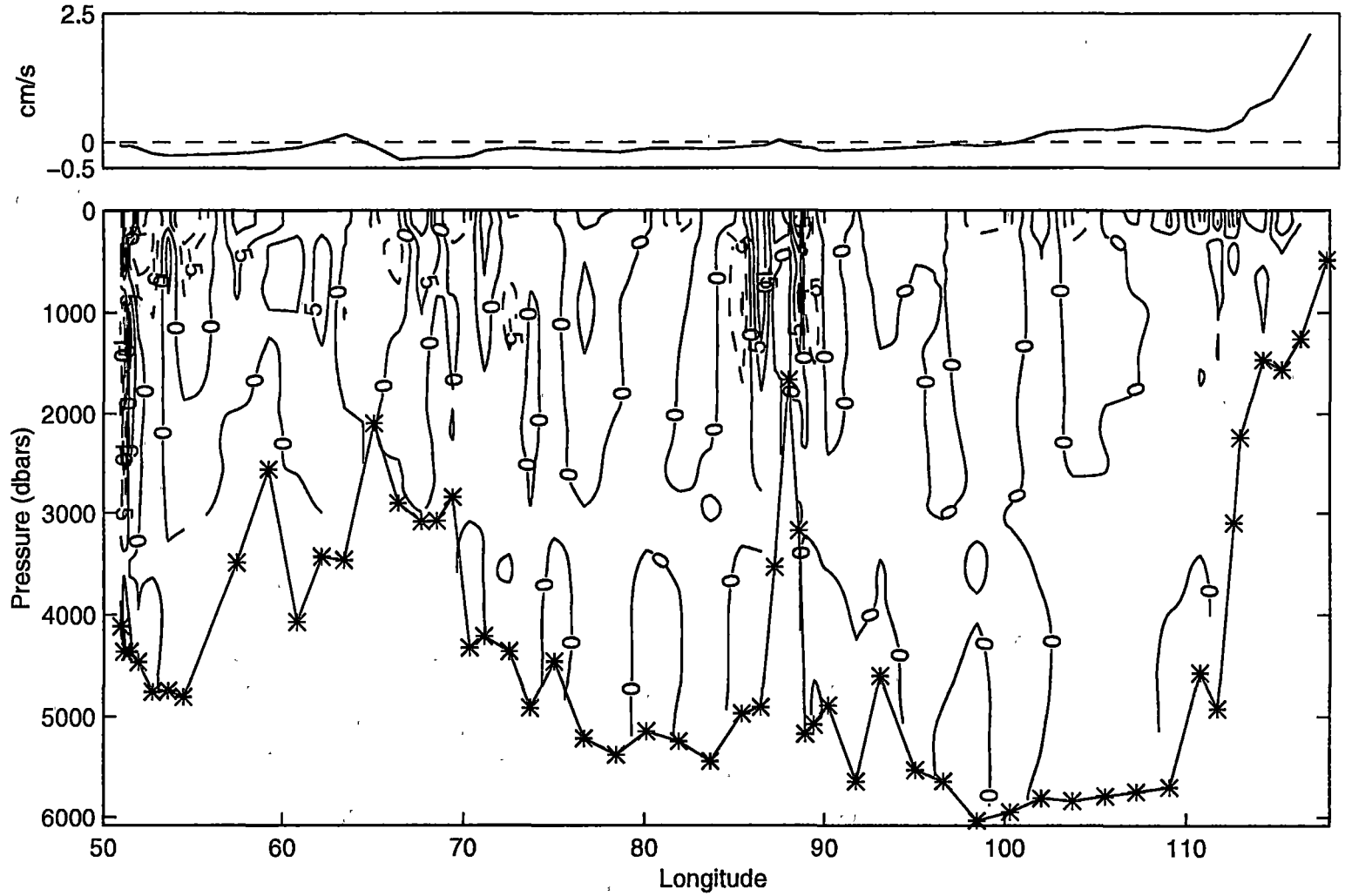

Figure 5.10: Absolute velocity at the Indian 18°S section. Solid and dashed contours refer to north and south velocities, respectively. Upper plot is reference level velocity.

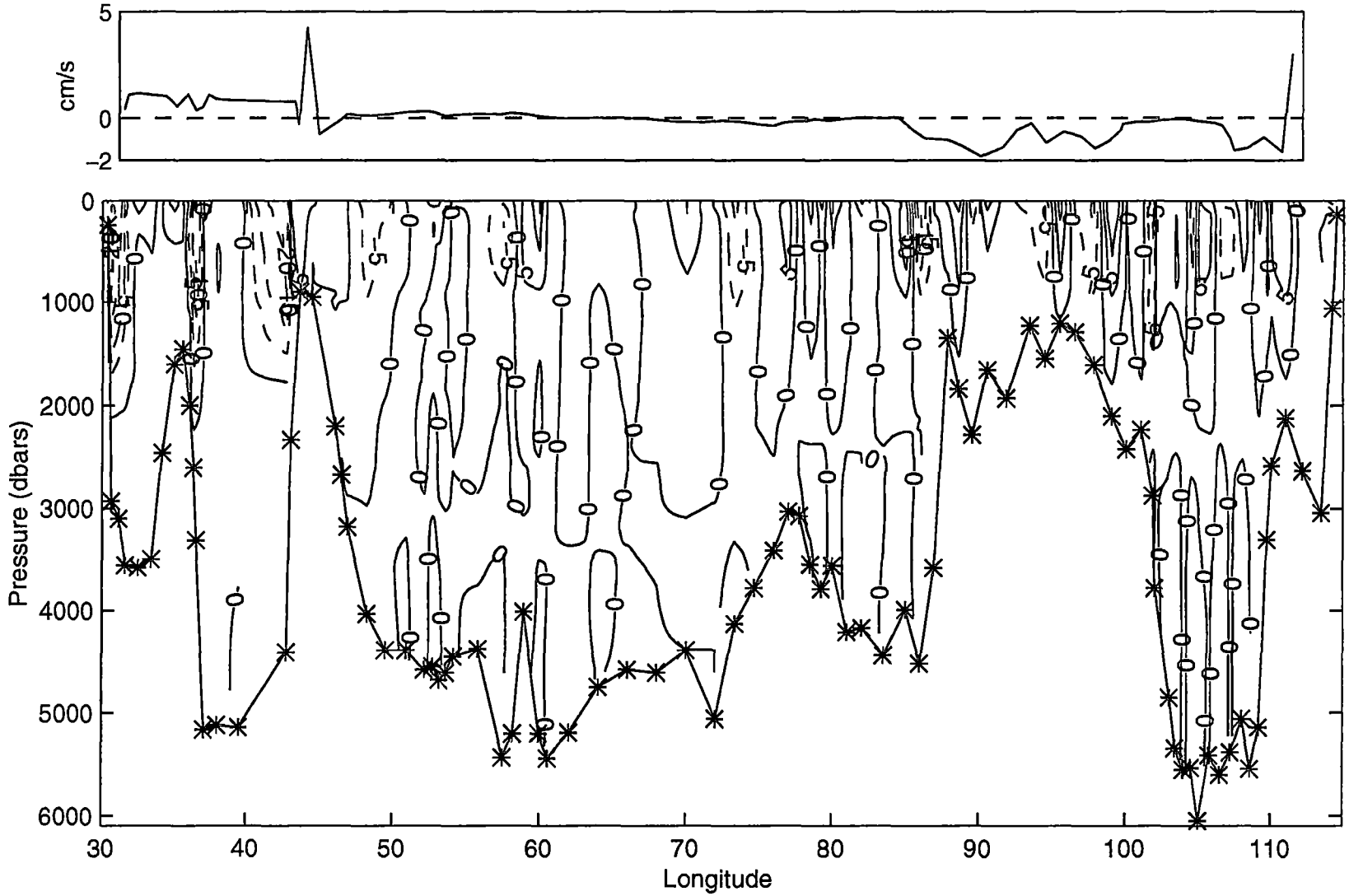

Figure 5.11: Absolute velocity at the Indian 32°S section. Solid and dashed contours refer to north and south velocities, respectively. Upper plot is reference level velocity.

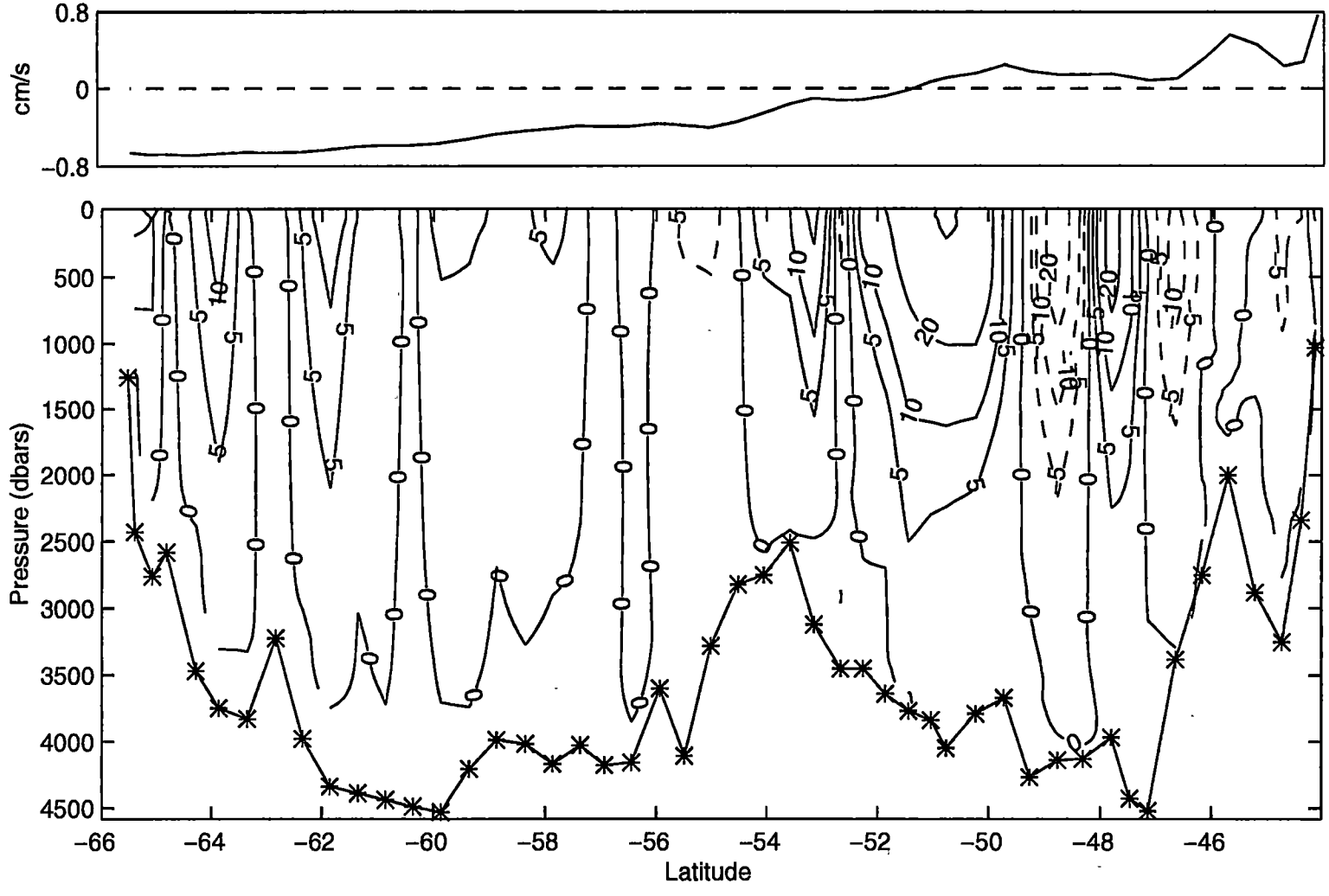

Figure 5.12: Absolute velocity at the section south of Australia. Solid and dashed contours refer to east and west velocities, respectively. Upper plot is reference level velocity.

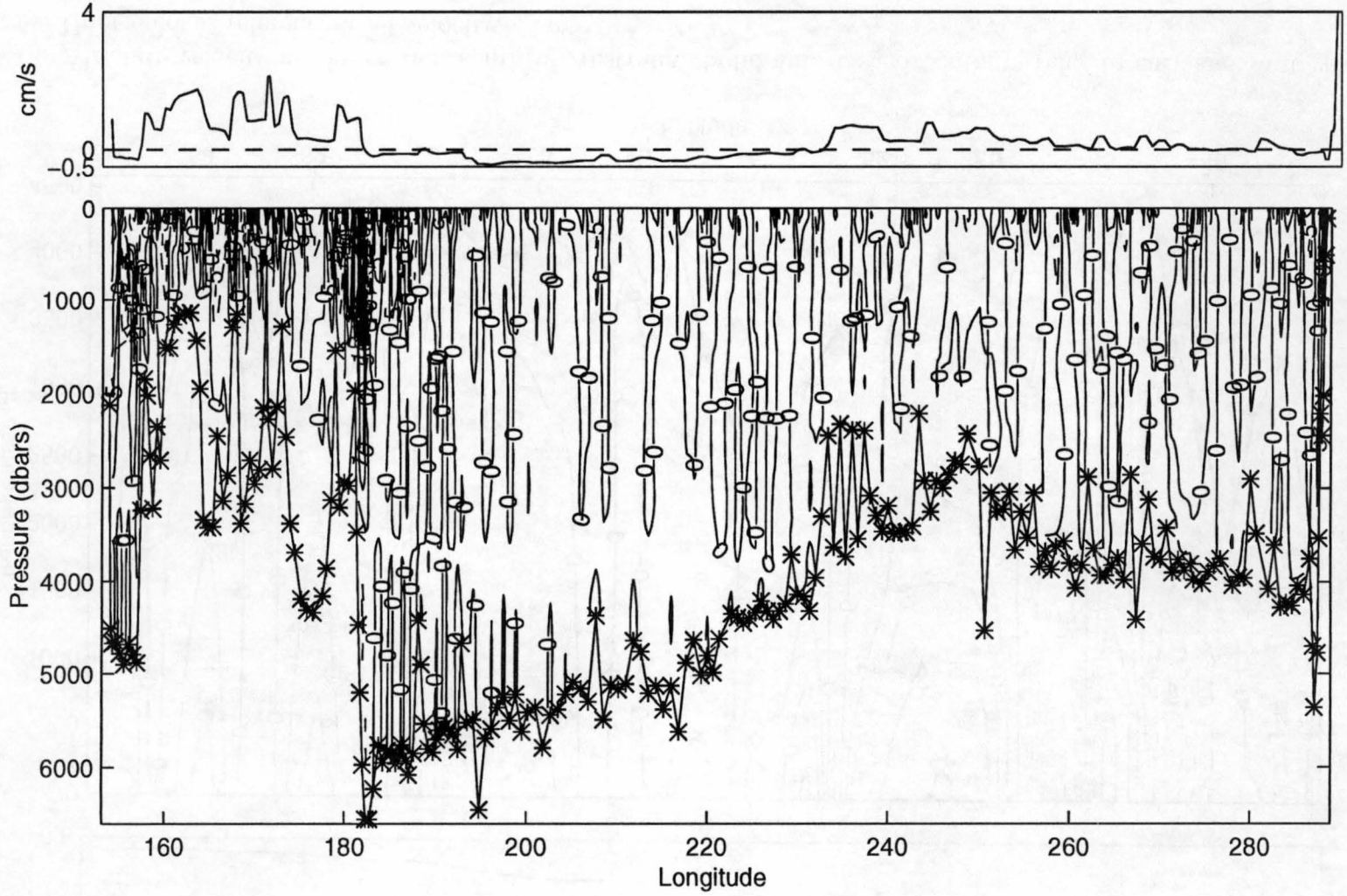

Figure 5.13: Absolute velocity at the Pacific 32°S section. Solid and dashed contours refer to north and south velocities, respectively. Upper plot is reference level velocity.

climatologies to be modified making them consistent with the hydrographic data.

In the following discussion graphs for each region show the inverse corrections to the heat and freshwater fluxes and Ekman transport at the outcropping neutral surfaces. In these graphs a positive heat flux represents a heat gain to the ocean from the atmosphere, negative heat flux is a heat loss from the ocean. The freshwater flux is expressed as evaporation minus precipitation and runoff, where a positive flux represents a loss of freshwater from the ocean and a negative flux is a freshwater gain from precipitation or runoff. A positive Ekman transport means a transport toward lighter neutral densities and generally indicate a northward transport as denser neutral surfaces outcrop with increasing latitude and a negative Ekman transport means a transport towards denser layers and represents a southward Ekman flux.

Within the subtropical Atlantic region (BI) the heat flux corrections are less than 10% and generally reduces the COADS heat flux at all outcropping neutral surfaces (Figure 5.14). The corrected heat flux results in a heat gain to the ocean (positive heat flux), at most, outcropping neutral surfaces for the subtropical Atlantic.

The freshwater correction terms are generally less than 20% resulting in minor changes to the freshwater flux in the subtropical Atlantic region (Figure 5.15). The correction terms increase the size of the freshwater loss over neutral surfaces 5,6 and decrease the freshwater loss over neutral surfaces 7,8 and 9 respectively (positive freshwater flux represents a net loss of freshwater from the ocean, while a negative freshwater flux represent a freshwater gain over the ocean). At neutral surface 10 the inverse correction is large (80 $cmyear^{-1}$) and results in a change in sign of the freshwater flux - from an original precipitation gain (-20 $cmyear^{-1}$) to a corrected freshwater loss, by evaporation, of 60 $cmyear^{-1}$. At the remaining outcropping neutral surfaces the inverse corrections are small resulting in only minor changes to the GASP freshwater flux.

A comparison of GASP and the inverse corrected GASP freshwater fluxes with two freshwater climatologies: ECMWF (Keith 1995) derived from a numerical weather prediction model and; the Baumgartner and Reichel (1975)

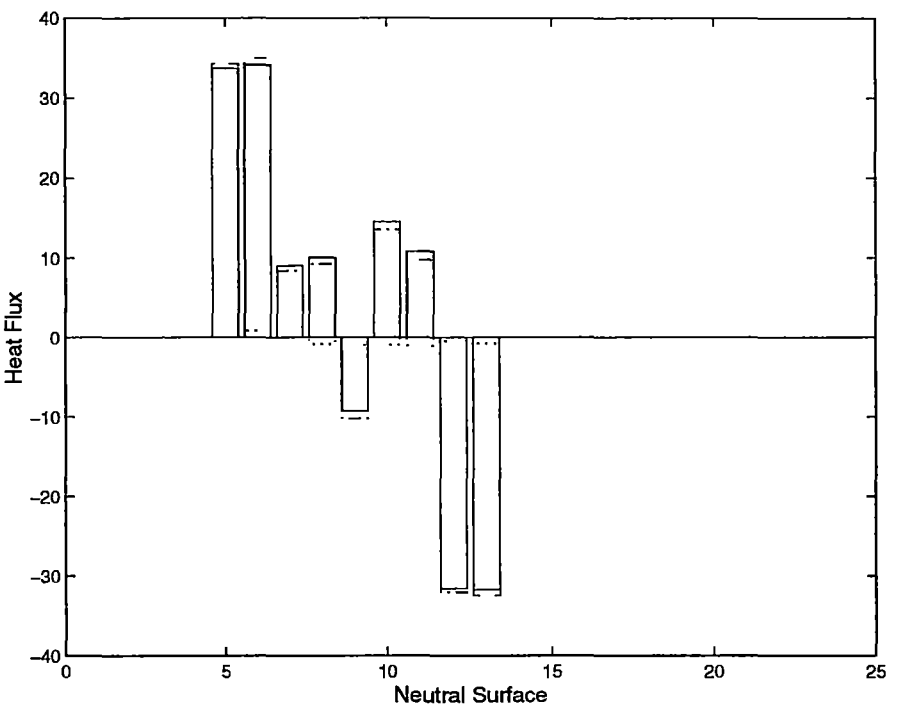

Figure 5.14: The COADS heat flux (Wm^{-2}) for subtropical Atlantic (BI) integrated over surface outcrop region. COADS (solid), Inverse Correction (dot), New Heat (dot-dash) Positive - heat gain to oceans, Negative - heat loss from ocean

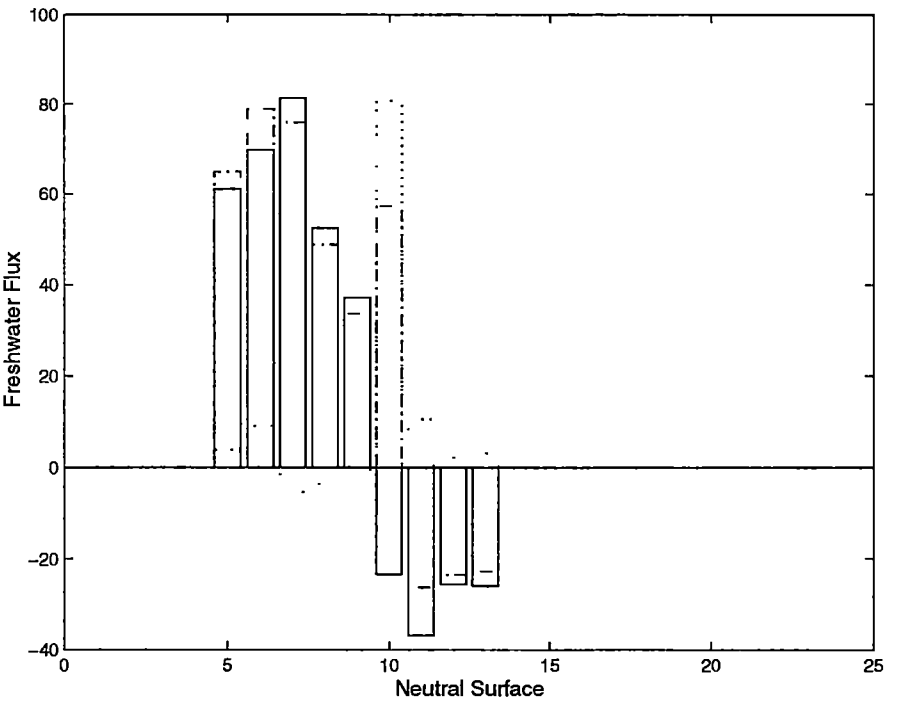

Figure 5.15: Freshwater flux ($cmyear^{-1}$) for subtropical Atlantic (BI) integrated over surface outcrop region. Freshwater (solid), Inverse Correction (dot), New Freshwater (dot-dash)

freshwater climatology is shown in Figure 5.16. (The freshwater flux from the numerical weather prediction model is derived assuming total column moisture balance). The sign of the freshwater flux, for all climatologies, agrees, apart from outcropping neutral surface 10. At this outcropping neutral surface the inverse correction changes the sign of the freshwater flux, which now agrees with the other climatologies, although the size of the freshwater loss is larger than ECMWF and Baumgartner and Reichel (hereafter B&R). Over the lighter outcropping neutral surfaces (5,6,7, and 8) the GASP and inverse corrected GASP freshwater fluxes are similar to the B&R freshwater flux, while at neutral surface 9 the GASP and inverse corrected GASP have a smaller freshwater loss than the other climatologies. Over the denser outcropping surfaces (11,12 and 13) the freshwater gains of GASP , inverse corrected GASP agree with the ECMWF and B&R freshwater fluxes.

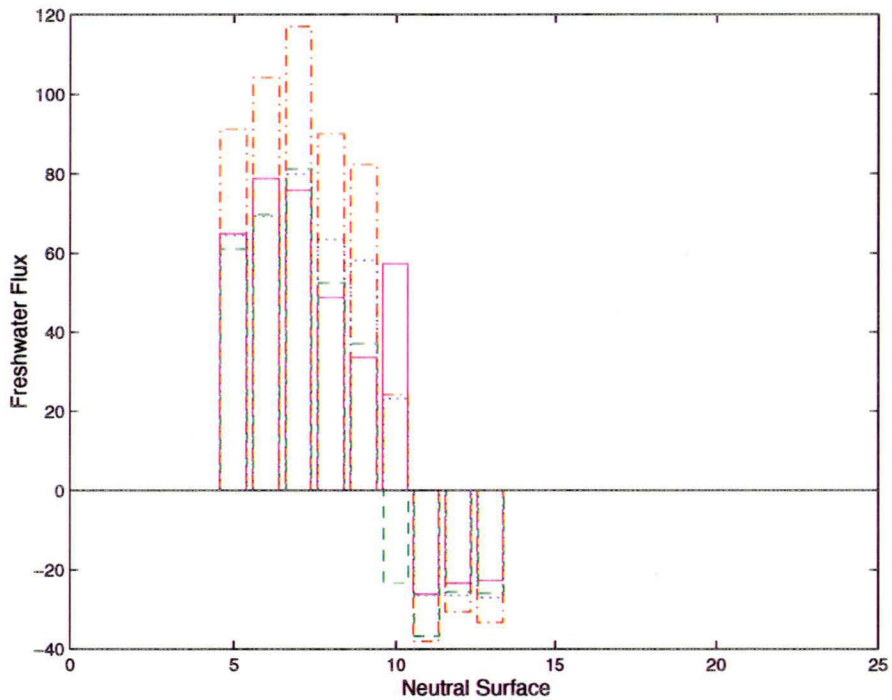

Figure 5.16: Comparison of Inverse corrected GASP (solid, magenta) and GASP Freshwater Flux (dashed, green) with freshwater flux derived from: Baumgartner and Reichel (1975) (dot, dark blue) (Keith, 1995); ECMWF (dash-dot, red) (Keith, 1995), for the subtropical Atlantic (BI) ($cmyear^{-1}$)

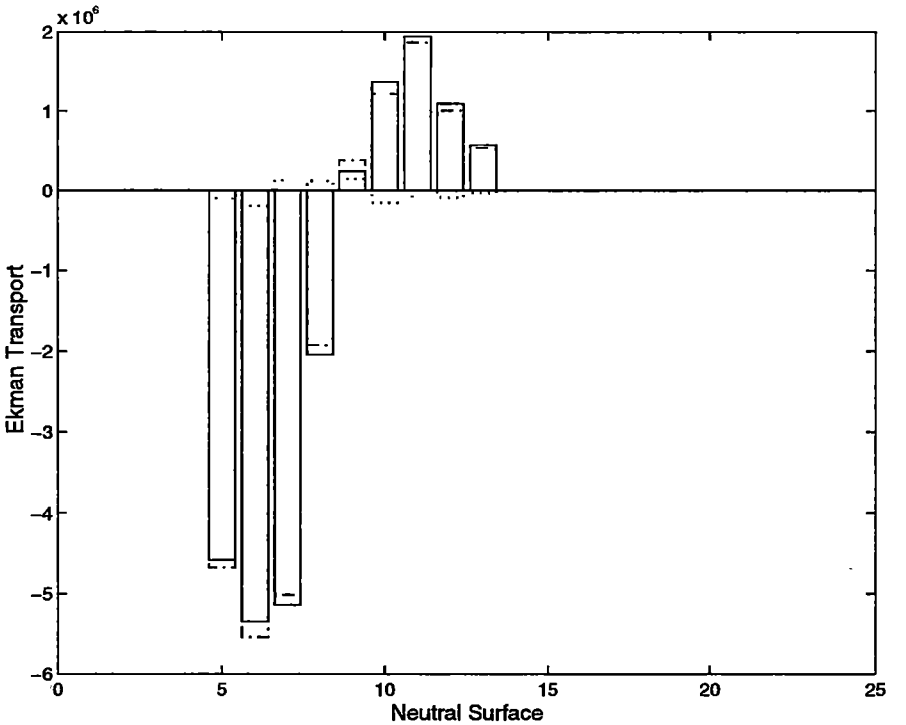

Figure 5.17: The Ekman transport ($m^3 s^{-1}$) for subtropical Atlantic (BI) integrated over surface outcrop region. Ekman(solid), Inverse Correction (dot), New Ekman (dot-dash)

The inverse corrections to the Ekman fluxes are small (< 20%) at all outcropping neutral surfaces (Figure 5.17). The Ekman fluxes highlight the dominance of the atmospheric anti-cyclone over the subtropical region with southward Ekman flux across the lightest most northern outcropping surfaces (associated with the easterly trade winds) and northward Ekman flux over the southern denser outcropping surfaces (associated with the westerly winds).

In the Southern Ocean Atlantic (BII) sector the inverse corrections to the annual mean heat flux less than 15% (Figure 5.18). The lightest and densest outcropping neutral surfaces, 7 and 16 respectively, experience the largest heat fluxes. At neutral surface 7 the ocean gains heat from the atmosphere while close to the Antarctic continent the densest outcropping surface looses heat to the atmosphere.

The inverse correction to the GASP freshwater flux are less 5% over the lightest outcropping neutral surfaces (7,8 and 9), maintaining the small net

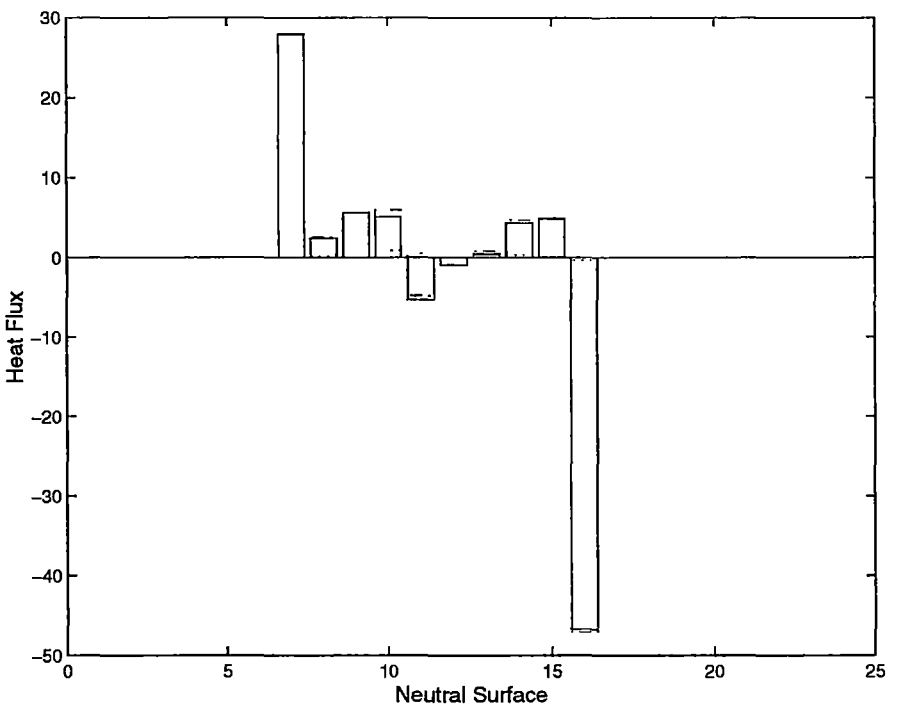

Figure 5.18: The COADS heat flux (Wm^{-2}) for Southern Ocean Atlantic (BII) sector integrated over surface outcrop region. COADS (solid), Inverse Correction (dot), New Heat (dot-dash)

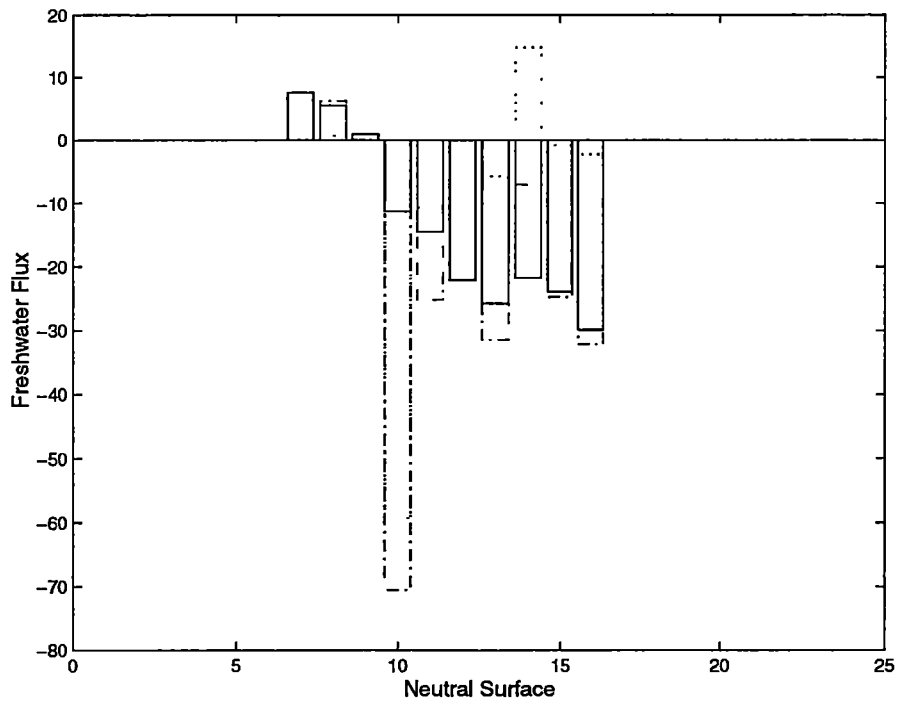

Figure 5.19: Comparison of Freshwater flux ($cmyear^{-1}$) over Southern Ocean Atlantic (BII) sector integrated over surface outcrop region. Freshwater (solid), Inverse Correction (dot), New Freshwater (dot-dash)

evaporation (Figure 5.19). Over the remaining outcropping neutral surfaces (10 to 16) there is a net addition of freshwater (5 to 10 $cmyear^{-1}$), with some large inverse corrections (neutral surfaces 10, 11 and 14 60 to 15 $cmyear^{-1}$). The inverse corrections to neutral surfaces 10 and 11 increase the freshwater gains in these while the correction at neutral surface 14 decreases the freshwater gain.

The comparison of the inverse freshwater and GASP freshwater with ECMWF and B&R is shown in Figure 5.20. At the lightest outcropping neutral surfaces (7,8 and 9) the GASP and inverse corrected freshwater fluxes are smaller than the ECMWF and B&R freshwater fluxes. At outcropping neutral surfaces 10 and 11 the sign of the freshwater flux does not agree between all climatologies. B&R suggest that the basin is still losing freshwater while GASP, inverse corrected GASP and ECMWF suggest that at these outcropping surfaces the Southern Ocean Atlantic (BII) region is gaining freshwater. Across the remaining outcropping neutral surfaces (11 to 16) all climatologies are gaining freshwater. The largest difference between the inverse corrected GASP

and other climatologies is at outcropping surfaces 10. The inverse correction suggests large freshwater gain ($70 cm year^{-1}$), while B&R has a freshwater loss ($20 cm year^{-1}$) and GASP and ECMWF a freshwater gain ($15 cm year^{-1}$). Within the remaining outcropping neutral surfaces (11 to 16) the magnitude of the freshwater flux from the inverse corrected GASP either agrees with ECMWF or B&R or both.

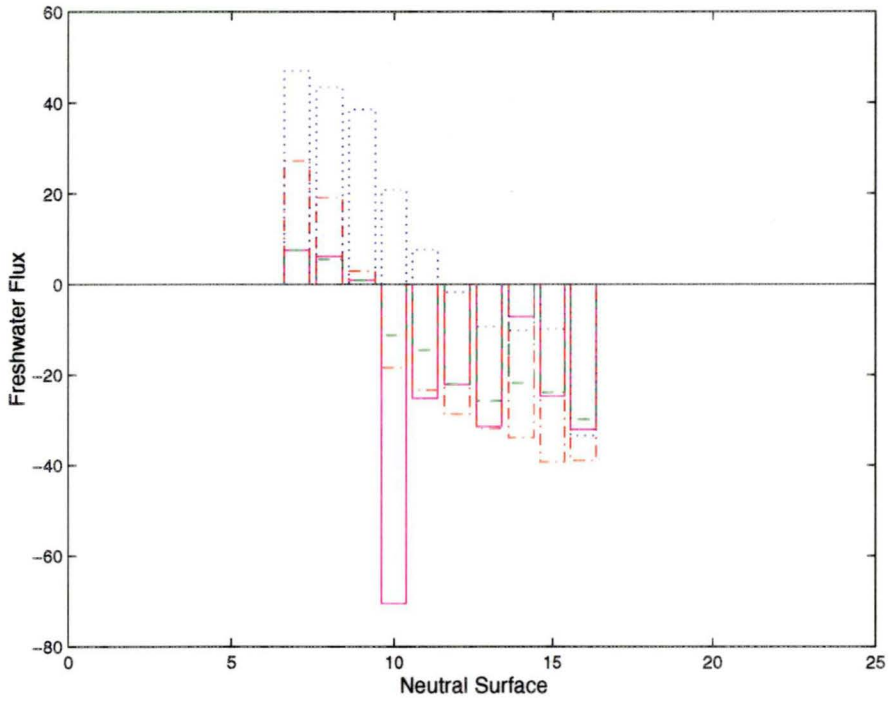

Figure 5.20: Comparison of the Inverse corrected (solid, magenta) GASP Freshwater Flux (dashed, green) with freshwater fluxes derived from: Baumgartner and Reichel (1975) (dot, dark blue); ECMWF (dash-dot, red) (Keith, 1995), for the Southern Ocean Atlantic (BII) sector ($cmyear^{-1}$).

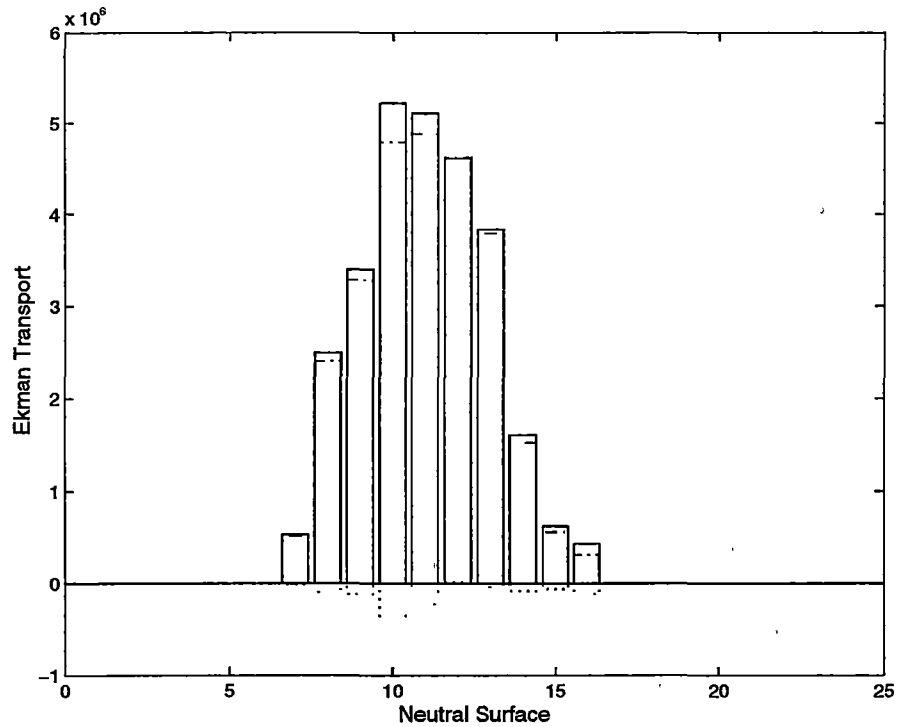

Figure 5.21: The Ekman transport ($m^3 s^{-1}$) Southern Ocean Atlantic (BII) sector. Ekman(solid), Inverse Correction (dot), New Ekman (dot-dash)

Within the Southern Ocean Atlantic (BII) sector there are only minor inverse corrections ($< 10\%$) to the Ekman flux (Figure 5.21). The Ekman flux is northward across all outcropping neutral surfaces reflecting the persistent westerly wind regime over the Southern Ocean.

The heat loss from the ocean to the atmosphere over the subtropical Indian Ocean (BIV) is reduced by the inverse corrections (Figure 5.22). The correction are between $1 W m^{-2}$ to $3 W m^{-2}$.

The inverse correction to the GASP freshwater flux over the subtropical Indian Ocean results in smaller freshwater fluxes over the outcropping neutral surfaces (Figure 5.23). The inverse corrections are largest at outcropping neutral surface 3 of 38 $cm year^{-1}$ while for remaining neutral surfaces the correction is less than 10 $cm year^{-1}$ (Figure 5.23).

Figure 5.24 show that the inverse corrected freshwater flux is the smallest flux of all climatologies. The ECMWF has the largest freshwater losses over the outcropping surfaces (Figure 5.24). The B&R freshwater flux is $20 cm year^{-1}$ to

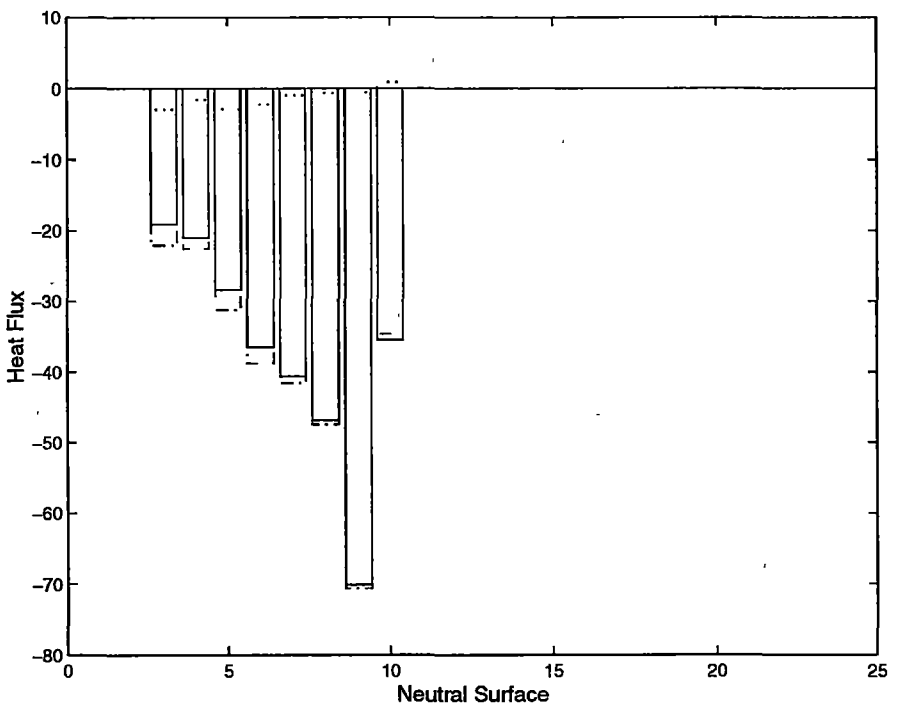

Figure 5.22: The COADS heat flux (Wm^{-2}) for subtropical Indian (BIV) integrated over surface outcrop region. COADS (solid), Inverse Correction (dot), New Heat (dot-dash)

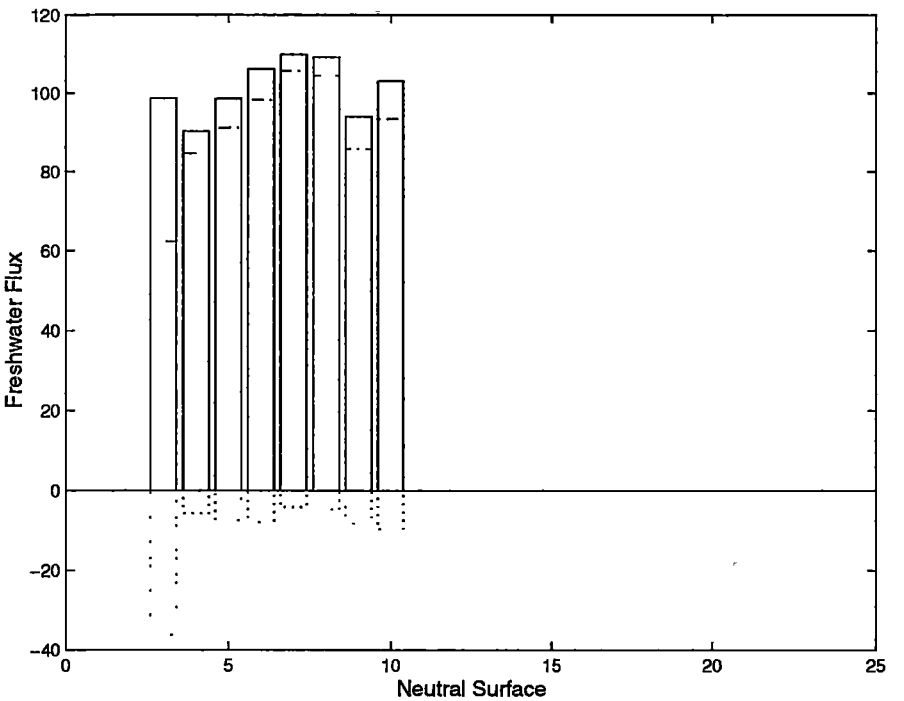

Figure 5.23: The Freshwater flux ($cmyear^{-1}$) over subtropical Indian Ocean (BIV) integrated over surface outcrop region. Freshwater (solid), Inverse Correction (dot), New Freshwater (dot-dash)

$40cmyear^{-1}$ small than the the ECMWF, while the GASP and inverse corrected GASP freshwater flux is $60cmyear^{-1}$ to $90cmyear^{-1}$ smaller than the ECMWF freshwater loss.

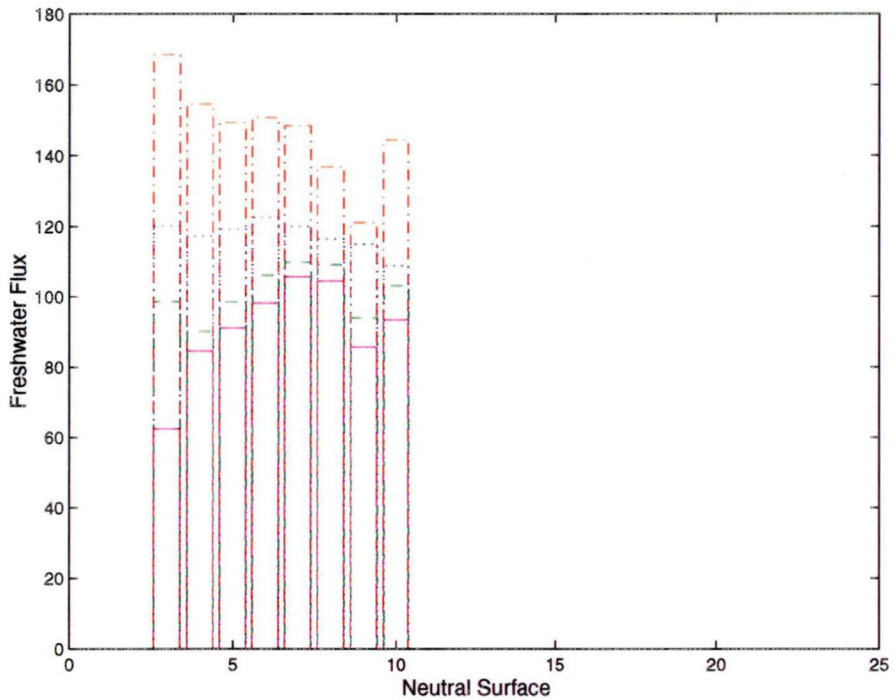

Figure 5.24: Comparison of Inverse corrected (solid, magenta) GASP Freshwater Flux (dashed, green) with freshwater derived from: Baumgartner and Reichel (1975) (dot, dark blue) (Keith, 1995); ECMWF (dash-dot, red) (Keith, 1995) for the subtropical Indian Ocean ($cmyear^{-1}$)

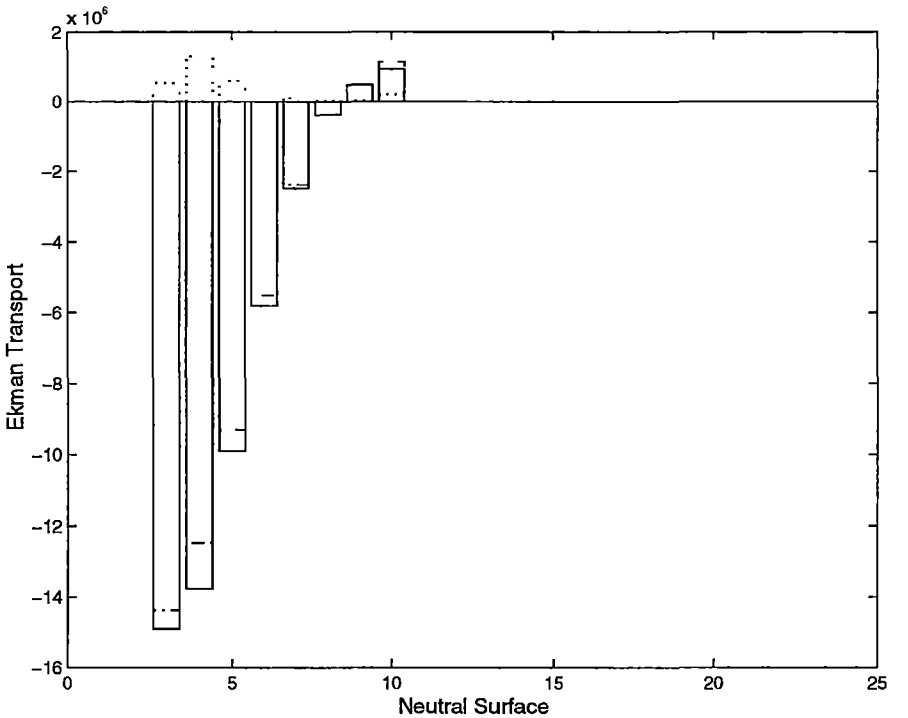

Figure 5.25: The Ekman transport ($m^3 s^{-1}$) for subtropical Indian (BIV) integrated over surface outcrop region. Ekman(solid), Inverse Correction (dot), New Ekman (dot-dash)

Corrections to the Ekman transport over outcropping neutral surfaces in the subtropical Indian Ocean result in a small decrease in Ekman flux (towards denser layers) in the region (Figure 5.25). The correction terms are generally less than $1 \times 10^6 m^3 s^{-1}$. The Ekman flux is southward (towards denser layers) across most outcropping neutral surfaces, indicating the dominance of the easterly wind regime over the region. The most southern outcropping neutral surfaces (9 and 10) have small northward (towards lighter layers) Ekman fluxes, highlighting the beginnings of the westerly wind regime which dominates over the Southern Ocean.

Figure 5.26 shows that the inverse heat corrections are small (less than 5%), generally resulting in minor increases in the heat flux over the outcropping neutral surfaces. Over the lighter outcropping layers (6 to 10) the ocean is losing heat to the atmosphere. These layers outcrop in the northern region and are associated with the extension and retroflection of the Agulhas Current south of Africa and the southern limb of the subtropical gyre. Further south the

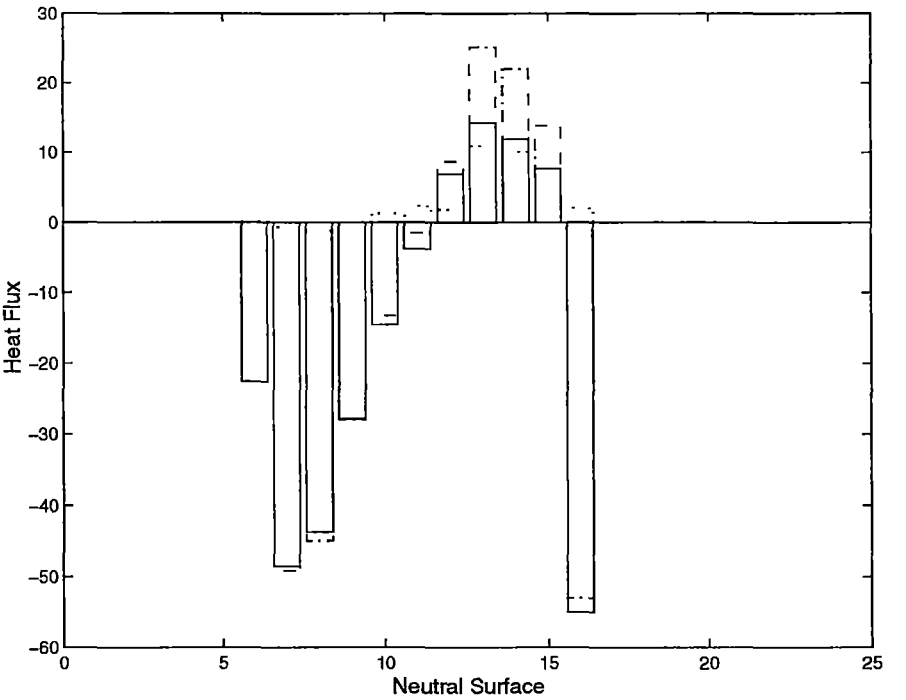

Figure 5.26: The COADS heat flux (Wm^{-2}) over Southern Ocean Indian sector (BV) integrated over surface outcrop region. COADS (solid), Inverse Correction (dot), New Heat (dot-dash)

outcropping neutral surfaces (12 to 15) the inverse correction is larger (50%) resulting in larger heat gains from the atmosphere while the densest outcropping neutral surfaces immediately adjacent to the Antarctic continent lose heat to the atmosphere.

The inverse correction to the GASP freshwater flux result in only minor changes to the freshwater flux (5 $cmyear^{-1}$), apart from outcropping neutral surfaces 15 and 16 where the inverse correction increases the freshwater flux by 35 $cmyear^{-1}$ (Figure 5.27). The freshwater flux changes sign over the Southern Ocean Indian sector, with the northern region (outcropping neutral surfaces 6 to 9) being a net evaporative region and the southern region (outcropping neutral surfaces 10 to 16) a net precipitation region.

A comparison of the GASP and inverse corrected GASP freshwater flux with the ECMWF and B&R freshwater climatologies is shown in Figure 5.28. Over the lightest neutral surfaces (6 to 9) the GASP and inverse corrected GASP freshwater flux are smaller than the ECMWF and B&R freshwater flux.

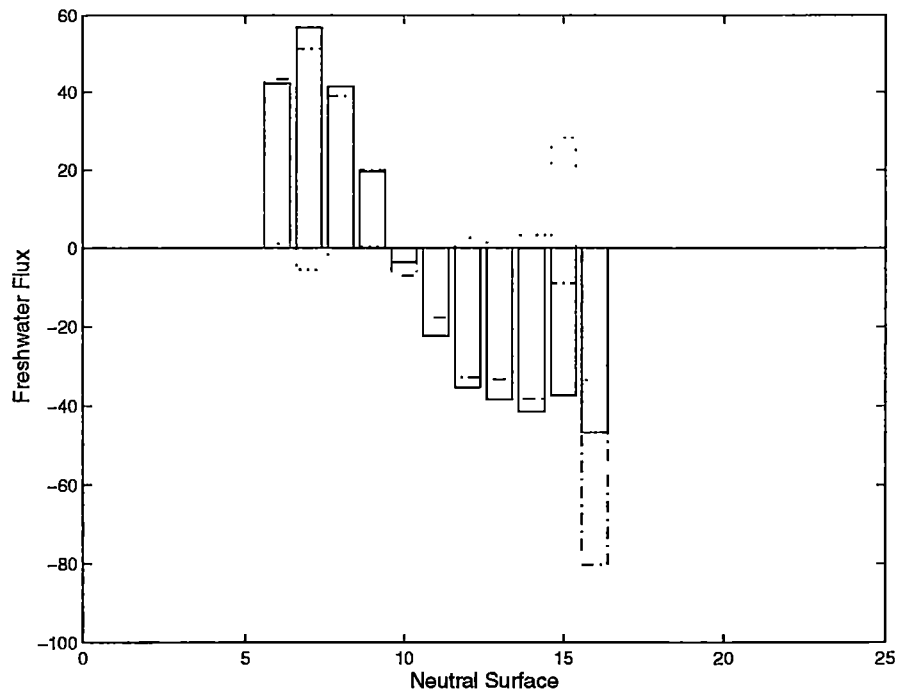

Figure 5.27: Freshwater flux ($cmyear^{-1}$) for Southern Ocean Indian sector (BV) integrated over surface outcrop region. Freshwater (solid), Inverse Correction (dot), New Freshwater (dot-dash)

At outcropping neutral surface 10 the GASP and inverse corrected GASP have a small freshwater gain (-ve flux) while the ECMWF and B&R climatologies still maintain a small freshwater loss (+ve flux). The freshwater flux over the denser outcropping neutral surfaces (10 to 14) are similar for all climatologies, while at the densest outcropping neutral surfaces, 15 and 16, the inverse correction decreases and increases the size of the freshwater flux, respectively.

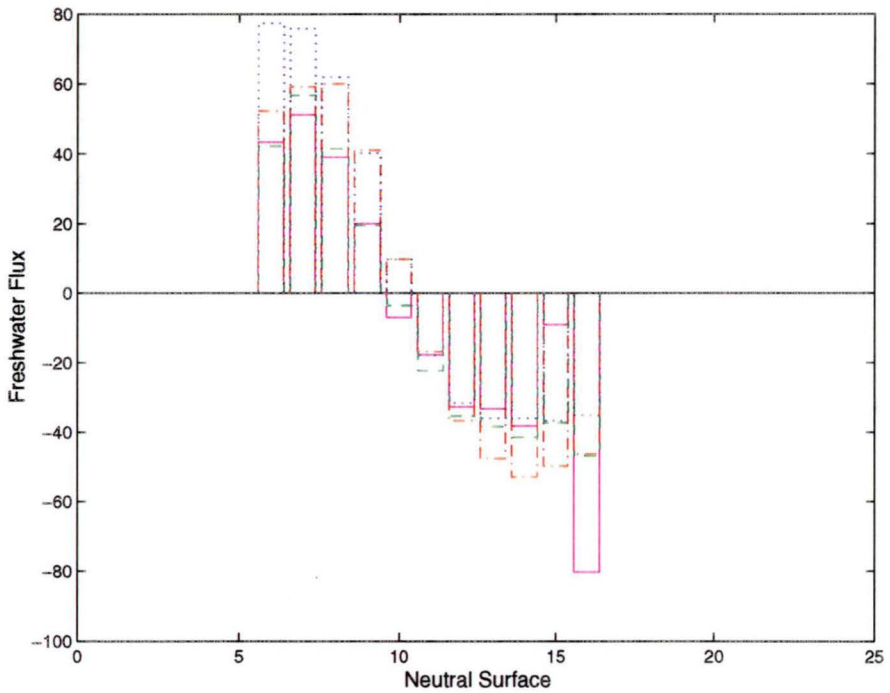

Figure 5.28: Comparison of Inverse corrected (solid, magenta) GASP Freshwater Flux (dashed, green) with freshwater derived from: Baumgartner and Reichel (1975) (dot, dark blue); ECMWF (dash-dot, red) (Keith, 1995) for the Southern Ocean Indian sector

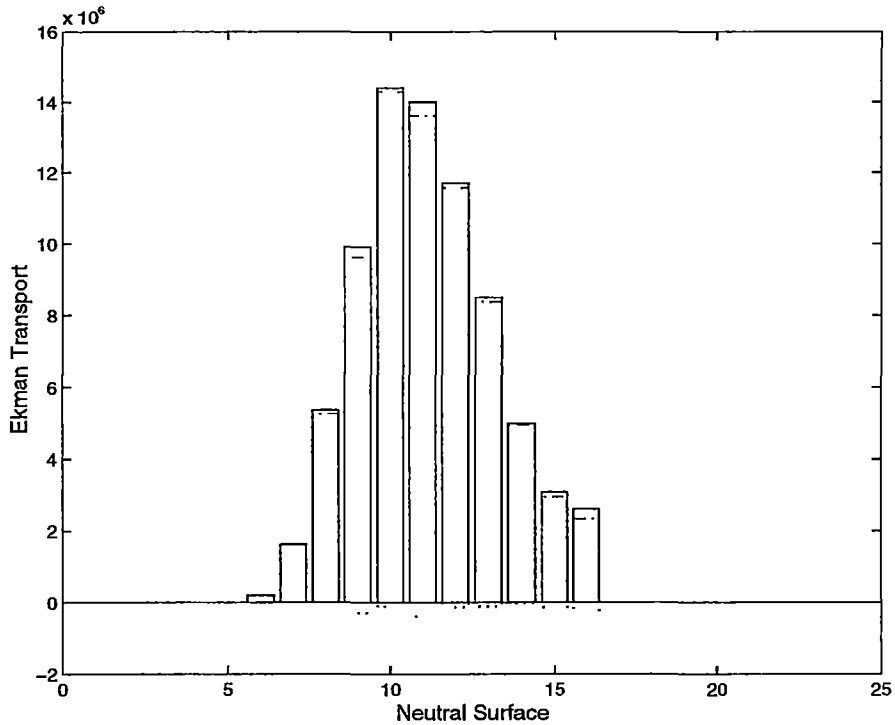

Figure 5.29: The Ekman transport ($m^3 s^{-1}$) for Southern Ocean Indian sector (BV) integrated over surface outcrop region. Ekman(solid), Inverse Correction (dot), New Ekman (dot-dash)

The inverse corrections to the Ekman transports are small less than 2% (Figure 5.29). The Ekman transports are northward (towards lighter layers) with largest transports at outcropping neutral surfaces 10 and 11, on either side of these outcropping neutral surfaces the northward Ekman transport decreases. The northward Ekman transports are due to the dominance of the strong westerly wind over the Southern Ocean.

Over the Southern Ocean Pacific (BVI) sector the inverse corrections to the heat flux are small (< 2%) over the lightest outcropping neutral surfaces (7 to 11) and densest neutral surfaces (17 to 20). The inverse corrections are larger over outcropping neutral surfaces 12 to 15, between 18 to 10 Wm^{-2}, resulting in a change of sign of the heat flux at outcropping layers 13, 14 and 15 (Figure 5.30). This heat gain (neutral surfaces 13 to 15) occurs over the outcropping AAIW which could gain heat at their northern outcropping boundaries. The inverse corrected heat flux over the Southern Ocean Pacific

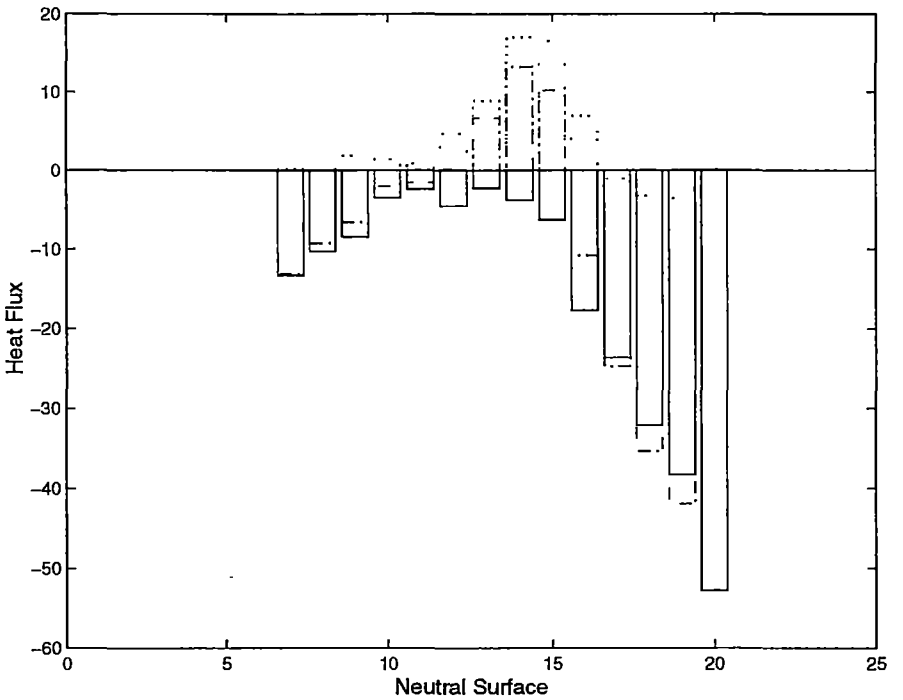

Figure 5.30: The COADS heat flux (Wm^{-2}) for Southern Ocean Pacific sector (BVI) integrated over surface outcrop region. COADS (solid), Inverse Correction (dot), New Heat (dot-dash)

(BVI) region now has a similar similar structure to the Southern Ocean Indian sector heat flux (Figure 5.26). Across the lightest (7 to 11) and densest (16 to 20) there is a heat loss from the ocean to the atmosphere, while over outcropping surfaces 13 to 15 there is a heat gain to the ocean from the atmosphere.

The freshwater correction terms are small, less than 5 $cmyear^{-1}$, over the lighter outcropping neutral surfaces (7 to 16), while over the denser and more southern outcropping neutral surfaces the inverse corrections are larger (between 80 $cmyear^{-1}$ to 20 $cmyear^{-1}$) resulting in larger freshwater fluxes (freshwater gain) (Figure 5.31). The largest corrections occur at outcropping neutral surface 17 and 18 which outcrop for most of the year, the denser outcropping neutral surfaces (19 and 20) only surface in winter and early spring. These dense neutral surfaces outcrop adjacent to the Antarctic continent in the Ross Sea and along the Adelie coast (Figure 5.32). Within this region Jacobs et al. (1985) estimates a freshwater input of glacial and basal ice sources of

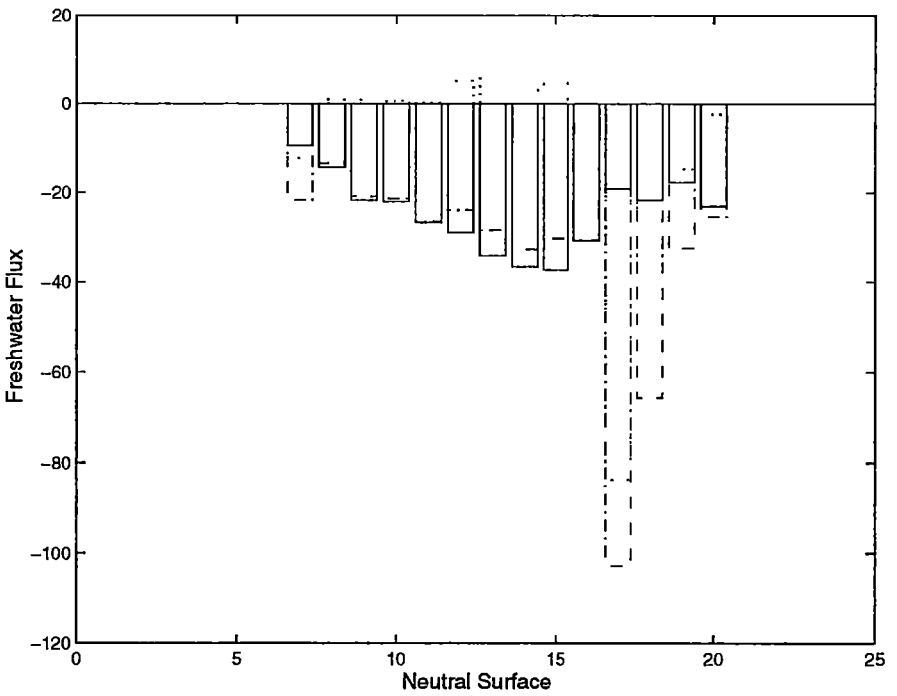

Figure 5.31: The Freshwater flux ($cmyear^{-1}$) over the Southern Ocean Pacific sector (BVI). Freshwater (solid), Inverse Correction (dot), New Freshwater (dot-dash)

$\approx 36 cmyear^{-1}$. They highlight that estimates of freshwater inputs from ice melt are highly dependent on estimates of iceberg calving, melting under ice shelves and ice wall melting which vary widely.

The GASP, inverse corrected GASP and B&R freshwater fluxes agree in both sign (freshwater gain) and magnitude at most outcropping neutral surfaces, apart from the larger freshwater fluxes of the inverse over the densest outcropping neutral surfaces (Figure 5.33). The ECMWF freshwater flux agrees with the other climatologies over outcropping neutral surfaces 9 to 16 (freshwater gain), but over the lightest (7 and 8) and densest (17 to 20) outcropping neutral surfaces the freshwater flux opposes the GASP, inverse corrected GASP and B&R freshwater flux.

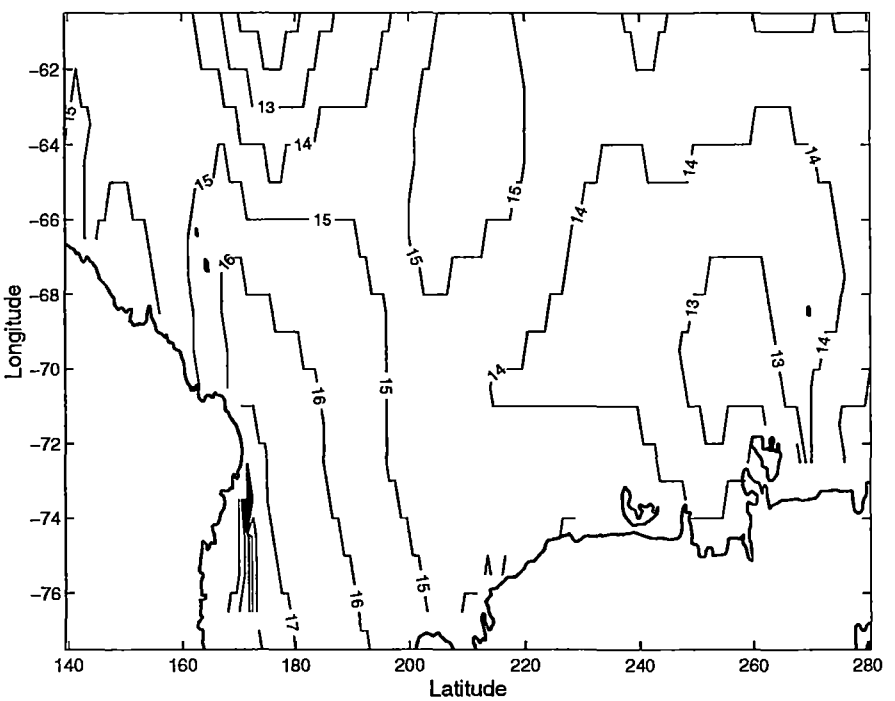

Figure 5.32: Outcropping position of neutral surfaces in the far southwestern region of the Southern Ocean Pacific (BVI) region. Contour labels are neutral surface numbers.

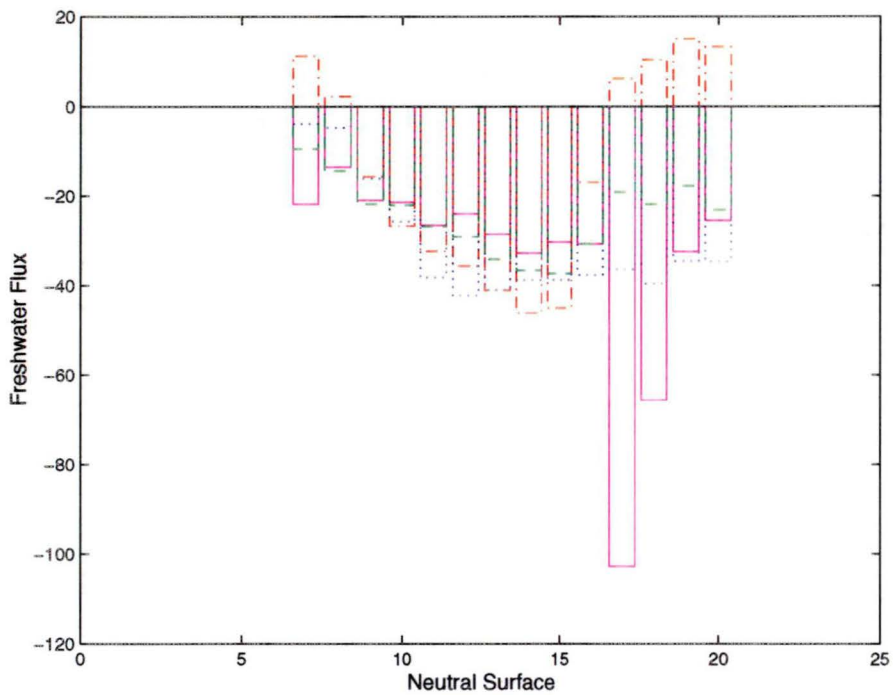

Figure 5.33: Comparison of Inverse corrected (solid, magenta) GASP Freshwater Flux (dashed, green) with freshwater derived from: Baumgartner and Reichel (1975) (dot, dark blue); ECMWF (dash-dot, red) (Keith, 1995) for the Southern Ocean Pacific (BVI) sector ($cmyear^{-1}$)

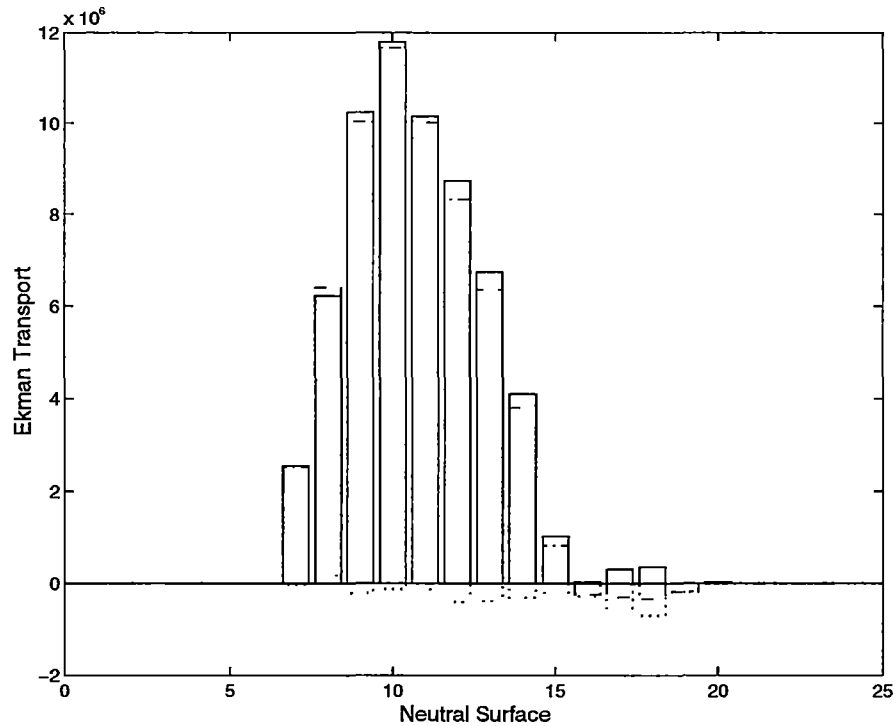

Figure 5.34: The Ekman transport ($m^3 s^{-1}$) for Southern Ocean Pacific sector. Ekman(solid), Inverse Correction (dot), New Ekman (dot-dash)

The inverse Ekman correction transport are small (< 3%) and result in only minor changes to the Ekman transport over outcropping neutral surfaces 7 to 15 (Figure 5.34). Although the corrections are small over the denser outcropping neutral surfaces (16 to 20) they result in a corrected southward (towards denser layer) Ekman transport. The northward Ekman transport (towards lighter layers) at most outcropping neutral surfaces indicates the persistence and strength of the westward winds over the Southern Ocean, while the small southward (towards denser layers) Ekman transport at the densest outcropping neutral surfaces is due to the easterly wind which dominates adjacent to the Antarctic continent.

In the inverse model the weights imposed on the air-sea fluxes reflected a reasonable confidence in the climatologies. The inverse corrections to the COADS heat flux and Ekman flux driven by Hellerman and Rosenstein wind stress are generally small, less than 10% and 5% respectively. The GASP freshwater fluxes experience the largest inverse adjustments. On a regional

comparisons the largest corrections to the heat and freshwater fluxes occur in the Southern Ocean Pacific sector. The circulation obtained from this inverse model is still consistent with our understanding of the circulation of the Southern Ocean (shown in later section), although the strength of the deep overturning cell in the Pacific is larger than previous estimates (Warren 1981b; Wunsch et al. 1983; Macdonald 1993).

In Appendix E, Table E.12 to Table E.16 the Ekman, heat flux and freshwater flux components in the total mass transformation are shown. These tables shown that, in general, the freshwater flux is the smallest component in the total mass transformation.

The comparison of the inverse corrected GASP, ECMWF, and Baumgartner and Reichel freshwater fluxes in this section highlight the variability the freshwater flux between these climatologies. A comparison of the differences in the freshwater transformations between the different climatologies was undertaken, although it is not shown here. The different freshwater climatologies results in similar (not significant) transformations. The major exception to this was when the transformation were calculated using the da Silva et al. (1994) COADS freshwater climatology. The COADS freshwater flux is comparable to the other climatologies north of 30°S resulting in similar transformations. South of 30°S the COADS freshwater flux has large net precipitation, particularly in the Southern Ocean Indian and Pacific sectors where the difference is 0(2). The calculated transformations using the COADS data in the Southern Ocean Indian and Pacific sectors was as large as $40\times10^{6}m^{3}s^{-1}$. Because of the significant difference south of 30°S between the COADS freshwater and other climatologies and the resulting large transformations I rejected the COADS freshwater climatology. Although the GASP, ECMWF, and Baumgartner and Reichel freshwater climatologies show variability these result in non-significant difference in the transformation. The GASP freshwater flux was chosen because I had access to monthly E-P data.

Similar comparison of the heat transformation resulting from different heat flux climatologies can be undertaken. These were not performed in this study and the COADS heat flux was used because of it good spatial and temporal coverage at high latitudes. The Hellerman and Rosenstein wind

climatology was chosen due to it coverage of high southern latitudes.

The small inverse corrections to the COADS heat (apart from the southern area of the Southern Ocean Pacific region) and Hellerman and Rosenstein wind data suggest that these climatologies are consistent with the hydrography. The inverse corrections to the freshwater flux and comparison with other climatologies suggest that this is the most variable air-sea flux, but generally results in the smallest influence on the total transformation. The corrections to the heat and freshwater climatologies south of 50°S (outcropping layers 12 to 19) in the Southern Ocean Pacific (BVI) region suggest that the climatologies in this area are not as consistent with the hydrography as other regions of the Southern Ocean. The inconsistency of the air-sea heat, freshwater and wind in the southern region of the Southern Ocean Pacific sector highlights the data spareness in this region.

5.3.2 Interior Dianeutral Fluxes

The inclusion of air-sea forcing at outcropping neutral surfaces results in changes to the interior dianeutral property fluxes. The following discussion describes the interior dianeutral fluxes. The interior dianeutral property fluxes, across those dianeutral surfaces that have surface expressions, represent the mechanism by which sea-surfaces fluxes are dispersed into the interior of the ocean. Before discussing the dianeutral property fluxes the reader is reminded that the dianeutral property advection is the layer property mean $\times$ dianeutral mass flux, and the dianeutral effective property diffusion is the remainder of the total dianeutral property flux once the advective component is removed. The dianeutral effective diffusion incorporates not only the actual diffusion but also other eddy processes. The dianeutral unknowns are solved like a "velocity" term, where the property flux is the "velocity" term times the concentration and neutral surface area.

In the subtropical Atlantic (BI) the advective dianeutral flux is downwards across the upper thermocline neutral surfaces (5 and 6) and upward across the main thermocline neutral surfaces (7 to 11). This results in a redistribution of upper thermocline (5 and 6) and lower thermocline (10 and 11) layers into thermocline (7, 8 and 9) layers (Figure 5.35).

a)

b)

c)

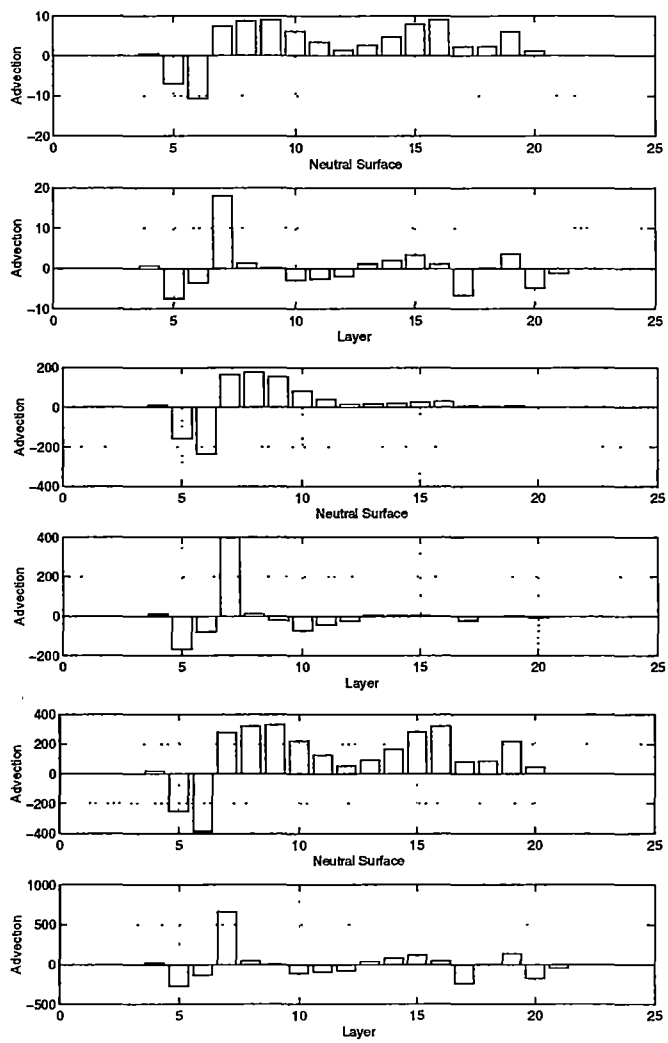

Figure 5.35: subtropical Atlantic (BI) dianeutral advection a) mass b) heat c) salt (prop$\times 10^6 m^3 s^{-1}$). Upper plot - flux across neutral surface, +ve upwards flux, -ve downwards flux. Lower plot - mass convergence within layer, +ve mass gain (convergence), -ve mass loss (divergence)

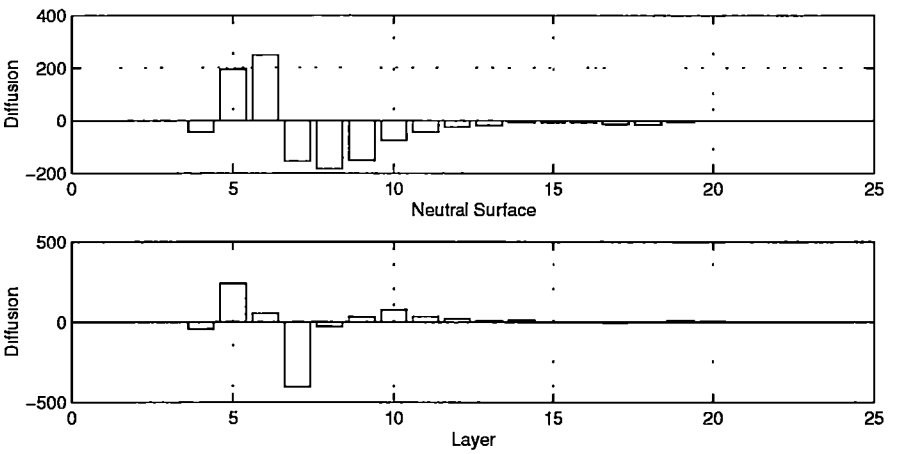

Figure 5.36: subtropical Atlantic (BI) dianeutral heat effective diffusion ($\times 10^6$ °C $m^3 s^{-1}$). Upper plot - effective heat diffusion flux across neutral surface, +ve upwards flux, -ve downwards flux. Lower plot - resultant heat convergence within layer, +ve heat flux gain (convergence), -ve heat flux loss (divergence)

The effective heat diffusion is upwards across the upper thermocline layers (5 and 6) and downwards across remaining thermocline surfaces (7 to 10), resulting in the conversion of heat from thermocline layers 7 to 8 into both the upper thermocline (layers 5 and 6) and lower thermocline layer 9 and 10 (Figure 5.36).

The effective salt diffusion oscillates between upwards and downwards across the upper thermocline layers (4 to 6), while it is downward for remaining thermocline layers (7 to 10). This results in a small flux of salt from layer 5 into the overlying layer (4), with most of the salt flux from this layer moving into layer 6. There is also a flux of salt from layer 7 into layer 6 and into denser thermocline layers.

The property dianeutral "velocity" is largest across the thermocline neutral surfaces (4 to 7) (Figure 5.38). The mass and salt "velocities" have a similar structure, while the heat "velocity" is downwards across the thermocline layers.

Dianeutral advection of mass, heat and salt, in the Southern Ocean Atlantic sector is downwards across thermocline and intermediate neutral surfaces (Figure 5.39). This results in a flux of thermocline water (layer 10) into intermediate water (layer 11,12).

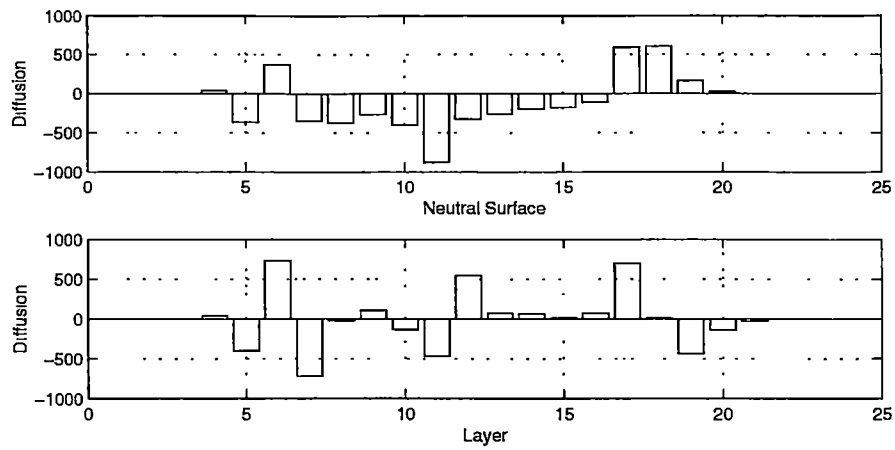

Figure 5.37: subtropical Atlantic (BI) dianeutral salt effective diffusion ($\times 10^6$ psu $m^3 s^{-1}$) Upper plot - effective salt diffusion flux across neutral surface, +ve upwards flux, -ve downwards flux. Lower plot - resultant salt convergence within layer, +ve salt flux gain (convergence), -ve salt flux loss (divergence)

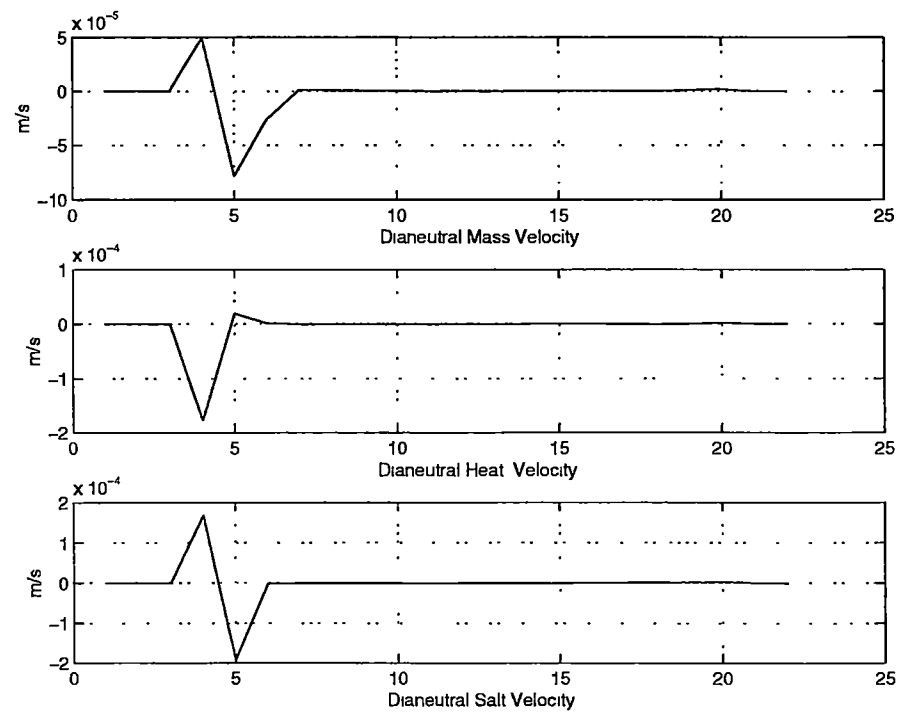

Figure 5.38: subtropical Atlantic (BI) Mass, Heat and Salt Dianeutral "velocity" (ms^{-1}). +ve -upwards, -ve -downwards.

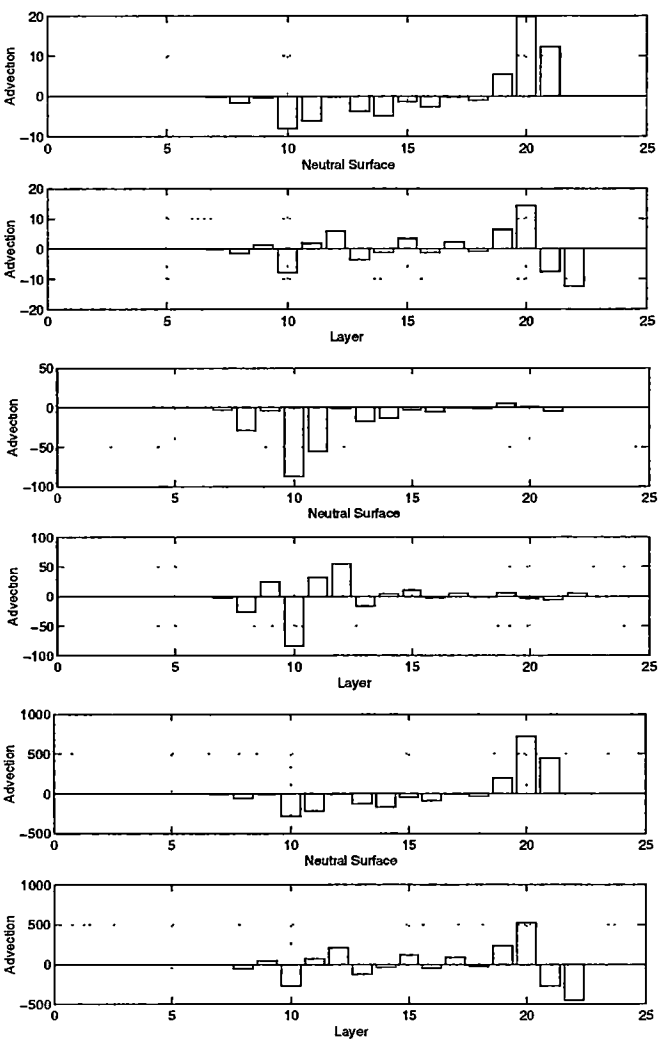

a)

b)

c)

Figure 5.39: Southern Ocean Atlantic (BII) dianeutral advection a) mass b) heat c) salt (prop$\times 10^6 m^3 s^{-1}$) Upper plot - flux across neutral surface, +ve upwards flux, -ve downwards flux. Lower plot - mass convergence within layer, +ve mass gain (convergence), -ve mass loss (divergence)

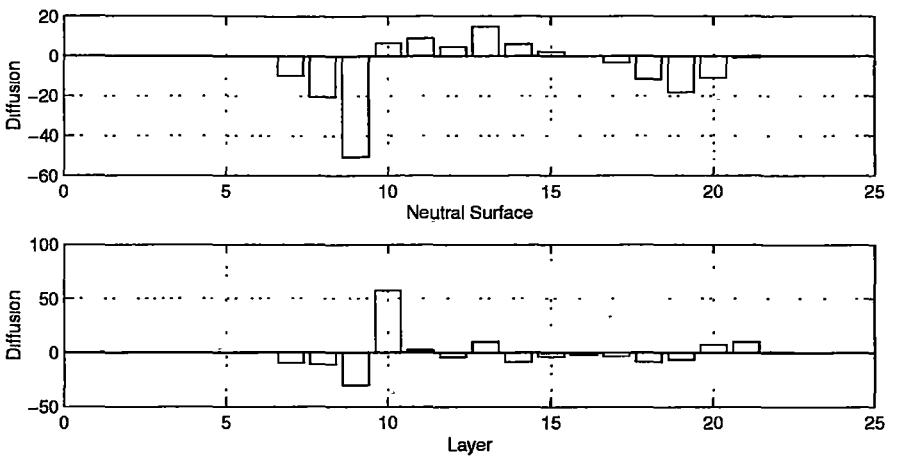

Figure 5.40: Southern Ocean Atlantic (BII) dianeutral heat effective diffusion ($\times 10^6$ °C $m^3 s^{-1}$) Upper plot - effective heat diffusion flux across neutral surface, +ve upwards flux, -ve downwards flux. Lower plot - resultant heat convergence within layer, +ve heat flux gain (convergence), -ve heat flux loss (divergence)

The effective heat diffusion is downwards across thermocline layers 7, 8 and 9 and upwards across all remaining neutral surfaces (Figure 5.40). This results in the major heat flux from thermocline layer (7,8 and 9) and intermediate layers (12 to 15) into layers 10 and 11.

The effective salt diffusion alternates between upward and downward effective diffusion across thermocline and intermediate neutral surfaces (Figure 5.41). The effective diffusion results in a salt flux from layer 9 into layer 8 and a redistribution of salt from layer 10 into upper intermediate layers (11 and 12). The other major effective salt diffusion is the flux of salt from layer 16 and 17 (NADW) into underlying CDW (layers 18 and 19).

The small changes to the dianeutral property fluxes result in only minor changes to the dianeutral mass, heat and salt "velocity" (Figure 5.42) structure between this model and the previous model (model_int, Figure 4.18). The dianeutral "velocities" are dominated by dianeutral mixing between NADW, CDW and AABW.

Within the subtropical Indian Ocean there are significant changes to the dianeutral property flux across neutral surfaces that outcrop. The advective property flux is now directed upwards across thermocline neutral surfaces (3 to 9) and downwards across lower thermocline (10) and upper intermediate neutral

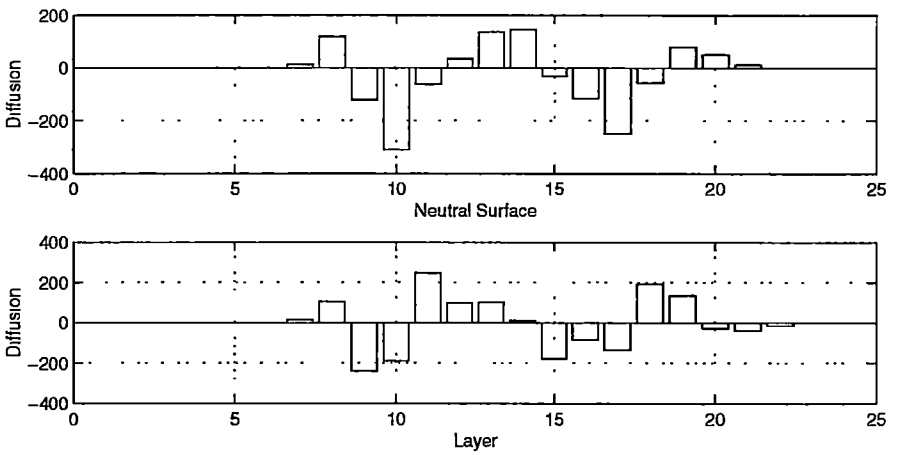

Figure 5.41: Southern Ocean Atlantic (BII) Dianeutral Effective Salt Diffusion ($\times 10^6$ psu $m^3 s^{-1}$) Upper plot - effective salt diffusion flux across neutral surface, +ve upwards flux, -ve downwards flux. Lower plot - resultant salt convergence within layer, +ve salt flux gain (convergence), -ve salt flux loss (divergence)

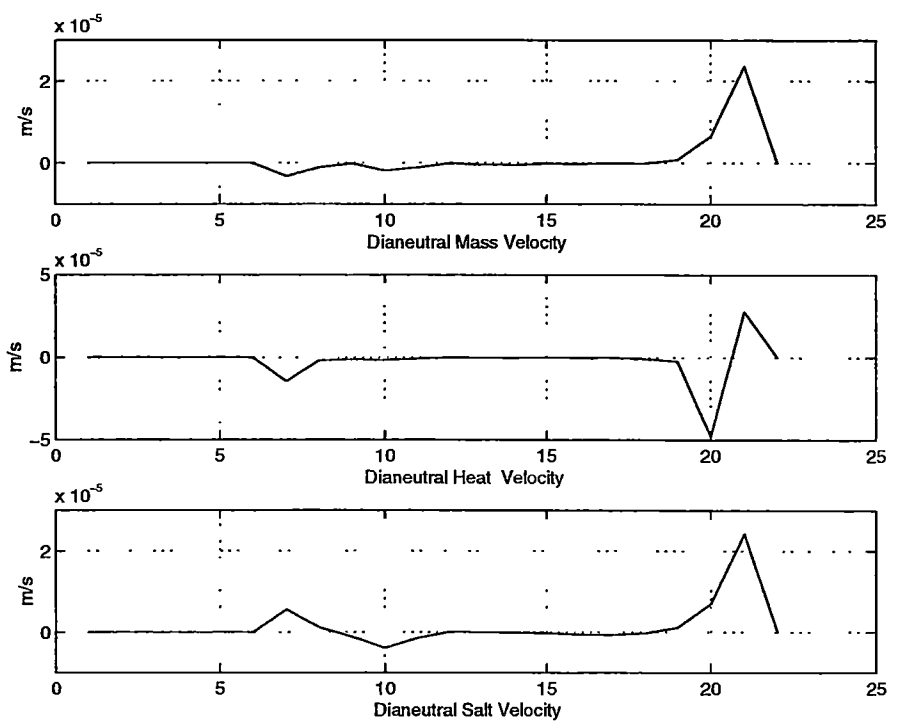

Figure 5.42: Southern Ocean Atlantic (BII) Mass, Heat and Salt Dianeutral "velocity" (ms^{-1}). +ve -upwards, -ve -downwards.

surfaces (11,12) (Figure 5.43). This results in a transfer of lower thermocline layers (6,7 and 8) into upper thermocline layers (3,4 and 5) and also a transfer of lower thermocline layers (9 and 10) into upper intermediate layers (12, 13 and 14).

The effective heat diffusion is now downwards across all neutral surfaces, with the largest downward effective diffusion across upper thermocline surfaces 5 and 6 (Figure 5.44). This results in a flux of heat from upper thermocline layer (3, 4 and 5) into underlying thermocline layers (6 to 10).

The effective salt diffusion is similar to the previous model (model_int, Figure 4.21) with large upward effective salt diffusion occurring across neutral surface 11 (Figure 5.45). The effective salt diffusion in thermocline layers is slightly smaller than the previous model (model_int). This results in the redistribution of salt from layer (12) into overlying thermocline layers (8,9,10,11).

The most significant change to the dianeutral property "velocity" occurs across the thermocline surfaces. There is now an upward dianeutral mass and salt "velocity" across the upper thermocline neutral surfaces (3 and 4) and an upward dianeutral heat "velocity" across layer 3 and a small, but constant, downward heat "velocity"' across remaining thermocline neutral surfaces (4 to 10) and upper intermediate neutral surfaces (surface 11, 12 and 13) (Figure 5.46) (cf Figure 4.22).

In the Southern Ocean Indian sector the dianeutral advective flux is upwards across the upper thermocline surfaces (7 and 8) and downward across lower thermocline (9 and 10) and intermediate surfaces (11 to 15) (Figure 5.47). This results in a transfers of lower thermocline layers (8) into upper thermocline layers (6 and 7) and a transfer of lower thermocline layers (10) and upper intermediate water (layer 11,12 and 13) into lower intermediate layers (14 and 15).

The effective heat diffusion is downwards across the thermocline (7 to 10) and upper intermediate neutral surfaces (11) (Figure 5.48). There is a smaller upward heat effective diffusion across remaining neutral surfaces (12 to 19). This results in a redistribution of heat from the thermocline (layers 6, 7, 8 and 9) into upper intermediate layers (11, 12 and 13).

a)

b)

c)

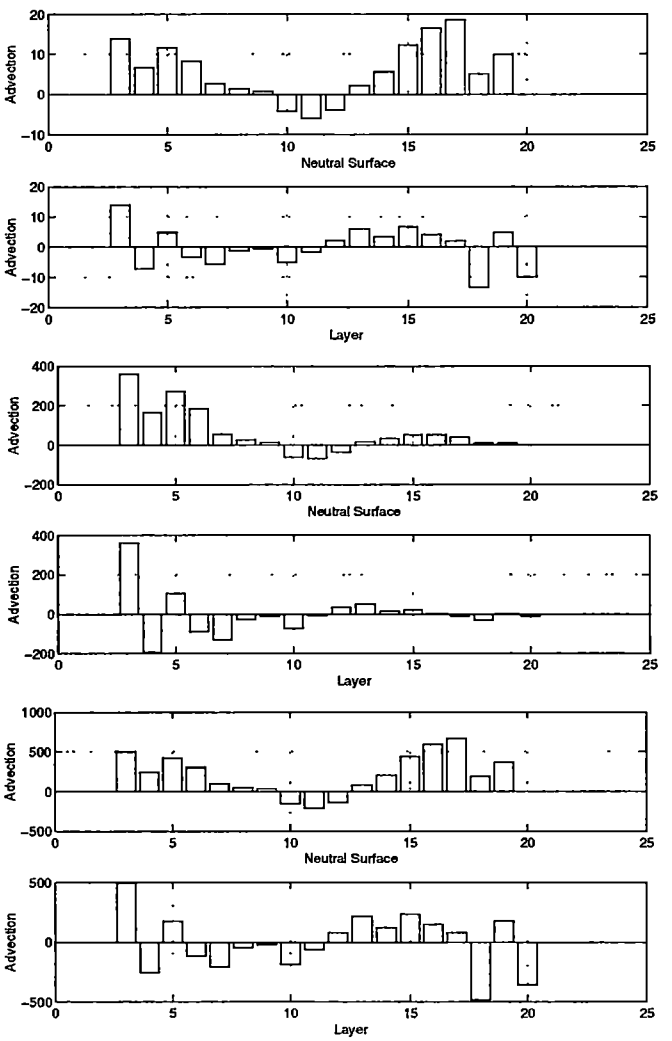

Figure 5.43: subtropical Indian Ocean (BIV) dianeutral advection a) mass b) heat c) salt (prop$\times 10^6 m^3 s^{-1}$) Upper plot - flux across neutral surface, +ve upwards flux, -ve downwards flux. Lower plot - mass convergence within layer, +ve mass gain (convergence), -ve mass loss (divergence)

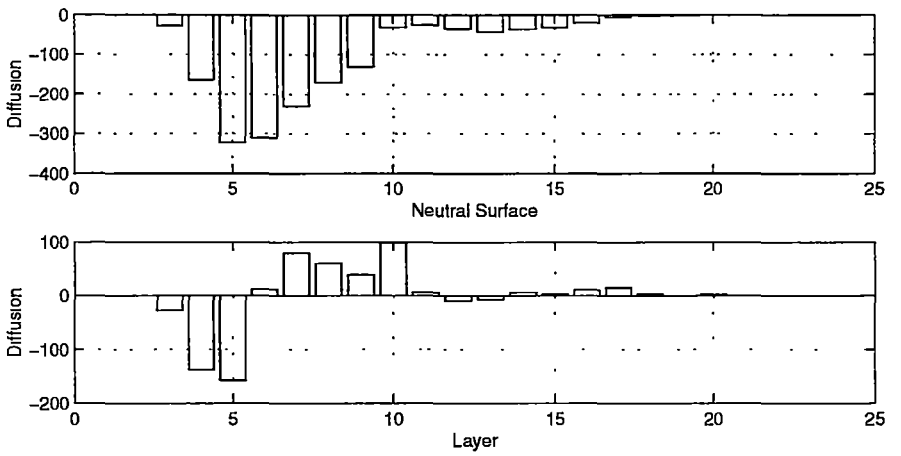

Figure 5.44: subtropical Indian Ocean (BIV) Dianeutral Effective Heat Diffusion ($\times 10^6$ °C $m^3 s^{-1}$) Upper plot - effective heat diffusion flux across neutral surface, +ve upwards flux, -ve downwards flux. Lower plot - resultant heat convergence within layer, +ve heat flux gain (convergence), -ve heat flux loss (divergence)

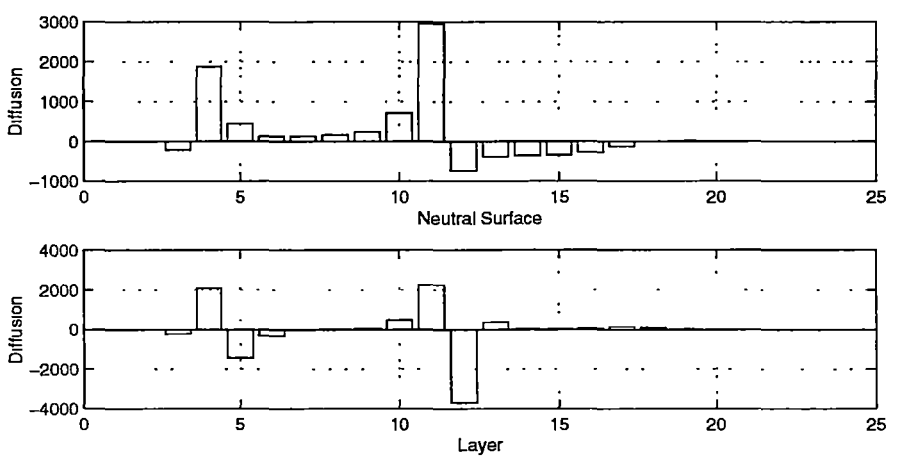

Figure 5.45: subtropical Indian Ocean (BIV) dianeutral salt effective diffusion ($\times 10^6$ psu $m^3 s^{-1}$) Upper plot - effective salt diffusion flux across neutral surface, +ve upwards flux, -ve downwards flux. Lower plot - resultant salt convergence within layer, +ve salt flux gain (convergence), -ve salt flux loss (divergence)

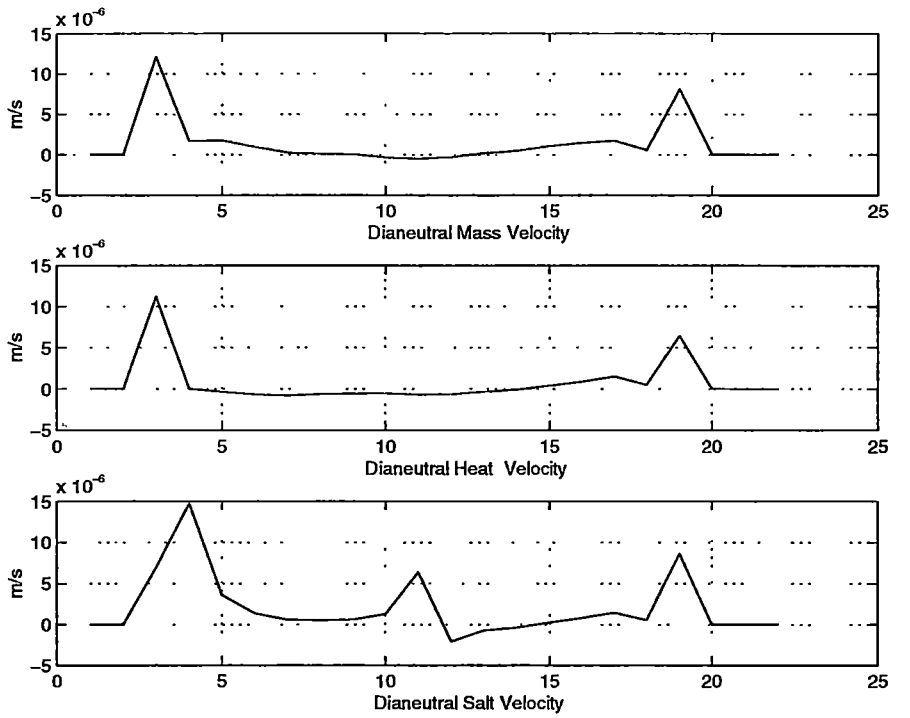

Figure 5.46: subtropical Indian Ocean (BIV) Mass, Heat and Salt Dianeutral "velocity" (ms^{-1}). +ve -upwards, -ve -downwards.

The effective salt diffusion is downwards across thermocline neutral surfaces (7, 8 and 9) and upward lower intermediate (11 to 15), deep (16 to 18) and bottom (19 and 20) neutral surfaces (Figure 5.49). This results in a flux of salt from the upper thermocline (layers 7, 8 and 9) into lower thermocline (10) and upper intermediate layers (12 and 13).

The property dianeutral "velocities" are shown in Figure 5.50. Mass and salt have a downward dianeutral "velocity" across thermocline and intermediate neutral surfaces. The heat "velocity" is upward across the lightest neutral surface (6) and downwards across the main thermocline and intermediate neutral surfaces.

The dianeutral advective fluxes in the Southern Ocean Pacific (BVI) sector (BVI) are downwards across all neutral surfaces (Figure 5.51). Within the downward advection there are two local maxima, across intermediate neutral surfaces (12, 13 and 14) and deep (17 and 18) neutral surfaces. This results in a redistribution of upper thermocline water (7 and 8) into lower thermocline (9

a)

b)

c)

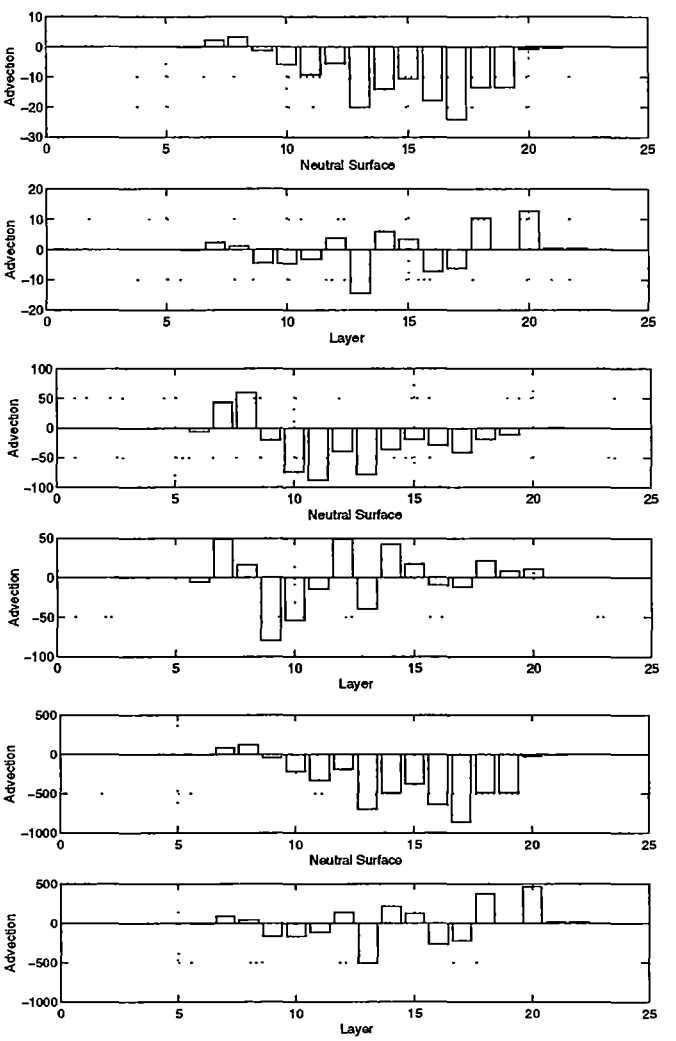

Figure 5.47: Southern Indian Ocean (BV) dianeutral advection a) mass b) heat c) salt (prop$\times 10^6 m^3 s^{-1}$) Upper plot - flux across neutral surface, +ve upwards flux, -ve downwards flux. Lower plot - mass convergence within layer, +ve mass gain (convergence), -ve mass loss (divergence)

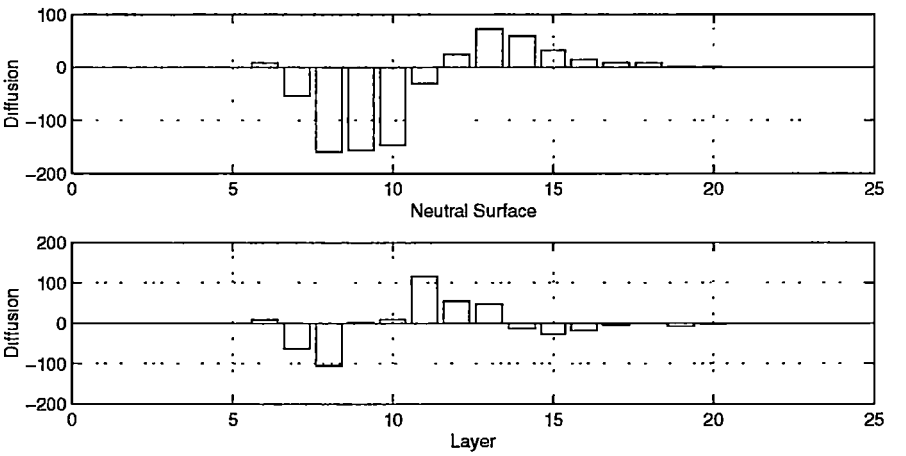

Figure 5.48: Southern Indian Ocean dianeutral heat effective diffusion ($\times 10^6$ °C $m^3 s^{-1}$) Upper plot - effective heat diffusion flux across neutral surface, +ve upwards flux, -ve downwards flux. Lower plot - resultant heat convergence within layer, +ve heat flux gain (convergence), -ve heat flux loss (divergence)

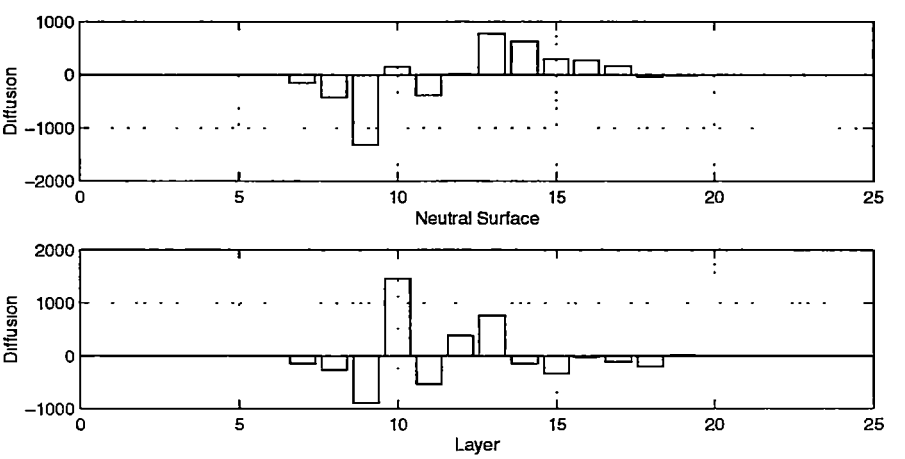

Figure 5.49: Southern Indian Ocean (BV) dianeutral salt effective diffusion ($\times 10^6$ psu $m^3 s^{-1}$) Upper plot - effective salt diffusion flux across neutral surface, +ve upwards flux, -ve downwards flux. Lower plot - resultant salt convergence within layer, +ve salt flux gain (convergence), -ve salt flux loss (divergence)

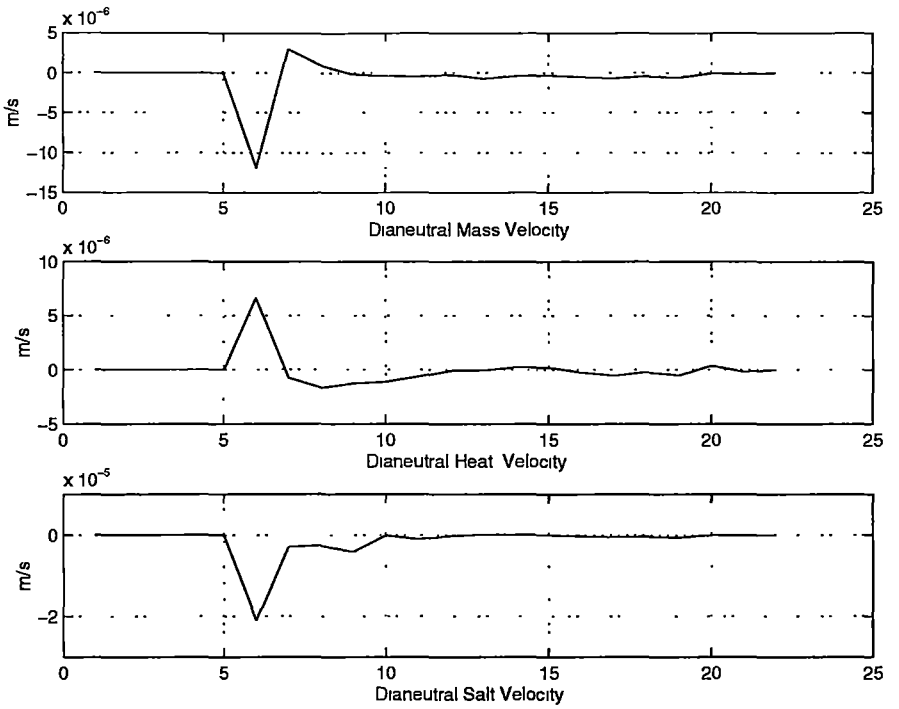

Figure 5.50: Southern Indian Ocean (BV) Mass, Heat and Salt Dianeutral "velocity" (ms^{-1}). +ve -upwards, -ve -downwards.

and 10) and upper intermediate layers (11), a transfer of intermediate layer (12) into lower intermediate layers (13, 14 and 15) and a transfer of deep layers (16,17 and 18) into lower deep layers (19) and bottom layers (19 and 20).

The effective heat diffusion is downwards across thermocline (7 and 8) neutral surfaces and upwards across remaining neutral surfaces (Figure 5.52). This results in a redistribution of heat from the thermocline (layers 7 and 8) into the lower thermocline (layer 9) and smaller redistribution of heat from intermediate (15) and deep (16 to 19) into remaining intermediate layers (12 to 14) and bottom layers (20)

The effective salt diffusion is upwards across thermocline (7 and 9), lower intermediate (13 and 15) and deep (16 to 19) neutral surfaces, and downwards across lower thermocline (10) and upper intermediate (11 to 12) neutral surfaces. This results in a flux of salt from thermocline layer (9) into upper thermocline layers (7 and 8) and a flux of salt from lower thermocline layers (10) and deep layers (16 to 18) into intermediates layers (12 to 15).

The deep and bottom dianeutral mass "velocity" (Figure 5.54) is larger

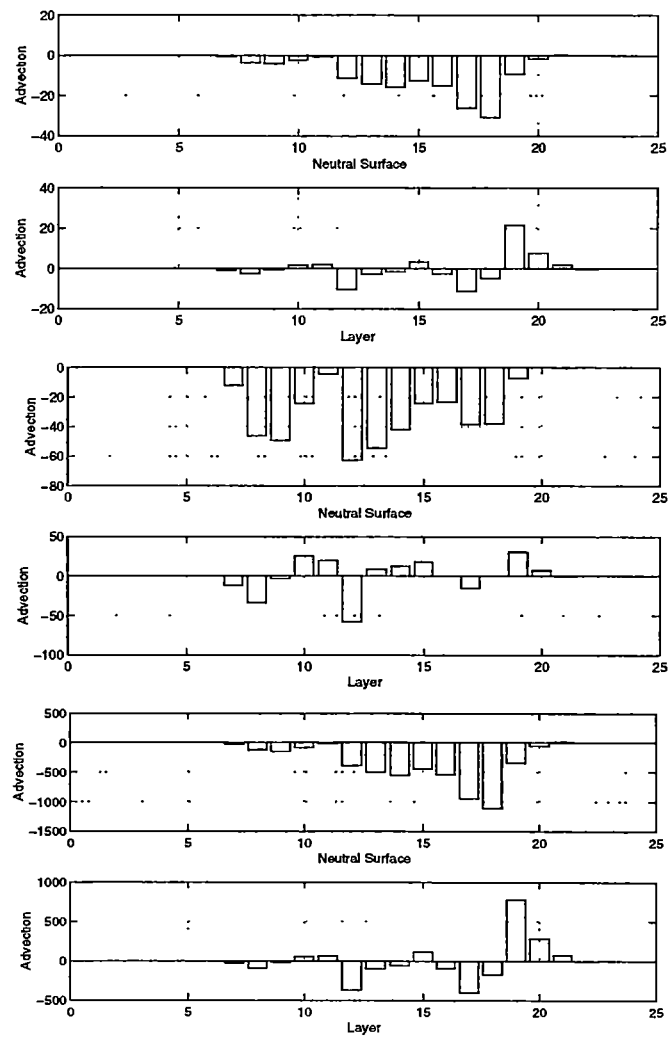

a)

b)

c)

Figure 5.51: Southern Ocean Pacific (BVI) Ocean dianeutral advection a) mass b) heat c) salt (prop$\times 10^6 m^3 s^{-1}$) Upper plot - flux across neutral surface, +ve upwards flux, -ve downwards flux. Lower plot - mass convergence within layer, +ve mass gain (convergence), -ve mass loss (divergence)

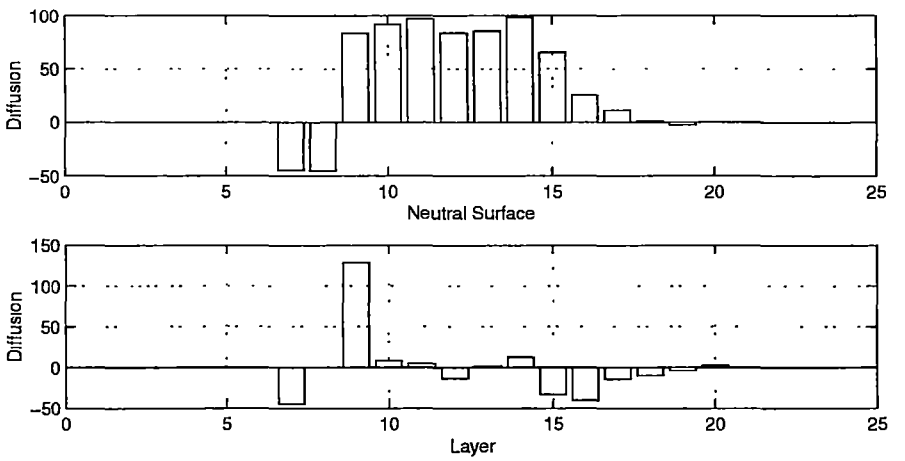

Figure 5.52: Southern Ocean Pacific (BVI) dianeutral heat effective diffusion ($\times 10^6$ °C $m^3 s^{-1}$) Upper plot - effective heat diffusion flux across neutral surface, +ve upwards flux, -ve downwards flux. Lower plot - resultant heat convergence within layer, +ve heat flux gain (convergence), -ve heat flux loss (divergence)

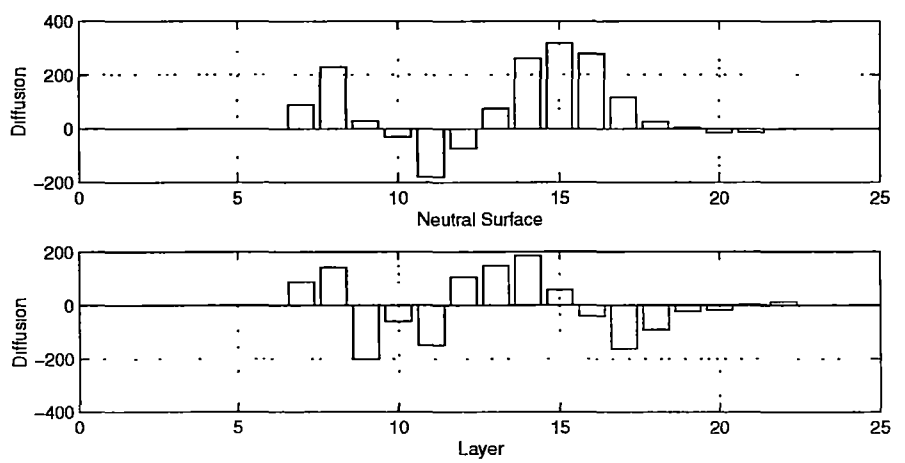

Figure 5.53: Southern Ocean Pacific (BVI) dianeutral salt effective diffusion ($\times 10^6$ psu $m^3 s^{-1}$) Upper plot - effective salt diffusion flux across neutral surface, +ve upwards flux, -ve downwards flux. Lower plot - resultant salt convergence within layer, +ve salt flux gain (convergence), -ve salt flux loss (divergence)

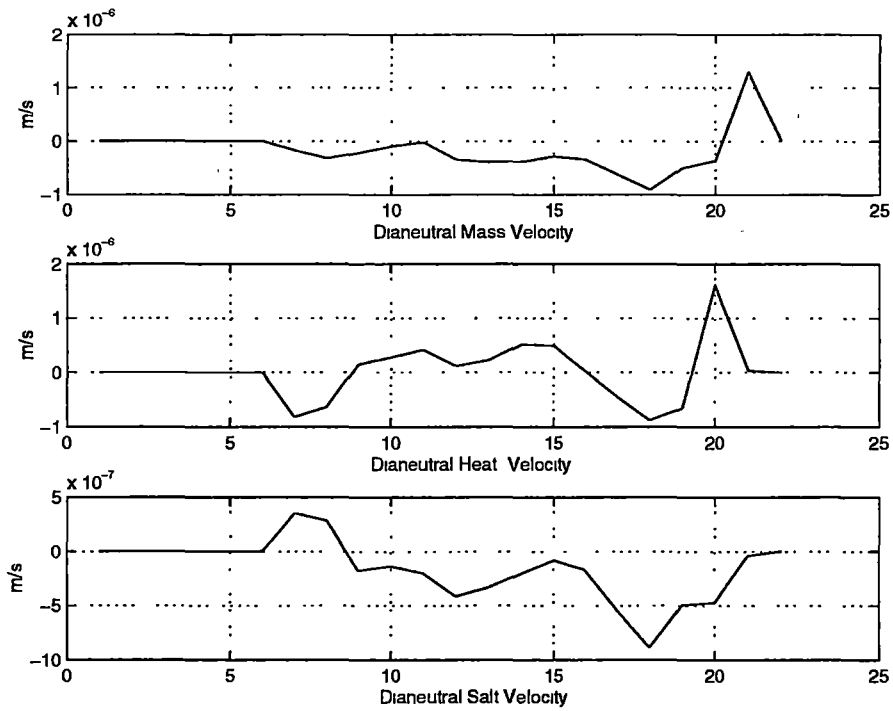

Figure 5.54: Southern Ocean Pacific (BVI) Mass, Heat and Salt Dianeutral "velocity" (ms^{-1}). +ve -upwards, -ve -downwards.

than the the previous model (model_int, Figure 4.30, while the heat and salt dianeutral velocities are similar. The "velocities" are smaller than the comparable dianeutral property "velocities" in the Southern Ocean Atlantic (BII) sector (Figure 5.42).

5.4 Circulation- Air-Sea and Interior Influences

This section principally describes the sea-surfaces and interior dianeutral fluxes in terms of water mass formation and interior "consumption". The interior dianeutral fluxes include near-surface process (such as the $\overline{e'c'}$ terms which are large near the surfaces outcrop layers in FRAM) as well as basin dianeutral fluxes. There is also a brief discussion for each region on the total layer property fluxes.

The total section fluxes are shown in Table 5.1. There are some differences in the total section fluxes between this model, which explicitly includes

sea-surface forcing terms, and the previous model, model_int (Table 4.1). These difference result in smaller or larger property fluxes at each station effecting the strength of boundary currents and overturning cells, but in general do not change the circulation pattern discussed in Chapter 4. The mass and heat divergence in each region are due to the loss/gain of heat or freshwater.

The addition of air-sea forcing terms results in some changes to the total and layer by layer property fluxes, although the derived circulation is the same as the previous model. The following sections discuss, for each ocean region, the interaction between the interior dianeutral fluxes across outcropping neutral surfaces and sea-surface fluxes, highlighting the water mass fluxes that occur in the regions and the mechanisms which result in the conversions.

5.4.1 Atlantic Region

In the subtropical Atlantic (BI) the mass flux driven by air-sea fluxes (Equation 5.2) across upper thermocline (5 and 6) outcropping neutral surfaces results in a mass flux towards lighter neutral density layers, while across the remaining outcropping neutral surfaces the sea-surface transformation is towards denser layers (Figure 5.55 upper plot, dots). The sea-surface transformation is generally dominated by the buoyancy change due to heating at the outcropping neutral surfaces, although the heat flux influence decreases with increasing neutral density (Appendix E, Table E.12). The difference in sea-surface transformations across outcropping neutral surfaces results in a convergence of upper thermocline layers (7) into lighter thermocline layers (5 and 6), while the small difference in sea-surface transformations across lower thermocline neutral surfaces (7 to 10) results in a convergence into lower thermocline (8 to 10) and lower intermediate (11 and 12) layers (Figure 5.55 middle plot, dots).

Also plotted in Figure 5.55 are the interior dianeutral mass fluxes across the sea-surface outcropping neutral surfaces (dot-dashed). The interior fluxes indicate the extent to which mass convergence driven by air-sea fluxes is balanced by mixing in the interior of the ocean. Interior convergence into thermocline layers (7) is achieved by downward transport of upper thermocline layers (5 and 6) and upward flux across denser thermocline layer (8 to 10) (Figure 5.55 upper and middle plot, dot-dashed).

section	Mass($\times 10^6 m^3 s^{-1}$)	Heat($\times 10^6$ °C $m^3 s^{-1}$)	Salt($\times 10^6 kgs^{-1}$)	Freshwater($\times 10^9 kgs^{-1}$)	Silica ($kmols^{-1}$)
SAVE2	-0.69±11.5	111.82±49.46	-24.47±46.46	-0.78±11.5	-7.38±485.7
SAVE4	-0.19±7.7	77.00±25.9	-4.38±97.3	-0.22±7.7	346.84±476.7
Drake P	131.80±1.3	335.51±2.3	4673.8±18.9	131.00±1.3	8830.2±124.5
S. Africa	132.00±7.9	261.46±16.8	4674.3±98.5	131.18±7.9	8631.4±680.9
Weddell Sea	0.04±3.9	-24.39±1.5	1.61±52.8	0.07±3.9	196.8±501.4
Ind18	-11.28±8.4	-331.62±42.7	-401.84±74.4	-11.09±8.3	417.0±808.3
Ind32	-10.95±10.1	-234.07±56.1	-390.38±88.1	-10.78±10.1	430.6±638.4
S. Aust	143.11±4.9	440.34±12.6	5074.8±70.0	142.24±4.9	7805.4±387.3
Pac32	11.66±15.8	28.60±67.3	416.64±212.1	11.63±15.6	1539.5±1300.3

Table 5.1: Total property flux for all sections. +ve - northwards or eastward flux, -ve - southward or westward flux. Units: mass $\times 10^6 m^3 s^{-1}$ and heat $\times 10^6$ °C $m^3 s^{-1}$ calculated relative to 0°C, salt $\times 10^6 kgs^{-1}$, freshwater $\times 10^9 kgs^{-1}$ and silicate $kmols^{-1}$

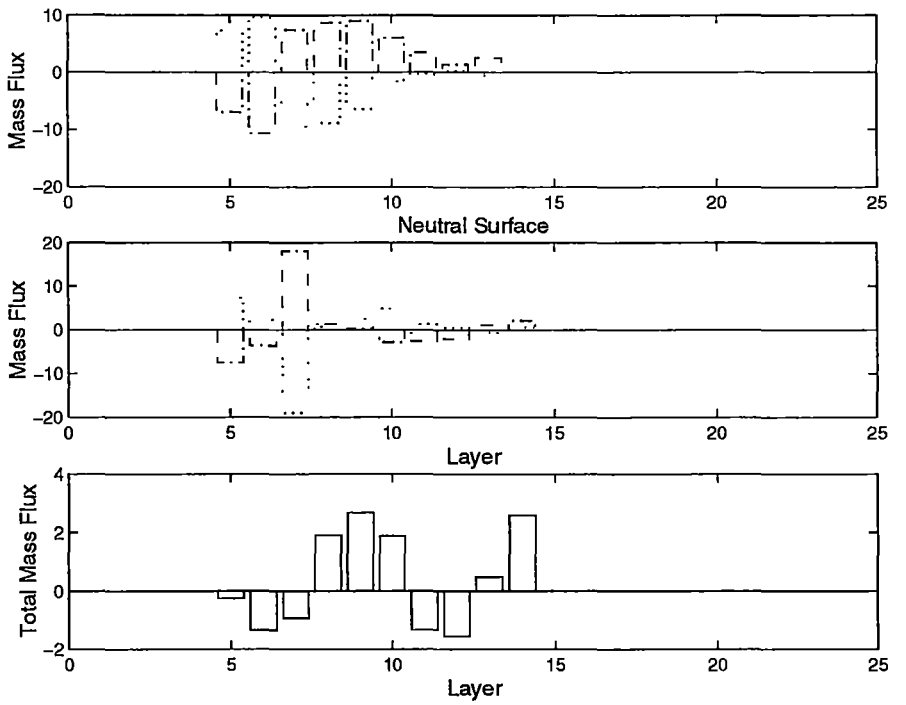

Figure 5.55: subtropical Atlantic (BI) dianeutral mass flux. Sea-surface transformation (dots), interior dianeutral mass flux (dot-dash) and total mass convergence in layers (solid) ($\times 10^6 m^3 s^{-1}$). Upper plot - mass flux across neutral surfaces, +ve towards lighter neutral density/upwards -ve towards denser neutral density/downwards. Middle plot - mass convergence into neutral density layers by surface and internal processes, +ve mass gain (convergence) -ve mass loss (divergence) Bottom Plot - Total mass convergence into neutral density layers by surface and internal processes +ve mass gain (convergence) -ve mass loss (divergence). Note change of scale of lower plot

The sea-surface and interior mass convergences and divergences are not in complete balance which result in small total mass convergences (Figure 5.55, lower plot). Sea-surface and interior dianeutral fluxes result in a total mass convergence of upper thermocline layers (5,6 and 7) into lower thermocline layer (8,9 and 10). It is principally interior convergences from upper intermediate layers (11 and 12) into lower intermediate layers (14) that result in the small total mass convergence into layer 14.

The sea-surface and interior dianeutral salt fluxes are shown in Figure 5.56. Across the thermocline layers (5) the sea-surface and interior salt fluxes transfer salt into lower thermocline layers (6 to 9), while the salt transfer from lower thermocline (10) and upper intermediate (11) layers into lower

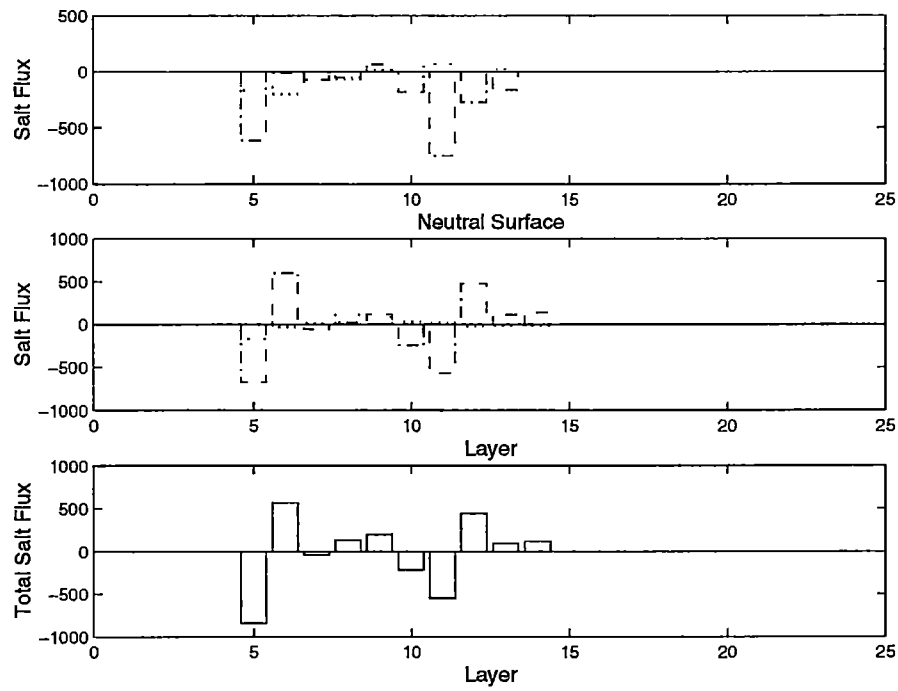

Figure 5.56: subtropical Atlantic (BI) dianeutral salt flux. Sea-surface transformation (dots), interior dianeutral salt flux (dot-dash) and total salt convergence in layers (solid) ($\times 10^6$ psu $m^3 s^{-1}$). Upper plot - salt flux across neutral surfaces, +ve towards lighter neutral density/upwards -ve towards denser neutral density/downwards. Middle plot - salt convergence into neutral density layers by surface and internal processes, +ve salt gain (convergence) -ve salt loss (divergence) Bottom Plot - Total salt convergence into neutral density layers by surface and internal processes +ve salt gain (convergence) -ve salt loss (divergence).

intermediate (12, 13 and 14) is achieved by interior dianeutral salt fluxes. Layers 12, 13 and 14 define SAMW and AAIW in the subtropical Atlantic Ocean, the input of salt into SAMW and AAIW is achieved by interior mixing processes. This salt flux into SAMW and AAIW is the mechanism by which the salinity of these water mass is increased in the subtropical Atlantic Ocean, as evident by the increased salinity of SAMW and AAIW between SAVE 4 (Figure 3.6) and SAVE 2 (Figure 3.3).

Across the outcropping neutral surfaces in the Southern Ocean Atlantic sector the sea-surface mass fluxes are dominated by the buoyancy heat flux and Ekman flux (Appendix E, Table E.13). The sea-surface mass flux are towards lighter layers across all outcropping neutral surfaces (Figure 5.57 upper plot, dots). This results in a sea-surface transport of lower intermediate layers (14

and 15) into upper intermediate (11, 12 and 13) and lower thermocline layers (10) (Figure 5.57 middle plot, dots). The interior dianeutral mass flux across the outcropping neutral surfaces is downwards and smaller than the sea-surface mass fluxes (Figure 5.57, upper plot dot-dash). The interior dianeutral fluxes result in the transfer of lower thermocline (layer 10) into upper intermediate (11 and 12) layers, and a smaller transfer of intermediate layers (13 and 14) into lower intermediate layers (15) (Figure 5.57 middle plot, dot-dashed).

The sea-surface flux into lower thermocline layers (10) and upper intermediate layers (11, 12 and 13) from intermediate layers (14 and 15) is dispersed into upper intermediate layers (11 and 12) by interior mixing processes (Figure 5.57 middle plot). This results in the total mass convergence into upper intermediate layers (11 and 12) by a sea-surface flux of lower intermediate layers (14 and 15) and interior dianeutral mixing from lower thermocline layers (10) (Figure 5.57, lower plot). Within the Southern Ocean Atlantic sector intermediate layers 11 and 12 are representative of SAMW, while layers 13, 14 and 15 are representative of AAIW. The total mass convergence into SAMW is driven by air-sea flux driven convergence from AAIW and interior mixing from thermocline water (layer 10). This indicates that in the Southern Ocean Atlantic sector lower intermediate water (AAIW) is converted into upper intermediate water (SAMW) by both air-sea flux and interior dianeutral mass flux.

The sea-surface and interior dianeutral heat fluxes are shown in Figure 5.58. The sea-surface heat fluxes are towards lighter layers across all outcropping neutral surfaces (Figure 5.58 upper plot, dots). This results in a sea-surfaces heat flux of intermediate (11 to 15) layers into thermocline (7 to 10) layers (Figure 5.58 middle plot, dots). The interior dianeutral heat flux is downwards across thermocline (7 to 10) and upper intermediate (11) layers and upward across remaining intermediate (12 to 15) layers (Figure 5.58 upper plot, dot-dashed). This results in a transfer of heat from thermocline (7 to 10) and a small transfer from lower intermediate (13 to 15) layer into upper intermediate (11 and 12) layers. The interior dianeutral heat fluxes dominate the convergence of heat in SAMW (layer 11 and 12) (Figure 5.58, lower plot). The dianeutral heat convergence into SAMW, principally from downward heat flux of overlying

thermocline layer highlights the mechanism which increases the temperature of SAMW.

The interior dianeutral salt fluxes across outcropping neutral surfaces are larger than the sea-surface salt transport with the Southern Ocean Atlantic sector (Figure 5.59). The interior dianeutral salt fluxes are downwards across all neutral surfaces, with two local maxima across: lower thermocline layers (9 and 10) and; deep layers (16). This results in a flux of salt from the thermocline (9 and 10) into the SAMW (upper intermediate layers 11 and 12) and a flux of salt from upper deep layer (16 and 17) into lower deep (18 and 19) layers (the lower deep layers are not shown as they do not have sea-surface outcrop expressions). The deep layers (16 and 17) represent the salinity maximum NADW, the salt flux from these layers into fresher CDW shows the mechanism which results in the high salinity LCDW.

The position of the neutral surfaces in winter (July) and corresponding sea surface temperature and salinity in the Southern Ocean Atlantic sector are shown in Figure 5.60. The outcropping AAIW layers (between neutral surfaces 12 to 15) are south of 45°S and are colder and fresher than the temperature and salinity values generally used to describe AAIW in the Southern Ocean Atlantic (BII) sector (at 45°S 3.5°C and 34.2 psu and at 30°S 4°C and 34.3 psu (Piola and Georgi 1982)). The cold, fresh outcropping properties of neutral surfaces 12 to 15 identify Antarctic Surface Water (AASW). The sea-surface forcing results in cold and fresh AASW water being converted into SAMW and thermocline water, while the downward dianeutral interior mass flux of thermocline water into SAMW results from the downward heat and salt fluxes from the thermocline into SAMW. The transfer of thermocline water into SAMW results in the warming and increased the salinity of SAMW in the Atlantic region.

The addition of the air-sea flux result in changes to the layer-by-layer mass flux between this model (Figure 5.61) and the previous model (model_int, Figure 4.32), although the circulation pattern discussed in Chapter 4 is the same. The major change occurs in the deep (16 to 18) and bottom (19 to 22). In this model the northward mass flux of deep water across the Argentine basin is $27\times10^6 m^3 s^{-1}$. Most of this water returns to the Southern Ocean across the mid-Atlantic ridge. The Weddell Sea Deep (layer 21) and Bottom (layer 22)

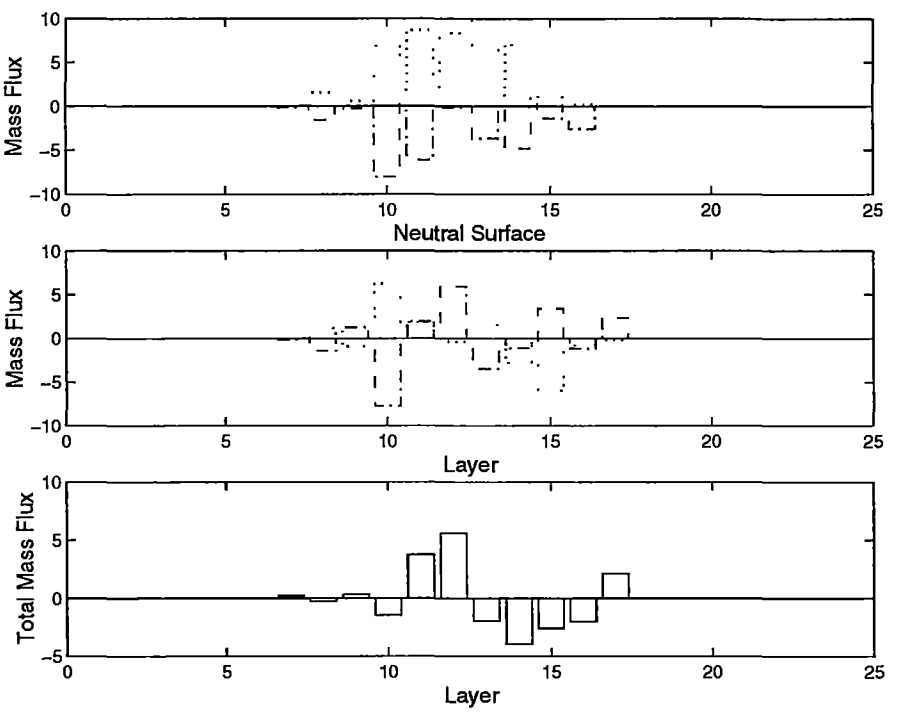

Figure 5.57: Southern Ocean Atlantic (BII) sector dianeutral mass flux. Sea-surface transformation (dots), interior dianeutral mass flux (dot-dash) and total mass convergence in layers (solid) ($\times 10^6 m^3 s^{-1}$). Upper plot - mass flux across neutral surfaces, +ve towards lighter neutral density/upwards -ve towards denser neutral density/downwards. Middle plot - mass convergence into neutral density layers by surface and internal processes, +ve mass gain (convergence) -ve mass loss (divergence) Bottom Plot - Total mass convergence into neutral density layers by surface and internal processes +ve mass gain (convergence) -ve mass loss (divergence).

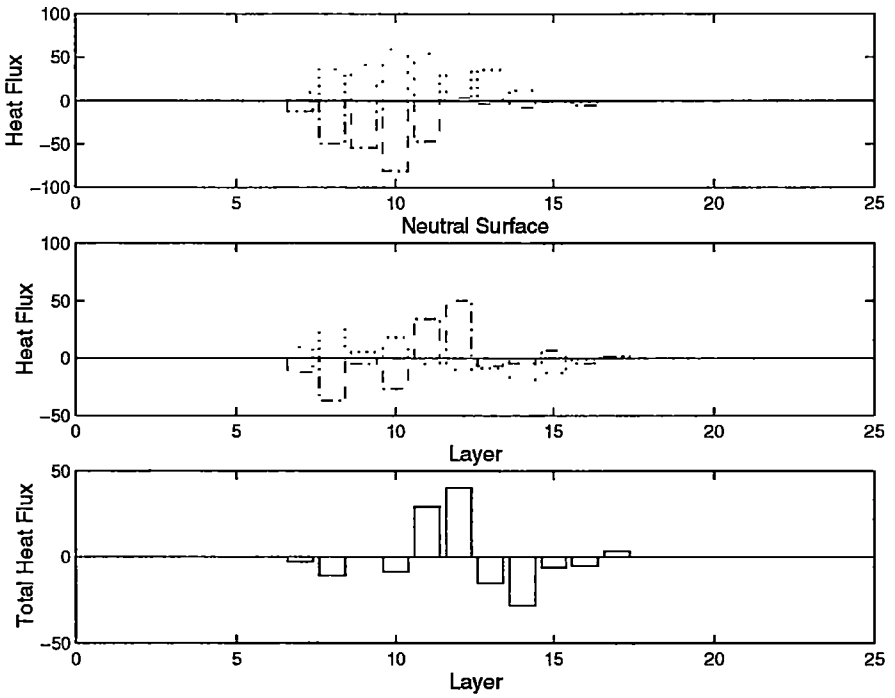

Figure 5.58: Southern Ocean Atlantic (BII) sector (BII) dianeutral heat flux. Sea-surface transformation (dots), interior dianeutral heat flux (dot-dash) and total heat convergence in layers (solid) ($\times 10^6$ °C $m^3 s^{-1}$). Upper plot - heat flux across neutral surfaces, +ve towards lighter neutral density/upwards -ve towards denser neutral density/downwards. Middle plot - heat convergence into neutral density layers by surface and internal processes, +ve heat gain (convergence) -ve heat loss (divergence) Bottom Plot - Total heat convergence into neutral density layers by surface and internal processes +ve heat gain (convergence) -ve heat loss (divergence).

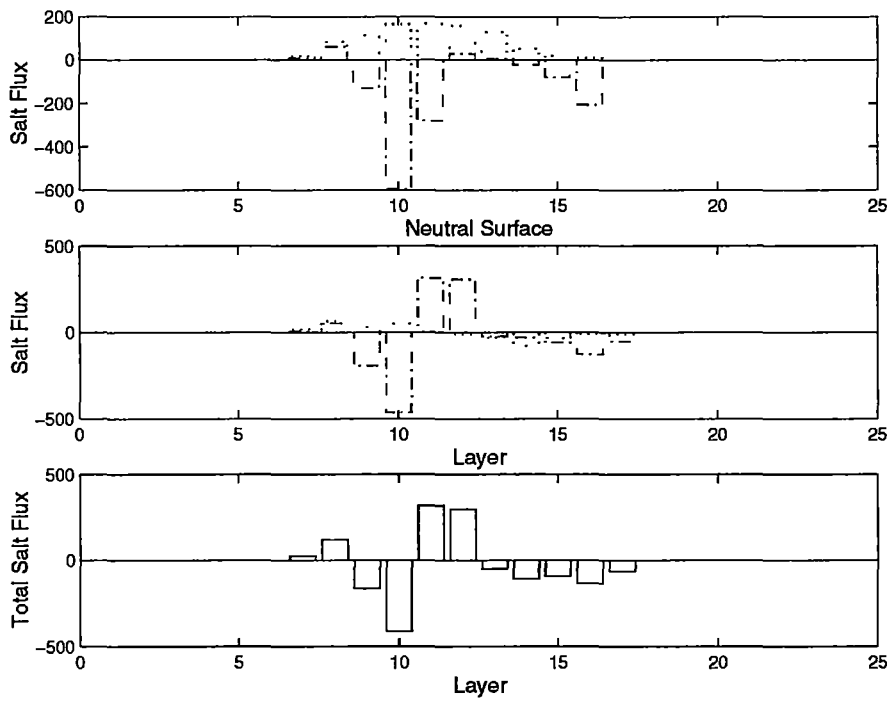

Figure 5.59: Southern Ocean Atlantic (BII) sector dianeutral salt flux. Sea-surface transformation (dots), interior dianeutral salt flux (dot-dash) and total salt convergence in layers (solid) ($\times 10^6$ psu $m^3 s^{-1}$). Upper plot - salt flux across neutral surfaces, +ve towards lighter neutral density/upwards -ve towards denser neutral density/downwards. Middle plot - salt convergence into neutral density layers by surface and internal processes, +ve salt gain (convergence) -ve salt loss (divergence) Bottom Plot - Total salt convergence into neutral density layers by surface and internal processes +ve salt gain (convergence) -ve salt loss (divergence).

a)

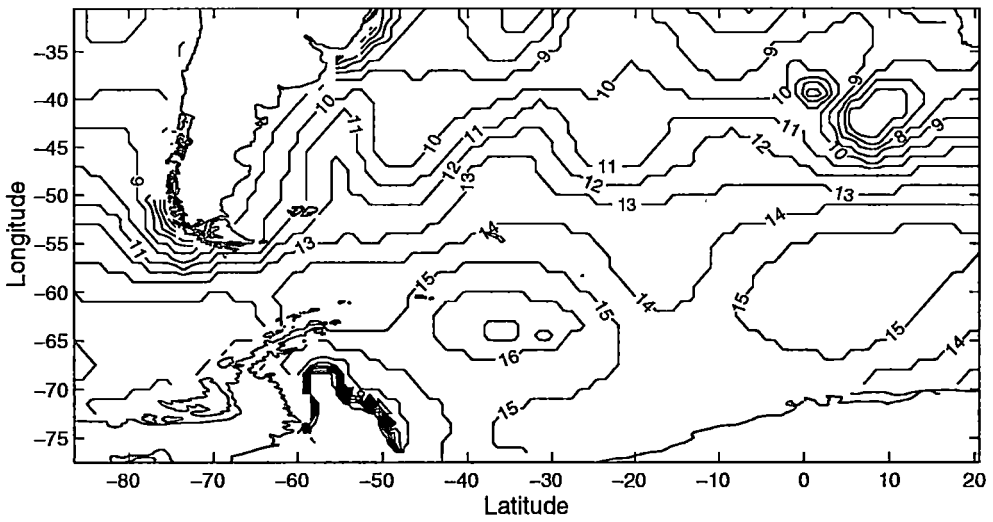

b)

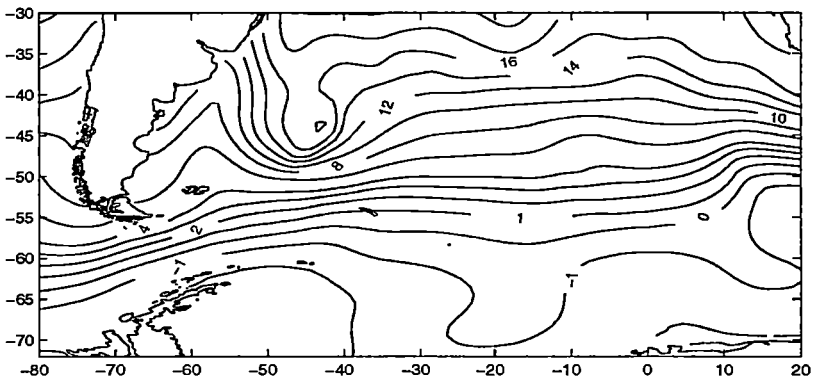

c)

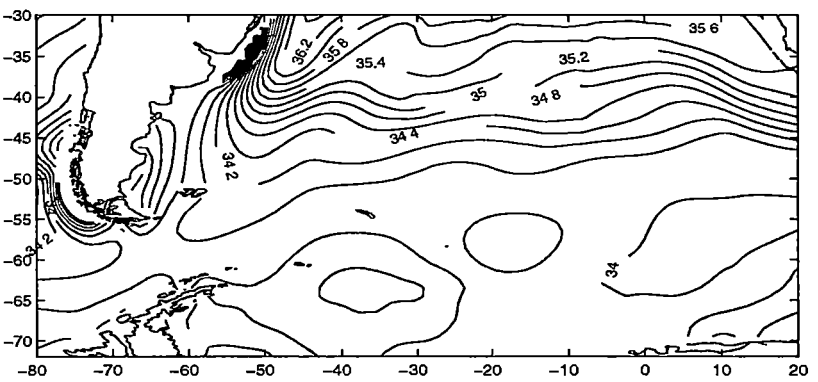

Figure 5.60: Southern Ocean Atlantic (BII) sector June sea-surface a) neutral density outcropping position, contour label are neutral surface numbers b) temperature (°C) and c) salinity (psu)

water which enters the Southern Ocean sector across the Wedsea section is nearly completely modified into generic AABW and LCDW (layer 21). The modification of the extreme Weddell Sea bottom water results in an increased eastward flow of deep water (CDW, layer 19) across the section south of Australia. The increased eastward flow of CDW south of Africa increase the eastward silica flux, which now balance the silica flux in the Southern Ocean Atlantic sector.

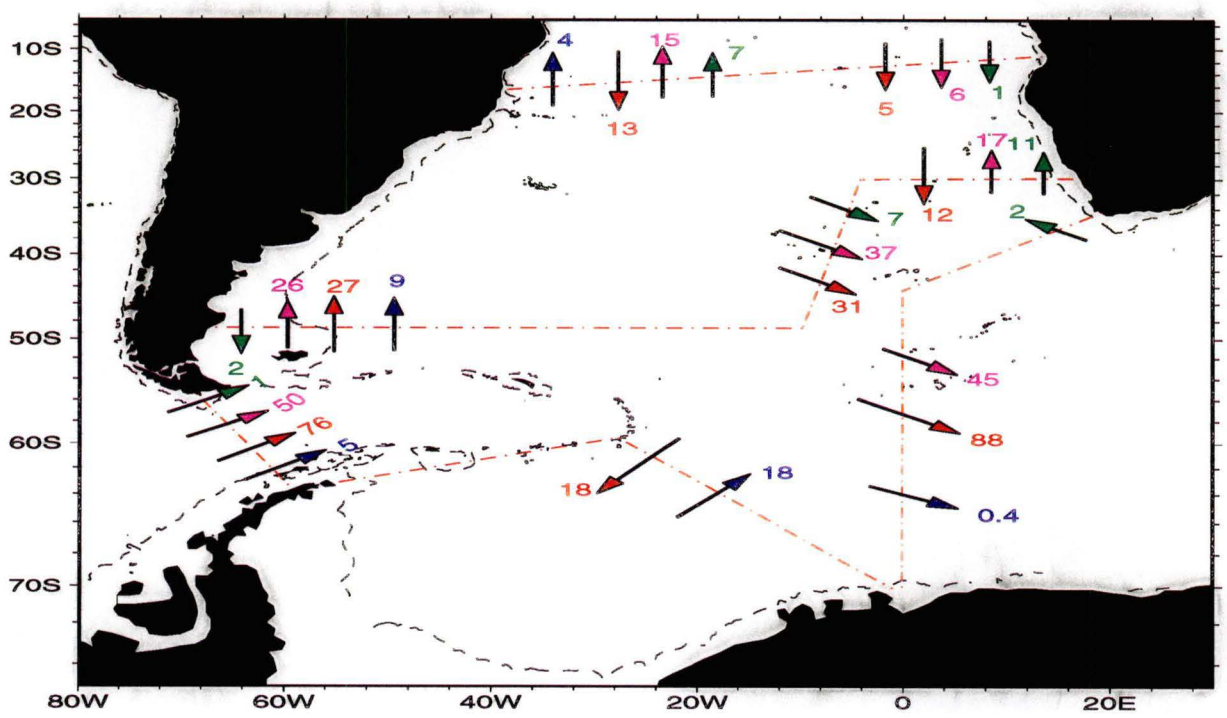

Figure 5.61: Transport ($\times 10^6 m^3 s^{-1}$) of particular layers in the Atlantic Region. Thermocline layers 5 to 10 (green), Intermediate layers 11 to 15 (magenta), Deep layers 16 to 18 across SAVE2, SAVE4 and 16 to 19 across Drake Passage, south Africa and Weddell Sea (red) and Bottom layers 20 to 22 (dark blue). Dashed line 1000 dbar contour

5.4.2 Indian Region

In the subtropical Indian Ocean (BIV) the sea-surface transformations across outcropping neutral surfaces are towards denser layers (Figure 5.62, upper plot dots). (The individual components of the sea-surface transformation are given in Appendix E, Table E.14). This results in a sea-surface transfer of upper thermocline (3, 4 and 5) into lower thermocline (6 to 10) layers (Figure 5.62 middle plot, dots). The interior dianeutral mass flux across outcropping neutral surfaces is upwards, but smaller than the downward sea-surface transformation (Figure 5.62, upper plot dot-dash). The warm, fresh upper thermocline layers (3 and 4) enters the subtropical Indian Ocean across 18°S. These warm fresh thermocline waters are converted into denser thermocline layers (5 to 10) by sea-surface processes.

In the Southern Ocean Indian sector the sea-surface transformations across the thermocline neutral surfaces (6 to 10) are towards denser layers, while the remaining outcropping neutral surfaces (11 to 16) have a sea-surface transformation towards lighter layers (Figure 5.63 upper plot, dots). This results in a sea-surface transport of upper thermocline layers (7 and 8) into lower thermocline layers (9 and 10) and a transport of lower intermediate layers (14 and 15) into upper intermediate layers (11, 12 and 13) (Figure 5.63 middle plots, dots). The upper thermocline layers (6,7,8) identify the southward extension of the Agulhas Current adjacent to the south African coast (Figure 5.66). The sea-surface transformation across these outcropping neutral surfaces is driven by the buoyancy heat loss (Appendix E, Table E.15). The loss of heat from the ocean to the atmosphere results in the convergence of mass from the lightest thermocline layer (6, 7 and 8) associated with the Agulhas Current into denser thermocline layers (9 and 10). The transport of lower intermediate layers (14 and 15) to upper thermocline layers (11 to 13) results from northward Ekman flux, heating of sea-surfaces and freshwater inputs (Appendix E, Table E.15).

The interior dianeutral mass fluxes are downward across intermediate layer (11 to 15), with small upward fluxes across the lightest dianeutral surfaces (7 and 8) (Figure 5.63 upper plot, dot-dashed). This results in a small transport

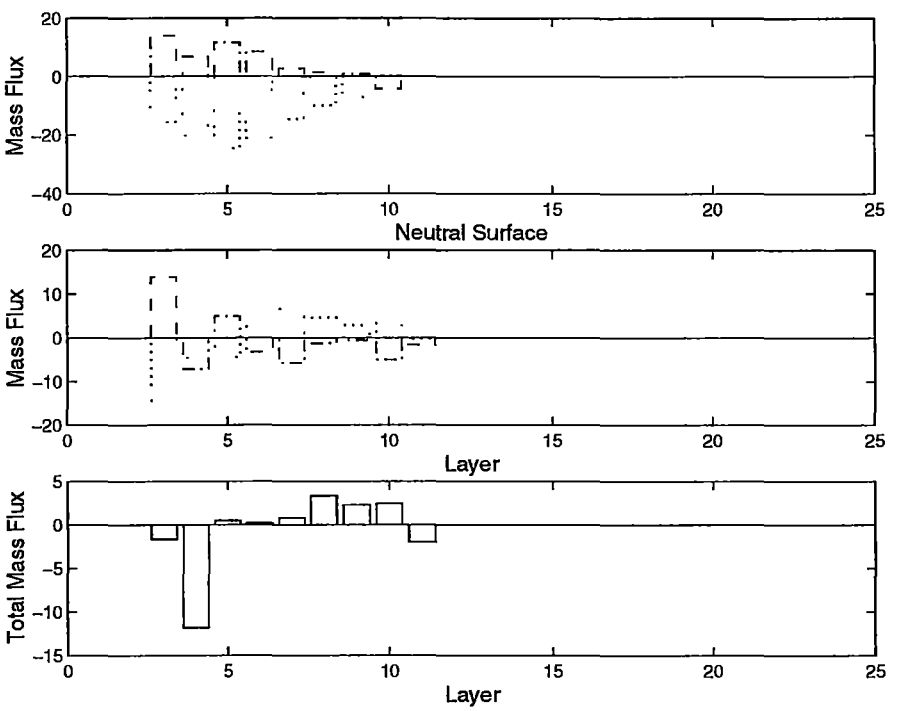

Figure 5.62: subtropical Indian (BIV) dianeutral mass flux. Sea-surface transformation (dots), interior dianeutral mass flux (dot-dash) and total mass convergence in layers (solid) ($\times 10^6 m^3 s^{-1}$). Upper plot - mass flux across neutral surfaces, +ve towards lighter neutral density/upwards -ve towards denser neutral density/downwards. Middle plot - mass convergence into neutral density layers by surface and internal processes, +ve mass gain (convergence) -ve mass loss (divergence) Bottom Plot - Total mass convergence into neutral density layers by surface and internal processes +ve mass gain (convergence) -ve mass loss (divergence).

of lower thermocline layers (9) into upper thermocline layers (7 and 8), a transfer of lower thermocline layers (10) into upper intermediate layers (12) (Figure 5.63 middle plot, dot-dashed). There is also a transfer of intermediate layer (13) into lower intermediate layers (14 and 15).

The sea-surface and interior dianeutral fluxes convert thermocline layers to upper intermediate layers (11 and 12). There is also a transfer into upper intermediate layers (11, 12 and 13) from lower intermediate layers (14 and 15) by sea-surface processes (Figure 5.63 lower plot).

The heat and salt sea-surface and interior dianeutral fluxes show that the heat and salt flux into the upper intermediate layers (11, 12 and 13) is principally driven by interior dianeutral fluxes from thermocline layers (6 to 10) (Figure 5.64 and Figure 5.65). These thermocline layers are generally associated with the Agulhas Current extension and retroflection south of Africa.

In the Southern Ocean Indian sector the Agulhas extension and its retroflection south of Africa are characterised by thermocline layers (7,8 and 9), upper intermediate layers (11, 12 and 13) describe SAMW while the lower intermediate layers (14 and 15) are associated with the cold, fresh Antarctic surface water. The outcropping position of the neutral surfaces, sea-surface temperature and salinity are shown in Figure 5.66. The Agulhas Current and retroflection are warm and salty and the sea-surface temperature and salinity associated with outcropping cold, fresh Antarctic surface water (14 and 15) are colder and fresher than the temperature and salinity characteristics of SAMW in the Southern Ocean Indian sector (McCartney 1977). SAMW cools and freshens as it moves eastward in the Southern Ocean Indian sector. The sea-surface and interior dianeutral flux of Agulhas thermocline layers into SAMW, highlighted above, result in the warm, saline SAMW found in the western Southern Ocean Indian sector. The Agulhas thermocline water converted into SAMW moves eastward with the Antarctic Circumpolar Current, resulting in an increase flux of SAMW south of Australia. As the SAMW moves eastward across the Southern Ocean Indian sector the northward sea-surface transformation of colder and fresher Antarctic surface water into SAMW results in the gradual cooling and freshening of SAMW noted within previous studies (McCartney 1977).

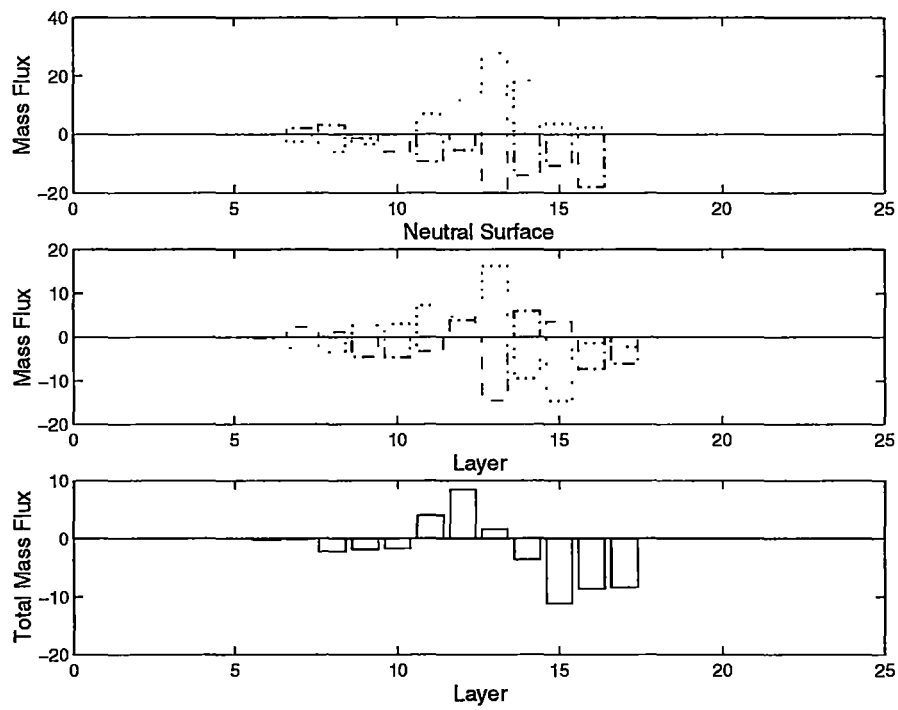

Figure 5.63: Southern Ocean Indian sector (BV) dianeutral mass flux. Sea-surface transformation (dots), interior dianeutral mass flux (dot-dash) and total mass convergence in layers (solid) ($\times 10^6 m^3 s^{-1}$). Upper plot - mass flux across neutral surfaces, +ve towards lighter neutral density/upwards -ve towards denser neutral density/downwards. Middle plot - mass convergence into neutral density layers by surface and internal processes, +ve mass gain (convergence) -ve mass loss (divergence) Bottom Plot - Total mass convergence into neutral density layers by surface and internal processes +ve mass gain (convergence) -ve mass loss (divergence).

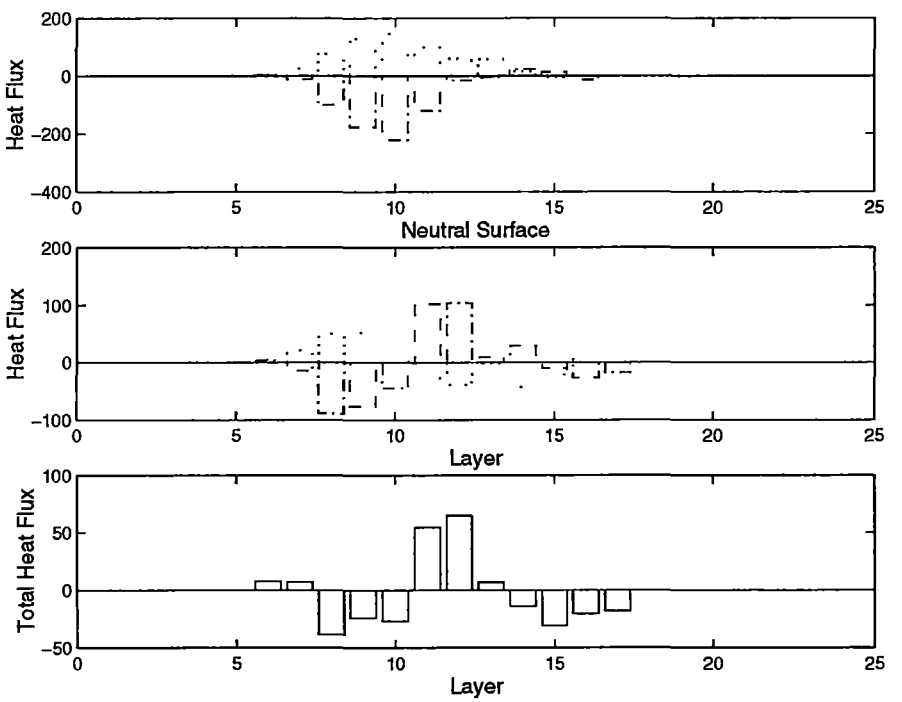

Figure 5.64: Southern Ocean Indian sector (BV) dianeutral heat flux. Sea-surface transformation (dots), interior dianeutral heat flux (dot-dash) and total heat convergence in layers (solid) ($\times 10^6$ °C $m^3 s^{-1}$). Upper plot - heat flux across neutral surfaces, +ve towards lighter neutral density/upwards -ve towards denser neutral density/downwards. Middle plot - heat convergence into neutral density layers by surface and internal processes, +ve heat gain (convergence) -ve heat loss (divergence) Bottom Plot - Total heat convergence into neutral density layers by surface and internal processes +ve heat gain (convergence) -ve heat loss (divergence).

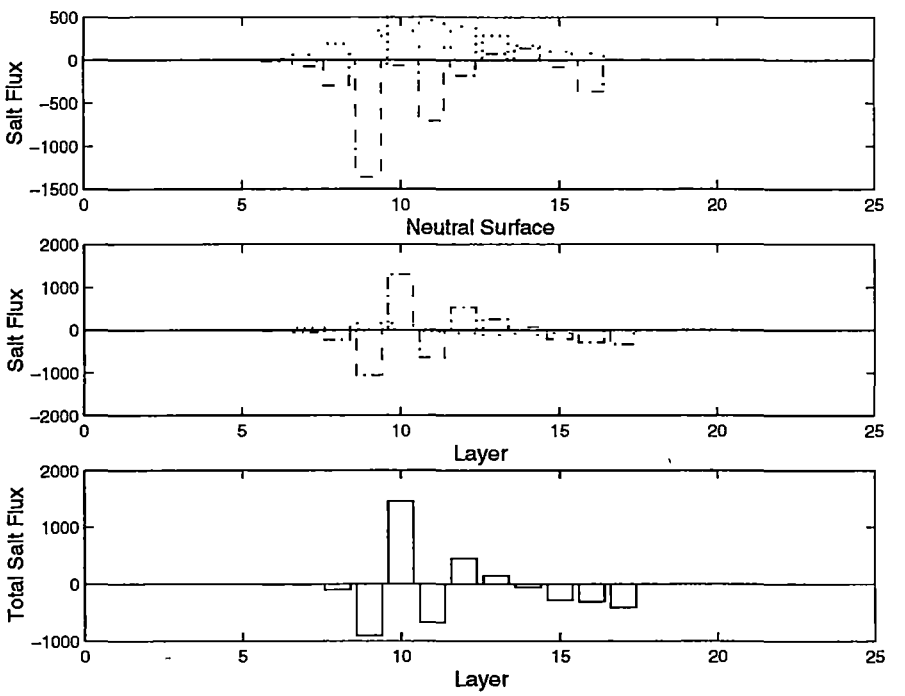

Figure 5.65: Southern Ocean Indian sector (BV) dianeutral salt flux. Sea-surface transformation (dots), interior dianeutral salt flux (dot-dash) and total salt convergence in layers (solid) ($\times 10^6$ psu $m^3 s^{-1}$). Upper plot - salt flux across neutral surfaces, +ve towards lighter neutral density/upwards -ve towards denser neutral density/downwards. Middle plot - salt convergence into neutral density layers by surface and internal processes, +ve salt gain (convergence) -ve salt loss (divergence) Bottom Plot - Total salt convergence into neutral density layers by surface and internal processes +ve salt gain (convergence) -ve salt loss (divergence).

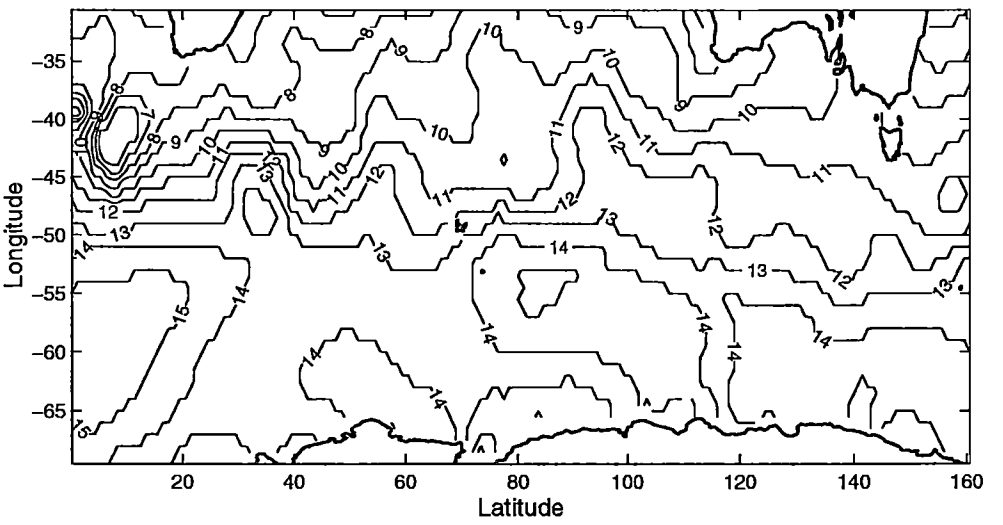

a)

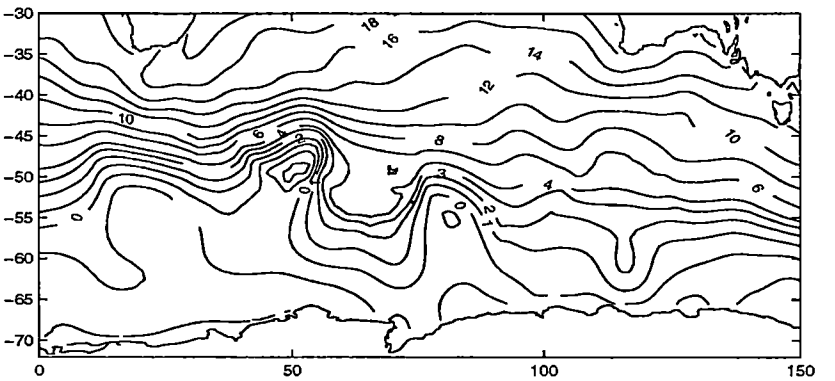

b)

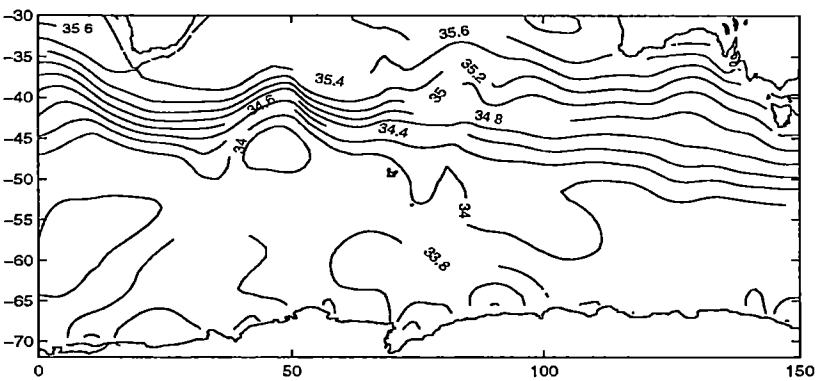

c)

Figure 5.66: Southern Ocean Indian sector June sea-surface a) neutral density outcropping position, contour label are neutral surface numbers b) temperature (°C) and c) salinity (psu)

The deep (16 to 18) and bottom (19 to 20) transport differs between this model (Figure 5.67) and the previous model (model_int, Figure 4.40). Similar amounts of Southern Ocean deep (layers 16 to 18) and bottom (layers 19 to 20) water move northwards across 32°S into the Indian Ocean in the two model, but at 18°S the northward transport of bottom water is increased to $14\times10^6 m^3 s^{-1}$ n this model. The northward flow of bottom water at 18°S is balanced by an overall southward flow of Indian Deep Water (layers 16 to 18). The northward flow of bottom water at the Ind18 section results in a change of sign of the silica flux between these two models.

The inclusion of air-sea fluxes doesn't change the size of the deep overturning cell in the Indian ocean but does result in changes to the region where the modification to slightly less dense water occurs. Southern Ocean deep and bottom water is now modified to slightly less dense IDW and lower intermediate water between 32°S and 18°S and north of 18°S.

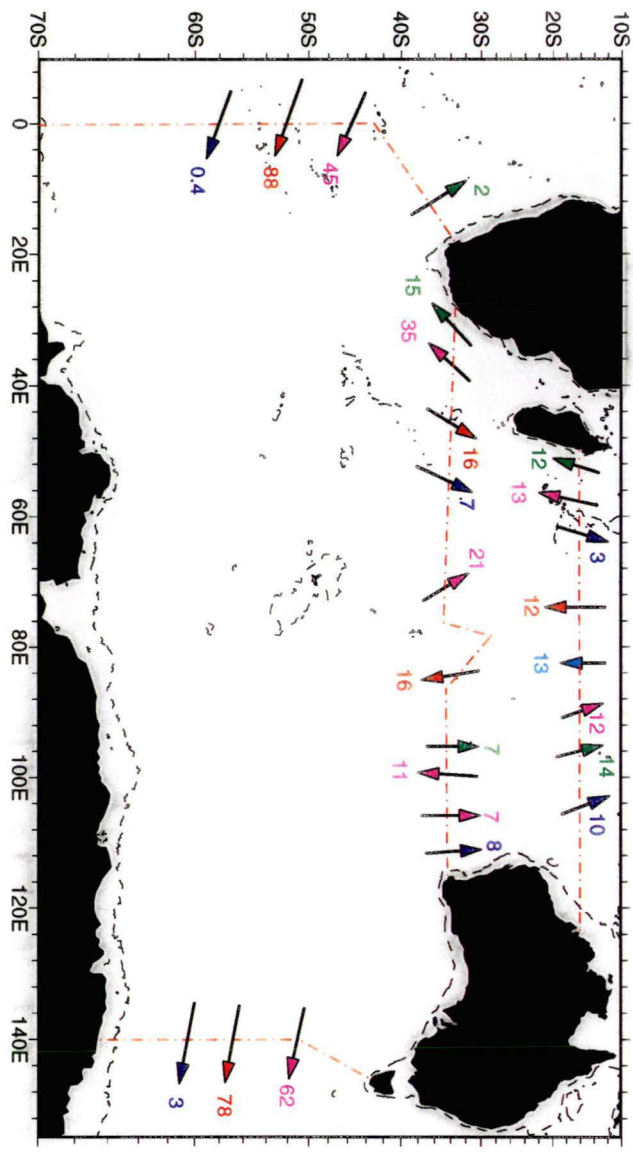

Figure 5.67: Transport ($\times 10^6 m^3 s^{-1}$) of particular layers in the Indian Region. Surface layers 3 and 4 (light blue), Thermocline layers 5 to 10 (green), Intermediate layers 11 to 15 (magenta), Deep layers 16 to 18 across Ind18, Ind32 and 16 to 19 south of Africa and Australia (red) and Bottom layers 20 to 22 (dark blue). Dashed line 1000 dbar contour.

5.4.3 Pacific Region

In the Southern Ocean Pacific (BVI) sector (BVI) the sea-surface transformations are toward lighter layers across outcropping intermediate (11 to 15) and thermocline (7 to 10) neutral surfaces, while across deep (16 to 19) outcropping neutral surfaces the sea-surface transformations are small and directed towards denser layers (Figure 5.68 upper plot, dots). This results in a transfer of lower intermediate layers (15) into intermediate layers (13 and 14), and a transfer of upper intermediate layers (11 and 12) into lower thermocline layers (8 and 9) (Figure 5.68 middle plot, dots). The sea-surface transformations across intermediate and thermocline outcropping neutral surfaces are dominated by the northward Ekman flux (Appendix E, Table E.16).

The interior dianeutral mass fluxes are downward (into denser layers) across most neutral surfaces, apart from small upward fluxes across neutral surfaces 10 and 11 (Figure 5.68 upper plot, dash-dot). The interior dianeutral fluxes result in a transfer of thermocline layers (8 and 9) into lower thermocline layers (10), a flux of intermediate (12 and 13) layers into lower intermediate (14 and 15) (Figure 5.68 middle plot, dash-dot). The largest interior flux occurs between upper deep (17 and 18) and lower deep (19) and bottom (20 and 21) layers.

The sea-surface and interior dianeutral heat flux from upper intermediate layers (11 and 12) into thermocline layers result in the warming of thermocline layers in the Southern Ocean Pacific (BVI) sector (Figure 5.69). There are smaller interior heat fluxes between lower intermediate (13 to 15) and deep layers (16 to 19), which result in the loss of heat from upper deep layer (16 to 18) into lower intermediate (13 and 14) and lower deep (19) and bottom (20) layers.

The sea-surface salt fluxes are towards lighter layers and transfer salt from the intermediate (11 to 15) into the thermocline (7 to 10) layers (Figure 5.70 upper and lower plots, dots). The sea-surface salt fluxes and smaller interior dianeutral salt fluxes into thermocline layers result in a net salt convergence into the thermocline layers (7 and 8). The downward interior salt fluxes across thermocline (11 to 14) and deep (17 to 19) layers is larger than the upward

sea-surfaces salt fluxes across these layers. This results in a salt convergence from intermediate (11 and 12) into lower intermediate (13 to 15) layers, and a flux of salt from deep (17 and 18) layers into deep and bottom (19 to 21) layers. The salt transfer between deep and bottom layer is driven completely by interior dianeutral fluxes.

As shown in, Section 4.3 the total eastward mass transport within SAMW, south of Australia, is larger than the eastward mass flux of SAMW at Drake Passage and south of Africa. The increased eastward mass transport of SAMW south of Australia results from the return flow of Indonesian through-flow water. As shown the Agulhas thermocline water is converted into SAMW in the Southern Ocean Indian sector, these waters move eastward with the Antarctic Circumpolar Current south of Australia. In the Southern Ocean Pacific (BVI) sector SAMW (layers 11, 12 and 13) is converted into warmer, more saline thermocline (7, 8, 9 and 10) layers by sea-surface and interior dianeutral processes, as highlighted. The mass and salt flux is principally driven by sea-surface transformation while sea-surface and interior dianeutral fluxes result in the heat transfer. The thermocline waters move northward into the subtropical Pacific Ocean, closing the Indian-Pacific interbasin exchange.

Within this region AAIW is described by lower intermediate layers (13, 14 and 15). There are small mass and salt fluxes into AAIW from SAMW (layers 11 and 12). This indicates that SAMW is converted into AAIW by both sea-surface and interior mixing processes. A large area of the sea surface in the southeast Southern Ocean Pacific (BVI) sector has the appropriate temperature and salinity values of SAMW/AAIW (Figure 5.71). The sea-surface and interior mixing processes, in the southeast Pacific, may act to homogenise the SAMW/AAIW properties without resulting in changes to the neutral density. This may account for the small mass, heat and salt convergence between SAMW and AAIW shown in this study.

The interior dianeutral property fluxes between upper deep layers (16 and 17, Pacific Deep Water and UCDW), lower deep water (18 and 19, CDW) and bottom water (20 and 21 AABW ALBW/RSBW) highlight the mixing occurring between these water masses. The interior mixing that occurs between these layers is much larger than the sea-surface transfer of upper deep layer (16

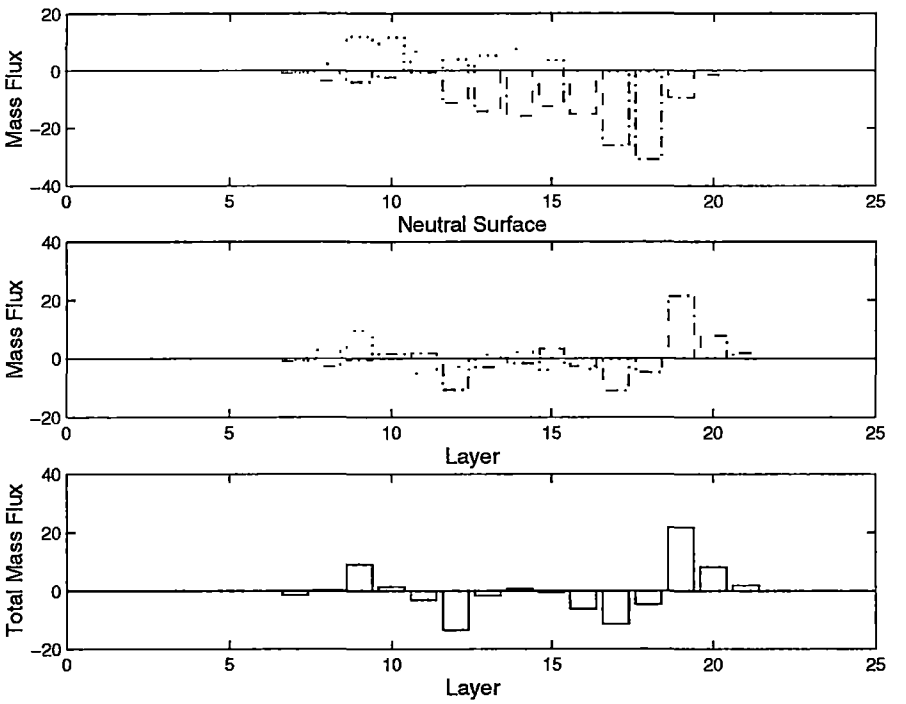

Figure 5.68: Southern Ocean Pacific (BVI) sector (BVI) dianeutral mass flux. Sea-surface transformation (dots), interior dianeutral mass flux (dot-dash) and total mass convergence in layers (solid) ($\times 10^6 m^3 s^{-1}$). Upper plot - mass flux across neutral surfaces, +ve towards lighter neutral density/upwards -ve towards denser neutral density/downwards. Middle plot - mass convergence into neutral density layers by surface and internal processes, +ve mass gain (convergence) -ve mass loss (divergence) Bottom Plot - Total mass convergence into neutral density layers by surface and internal processes +ve mass gain (convergence) -ve mass loss (divergence)

and 17) to lower deep layers (18 and 19). The interior mixing of CDW (layer 17 to 19) represent two mixing components. Firstly, the mixing of these salty waters with cold, fresh Antarctic surface water over the continental slope adjacent to the Antarctic continent which results in the production Southern Ocean Pacific Antarctic bottom water (ALBW and RSBW) and, secondly the mixing north of the bottom water formation region of CDW with this extreme AABW which results in the generic AABW seen leaving the region across 32°S and at Drake Passage.

Figure 5.72 shows the layer fluxes across the Southern Ocean Pacific sector. The major difference between the circulation described in this figure and the previous model (model_int, Figure 4.48) is the increased northward

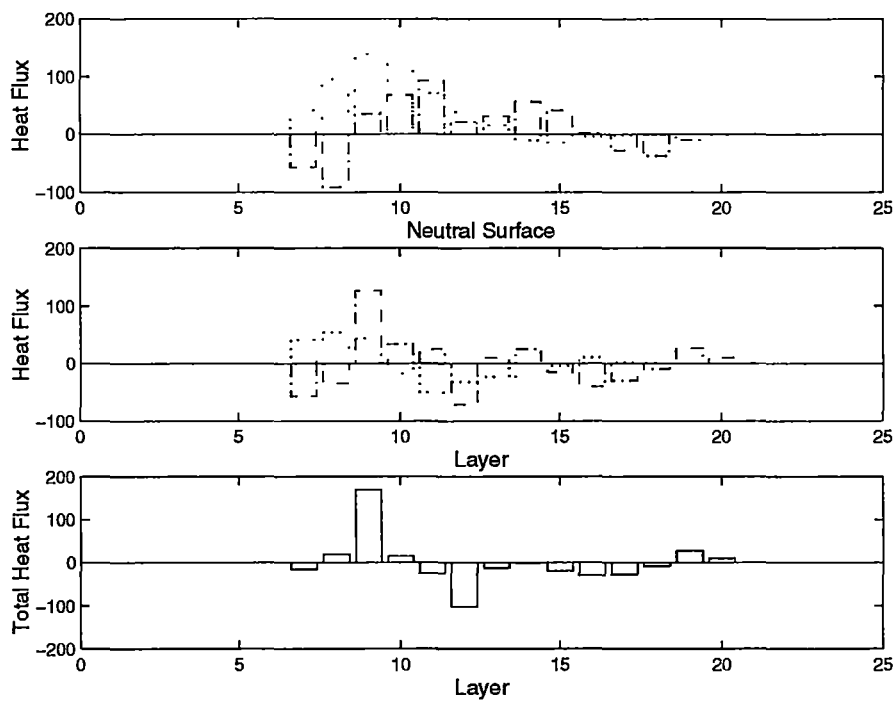

Figure 5.69: Southern Ocean Pacific (BVI) sector (BVI) dianeutral heat flux. Sea-surface transformation (dots), interior dianeutral heat flux (dot-dash) and total heat convergence in layers (solid) ($\times 10^6$ °C $m^3 s^{-1}$). Upper plot - heat flux across neutral surfaces, +ve towards lighter neutral density/upwards -ve towards denser neutral density/downwards. Middle plot - heat convergence into neutral density layers by surface and internal processes, +ve heat gain (convergence) -ve heat loss (divergence) Bottom Plot - Total heat convergence into neutral density layers by surface and internal processes +ve heat gain (convergence) -ve heat loss (divergence)

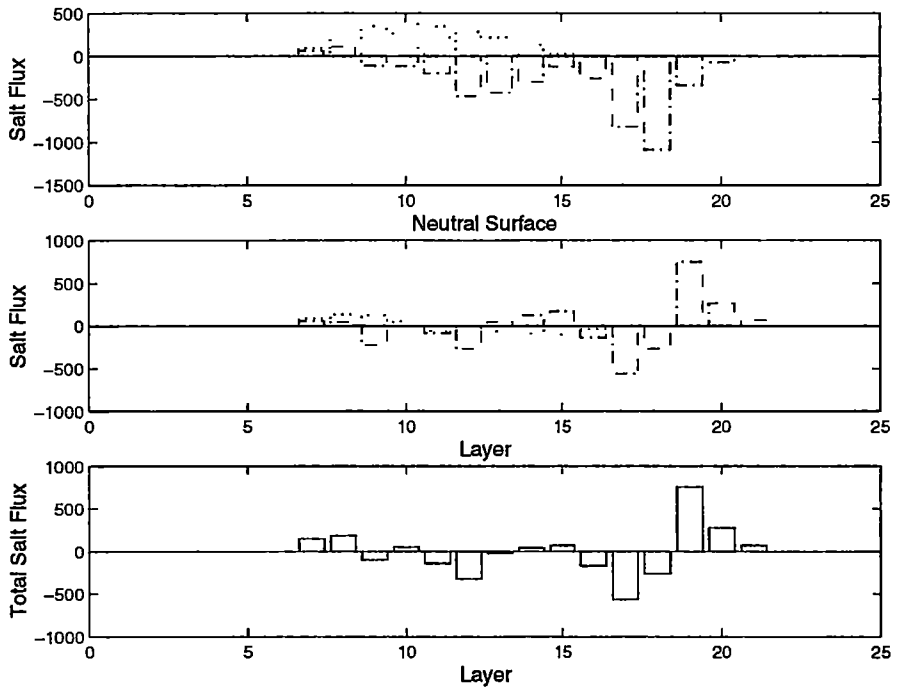

Figure 5.70: Southern Ocean Pacific (BVI) sector (BVI) dianeutral salt flux. Sea-surface transformation (dots), interior dianeutral salt flux (dot-dash) and total salt convergence in layers (solid) ($\times 10^6$ psu $m^3 s^{-1}$). Upper plot - salt flux across neutral surfaces, +ve towards lighter neutral density/upwards -ve towards denser neutral density/downwards. Middle plot - salt convergence into neutral density layers by surface and internal processes, +ve salt gain (convergence) -ve salt loss (divergence) Bottom Plot - Total salt convergence into neutral density layers by surface and internal processes +ve salt gain (convergence) -ve salt loss (divergence)

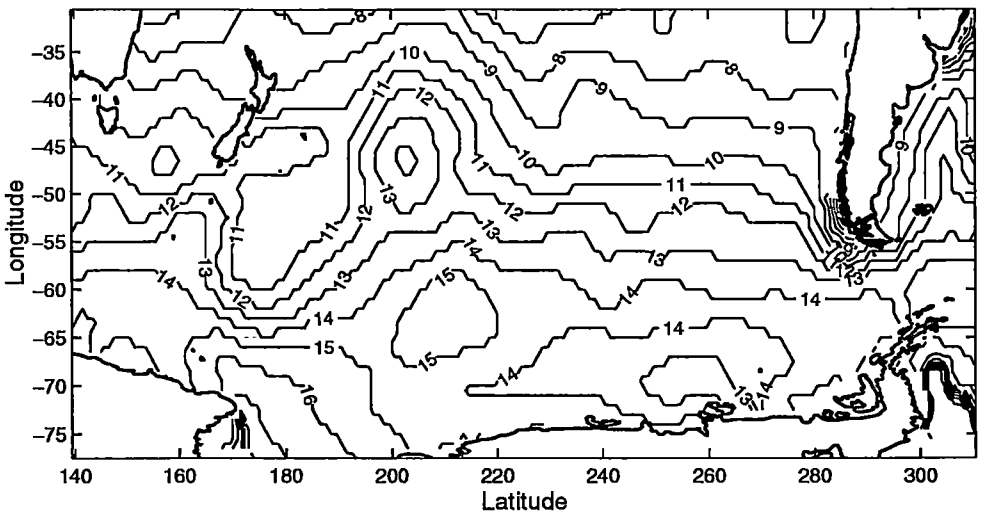

a)

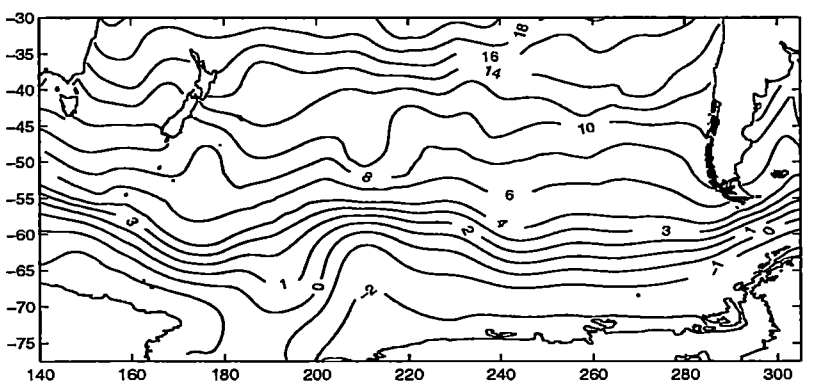

b)

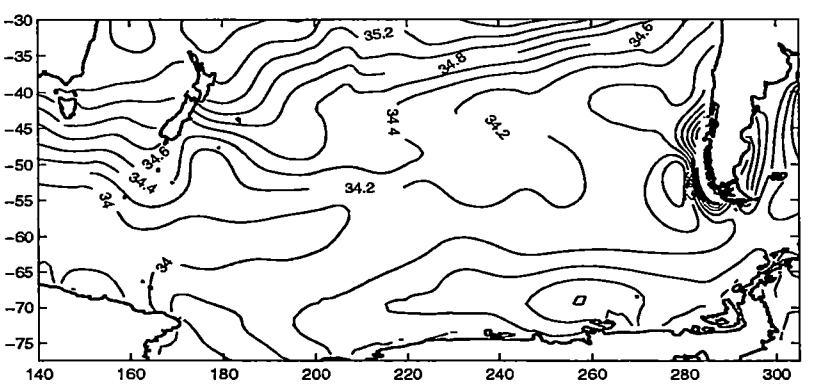

c)

Figure 5.71: Southern Ocean Pacific (BVI) sector June sea-surface a) neutral density outcropping position, contour label are neutral surface numbers b) temperature (°C) and c) salinity (psu)

transport of the deep (16 to 19, CDW) layers of the deep western boundary current in the Southwest Pacific basin. The deep and bottom water moving northwards into the Pacific basin are converted into slightly less dense NPDW (layers 16 and 17) and lower intermediate water which subsequently return to the Southern Ocean Pacific sector as low oxygen NPDW in the Tasman Sea and east 240°W in the eastern Pacific basin. The increased northward flow of CDW water results in an increased northward flux of silica and an increase in size of the deep overturning circulation from $24\times10^{6}m^{3}s^{-1}$ 32 $\times10^{6}m^{3}s^{-1}$. Previous estimates of the deep overturning circulation in the Pacific vary from $7\times10^{6}m^{3}s^{-1}$ to $20\times10^{6}m^{3}s^{-1}$ (Warren 1981b; Wunsch et al. 1983; Macdonald 1993; Macdonald 1995).

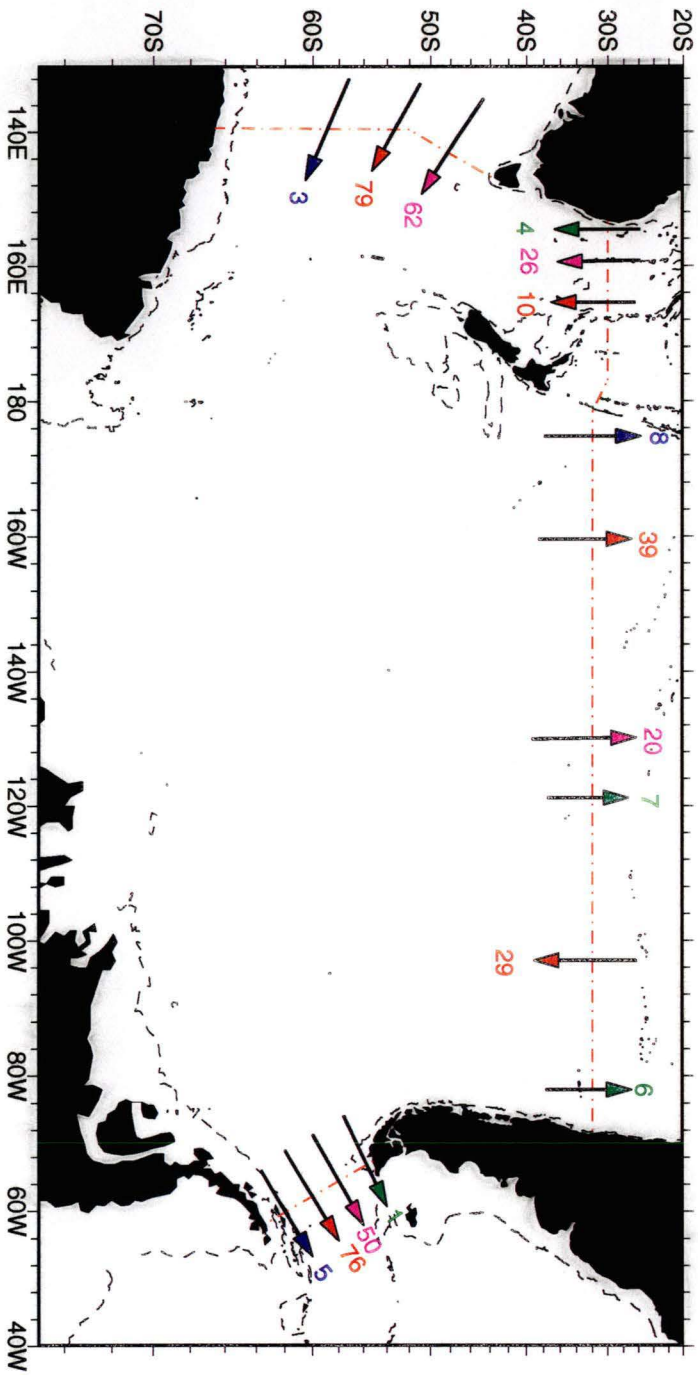

Figure 5.72: Transport ($\times 10^6 m^3 s^{-1}$) of particular layers in the Pacific Region. Thermocline layers 5 to 10 (green), Intermediate layers 11 to 15 (magenta), Deep layers 16 to 19 (red), and Bottom layers 20 to 22 (dark blue). Dashed line 1000 dbar contour.

5.5 Concluding Remarks

The model presented in this chapter is the first inverse model, to my knowledge, that gives estimates of water mass formation by air-sea fluxes and interior "consumption" rates. The partitioning of the dianeutral property fluxes into sea-surface (by air-sea forcing) and interior processes results in changes to the lateral property fluxes at the hydrographic boundaries. (The reader is reminded that the interior dianeutral fluxes include near-surface processes including dianeutral fluxes in the surface mixed layer as well as basin dianeutral fluxes). The inverse method makes only small corrections to the COADS heat, GASP freshwater climatologies and Ekman transports (resulting from the Hellerman and Rosenstein wind data), apart from the far Southern Ocean Pacific region. The important result of partitioning of the dianeutral property fluxes into sea-surface and interior dianeutral fluxes is that I am able to determine and quantify the mechanisms which result in water mass formation and conversion.

In the subtropical Atlantic (BI) the interior dianeutral salt flux into SAMW/AAIW from the overlying thermocline (-500$\times 10^6$ psu $m^3 s^{-1}$) represents the mechanism by which the salinity of these layers increase as they move northwards in the subtropical gyre. In the Southern Ocean Atlantic (BII) sector there is a transfer of AASW and AAIW into SAMW by both sea-surface and interior dianeutral fluxes. AASW ($8\times 10^6 m^3 s^{-1}$) is converted to SAMW and lower thermocline water by sea-surface processes. The interior dianeutral fluxes ($8\times 10^6 m^3 s^{-1}$) redistribute the sea-surface produced thermocline water into SAMW density water. Essentially all of the net production of SAMW ($8\times 10^6 m^3 s^{-1}$) in the Southern Ocean Atlantic sector is exported to the subtropical Atlantic in the eastern Cape basin. The export of SAMW into the subtropical Atlantic results in the difference in eastward transport of intermediate water between Drake Passage ($50\times 10^6 m^3 s^{-1}$) and south of Africa ($45\times 10^6 m^3 s^{-1}$). The net export of SAMW into the subtropical Atlantic highlights that it is SAMW which essential ventilates the subtropical gyre. The dianeutral heat and salt fluxes, in the Southern Ocean Atlantic sector, from the thermocline into SAMW are responsible for the warming and increased salinity

of SAMW which is exported to the subtropical Atlantic.

The warm, slightly fresher thermocline water ($15\times10^6 m^3 s^{-1}$) that moves southward across 18°S in Indian Ocean is transfered into lower thermocline water by sea-surface transformations. The air-sea modified thermocline water moves southward into the Southern Ocean Indian sector across 32°S in the Agulhas Current. In the Southern Ocean Indian sector the combination of sea-surface ($4\times10^6 m^3 s^{-1}$) transformation and interior ($6\times10^6 m^3 s^{-1}$) dianeutral flux transfers $10\times10^6 m^3 s^{-1}$ of thermocline Agulhas (Indian) water into SAMW. As the SAMW moves eastward with the ACC Antarctic surface water ($27\times10^6 m^3 s^{-1}$) is advected across the Polar Front Zone by sea-surfaces processes resulting in the cooling and freshening of SAMW/AAIW in the Southern Ocean Indian sector. The downward interior dianeutral mass flux across SAMW and AAIW "consumes" approximately $11\times10^6 m^3 s^{-1}$ of the sea-surface production transferring it into denser AAIW and deep layer. The sea-surface and interior dianeutral fluxes acting across thermocline layers and the net production of SAMW from sea-surface processes across the Polar Front Zone results in a total production of SAMW/AAIW ($25\times10^6 m^3 s^{-1}$) in the Southern Ocean Indian sector. Of the $25\times10^6 m^3 s^{-1}$ of SAMW/AAIW produced in the Southern Ocean Indian sector, $10\times10^6 m^3 s^{-1}$ of principally SAMW is exported into the subtropical Indian Ocean in the Crozet, Central and Perth basins highlighting that SAMW is the main water mass that ventilates the subtropical gyre. The remaining $15\times10^6 m^3 s^{-1}$ is exported into the Southern Ocean Pacific sector south of Australia accounting for the increased eastward transport of intermediate water south of Australia ($62\times10^6 m^3 s^{-1}$) relative to south of Africa ($45\times10^6 m^3 s^{-1}$).

In the Southern Ocean Pacific (BVI) sector SAMW is transferred into warmer thermocline water by sea-surface ($12\times10^6 m^3 s^{-1}$) with only a small "consumption" by downward dianeutral interior fluxes ($2\times10^6 m^3 s^{-1}$). The thermocline water moves north across 32°S into the Pacific Ocean. It is these sea-surface and interior dianeutral fluxes that show the circulation path of Indonesian throughflow water between the Indian and Pacific Oceans, describing it, essentially, as a circum-Australia circulation. Sea-surface transformation of AASW ($8\times10^6 m^3 s^{-1}$) to SAMW is completely "consumed"

by larger downward dianeutral interior fluxes ($12\times10^6 m^3 s^{-1}$). This results in a small net production of AAIW in the Southern Ocean Pacific sector. As highlighted previously a large area of the southeast Southern Ocean Pacific sector has the appropriate sea-surface temperature and salinity values of SAMW/AAIW. The sea-surface and interior dianeutral processes, in the southeast Pacific, may act to homogenise the SAMW/AAIW properties without resulting in changes in neutral density, accounting for the small mass, heat and salt convergence between SAMW and AAIW shown in this study.

The addition of the air-sea fluxes results in a similar overall circulation in the Atlantic region when compared to the previous model (model_int). In the Indian region the same size ($25\times10^6 m^3 s^{-1}$) deep overturning circulation is maintained but in this model the conversion of AABW and CDW to IDW and intermediate water occurs in both the subtropical Indian Ocean (between 18°S and 32°S) and north of 18°S. The strength of the Pacific deep overturning circulation is increased to $30\times10^6 m^3 s^{-1}$ (from $24\times10^6 m^3 s^{-1}$ in model_int). This may result from inconsistent COADS heat flux estimates highlighted by the inverse corrections applied to the heat flux in this region. (Although the inverse methods adds small corrections to the freshwater and heat fluxes at the outcropping neutral surfaces these correction when integrated must equal the total box divergence of heat and freshwater prescribed by their climatologies). The increased overturning circulation results in a large northward flux of silica ($1539.5 \pm 1300.3 kmols^{-1}$) which is not consistent with recent studies (Trèguer et al. 1995). These studies show that the Southern Ocean is a sink of silica which is input into the marine environment principally by equatorial and temperate rivers. The estimated sink of silica into marine sediments in the Southern Ocean would result a total southward flux of $170 kmols^{-1}$ of silica at 30°S.

The addition of the air-sea fluxes to the inverse model results in a global meridional heat flux at 30°S of -0.55 PW. This southward heat flux is smaller than previous estimates of $-0.9 \pm 0.3 PW$ (Macdonald and Wunsch 1996), -1.62 PW (Hsiung 1985) and, -1.75 PW (Hastenrath 1982). The freshwater divergence between SAVE2 and SAVE4 of $0.56\times10^9 kgs^{-1}$ and between Ind18 and Ind32 of $0.31\times10^9 kgs^{-1}$ are slightly larger and smaller than freshwater

divergences estimated by Wijffels et al. (1992), respectively.

This chapter shows that it is possible to partition the dianeutral property fluxes into sea-surface and interior dianeutral fluxes. The model shown in this chapter is used to test alternative circulation hypotheses in Chapter 6.

Chapter 6

Testing Alternative Circulation Hypotheses

Ocean circulation theories can easily be tested using inverse models. Using the previous inverse model (model_surf), this chapter examines the differences in the circulation when a smaller southward heat flux is imposed on the Weddell Sea and what circulation changes result when a large northward Malvinas Current is imposed immediately adjacent to the South American coast. Finally I discuss the thermocline and intermediate inter-basin exchanges between the Atlantic, Indian and Pacific Basins resulting from these experiments.

6.1 Decreasing the Weddell Sea Heat Flux

The size of the overturning Weddell Sea circulation is dependent on the imposed heat flux in the region. In the previous models (model_int and model_surf) the Weddell Sea heat flux was constrained to be 31 Wm^{-2} (0.1PW) based on Gordon (1981b). An estimated heat flux of 31 Wm^{-2} (0.1PW) results in an overturning cell of $18{\times}10^{6}m^{3}s^{-1}$, which includes an outflow of $6.5{\times}10^{6}m^{3}s^{-1}$ of Weddell Sea Deep water and $12{\times}10^{6}m^{3}s^{-1}$ of Weddell Bottom Water. Recent estimates of the heat flux over the Weddell Sea vary from 10 Wm^{-2} to 41 Wm^{-2} (Gordon 1981b; Gordon and Huber 1990; Fahrbach et al. 1994; Barnier et al. 1995). These studies suggest that higher heat flux values (41 to 31 Wm^{-2}) are representative of the winter heat flux, while the lower values (20 to 10 Wm^{-2}) are representative of the annual mean heat flux over the Weddell Sea.

In this model (model_wsh) the smaller estimated heat flux of 16 Wm^{-2} from Gordon and Huber (1990) is used as a constraint across the Weddell Sea, while still maintaining a net zero mass flux across the section. This heat flux corresponds to an actual heat loss, over the Weddell Sea of 0.05 PW.

6.1.1 Resultant Circulation

Constraining the heat flux into the Weddell Sea to the smaller annual mean heat flux of Gordon and Huber (1990) (16 Wm^{-2}) results in an overturning circulation in the Weddell Sea of $11\times10^{6}m^{3}s^{-1}$. The $12\times10^{6}m^{3}s^{-1}$ overturning cell is composed of a northward flux, into the Southern Ocean Atlantic sector, of $2\times10^{6}m^{3}s^{-1}$ Weddell Sea Deep Water and $10\times10^{6}m^{3}s^{-1}$ Weddell Sea Bottom Water.

The total property flux across each of the other sections is the same as previous models. The reader is referred to Appendix F, Table F.1 to Table F.7 for individual total section property fluxes. The major change in the layer property fluxes is seen at the SAfrica section in the deep (layers 17 to 19) and bottom (layers 20 to 22) layers. The total mass flux (of $132\times10^{6}m^{3}s^{-1}$) is maintained but there is a decrease in the eastward transport of bottom water from $0.4\times10^{6}m^{3}s^{-1}$ (model_surf) to $-2\times10^{6}m^{3}s^{-1}$ in the Current model (model_wsh). The small westward bottom water transport results from the difference between small eastward flow in layer 20 and opposing westward flow in extreme Weddell Sea deep and bottom water (layers 21 and 22) (Appendix F, Table F.4). The small westward flow of bottom water is balanced by a slight increase in eastward flow within all deep (16 to 19) and intermediate (11 and 15) layers Figure 6.1 shows that the small increases in transport in the deep layers (16 to 19) result from smaller southward transports of these layers into the Weddell Sea and an increased downward dianeutral flux across deep layers (19 and 18). These results highlight that the reduced bottom flow is compensated by small increases ($< 0.5\times10^{6}m^{3}s^{-1}$) within all deep and intermediate layers, maintaining the total section fluxes across bounding hydrographic sections. The larger downward dianeutral mass fluxes from deep layers (17, 18 and 19) compensates the smaller upward flux from Weddell Sea Deep and Bottom water (21 an 22), resulting in only a small decrease in

eastward flow of AABW (layer 20).

In the previous models (model_int and model_surf) the small northward transport of AABW (layer 19) in the Angola Basin at SAVE2 is contrary to previous studies (Warren and Speer 1991; McCartney and Curry 1993). In this model there is a slight increase in the southward transport of AABW ($0.98\times10^{6}m^{3}s^{-1}$) in the Angola Basin (from $0.56\times10^{6}m^{3}s^{-1}$ in model_surf), in agreement with those earlier studies.

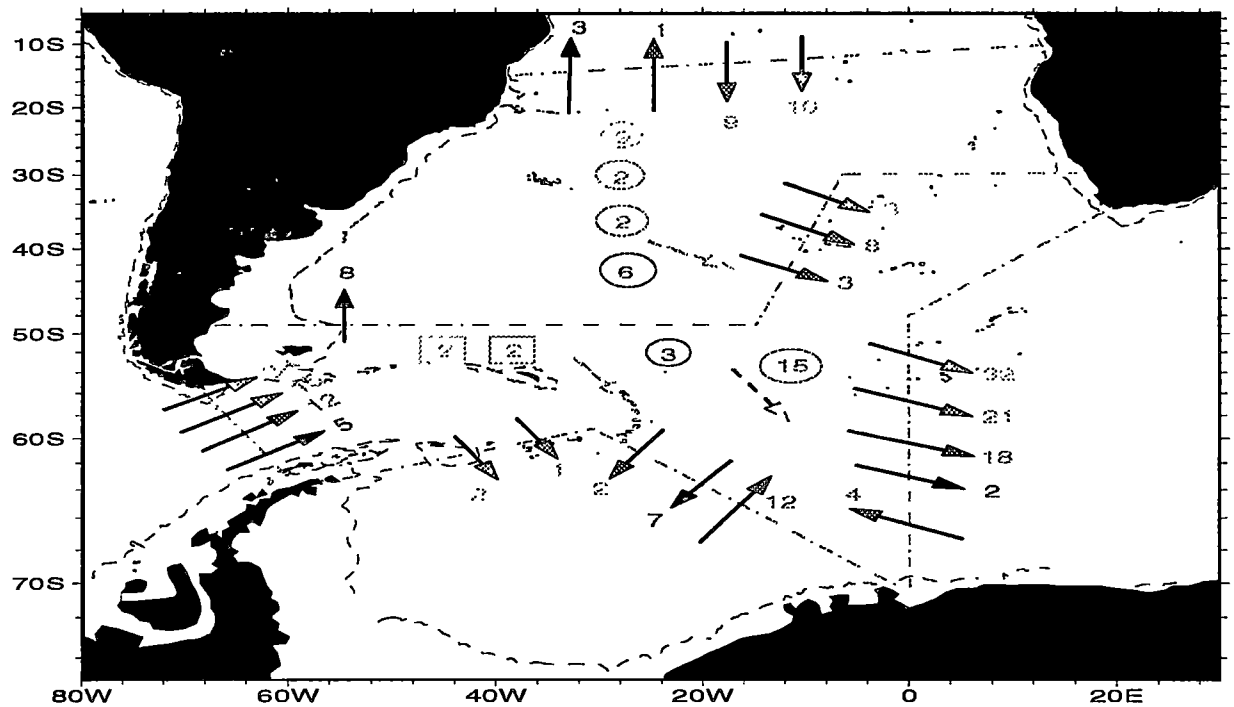

Figure 6.1: Mass transport and dianeutral flux ($\times 10^6 m^3 s^{-1}$) within Deep and Bottom water in the Atlantic Region (BI,BII) for model_wsh. Upward Dianeutral flux- circle, Downward Dianeutral Flux - square, dashed arrow represent net production within layers due to dianeutral flux. UCDW/NADW (layer 17, light blue), UCDW/NADW/LCDW (layer 18, green), LCDW/AABW (layer 19, magenta), AABW (layer 20, dark blue), and extreme AABW (layer 21 and 22, red)

6.1.2 Comments

Halving the total heat flux into the Weddell Sea results in a smaller overturning circulation in the Weddell Sea. The smaller input of Weddell Sea Deep and Bottom water does not dramatically change the circulation in the Southern Ocean Atlantic sector or adjoining regions. Small increases in the eastward flow of intermediate and deep water maintain the overall eastward flow south of Africa. Larger downward dianeutral mass fluxes across deep layers (18 and 19), in the Southern Ocean Atlantic sector, partially compensate the decreased production of AABW, so that the eastward flow of AABW (layer 20) south of Africa is almost unchanged.

The larger estimated Weddell Sea Heat Flux applied in model_int and model_surf of 31 Wm^{-2} comes from an early study of Gordon (1981b). Recent studies by Gordon and Huber (1990), Fahrbach et al. (1994) and Barnier et al. (1995) estimate mean annual Weddell Sea heat fluxes of 16 Wm^{-2}, 19 Wm^{-2} and 10 Wm^{-2}, respectively, while Gordon and Huber (1990) estimate a winter heat flux of 41 Wm^{-2}. This suggests that higher heat flux values (41 Wm^{-2} and 31 Wm^{-2}) are representative of the winter heat flux, while the lower values (20 to 10 Wm^{-2}) are indicative of the the annual mean heat flux over the Weddell Sea. Therefore within this inverse model, in which the mean circulation is derived, it is more appropriate to use the smaller heat flux estimates in the Weddell Sea.

6.2 Large Northward Malvinas Current

As discussed in Chapter 4, Section 4.3 the northward Malvinas Current transports, immediately adjacent to the South American coast, is $19\times10^6 m^3 s^{-1}$, and in model_surf $18\times10^6 m^3 s^{-1}$. These northward transport agrees with previous estimates (Gordon and Greengrove 1986; Piola and Bianchi 1990). The size of the northward transport associated with the Malvinas Current has recently been questioned by Peterson and Stramma (1991) and Peterson (1992). They show the connection between the water north of the Subantarctic Front (SAF) in the Drake Passage and the Malvinas Current. The continuity of water properties from Drake Passage to the northward Malvinas Current is shown by

the depth of the 4°C isotherm, which can be used to identify the position of the SAF (Figure 6.2). Peterson and Stramma (1991) and Peterson (1992) argue that because the Malvinas Current is the northward extension of the SAF, the Malvinas Current transport must be close to the transport north of the SAF in Drake Passage: $60\times10^{6}m^{3}s^{-1}$ to $70\times10^{6}m^{3}s^{-1}$.

The inverse method allows us to easily impose a large northward Malvinas Current and analyse the resultant circulation. Changes, if any, to the circulation in the subtropical Atlantic Ocean, Southern Ocean Atlantic sector or adjacent ocean basins will enable us to determine whether a large northward Malvinas Current is consistent with our understanding of the circulation of the Southern Ocean and adjacent ocean basins.

6.2.1 Malvinas Current Constraint

The large northward Malvinas Current can be applied to the inverse method by either constraining the total mass transport in the six station pairs adjacent to the South American coast to be $60\times10^{6}m^{3}s^{-1}$, or applying a non-zero reference velocity at those station pairs such that the combined baroclinic ($12.66\times10^{6}m^{3}s^{-1}$) and barotropic transport equal the hypothesised $60\times10^{6}m^{3}s^{-1}$ northward transport. The latter method is employed here. To achieve a northward barotropic transport of $47\times10^{6}m^{3}s^{-1}$ in the six station pairs adjacent South America a non-zero reference velocity of $0.132ms^{-1}(13.2cms^{-1})$ is required. This large reference velocity is comparable to the mean current speed (10 days) of a mooring placed 91 m above the bottom (1524 m) on the northern edge of the Falkland Plateau in the SAF, of 17 cms^{-1} (Peterson and Whitworth 1989; Peterson 1992).

The reference velocity imposed on the six station pairs results in a northward barotropic transport of $47\times10^{6}m^{3}s^{-1}$, which combined with the baroclinic transport gives a total northward transport of $59.66\times10^{6}m^{3}s^{-1}$. Within this model I also constrain the northward flow of AABW (colder than 0.2°C) in the Brazil basin to be $6\times10^{6}m^{3}s^{-1}$ based on estimates of Whitworth et al. (1991) and the northward flow of water below 2000 dbars across the stations pair near the WOCE PCM9 mooring array in the Southwest Pacific basin to be $11\times10^{6}m^{3}s^{-1}$ (Whitworth et al. 1996). These additional constraints

are added to the previous model constraints (while retaining the smaller Weddell Sea heat flux of $16Wm^{-2}$).

6.2.2 Reference Velocity

The reader is reminded that the inverse model selects a solution which simultaneously minimises the misfit of the conservation equations and the deviation from the initial choice of reference velocity. In this model (model_malv) the initial choice of reference velocity is $0.132ms^{-1}$ at the first six stations pairs adjacent to the South American coast and $0ms^{-1}$ for the remaining station pairs. A comparison of the inverse modification to the initial choice of reference velocity, at the station pairs adjacent to the South American coast, between this model (model_malv) (Figure 6.3, upper plot) and model_int (Figure 4.3) shows that the correction in the present model is smaller than model_int. The remaining station pairs have a similar structure in both models. The absolute velocity profile between model_malv and model_int differs only at the six station pairs adjacent to South America, with larger northward velocities evident in model_malv (Figure 6.3 and Figure 4.3, lower plot).

6.2.3 Property Fluxes and Resultant Circulation

The total section property fluxes are shown in Table 6.1. There are some significant changes to the total section property fluxes across most sections when compared to the previous model (model_surf). These include changes to the mass, heat and salt fluxes at SAVE2 and SAVE4, larger eastward property fluxes at Drake Passage and south of Africa and smaller property fluxes south of Australia. There is also a decrease in the south and north meridional property fluxes across the Indian (Ind18 and Ind32) and the Pacific 32°S sections, respectively.

Atlantic

The layer mass flux at SAVE2, SAVE4, DrakeP, SAfrica and Wedsea are shown in Figure 6.4. At SAVE2 notable changes to the mass flux occurs within deep and bottom layers. The southward transport of NADW (layers 16,17 and 18) across SAVE 2 in this model (model_malv) agrees with previous models

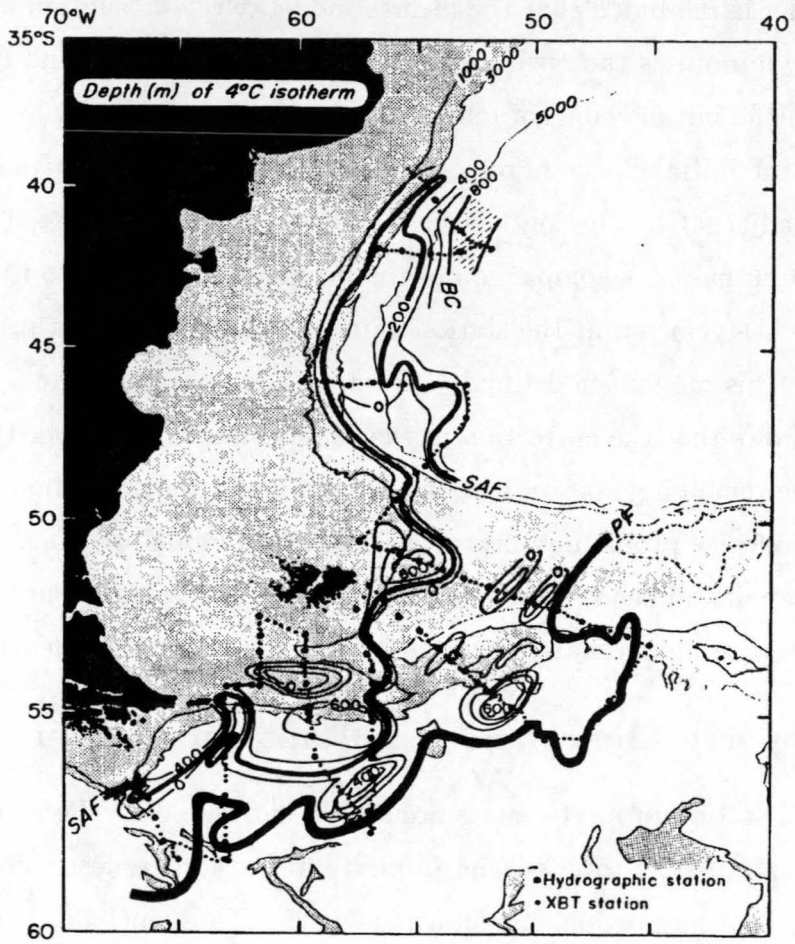

Figure 6.2: Depth of the 4°C isotherm (m) observed from the R/V *Atlantis II* during the austral winter of 1980. The course of the Subantarctic Front (SAF) is approximated by the 200m contour, while the Polar Front (PF) is depicted with the heaviest line. The hatched area represents central water bounded by the Brazil Current (BC) (from Peterson and Stramma 1991)

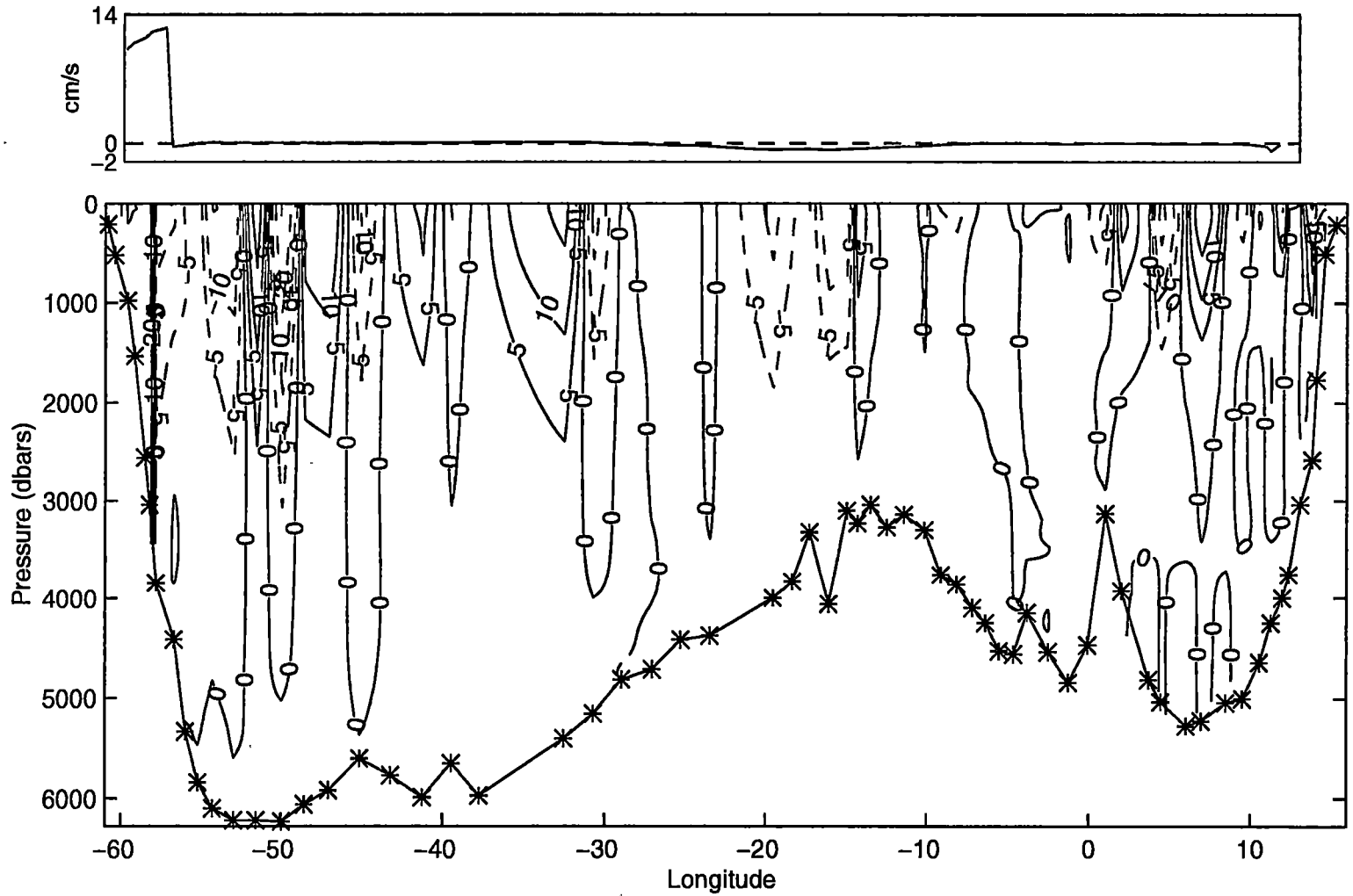

Figure 6.3: Absolute velocity SAVE 4 ($cms-1$) for model with an imposed large Malvinas velocity. Solid and dashed contours refer to north and south velocities, respectively. Upper plot is reference level velocity ($cms-1$).

section	Mass($\times 10^6 m^3 s^{-1}$)	Heat($\times 10^6$ °C $m^3 s^{-1}$)	Salt($\times 10^6 kg s^{-1}$)	Freshwater($\times 10^9 kg s^{-1}$)	Silica ($kmol s^{-1}$)
SAVE2	-0.74±11.4	114.19±49.4	-26.79±45.0	-0.83±11.3	13.38±474.5
SAVE4	-0.36±10.3	79.51±30.7	-11.68±134.6	-0.40±10.2	149.57±707.3
Drake P	133.40±1.2	339.11±2.1	4732.2±17.9	132.67±1.2	8975.2±117.9
S. Africa	133.4±6.4	274.38±12.6	4739.9±79.2	132.99±6.3	8625.8±560.5
Weddell Sea	0.03±3.6	-12.59±1.4	0.24±48.1	0.04±3.6	23.26±456.49
Ind18	-8.30±5.1	-315.59±25.7	-295.15±44.7	-8.13±5.0	690.74±485.4
Ind32	-7.98±7.6	-218.07±42.9	-283.79±65.8	-7.822±7.6	625.15±469.6
S. Aust	141.98±3.4	437.29±7.8	5033.8±47.6	141.10±3.4	7719.5±278.6
Pac32	8.86±14.2	21.98±60.7	316.72±190.48	8.84±14.1	1241.9±1173.9

Table 6.1: Total property fluxes across all sections for imposed large Malvinas transport. +ve - northward or eastward flux, -ve -southward or westward flux. Units: mass $\times 10^6 m^3 s^{-1}$ and heat $\times 10^6$ °C $m^3 s^{-1}$ calculated relative to 0°C, salt $\times 10^6 kg s^{-1}$, freshwater $\times 10^9 kg s^{-1}$ and silicate $kmol s^{-1}$

(model_int, model_surf and model_whs), but the division of this transport between the Angola and Brazil basin has changed. In this model (model_malv) most of the NADW moves southwards in the western boundary current in the Brazil basin, and only a small southward flux occurs in the Angola basin ($3\times10^{6}m^{3}s^{-1}$, layers 16 and 17). The southward transport (and magnitude) of NADW principally in the Brazil basin agrees with previous studies (Reid et al. 1977; McCartney 1993).

The mass flux of the individual layers in the Angola basin Appendix F,Table F.10) shows that the total southward flow within deep layers results from southward flow within layer 16 and 17 (1000 to 2000 dbars) and opposing smaller northward flow within layer 18. Warren and Speer (1991) suggest a southward flow at 2000 dbars (layers 16 and 17) and estimate a northward flow between 2400 and 4000 dbars (layer 18) of $1.76\times10^{6}m^{3}s^{-1}$. In the Angola basin, AABW (layer 19) transport is southward ($1.93\times10^{6}m^{3}s^{-1}$) is slightly larger than the southward transport within model_surf and model_wsh. The weak southward AABW transport in this model (and model_surf and model_wsh) is consistent with previous studies which indicate a southward transport of AABW in the northern Angola basin (Warren and Speer 1991; McCartney and Curry 1993).

At SAVE4 major changes to the property flux occur within deep (layer 16 to 19) and intermediate (layer 11 to 15) water in the Argentine basin and over the mid-Atlantic ridge and deep water (layer 16 to 18) in the Cape basin (Figure 6.4). The northward transport of intermediate water entering the subtropical Atlantic (BI) in the Argentine basin is increased. There is also an equivalent increase in the southward flow of intermediate water over the mid-Atlantic ridge. The increase of intermediate water transport in the Argentine basin and over the mid-Atlantic ridge reflects the effect of the large Malvinas Current constraint, which forces intermediate water northward in the Malvinas Current. The intermediate water then turns eastward with the SAF, near the Brazil-Malvinas Confluence zone, and returns to the Southern Ocean Atlantic over the mid-Atlantic ridge. The sharp northward turning of the SAF and subsequent eastward flow in the subtropical Atlantic has been described previously (Ikeda et al. 1989; Reid 1989; Peterson and Whitworth 1989;

Peterson and Stramma 1991)

Over the mid-Atlantic ridge the southward deep water (layer 16 to 19) flow is increased from $30\times10^6 m^3 s^{-1}$ (model_wsh) to $58\times10^6 m^3 s^{-1}$. This increase results from the increased northward flow in the Argentine basin at SAVE4 and the increased southward flow of NADW at SAVE2 in the Brazil basin. The southward flow of NADW (layer 16,17 and 18) in the Angola and Cape Basins is decreased, again due to the concentration of NADW transport near the western boundary of the Brazil basin. Although most of the NADW enters the subtropical Atlantic adjacent to the western boundary, the highest salinity NADW is found in the Angola and Cape basins (Figure 3.6). The highest salinity NADW reaches the southern Angola and Cape basins directly from the northern Angola basin, where I have already highlighted the southward flow of layers 16 and 17 over the Guinea Rise. NADW that forms the deep branch of the Brazil Current flows adjacent to the coast to 40°S, at which point it continues to flow southward but is displaced offshore by the northward flowing CDW in the Malvinas Current (Reid et al. 1977). The juxtaposition of northward flowing CDW and southward flowing NADW form a deep extension of the Brazil-Malvinas Confluence (surface Brazil-Malvinas Confluence is found between 32°S and 38°S) (Georgi 1981). Provost et al. (1995) highlight strong mixing between NADW and CDW over the South American continental slope. The mixing between CDW and NADW results in the dilution of NADW salinity and oxygen characteristics in the Argentine basin, which is shown by the reduced salinity and oxygen maxima of NADW over the mid-Atlantic ridge at SAVE 4 where NADW enters the Southern Ocean (Figure 3.5 and Figure 3.7). The mixing of NADW with CDW also accounts for the increase in salinity and oxygen concentration between CDW entering the Southern Ocean Atlantic sector via Drake Passage and CDW which moves southward across the mid-Atlantic ridge (Figure 3.6, Figure 3.7, Figure 3.10 and Figure 3.11).

The strength of the Antarctic Circumpolar Current (ACC) at Drake Passage and south of Africa is increased by $1\times10^6 m^3 s^{-1}$ from $132\times10^6 m^3 s^{-1}$, in previous models to $133\times10^6 m^3 s^{-1}$ in this model. The increase is contained in the deep layers (Figure 6.4).

Figure 6.5 shows the dianeutral mass flux occurring between deep and

bottom water layers in the subtropical Atlantic and Southern Ocean Atlantic sector. The direction of the dianeutral mass flux across layers is the same as previous models (Appendix E, Figure 6.1) but the magnitude of these dianeutral fluxes is smaller or larger across particular neutral surfaces. There is a smaller upward dianeutral flux and a larger upward dianeutral flux from AABW (layer 20) within the subtropical Atlantic. In the Southern Ocean Atlantic sector there is a larger downward dianeutral flux across all deep layers (17 and 18). These dianeutral fluxes result in small changes in the mass flux of individual layers in the deep and bottom water classes.

In model_surf the heat flux across SAVE4 is 0.33±0.11 PW this model increases the heat flux, slightly, to 0.34±0.13 PW). The increased northward heat flux at SAVE4 results from a decreased southward heat flux within deep water (layers 16 to 19) (Figure 6.6), while the increased northward heat flux at SAVE2 results from a small increase in the northward heat flux within intermediate water (layers 11 to 15) and thermocline water (layers 5 to 10).

Within this model the southward salt flux is increased across SAVE4 to $12 \pm 134 \times 10^6 kgs^{-1}$ which results in an improved salt balance within the subtropical Atlantic (Figure 6.7). This southward salt flux at SAVE2 ($24 \pm 46 \times 10^6 kgs^{-1}$) is similar to the Atlantic salt flux calculated by Wijffels et al. (1992).

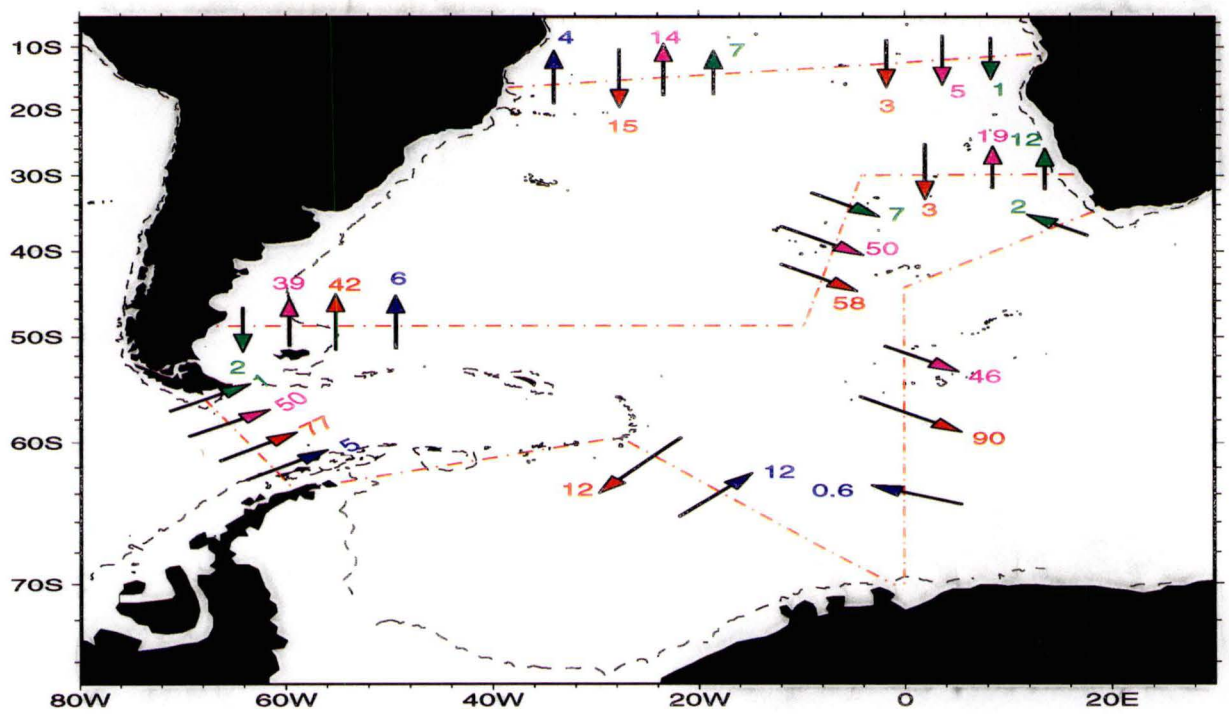

Figure 6.4: Transport ($\times 10^6 m^3 s^{-1}$) of particular layers in the Atlantic Region for the model_malv. Thermocline layers 5 to 10 (green), Intermediate layers 11 to 15 (magenta), Deep layers 16 to 18 across SAVE2, SAVE4 and 16 to 19 across Drake Passage, south Africa and Weddell Sea (red) and Bottom layers 20 to 22 (dark blue)

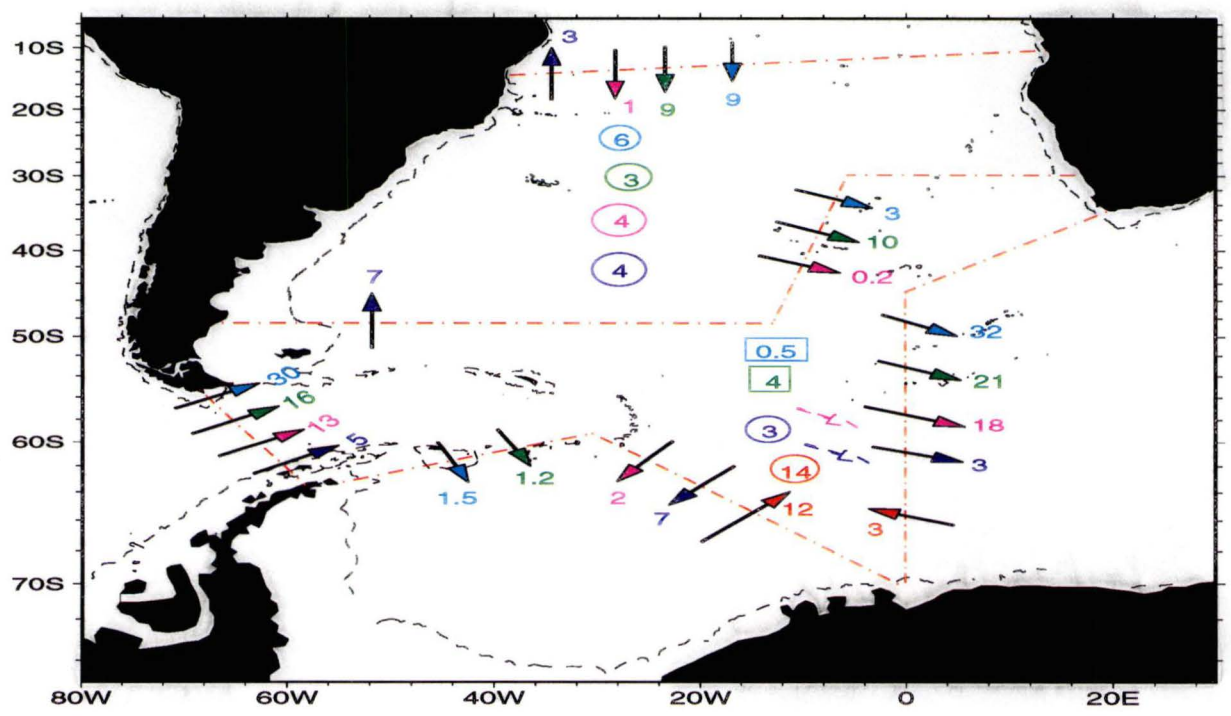

Figure 6.5: Mass transport and dianeutral flux ($\times 10^6 m^3 s^{-1}$) within Deep and Bottom water in the Atlantic Region (BI,BII) for the model_malv. Upward Dianeutral flux- circle, Downward Dianeutral Flux - square, dashed arrow represent net production within layers due to dianeutral flux. UCDW/NADW (layer 17, light blue), UCDW/NADW/LCDW (layer 18, green), LCDW/AABW (layer 19, magenta), AABW (layer 20, dark blue), and extreme AABW (layer 21 and 22, red).

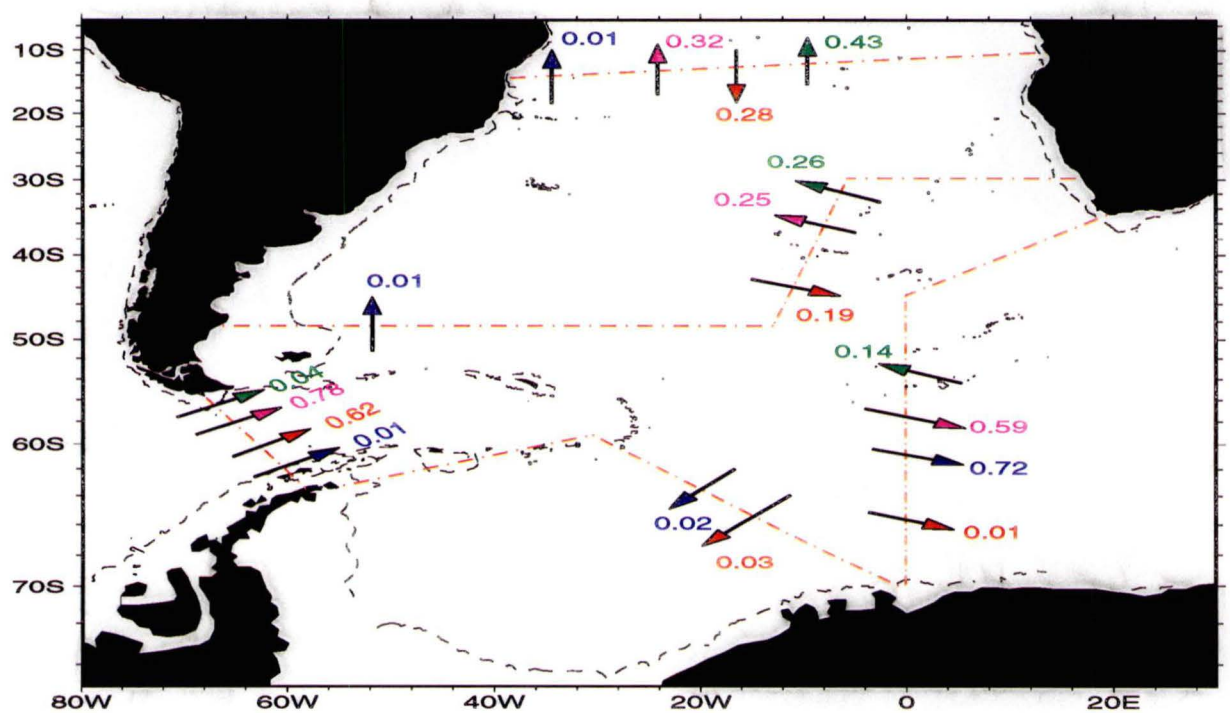

Figure 6.6: Heat flux (PW) of particular layers in the Atlantic Region for the model_malv. Thermocline layers 5 to 10 (green), Intermediate layers 11 to 15 (magenta), Deep layers 16 to 18 across SAVE2, SAVE4 and 16 to 19 across Drake Passage, south Africa and Weddell Sea (red) and Bottom layers 20 to 22 (dark blue)

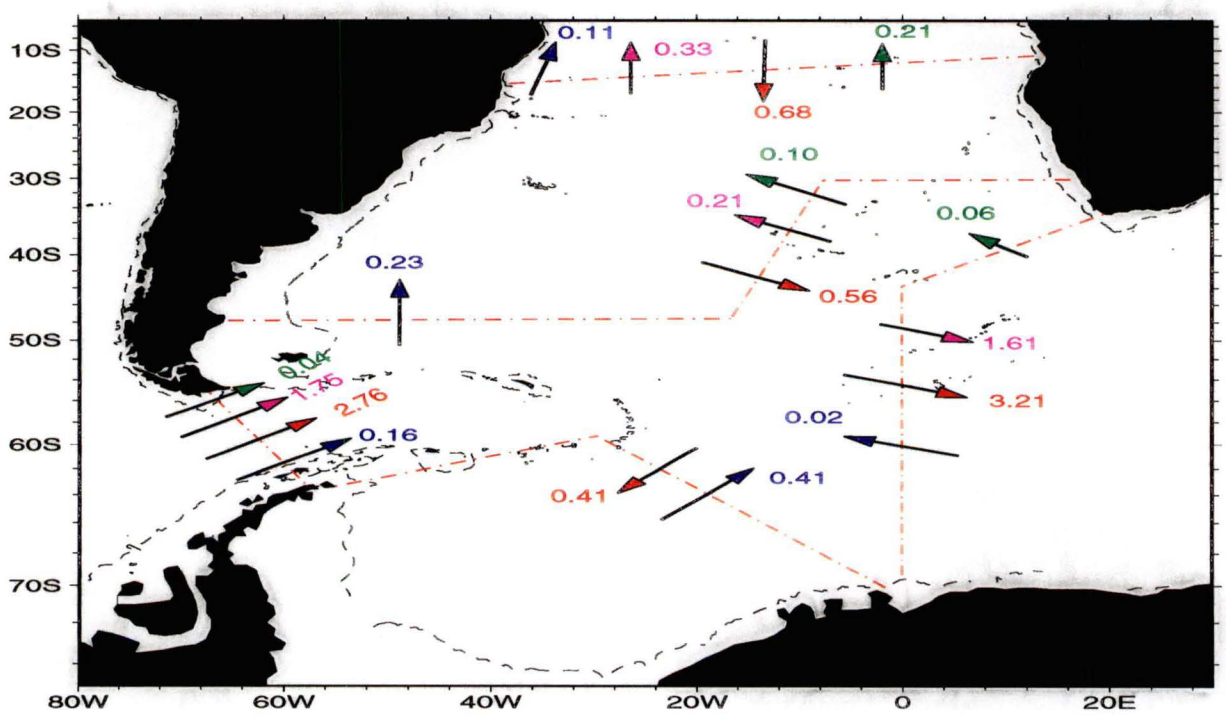

Figure 6.7: Salt flux ($\times 10^{-9} kg.s^{-1}$) of particular layers in the Atlantic Region for the model_malv. Thermocline layers 5 to 10 (green), Intermediate layers 11 to 15 (magenta), Deep layers 16 to 18 across SAVE2, SAVE4 and 16 to 19 across Drake Passage, south Africa and Weddell Sea (red) and Bottom layers 20 to 22 (dark blue)

Indian

In the previous models (model_surf and model_wsh) the southward mass flux through the Indian sections, Ind18 and Ind32, is $11\pm8\times10^6 m^3 s^{-1}$. In this model the southward mass flux in the Indian Ocean is reduced to $8\pm5\times10^6 m^3 s^{-1}$. A comparison of the layer fluxes across Ind18 and Ind32 highlights water layers where the changes occur (Figure 6.8 and Figure 4.40). At Ind18 the decrease in the southward mass flux results from slight decreases ($1\times10^6 m^3 s^{-1}$) in the southward flux within the surface layers (3 and 4), western boundary thermocline (layers 5 to 10) and intermediate (layers 11 to 15) water and NIDW (layers 16 to 18) in the central basin and an increased ($2\times10^6 m^3 s^{-1}$) northward flux of deep water (layers 16 to 18) over the Central Indian ridge. At Ind32 small changes in the flux of most layers ($1\times10^6 m^3 s^{-1}$) account for the decreased southward mass flux. These include decreased mass transport in western boundary thermocline water (layers 6 to 10), intermediate water (layers 12 to 15) over Ninetyeast ridge/Broken Plateau and deep water (layers 16 to 18) in the Perth basin and increased northward bottom water (layers 19 and 20) in the combined basins west of the Ninetyeast ridge.

The size of the deep overturning cell in the Indian ocean north of 32°S in this model is similar to model_surf and model_wsh. In these models the northward flux of deep and bottom water across 32°S is similar to the initial model (model_int) but the modification of the Southern Ocean deep and bottom water to slightly less dense IDW and lower thermocline water occurs north of 18°S and between 18°S and 32°S in nearly equal proportions. Figure 6.9 shows a schematic of the overturning circulation north of 18°S of this model (model_malv). There is now a northward $13\times10^6 m^3 s^{-1}$ transport of bottom and deep water across 18°S which returns southward to the subtropical Indian Ocean as slightly less dense IDW and intermediate water. (The overturning cell of model_int is shown in Figure 4.41) The effect of the larger northward transport of deep and bottom water across 18°S results in smaller upward dianeutral fluxes across bottom and deep layers in the subtropical Indian ocean (Figure 6.10) compared to model_int dianeutral fluxes (Figure 4.42). Although the region where the conversion of Southern Ocean bottom and deep water in

this model (and model_surf and model_int) is different from model_int all model maintain the overturning cell below 1000 db. Briefly, some of the deep and bottom water which enters the subtropical Indian ocean from the south across Ind32 is converted into upper deep (layer 17 and 16) and intermediate water (layers 13 to 15) which returns to the Southern Ocean Indian sector in eastern basins. The remaining bottom (layers 19 and 20), deep (layers 18 to 16) and intermediate (layer 15 to 11) water move northward across the Ind18 section where they are converted to NIDW (layer 17 and 16) and thermocline water (layers 10 to 4) which return southward across Ind18 to the subtropical Indian Ocean in the eastern basin (NIDW) and in the East Madagascar Current (EMC) on the western boundary (thermocline, intermediate water).

The layer heat and salt flux in the Indian region are shown in Figure 6.11 and Figure 6.12, respectively. The large southward heat flux at 18°S is associated with the upper thermocline layers (3 and 4), which is dispersed into underlying thermocline layer (6 to 10) in the subtropical Indian region. The northward salt flux associated with the northward deep and bottom transport at 18°S is returned southward in IDW (layers 17 to 18) and intermediate water (layer 11 to 15), while the overall southward salt flux results from the southward transport of Indonesian through-flow water in the Indian Ocean. The heat and salt fluxes reflect the changes the total mass flux and result in decreases in the southward heat flux (-1.42±0.18 PW) and salt flux ($-401.8 \pm 74 \times 10^6 kgs{-}1$) from previous model (model_surf) to -1.35±0.11 PW and $-295.1 \pm 45 \times 10^6 kgs{-}1$ at 18°S. Assuming salt balance to calculate the size of the Indonesian through-flow, in a similar manner to Section 4.3.2, the estimated size of the Indonesian through-flow is $8.3{\times}10^6 m^3 s^{-1}$. Removing the heat flux associated with the Indonesian Throughflow (assuming a temperature of 24°C) at 30°S gives a southward het flux of -0.09 PW. The sign of the heat flux agrees with previous estimates but is smaller (Table 4.3).

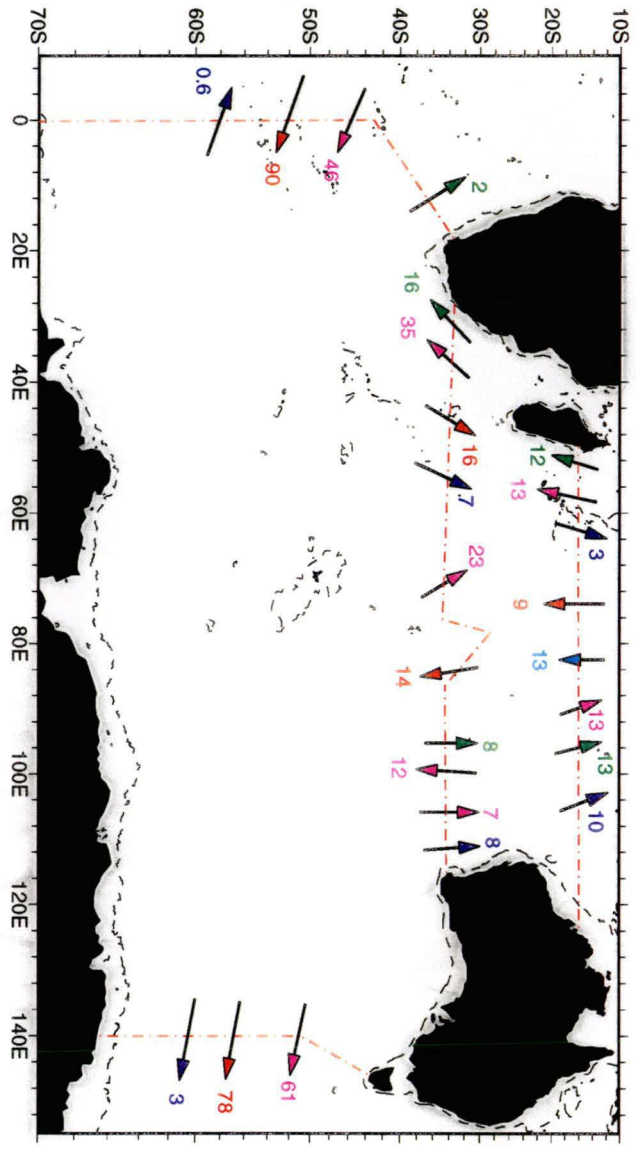

Figure 6.8: Transport ($\times 10^6 m^3 s^{-1}$) of particular layers in the Indian Region for the model_malv. Surface layers 3 and 4 (light blue), Thermocline layers 5 to 10 (green), Intermediate layers 11 to 15 (magenta), Deep layers 16 to 18 across Ind18, Ind32 and 16 to 19 south of Africa and Australia (red) and Bottom layers 20 to 22 (dark blue)

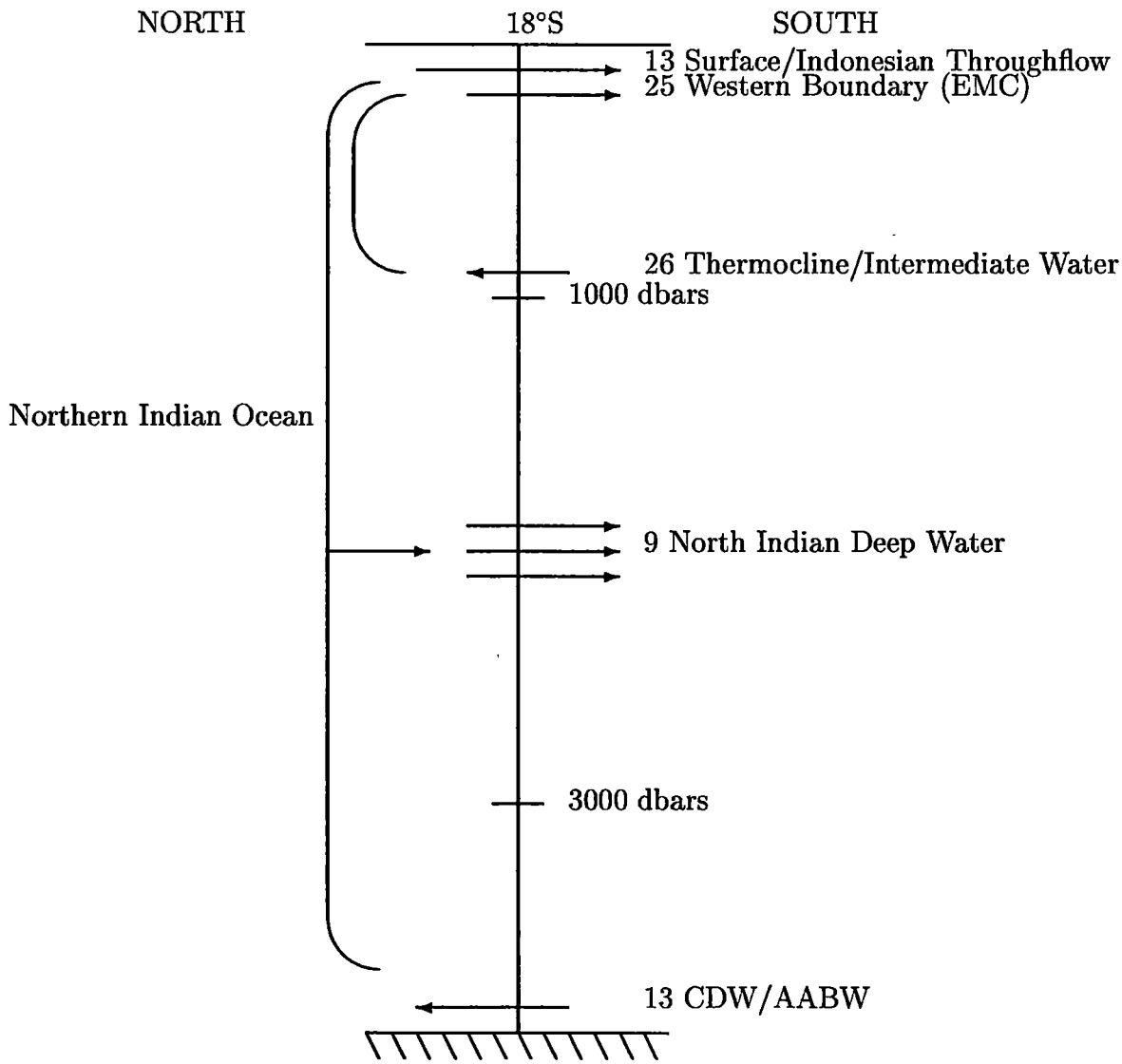

Figure 6.9: Schematic of overturning cell ($\times 10^6 m^3 s^{-1}$) north of 18°S in the Northern Indian Ocean for the model_malv. Thermocline and intermediate water moves northward across 18°S and balances the southward flow of thermocline and intermediate within the EMC. AABW and CDW move northward across 18°S. In the northern Indian Ocean dianeutral fluxes convert AABW and CDW into North Indian Deep Water and intermediate and thermocline water which flow southward across 18°S.

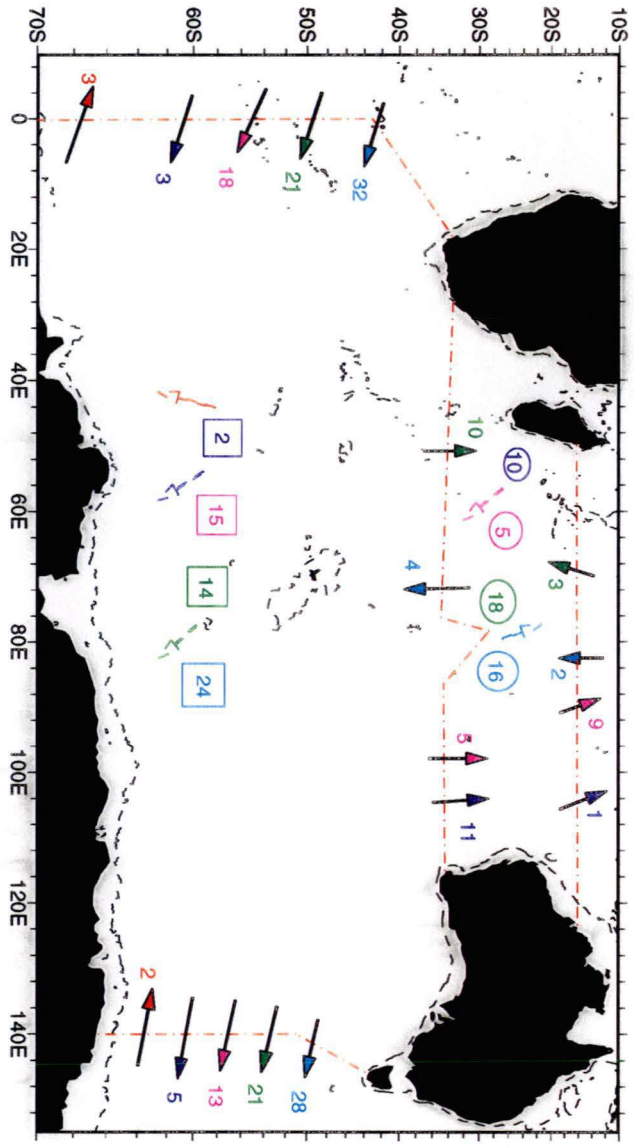

Figure 6.10: Mass transport and dianeutral flux ($\times 10^6 m^3 s^{-1}$) within Deep and Bottom water in the Indian Region for the model_malv. Upward Dianeutral flux- circle, Downward Dianeutral Flux - square, dashed arrow represent net production within layers due to dianeutral flux. UCDW/PDW (layer 17, light blue), UCDW/LCDW (layer 18, green), LCDW/AABW (layer 19, magenta), AABW (layer 20, dark blue), and extreme AABW (layer 21 and 22, red).

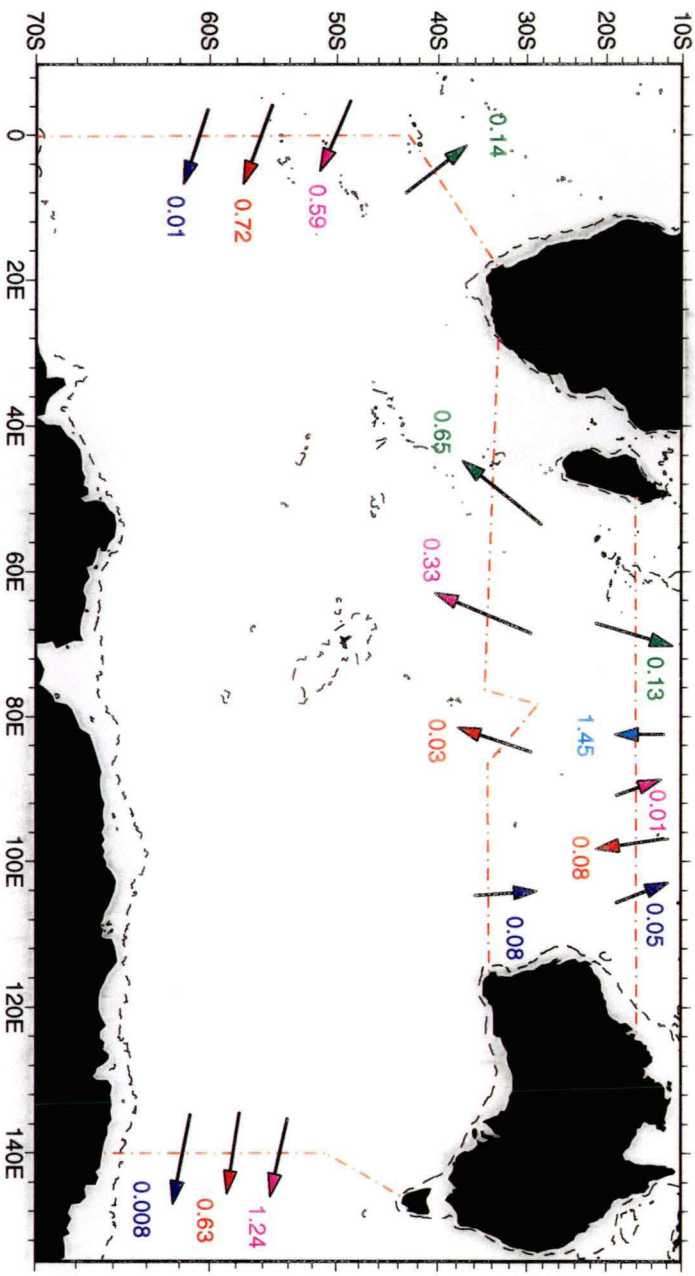

Figure 6.11: Heat flux (PW) of particular layers in the Indian Region for the model_malv. Thermocline layers 5 to 10 (green), Intermediate layers 11 to 15 (magenta), Deep layers 16 to 18 across SAVE2, SAVE4 and 16 to 19 across Drake Passage, south Africa and Weddell Sea (red) and Bottom layers 20 to 22 (dark blue)

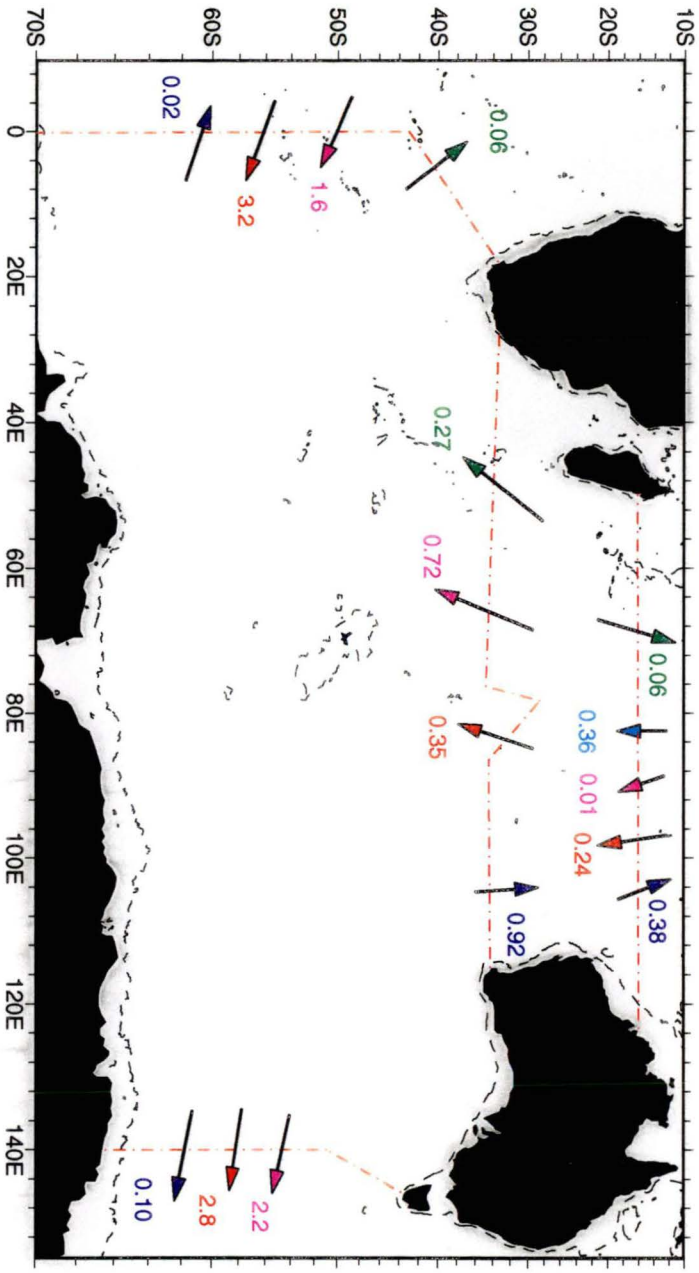

Figure 6.12: Salt flux ($\times 10^9 kgs^{-1}$) of particular layers in the Indian Region for the model_malv. Thermocline layers 5 to 10 (green), Intermediate layers 11 to 15 (magenta), Deep layers 16 to 18 across SAVE2, SAVE4 and 16 to 19 across Drake Passage, south Africa and Weddell Sea (red) and Bottom layers 20 to 22 (dark blue)

The changes to the overturning circulation in the Indian Ocean result in an increased northward silica flux across 32°south from $213 \pm 490 kmols^{-1}$ in model_int to $624 \pm 470 kmols^{-1}$ in this model (model_malv). Table 6.2 gives the comparison of layers silica flux from this model with model_int and the Toole and Warren (1993) and Robbins and Toole (1997) studies. The total southward mass flux is $8 \times 10^6 m^3 s^{-1}$ in mod_malv ($15 \times 10^6 m^3 s^{-1}$ mod_int). The northward silicate flux is larger in model_malv. The major change in the silica balance between model_malv and model_int occurs in layers 14 to 17 (T&W and R&T layers 4 and 5). The decreased southward silica flux results from smaller southward mass transport in the upper deep layers (16 and 17) between the inverse models. Figure 6.13 highlights the difference in the overturning cell between the T&W and R&T and this study. In this study the northward bottom and deep flow across 32°S is balanced by returning southward flow below 1000 dbars (layers 14 to 17). The return flow in these layers results in the small northward silica flux at 32°S.

Figure 6.14 shows a comparison of the vertical velocity for the Indian Ocean between the T&W, R&T and model_malv. (The T&W and R&T vertical velocities are interpolated onto the mean depth of the neutral surface used in this study). The vertical velocities of T&W and the R&T study are for the entire Indian Ocean north of 32°S, while the vertical velocities mod_malv are the area between 32°S and 18°S. The major difference is the large vertical velocity across the deepest neutral surface in model_malv. As Table 6.2 shows $11 \times 10^6 m^3 s^{-1}$ of bottom water (layer 20) enters the Indian Ocean in the inverse model compared to only $1 \times 10^6 m^3 s^{-1}$ in the T&W and R&T studies. Most of the $11 \times 10^6 m^3 s^{-1}$ upwells into layer 19 between 32°S and 18°S. At 18°S $10 \times 10^6 m^3 s^{-1}$ of AABW/CDW (layer 19) moves northward into the northern Indian Ocean where it is modified into IDW (layer 17 and 16), intermediate (layer 15 to 11) and thermocline water (layers 10 to 5) (Figure 6.9). Between 3000 dbars and 1000 dbars model_malv has a slightly larger vertical velocity, while the small downwelling at 600 dbars highlights that the overturning cell is contained below 1000 dbars.

Layers		Mass ($\times 10^6 m^3 s^{-1}$)				Silica ($kmols^{-1}$)			
T&W,R&T	int/malv	T&W	R&T	int	malv	T&W	R&T	int	malv
1	1-10	-21	-16	-8	-8	-97	-31	-83	-28
2	11-12	-0.7	4	-1	1	-85	-64	-68	-62
3	13	-8	-4	-5	-5	-305	-226	-147	-132
4	14-15	-5	-3	-14	-12	-316	-208	-806	-729
5	16-17	-0.5	-4	-12	-10	-73	-417	-1155	-973
6	18	11	2	10	10	731	-216	627	692
7	19	14	10	4	5	1509	1110	330	407
8	20	1	1	11	11	169	170	1463	1449
Total		-10	-10	-15	-8	1532	21	213±490	624±470

Table 6.2: A comparison of the layer silica flux ($kmols^{-1}$) and the mass transport ($\times 10^6 m^3 s^{-1}$) between Toole and Warren (1993) (T&W), Robbins and Toole (1997) (R&T), model_int and this model (mod_malv) +ve northward flux, -ve southward flux

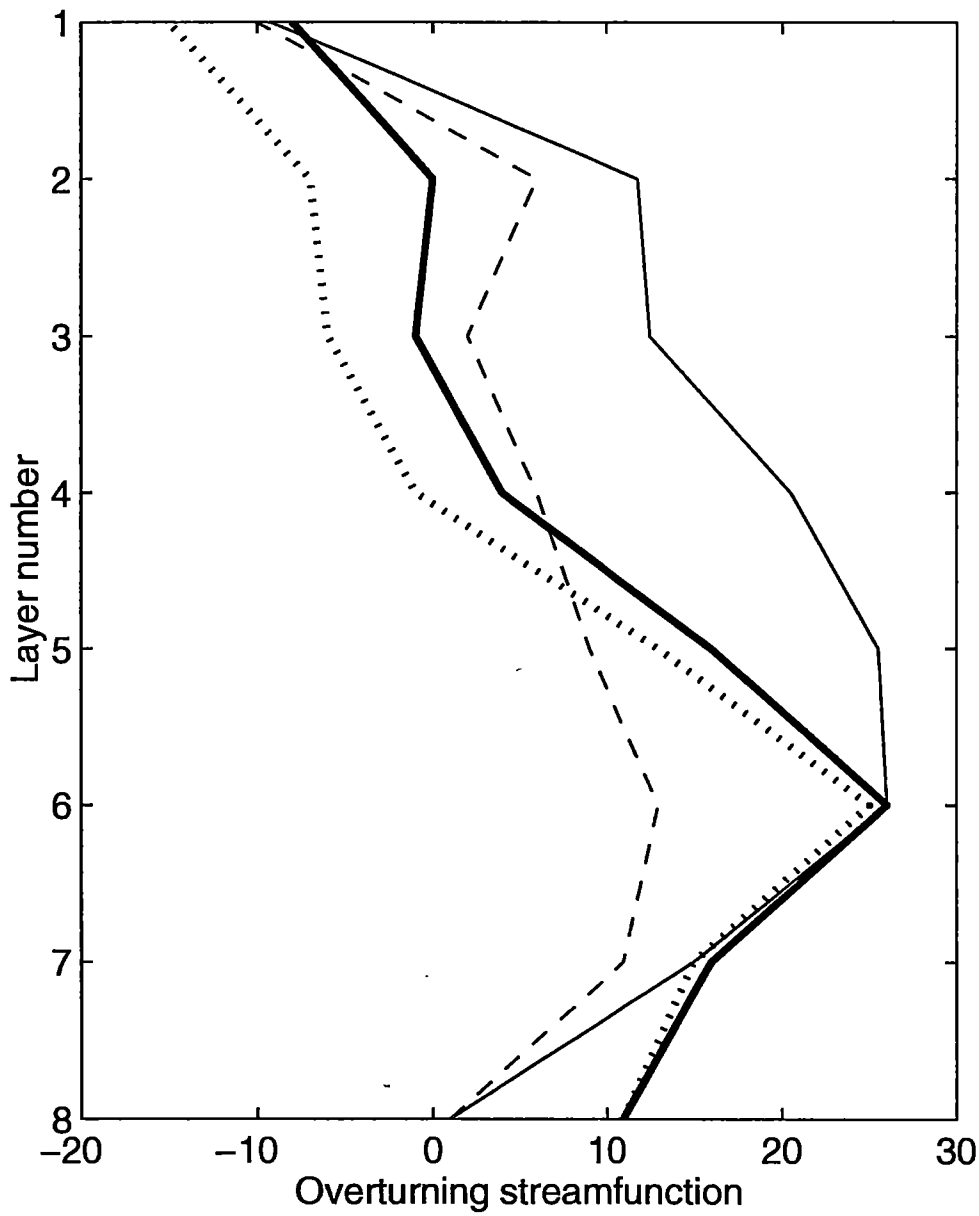

Figure 6.13: Comparison of overturning streamfunction ($\times 10^6 m^3 s^{-1}$) between Toole and Warren (1993) (T&W) solid line, Robbins and Toole (1997) (R&T) dashed line, model_int bold dotted line and model_malv bold solid line for the model_malv (using T&W and R&T layers).

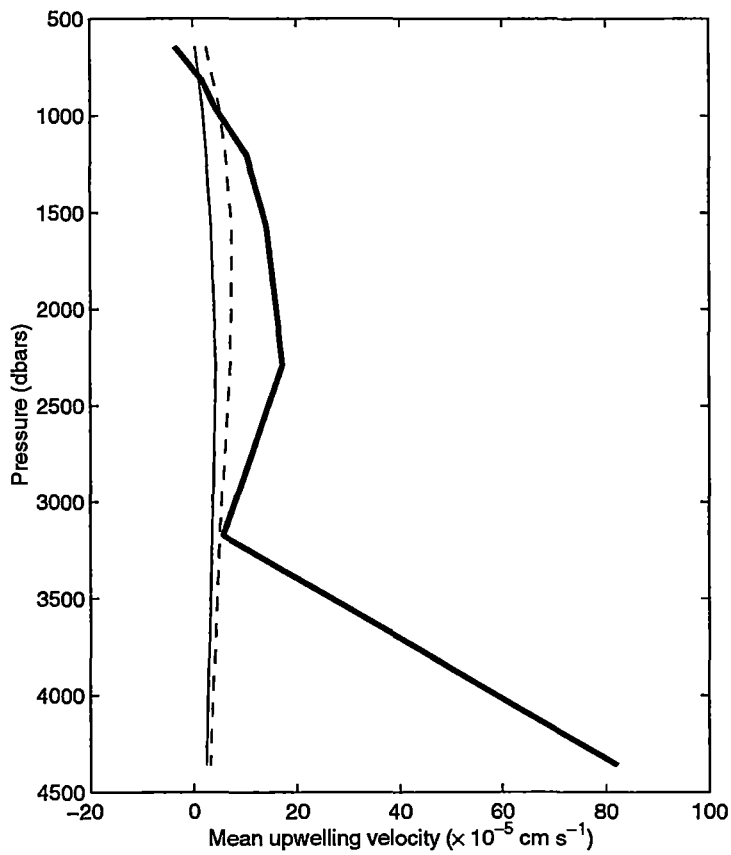

Figure 6.14: Comparison of the vertical velocity ($\times 10^{-5} cms^{-1}$) for the Indian Ocean between Toole and Warren (1993) (T&W) solid line, Robbins and Toole (1997) (R&T) dashed line, and model_malv bold solid line.

Pacific

The total mass flux across the SR3 section decreases from $143\pm4.9\times10^6 m^3 s^{-1}$ (model_surf) to $142\pm2.1\times10^6 m^3 s^{-1}$ in this model. The small decrease results from the smaller Indonesian through-flow being partially compensated by an increase ACC transport, as shown by increased eastward flow within Drake Passage and south of Africa. Across Pac32 section the total mass transport decreases from $12\pm15.8\times10^6 m^3 s^{-1}$ to $9\pm14.2\times10^6 m^3 s^{-1}$. The decrease results from a smaller northward flow in deep (layer 16 to 19), intermediate (layers 11 to 15) and thermocline (layers 7 to 10) layers in the southwest Pacific basin and smaller southward deep (layers 16 to 19) in the Tasman Sea and eastern Pacific (Figure 6.15).

The decrease in net northward mass transport in the thermocline, intermediate and deep layers results in only small changes in deep (layers 16 to 18) and bottom (layers 19 to 21) transport in the Southern Ocean Pacific sector. This results in similar deep and bottom layer transport in the Southern Ocean Pacific between this model and model_surf. The slightly smaller northward mass flux in deep layers results in a small decrease in the northward silica flux across PAC32. The mass transport and the dianeutral mass flux of deep and bottom layers is shown in Figure 6.16. The downward dianeutral mass flux from UCDW (layer 17) and UCDW/LCDW (layer 18) in Figure 6.16 are larger than those of model_int (Figure 4.49), while the downward dianeutral fluxes from LCDW/AABW (layer 19) and AABW (layer 20) are similar between models. The larger dianeutral flux into LCDW and AABW (layer 19) in this model (and model_surf) balance the large northward flux of this layer across the PAC32 section.

The smaller northward mass flux in thermocline, intermediate and deep layers in the Southwest Pacific basin result in an small decrease in northward heat and salt flux across 32°S. In the previous models (model_surf and model_wsh) the heat and salt flux are 0.12±0.28 PW and $416.64 \pm 212.1 \times 10^6 kgs{-}1$ while in this model the heat and salt is 0.09±0.26PW and $317 \pm 190.5 \times 10^6 kgs{-}1$. The layer heat and salt fluxes are shown Figure 6.17 and Figure 6.18, respectively. The northward heat flux of

thermocline (7 to 10) and bottom layer (20 and 21) area balanced by returning warmer intermediate (11 to 15) and deep (16 to 19) layers, while the northward salt flux in bottom (20 and 21) layers dominates the overall northward flux.

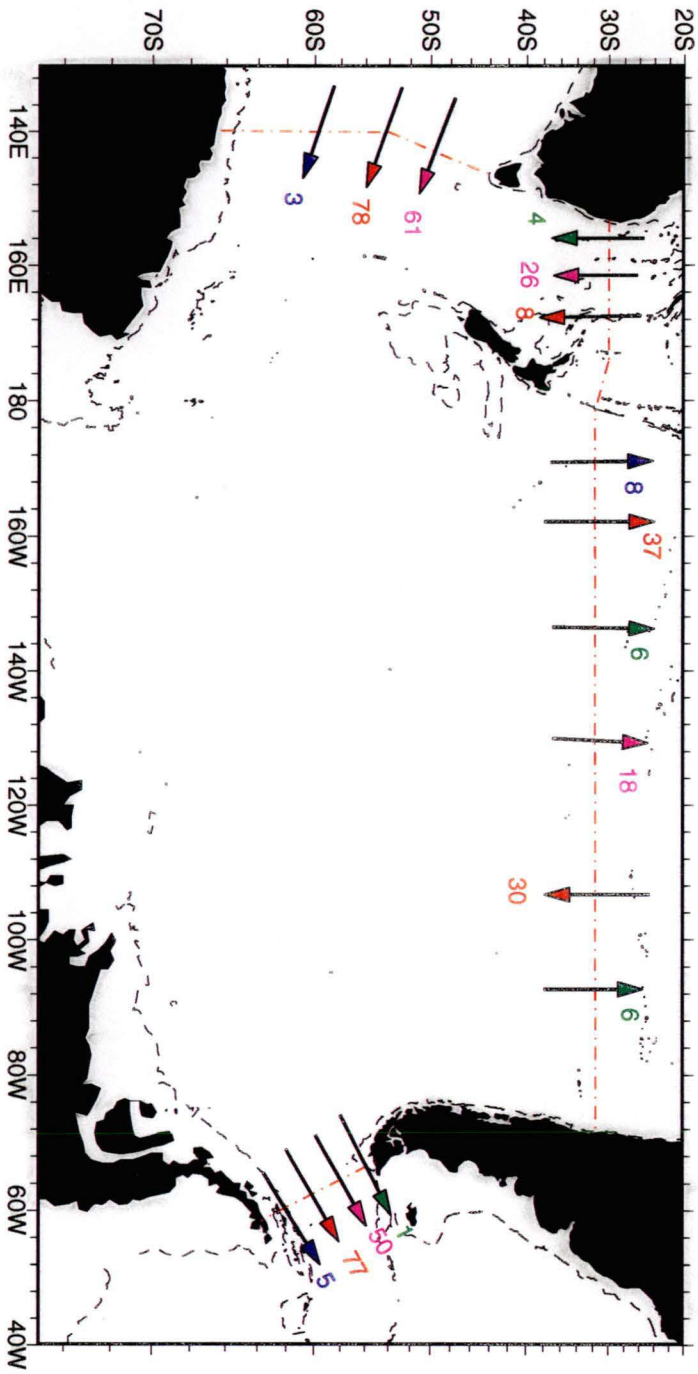

Figure 6.15: Transport ($\times 10^6 m^3 s^{-1}$) of particular layers in the Pacific Region for the model_malv. Thermocline layers 5 to 10 (green), Intermediate layers 11 to 15 (magenta), Deep layers 16 to 18 across Pac32 and 16 to 19 across south of Australia, Drake Passage (red) and Bottom layers 20 to 22 (dark blue)

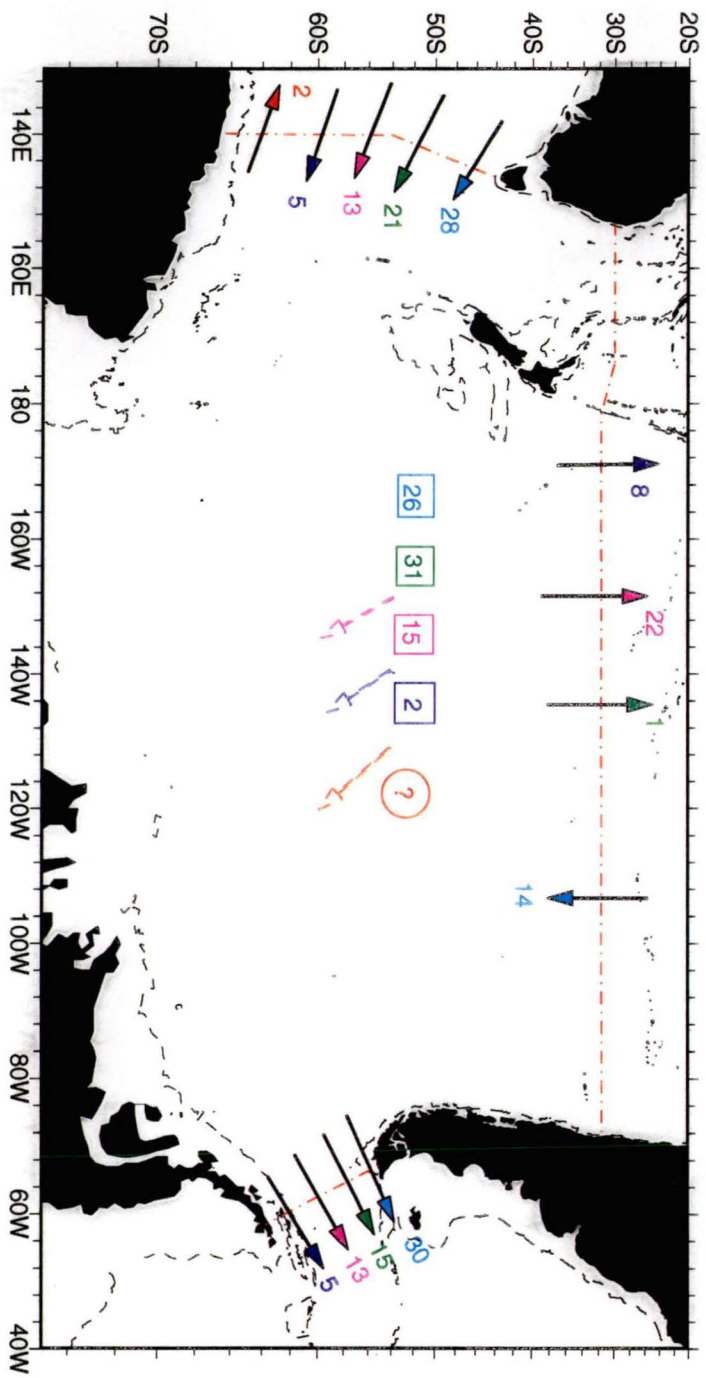

Figure 6.16: Mass transport and dianeutral flux ($\times 10^6 m^3 s^{-1}$) within Deep and Bottom water in the Pacific Region (BVI) for the model_malv. Upward Dianeutral flux- circle, Downward Dianeutral Flux - square, dashed arrow represent net production within layers due to dianeutral flux. UCDW/PDW (layer 17, light blue), UCDW/LCDW (layer 18, green), LCDW/AABW (layer 19, magenta), AABW (layer 20, dark blue), and extreme AABW (layer 21 and 22, red).

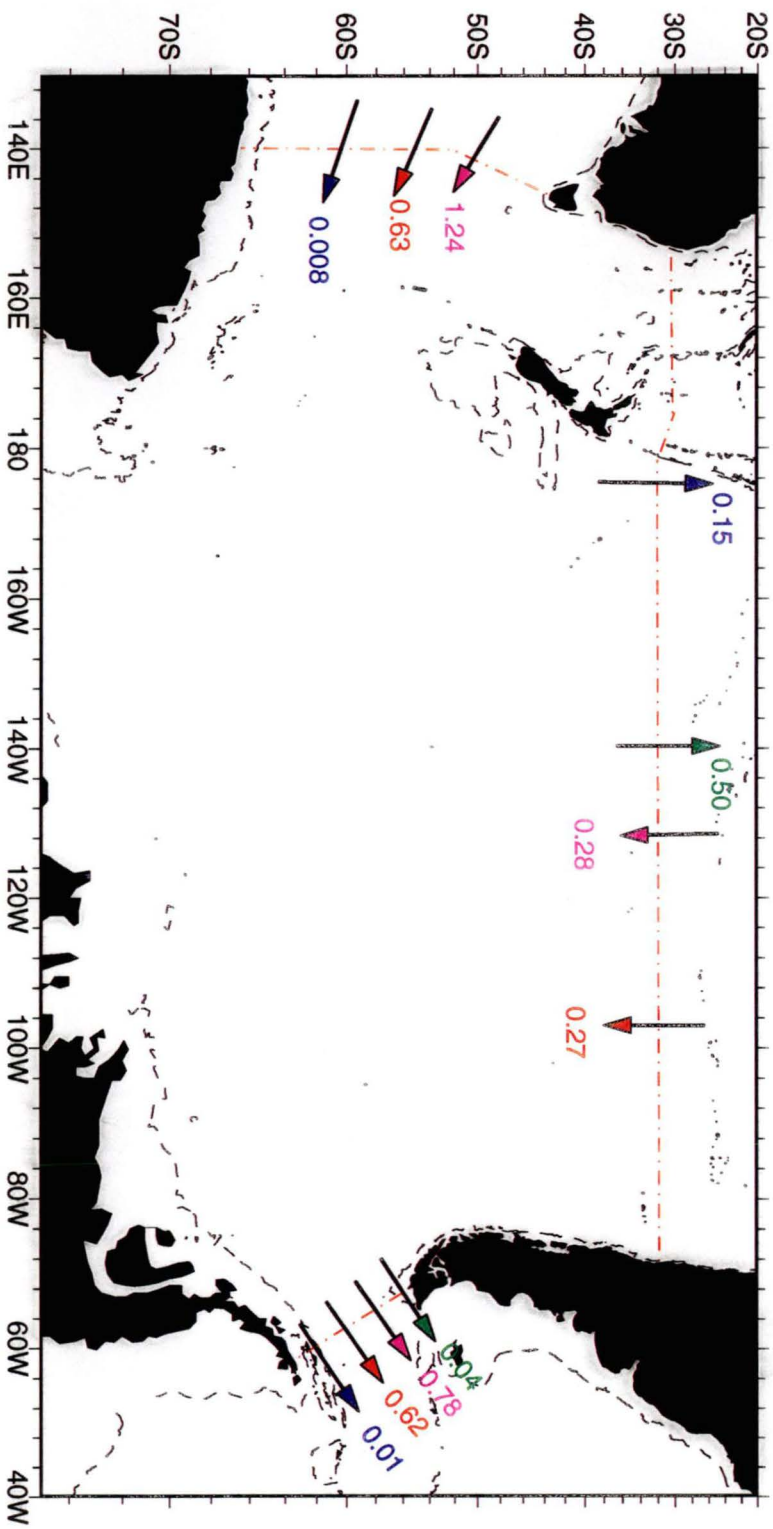

Figure 6.17: Heat flux (PW) of particular layers in the Pacific Region for the model_malv. Thermocline layers 5 to 10 (green), Intermediate layers 11 to 15 (magenta), Deep layers 16 to 18 across SAVE2, SAVE4 and 16 to 19 across Drake Passage, south Africa and Weddell Sea (red) and Bottom layers 20 to 22 (dark blue)

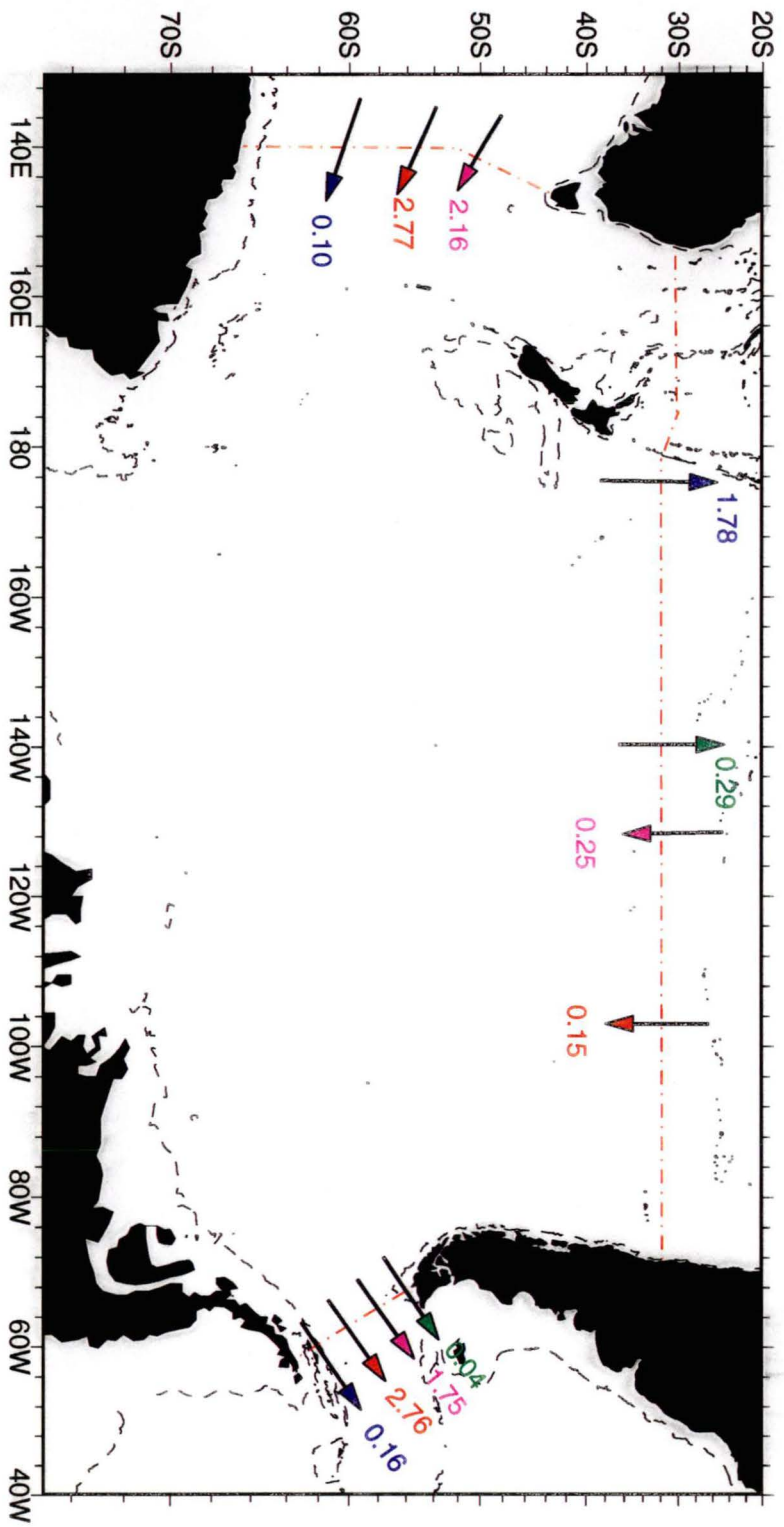

Figure 6.18: Salt flux ($\times 10^9 kgs^{-1}$) of particular layers in the Pacific Region for the model_malv. Thermocline layers 5 to 10 (green), Intermediate layers 11 to 15 (magenta), Deep layers 16 to 18 across SAVE2, SAVE4 and 16 to 19 across Drake Passage, south Africa and Weddell Sea (red) and Bottom layers 20 to 22 (dark blue)

6.2.4 Validity of Assumptions

The imposition of a large northward Malvinas Current and an northward AABW mass flux ($6\times10^6 m^3 s^{-1}$) in the Argentine basin results in some improvements in the circulation of the previous models (model_surf and model_wsh). These changes include an increase in the size of the ACC by $1\times10^6 m^3 s^{-1}$, contained within deep water (layer 16 to 18). Other changes improve the implied circulation, when compared to previous studies, including the southward transport of NADW in the western basin at SAVE2 and the sharp northward movement of the SAF in the Argentine basin and eastward return over the mid-Atlantic ridge.

The additional constraints imposed within this model, although confined to the Atlantic Ocean, result in small changes to layer mass, heat and salt fluxes in the Indian and Pacific Oceans and a smaller Indonesian through-flow of $8\pm5.1\times10^6 m^3 s^{-1}$. An Indonesian through-flow of $8\times10^6 m^3 s^{-1}$ agrees with smaller the more recent estimates of (Cresswell et al. 1993; Meyers et al. 1995). The deep overturning circulation of the Indian and Pacific oceans are essentially unaffected by the additional constraints on the size of the northward Malvinas Current and AABW mass transport in the Argentine basin.

The circulation derived with a large Malvinas Current and $6\times10^6 m^3 s^{-1}$ northward AABW transport in the Argentine basin results in a circulation for the Southern Ocean and adjacent ocean basins which is consistent with our current understanding of ocean circulation within this region. The model improves the circulation path of NADW in the subtropical Atlantic Ocean and the smaller Indonesian throughflow agrees with other recent estimates.

6.3 Thermohaline Circulation: Upper Closure

The NADW that flows southward in the South Atlantic is eventually entrained into the Antarctic Circumpolar Current (ACC). It is modified in the ACC to form CDW which is dispersed by the ACC into the Indian and Pacific Oceans. The deep NADW exported from the Atlantic and dispersed into the Southern, Indian and Pacific Oceans is compensated in the Atlantic by a return northward flow of intermediate and thermocline water. This overturning

circulation is known as the global thermohaline circulation. The closure of the global thermohaline circulation by warmer thermocline and intermediate water masses results in the northward heat flux in the Atlantic Ocean.

Recently, much discussion has centred on which water mass, thermocline or intermediate, is principally responsible for the thermohaline closure and the circulation path taken by these waters that eventually close the thermohaline circulation (Gordon 1986; Rintoul 1991; Gordon et al. 1992; Macdonald 1993; Saunders and King 1995; Schmitz 1995). These studies categorise the upper branch of the thermohaline circulation path as either "cold water path" or "warm water path". The "cold water path" balances the export of NADW with inflow of intermediate water which enters the South Atlantic via Drake Passage (Rintoul 1991; Gordon et al. 1992; Macdonald 1993; Schmitz 1995). Gordon et al. (1992) highlights a complicated circulation path by which colder intermediate water entering via Drake Passage closes the thermohaline circulation. He suggests that the colder intermediate water from Drake Passage moves northwards into the South Atlantic at the eastern boundary after a sojourn in the southwest Indian Ocean. The "warm water path" closes the thermohaline circulation by conversion of deep water into intermediate water in the subtropical Indian and Pacific Oceans and subsequent further warming to thermocline water in the subtropical Indian and Pacific. This warm thermocline water eventually returns to the South Atlantic south of Africa by eddies from the Agulhas Current which move northwest-wards into the South Atlantic in the Benguela Current (Gordon 1986; Saunders and King 1995).

In the following section the mass transport of thermocline and intermediate water across DrakeP, SAVE4, SAVE2, SAfrica, Ind32 and Ind18 sections are divided into three temperature classes. From the mass transport of these finer temperature classes the path by which thermocline and intermediate water close the thermohaline circulation is discussed.

6.3.1 Water Mass Transfer

Within the Southern Ocean and adjacent ocean basins six hydrographic sections (SAVE2, SAVE4, DrakeP, SAfrica, Ind32 and Ind18) are involved in the Indian-Atlantic and southern Pacific-Atlantic interbasin exchange which

closes the global thermohaline circulation. To differentiate the importance of particular thermocline and intermediate water masses in the thermohaline closure these layers are divided into three temperature classes from the surface to 1500 dbars. These temperatures classes, and the neutral density layers are:

θ >13°C	thermocline water (layers 1-10)
13°C > θ > 10°C	upper intermediate water (SAMW layers 11-12)
θ < 10°C	lower thermocline water (AAIW layers 13 to 15)

The mass transport in each temperature class is shown in Figure 6.19. At Drake Passage no water warmer than 10°C enters into the Southern Ocean Atlantic sector. The Malvinas Current constraint ($50 \times 10^6 m^3 s^{-1}$) results in a northward transport of water colder than 10°C and slightly warmer water (13°C > θ > 10°C) across the SAVE4, in the Argentine basin. The SAMW is produced locally in the Southern Ocean Atlantic sector (see Chapter 5). As detailed in Section 6.2.1, SAMW (layers 11 and 12) and AAIW (layers 13, 14 and 15) move northwards adjacent the South American coast in the Malvinas Current. Between 38°S and 33°S the northward Malvinas Current meets the southward Brazil Current forming the Brazil-Malvinas Confluence, which moves eastward across the Atlantic forming the South Atlantic Current (SAC). At the Brazil-Malvinas Confluence the northward flowing SAMW/AAIW (which is at the sea-surface) in the Malvinas Current is over-ridden or capped by the less dense southward flowing warm, salty subtropical thermocline water in the Brazil Current. The over-riding or capping of SAMW/AAIW by warm, salty thermocline water results in the salinity minimum signature of AAIW, evident as this water moves eastward over the mid-Atlantic ridge. The AAIW salinity minimum is enhanced as it forms a low salinity wedge between two relatively salty waters namely, thermocline water and NADW. Mixing between the subtropical thermocline water and SAMW/AAIW also occurs at the Brazil-Malvinas Confluence and along the SAC. This results in the large property changes in the SAMW/AAIW layers, between the colder, fresher water

in the Argentine Basin and the warmer, saltier water moving eastward across the mid-Atlantic ridge (Figure 6.20 and Figure 6.21). (NB. The warmer, saltier and lower oxygen stations in the Argentine basin result from subtropical meanders on the Brazil-Malvinas Confluence at 40°S, Figure 3.5 and Figure 3.6). Schmitz (1996b) and Schmitz (1995) also suggest strong mixing between SAMW/AAIW and subtropical thermocline water in the southwest Atlantic, resulting in major changes to the property characteristics of SAMW/AAIW in the Atlantic.

The warm, salty modified variety of AAIW and SAMW, produced locally in the southwest Atlantic, move eastward across the mid-Atlantic ridge along with thermocline water (Figure 6.19). The mass fluxes in the three temperature classes south of Africa are shown for the stations between 0°E and 20°E and the remaining stations at 0°E. The stations between 0°E and 20°E are west of the mean position of the Agulhas retroflection between 16°E to 20°E (Lutjeharms and Van Ballegooyen 1988). Therefore it is appropriate to assume that most of this water enters the Atlantic Ocean in the Benguela Current. The transport associated with the thermocline and SAMW are $3\times10^6 m^3 s^{-1}$ and $2\times10^6 m^3 s^{-1}$ respectively, with the largest transport in the colder AAIW water class. The small amount of thermocline and SAMW entering the Atlantic between 0°E and 20°E, south of Africa, highlights that most of this water that moves southward in the Agulhas Current (at 32°S) turn eastward south of Africa with the Agulhas retroflection. The Indian Ocean thermocline water and SAMW is then either recirculated into the Indian Ocean in the Crozet and Central Indian Basins or is cooled and freshened, by air-sea fluxes and dianeutral interior mixing, as it moves eastward with the ACC (as discussed in Chapter 5). The mass exchanges of thermocline ($3\times10^6 m^3 s^{-1}$) and warm, salty SAMW ($2\times10^6 m^3 s^{-1}$) from the Indian Ocean to the Atlantic Ocean agrees with previous studies (Harris et al. 1978; Gordon and Haxby 1990; Boddem and Schlitzer 1995). The 0°E portion of the section south of Africa is dominated by AAIW (lower thermocline layers 12 to 15) in the ACC.

The global thermohaline circulation is closed in the eastern basins of SAVE 4 by the northward transport of thermocline and intermediate water in the Benguela Current. The $10\times10^6 m^3 s^{-1}$ thermocline transport is dominated by the Atlantic subtropical thermocline water that moves eastward across the

mid-Atlantic ridge. Although the SAC is the primary source of thermocline water in the Benguela Current the temperature-salinity diagram shows that the input of salty, warm Indian Ocean Water results in changes in the property characteristics between Benguela and SAC thermocline water (Figure 6.20). The temperature-salinity properties of Benguela Current thermocline and SAMW highlight that the Indian Ocean is a major source of heat and salt to the Atlantic Ocean. The northward transport in the Benguela Current is dominated by intermediate water (cooler than 10°C) emphasising that the thermohaline circulation is closed by intermediate water.

This study and most recent studies (Macdonald 1993; Peterson and Stramma 1991; Gordon et al. 1992; Schmitz 1995) show that the thermohaline circulation is closed by intermediate water that enters the Atlantic through Drake Passage- the so called "cold water path". Although there is consensus that intermediate water flows north in the eastern Atlantic to close the thermohaline circulation, there is still debate on the circulation path of the intermediate water before it moves northward into the Atlantic Ocean. Stramma and Peterson (1990) suggest that the SAC is the primary source of Benguela Current. Schmitz (1995) highlights the modification of Intermediate water (SAMW/AAIW), which enters the Atlantic through Drake Passage, occurs in the Brazil-Malvinas Confluence zone and eastward with the SAC. This warmer and saltier intermediate water flows northward with the Benguela Current. Gordon et al. (1992) highlighting the differences in the equilibrium ratio of chlorofluoromethane 11 (CFM-11) to chlorofluoromethane 12 (CFM-12) between the Benguela Current and the SAC shows that the SAC does not flow directly into the Benguela Current. They determine that intermediate water in the Benguela Current is a mixture of South Atlantic and Indian Ocean water, using the difference in ratio of chlorofluoromethane 11 (CFM-11) to chlorofluoromethane 12 (CFM-12) between Indian Ocean SAMW and AAIW (Agulhas Current) and SAC (Atlantic Ocean) in the Agulhas Retroflection. The temperature-salinity and temperature-oxygen diagrams, for intermediate water colder than 10°C, show that the intermediate water in the Benguela Current results from a mixture of colder and fresher Atlantic Ocean intermediate water with warmer and saltier Indian Ocean intermediate water (Figure 6.20 and

Figure 6.21).

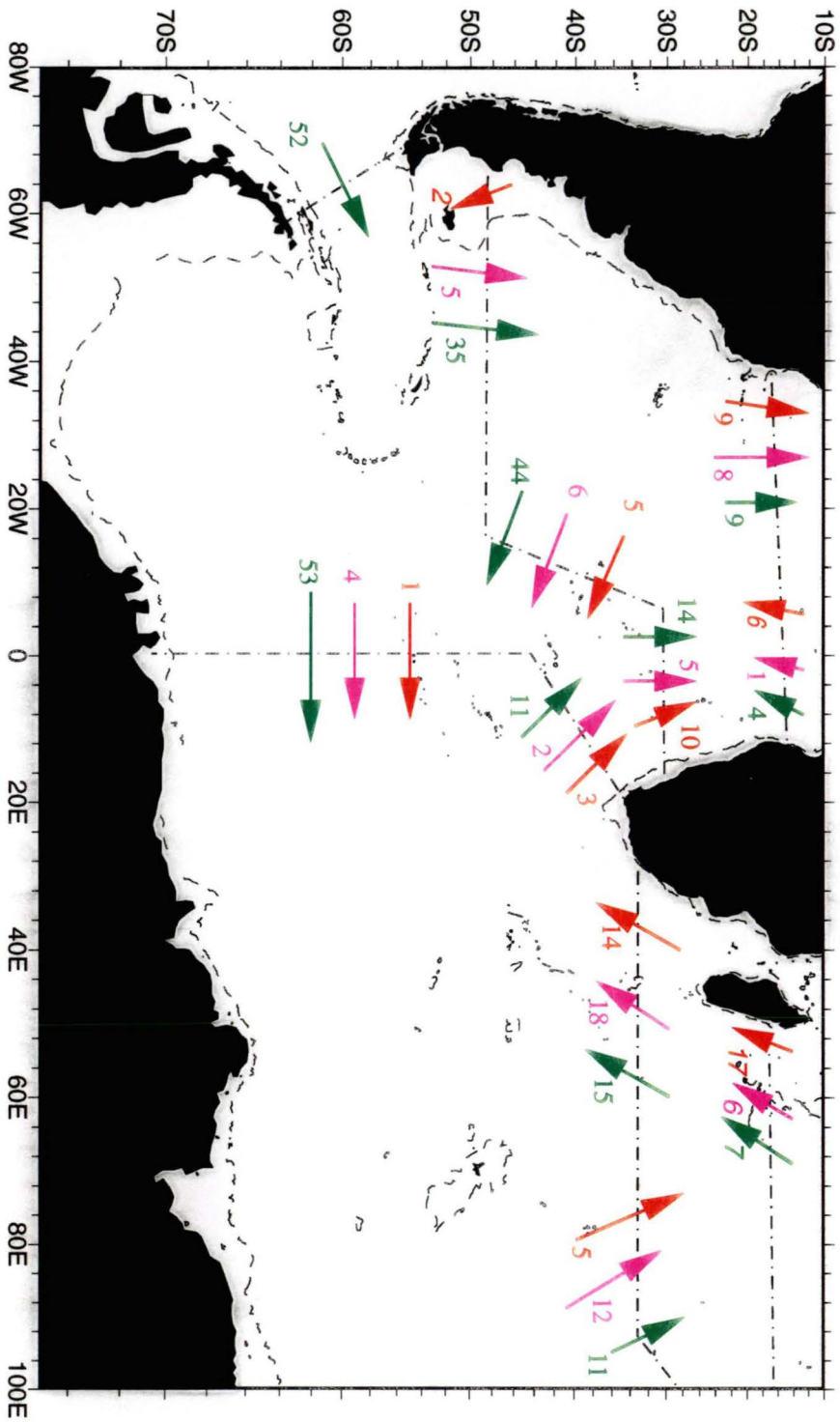

Figure 6.19: Mass Transport of layer above 1500 dbars subdivided into three temperature class across section involved in the Atlantic-Indian interbasin circulation. Thermocline - red ($\theta > 13$°C), Upper Intermediate (SAMW) - magenta

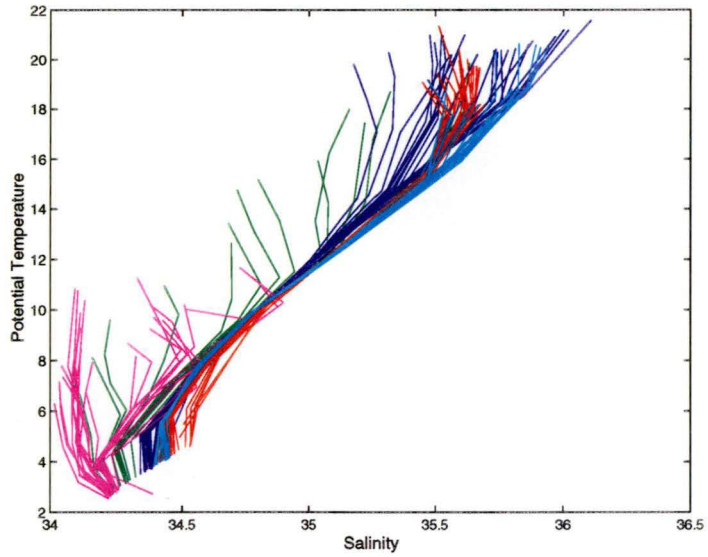

Figure 6.20: Potential Temperature-Salinity Diagram of stations involved in the Pacific-Atlantic-Indian Interbasin exchange SAVE 4: Argentine Basin (Magenta), South Atlantic Current (green), Benguela Current (dark blue), and Ind32: Agulhas Current (red), Crozet and Central Basins (light blue)

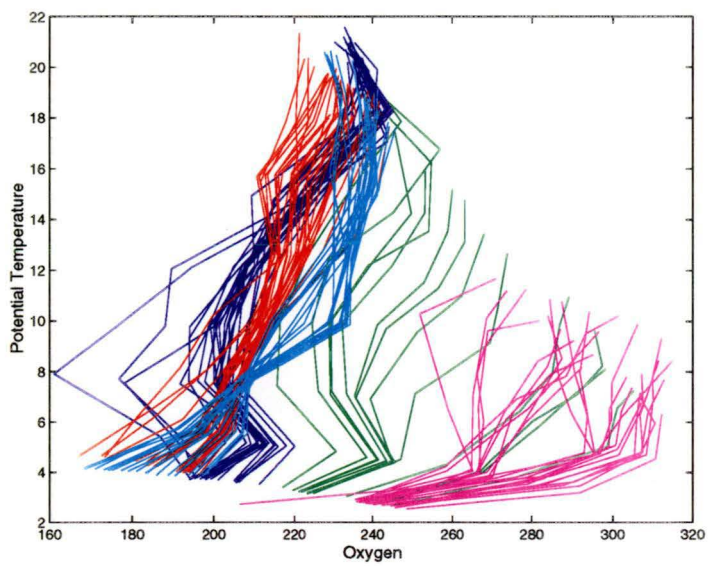

Figure 6.21: Potential Temperature-Oxygen diagram of stations involved in the Pacific-Atlantic-Indian Interbasin exchange SAVE 4: Argentine Basin (Magenta), South Atlantic Current (green), Benguela Current (dark blue), and Ind32: Agulhas Current (red), Crozet and Central Basins (light blue)

6.3.2 Pacific-Atlantic-Indian Circulation

A schematic of the Pacific-Atlantic-Indian circulation derived from this study is shown in Figure 6.22. This circulation pattern is consistent with the hydrographic sections used in the study and conservation of mass, heat and salt for the entire Southern Ocean and adjacent ocean basins. There are similarities with previous conceptual cartoons of the thermohaline and intermediate water circulation in the Atlantic and Indian Oceans given by Gordon et al. (1992) and Schmitz (1995).

The global thermohaline circulation is principally closed by intermediate (AAIW/SAMW) water that enters the Atlantic Ocean through Drake Passage (Figure 6.19 and Figure 6.22). Modification of intermediate water occurs in the southwest Atlantic ocean in the Brazil-Malvinas Confluence. The resulting warmer and saltier SAMW and some Atlantic thermocline water feeds directly into the Benguela Current in the eastern Atlantic Ocean. The remaining intermediate water (colder, fresher SAMW and AAIW), which principally balances the thermohaline circulation, make a sojourn into the southwest Indian Ocean. The Atlantic intermediate water is then modified within the southwest Indian Ocean, eventually returning to the Atlantic south of Africa and closing the global thermohaline circulation. There is only a small transport of warm, salty Indian thermocline water ($3\times10^6 m^3 s^{-1}$) into the Atlantic.

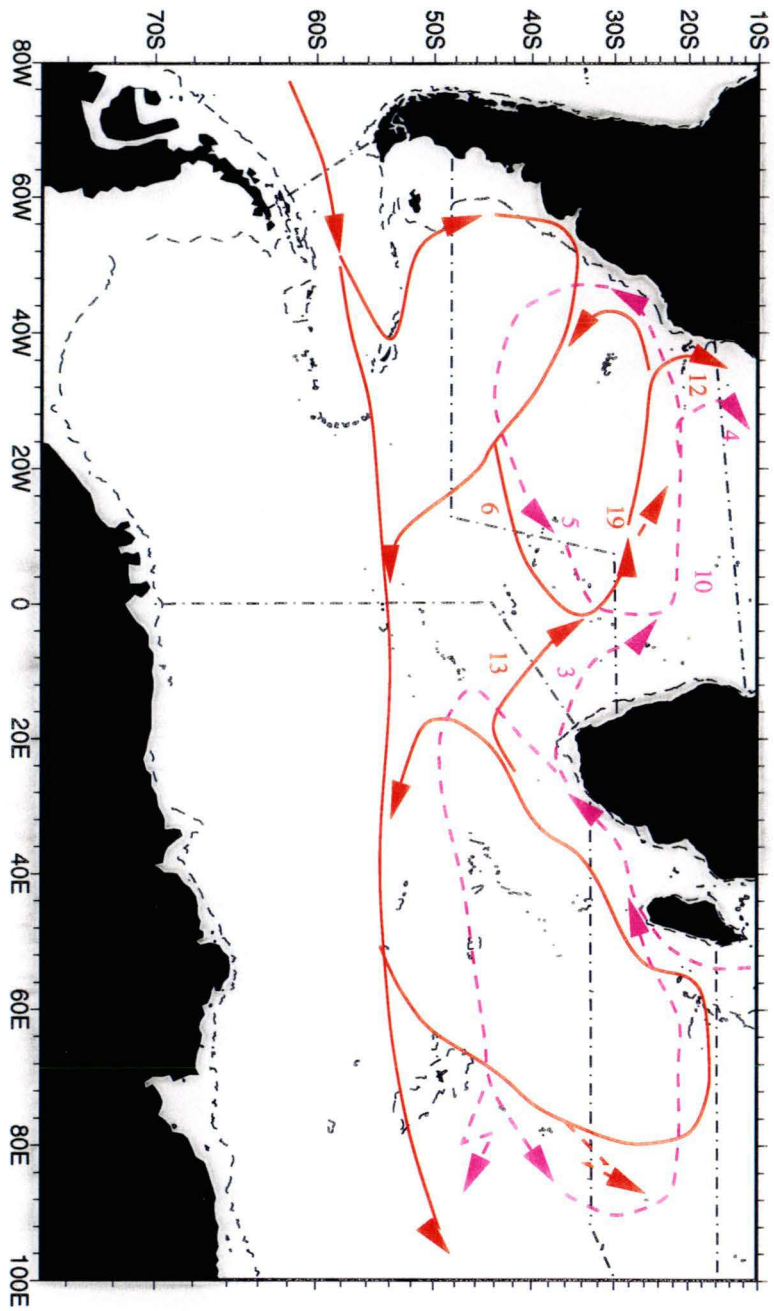

Figure 6.22: Schematic of major circulation path of thermocline and Intermediate water (SAMW/AAIW) which close the global thermohaline circulation. Intermediate Water (SAMW/AAIW) - red, Thermocline (Atlantic and Indian) - magenta. Dashed arrows represent conversion by either air-sea and interior dianeutral fluxes of thermocline water to intermediate water, or vice-versa.

Chapter 7

Final Remarks

This study shows that when the dianeutral and sea-surface property fluxes are included in an inverse model the mechanisms by which water masses transfer mass, heat and salt can be described. The interpretation of the sea-surface and interior dianeutral provided in this study is plausible, but not unique.

7.1 Region Circulation

The salient features of the Southern Ocean and adjacent ocean basins circulation found in this study are highlighted below.

Atlantic Region

The sea-surface and interior dianeutral fluxes show that $8\times10^6 m^3 s^{-1}$ of AASW is converted to lower thermocline water and SAMW. The interior dianeutral mass fluxes redistribute this water into "pure" SAMW, while the interior dianeutral heat and salt fluxes increase the temperature and salinity of SAMW within the Southern Ocean Atlantic sector. The $8\times10^6 m^3 s^{-1}$ of SAMW produced within the Southern Ocean Atlantic sector is exported into the subtropical Atlantic Ocean and is the major water source that ventilates the subtropical gyre.

Schmitz (1996a) and Schmitz (1996b) provide a conceptual cartoon of the meridional transport in the Atlantic. The results from this study quantify the lateral and dianeutral transports between different water masses in a mass, heat and salt conserving inverse model. Figure 6.4 shows these lateral and dianeutral fluxes for bottom and deep layers. At SAVE2 $20\times10^6 m^3 s^{-1}$ of NADW moves

southward into the subtropical Atlantic, where its is transfered ($6\times10^6 m^3 s^{-1}$) into slightly less dense deep water (Schmitz (1996b) UNADW his figure II-155) and eventually moves southward into the Southern Ocean across the mid-Atlantic ridge. AABW ($7\times10^6 m^3 s^{-1}$) moves northward across SAVE4 into the subtropical Atlantic while it continues to move northward in the deep western boundary current $4\times10^6 m^3 s^{-1}$ upwells into overlying NADW and $3\times10^6 m^3 s^{-1}$ eventually moves northward across SAVE2. In the Southern Ocean Atlantic sector the eastward ACC dominates the lateral transport, but important dianeutral transports occur which result in changes to the characteristics of CDW and AABW between Drake Passage and south of Africa. These dianeutral fluxes are: $4\times10^6 m^3 s^{-1}$ of NADW into CDW/AABW, resulting in the salinity maximum of LCDW; $14\times10^6 m^3 s^{-1}$ of WSDW/WSBW into AABW/CDW which then moves northward into the subtropical gyre and eastward with the ACC.

Table 7.1 shows a comparison of the meridional property fluxes at 30°S for the Atlantic between this study (model_malv) and previous regional (Saunders and King (1995)) and global studies (Macdonald (1993) and Macdonald and Wunsch (1996)). The zero mass and small southward transport at 30°S in these studies are applied constraints. The small southward mass transport in model_malv is consistent with the constraints of the other models. The heat flux of model_malv agrees with the Macdonald (1993) studies and is smaller than the estimates of Saunders and King (1995) and Macdonald and Wunsch (1996). The Saunders and King (1995) study estimates a small northward salt flux and southward silica flux while model_malv has a southward salt flux and northward silica flux. The southward salt flux of model_malv agree in direction with the estimate of Wijffels et al. (1992) but is approximately half the size of their estimated flux. The northward silica flux is smaller but of similar sign to that estimates by Macdonald (1993).

Indian Region

In the Indian region $8\times10^6 m^3 s^{-1}$ of warm, fresh Indonesian throughflow water is transferred into slightly denser thermocline water in the subtropical Indian Ocean. The thermocline water moves southward across 32°S in the

Property	S&K	Md	M&W	mod_malv
Mass ($\times 10^6 m^3 s^{-1}$)	0	-0.8		-0.36±10.3
Heat (PW)	0.53	0.3±0.8	0.5	0.34±0.13
Salt ($\times 10^6 kgs^{-1}$)	0.82			-11.7±134.6
Silica ($kmols^{-1}$)	-233	360±2407		150±707

Table 7.1: Comparison of meridional property fluxes at 30°S in the Atlantic between model_malv, Saunders and King (S&K) (1995), Macdonald (Md) (1993) and Macdonald and Wunsch (M&W) (1996). Fluxes from Macdonald (1993) are for her model B. The heat fluxes are based on a 0°C reference. +ve -northwards, -ve -southwards

Agulhas Current. The Agulhas thermocline water looses heat resulting in the sea-surface mass ($4\times10^6 m^3 s^{-1}$) transfer of thermocline water into SAMW. There is also an interior dianeutral flux ($6\times10^6 m^3 s^{-1}$) of thermocline water into SAMW. The sea-surface and interior dianeutral flux of thermocline water ($10\times10^6 m^3 s^{-1}$) into SAMW south of Africa highlights the dianeutral processes that result in the transfer of Indonesian throughflow water to warm, salty SAMW in the southwest Indian Ocean SAMW is cooled and freshened as it moves eastward with the ACC by a net sea-surface flux of AASW ($16\times10^6 m^3 s^{-1}$) across the Polar Front Zone. The sea-surface and interior dianeutral fluxes in the Southern Ocean Indian sector result in a net production of SAMW ($25\times10^6 m^3 s^{-1}$). The $25\times10^6 m^3 s^{-1}$ of locally produced SAMW exits the Southern Ocean Indian sector northward across 32°S ($10\times10^6 m^3 s^{-1}$), ventilating the subtropical gyre, while the remaining $15\times10^6 m^3 s^{-1}$ exit with the eastward ACC south of Australia.

A large deep overturning circulation ($26\times10^6 m^3 s^{-1}$) is found north 32°S. The strength of the overturning cell similar to that proposed by Toole and Warren (1993). The difference between this study and the study of Toole and Warren (1993) is the vertical extent of the overturning circulation. The inverse model (model_malv) maintains the overturning circulation below 1000 dbars between 18°S and 32°S, while north of 18°S the vertical overturning cell extends into intermediate and thermocline water (500 dbars). A schematic of the overturning circulation north of 18°S is shown in Figure 6.9. In the subtropical Indian Ocean the interior dianeutral fluxes transfer $16\times10^6 m^3 s^{-1}$ of AABW and

Property	T&W	Md	R&T	M&W	mod_malv
Mass ($\times 10^6 m^3 s^{-1}$)	-6.6	-10	-9.8		-7.98±7.6
Heat (PW)	-1.67	-1.3±1.4		-1.3	-0.94±0.18
Salt ($\times 10^6 kgs^{-1}$)	-236.8				-283.79±134.6
Silica ($kmols^{-1}$)	1532	708±3820	21		625±470

Table 7.2: Comparison of meridional property fluxes at 30°S in the Indian between model_malv, Toole and Warren (T&W) (1993), Macdonald (Md) (1993), Robbins and Toole (R&T) (1997) and Macdonald and Wunsch (M&W) (1996). Fluxes from Macdonald (1993) are for her model B. The heat fluxes are based on a 0°C reference. +ve -northwards, -ve -southwards

CDW/NADW into upper deep water (IDW). The IDW produced between 32°S and 18°S combines with the IDW (or NIDW) produced north of 18°S returning to the Southern Ocean Indian sector as slightly less saline, oxygen poor IDW in the Central and Perth basins and over the Ninetyeast ridge. The overturning circulation of this study is similar to the sketched by Schmitz (1996b), although the strength of his schematic overturning circulation is half that found in this study.

Recent estimates of the meridional transport at 30°S in the Indian Ocean are shown Table 7.2. The $10 \times 10^6 m^3 s^{-1}$ southward transport is a constraint in the Macdonald (1993) study. All studies have a similar southward transport at 30°S which indicates the strength of the Indonesian throughflow transport. The difference in the heat flux between model_malv and previous studies reflect the strength of the overturning circulation and the vertical extent of the overturning cell. The southward salt flux in both studies results from the input of Pacific water into the Indian Ocean - Indonesian throughflow. The difference in the northward silica fluxes are due to the difference, between the studies, in the strength and vertical extent of the overturning circulation. Model_malv and the Toole and Warren (1993) study have a similar sized overturning circulation, but the overturning cell is contained below 1000 dbars model_malv resulting in a smaller net northward silica flux.

Pacific

In the Southern Ocean Pacific sector the increased eastward transport of SAMW/AAIW south of Australia is transfered ($12\times10^6 m^3 s^{-1}$) by sea-surface processes into thermocline water. The thermocline water moves northward across 32°S. This shows that the circulation path of the Indonesian throughflow between the Indian and Pacific Oceans is essentially as a circum-Australia circulation feature. The sea-surface transfer of AASW ($8\times10^6 m^3 s^{-1}$) across the Polar Front Zone is "consumed" by interior dianeutral transport ($12\times10^6 m^3 s^{-1}$) of SAMW into AAIW, which results in a small net production of AAIW ($4\times10^6 m^3 s^{-1}$).

A large bottom and deep ($30\times10^6 m^3 s^{-1}$) overturning circulation is proposed in this study, although the strength of the overturning circulation is forced by suspicious air-sea heat fluxes. A major concern of the strong overturning circulation is the resulting large northward silica flux ($1242 \pm 1174 kmols^{-1}$). Studies of the global silica balance result in a small total southward silica flux into the Southern Ocean. The northward transport of AABW and CDW is balanced by southward transport, across 32°S, of slightly less saline, low oxygen PDW. This overturning circulation quantifies the Pacific meridional schematic of Schmitz (1996b). In the Southern Ocean Pacific sector downward dianeutral transport occurs across all deep layer. The downward dianeutral transport of UCDW/IDW (26) into LCDW results in the differences in CDW characteristic south of Australia and Drake Passage (oxygen minimum). The dianeutral flux of PDW/UCDW into LCDW replaces the LCDW ($31\times10^6 m^3 s^{-1}$) which is transfered into AABW. A net production of generic AABW and extreme AABW (ALBW/RSBW) occurs in the Southern Ocean Pacific region. I am unable to quantify the production of ALBW/RSBW as I lack a section parallel to the Antarctic continent. Some locally produced ALBW/RSBW ($2\times10^6 m^3 s^{-1}$) moves westward south of Australia. As the remaining ALBW/RSBW ($?\times10^6 m^3 s^{-1}$) moves northward and eastward in the ACC downward dianeutral flux from LCDW ($15\times10^6 m^3 s^{-1}$) modifies it to the generic AABW which exit the region northwards across 32°S and eastward through Drake Passage.

Property	W,H&G	Md	M&W	mod_malv
Mass ($\times 10^6 m^3 s^{-1}$)	0.08	10.8		8.86±14.2
Heat (PW)	-0.1	0.3±1.2	-0.04	0.09±0.26
Salt ($\times 10^6 kgs^{-1}$)	12.3			316.72±190.5
Silica ($kmols^{-1}$)	-392	-499±3650		1242±1174

Table 7.3: Comparison of meridional property fluxes at 30°S in the Pacific between model_malv, Wunsch, Hu and Grant (W,H&G) (1983), Macdonald (Md) (1993) and Macdonald and Wunsch (M&W) (1996). Fluxes for Wunsch, Hu and Grant (1983) are their model S-1B, Macdonald (1993) are for her model B. The heat fluxes are based on a 0°C reference. +ve -northwards, -ve -southwards

The meridional property fluxes at 30°S in the Pacific show the greatest variability between studies. The northward transport between model_malv and Macdonald (1993) are in good agreement and essentially balance the Indonesian throughflow and Pacific-Atlantic interocean transport through Bering Strait. The heat fluxes of model_malv and Macdonald and Wunsch (1996) are small but of opposite sign. The difference in the salt and silica flux reflected the difference in the strength of the deep overturning circulation between this study and the previous studies.

Meridional Fluxes

Comparison of the global meridional property fluxes at 30°S is given in Table 7.4. The northward mass flux in mod_malv indicates that there is a net input of freshwater (precipitation) over the Southern Ocean. The southward heat flux is smaller than previous estimates. The smaller southward heat flux in model_malv is due to the smaller southward heat flux in the Indian Ocean in this model. The salt flux should be zero. The small northward salt flux of model_malv is due to the divergence of salt in the Subtropical Atlantic Ocean (BI) between SAVE2 and SAVE4. The total northward silica flux results from the northward export of AABW and CDW from the Southern Ocean into the adjacent ocean basins and is dominated by the northward flux across 32°S in the Pacific. Studies of the global silica balance estimate a total southward flux of silica ($170 kmols^{-1}$) into the Southern Ocean (Trèguer et al. 1995). The large northward silica flux from this study may indicate that the strength of the

Property	Md	M&W	mod_malv
Mass ($\times 10^6 m^3 s^{-1}$)	0.0		0.52
Heat (PW)	-0.7	-0.9±0.3	-0.51
Salt ($\times 10^6 kgs^{-1}$)			21.2
Silica ($kmols^{-1}$)			2017

Table 7.4: Comparison of global meridional property fluxes at 30°S between model_malv, Macdonald (Md) (1993) and Macdonald and Wunsch (M&W) (1996). Fluxes for Macdonald (1993) are for her model B. The heat fluxes are based on a 0°C reference. +ve -northwards, -ve -southwards

overturning circulation is too large or that the returning arm of this circulation is too shallow. The reader is reminded that the increase in the northward silica flux across 30°south in the Indian and Pacific Oceans occurred when the air-sea fluxes were added. This may indicate some inconsistencies between the hydrographic data and the COADS air-sea heat flux.

7.2 Future Directions

This study quantifies the air-sea and interior dianeutral fluxes. It highlights the regions of the Southern Ocean where the air-sea fluxes modify AASW to SAMW/AAIW and how the dianeutral property fluxes either "consume" SAMW/AAIW transferring it to warmer thermocline or colder deep water or add to the overall production of SAMW/AAIW with a region. The dianeutral mixing between extreme AABW (WSDW, WSBW, ALBW and RSBW), AABW, CDW and northern origin deep water (NADW, IDW and PDW) shown in this study for the Atlantic, Indian and Pacific quantifies the dianeutral mixing processes between these water masses. The dianeutral mass flux describe the volume changes and the heat and salt dianeutral fluxes highlights the dianeutral processes that result in the property changes of water masses between the Southern Ocean choke point sections.

The sea-surface and interior dianeutral fluxes described in this study represent a the mean dianeutral property flux over the entire box region. These regions generally contain different dynamical areas, such as complex bottom topography, and active ocean front (Antarctic Polar Front, Subantarctic Front,

Brazil-Malvinas Confluence and Agulhas retroflection) where enhanced sea-surfaces and interior mixing could occur. Further development of inverse methods in determining the strength and regional variability of dianeutral processes would be to design inverse models which use hydrographic sections to encompass dynamically similar regions, such as the Brazil-Malvinas Confluence, the Polar Front Zone and the Agulhas retroflection region. The data collected during WOCE now enables such regions to be enclosed. An inverse model which has smaller and similar dynamical regions would enable us to investigate the variability of dianeutral fluxes and determine those regions that are active sites of water mass formation and modification. These studies may also benefit numerical models by providing information on the spatial variations of dianeutral mixing, which could then be incorporated into the numerical models

Appendix A

Assessment of the Non-Synoptic Error

Oceanographers have known for sometime that the ocean varies on seasonal time-scales, and recently decadal and longer time-scale variability have been found. The seasonal and decadal time-scale variabilities are an inherent problem with ocean circulations derived by inverse methods because one-time, non-synoptic hydrographic sections form the boundaries of the box regions. In this appendix I discuss changes to the derived circulation when a different section (season and year) south of Australia is used.

A.1 The Non-Synoptic Problem

One of the underlying assumptions of inverse methods is that the hydrographic data describe a near steady-state ocean circulation or that the one-time hydrographic sections represent the mean, long-term property fluxes (Wunsch 1982; Wunsch 1996). Conversely, the non-synoptic hydrographic the sections are potentially the largest source of error (Wunsch 1996).

Knowledge of the seasonal variability of the ocean is confined to a few regions, including the Gulf Stream, Drake Passage and the Indonesian through-flow (Niiler and Richardson 1973; Whitworth 1980; Fieux et al. 1994; Meyers et al. 1995). The gyre scale seasonal variability is still unknown for most ocean basins, while recent studies have shown decadal variability within ocean gyres (Bindoff and Church 1992). Although these studies highlight the variability between different one-time hydrographic section we still do not have

a clear picture of the true time averaged ocean circulation.

The question of whether the circulation, derived from inverse methods, represents the mean ocean circulation still needs to be addressed. A way of testing the stability (or mean-ness) of the circulation derived from the inverse method is to replace particular hydrographic sections with other realisation of these sections.

The World Ocean Circulation Experiment (WOCE) has included some repeat hydrographic sections which are specifically designed to provide information on the seasonal and annual variability of the ocean. The section south of Australia (SR3) is one of the repeat WOCE sections in the Southern Ocean. This section has been occupied six times between 1992 and 1996, encompassing all seasons. The multiplicity of the section south of Australia (WOCE-SR3) allows investigation into the stability of the circulation derived in this study.

The year and season of the sections used in the previous models and another realisation of the section south of Australia are shown in Table A.1. The sections used in this study were occupied in different years, although there is seasonal continuity between sections. The two sections south of Australia are separated by 18 months and were occupied in different seasons, summer and winter. Changing the section south of Australia, from the 1994 to 1995 realisation in this model, introduces both annual and seasonal differences.

A.2 Variations to the Circulation

A.2.1 Relative transport

The difference between the relative layer fluxes (reference levels is deepest common depth) between the two section south of Australia is shown in Figure A.1.

The differences in layer relative flux between the two sections south of Australia include: the lightest layer (11) is present in the 1994 summer section (solid line) but not in the 1995 winter section (dashed line) and there is a smaller eastward flux in layer 12 during the winter section (1995); the 1995 winter section has a larger eastward transport within intermediate layers (13, 14

Section	Year	Season	Comments
SAVE 2	1988	Summer	
SAVE 4	1989	Summer	
Drake P	1990	Summer	
S. Africa	1984	Summer	all models
Weddell Sea	1984	Summer	
Ind18	1976	Winter	
Ind32	1987	Summer	
S. Aust (SR3)	1994	Summer	all previous models
S. Aust (SR3)	1995	Winter	this model (model_var)
Pac32	1992	Winter	all models

Table A.1: Detail of the hydrographic section (month and year) used in this study. The models discussed in the previous chapters use SR3_1994 as the section south of Australia, while this model (model_var) uses SR3_1995. Comments indicate which sections are used in the models in this study

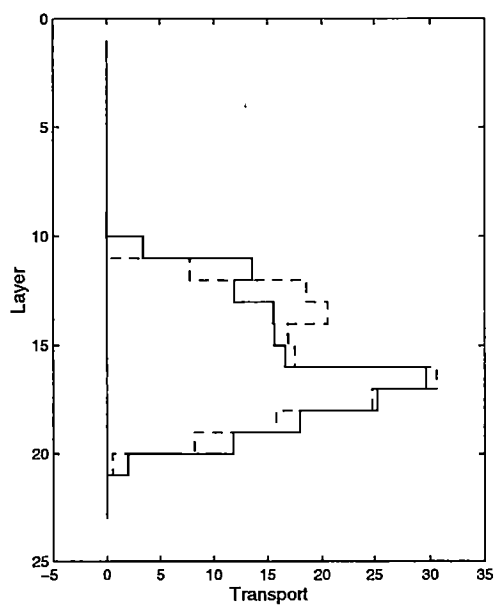

Figure A.1: Comparison of the relative transport (reference level is deepest common depth) between the 1994 summer (solid line) and the 1995 winter (dashed line) section south of Australia (WOCE SR3) (+ve is eastward).

and 15, SAMW/AAIW), and deep layers (16 and 17, UCDW) and; the eastward flow of deep (18 and 19, LCDW/AABW) and bottom (20, AABW) is largest in the 1994 summer section (solid line). Although there are differences in the layer mass transports between the summer 1994 and winter 1995 sections south of Australia the total eastward relative mass transports are similar, $161 \times 10^6 m^3 s^{-1}$ and $163 \times 10^6 m^3 s^{-1}$ respectively.

A.2.2 Absolute Property Flux changes

The total property fluxes across all sections used in this model (model_var), including the winter 1995 section south of Australia, are shown in Table A.2. A comparison of the total property fluxes in this model with the previous model (model_malv, Table 6.1) highlight the changes between the models. There is a decrease in the eastward property fluxes at Drake Passage and south of Africa and an increase south of Australia, while at the meridional section within the Indian and Pacific oceans there is an increase in the southward and northward property fluxes, respectively. There are only small changes in the property fluxes at the SAVE2, SAVE4 and the Weddell Sea. The layer property differences between this model (model_var) and the previous model (model_malv) are shown in Table A.3 to Table A.10. These show that the transport differences are distributed throughout water column resulting in layer flux difference of $< 1 \times 10^6 m^3 s^{-1}$, apart from south of Australia (which is the section that has been changed).

The smaller eastward transport at Drake Passage and south of Africa are principally in the deep and bottom layers (17 to 22). This results in the difference in the salt and silicate fluxes, while the smaller differences in the heat flux reflects the small transport differences in the intermediate (11 to 15) and thermocline (layer 10 and above) transports.

In the Indian Ocean there is a net southward transport increase of $7 \times 10^6 m^3 s^{-1}$. At Ind18 the mass difference is mostly contained in the deep layers (16 to 19) (Table A.5). The increased southward transport in the deep layers result in a smaller northward silica flux and smaller southward salt flux. The increases in the heat flux reflect the small increase in the southward transport within the thermocline. The $7 \times 10^6 m^3 s^{-1}$ increase in the southward

section	Mass ($\times 10^6 m^3 s^{-1}$)	Heat ($\times 10^6$ °C $m^3 s^{-1}$)	Salt ($\times 10^6 kgs^{-1}$)	Freshwater ($\times 10^9 kgs^{-1}$)	Silica ($kmols-1$)
SAVE2	-0.74±11.33	112.81±48.9	-26.86±44.5	-0.82±11.2	24.89±469.9
SAVE4	-0.37±10.1	78.13±30.0	-11.78±131.6	-0.41±9.9	168.50±690.4
Drake P	131.27±1.2	335.69±2.1	4654.4±17.6	130.51±1.2	8751.6±116.4
S. Africa	131.67±6.2	272.35±12.4	4662.2±77.9	130.83±6.2	8398.8±552.6
Weddell Sea	0.03±3.6	-12.59±1.4	0.23±47.7	0.04±3.5	23.14±452.9
Ind18	-15.15±5.1	-355.92±25.8	-540.30±44.8	-14.94±5.0	91.746±486.4
Ind32	-14.82±7.7	-258.14±43.0	-528.82±66.0	-14.62±7.6	221.89±470.8
S. Aust	146.63±3.5	475.60±8.3	5202.3±49.5	145.73±3.6	7969.7±288.3
Pac32	15.71±13.9	63.69±59.1	562.18±185.4	15.64±13.8	1701.5±1144.1

Table A.2: Total section flux for each property when a different realisation of the section south of Australia (SR3_1995). Positive represent northwards and eastward fluxes. Units: mass $\times 10^6 m^3 s^{-1}$, heat $\times 10^6$ °C $m^3 s^{-1}$, salt $\times 10^6 kgs^{-1}$, freshwater $\times 10^9 kgs^{-1}$ and silica $kmols-1$

transport at Ind32 results from small decreases in the northward transport and small increases in the southward transport in all layers (Table A.6). The balance of smaller northward transport of CDW (layers 16 to 18) and AABW (layer 19 to 20) and larger southward flux of IDW (layer 17 to 18) result in a decrease in the northward silica flux. The increase in the southward heat flux result from a slight increase in the southward flux within thermocline (7 to 10) and intermediate layers (11 to 15).

The total eastward transport south of Australia increase from $142\times10^6 m^3 s^{-1}$ in model_malv to $147\times10^6 m^3 s^{-1}$ within this model (model_var). The larger eastward transport results from an increased eastward flux within intermediate layers (13 to 15) and upper deep layers (16 to 17), and a decrease in the eastward transport of lower deep (18 and 19) and bottom layers (20). There is also a decrease in the westward transport of Pacific origin extreme AABW (layer 21) (Figure A.2, Table A.7). The large decrease in the eastward transport of upper intermediate layers (11 and 12) is because these layers are not present in the winter section (SR3_1995, model_var) or occupy a smaller area. The loss of these layers south of Australia result in an increase conversion of thermocline (9 and 10) and upper intermediate (11 and 12) layers into lower intermediate (13 to 15) by interior dianeutral fluxes within the Southern Ocean Indian region (BV). The use of the winter SR3_1995 section south of Australia results in a redistribution of water within intermediate layers with only a total increase of $5\times10^6 m^3 s^{-1}$. The increased eastward transport within upper deep layers (16 to 17) result from the increase southward flux of these layers at the Ind32 and smaller downward interior dianeutral fluxes across these layers within the Southern Ocean Indian region (BV). The smaller downward interior dianeutral fluxes across upper deep layer (16 to 17) and smaller eastward transport of lower deep (18 and 19) and bottom (20) layers south of Africa result in a decreased eastward transport of lower deep and bottom layers (layer 19 and 20) south of Australia (Figure A.2). The increased eastward heat flux south of Australia is due to the increased eastward intermediate layer transport, while the larger eastward salt and silicate fluxes result from increased intermediate and upper deep layer transport south of Australia.

Across the 32°S Pacific section the transport increases by $7\times10^6 m^3 s^{-1}$

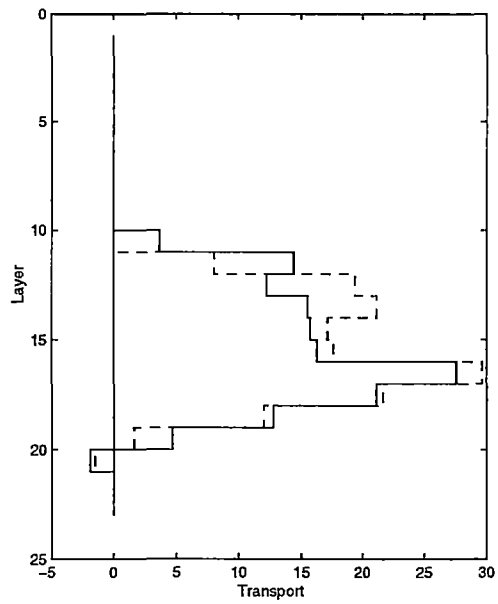

Figure A.2: Comparison of the total layer transport between the 1994 summer (solid line, model_malv) and the 1995 winter (dashed line, model_var) section south of Australia (WOCE SR3) (+ve is eastward).

between this model and the previous model (model_malv). This increase results from small increases and decreases in the northward and southward transport in the Southwest Pacific and Tasman Basins and over the Tonga-Kermadac ridge in all layers (Table A.8). The dianeutral interior mass convergence from lower intermediate layers (13 to 15) to upper intermediate (11 to 12) and thermocline layers (7 to 10) is larger in this model. This redistributes the increased eastward transport of lower thermocline layers, south of Australia, into thermocline (7 to 10) and upper intermediate (11 and 12). The thermocline and upper intermediate layers move northwards into the subtropical Pacific Ocean. The increased northward transport of thermocline and upper intermediate layers results in the increased northward heat flux, while the larger and smaller northward and resulting southward transport of deep (16 to 19) layer results in the increase in the northward salt and silica flux.

A.3 Non-synoptic sections and the Mean Circulation

The inclusion of a different section south of Australia results in changes to the total property flux across the bounding hydrographic sections. These changes are distributed throughout the entire water column.

The largest changes to the total section property fluxes occur across the meridional Indian and Pacific sections. The estimated $15\times10^6 m^3 s^{-1}$ southward transport in the Indian ocean is still in agreement with previous estimates of the Indonesian through-flow, although it would be considered on the high side of the mean transport (Fieux et al. 1994; Meyers et al. 1995; Fieux et al. 1996). The total transport south of Australia varies from $142\times10^6 m^3 s^{-1}$ to $147\times10^6 m^3 s^{-1}$ between the summer 1994 and winter 1995 sections. These transport estimates agree with the the mean transport of $150\times10^6 m^3 s^{-1}$ derived from five repeat sections of SR3 south of Australia (Bindoff et al. 1997).

The difference in the ocean circulation derived using a different section south of Australia result in only minor changes to the property fluxes in the Atlantic Ocean and at Drake Passage and south of Africa. The strength of the Indonesian throughflow is sensitive to the section south of Australia and these changes are mainly contained in the intermediate layers (13 and 14) south of Australia. The circulation derived does appear to represent a mean circulation, supporting the initial assumption that the hydrographic data describe a near steady-state ocean circulation.

Layer	Total
1	0.00
2	0.00
3	0.00
4	0.00
5	0.00
6	0.00
7	0.00
8	0.00
9	0.00
10	-0.01
11	-0.01
12	-0.01
13	-0.02
14	-0.08
15	-0.13
16	-0.16
17	-0.38
18	-0.38
19	-0.53
20	-0.48
21	0.00
22	0.00
23	0.00

Table A.3: Difference of the layer mass flux at Drake Passage between model_var and model_malv ($\times 10^6 m^3 s^{-1}$). +ve - larger eastward flux in model_var, -ve - smaller eastward flux in model_var

Layer	Total
1	0.00
2	0.00
3	0.00
4	0.00
5	0.00
6	0.00
7	0.00
8	0.00
9	0.00
10	0.00
11	-0.01
12	-0.02
13	-0.02
14	-0.08
15	-0.09
16	-0.11
17	-0.23
18	-0.17
19	-0.45
20	-0.52
21	-0.38
22	-0.11
23	0.00

Table A.4: Difference of the layer mass flux south of Africa between model_var and model_malv ($\times 10^6 m^3 s^{-1}$). +ve - larger eastward flux in model_var, -ve - smaller eastward flux in model_var

Layer	Mascarene	Central Ridge	Central Basin	West Aust.	Total
1	0.00	0.00	0.00	0.00	0.00
2	0.00	0.00	0.00	0.00	0.00
3	0.00	0.00	0.00	-0.03	-0.04
4	-0.02	-0.04	-0.02	-0.03	-0.12
5	-0.02	-0.03	-0.01	-0.03	-0.09
6	-0.01	-0.03	-0.01	-0.02	-0.09
7	-0.02	-0.02	-0.01	-0.03	-0.07
8	-0.02	-0.03	-0.02	-0.02	-0.09
9	-0.02	-0.04	-0.02	-0.03	-0.12
10	-0.02	-0.06	-0.04	-0.05	-0.17
11	-0.04	-0.08	-0.05	-0.05	-0.20
12	-0.05	-0.12	-0.07	-0.08	-0.33
13	-0.04	-0.10	-0.06	-0.25	-0.45
14	-0.04	-0.09	-0.06	-0.10	-0.30
15	-0.10	-0.18	-0.12	-0.18	-0.57
16	-0.13	-0.33	-0.19	-0.27	-0.92
17	-0.24	-0.59	-0.40	-0.04	-1.26
18	-0.35	-0.55	-0.37	-0.04	-1.33
19	-0.20	0.00	-0.56	0.06	-0.70
20	-0.02	0.00	0.00	0.00	-0.02
21	0.00	0.00	0.00	0.00	0.00
22	0.00	0.00	0.00	0.00	0.00
23	0.00	0.00	0.00	0.00	0.00

Table A.5: Difference of the layer mass flux at Indian 18S between model_var and model_malv ($\times 10^6 m^3 s^{-1}$). +ve - smaller southward/larger northward flux in model_var, -ve - larger southward/smaller northward flux in model_var

Layer	Natal	Mozam	Mada	Crozet	Central	Ninety R	Perth	Total
1	0.00	0.00	0.00	0.00	0.00	0.00	0.00	0.00
2	0.00	0.00	0.00	0.00	0.00	0.00	0.00	0.00
3	0.00	0.00	0.00	0.00	0.00	0.00	0.00	0.00
4	0.00	0.00	0.00	0.00	0.00	0.00	0.00	0.00
5	0.00	0.00	0.00	0.00	0.00	0.00	0.00	0.00
6	0.00	0.00	0.00	0.00	0.00	0.00	0.00	0.00
7	0.00	0.00	0.00	0.00	0.00	0.00	0.00	0.00
8	-0.01	-0.01	-0.01	0.00	0.00	-0.01	0.00	-0.04
9	-0.03	-0.01	-0.03	-0.02	-0.02	-0.03	-0.01	-0.15
10	-0.10	-0.06	-0.10	-0.04	-0.03	-0.08	-0.06	-0.46
11	-0.06	-0.05	-0.13	-0.10	-0.07	-0.17	-0.08	-0.65
12	-0.04	-0.03	-0.07	-0.05	-0.07	-0.24	-0.14	-0.63
13	-0.03	-0.08	-0.17	-0.04	-0.03	-0.11	-0.06	-0.52
14	-0.05	-0.03	-0.05	-0.05	-0.04	-0.11	-0.06	-0.37
15	-0.05	-0.03	-0.05	-0.07	-0.06	-0.25	-0.14	-0.64
16	-0.08	-0.05	-0.07	-0.09	-0.13	-0.12	-0.16	-0.71
17	-0.09	-0.07	-0.14	-0.16	-0.13	-0.08	-0.25	-0.94
18	-0.10	-0.09	-0.14	-0.29	-0.16	0.00	-0.07	-0.84
19	-0.01	-0.05	-0.23	-0.17	-0.17	0.00	-0.06	-0.68
20	0.00	-0.06	-0.02	-0.10	0.00	0.00	-0.02	-0.19
21	0.00	0.00	0.00	0.00	0.00	0.00	0.00	0.00
22	0.00	0.00	0.00	0.00	0.00	0.00	0.00	0.00
23	0.00	0.00	0.00	0.00	0.00	0.00	0.00	0.00

Table A.6: Difference of the layer mass flux at Indian 32S between model_var and model_malv ($\times 10^6 m^3 s^{-1}$). +ve - smaller southward/larger northward flux in model_var, -ve - larger southward/smaller northward flux in model_var

Layer	Total
1	0.00
2	0.00
3	0.00
4	0.00
5	0.00
6	0.00
7	0.00
8	0.00
9	0.00
10	-0.01
11	-3.67
12	-6.34
13	7.12
14	5.70
15	1.36
16	1.34
17	2.04
18	0.58
19	-0.78
20	-3.06
21	0.38
22	0.00
23	0.00

Table A.7: Difference of the layer mass flux south of Australia between model_var and model_malv ($\times 10^6 m^3 s^{-1}$). +ve - larger eastward/smaller westward (layer 21) flux in model_var, -ve - smaller eastward flux in model_var

Layer	Chile	South West Pacific	Tonga-Kermadac	Tasman	Total
1	0.00	0.00	0.00	0.00	0.00
2	0.00	0.00	0.00	0.00	0.00
3	0.00	0.00	0.00	0.00	0.00
4	0.00	0.00	0.00	0.00	0.00
5	0.00	0.00	0.00	0.00	0.00
6	0.00	0.00	0.00	0.00	0.00
7	-0.04	0.00	0.00	0.02	-0.02
8	-0.02	0.02	0.07	0.04	0.11
9	-0.06	0.08	0.35	0.03	0.40
10	-0.05	0.11	0.36	0.03	0.45
11	-0.05	0.07	0.32	0.03	0.37
12	-0.05	0.11	0.33	0.03	0.42
13	-0.17	0.28	0.45	0.06	0.62
14	-0.17	0.18	0.47	0.06	0.54
15	-0.16	0.18	0.42	0.06	0.50
16	-0.29	0.25	0.42	0.11	0.48
17	-0.67	0.89	0.80	0.20	1.22
18	-0.42	0.78	0.05	0.15	0.56
19	0.00	0.76	0.00	0.34	1.10
20	0.00	0.09	0.00	0.00	0.09
21	0.00	0.00	0.00	0.00	0.00
22	0.00	0.00	0.00	0.00	0.00
23	0.00	0.00	0.00	0.00	0.00

Table A.8: Difference of the layer mass flux at Pacific 32S between model_var and model_malv ($\times 10^6 m^3 s^{-1}$). +ve - larger northward/smaller southward flux in model_var, -ve - smaller northward/larger southward flux in model_var

Layer	SV2	SV4	Drake	SAfrica	Ind18	Ind32	Wedsea	SAust	Pac
1	0.00	0.00	0.00	0.00	0.00	0.00	0.00	0.00	0.00
2	0.00	0.00	0.00	0.00	0.00	0.00	0.00	0.00	0.00
3	0.00	0.00	0.00	0.00	0.00	-0.83	0.00	0.00	0.00
4	0.00	0.00	0.00	0.00	0.00	-3.08	0.00	0.00	0.00
5	-0.05	0.00	0.00	0.00	0.00	-2.01	0.00	0.00	0.00
6	-0.13	0.00	0.00	0.00	0.00	-1.90	-0.01	0.00	0.00
7	-0.02	-0.05	0.00	0.00	0.00	-1.57	-0.02	0.00	-0.29
8	-0.25	-0.06	0.00	0.04	0.00	-1.78	-0.71	0.00	2.22
9	-0.20	-0.09	0.00	0.02	0.00	-2.01	-2.79	0.00	7.38
10	-0.29	-0.19	-0.03	0.11	0.00	-2.54	-6.89	0.01	6.92
11	-0.16	-0.28	-0.05	0.02	0.00	-2.62	-8.21	-27.39	4.61
12	-0.01	-0.44	-0.04	-0.10	0.00	-3.35	-6.27	-42.08	4.07
13	-0.05	-0.16	-0.12	-0.11	0.00	-3.47	-3.52	45.76	4.63
14	-0.14	-0.21	-0.27	-0.25	0.00	-1.90	-2.07	53.04	3.15
15	-0.14	-0.01	-0.26	-0.21	0.00	-2.95	-2.53	3.34	2.25
16	-0.18	0.01	-0.34	-0.24	0.00	-3.65	-2.25	2.95	1.60
17	-0.36	0.01	-0.80	-0.49	0.00	-3.25	-2.38	2.67	2.81
18	-0.07	-0.06	-0.63	-0.29	0.01	-2.38	-1.64	1.14	0.90
19	0.64	0.13	-0.60	-0.52	0.00	-0.99	-0.90	-0.58	1.36
20	0.02	0.03	-0.28	-0.16	0.00	-0.02	-0.15	-0.69	0.09
21	0.00	-0.01	0.00	0.10	0.01	0.00	0.00	0.12	0.00
22	0.00	0.00	0.00	0.05	0.00	0.00	0.00	0.00	0.00
23	0.00	0.00	0.00	0.00	0.00	0.00	0.00	0.00	0.00

Table A.9: Difference of the Total Layer Heat Flux for each section between model_var and model_malv (°C $\times 10^6 m^3 s^{-1}$). +ve - larger eastward/northward (smaller southward) flux in model_var, -ve - smaller eastward/northward (larger southward) flux in model_var

Layer	SV2	SV4	Drake	SAfrica	Ind18	Ind32	Wedsea	SAust	Pac
1	0.00	0.00	0.00	0.00	0.00	0.00	0.00	0.00	0.00
2	0.00	0.00	0.00	0.00	0.00	0.00	0.00	0.00	0.00
3	0.00	0.00	0.00	0.00	0.00	-1.13	0.00	0.00	0.00
4	0.00	0.00	0.00	0.00	0.00	-4.39	0.00	0.00	0.00
5	-0.07	0.00	0.00	0.00	0.00	-3.05	0.00	0.00	0.00
6	-0.17	0.00	0.00	0.00	0.00	-3.10	-0.02	0.00	0.00
7	-0.04	-0.10	0.00	0.00	0.00	-2.76	-0.03	0.00	-0.62
8	-0.40	-0.11	0.00	0.07	0.00	-3.36	-1.31	0.00	4.05
9	-0.36	-0.19	0.00	0.04	0.00	-4.18	-5.64	0.00	14.70
10	-0.68	-0.47	-0.11	0.22	0.00	-6.07	-16.91	-0.33	16.18
11	-0.48	-0.77	-0.20	-0.17	0.00	-7.48	-23.53	-128.35	13.43
12	-0.04	-1.75	-0.27	-0.63	0.00	-11.70	-22.80	-222.86	15.01
13	-0.28	-0.74	-0.87	-0.86	0.00	-16.24	-18.30	251.03	21.91
14	-0.93	-1.55	-2.80	-2.63	0.02	-10.59	-13.03	203.89	19.11
15	-1.23	0.15	-4.40	-3.31	0.01	-20.31	-22.80	48.05	17.80
16	-1.71	0.38	-5.62	-3.97	0.03	-32.85	-25.27	47.64	17.29
17	-3.50	0.52	-13.76	-8.40	0.07	-45.19	-33.56	72.75	43.69
18	-0.75	-0.35	-13.37	-6.24	0.04	-47.35	-30.37	20.73	20.09
19	9.62	3.90	-19.17	-15.96	0.02	-24.93	-24.49	-27.86	39.47
20	0.96	1.51	-17.16	-18.45	-0.19	-0.49	-6.97	-109.86	3.21
21	0.00	-0.54	0.00	-13.36	-0.03	0.00	0.00	13.65	0.00
22	0.00	0.00	0.00	-3.96	0.02	0.00	0.00	0.00	0.00
23	0.00	0.00	0.00	0.00	0.00	0.00	0.00	0.00	0.00

Table A.10: Difference of the Total Layer Salt Flux for each section between model_var and model_malv ($\times 10^6 kgs^{-1}$). +ve - larger eastward/northward (smaller southward) flux in model_var, -ve - smaller eastward/northward (larger southward) flux in model_var

Appendix B

Error Analysis

This chapter contains details of the error analysis given. The method described is the same given by Wunsch et al. (1983), Rintoul (1988) and Macdonald (1991) and is repeated here for completeness of the thesis.

The "true" velocity at the hydrographic section can be written as:

$$\begin{aligned} v &= v_{rel} + vE + b + \sum_{l=k+1}^{N} \alpha_l Q_l \\ &= A_1 + A_2 + A_3 + A_4 \end{aligned} \tag{B.1}$$

where

v_{rel} Relative velocity

vE Ekman velocity

b Reference velocity

Q Null space

The flux of property C across the hydrographic sections is then:

$$F_c = B_1 + B_2 + B_3 + B_4 \tag{B.2}$$

where B_1 is the flux due to the relative velocities, B_2 is the flux due to the Ekman and other velocities, while B_3 and B_4 are the fluxes due to the reference velocity and the null space, respectively, and can be written:

$$B_3 = C^t b = \sum_{l=1}^{k} \alpha_l C^t V_l \tag{B.3}$$

and

$$B_4 = \sum_{l=k+1}^{N} \alpha_l C^t Q_l \tag{B.4}$$

The errors in the total flux F_c result from the individual component of the flux. The errors in the relative flux (B_1) are due to noise in the observations, errors in B_2 result from error in the wind stress. The error in the reference velocity (B_3) result from noise in the hydrographic sections, while the B_4 is the flux of the unresolved the null-space.

The SVD provides an estimate of error for B_3 and B_4. The column and row weighted SVD shows the variance of the i'th solution element is

$$\frac{< b_i^2 >}{\alpha^2} = \sum_{i=1} k \frac{v_{ji}^2}{\sigma_i^2} \tag{B.5}$$

where $< b_i^2 >$ is the solution variance and α^2 is the problem variance. The problem variance is found by examining the residuals in the conservation equations:

$$\alpha^2 = \sum_{i=1} k \frac{(Ab + d)_i^2}{M - k} \tag{B.6}$$

The formal error in the flux of $C_i b_i$ is then given by:

$$< (\sum_i C_i b_i)(\sum_j C_j b_j) >= \alpha^2 \sum_i \sum_j C_i C_j \frac{(V_{li} V_{lj})}{\sigma_l^2} \tag{B.7}$$

where C_{ij} is the vertically integrated tracer concentration $C_j = \triangle x_j \int_{D_j}^{0} C_j \rho_j dz$. The square root of this value is the noise error in the reference velocity (B_3).

To estimate the error in B_4 we use the fact that the **V** and **Q** vectors form a complete set to rewrite the vector tracer concentrations C as:

$$C = \sum_{l=1}^{k} (C^t V_l) V_l + \sum_{l=k+1}^{N} (C^t Q_l) Q_l \tag{B.8}$$

From equation Equation B.4, following Wunsch et al. (1983), the squared magnitude of B_4 is:

$$|B_4|^2 \leq (\sum_i \alpha_i^2) C^t C \frac{C^t Q Q^t C}{C^t C} (\sum_i \alpha_i^2) C^t C \Delta \tag{B.9}$$

The null space error calculated is the transport of each property if there is an increase in the rms null-space (α) velocity of $1 cms^{-1}$. Δ can be determined in terms of $\mathbf{V}$ so that it is not nessary to calculate the null-spaced vectors.

$$\Delta \equiv \frac{C^t Q Q^t C}{C^t C} = 1 - \frac{C^t V V^t C}{C^t C} \tag{B.10}$$

where $C^t V V^t C$ is the squared projection of $\mathbf{C}$ onto the range of $\mathbf{A}$. If the problem is fully determined, or $\mathbf{C}$ is orthogonal to the null-space $\Delta = 0$, then the uncertainty due to B_4 is zero. In this problem the projection of $\mathbf{C}$ onto the null-space is small.

The error estimates given in the text are a combination of $B_3 + B_4$. These errors are calculated for both the lateral and dianeutral fluxes.

Appendix C

Accuracy of Inverse Methods

This chapter provides a comparsion of the layer mass, heat and salt inverse fluxes with the "true" and relative FRAM fluxes for each of the four boxes south of Australia used in the study which test the accuracy of inverse methods.

Sections	Property	Inverse	FRAM Total	FRAM Relative
1	Mass	−3.46	−3.55	0.28
	Heat	−48.81	−54.54	−38.49
	Salt	0.26	2.45	1.39
2	Mass	3.33	3.55	−5.51
	Heat	49.37	56.40	24.17
	Salt	−2.72	−2.55	0.26
3	Mass	24.42	21.54	32.93
	Heat	178.12	175.85	205.35
	Salt	−11.47	−10.74	−14.45
4	Mass	−28.43	−28.26	−42.01
	Heat	−164.2	−180.1	−215.94
	Salt	12.12	13.00	17.06
5	Mass	7.57	10.93	5.57
	Heat	43.55	63.83	30.50
	Salt	−2.82	−3.94	−2.26
6	Mass	122.41	124.60	132.89
	Heat	368.79	367.66	389.55
	Salt	−63.10	−63.66	−66.98
7	Mass	16.28	21.82	−1.96
	Heat	18.96	23.04	−0.55
	Salt	−6.6801	−8.27	−0.60
8	Mass	−167.29	−175.34	−153.22
	Heat	−574.00	−589.66	−529.08
	Salt	83.43	86.17	77.99
9	Mass	47.65	52.34	45.15
	Heat	42.86	44.39	41.81
	Salt	−17.28	−18.70	−16.49
10	Mass	−31.31	−30.52	−22.82
	Heat	−25.54	−22.56	−18.99
	Salt	10.47	10.28	7.82

Table C.1: Comparison of section property fluxes of inverse (mod_fram), "true" FRAM and "relative" FRAM (+ve is eastward and northward, -ve is westward or southward) Units: mass ($\times 10^6 m^3 s^{-1}$), heat ($\times 10^6$ °C $m^3 s^{-1}$)), salt ($\times 10^3$ (psu-35)$m^3 s^{-1}$)

Sections	Property	Inverse	FRAM Total	FRAM Relative
1	Mass	−2.33	−3.5	0.28
	Heat	−50.49	−54.54	−38.49
	Salt	2.19	0.24	0.14
2	Mass	2.20	3.55	−5.51
	Heat	51.04	56.40	24.17
	Salt	−2.33	−2.55	0.26
3	Mass	26.73	21.54	32.93
	Heat	186.01	175.85	205.35
	Salt	−12.25	−10.74	−14.45
4	Mass	−28.70	−28.26	−42.01
	Heat	−152.75	−180.06	−215.94
	Salt	12.26	13.00	17.06
5	Mass	4.40	10.93	5.57
	Heat	25.89	63.83	30.50
	Salt	−1.78	−3.94	−2.26
6	Mass	113.71	124.60	132.89
	Heat	352.70	367.66	389.55
	Salt	−59.73	−63.66	−66.98
7	Mass	16.37	21.82	−1.96
	Heat	18.25	23.04	−0.55
	Salt	−6.68	−8.27	−0.60
8	Mass	−158.95	−175.34	−153.22
	Heat	−545.74	−589.66	−529.08
	Salt	80.24	86.17	77.99
9	Mass	49.25	52.34	45.15
	Heat	43.60	44.39	41.81
	Salt	−17.76	−18.70	−16.49
10	Mass	−32.81	−30.52	−22.82
	Heat	−27.00	−22.56	−18.99
	Salt	10.96	10.28	7.82

Table C.2: Comparison of section property fluxes of inverse with explicit dianeutral fluxes (mod_expl), "true" FRAM and "relative" FRAM (+ve is eastward and northward, -ve is westward or southward) Units: mass ($\times 10^6 m^3 s^{-1}$), heat ($\times 10^6$ °C $m^3 s^{-1}$)), salt ($\times 10^3$ (psu-35)$m^3 s^{-1}$)

Sections	Property	Inverse	FRAM Total	FRAM Relative
1	Mass	−2.76	−3.55	0.28
	Heat	−46.81	−54.54	−38.49
	Salt	0.23	2.45	1.39
2	Mass	2.61	3.55	−5.51
	Heat	47.36	56.40	24.17
	Salt	−2.52	−2.55	0.26
3	Mass	25.81	21.54	32.93
	Heat	182.54	175.85	205.35
	Salt	−11.96	−10.74	−14.45
4	Mass	−30.30	−28.26	−42.01
	Heat	−169.68	−180.06	−215.94
	Salt	12.77	13.00	17.06
5	Mass	7.40	10.93	5.57
	Heat	42.31	63.83	30.50
	Salt	−2.78	−3.94	−2.26
6	Mass	121.92	124.60	132.89
	Heat	367.60	367.66	389.55
	Salt	−62.88	−39.39	−66.98
7	Mass	13.99	21.82	−1.96
	Heat	18.18	23.04	−0.55
	Salt	−5.94	−8.27	−0.60
8	Mass	−166.22	−175.34	−153.22
	Heat	−577.40	−589.66	−529.08
	Salt	83.22	86.17	77.99
9	Mass	45.11	52.34	45.15
	Heat	41.63	44.39	41.81
	Salt	−16.47	−18.70	−16.49
10	Mass	−31.70	−30.52	−22.82
	Heat	−25.16	−22.56	−18.99
	Salt	10.40	10.28	7.82

Table C.3: Comparison of section property fluxes of inverse (mod_fram) with 10% random error, "true" FRAM and "relative" FRAM (+ve is eastward and northward, -ve is westward or southward) Units: mass ($\times 10^6 m^3 s^{-1}$), heat ($\times 10^6$ °C $m^3 s^{-1}$)), salt ($\times 10^3$ (psu-35)$m^3 s^{-1}$)

Sections	Property	Inverse	FRAM Total	FRAM Relative
1	Mass	−3.17	−3.55	0.28
	Heat	−48.03	−54.54	−38.49
	Salt	2.49	2.45	1.39
2	Mass	3.02	3.55	−5.51
	Heat	48.56	56.40	24.17
	Salt	−2.63	−2.55	0.26
3	Mass	25.51	21.54	32.93
	Heat	181.59	175.85	205.35
	Salt	−11.86	−10.74	−14.45
4	Mass	−29.67	−28.26	−42.01
	Heat	−168.21	−180.06	−215.94
	Salt	12.56	13.00	17.06
5	Mass	7.47	10.93	5.57
	Heat	43.01	6.3.83	30.50
	Salt	−2.79	−3.94	−2.26
6	Mass	119.97	124.60	132.89
	Heat	365.37	367.66	389.55
	Salt	−62.18	−63.66	−66.98
7	Mass	16.78	21.82	−1.96
	Heat	19.21	23.04	−0.55
	Salt	−6.83	−8.27	−0.60
8	Mass	−166.43	−175.34	−153.22
	Heat	−574.81	−589.66	−529.08
	Salt	83.21	86.17	77.99
9	Mass	45.86	52.34	45.15
	Heat	41.65	44.39	41.81
	Salt	−16.72	−18.70	−16.49
10	Mass	−29.03	−30.52	−22.82
	Heat	−24.07	−22.56	−18.99
	Salt	9.76	10.28	7.82

Table C.4: Comparison of section property fluxes of inverse with explicit dia-neutral fluxes (mod_expl) and 10% random error, "true" FRAM and "relative" FRAM (+ve is eastward and northward, -ve is westward or southward) Units: mass ($\times 10^6 m^3 s^{-1}$), heat ($\times 10^6$ °C $m^3 s^{-1}$)), salt ($\times 10^3$ (psu-35)$m^3 s^{-1}$)

Appendix D

Model_Int: Basin and Layer fluxes

This chapter contains the layer mass flux in each basin of each section for model_int. The heat and salt flux are the total layer flux at each section, the individual basin and layer silica flux across the Indian 32°S is also shown.

Layer	Angola	Brazil	Total
1	0.00	0.00	0.00
2	0.00	0.00	0.00
3	0.00	0.00	0.00
4	0.00	0.00	0.00
5	0.04	-0.30	-0.26
6	-0.28	-1.05	-1.33
7	-1.17	0.39	-0.77
8	0.14	2.53	2.66
9	1.55	1.79	3.34
10	-1.63	3.61	1.98
11	-1.76	4.01	2.25
12	-1.10	3.02	1.92
13	-1.36	3.08	1.72
14	-1.47	3.05	1.59
15	-0.70	1.48	0.78
16	-1.06	0.54	-0.51
17	-4.04	-5.86	-9.90
18	-0.54	-8.00	-8.54
19	0.13	1.67	1.79
20	0.00	2.57	2.57
21	0.00	0.00	0.00
22	0.00	0.00	0.00
23	0.00	0.00	0.00

Table D.1: Layer Mass flux SAVE 2 ($\times 10^6 m^3 s^{-1}$) for the model_int (+ve North)

Layer	Argentine	Ridge	Angola	Cape	Total
1	0.00	0.00	0.00	0.00	0.00
2	0.00	0.00	0.00	0.00	0.00
3	0.00	0.00	0.00	0.00	0.00
4	0.00	0.00	0.00	0.00	0.00
5	0.00	0.00	0.00	0.00	0.00
6	0.00	0.00	0.00	0.00	0.00
7	0.00	0.00	0.00	0.19	0.19
8	0.00	-0.38	-0.69	1.90	0.82
9	0.00	-0.03	-0.47	1.28	0.78
10	-1.98	-1.38	-3.96	7.68	0.37
11	4.14	-2.43	-2.47	4.89	4.12
12	3.96	-1.63	-1.65	3.53	4.21
13	5.38	-4.79	-1.81	3.02	1.80
14	6.73	-7.45	-2.52	3.46	0.21
15	4.44	-6.00	-2.43	2.11	-1.88
16	4.11	-3.55	-2.56	0.81	-1.19
17	6.79	-3.16	-3.66	-2.31	-2.33
18	4.17	-2.42	-3.47	-5.42	-7.14
19	4.78	-2.82	-1.91	-4.35	-4.30
20	3.85	-0.05	0.00	-0.01	3.79
21	-0.02	0.00	0.00	0.00	-0.02
22	0.00	0.00	0.00	0.00	0.00
23	0.00	0.00	0.00	0.00	0.00

Table D.2: Layer Mass flux SAVE4 ($\times 10^6 m^3 s^{-1}$) for the model_int (+ve North, East)

Layer	Total
1	0.00
2	0.00
3	0.00
4	0.00
5	0.00
6	0.00
7	0.00
8	0.00
9	0.00
10	1.12
11	1.39
12	2.28
13	9.27
14	18.36
15	19.12
16	19.29
17	30.02
18	15.58
19	12.52
20	4.15
21	0.00
22	0.00
23	0.00

Table D.3: Layer Mass flux Drake Passage ($\times 10^6 m^3 s^{-1}$) for the model_int (+ve east)

Layer	Total
1	0.00
2	0.00
3	0.00
4	0.00
5	0.00
6	0.00
7	0.05
8	-1.05
9	-0.37
10	-0.65
11	1.00
12	3.91
13	5.82
14	13.69
15	17.22
16	17.15
17	29.25
18	16.82
19	14.92
20	7.84
21	5.94
22	2.10
23	0.00

Table D.4: Layer Mass flux South Africa ($\times 10^6 m^3 s^{-1}$) for the model_int (+ve east)

Layer	Total
1	0.00
2	0.00
3	0.00
4	0.00
5	0.00
6	0.00
7	0.00
8	0.00
9	0.00
10	0.00
11	0.00
12	0.00
13	0.39
14	-0.34
15	-0.33
16	0.29
17	-2.84
18	-2.81
19	-4.13
20	-8.70
21	6.46
22	12.01
23	0.00

Table D.5: Layer Mass flux Weddell Sea ($\times 10^6 m^3 s^{-1}$) for the model_int (+ve north)

Layer	Mascarene	Central Ridge	Central Basin	West Aust.	Total
1	0.00	0.00	0.00	0.00	0.00
2	0.00	0.00	0.00	0.00	0.00
3	-0.50	0.00	-1.60	0.67	-1.44
4	-4.63	-0.34	-3.03	-3.52	-11.52
5	-1.91	1.22	0.01	1.42	0.74
6	-2.17	1.19	-0.09	1.30	0.23
7	-1.01	0.95	0.12	0.79	0.86
8	-1.95	0.94	0.30	0.92	0.22
9	-2.03	0.91	0.16	1.24	0.29
10	-2.45	1.00	0.32	1.73	0.60
11	-3.18	1.34	0.49	1.66	0.31
12	-2.83	1.41	0.79	1.82	1.19
13	-2.44	0.58	0.24	5.75	4.13
14	-1.99	0.55	-0.11	1.31	-0.24
15	-2.29	0.99	-0.49	1.05	-0.75
16	-1.52	1.48	-1.01	1.16	0.12
17	-0.32	5.25	-3.30	-3.13	-1.51
18	-0.60	2.79	-5.67	-2.42	-5.90
19	2.04	0.00	-6.03	0.89	-3.10
20	1.04	0.00	0.00	0.00	1.04
21	0.00	0.00	0.00	0.00	0.00
22	0.00	0.00	0.00	0.00	0.00
23	0.00	0.00	0.00	0.00	0.00

Table D.6: Layer Mass flux Indian 18S ($\times 10^6 m^3 s^{-1}$) for the model_int (+ve north)

Layer	Natal	Mozam	Mada	Crozet	Central	Ninety R	Perth	Total
1	0.00	0.00	0.00	0.00	0.00	0.00	0.00	0.00
2	0.00	0.00	0.00	0.00	0.00	0.00	0.00	0.00
3	0.00	0.00	0.00	0.00	0.00	0.00	0.00	0.00
4	0.00	0.00	0.00	0.00	0.00	0.00	0.00	0.00
5	0.00	0.00	0.00	0.00	0.00	0.00	0.00	0.00
6	-0.21	0.00	0.00	0.00	0.00	0.00	0.00	-0.21
7	-0.14	0.00	0.00	0.00	0.00	0.02	0.00	-0.12
8	-2.29	-0.25	-0.23	0.07	-0.68	0.09	0.00	-3.28
9	-4.95	0.44	0.71	0.74	0.82	-0.04	0.07	-2.21
10	-7.98	1.01	-0.74	3.76	0.63	-0.71	1.81	-2.22
11	-7.37	-0.14	-4.07	8.68	2.84	-1.69	3.11	1.36
12	-4.84	-0.16	-1.41	1.90	1.95	-3.59	3.79	-2.36
13	-3.55	-0.43	-2.65	1.43	0.94	-1.57	1.11	-4.72
14	-3.41	0.11	-1.73	1.51	0.59	-1.82	0.13	-4.63
15	-2.49	0.10	-1.62	1.54	0.36	-4.62	-2.64	-9.37
16	-1.43	0.77	-1.59	1.44	-1.12	-2.31	-2.45	-6.68
17	1.14	3.52	-1.42	1.58	-0.87	-1.58	-7.36	-5.00
18	5.28	6.77	0.61	-1.01	-0.69	0.00	-1.51	9.45
19	0.84	2.23	-1.36	-0.27	0.43	0.00	2.12	3.99
20	0.00	1.65	0.63	3.10	0.00	0.00	5.89	11.27
21	0.00	0.00	0.00	0.00	0.00	0.00	0.00	0.00
22	0.00	0.00	0.00	0.00	0.00	0.00	0.00	0.00
23	0.00	0.00	0.00	0.00	0.00	0.00	0.00	0.00

Table D.7: Layer Mass flux Indian 32S ($\times 10^6 m^3 s^{-1}$) for the model_int (+ve north)

Layer	Total
1	0.00
2	0.00
3	0.00
4	0.00
5	0.00
6	0.00
7	0.00
8	0.00
9	0.00
10	0.03
11	3.84
12	15.21
13	12.65
14	15.89
15	16.28
16	16.84
17	29.09
18	22.24
19	13.82
20	4.57
21	-2.09
22	0.00
23	0.00

Table D.8: Layer Mass flux South Australia ($\times 10^6 m^3 s^{-1}$) for the model_int (+ve east)

Layer	Chile	South West Pacific	Tonga-Kermadac	Tasman	Total
1	0.00	0.00	0.00	0.00	0.00
2	0.00	0.00	0.00	0.00	0.00
3	0.00	0.00	0.00	0.00	0.00
4	0.00	0.00	0.00	0.00	0.00
5	0.00	0.00	0.00	0.00	0.00
6	0.00	0.00	0.00	0.00	0.00
7	1.16	0.00	0.00	-2.25	-1.09
8	2.59	-0.38	-3.76	2.10	0.55
9	2.12	0.60	7.38	-0.14	9.97
10	1.70	4.63	-4.36	-0.43	1.53
11	0.81	2.58	-2.43	-0.77	0.19
12	0.67	2.74	-3.22	-0.47	-0.28
13	2.15	6.38	-4.98	-0.49	3.06
14	1.25	3.06	-4.00	-0.31	-0.01
15	-0.60	1.96	-2.95	-0.59	-2.18
16	-5.04	1.45	-2.37	-0.90	-6.86
17	-10.26	2.49	-2.85	-1.13	-11.75
18	-4.08	2.20	-0.16	-0.30	-2.35
19	0.00	16.21	0.00	0.07	16.28
20	0.00	8.23	0.00	0.00	8.23
21	0.00	0.00	0.00	0.00	0.00
22	0.00	0.00	0.00	0.00	0.00
23	0.00	0.00	0.00	0.00	0.00

Table D.9: Layer Mass flux Pacific 32S ($\times 10^6 m^3 s^{-1}$) for the model_int (+ve north)

Layer	SV2	SV4	Drake	SAfrica	Wedsea	Ind18	Ind32	SAust	Pac
1	0.00	0.00	0.00	0.00	0.00	0.00	0.00	0.00	0.00
2	0.00	0.00	0.00	0.00	0.00	0.00	0.00	0.00	0.00
3	0.00	0.00	0.00	0.00	0.00	-36.74	0.00	0.00	0.00
4	0.00	0.00	0.00	0.00	0.00	-290.57	0.00	0.00	0.00
5	-7.54	0.00	0.00	0.00	0.00	16.44	0.00	0.00	0.00
6	-36.34	0.00	0.00	0.00	0.00	4.64	-4.74	0.00	0.00
7	-16.70	3.70	0.00	0.97	0.00	17.55	-2.59	0.00	-28.40
8	61.67	17.16	0.00	-20.51	0.00	3.83	-68.10	0.00	8.01
9	67.16	13.11	0.00	-6.56	0.00	4.81	-38.44	0.00	172.14
10	32.36	17.63	9.69	-11.78	0.00	8.78	-41.90	0.24	12.92
11	26.78	46.36	10.89	-3.65	0.00	3.33	19.48	29.22	-2.86
12	18.98	39.17	13.50	18.29	0.00	11.59	-24.92	109.11	-8.74
13	12.97	10.32	45.46	20.86	0.73	28.40	-33.72	63.79	12.66
14	6.39	0.25	68.86	38.11	-1.72	-2.15	-28.75	57.82	-3.61
15	2.22	-2.42	43.27	36.20	-0.59	-4.16	-37.47	45.73	-11.28
16	-2.19	-2.15	42.12	34.24	-0.22	-0.58	-22.31	40.83	-24.80
17	-36.69	-4.83	63.01	59.29	-5.21	-5.75	-11.83	62.46	-26.53
18	-25.12	-19.07	26.24	27.24	-3.05	-10.89	21.36	37.08	-4.56
19	2.84	-11.78	14.36	15.66	-3.58	-6.03	8.15	14.53	19.02
20	2.14	1.76	2.47	0.51	-2.21	1.02	9.37	1.67	8.73
21	0.00	-0.01	0.00	-1.67	-3.27	0.00	0.00	0.13	0.00
22	0.00	0.00	0.00	-0.99	-5.29	0.00	0.00	0.00	0.00
23	0.00	0.00	0.00	0.00	0.00	0.00	0.00	0.00	0.00

Table D.10: Total Layer Heat Flux for each section ($\times 10^6$ °C $m^3 s^{-1}$) for the model_int (+ve north/east)

Layer	SV2	SV4	Drake	SAfrica	Wedsea	Ind18	Ind32	SAust	Pac
1	0.00	0.00	0.00	0.00	0.00	0.00	0.00	0.00	0.00
2	0.00	0.00	0.00	0.00	0.00	0.00	0.00	0.00	0.00
3	0.00	0.00	0.00	0.00	0.00	-51.37	0.00	0.00	0.00
4	0.00	0.00	0.00	0.00	0.00	-411.92	0.00	0.00	0.00
5	-9.71	0.00	0.00	0.00	0.00	25.29	0.00	0.00	0.00
6	-56.18	0.00	0.00	0.00	0.00	6.92	-7.58	0.00	0.00
7	-28.99	6.45	0.00	1.78	0.00	30.16	-4.28	0.00	-42.17
8	98.16	36.10	0.00	-37.19	0.00	6.89	-120.11	0.00	20.81
9	122.31	25.84	0.00	-12.85	0.00	9.31	-82.37	0.00	375.00
10	69.12	41.09	39.28	-19.06	0.00	20.47	-83.86	0.00	67.98
11	80.13	140.05	48.86	42.13	0.00	9.32	43.73	0.00	18.86
12	69.04	135.84	80.00	141.25	0.00	39.93	-90.64	290.29	2.18
13	62.63	66.75	326.49	208.78	14.33	143.03	-172.25	698.88	119.99
14	58.95	28.68	647.11	487.88	-5.53	-11.15	-167.65	770.96	14.09
15	29.97	-51.27	674.76	614.14	-7.26	-31.59	-338.78	615.14	-64.43
16	-20.62	-73.60	685.04	620.31	22.85	-3.56	-244.77	639.75	-236.68
17	-366.52	-118.24	1075.90	1065.69	-53.06	-64.83	-186.58	1098.88	-422.60
18	-326.58	-378.02	561.11	660.00	-44.08	-223.43	332.53	798.90	-113.90
19	74.69	-94.68	448.16	539.09	-82.13	-116.73	137.92	445.62	577.80
20	116.29	156.79	138.83	235.26	-260.78	36.89	401.88	37.57	291.66
21	0.00	52.22	0.00	146.70	65.52	0.00	0.00	-63.64	0.00
22	0.00	0.00	0.00	53.72	349.50	0.00	0.00	0.00	0.00
23	0.00	0.00	0.00	0.00	0.00	0.00	0.00	0.00	0.00

Table D.11: Total Layer Salt Flux for each section ($\times 10^6 kgs{-}1$) for the model_int (+ve north/east)

Layer	Natal	Mozam	Mada	Crozet	Central	Ninety R	Perth	Total
1	0.000	0.000	0.000	0.000	0.000	0.000	0.000	0.000
2	0.000	0.000	0.000	0.000	0.000	0.000	0.000	0.000
3	0.000	0.000	0.000	0.000	0.000	0.000	0.000	0.000
4	0.000	0.000	0.000	0.000	0.000	0.000	0.000	0.000
5	0.000	0.000	0.000	0.000	0.000	0.000	0.000	0.000
6	-0.987	0.000	0.000	0.000	0.000	0.000	0.000	-0.987
7	-0.750	0.000	0.000	0.000	0.000	0.037	0.000	-0.713
8	-6.723	-0.543	-0.305	0.113	-0.956	0.263	0.000	-8.152
9	-17.876	0.865	1.659	1.053	1.749	-0.211	-0.225	-12.986
10	-24.801	4.360	-0.117	9.801	1.110	-1.937	3.694	-7.889
11	-43.802	0.282	-17.110	34.382	10.196	-4.272	5.823	-14.502
12	-65.890	-0.727	-12.711	16.428	11.703	-17.970	15.866	-53.302
13	-82.798	-13.143	-81.179	24.203	14.331	-21.324	13.272	-146.638
14	-128.250	-0.574	-50.264	40.166	18.164	-54.004	0.440	-174.321
15	-138.430	0.974	-73.832	68.821	16.636	-298.271	-208.031	-632.135
16	-99.267	49.382	-103.804	92.575	-108.568	-186.029	-196.858	-552.569
17	83.634	268.662	-113.828	129.500	-80.911	-155.887	-733.561	-602.390
18	387.434	545.300	64.374	-125.296	-72.126	0.000	-172.480	627.206
19	76.527	214.840	-237.524	-40.558	50.937	0.000	265.608	329.829
20	0.000	205.848	81.524	414.353	0.000	0.000	761.418	1463.142
21	0.000	0.000	0.000	0.000	0.000	0.000	0.000	0.000
22	0.000	0.000	0.000	0.000	0.000	0.000	0.000	0.000
23	0.000	0.000	0.000	0.000	0.000	0.000	0.000	0.000

Table D.12: Layer Silica flux Indian 32S $kmols^{-1}$) for the model_int ((+ve north)

layer	Advection	
	Surf.	Layers
1		
2		
3		
4	0.13±3.5	0.13
5	-0.13±3.4	-0.26
6	-1.46±3.3	-1.33
7	-2.42±3.2	-0.96
8	-0.58±3.0	1.84
9	1.99±3.0	2.56
10	3.60±2.8	1.61
11	1.72±2.7	-1.87
12	-0.57±2.6	-2.29
13	-0.65±2.5	-0.08
14	0.73±2.5	1.38
15	3.38±2.4	2.65
16	4.06±2.2	0.68
17	-3.50±2.1	-7.56
18	-4.89±1.9	-1.39
19	1.20±1.3	6.09
20	-0.02±0.8	-1.22
21		0.02
22		
23		

Table D.13: Dianeutral Interior Mass Flux Box I ($\times 10^6 m^3 s^{-1}$) for the model_int. Positive : upwards flux across surface, convergence into layer. Negative : downward flux across surface, divergence from layer.

layer	Advection	
	Surf.	Layers
1		
2		
3		
4		
5		
6		
7	0.24±0.8	0.24
8	0.02±1.1	-0.22
9	0.43±1.3	0.42
10	-0.96±1.4	-1.39
11	2.78±1.5	3.74
12	8.61±1.6	5.83
13	6.57±1.7	-2.04
14	2.45±1.7	-4.12
15	-0.99±1.8	-3.44
16	-4.61±1.8	-3.62
17	-4.87±1.8	-0.26
18	-7.96±1.8	-3.09
19	-5.73±1.9	2.23
20	10.45±1.4	16.18
21	9.91±0.8	-0.54
22		-9.91
23		

Table D.14: Dianeutral Interior Mass Flux Box II ($\times 10^6 m^3 s^{-1}$) for the model_int. Positive : upwards flux across surface, convergence into layer. Negative : downward flux across surface, divergence from layer.

layer	Advection	
	Surf.	Layers
1		
2		
3	-1.44±0.8	-1.44
4	-12.95±1.1	-11.52
5	-12.22±1.3	0.74
6	-11.78±1.5	0.44
7	-10.80±1.6	0.98
8	-7.30±1.7	3.50
9	-4.80±1.7	2.50
10	-1.98±1.8	2.82
11	-3.04±1.8.8	-1.06
12	0.52±1.8	3.55
13	9.37±1.9	8.85
14	13.75±1.9	4.39
15	22.37±1.9	8.62
16	29.17±2.0	6.80
17	32.67±1.8	3.50
18	17.32±1.4	-15.35
19	10.23±0.9	-7.09
20		-10.23
21		
22		
23		

Table D.15: Dianeutral Interior Mass Flux Box IV ($\times 10^6 m^3 s^{-1}$) for the model_int. Positive : upwards flux across surface, convergence into layer. Negative : downward flux across surface, divergence from layer.

layer	Advection	
	Surf.	Layers
1		
2		
3		
4		
5		
6	-0.21±0.8	-0.21
7	-0.38±1.1	-0.17
8	-2.62±1.3	-2.24
9	-4.46±1.5	-1.84
10	-6.00±1.6	-1.54
11	-1.80±1.6	4.20
12	7.14±1.7	8.94
13	9.25±1.8	2.11
14	6.84±1.8	-2.42
15	-3.47±1.9	-10.31
16	-10.46±1.9	-6.99
17	-15.62±1.9	-5.16
18	-0.75±1.7	14.87
19	2.13±1.7	2.89
20	10.13±1.4	8.00
21	2.10±0.8	-8.03
22		-2.10
23		

Table D.16: Dianeutral Interior Mass Flux Box V ($\times 10^6 m^3 s^{-1}$) for the model_int. Positive : upwards flux across surface, convergence into layer. Negative : downward flux across surface, divergence from layer.

layer	Advection	
	Surf.	Layers
1		
2		
3		
4		
5		
6		
7	-1.09±0.8	-1.09
8	-0.54±1.2	0.55
9	9.43±1.4	9.97
10	12.05±1.7	2.62
11	9.79±1.9	-2.26
12	-3.43±2.0	-13.21
13	-3.74±2.2	-0.32
14	-1.28±2.3	2.46
15	-0.62±2.5	0.67
16	-5.03±2.7	-4.42
17	-15.85±2.8	-10.82
18	-24.86±2.9	-9.00
19	-9.88±3.1	14.98
20	-2.07±3.2	7.81
21	0.02±3.3	2.09
22		-0.02
23	0.00	0.00

Table D.17: Dianeutral Interior Mass Flux Box VI ($\times 10^6 m^3 s^{-1}$) for the model_int. Positive : upwards flux across surface, convergence into layer. Negative : downward flux across surface, divergence from layer.

Appendix E

Model_surf: Explicit Sea-Surface Forcing

This chapter contains the basin layer and total layer mass flux and the heat and salt total layer fluxes for model_surf. It also contains tables of the inverse corrected mass transformation and formation and mass interior dianeutral flux.

Layer	Angola	Brazil	Total
1	0.00	0.00	0.00
2	0.00	0.00	0.00
3	0.00	0.00	0.00
4	0.00	0.00	0.00
5	0.04	-0.30	-0.25
6	-0.28	-1.06	-1.34
7	-1.17	0.40	-0.77
8	0.15	2.53	2.69
9	1.57	1.79	3.36
10	-1.60	3.61	2.02
11	-1.74	4.02	2.28
12	-1.10	3.02	1.93
13	-1.34	3.09	1.75
14	-1.40	3.08	1.68
15	-0.61	1.50	0.89
16	-0.96	0.58	-0.38
17	-3.85	-5.80	-9.66
18	-0.55	-7.96	-8.51
19	-0.56	1.63	1.07
20	0.00	2.56	2.56
21	0.00	0.00	0.00
22	0.00	0.00	0.00
23	0.00	0.00	0.00

Table E.1: Layer Mass flux SAVE 2 ($\times 10^6 m^3 s^{-1}$) for the model_surf (+ve North)

Layer	Argentine	Ridge	Angola	Cape	Total
1	0.00	0.00	0.00	0.00	0.00
2	0.00	0.00	0.00	0.00	0.00
3	0.00	0.00	0.00	0.00	0.00
4	0.00	0.00	0.00	0.00	0.00
5	0.00	0.00	0.00	0.00	0.00
6	0.00	0.00	0.00	0.00	0.00
7	0.00	0.00	0.00	0.16	0.16
8	0.00	-0.40	-0.70	1.88	0.78
9	0.00	-0.11	-0.48	1.26	0.68
10	-1.98	-1.52	-3.99	7.62	0.13
11	4.15	-2.81	-2.50	4.78	3.61
12	3.93	-2.07	-1.67	3.29	3.49
13	5.46	-5.31	-1.83	2.95	1.27
14	6.98	-8.40	-2.56	3.07	-0.91
15	5.07	-7.02	-2.47	2.07	-2.35
16	5.09	-4.72	-2.62	0.77	-1.48
17	8.90	-5.65	-3.79	-2.44	-2.99
18	5.96	-5.31	-3.76	-5.43	-8.53
19	6.93	-3.40	-1.90	-4.21	-2.58
20	7.36	-0.07	0.00	0.07	7.36
21	1.18	0.00	0.00	0.00	1.18
22	0.00	0.00	0.00	0.00	0.00
23	0.00	0.00	0.00	0.00	0.00

Table E.2: Layer Mass flux SAVE4 ($\times 10^6 m^3 s^{-1}$) for the model_surf (+ve North, East)

Layer	Total
1	0.00
2	0.00
3	0.00
4	0.00
5	0.00
6	0.00
7	0.00
8	0.00
9	0.00
10	1.11
11	1.38
12	2.27
13	9.18
14	18.16
15	18.94
16	19.08
17	29.61
18	15.21
19	12.34
20	4.52
21	0.00
22	0.00
23	0.00

Table E.3: Layer Mass flux Drake Passage ($\times 10^6 m^3 s^{-1}$) for the model_surf (+ve east)

Layer	Total
1	0.00
2	0.00
3	0.00
4	0.00
5	0.00
6	0.00
7	0.06
8	-1.03
9	-0.35
10	-0.48
11	1.50
12	4.36
13	6.35
14	14.79
15	18.37
16	18.85
17	31.85
18	20.22
19	17.18
20	2.94
21	-2.24
22	-0.35
23	0.00

Table E.4: Layer Mass flux South Africa ($\times 10^6 m^3 s^{-1}$) for the model_surf (+ve east)

Layer	Total
1	0.00
2	0.00
3	0.00
4	0.00
5	0.00
6	0.00
7	0.00
8	0.00
9	0.00
10	0.00
11	0.00
12	0.00
13	0.39
14	-0.34
15	-0.33
16	0.30
17	-2.84
18	-2.81
19	-4.12
20	-8.66
21	6.46
22	12.01
23	0.00

Table E.5: Layer Mass flux Weddell Sea ($\times 10^6 m^3 s^{-1}$) for the model_surf (+ve north)

Layer	Mascarene	Central Ridge	Central Basin	West Aust.	Total
1	0.00	0.00	0.00	0.00	0.00
2	0.00	0.00	0.00	0.00	0.00
3	-0.50	0.00	-1.59	0.43	-1.66
4	-4.66	-0.54	-2.99	-3.62	-11.81
5	-1.93	1.09	0.03	1.25	0.44
6	-2.21	1.07	-0.06	1.19	-0.02
7	-1.04	0.84	0.14	0.73	0.66
8	-1.98	0.79	0.34	0.87	0.02
9	-2.06	0.73	0.20	1.16	0.03
10	-2.48	0.72	0.37	1.59	0.20
11	-3.23	0.99	0.56	1.45	-0.24
12	-2.92	0.84	0.91	1.70	0.53
13	-2.50	0.10	0.34	3.84	1.78
14	-2.06	0.12	-0.04	0.99	-0.99
15	-2.47	0.18	-0.34	0.69	-1.95
16	-1.73	-0.06	-0.73	0.54	-1.98
17	-0.65	2.32	-3.22	-0.73	-2.29
18	-1.09	0.53	-4.53	1.03	-4.05
19	2.16	0.00	-3.34	10.16	8.98
20	1.08	0.00	0.00	0.00	1.08
21	0.00	0.00	0.00	0.00	0.00
22	0.00	0.00	0.00	0.00	0.00
23	0.00	0.00	0.00	0.00	0.00

Table E.6: Layer Mass flux Indian 18S ($\times 10^6 m^3 s^{-1}$) for the model_surf (+ve north)

Layer	Natal	Mozam	Mada	Crozet	Central	Ninety R	Perth	Total
1	0.00	0.00	0.00	0.00	0.00	0.00	0.00	0.00
2	0.00	0.00	0.00	0.00	0.00	0.00	0.00	0.00
3	0.00	0.00	0.00	0.00	0.00	0.00	0.00	0.00
4	0.00	0.00	0.00	0.00	0.00	0.00	0.00	0.00
5	0.00	0.00	0.00	0.00	0.00	0.00	0.00	0.00
6	-0.21	0.00	0.00	0.00	0.00	0.00	0.00	-0.21
7	-0.14	0.00	0.00	0.00	0.00	0.02	0.00	-0.12
8	-2.31	-0.25	-0.24	0.07	-0.68	0.11	0.00	-3.30
9	-5.00	0.40	0.69	0.76	0.84	0.01	0.09	-2.21
10	-8.03	0.87	-0.80	3.79	0.66	-0.59	1.89	-2.21
11	-7.46	-0.26	-4.12	8.78	2.92	-1.40	3.34	1.79
12	-4.91	-0.23	-1.44	1.96	2.03	-3.19	4.17	-1.60
13	-3.61	-0.46	-2.54	1.47	0.98	-1.39	1.27	-4.28
14	-3.48	0.02	-1.75	1.56	0.63	-1.63	0.29	-4.35
15	-2.58	0.00	-1.64	1.60	0.43	-4.15	-2.23	-8.57
16	-1.55	0.63	-1.62	1.52	-0.95	-2.07	-2.05	-6.08
17	0.90	3.20	-1.47	1.73	-0.74	-1.42	-6.58	-4.37
18	5.03	6.35	0.55	-0.72	-0.52	0.00	-1.27	9.42
19	0.81	1.98	-1.48	-0.08	0.58	0.00	2.33	4.15
20	0.00	1.29	0.60	3.12	0.00	0.00	5.98	10.99
21	0.00	0.00	0.00	0.00	0.00	0.00	0.00	0.00
22	0.00	0.00	0.00	0.00	0.00	0.00	0.00	0.00
23	0.00	0.00	0.00	0.00	0.00	0.00	0.00	0.00

Table E.7: Layer Mass flux Indian 32S ($\times 10^6 m^3 s^{-1}$) for the model_surf (+ve north)

Layer	Total
1	0.00
2	0.00
3	0.00
4	0.00
5	0.00
6	0.00
7	0.00
8	0.00
9	0.00
10	0.01
11	3.68
12	14.45
13	12.27
14	15.53
15	15.76
16	16.30
17	27.83
18	21.35
19	13.02
20	4.77
21	-1.87
22	0.00
23	0.00

Table E.8: Layer Mass flux South Australia ($\times 10^6 m^3 s^{-1}$) for the model_surf (+ve east)

Layer	Chile	South West Pacific	Tonga-Kermadac	Tasman	Total
1	0.00	0.00	0.00	0.00	0.00
2	0.00	0.00	0.00	0.00	0.00
3	0.00	0.00	0.00	0.00	0.00
4	0.00	0.00	0.00	0.00	0.00
5	0.00	0.00	0.00	0.00	0.00
6	0.00	0.00	0.00	0.00	0.00
7	0.80	0.00	0.00	-2.21	-1.41
8	2.26	-0.23	-3.98	2.17	0.21
9	1.50	1.14	6.42	-0.09	8.97
10	1.08	5.07	-5.42	-0.39	0.33
11	0.36	2.90	-3.37	-0.73	-0.84
12	0.16	3.25	-4.21	-0.42	-1.22
13	0.29	7.91	-6.35	-0.40	1.44
14	-0.38	4.00	-5.43	-0.22	-2.02
15	-2.05	2.89	-4.20	-0.49	-3.84
16	-7.58	2.74	-3.40	-0.73	-8.97
17	-15.94	7.66	-4.15	-0.71	-13.14
18	-5.79	7.30	-0.20	0.12	1.43
19	0.00	21.23	0.00	1.10	22.32
20	0.00	8.37	0.00	0.00	8.37
21	0.00	0.00	0.00	0.00	0.00
22	0.00	0.00	0.00	0.00	0.00
23	0.00	0.00	0.00	0.00	0.00

Table E.9: Layer Mass flux Pacific 32S ($\times 10^6 m^3 s^{-1}$) for the model_surf (+ve north)

Layer	SV2	SV4	Drake	SAfrica	Wedsea	Ind18	Ind32	SAust	Pac
1	0.00	0.00	0.00	0.00	0.00	0.00	0.00	0.00	0.00
2	0.00	0.00	0.00	0.00	0.00	0.00	0.00	0.00	0.00
3	0.00	0.00	0.00	0.00	0.00	-42.66	0.00	0.00	0.00
4	0.00	0.00	0.00	0.00	0.00	-298.04	0.00	0.00	0.00
5	-7.40	0.00	0.00	0.00	0.00	9.47	0.00	0.00	0.00
6	-36.60	0.00	0.00	0.00	0.00	-0.82	-4.72	0.00	0.00
7	-16.69	3.18	0.00	1.16	0.00	13.59	-2.57	0.00	-34.55
8	62.21	16.31	0.00	-20.15	0.00	0.09	-68.34	0.00	1.62
9	67.61	11.50	0.00	-6.36	0.00	0.58	-38.37	0.00	155.15
10	32.96	14.25	9.61	-9.66	0.00	3.03	-41.91	0.00	-4.51
11	27.19	40.51	10.77	1.44	0.00	-3.31	24.73	27.54	-14.75
12	19.04	32.91	13.41	22.08	0.00	4.91	-17.66	102.48	-17.62
13	13.23	6.69	44.98	24.47	0.73	11.66	-31.01	61.16	1.23
14	6.94	-4.74	68.09	43.19	-1.72	-7.08	-27.31	55.96	-14.63
15	2.72	-4.17	42.68	40.34	-0.59	-10.46	-34.59	43.83	-18.51
16	-1.67	-3.22	41.52	39.41	-0.22	-8.66	-20.46	39.24	-31.92
17	-35.88	-6.90	62.07	67.36	-5.21	-6.97	-10.38	59.40	-29.85
18	-25.11	-22.80	25.62	35.87	-3.05	-7.47	21.03	35.38	1.47
19	1.13	-10.06	14.12	20.54	-3.58	9.45	8.30	13.50	26.58
20	2.14	3.26	2.64	1.11	-2.21	1.06	9.18	1.73	8.88
21	0.00	0.28	0.00	0.54	-3.27	0.00	0.00	0.11	0.00
22	0.00	0.00	0.00	0.13	-5.29	0.00	0.00	0.00	0.00
23	0.00	0.00	0.00	0.00	0.00	0.00	0.00	0.00	0.00

Table E.10: Layer Heat Flux for each section ($\times 10^6$ °C $m^3 s^{-1}$) for the model_surf +ve north/east

Layer	SV2	SV4	Drake	SAfrica	Wedsea	Ind18	Ind32	SAust	Pac
1	0.00	0.00	0.00	0.00	0.00	0.00	0.00	0.00	0.00
2	0.00	0.00	0.00	0.00	0.00	0.00	0.00	0.00	0.00
3	0.00	0.00	0.00	0.00	0.00	-59.18	0.00	0.00	0.00
4	0.00	0.00	0.00	0.00	0.00	-421.47	0.00	0.00	0.00
5	-9.65	0.00	0.00	0.00	0.00	15.39	0.00	0.00	0.00
6	-50.90	0.00	0.00	0.00	0.00	-1.32	-7.59	0.00	0.00
7	-28.48	5.72	0.00	2.01	0.00	23.74	-4.26	0.00	-52.90
8	101.67	28.54	0.00	-37.31	0.00	0.43	-120.19	0.00	5.35
9	125.22	24.58	0.00	-12.87	0.00	1.09	-80.89	0.00	324.87
10	73.72	7.92	38.79	-18.08	0.00	7.54	-81.66	0.38	9.82
11	81.94	129.02	48.10	50.01	0.00	-8.47	64.91	128.90	-30.93
12	68.77	123.60	79.36	151.76	0.00	18.86	-57.79	509.55	-44.28
13	62.01	44.50	322.03	221.41	13.59	63.30	-152.38	430.24	49.93
14	59.08	-31.72	637.69	517.83	-12.06	-35.41	-154.65	545.12	-71.99
15	31.41	-82.21	666.35	645.70	-11.55	-69.45	-304.44	555.24	-136.32
16	-13.74	-52.54	675.67	666.88	10.10	-70.63	-216.40	577.14	-318.52
17	-348.05	-106.74	1057.35	1136.10	-101.29	-82.20	-156.14	993.29	-469.74
18	-307.54	-307.50	544.54	723.59	-100.24	-145.36	338.19	764.48	51.27
19	38.27	-93.36	442.20	615.01	-147.29	322.80	149.21	466.30	800.38
20	91.79	263.68	161.72	105.21	-310.55	38.50	393.71	171.03	299.70
21	0.00	42.11	0.00	-80.64	231.42	0.00	0.00	-66.90	0.00
22	0.00	0.00	0.00	-12.35	429.48	0.00	0.00	0.00	0.00
23	0.00	0.00	0.00	0.00	0.00	0.00	0.00	0.00	0.00

Table E.11: Layer Salt Flux for each section ($\times 10^6 kgs{-}1$) for the model_surf +ve north/east

Layer	Ekman		Heat		Fresh Water		Total	
	Trans.	Forma.	Trans.	Forma.	Trans.	Forma.	Trans.	Forma.
1								
2								
3								
4								
5	-4.67	-4.67	16.19	16.19	-4.25	-4.25	7.27	7.27
6	-5.53	-0.86	18.97	2.79	-3.86	0.38	9.58	2.31
7	-5.00	0.53	0.48	-18.50	-4.91	-1.05	-9.44	-19.02
8	-1.91	3.09	-2.62	-3.09	-4.28	0.63	-8.81	0.63
9	0.40	2.31	-3.70	-1.08	-3.11	1.18	-6.41	2.40
10	1.22	0.82	-3.41	0.28	0.59	3.70	-1.61	4.79
11	1.87	0.65	-2.79	0.63	0.58	-0.01	-0.34	1.27
12	0.99	-0.87	-1.15	1.64	0.30	-0.28	0.14	0.48
13	0.53	-0.47	-1.12	0.03	0.07	-0.23	-0.53	-0.67
14		-0.53		1.12		-0.07		0.53
15								
16								
17								
18								
19								
20								
21								
22								
23								

Table E.12: Inverse modified Mass Flux across outcropping neutral surface and Formation within layer for Box I ($\times 10^6 m^3 s^{-1}$) for the model_surf Positive - upwards flux across surface, convergence into layer Negative - downward flux across surface, divergence form layer

Layer	Ekman		Heat		Fresh Water		Total	
	Trans.	Forma.	Trans.	Forma.	Trans.	Forma.	Trans.	Forma.
1								
2								
3								
4								
5								
6								
7	0.52	0.52	0.59	0.59	-0.76	-0.76	0.36	0.36
8	2.42	1.90	-0.46	-1.05	-0.41	0.35	1.55	1.19
9	3.30	0.88	-2.37	-1.91	-0.33	0.08	0.59	-0.95
10	4.80	1.50	1.69	4.07	0.36	0.69	6.85	6.25
11	4.89	0.09	2.84	1.15	0.95	0.59	8.68	1.83
12	4.66	-0.23	2.08	-0.76	1.62	0.67	8.36	-0.32
13	3.87	-0.79	3.55	1.47	2.52	0.90	9.94	1.58
14	1.56	-2.31	2.40	-1.15	3.12	0.60	7.08	-2.86
15	0.53	-1.03	-0.23	-2.62	0.72	-2.39	1.03	-6.05
16	0.24	-0.29	-0.30	-0.07	0.20	-0.52	0.14	-0.89
17		-0.24		0.30		-0.20		-0.14
18								
19								
20								
21								
22								
23								

Table E.13: Inverse modified Mass Transformation across outcropping neutral surface and Formation within layer for Box II ($\times 10^6 m^3 s^{-1}$) for the model_surf Positive - upwards flux across surface, convergence into layer Negative - downward flux across surface, divergence form layer

Layer	Ekman		Heat		Fresh Water		Total	
	Trans.	Forma.	Trans.	Forma.	Trans.	Forma.	Trans.	Forma.
1								
2								
3	-14.37	-14.37	0.52	0.52	-1.73	-1.73	-15.58	-15.58
4	-12.49	1.88	-4.58	-5.10	-3.14	-1.41	-20.21	-4.64
5	-9.30	3.19	-11.12	-6.53	-4.19	-1.06	-24.61	-4.40
6	-5.53	3.77	-12.20	-1.09	-3.40	0.79	-21.14	3.47
7	-2.39	3.14	-9.70	2.51	-2.52	0.88	-14.60	6.54
8	-0.38	2.01	-7.92	1.78	-1.71	0.81	-10.00	4.60
9	0.49	0.87	-6.60	1.32	-1.08	0.62	-7.19	2.81
10	1.13	0.64	-0.52	6.07	-0.30	0.78	0.30	7.49
11		-1.13		0.52		0.30		-0.30
12								
13								
14								
15								
16								
17								
18								
19								
20								
21								
22								
23								

Table E.14: Inverse modified Mass Transformation across outcropping neutral surface and Formation within layer for Box IV ($\times 10^6 m^3 s^{-1}$) for the model_surf Positive - upwards flux across surface, convergence into layer Negative - downward flux across surface, divergence form layer

Layer	Ekman		Heat		Fresh Water		Total	
	Trans.	Forma.	Trans.	Forma.	Trans.	Forma.	Trans.	Forma.
1								
2								
3								
4								
5								
6	0.19	0.19	0.40	0.40	-0.57	-0.57	0.03	0.03
7	1.62	1.42	-3.18	-3.58	-0.97	-0.40	-2.53	-2.55
8	5.24	3.62	-9.64	-6.46	-1.53	-0.57	-5.93	-3.40
9	9.58	4.35	-11.27	-1.63	-1.59	-0.06	-3.28	2.65
10	14.28	4.70	-14.40	-3.12	-0.16	1.44	-0.27	3.01
11	13.62	-0.66	-9.20	5.20	2.52	2.68	6.95	7.22
12	11.59	-2.04	-5.33	3.87	5.33	2.81	11.59	4.64
13	8.38	-3.20	9.91	15.23	9.48	4.15	27.77	16.18
14	5.00	-3.38	2.26	-7.65	11.05	1.57	18.30	-9.47
15	3.03	-1.97	-1.38	-3.63	2.07	-8.98	3.72	-14.58
16	2.47	-0.56	-0.07	1.31	0.03	-2.04	2.43	-1.29
17		-2.47		0.07		-0.03		-2.43
18								
19								
20								
21								
22								
23								

Table E.15: Inverse modified Mass Transformation across outcropping neutral surface and Formation within layer for Box V ($\times 10^6 m^3 s^{-1}$) for the model_surf Positive - upwards flux across surface, convergence into layer Negative - downward flux across surface, divergence form layer

Layer	Ekman		Heat		Fresh Water		Total	
	Forma.	Trans.	Trans.	Forma.	Trans.	Forma.	Trans.	Forma.
1								
2								
3								
4								
5								
6								
7	2.51	2.51	-3.15	-3.15	0.05	0.05	-0.58	-0.58
8	6.39	3.88	-5.41	-2.26	1.32	1.27	2.30	2.88
9	10.00	3.61	-0.52	4.89	2.33	1.01	11.81	9.51
10	11.63	1.63	-2.67	-2.15	2.64	0.32	11.60	-0.20
11	10.00	-1.62	-7.29	-4.62	3.93	1.28	6.64	-4.96
12	8.33	-1.67	-8.86	-1.57	4.43	0.50	3.90	-2.74
13	6.41	-1.92	-6.81	2.05	5.64	1.21	5.25	1.35
14	3.92	-2.50	-5.32	1.49	8.98	3.34	7.58	2.33
15	0.96	-2.96	-1.82	3.50	4.53	-4.45	3.67	-3.91
16	-0.06	-1.02	-0.56	1.26	0.76	-3.77	0.13	-3.54
17	-0.06	0.00	-0.26	0.30	0.18	-0.58	-0.14	-0.27
18	-0.20	-0.14	-0.06	0.20	0.03	-0.15	-0.23	-0.09
19	-0.18	0.01	-0.02	0.03	0.01	-0.02	-0.20	0.03
20	0.02	0.21	-0.02	0.01	0.01	0.00	0.02	0.22
21		-0.02		0.02		-0.01		-0.02
22								
23								

Table E.16: Inverse modified Mass Transformation across outcropping neutral surface and Formation within layer for Box VI ($\times 10^6 m^3 s^{-1}$) for the model_surf Positive - upwards flux across surface, convergence into layer Negative - downward flux across surface, divergence form layer

layer	Advection	
	Surf.	Layers
1		
2		
3		
4	0.51±6.1	0.51
5	-7.00±5.8	-7.51
6	-10.65±5.6	-3.65
7	7.44±5.5	18.09
8	8.72±5.3	1.28
9	9.00±5.1	0.28
10	6.08±4.9	-2.92
11	3.47±4.7	-2.60
12	1.42±4.5	-2.06
13	2.57±4.3	1.15
14	4.64±4.2	2.08
15	7.88±3.9	3.24
16	8.98±3.7	1.10
17	2.31±3.4	-6.67
18	2.33±3.0	0.02
19	5.98±2.3	3.64
20	1.18±1.5	-4.80
21		-1.18
22		
23		

Table E.17: Dianeutral Interior Mass Flux Box I ($\times 10^6 m^3 s^{-1}$) for the model_surf. Positive : upwards flux across surface, convergence into layer. Negative : downward flux across surface, divergence from layer.

layer	Advection	
	Surf.	Layers
1		
2		
3		
4		
5		
6		
7	-0.13±1.4	-0.13
8	-1.56±1.8	-1.43
9	-0.29±2.2	1.28
10	-8.01±2.5	-7.72
11	-6.10±2.7	1.91
12	-0.18±2.8	5.93
13	-3.67±2.9	-3.49
14	-4.79±3.0	-1.12
15	-1.39±3.0	3.40
16	-2.57±3.0	-1.18
17	-0.25±2.8	2.32
18	-0.97±2.7	-0.71
19	5.42±2.6	6.38
20	19.86±2.3	14.45
21	12.35±1.4	-7.52
22		-12.35
23		

Table E.18: Dianeutral Interior Mass Flux Box II ($\times 10^6 m^3 s^{-1}$) for the model_surf. Positive : upwards flux across surface, convergence into layer. Negative : downward flux across surface, divergence from layer.

layer	Advection	
	Surf.	Layers
1		
2		
3	13.93±1.4	13.93
4	6.75±1.9	-7.18
5	11.62±2.3	4.87
6	8.35±2.6	-3.27
7	2.61±2.8	-5.74
8	1.34±2.9	-1.27
9	0.78±3.0	-0.56
10	-4.27±3.1	-5.05
11	-5.96±3.1	-1.70
12	-3.81±3.2	2.15
13	2.27±3.3	6.08
14	5.65±3.3	3.38
15	12.29±3.4	6.64
16	16.41±3.4	4.12
17	18.51±3.2	2.10
18	5.05±2.4	-13.45
19	9.90±1.5	4.84
20		-9.90
21		
22		
23		

Table E.19: Dianeutral Interior Mass Flux Box IV ($\times 10^6 m^3 s^{-1}$) for the model_surf. Positive : upwards flux across surface, convergence into layer. Negative : downward flux across surface, divergence from layer.

layer	Advection	
	Surf.	Layers
1		
2		
3		
4		
5		
6	-0.25±1.4	-0.25
7	2.11±1.9	2.36
8	3.23±2.3	1.12
9	-1.30±2.5	-4.53
10	-6.00±2.7	-4.70
11	-9.24±2.9	-3.24
12	-5.41±3.0	3.84
13	-19.96±3.1	-14.56
14	-14.08±3.1	5.88
15	-10.64±3.2	3.44
16	-17.93±3.3	-7.30
17	-24.04±3.3	-6.11
18	-13.50±3.0	10.54
19	-13.52±2.9	-0.01
20	-0.70±2.2	12.82
21	-0.34±1.4	0.36
22		0.34
23		

Table E.20: Dianeutral Interior Mass Flux Box V ($\times 10^6 m^3 s^{-1}$) for the model_surf. Positive : upwards flux across surface, convergence into layer. Negative : downward flux across surface, divergence from layer.

layer	Advection	
	Surf.	Layers
1		
2		
3		
4		
5		
6		
7	-0.83±1.4	-0.83
8	-3.51±2.0	-2.67
9	-4.06±2.5	-0.55
10	-2.42±2.9	1.63
11	-0.58±3.2	1.85
12	-11.22±3.5	-10.65
13	-14.17±3.8	-2.94
14	-15.83±4.1	-1.66
15	-12.56±4.3	3.26
16	-15.16±4.6	-2.59
17	-26.18±4.9	-11.02
18	-30.89±5.1	-4.71
19	-9.43±5.3	21.47
20	-1.52±5.6	7.90
21	0.36±5.8	1.89
22		-0.36
23		

Table E.21: Dianeutral Interior Mass Flux Box VI ($\times 10^6 m^3 s^{-1}$) for the model_surf. Positive : upwards flux across surface, convergence into layer. Negative : downward flux across surface, divergence from layer.

Appendix F

Alternative Circulation

This chapter contains the basin and total layer flux across SAVE2, SAVE4, DrakeP, SAfrica and Wedsea section and dianeutral flux for the subtropical Atlantic (BI) and Southern Ocean Atlantic (BII) region for the model_wsh. For the model_malv the basin and total layer mass flux for each section are shown as well as the dianeutral mass flux for each region.

Layer	Angola	Brazil	Total
1	0.00	0.00	0.00
2	0.00	0.00	0.00
3	0.00	0.00	0.00
4	0.00	0.00	0.00
5	0.05	-0.29	-0.25
6	-0.28	-1.06	-1.34
7	-1.17	0.40	-0.77
8	0.16	2.54	2.70
9	1.59	1.79	3.37
10	-1.57	3.61	2.04
11	-1.73	4.03	2.30
12	-1.10	3.03	1.93
13	-1.34	3.10	1.77
14	-1.37	3.10	1.73
15	-0.57	1.52	0.95
16	-0.91	0.60	-0.31
17	-3.76	-5.75	-9.51
18	-0.60	-7.91	-8.51
19	-0.98	1.62	0.64
20	0.00	2.56	2.56
21	0.00	0.00	0.00
22	0.00	0.00	0.00
23	0.00	0.00	0.00

Table F.1: Layer Mass flux SAVE 2 ($\times 10^6 m^3 s^{-1}$) for model_wsh .(+ve North)

Layer	Argentine	Ridge	Angola	Cape	Total
1	0.00	0.00	0.00	0.00	0.00
2	0.00	0.00	0.00	0.00	0.00
3	0.00	0.00	0.00	0.00	0.00
4	0.00	0.00	0.00	0.00	0.00
5	0.00	0.00	0.00	0.00	0.00
6	0.00	0.00	0.00	0.00	0.00
7	0.00	0.00	0.00	0.16	0.16
8	0.00	-0.40	-0.70	1.88	0.78
9	0.00	-0.10	-0.48	1.26	0.68
10	-1.98	-1.52	-3.99	7.62	0.14
11	4.15	-2.79	-2.50	4.78	3.64
12	3.94	-2.04	-1.67	3.30	3.52
13	5.45	-5.28	-1.83	2.95	1.29
14	6.97	-8.35	-2.56	3.09	-0.84
15	5.04	-6.96	-2.47	2.07	-2.32
16	5.04	-4.66	-2.62	0.77	-1.47
17	8.79	-5.51	-3.79	-2.44	-2.95
18	5.87	-5.14	-3.74	-5.43	-8.46
19	6.82	-3.37	-1.91	-4.22	-2.67
20	7.18	-0.07	0.00	0.06	7.18
21	1.12	0.00	0.00	0.00	1.12
22	0.00	0.00	0.00	0.00	0.00
23	0.00	0.00	0.00	0.00	0.00

Table F.2: Layer Mass flux SAVE4 ($\times 10^6 m^3 s^{-1}$) for model_wsh (+ve North, East)

Layer	Total
1	0.00
2	0.00
3	0.00
4	0.00
5	0.00
6	0.00
7	0.00
8	0.00
9	0.00
10	1.11
11	1.37
12	2.27
13	9.15
14	18.10
15	18.89
16	19.02
17	29.49
18	15.11
19	12.31
20	4.69
21	0.00
22	0.00
23	0.00

Table F.3: Layer Mass flux Drake Passage ($\times 10^6 m^3 s^{-1}$) for model_wsh (+ve east)

Layer	Total
1	0.00
2	0.00
3	0.00
4	0.00
5	0.00
6	0.00
7	0.06
8	-1.03
9	-0.35
10	-0.46
11	1.57
12	4.43
13	6.44
14	14.97
15	18.56
16	19.13
17	32.30
18	20.75
19	17.59
20	2.15
21	-3.64
22	-0.78
23	0.00

Table F.4: Layer Mass flux South Africa ($\times 10^6 m^3 s^{-1}$) for model_wsh (+ve east)

Layer	Total
1	0.00
2	0.00
3	0.00
4	0.00
5	0.00
6	0.00
7	0.00
8	0.00
9	0.00
10	0.00
11	0.00
12	0.00
13	0.41
14	-0.16
15	-0.21
16	0.65
17	-1.52
18	-1.25
19	-2.30
20	-7.16
21	1.83
22	9.75
23	0.00

Table F.5: Layer Mass flux Weddell Sea ($\times 10^6 m^3 s^{-1}$) for model_wsh (+ve north)

Layer	SV2	SV4	Drake	SAfrica	Wedsea	Ind18	Ind32	SAust	Pac
1	0.00	0.00	0.00	0.00	0.00	0.00	0.00	0.00	0.00
2	0.00	0.00	0.00	0.00	0.00	0.00	0.00	0.00	0.00
3	0.00	0.00	0.00	0.00	0.00	-42.29	0.00	0.00	0.00
4	0.00	0.00	0.00	0.00	0.00	-297.49	0.00	0.00	0.00
5	-7.31	0.00	0.00	0.00	0.00	9.94	0.00	0.00	0.00
6	-36.69	0.00	0.00	0.00	0.00	-0.43	-4.72	0.00	0.00
7	-16.67	3.21	0.00	1.19	0.00	13.87	-2.56	0.00	-33.96
8	62.51	16.35	0.00	-20.12	0.00	0.38	-68.18	0.00	2.00
9	67.86	11.59	0.00	-6.34	0.00	0.90	-37.85	0.00	155.86
10	33.35	14.41	9.58	-9.40	0.00	3.47	-40.72	0.05	-3.89
11	27.46	40.82	10.73	2.16	0.00	-2.82	25.99	27.86	-14.31
12	19.07	33.25	13.38	22.66	0.00	5.44	-15.99	103.72	-17.34
13	13.36	6.90	44.82	25.03	0.83	12.74	-30.07	61.64	1.76
14	7.24	-4.46	67.82	44.01	-1.24	-6.73	-27.01	56.28	-14.02
15	3.00	-4.07	42.48	41.01	-0.44	-9.98	-33.95	44.18	-18.11
16	-1.38	-3.15	41.32	40.24	0.18	-8.05	-20.12	39.44	-31.41
17	-35.39	-6.78	61.79	68.71	-2.46	-6.76	-10.47	59.63	-29.64
18	-25.14	-22.60	25.44	37.19	-0.53	-7.57	20.60	35.28	1.14
19	0.11	-10.16	14.08	21.39	-1.65	8.58	7.87	13.38	25.89
20	2.14	3.18	2.73	1.21	-1.50	1.06	9.00	1.58	8.81
21	0.00	0.27	0.00	0.92	-1.58	0.00	0.00	0.12	0.00
22	0.00	0.00	0.00	0.33	-4.21	0.00	0.00	0.00	0.00
23	0.00	0.00	0.00	0.00	0.00	0.00	0.00	0.00	0.00

Table F.6: Layer Heat Flux for each section ($\times 10^6$ °C $m^3 s^{-1}$) for model_wsh +ve north/east

Layer	SV2	SV4	Drake	SAfrica	Wedsea	Ind18	Ind32	SAust	Pac
1	0.00	0.00	0.00	0.00	0.00	0.00	0.00	0.00	0.00
2	0.00	0.00	0.00	0.00	0.00	0.00	0.00	0.00	0.00
3	0.00	0.00	0.00	0.00	0.00	-58.68	0.00	0.00	0.00
4	0.00	0.00	0.00	0.00	0.00	-420.68	0.00	0.00	0.00
5	-9.53	0.00	0.00	0.00	0.00	16.11	0.00	0.00	0.00
6	-51.01	0.00	0.00	0.00	0.00	-0.68	-7.58	0.00	0.00
7	-28.45	5.77	0.00	2.06	0.00	24.25	-4.25	0.00	-51.80
8	102.15	28.62	0.00	-37.25	0.00	0.98	-119.92	0.00	6.09
9	125.67	24.76	0.00	-12.82	0.00	1.79	-79.84	0.00	326.50
10	74.66	8.34	38.67	-17.33	0.00	8.61	-78.47	0.52	11.55
11	82.70	129.99	47.92	52.60	0.00	-7.04	68.57	129.96	-29.45
12	68.89	124.98	79.20	154.32	0.00	20.71	-51.64	514.58	-43.15
13	62.61	45.56	320.91	224.44	14.33	68.65	-146.84	432.55	52.87
14	60.85	-29.50	635.40	524.31	-5.74	-33.47	-152.70	546.70	-67.75
15	33.67	-81.21	664.37	652.50	-7.36	-66.22	-298.43	557.83	-132.87
16	-11.01	-51.88	673.47	676.87	22.50	-65.01	-212.65	579.04	-313.09
17	-342.82	-105.25	1053.05	1151.91	-54.11	-78.68	-157.38	995.76	-466.32
18	-307.59	-304.79	540.70	742.49	-44.61	-147.19	330.20	761.32	43.58
19	22.89	-96.75	441.20	629.89	-82.13	298.23	136.89	460.96	780.53
20	91.85	257.10	167.83	77.11	-256.47	38.44	385.68	157.09	297.44
21	0.00	39.99	0.00	-130.99	65.43	0.00	0.00	-75.17	0.00
22	0.00	0.00	0.00	-27.78	348.77	0.00	0.00	0.00	0.00
23	0.00	0.00	0.00	0.00	0.00	0.00	0.00	0.00	0.00

Table F.7: Layer Salt Flux for each section ($\times 10^6 kgs{-}1$) for the model_wsh +ve north/east

layer	Advection	
	Surf.	Layers
1		
2		
3		
4	0.51±6.1	0.51
5	-6.99±5.9	-7.51
6	-10.64±5.7	-3.65
7	7.44±5.5	18.09
8	8.73±5.3	1.29
9	9.02±5.1	0.29
10	6.11±5.0	-2.91
11	3.50±4.8	-2.61
12	1.41±4.8	-2.09
13	2.55±4.3	1.14
14	4.61±4.2	2.06
15	7.88±3.9	3.27
16	9.04±3.7	1.16
17	2.47±3.4	-6.57
18	2.42±3.0	-0.05
19	5.73±2.3	3.31
20	1.12±1.5	-4.61
21		-1.12
22		
23		

Table F.8: Dianeutral Interior Mass Flux Box II for model_wsh ($\times 10^6 m^3 s^{-1}$). Positive : upwards flux across surface, convergence into layer. Negative : downward flux across surface, divergence from layer.

layer	Advection	
	Surf.	Layers
1		
2		
3		
4		
5		
6		
7	-0.13±1.4	-0.13
8	-1.56±1.9	-1.43
9	-0.27±2.3	1.28
10	-7.96±2.5	-7.69
11	-5.95±2.7	2.01
12	0.09±2.9	6.04
13	-3.29±2.9	-3.37
14	-4.28±3.0	-0.99
15	-0.73±3.0	3.55
16	-1.89±3.1	-1.16
17	-0.28±3.1	1.61
18	-1.84±2.8	-1.56
19	3.07±2.7	4.91
20	14.87±2.3	11.80
21	10.52±1.5	-4.35
22		-10.52
23		

Table F.9: Dianeutral Interior Mass Flux Box II for model_wsh ($\times 10^6 m^3 s^{-1}$). Positive : upwards flux across surface, convergence into layer. Negative : downward flux across surface, divergence from layer.

Layer	Angola	Brazil	Total
1	0.00	0.00	0.00
2	0.00	0.00	0.00
3	0.00	0.00	0.00
4	0.00	0.00	0.00
5	0.06	-0.29	-0.23
6	-0.28	-1.17	-1.44
7	-1.16	0.39	-0.78
8	0.21	2.49	2.70
9	1.65	1.73	3.38
10	-1.44	3.52	2.08
11	-1.60	3.96	2.36
12	-1.03	2.98	1.95
13	-1.19	3.05	1.85
14	-1.06	3.01	1.96
15	-0.17	1.39	1.22
16	-0.46	0.38	-0.08
17	-2.76	-6.42	-9.18
18	0.14	-8.97	-8.84
19	-1.93	1.23	-0.70
20	0.00	3.01	3.01
21	0.00	0.00	0.00
22	0.00	0.00	0.00
23	0.00	0.00	0.00

Table F.10: Layer Mass flux SAVE 2 ($\times 10^6 m^3 s^{-1}$) for model_malv (+ve North)

Layer	Argentine	Ridge	Angola	Cape	Total
1	0.00	0.00	0.00	0.00	0.00
2	0.00	0.00	0.00	0.00	0.00
3	0.00	0.00	0.00	0.00	0.00
4	0.00	0.00	0.00	0.00	0.00
5	0.00	0.00	0.00	0.00	0.00
6	0.00	0.00	0.00	0.00	0.00
7	0.00	0.00	0.00	0.13	0.13
8	0.00	-0.39	-0.62	1.97	0.96
9	0.00	-0.33	-0.38	1.33	0.63
10	-1.74	-1.79	-3.65	8.11	0.93
11	5.01	-4.26	-2.22	5.02	3.55
12	4.85	-3.84	-1.45	3.34	2.90
13	7.50	-7.65	-1.57	3.17	1.45
14	12.26	-13.01	-2.13	2.62	-0.26
15	9.85	-12.17	-1.99	2.73	-1.58
16	8.85	-10.51	-1.99	1.68	-1.98
17	17.14	-17.78	-2.34	-0.18	-3.17
18	9.38	-17.30	-0.88	-1.45	-10.24
19	7.59	-6.57	-0.16	-1.05	-0.20
20	4.92	-0.75	0.00	1.10	5.26
21	1.25	0.00	0.00	0.00	1.25
22	0.00	0.00	0.00	0.00	0.00
23	0.00	0.00	0.00	0.00	0.00

Table F.11: Layer Mass flux SAVE4 ($\times 10^6 m^3 s^{-1}$) for model_malv (+ve North, East)

Layer	Total
1	0.00
2	0.00
3	0.00
4	0.00
5	0.00
6	0.00
7	0.00
8	0.00
9	0.00
10	1.12
11	1.39
12	2.28
13	9.23
14	18.29
15	19.09
16	19.25
17	29.98
18	15.56
19	12.68
20	4.58
21	0.00
22	0.00
23	0.00

Table F.12: Layer Mass flux Drake Passage ($\times 10^6 m^3 s^{-1}$) for model_malv (+ve east)

Layer	Total
1	0.00
2	0.00
3	0.00
4	0.00
5	0.00
6	0.00
7	0.06
8	-1.01
9	-0.35
10	-0.40
11	1.66
12	4.46
13	6.45
14	14.95
15	18.54
16	19.09
17	32.30
18	21.25
19	17.46
20	2.72
21	-2.78
22	-0.54
23	0.00

Table F.13: Layer Mass flux South Africa ($\times 10^6 m^3 s^{-1}$) for model_malv (+ve east)

Layer	Total
1	0.00
2	0.00
3	0.00
4	0.00
5	0.00
6	0.00
7	0.00
8	0.00
9	0.00
10	0.00
11	0.00
12	0.00
13	0.41
14	-0.16
15	-0.21
16	0.66
17	-1.50
18	-1.24
19	-2.29
20	-7.23
21	1.82
22	9.76
23	0.00

Table F.14: Layer Mass flux Weddell Sea ($\times 10^6 m^3 s^{-1}$) for model_malv (+ve north)

Layer	Mascarene	Central Ridge	Central Basin	West Aust.	Total
1	0.00	0.00	0.00	0.00	0.00
2	0.00	0.00	0.00	0.00	0.00
3	-0.50	0.00	-1.59	0.44	-1.65
4	-4.65	-0.53	-2.98	-3.61	-11.77
5	-1.92	1.10	0.03	1.26	0.47
6	-2.21	1.08	-0.06	1.19	0.01
7	-1.03	0.84	0.14	0.74	0.69
8	-1.97	0.80	0.35	0.87	0.05
9	-2.05	0.74	0.21	1.17	0.08
10	-2.47	0.74	0.39	1.60	0.27
11	-3.21	1.02	0.58	1.46	-0.16
12	-2.90	0.89	0.94	1.73	0.66
13	-2.48	0.14	0.37	3.90	1.93
14	-2.04	0.15	-0.01	1.02	-0.88
15	-2.43	0.25	-0.29	0.75	-1.72
16	-1.67	0.06	-0.64	0.64	-1.62
17	-0.55	2.53	-3.04	-0.69	-1.76
18	-0.94	0.74	-4.34	1.09	-3.44
19	2.25	0.00	-3.04	10.24	9.45
20	1.09	0.00	0.00	0.00	1.09
21	0.00	0.00	0.00	0.00	0.00
22	0.00	0.00	0.00	0.00	0.00
23	0.00	0.00	0.00	0.00	0.00

Table F.15: Layer Mass flux Indian 18S ($\times 10^6 m^3 s^{-1}$) for model_malv (+ve north)

Layer	Natal	Mozam	Mada	Crozet	Central	Ninety R	Perth	Total
1	0.00	0.00	0.00	0.00	0.00	0.00	0.00	0.00
2	0.00	0.00	0.00	0.00	0.00	0.00	0.00	0.00
3	0.00	0.00	0.00	0.00	0.00	0.00	0.00	0.00
4	0.00	0.00	0.00	0.00	0.00	0.00	0.00	0.00
5	0.00	0.00	0.00	0.00	0.00	0.00	0.00	0.00
6	-0.21	0.00	0.00	0.00	0.00	0.00	0.00	-0.21
7	-0.14	0.00	0.00	0.00	0.00	0.02	0.00	-0.12
8	-2.31	-0.24	-0.23	0.07	-0.68	0.11	0.00	-3.28
9	-4.99	0.40	0.70	0.77	0.85	0.02	0.09	-2.15
10	-7.99	0.90	-0.76	3.81	0.67	-0.57	1.91	-2.03
11	-7.44	-0.23	-4.07	8.83	2.95	-1.36	3.37	2.04
12	-4.89	-0.21	-1.41	1.98	2.06	-3.12	4.22	-1.38
13	-3.60	-0.43	-2.48	1.49	0.99	-1.36	1.29	-4.10
14	-3.46	0.04	-1.72	1.58	0.65	-1.60	0.31	-4.21
15	-2.56	0.02	-1.61	1.64	0.45	-4.09	-2.19	-8.34
16	-1.52	0.66	-1.58	1.57	-0.90	-2.04	-1.99	-5.80
17	0.94	3.25	-1.40	1.81	-0.68	-1.40	-6.49	-3.95
18	5.08	6.41	0.62	-0.57	-0.45	0.00	-1.23	9.85
19	0.81	2.02	-1.35	0.02	0.67	0.00	2.39	4.55
20	0.00	1.33	0.62	3.18	0.00	0.00	6.01	11.14
21	0.00	0.00	0.00	0.00	0.00	0.00	0.00	0.00
22	0.00	0.00	0.00	0.00	0.00	0.00	0.00	0.00
23	0.00	0.00	0.00	0.00	0.00	0.00	0.00	0.00

Table F.16: Layer Mass flux Indian 32S ($\times 10^6 m^3 s^{-1}$) for model_malv (+ve north)

Layer	Total
1	0.00
2	0.00
3	0.00
4	0.00
5	0.00
6	0.00
7	0.00
8	0.00
9	0.00
10	0.01
11	3.67
12	14.38
13	12.22
14	15.48
15	15.69
16	16.20
17	27.60
18	21.14
19	12.77
20	4.69
21	-1.89
22	0.00
23	0.00

Table F.17: Layer Mass flux South Australia ($\times 10^6 m^3 s^{-1}$) for model_malv (+ve east)

Layer	Chile	South West Pacific	Tonga-Kermadac	Tasman	Total
1	0.00	0.00	0.00	0.00	0.00
2	0.00	0.00	0.00	0.00	0.00
3	0.00	0.00	0.00	0.00	0.00
4	0.00	0.00	0.00	0.00	0.00
5	0.00	0.00	0.00	0.00	0.00
6	0.00	0.00	0.00	0.00	0.00
7	0.79	0.00	0.00	-2.21	-1.42
8	2.25	-0.25	-3.97	2.17	0.20
9	1.48	1.09	6.48	-0.09	8.96
10	1.06	5.01	-5.36	-0.39	0.32
11	0.35	2.86	-3.32	-0.73	-0.84
12	0.14	3.19	-4.15	-0.42	-1.24
13	0.25	7.74	-6.28	-0.41	1.30
14	-0.43	3.89	-5.34	-0.22	-2.11
15	-2.10	2.78	-4.13	-0.49	-3.94
16	-7.67	2.58	-3.34	-0.74	-9.17
17	-16.17	7.08	-4.09	-0.73	-13.91
18	-6.05	6.76	-0.20	0.10	0.61
19	0.00	20.74	0.00	1.04	21.78
20	0.00	8.32	0.00	0.00	8.32
21	0.00	0.00	0.00	0.00	0.00
22	0.00	0.00	0.00	0.00	0.00
23	0.00	0.00	0.00	0.00	0.00

Table F.18: Layer Mass flux Pacific 32S ($\times 10^6 m^3 s^{-1}$) for model_malv (+ve north)

Layer	SV2	SV4	Drake	SAfrica	Ind18	Ind32	Wedsea	SAust	Pac
1	0.00	0.00	0.00	0.00	0.00	0.00	0.00	0.00	0.00
2	0.00	0.00	0.00	0.00	0.00	0.00	0.00	0.00	0.00
3	0.00	0.00	0.00	0.00	0.00	-42.42	0.00	0.00	0.00
4	0.00	0.00	0.00	0.00	0.00	-296.84	0.00	0.00	0.00
5	-6.94	0.00	0.00	0.00	0.00	10.21	0.00	0.00	0.00
6	-39.56	0.00	0.00	0.00	0.00	-0.10	-4.72	0.00	0.00
7	-16.80	2.62	0.00	1.18	0.00	14.19	-2.56	0.00	-34.79
8	62.47	20.22	0.00	-19.92	0.00	0.80	-68.06	0.00	1.34
9	68.00	11.47	0.00	-6.25	0.00	1.38	-37.29	0.00	155.10
10	33.87	26.36	9.66	-8.54	0.00	4.03	-39.16	-0.01	-4.60
11	28.30	38.20	10.85	3.34	0.00	-2.28	27.95	27.39	-14.69
12	19.31	24.32	13.47	23.03	0.00	6.25	-15.42	101.83	-17.73
13	14.16	4.36	45.25	25.34	0.82	12.83	-29.74	60.88	0.35
14	8.76	-4.13	68.56	44.12	-1.24	-6.36	-26.49	55.73	-15.00
15	4.37	-2.41	43.07	41.10	-0.43	-9.30	-33.68	43.60	-18.83
16	-0.40	-4.76	41.95	40.23	0.18	-7.22	-19.58	38.99	-32.51
17	-34.58	-9.95	62.88	68.79	-2.44	-5.58	-9.32	58.88	-31.48
18	-26.42	-26.69	26.20	38.46	-0.52	-6.37	21.88	35.01	0.10
19	-2.94	-3.44	14.52	21.20	-1.67	10.10	8.82	13.21	25.90
20	2.58	3.03	2.70	1.39	-1.52	1.07	9.30	1.69	8.82
21	0.00	0.30	0.00	0.70	-1.57	0.00	0.00	0.11	0.00
22	0.00	0.00	0.00	0.22	-4.21	0.00	0.00	0.00	0.00
23	0.00	0.00	0.00	0.00	0.00	0.00	0.00	0.00	0.00

Table F.19: Layer Heat Flux for each section ($\times 10^6$ °C $m^3 s^{-1}$) for model_malv +ve north/east

Layer	SV2	SV4	Drake	SAfrica	Ind18	Ind32	Wedsea	SAust	Pac
1	0.00	0.00	0.00	0.00	0.00	0.00	0.00	0.00	0.00
2	0.00	0.00	0.00	0.00	0.00	0.00	0.00	0.00	0.00
3	0.00	0.00	0.00	0.00	0.00	-58.85	0.00	0.00	0.00
4	0.00	0.00	0.00	0.00	0.00	-419.76	0.00	0.00	0.00
5	-9.01	0.00	0.00	0.00	0.00	16.51	0.00	0.00	0.00
6	-54.92	0.00	0.00	0.00	0.00	-0.14	-7.58	0.00	0.00
7	-28.60	4.72	0.00	2.05	0.00	24.79	-4.25	0.00	-53.36
8	102.21	35.30	0.00	-36.88	0.00	1.76	-119.69	0.00	4.79
9	125.95	23.14	0.00	-12.63	0.00	2.74	-78.70	0.00	324.55
10	75.95	37.14	39.00	-15.23	0.00	9.91	-74.88	0.33	9.34
11	84.94	126.25	48.44	55.74	0.00	-5.56	74.12	128.35	-30.98
12	69.56	102.22	79.70	155.10	0.00	23.52	-49.66	506.79	-45.01
13	65.73	50.60	323.84	225.16	14.33	68.67	-146.00	428.60	44.82
14	68.94	-9.46	642.09	523.49	-5.58	-31.34	-149.53	543.19	-75.03
15	43.14	-54.95	671.34	651.79	-7.28	-61.49	-296.33	552.62	-139.68
16	-2.86	-70.13	681.61	675.48	22.80	-57.74	-206.52	573.77	-325.80
17	-330.84	-113.65	1070.55	1152.23	-53.25	-63.04	-141.12	985.22	-497.41
18	-319.46	-368.59	556.90	760.64	-44.14	-123.56	353.86	756.92	21.91
19	-25.42	-7.48	454.56	625.10	-81.94	339.69	163.46	457.30	780.84
20	107.88	188.48	164.14	97.35	-259.20	38.75	399.03	168.19	297.72
21	0.00	44.73	0.00	-100.13	65.35	0.00	0.00	-67.49	0.00
22	0.00	0.00	0.00	-19.41	349.16	0.00	0.00	0.00	0.00
23	0.00	0.00	0.00	0.00	0.00	0.00	0.00	0.00	0.00

Table F.20: Layer Salt Flux for each section ($\times 10^6 kgs{-}1$) forthe model_malv +ve north/east

Layer	Natal	Mozam	Mada	Crozet	Central	Ninety R	Perth	Total
1	0.000	0.000	0.000	0.000	0.000	0.000	0.000	0.000
2	0.000	0.000	0.000	0.000	0.000	0.000	0.000	0.000
3	0.000	0.000	0.000	0.000	0.000	0.000	0.000	0.000
4	0.000	0.000	0.000	0.000	0.000	0.000	0.000	0.000
5	0.000	0.000	0.000	0.000	0.000	0.000	0.000	0.000
6	-0.982	0.000	0.000	0.000	0.000	0.000	0.000	-0.982
7	-0.746	0.000	0.000	0.000	0.000	0.038	0.000	-0.707
8	-6.757	-0.542	-0.316	0.114	-0.944	0.297	0.000	-8.147
9	-17.985	0.797	1.650	1.110	1.792	-0.108	-0.186	-12.931
10	-22.639	3.928	-0.171	9.922	1.177	-1.710	3.761	-5.732
11	-44.187	-0.221	-17.120	34.973	10.546	-3.375	6.363	-13.022
12	-66.424	-1.206	-12.780	17.058	12.312	-15.540	17.975	-48.605
13	-83.701	-12.253	-73.531	25.142	15.160	-18.448	15.822	-131.809
14	-130.077	-2.700	-50.026	42.282	19.927	-47.442	5.833	-162.201
15	-141.972	-3.083	-73.416	73.413	21.302	-264.308	-178.556	-566.619
16	-105.863	41.912	-103.063	101.091	-88.608	-164.180	-161.307	-480.018
17	68.601	248.140	-111.676	149.874	-62.765	-137.400	-647.273	-492.498
18	372.621	516.284	65.559	-74.783	-46.466	0.000	-140.726	692.489
19	73.744	193.706	-236.407	-2.776	79.794	0.000	298.698	406.759
20	0.000	167.022	79.727	425.390	0.000	0.000	777.037	1449.175
21	0.000	0.000	0.000	0.000	0.000	0.000	0.000	0.000
22	0.000	0.000	0.000	0.000	0.000	0.000	0.000	0.000
23	0.000	0.000	0.000	0.000	0.000	0.000	0.000	0.000

Table F.21: Layer Silica flux Indian 32S ($kmols^{-1}$) for the model_malv +ve north

layer	Advection	
	Surf.	Layers
1		
2		
3		
4	0.37±5.5	0.37
5	-7.12±5.2	-7.50
6	-10.87±5.1	-3.74
7	7.24±4.9	18.11
8	8.36±4.7	1.12
9	8.71±4.6	0.35
10	5.07±4.5	-3.64
11	2.59±4.3	-2.48
12	1.16±4.1	-1.44
13	2.23±3.8	1.07
14	3.91±3.7	1.68
15	6.71±3.5	2.80
16	8.61±3.2	1.90
17	2.60±2.9	-6.00
18	4.01±2.6	1.40
19	3.50±2.2	-0.51
20	1.25±1.4	-2.25
21		-1.25
22		
23		

Table F.22: Dianeutral Interior Mass Flux Box I for model_malv ($\times 10^6 m^3 s^{-1}$). Positive : upwards flux across surface, convergence into layer. Negative : downward flux across surface, divergence from layer.

layer	Advection	
	Surf.	Layers
1		
2		
3		
4		
5		
6		
7	-0.16±1.2	-0.16
8	-1.40±1.7	-1.24
9	-0.14±2.0	1.26
10	-6.98±2.3	-6.84
11	-5.02±2.4	1.96
12	0.39±2.6	5.41
13	-2.91±2.6	-3.29
14	-3.56±2.7	-0.65
15	0.50±2.8	4.06
16	-1.44±2.8	-1.94
17	-0.53±2.7	0.90
18	-3.84±2.6	-3.31
19	3.03±2.3	6.87
20	13.66±2.0	10.63
21	10.30±1.3	-3.35
22		-10.30
23		

Table F.23: Dianeutral Interior Mass Flux Box II for model_malv ($\times 10^6 m^3 s^{-1}$). Positive : upwards flux across surface, convergence into layer. Negative : downward flux across surface, divergence from layer.

layer	Advection	
	Surf.	Layers
1		
2		
3	13.94±1.3	13.94
4	6.81±1.8	-7.13
5	11.71±2.1	4.90
6	8.47±2.3	-3.24
7	2.76±2.5	-5.71
8	1.51±2.6	-1.25
9	0.94±2.7	-0.57
10	-4.23±2.8	-5.16
11	-6.10±2.8	-1.87
12	-4.05±2.9	2.05
13	2.01±2.9	6.05
14	5.36±2.8	3.35
15	11.99±2.8	6.63
16	16.19±2.8	4.20
17	18.40±2.6	2.21
18	5.12±2.0	-13.28
19	10.04±1.3	4.91
20		-10.04
21		
22		
23		

Table F.24: Dianeutral Interior Mass Flux Box IV for model_malv ($\times 10^6 m^3 s^{-1}$). Positive : upwards flux across surface, convergence into layer. Negative : downward flux across surface, divergence from layer.

layer	Advection	
	Surf.	Layers
1		
2		
3		
4		
5		
6	-0.25±1.3	-0.25
7	2.11±1.7	2.36
8	3.23±2.0	1.12
9	-1.25±2.3	-4.48
10	-5.83±2.5	-4.58
11	-8.9±2.69	-3.16
12	-5.11±2.7	3.89
13	-19.64±2.8	-14.53
14	-13.82±2.8	5.81
15	-10.39±2.9	3.43
16	-17.74±2.9	-7.35
17	-24.11±2.9	-6.37
18	-14.38±2.7	9.73
19	-14.53±2.6	-0.15
20	-1.42±2.0	13.11
21	-0.53±1.3	0.89
22		0.53
23		

Table F.25: Dianeutral Interior Mass Flux Box V for model_malv ($\times 10^6 m^3 s^{-1}$). Positive : upwards flux across surface, convergence into layer. Negative : downward flux across surface, divergence from layer.

layer	Advection	
	Surf.	Layers
1		
2		
3		
4		
5		
6		
7	-0.85±1.3	-0.85
8	-3.53±1.8	-2.69
9	-4.09±2.3	-0.56
10	-2.46±2.6	1.63
11	-0.59±2.9	1.87
12	-11.18±3.2	-10.58
13	-14.17±3.5	-2.99
14	-15.74±3.7	-1.57
15	-12.36±3.9	3.38
16	-14.89±4.2	-2.54
17	-26.09±4.4	-11.20
18	-31.06±4.6	-4.97
19	-9.55±4.8	21.52
20	-1.56±5.0	7.99
21	0.35±5.3	1.90
22		-0.35
23		

Table F.26: Dianeutral Interior Mass Flux Box VI for model_malv ($\times 10^6 m^3 s^{-1}$). Positive : upwards flux across surface, convergence into layer. Negative : downward flux across surface, divergence from layer.

References

Andrews, J., M. Lawrence and C. S. Nilsson, 1980: Observations of the Tasman Front, *Journal of Physical Oceanography*, **10**, 1854–1869.

Banks, H., J. Bullister, S. Bacon and H. Bryden, 1995: The Deep Western Boundary Current at 17°S in the Pacific Ocean, *International WOCE Newsletter*, **19**, 3–5.

Barnier, B., L. Siefridt and P. Marchesiello, 1995: Thermal forcing for a Global Ocean Circulation using a three year climatology of ECMWF analysis, *Journal of Marine Systems*, **6**, 363–380.

Baumgartner, A., and E. Reichel, 1975: *The World water balance*, p. 179, Elsevier.

Bennett, A. F., 1978: Poleward Heat fluxes in the Southern Hemisphere, *Journal of Physical Oceanography*, **8**, 789–798.

———, 1983: The South Pacific including the East Australian Current, in *Eddies in Marine Science*, edited by A. R. Robinson, pp. 219–244, Springer-Verlag Berlin Heidelberg.

Bindoff, N. L., and J. A. Church, 1992: Warming of the water column in the south-west Pacific, *Nature*, **357**.

———, D. Nechaev, S. Rintoul, J. Schröter and M. Yaremchuk, 1997: Oceanic Fluxes between Tasmania and Antarctica, In preparation.

Boddem, J., and R. Schlitzer, 1995: Interocean exchange and meridional Mass and Heat fluxes in the South Atlantic, *Journal of Geophysical Research*, **100**, 15821–15834.

Budd, W. F., P. A. Reid and L. J. Minty, 1995: Antarctic Moisture Flux and net Accumulation from Global Atmospheric Analyses, *Annals of Glaciology*, **21**, 149–156.

Carmack, E. C., 1977: Water characteristics of the Southern Ocean south of the Polar Front, in *Voyage of Discovery*, edited by M. Angel, pp. 15–37, Pergamon Press.

———, 1990: Large scale Physical Oceanography of Polar Oceans, in *Polar Oceanography Part A: Physical Science*, edited by W. O. Smith Jr., Academic Press Inc. San Diego, California.

Chelton, D. B., Mestas-Nuñez and F. J. Freilich, 1990: Global wind stress and Sverdrup circulation from the Seasat scatterometer, *Journal of Physical Oceanography*, **20**, 1175–1205.

Church, J., G. Cresswell and J. S. Godfrey, 1989: The Leeuwin Current, in *Poleward Flows along Eastern Ocean Boundaries*, edited by S. Neshyba, C. Mooers, R. Smith, and R. Barber, pp. 230–254, Springer-Verlag, New York.

Coachman, L., and K. Aagaard, 1988: Transport through Bering Strait: Anuual and interannual variability, *Journal of Geophysical Research*, **93**, 15535–15539.

Cresswell, G. R., A. Frische, J. Peterson and D. Quadfasel, 1993: Circulation in the Timor Sea, *Journal of Geophysical Research*, **98**, 14379–14389.

da Silva, A. M., C. C. Young and S. Levitus, 1994: Atlas of Surface Marine Data 1994: Volume 1 Algorithms and Procedures, *Tech. Rep. 6*, , NOAA, NESDIS.

Deacon, G. E. R., 1937: *The hydrology of the Southern Ocean*, vol. 15, pp. 3–122, Cambridge University Press.

———, 1982: Physical and biological zonation in the Southern Ocean, *Deep-Sea Research*, **29**, 1–15.

DeMaster, D. J., 1981: The supply and accumulation of silica in the marine environment, *Geochimica et Comsochimica Acta*, **45**, 1715–1732.

Dickson, R. R., and J. Brown, 1994: The production of North Atlantic Deep Water: Sources, rates and pathways., *Journal of Geophysical Research*, **99**, 12319–12341.

Edwards, R. J., and W. J. Emery, 1982: Australasian Southern Ocean frontal structure during summer 1976-77, *Australian Journal of Marine Freshwater Research*, **33**, 3–22.

Emery, W. J., 1977: Antarctic Polar Front Zone from Australia to the Drake Passage, *Journal of Physical Oceanography*, **7**, 811–822.

Fahrbach, E., G. Rohardt, M. Schröder and V. Strass, 1994: Transport and Structure of the Weddell Sea, *Annales Geophysics*, **12**, 840–855.

Fieux, M., P. Andrie, P. Delecluse, A. G. Ilahude, A. Kartavtse, F. Mantisi, R. Molcard and J. C. Swallow, 1994: Measurements within the Pacific-Indian oceans throughflow region, *Deep-Sea Research*, **41**, 101–130.

———, R. Molcard and A. G. Ilahude, 1996: Geostrophic transport of the Pacific-Indian oceans throughflow, *Journal of Geophysical Research*, **101**, 12421–12432.

Fine, R. A., 1993: Circulation of Antarctic Intermediate Water in the South Indian Ocean, *Deep-Sea Research*, **40**, 2021–2042.

———, M. J. Warner and R. F. Weiss, 1988: Water mass modification at the Agulhas Retroflection: chlorofluoromethane studies, *Deep-Sea Research*, **35**, 311–332.

Foster, T. D., and J. H. Middelton, 1980: Bottom water formation in the western Weddell Sea, *Deep-Sea Research*, **26**, 743–762.

FRAM, Group, 1991: An eddy-resolving model of the Southern Ocean, *EOS Transactions, American Geophysical Union*, **72**, 174–175.

Fu, L.-L., 1981: The general circulation and meridional heat transports of the subtropical South Atlantic determined by inverse methods, *Journal of Physical Oceanography*, **11**, 1171–1193.

———, 1986: Mass, Heat and Freshwater fluxes in the South Indian Ocean, *Journal of Physical Oceanography*, **16**, 1683–1693.

Garzoli, S. L., and G. Garraffo, 1989: Transport, frontal motions and eddies at the Brazil-Malvinas Confluence, *Deep-Sea Research*, **36**, 681–703.

Georgi, D. T., 1979: Modal properties of Antarctic Intermediate Water in the South East Pacific and South Atlantic, *Journal of Physical Oceanography*, **9**, 456–468.

———, 1981: On the relationship between the large-scale property variations and fine structure in the Circumpolar Deep Water, *Deep-Sea Research*, **86**, 6556–6566.

Georgi, D. T., and J. M. Toole, 1982: The Antarctic Circumpolar Current and the Oceanic Heat and Freshwater budgets, *Journal of Marine Research*, **40**, 183–197.

Gill, A. E., 1973: Circulation and Bottom Water production in the Weddell Sea, *Deep-Sea Research*, **20**, 111–140.

Godfrey, J. S., and K. Ridgway, 1985: The large-scale environment of the poleward-flowing Leeuwin Current, Western Australia: Longshore Steric Height gradients, wind stresses and geostrophic flow, *Journal of Physical Oceanography*, **15**, 481–495.

Gordon, A. L., 1971: Antarctic Polar Front Zone, in *Antarctic Oceanology I*, edited by J. L. Reid, pp. 205–221, American Geophysical Union , Washington D.C.

———, 1972: Oceanography of Antarctic Waters, in *Antarctic Oceanology I*, vol. 19 of *Antarctic Research Series*, edited by J. L. Reid, pp. 71–78, American Geophysical Union, Washington D.C.

Gordon, A. L., 1975: An Antarctic Oceanographic section along 170°E, *Deep-Sea Research*, **22**, 357–377.

———, 1981a: South Atlantic thermocline ventilation, *Deep-Sea Research*, **28**, 1239–1264.

Gordon, A. L., 1986: Interocean Exchange of Thermocline Water, *Journal of Geophysical Research*, **91**, 5037–5046.

———, 1989: Brazil-Malvinas Confluence - 1984, *Deep-Sea Research*, **28**, 1239–1264.

Gordon, A. L., and C. L. Greengrove, 1986: Geostrophic circulation of the Brazil-Falkland confluence, *Deep-Sea Research*, **33**, 573–585.

———, and W. F. Haxby, 1990: Agulhas Eddies invade the South Atlantic: Evidence from Geosat altimeter and ship-board conductivity-temperature-depth survey, *Journal of Geophysical Research*, **95**, 3117–3125.

Gordon, A. L., and B. A. Huber, 1990: Southern Ocean winter Mixed Layer, *Journal of Geophysical Research*, **95**, 11655–11672.

———, D. G. Marinson and H. W. Taylor, 1981: The wind-driven circulation in the Weddell-Enderby Basin, *Deep-Sea Research*, **28**, 151–163.

Gordon, A. L., and P. Tchernia, 1972: Waters of the Continental margin off the Adélie Coast Antarctic, in *Antarctic Oceanology II: The Australian-New Zealand Sector*, vol. 19 of *Antarctic Research Series*, edited by D. E. Hayes, pp. 59–69, American Geophysical Union, Washington D.C.

Gordon, A., 1981b: Seasonality of Southern Ocean Sea Ice, *Journal of Geophysical Research*, **86**, 4193–4197.

Gordon, A, L., R. F. Weiss, W. M. Smethie, Jr. and M. J. Warner, 1992: Thermocline and Intermediate Water Communication between the South Atlantic and Indian Oceans, *Journal of Geophysical Research*, **97**, 7223–7240.

Gründlingh, M. L., 1980: On the volume transport of the Agulhas Current, *Deep-Sea Research*, **27**, 557–563.

———, R. A. Carter and R. C. Stanton, 1991: Circulation and water properties of the southwest Indian Ocean Spring 1987, *Progress in Oceanography*, **28**, 305–342.

Hamon, B. V., 1965: The East Australian Current 1960-1964, *Deep-Sea Research*, **12**, 899–921.

Harris, J. L., 1996: Southern Ocean circulation from Hydrographic data: A Finite Difference Inverse Model, Ph.D. thesis, Institute of Antarctic and Southern Ocean Studies, University of Tasmania.

Harris, T. F., R. Legeckis and D. van Forrest, 1978: Satellite infra-red images in the Agulhas current system, *Deep-Sea Research*, **25**, 543–548.

Hastenrath, S., 1982: On Meridional Heat transport in the World Ocean, *Journal of Physical Oceanography*, **12**, 922–927.

Hellerman, S., and M. Rosenstein, 1983: Normal Monthly Wind Stress over the World Ocean with error estimates, *Journal of Physical Oceanography*, **13**, 1093–1104.

Hofmann, E. E., and T. Whitworth, III., 1985: A synoptic description of the flow at Drake Passage from Year-Long Measurements, *Journal of Geophysical Research*, **90**, 7177–7187.

Hogg, N. G., P. Biscaye, W. Gardner and W. J. Schmitz, Jr., 1982: On the transport and modification of Antarctic Bottom Water in the Vema Channel, *Journal of Marine Research*, **40**, 231–263.

Hogg, N., 1987: A least-squares fit of the advective-diffusive equations to Levitus atlas data, *Journal of Marine Research*, **45**, 347–375.

Hsiung, J., 1985: Estimates of Global Meridional heat transports, *Journal of Physical Oceanography*, **15**, 1405–1413.

Ikeda, Y., G. Seidler and M. Zwiery, 1989: On the variability of Southern Ocean front location between Southern Brazil and the Antarctic Peninsula, *Journal of Geophysical Research*, **94**, 4757–4762.

Jackett, D., and T. McDougall, 1997: A Neutral Density variable for the Worlds Oceans, *Journal of Physical Oceanography*, **27**, 237–263.

Jacobs, S., 1986: Injecting Ice-Shelf Water and Air into the Deep Antarctic Ocean, *Nature*, **321**, 196–197.

Jacobs, S. S., R. G. Fairbanks and Y. Horibe, 1985: Origin and evolution of water masses near the Antarctic continental margin, in *Oceanology of the Antarctic Continental Shelf*, vol. 43 of *Antarctic Research Series*, edited by S. S. Jacobs, pp. 59–85, American Geophysical Union, Washington D.C.

Johnson, G. C., and J. M. Toole, 1993: Flow of deep and bottom water in the Pacific at 10 ° N, *Deep-Sea Research*, **40**, 371–394.

Keith, D. W., 1995: Meridional energy transports: uncertainty in zonal means, *Tellus*, **47**, 30–44.

Killworth, P., and G. Bigg, 1988: An intercomparison of inverse methods using an eddy resolving general circulation model, *Journal of Physical Oceanography*, **18**, 987–1008.

Kort, V. G., 1966: Frontal Zones of the Southern Ocean, in *Symposium on Antarctic Oceanology*, W.Heffer and Son Ltd, Cambridge.

Lanczos, C., 1961: *Linear Differential Operators*, p. 564, Van Nostrand.

Lawson, C., and R. Hanson, 1974: *Solving Least Squares Problem*, p. 340, Prentice-Hall, Inc.

Levitus, S., 1982: Climatological Atlas of the World Ocean, *Tech. rep.*, p. 173, NOAA.

———, and T. Boyer, 1994: World Ocean Atlas 1994, *Tech. rep.*, p. 201, NOAA.

Lutjeharms, J. R. E., N. D. Bang and C. P. Duncan, 1981: Characteristics of the current east and south of Madagascar, *Deep-Sea Research*, **28**, 879–899.

———, and R. C. Van Ballegooyen, 1988: The Retroflection of the Agulhas Current, *Journal of Physical Oceanography*, **18**, 1570–1583.

Macdonald, A. M., 1993: Property fluxes at 30°S and their Implication for the Pacific-Indian throughflow and the Global Heat Budget, *Journal of Geophysical Research*, **98**, 6851–6868.

———, and C. Wunsch, 1996: An estimate of Global Ocean circulation and Heat fluxes, *Nature*, **382**, 436–439.

Macdonald, A., 1991: Mass,Heat,Oxygen and Nutrient fluxes at 30°S and their implication for the Pacific-Indian through flow and the Global Heat budget, Master's thesis, MIT/WHOI.

———, 1995: Oceanic fluxes of Mass, Heat and Freshwater: A Global estimate and perspective, Ph.D. thesis, MIT/WHOI.

Mantyla, A. W., and J. L. Reid, 1995: On the origins of deep and bottom waters of the Indian Ocean, *Journal of Geophysical Research*, **100**, 2417–2439.

McCartney, M. S., 1977: Subantarctic Mode Water, *Deep-Sea Research*, **24**, 103–119.

———, 1993: Crossing of the Equator by the Deep Western Boundary Current in the western Atlantic Ocean, *Journal of Physical Oceanography*, **23**, 1953–1974.

McCartney, M. S., and R. A. Curry, 1993: Transequatorial flow of Antarctic Bottom Water in the western Atlantic Ocean: Abyssal Geostrophy at the Equator, *Journal of Physical Oceanography*, **23**, 1264–1276.

McDougall, T., 1987a: Neutral Surfaces, *Journal of Physical Oceanography*, **17**, 1950–1964.

———, 1987b: Neutral Surfaces in the ocean: Implications for modelling, *Geophysical Research Letters*, **14**(8), 797–800.

McDougall, T., 1991: Parameterising mixing in inverse models, in *Dynamics of Oceanic Internal gravity Waves*, edited by D. Muller, and D. Henderson, Sixth 'Aha Hulika'a Hawaiian Winter Workshop, pp. 355–386, University of Hawaii at Monoa.

McIntosh, P., and S. Rintoul, 1997: Do Box Inverse Models Work?, *Journal of Physical Oceanography*, **27**, 291–208.

Menke, W., 1984: *Geophysical Data Analysis: discrete Inverse Theory*, p. 260, Academic Press.

Mestas-Nuñez, A. M., D. B. Chelton, M. H. Freilich and J. G. Richman, 1994: An Evaluation of ECMWF-based climatological wind stress fields, *Journal of Physical Oceanography*, **24**, 1532–1549.

Metzl, N., B. Moore and A. Poisson, 1990: Resolving the intermediate and deep advective flows in the Indian Ocean by using temperature, salinity, oxygen and phosphate data: the interplay of biogeochemical and geophysical tracers, in *Geochemical Variability in the Oceans, Ice and Sediments*, vol. 89 of *Palaogeography, Palaeoclimatology, Palaeoecology (Global and Planetary Change Section)*, edited by L. P. Labeyrie, and C. Jeandel, pp. 81–111, Elsevier Science.

Meyers, G., R. J. Bailey and A. P. Worby, 1995: Geostrophic transport of Indonesian throughflow, *Deep-Sea Research*, **42**, 1163–1174.

Molinelli, E. T., 1981: The Antarctic influence on Antarctic Intermediate Water., *Journal of Marine Research*, **39**, 267–293.

Muench, R. D., 1990: Mesoscale phenomena in the Polar Oceans, in *Polar Oceanography Part A: Physical Science*, edited by W. O. Smith Jr., pp. 223–285, Academic Press Inc. San Diego, California.

Nelson, D. M., P. Tréguer, M. A. Brzezinski, A. Leynaert and B. Qu'eguiner, 1995: Production and dissolution of biogenic silica in the ocean: Revised global estimates, comparison with regional data and relationship to biogenic sedimentation, *Global Biogeochemical Cycle*, **9**, 359–372.

Niiler, P. P., and W. S. Richardson, 1973: Seasonal variability of the Florida Current, *Journal of Marine Research*, **31**, 144–167.

Nowlin, Jr., W. D., and M. Clifford, 1982: The kinematic and thermohaline zonation of the Antarctic Circumpolar Current at Drake Passage, *Journal of Marine Research*, **24**, 481–507.

———, and J. M. Klinck, 1986: The Physics of the Antarctic Circumpolar Current, *Review of Geophysics*, **24**, 469–491.

Olbers, D., 1991: Diffusion parametrizations for the climatological circulation of the North Atlantic and the Southern Ocean, in *Dynamics of Oceanic Internal gravity Waves*, edited by D. Muller, and D. Henderson, Sixth 'Aha Hulika'a Hawaiian Winter Workshop, pp. 181–203, University of Hawaii at Monoa.

Orsi, A. H., W. D. Nowlin, Jr. and T. Whitworth, III, 1993: On the circulation and stratification of the Weddell Gyre., *Deep-Sea Research*, **40**, 169–203.

Parker, R., 1977: Understanding Inverse Theory, *Annual Review Earth and Planetary Science*, **5**, 35–64.

Patterson, S. L., and T. Whitworth, III., 1990: Physical Oceanography, in *Antarctic Sector of the Pacific*, edited by G. P. Glasby, pp. 55–93, Elevier Science Publishing , Amsterdam.

Peterson, R. G., and ———, 1989: The Subantarctic and Polar fronts in relation to deep water masses through the southwestern Atlantic, *Journal of Geophysical Research*, **94**, 10817–10838.

Peterson, R., 1992: The boundary currents in the western Argentine basin, *Deep-Sea Research*, **39**, 623–644.

———, and L. Stramma, 1991: Upper-level circulation in the South Atlantic Ocean, *Progress in Oceanography*, **26**, 1–73.

Piola, A. R., and A. A. Bianchi, 1990: Geostrophic mass transport at the Brazil-Malvinas Confluence, *EOS*, **71**(17), 542.

———, and D. T. Georgi, 1982: Circumpolar properties of Antarctic Intermediate Water and Subantarctic Mode Water., *Deep-Sea Research*, **29**, 687–711.

Provost, C., S. Gana, V. Garçon, K. Maamaatuaiahutapu and M. England, 1995: Hydrographic conditions in the Brazil-Malvinas Confluence during austral summer 1990, *Journal of Geophysical Research*, **100**, 10655–10678.

Read, J. F., and R. T. Pollard, 1993: Structure and Transport of the Antarctic Circumpolar Current and Agulhas Return Current at 40°S, *Journal of Geophysical Research*, **98**, 12281–12295.

Reid, J. L., 1989: On the total geostrophic circulation of the South Atlantic Ocean: Flow patterns, tracers and transports, *Progress in Oceanography*, **23**, 149–244.

———, W. D. Nowlin, Jr. and W. C. Patzert, 1977: On the Characteristics and Circulation of the Southwestern Atlantic Ocean, *Journal of Geophysical Research*, **7**, 62–91.

Ridgway, K. R., and J. S. Godfrey, 1994: Mass and heat budgets in the East Australian current: A direct approach, *Journal of Geophysical Research*, **99**, 3231–3248.

Rintoul, S. R., 1997: On the origin and influence of the Antarctic Bottom Water of the Southeast Indian Ocean , in *Oceanology of the Antarctic Continental Margin*, vol. Antarctic Research Series, edited by S. Jacobs, American geophysical Union, submitted.

Rintoul, S., 1988: Mass, Heat, Salt and Nurient fluxes in the Atlantic Ocean determined by inverse methods, Ph.D. thesis, MIT/WHOI.

———, 1991: South Atlantic interbasin exchange., *Journal of Geophysical Research*, **96**, 2675–2592.

Rintoul, S., and C. Wunsch, 1990: Mass, Heat, Salt and Nurient fluxes and budgets in the North Atlantic Ocean, *Deep-Sea Research*, **38**, 355–377.

Robbins, P. E., and J. M. Toole, 1997: The dissolved silica budget as a constraint on the meridional overturning circulation of the Indian Ocean, *Deep-Sea Research*, **44**, 879:906.

Roden, G. I., 1986: Thermohaline fronts and baroclinic flow in the Argentine Basin during the austral spring of 1984, *Journal of Geophysical Research*, **91**, 5075–5093.

Roemmich, D., 1980: The application of Inverse methods to problems of Ocean Circulation, Ph.D. thesis, MIT/WHOI.

Roether, W., R. Schlitzer, A. Putzka, P. Beining, K. Bulsiewicz, G. Rohardt and F. Delahoyde, 1993: A chlorofluoromethane and hydrographic section across Drake Passage: Deep water Ventilation and Meridional property transport., *Journal of Geophysical Research*, **98**, 14423–14435.

Sætre, R., and A. J. da Silva, 1984: The circulation of the Mozambique Channel, *Deep-Sea Research*, **31**, 485–508.

Saunders, P. M., and B. R. King, 1995: Oceanic Fluxes on the WOCE A11 Section, *Journal of Physical Oceanography*, **25**, 1942–1957.

Savchenko, V. G., W. G. Emery and O. A. Vladimirov, 1978: A cyclonic eddy in the Antarctic Circumpolar Current south of Australia, *Journal of Physical Oceanography*, **8**, 825–837.

Schmitt, R. W., P. S. Bogden and C. E. Dorman, 1989: Evaportaion minus Precipitation and density fluxes for the North Atlantic, *Journal of Physical Oceanography*, **19**, 1208–1221.

Schmitz, Jr., W. J., 1995: On the Interbasisn-Scale Thermohaline Circulation, *Reviews of Geophysics*, **33**, 151–173.

———, 1996a: On the World Ocean Circulation. Volume I: Some Global features/North Atlantic Circulation, *Tech. Rep. WHOI-96-03*, p. 140, Woods Hole Oceanographic Institute.

Schmitz, Jr., W. J., 1996b: On the World Ocean Circulation. Volume II: The Pacific and Indian Oceans/A global update, *Tech. Rep. WHOI-96-08*, p. 237, Woods Hole Oceanographic Institute.

Schott, F., M. Fieux, J. Swallow and R. Zantopp, 1988: The boundary currents east and north of Madagascar 2. Direct measurements and model comparisons, *Journal of Geophysical Research*, **93**, 4963–4774.

Sievers, H. A., and W. J. Emery, 1978: Variability of the Antarctic Polar Frontal Zone in the Drake Passage - Summer 1976-1977, *Journal of Geophysical Research*, **83**, 3010–3022.

———, and W. D. Nowlin, Jr., 1984: The Stratification and water masses at Drake Passage, *Journal of Geophysical Research*, **89**, 10489–10514.

Sievers, H. A., and ———, 1988: Upper Ocean Characteristics in Drake Passage and adjoining areas of the Southern Ocean 39°W - 95°W, in *Antarctic Ocean and Resources Variability*, edited by D. Sahrhage, Springer-Verlag, Berlin Heidelberg.

Smith, R. L., A. Huyer, J. S. Godfrey and J. A. Church, 1991: The Leeuwin Current off Western Australia 1986 - 1987, *Journal of Physical Oceanography*, **21**, 323–345.

Speer, K., and E. Tziperman, 1992: Rates of Water Mass Formation in the North Atlantic Ocean, *Journal of Physical Oceanography*, **22**, 93–104.

Speer, K. G., and W. Zenk, 1993: The flow of Antarctic Bottom Water into the Brazil Basin, *Journal of Physical Oceanography*, **23**, 2667–2682.

Stommel, H., and G. Veronis, 1981: Variational inverse method for study of oceanic circulation, *Deep-Sea Research*, **28**, 1147–1160.

Stramma, L., 1992: The South Indian Ocean Current, *Journal of Physical Oceanography*, **22**, 421–430.

———, Y. Ikeda and R. G. Peterson, 1990: Geostrophic transport in the Brazil Current region north of 20°s, *Deep-Sea Research*, **37**, 1875–1886.

Stramma, L., and R. G. Peterson, 1990: The South Atlantic Current, *Journal of Physical Oceanography*, **20**, 846–859.

———, ——— and M. Tomczak, 1995: The South Pacific Current, *Journal of Physical Oceanography*, **25**, 77–91.

Suga, T., and L. D. Talley, 1995: Antarctic Intermediate Water circulation in the tropical and subtropical South Atlantic, *Journal of Geophysical Research*, **100**, 13441–13453.

Sverdrup, H. U., M. W. Johnson and R. H. Fleming, 1946: *The Oceans, Their Physics, Chemistry and General Biology*, p. 1087, Prentice-Hall, Inc. New York.

Swallow, J., M. Fieux and F. Schott, 1988: The boundary currents east and north of Madagascar 1. Geostrophic currents and transports, *Journal of Geophysical Research*, **93**, 4951–4962.

Tarantola, A., 1987: *Inverse Problem Theory. Methods for data fitting and model parameter estimation*, p. 613, Elsevier Science Publishers.

Taylor, H., A. L. Gordon and E. Molinelli, 1978: Climate characteristics of the Antarctic Polar Front Zone, *Journal of Geophysical Research*, **83**, 4572–4578.

Tchernia, P., 1980: *Descriptive Physical Oceanography*, p. 253, Pergamon Press, Oxford England.

Toole, J. M., and M. E. Raymer, 1985: Heat and fresh water budgets of the Indian Ocean - revisited, *Deep-Sea Research*, **32**, 917–928.

———, and B. A. Warren, 1993: A hydrographic section across the Subtropical South Indian Ocean, *Deep-Sea Research*, **40**, 1973–2019.

Trèguer, P., D. M. Nelson, A. J. Van Bennekorn, D. J. DeMaster, A. Leynaert and B. Quèguiner, 1995: The Silica balance in the world ocean: A reestimate, *Science*, **268**, 375–379.

Trenberth, K. E., J. Olson and W. G. Large, 1990: The mean annual cycle in Global Ocean wind stress, *Journal of Physical Oceanography*, **20**, 1742–1760.

Tziperman, E., 1986: On the role of Interior Mixing and Air-Sea fluxes in determining the stratification and circulation of the Oceans, *Journal of Physical Oceanography*, **16**, 680–693.

Warren, B., 1981a: Transindian hydrographic section at Lat. 18 S : Property distribution and circulation in the South Indian Ocean, *Deep-Sea Research*, **28**, 759–788.

Warren, B. A., 1981b: Deep Circulation of the World Ocean, in *Evolution of Physical Oceanography*, edited by B. A. Warren, and C. Wunsch, pp. 6–41, MIT Press,

Cambridge Massachusetts.

———, 1982: The deep water of the Central Indian Basin, *Journal of Marine Research*, **40**, 823–860.

Warren, B. A., and K. G. Speer, 1991: Deep Circulation in the eastern South Atlantic Ocean, *Deep-Sea Research*, **38**, S281–S322.

Whitworth, III., T., 1980: Zonation and geostrophic flow of the Antarctic Circumpolar Current at Drake Passage, *Deep-Sea Research*, **27**, 497–507.

———, and W. D. Nowlin, Jr., 1987: Water masses and currents of the Southern Ocean at the Greenwich Meridian, *Journal of Geophysical Research*, **92**, 6462–6476.

Whitworth, III., T., ———, R. D. Pillsbury and R. F. Weiss, 1991: Observations of the Antarctic Circumpolar Current and deep boundary current in the Southwest Atlantic, *Journal of Geophysical Research*, **96**, 15105–15118.

———, B. A. Warren, W. D. Nowlin, Jr., R. D. Pillsbury and M. I. Moore, 1996: On the deep western-boundary current in the Southwest Pacific Basin, *Progress in Oceanography*, submitted.

Wijffels, S. E., R. W. Schmitt, H. L. Bryden and A. Stigebrandt, 1992: Transport of Freshwater by the Oceans, *Journal of Physical Oceanography*, **22**, 155–162.

Wijffels, S., 1993: Exchanges between Hemispheres and Gyres: A direct approach to the Mean Circulation of the Equatorial Pacific, Ph.D. thesis, MIT/WHOI.

Wooster, W. S.and Gilmartin, M., 1961: The Peru-Chile undercurrent, *Journal of Marine Research*, **19**, 97–122.

Wunsch, C., 1978: The North Atlantic General Circulation West of 50W Determined by Inverse Methods, *Reviews of Geophysics and Space Physics*, **16**(4), 583–620.

———, 1982: Towards the General Circulation of the North Atlantic Ocean, *Progress in Oceanography*, **11**, 1–59.

Wunsch, C., 1984: An eclectic Atlantic Ocean circulation model I The meridonal flux of heat, *Journal of Physical Oceanography*, **14**, 1712–1732.

———, 1996: *The Ocean Circulation Inverse Problem*, p. 441, Cambridge University Press.

Wunsch, C., D. Hu and B. Grant, 1983: Mass, Heat Salt and Nutrient fluxes in the South Pacific Ocean, *Journal of Physical Oceanography*, **13**, 725–753.

Wyrtki, K., 1962a: Geopotential topographies and associated circulation in the western South Pacific Ocean, *Australian Journal of Marine and Freshwater Research*, **13**, 89–105.

———, 1962b: The subsurface Water Masses in the Western South Pacific Ocean, *Australian Journal of Marine and Freshwater Research*, **13**, 18–47.

Wyrtki, K., 1971: *Ocean Atlas of the International Indian Ocean Experiment*, p. 531, National Science Foundation, Washington D.C.